

Biological Effects of Intense Terahertz Pulses

by

Cameron M. Hough

A thesis submitted in partial fulfillment of the requirements for the degree of

Doctor of Philosophy

in

Medical Physics

Department of Oncology
University of Alberta

© Cameron M. Hough, 2021

Abstract

Terahertz (THz) radiation is a non-ionizing form of electromagnetic (EM) energy that occupies a broad frequency region at the interface between conventional microwave and infrared bands. The strong coupling between THz excitations and natural oscillatory dynamics in biological systems has motivated the development of novel biomedical imaging and spectroscopy technologies, with unique advantages for improved diagnostic power for diseases such as cancer. However, while THz radiation is non-ionizing, and therefore considered a non-destructive probe, the coupling to vibrational or rotational modes implies that external excitation with intense pulses of THz energy could non-thermally dysregulate structural dynamics of important structures (e.g., proteins, nucleic acids, or membrane structures) such that the associated function is compromised. These may then induce biological effects via a non-thermal interaction mechanism that is unique to the THz band, and therefore must be characterized to establish safe exposure levels for existing technologies, or to develop potentially novel clinical technologies. Historically, the study of biological systems with THz radiation has been hindered by high attenuation in aqueous media, and the lack of available sources that operate efficiently at THz frequencies. However, recent developments in laser-based source technologies have dramatically increased THz generation capabilities. This has led to a resurgence of research interest in biological systems and biomedical applications for this under-explored regime of the EM spectrum.

For this thesis project, a system for THz exposure and analysis of biological systems is developed, and exposure studies are performed at the molecular, cellular, and tissue scale of biological organization. The radiation source utilizes nonlinear properties of crystal structures to generate and detect highly intense, picosecond-duration pulses of EM energy via optical rectification in lithium niobate and electro-optic sampling in gallium phosphide, respectively. Each

single-cycle pulse has a peak electric field strength of up to 640 kV/cm, a broad frequency spectrum peaked at roughly 1.0 ± 0.8 THz, and excites the associated dynamics in exposed samples under study. The pulsed radiation beam is delivered to an environmentally-controlled sample housing. Molecular-level experiments investigate structural changes to polymerized microtubules in solution in real-time via fluorescence microscopy. Cellular-level experiments characterize transient and long-term changes of membrane permeability in monolayer cell cultures induced by THz exposure. At the tissue level, the effects on 3D human skin models are investigated by measuring global differential gene expression for varying THz intensities. These data are used to determine biological processes and molecular signaling pathways that are likely to be dysregulated by THz exposures, particularly focusing on dysregulation of cancer-related processes.

Intense THz pulses are found to induce significant non-thermal effects at all investigated levels of biological organization. At the molecular scale, disassembly of polymerized microtubules is observed to occur within minutes of an applied train of THz pulses, and this depends on the intensity and frequency content of the applied pulse. At the cellular level, detectable increases of membrane permeability are observed in human and rat cancer cell lines. At the tissue-level, THz exposure induces a large differential gene expression response (1088 genes downregulated, 593 genes upregulated). Processes predicted to be most significantly dysregulated are related to epidermal differentiation, cellular binding/adhesion, and cytokine activity. Several pathways that are commonly implicated in human cancers (e.g., Ras signaling and Calcium signaling) are predicted to be suppressed in an intensity-dependent fashion, and these are predominantly due to a subset of only 42 genes dominantly responsible for THz-induced dysregulation of cancer-related processes. Importantly, the dysregulations observed at the tissue scale are directly related to the structural effects observed in microtubule and cell samples.

As innovation for applications of THz technologies continues to progress, human exposure levels can be expected to increase. Current technologies intended for human exposure (e.g.,

diagnostic imaging or security screening) are likely well-below the required intensity to induce significant biological or health effects. However, this thesis shows that intense THz pulses with high peak electric fields are sufficient to induce significant non-thermal biological effects at multiple scales of biological organization. Conclusions from these investigations are discussed in the context of potential clinical therapeutic applications of THz radiation, with the goal of targeted inhibition of pro-mitotic activity in diseased tissue.

Preface

This thesis work reports original research investigations by me, Cameron M. Hough. The project was jointly supervised by Dr. F. A. Hegmann (Condensed Matter, Department of Physics) and Dr. B. J. Warkentin (Medical Physics, Cross Cancer Institute (CCI), Department of Oncology) at the University of Alberta (U of A). Significant support, guidance, and assistance from many other experts, collaborators, peers, and trainees made this project possible.

The research conducted was part of the development of experimentation of biological systems with terahertz radiation in the Ultrafast Nanotools laboratory, led by F. A. Hegmann. The original work was conceptualized and initiated by Dr. L. V. Titova and F. A. Hegmann, in collaboration with Dr. O. V. Kovalchuk at the University of Lethbridge (U of L).

The project of designing and constructing the terahertz radiation source, fluorescent microscope, and biological exposure chamber described in Chapters 3, 4, and 5 was led by me, including: selecting, ordering, and installing terahertz source and microscope components, collecting data and performing extensive characterization of terahertz pulse and beam parameters, designing novel analysis software, and designing the temperature-regulated sample holder. Terahertz source construction was in collaboration with D. N. Purschke, with assistance by Dr. M. Narreto and C. Huang. The multi-mode operation of the terahertz source is due to implementing a rotating off-axis parabolic mirror on a programmable stage, suggested by F. A. Hegmann. F. A. Hegmann also assisted in data collection and interpretation, as well as project conceptualization. P. Nguyen performed the COMSOL simulations presented in Chapter 5 for characterization of near-field enhancement for exposures with sharp conductive tips. B. Shi, G. Popowich, and J. Chaulk assisted with AutoCAD designs, machining, and general technical support.

The exposure experiments presented in Chapters 7, 8, and 9 were led by me, in collaboration with both internal and external laboratories. Fluorescently-labelled microtubule samples were provided by Dr. J. A. Tuszynski from the U of A. A. P. Kalra and C. Bell provided training for sample preparation, and assisted with some exposures. Cell samples were provided by Dr. M. Kulka (National Research Council, NRC) and Dr. R. Mirzayans (CCI). Cellular samples were grown, maintained, and passaged in collaboration with Drs. N. A. Puga, B. Duguay, S. Willows, and S. Ayyalasomayajula in the Kulka lab, and B. Andrais in the Mirzayans lab. Some microscopy was performed at the CCI imaging facility, led by Dr. X. Sun, who also provided assistance for designing the fluorescence microscope for the terahertz exposure system. For tissue samples,

measurements of gene expression were overseen by O. V. Kovalchuk, R. Rodriguez-Juarez, and R. Rodriguez-Juarez, and calculation of preliminary gene expression statistics were provided by A. Golubov and I. Ilnytsky (U of L). C. Huang and P. J. Oliva assisted in exposure experiments and data acquisition. Exposure studies investigating frequency-dependence using terahertz bandpass filters were suggested by F. A. Hegmann.

The material in Chapter 7 is published as two articles: C. M. Hough, D. N. Purschke, C. Huang, L. V. Titova, O. V. Kovalchuk, B. J. Warkentin, and F. A. Hegmann, “Topology-Based Prediction of Pathway Dysregulation Induced by Intense Terahertz Pulses in Human Skin Tissue Models,” *Journal of Infrared, Millimeter, and Terahertz Waves*. vol. 39, pp. 887 – 898, 2018, and C. M. Hough, D. N. Purschke, C. Huang, L. V. Titova, O. V. Kovalchuk, B. J. Warkentin, and F. A. Hegmann, “Intense terahertz pulses inhibit *Ras signaling* and other cancer-associated signaling pathways in human skin tissue models,” *Journal of Physics: Photonics*. vol. 3, no. 034004, pp. 1 – 14, 2021. I was responsible for leading the project, including experimental design, sample preparation, performing terahertz exposures, transporting samples to U of L, measuring gene expression (in collaboration with the Kovalchuk lab), analyzing the data (including novel statistical analysis methods for target gene identification), and composing the manuscripts. L. V. Titova, O. V. Kovalchuk, and F. A. Hegmann conceived of the study, and provided valuable discussions and feedback. B. J. Warkentin and F. A. Hegmann provided overall project guidance and oversight.

An altered version of Chapter 9 has been accepted for publication: C. M. Hough, D. N. Purschke, C. Bell, A. P. Kalra, P. J. Oliva, C. Huang, J. A. Tuszynski, B. J. Warkentin, and F. A. Hegmann, “Disassembly of microtubules by intense terahertz pulses,” Accepted by *Biomedical Optics Express*, August 2021. I was similarly responsible for leading the project, including experimental design, preparing polymerized microtubules, performing terahertz exposures, collecting image data, analyzing data, and composing the manuscript. A. P. Kalra and C. Bell assisted in sample processing, and P. J. Oliva assisted in exposures. F. A. Hegmann, B. J. Warkentin, and J. A. Tuszynski provided project guidance and oversight, as well as significant insight for data interpretation and presentation.

Chapters 1 and 2, containing introductory and review material, Chapter 6, containing a novel framework for coherent terahertz dosimetry, and the concluding Chapter 10, were written independently. B. J. Warkentin and F. A. Hegmann provided thorough feedback and editorial suggestions of the entire thesis.

Results from this research were selected for several oral, keynote, and plenary presentations, including six international terahertz conferences and workshops (IRMMW-THz 2017 – 2020, 8th THz-Bio Workshop 2017, and 6th SICAST 2017) and one Canadian medical physics conference (COMP 2019). These have been published in the corresponding conference proceedings.

Peer-reviewed journal publications:

1. C. M. Hough, D. N. Purschke, C. Bell, A. P. Kalra, P. J. Oliva, C. Huang, J. A. Tuszynski, B. J. Warkentin, & F. A. Hegmann. Microtubule disassembly by intense terahertz pulses. Accepted by *Biomedical Optics Express*. August 2021.
2. C. M. Hough, D. N. Purschke, C. Huang, L. V. Titova, O. V. Kovalchuk, B. J. Warkentin, & F. A. Hegmann. Intense Terahertz Pulses Inhibit Ras Signaling and Other Cancer-associated Signaling Pathways in Human Skin Tissue Models. *Journal of Physics: Photonics*. vol. 3, no. 034004, pp. 1 – 14, 2021.
3. S. Ayyalosomayajula, S. Willows, C. Hough, F. Hegmann, and M. Kulka. Terahertz Radiation Does Not Alter Nuclear Envelope of Rat Basophilic Leukemia Cells to Propidium Iodide. *Spectrum*. no. 7, pp. 1 – 11, 2021.
4. C. M. Hough, David N. Purschke, Chenxi Huang, Lyubov V. Titova, Olga Kovalchuk, Brad J. Warkentin, & Frank A. Hegmann. Topology-based prediction of pathway dysregulation induced by intense terahertz pulses in human skin tissue models. *Journal of Infrared, Millimeter, and Terahertz Waves*. vol. 39, pp. 887 – 898, 2018.
5. C. M. Hough, D. N. Purschke, C. Huang, L. V. Titova, O. V. Kovalchuk, B. J. Warkentin, & F. A. Hegmann. (Invited Paper) Global gene expression in human skin tissue induced by intense terahertz pulses. *Terahertz Science and Technology*. vol. 11, no. 1, pp. 28 – 33, 2018.
6. I. Santelices, D. Friesen, C. Bell, C. Hough, J. Xiao, P. Kar, H. Freedman, V. Rezanian, J. Lewis, K. Shankar, & J. Tuszynski. Response to Alternating Electric Fields of Tubulin Dimers and Microtubule Ensembles in Electrolytic Solutions. *Scientific Reports*. vol. 7, no. 9594, pp. 1 – 11, 2017.

Published conference proceedings:

1. C. M. Hough, D. N. Purschke, C. Huang, L. V. Titova, O. V. Kovalchuk, B. J. Warkentin, F. A. Hegmann. Genomic Signature of Membrane Permeation Induced by Intense THz Pulses. *45th International Conference on Infrared, Millimeter, and Terahertz Waves (IRMMW-THz)*. DOI: 10.1109/IRMMW-THz46771.2020.9370436. September, 2020.

2. C. M. Hough, D. N. Purschke, C. Huang, L. V. Titova, O. V. Kovalchuk, B. J. Warkentin, & F. A. Hegmann. Intense Terahertz Pulses Suppress Cancer-related Pro-mitotic Signaling Pathways in Human Skin. *The Canadian Organization of Medical Physicists (COMP) 65th Annual Scientific Meeting (ASM)*. DOI: 10.1002/mp.13794. September, 2019.
3. C. M. Hough, D. N. Purschke, C. Huang, L. V. Titova, O. V. Kovalchuk, B. J. Warkentin, & F. A. Hegmann. Genomic Mechanisms of THz-Induced Cancer Dysregulation in Human Skin. *44th International Conference on Infrared, Millimeter, and Terahertz Waves (IRMMW-THz)*. DOI: 10.1109/IRMMW-THz.2019.8874132. September, 2019.
4. C. M. Hough, D. N. Purschke, C. Huang, L. V. Titova, O. V. Kovalchuk, B. J. Warkentin, & F. A. Hegmann. Intensity-dependent Suppression of Calcium Signaling in Human Skin Tissue Models Induced by Intense Terahertz Pulses. *43rd International Conference on Infrared, Millimeter, and Terahertz Waves (IRMMW-THz)*. DOI: 10.1109/IRMMW-THz.2018.8509862. August, 2018.
5. C. M. Hough, D. N. Purschke, C. Huang, L. V. Titova, O. V. Kovalchuk, B. J. Warkentin, & F. A. Hegmann. Biological Effects of Intense THz Pulses on Human Skin Tissue Models. *42nd International Conference on Infrared, Millimeter, and Terahertz Waves (IRMMW-THz)*. DOI: 10.1109/IRMMW-THz.2017.8066865. October, 2017.

Conference presentations:

- Invited plenary presentations
 1. Global Gene Expression Dynamics in Human Skin Tissue Models Induced by Intense Terahertz Pulses. *6th Shenzhen International Conference on Advanced Science and Technology*. Shenzhen, China. December, 2017.
- Invited keynote presentations
 1. Genomic Mechanisms of THz-Induced Cancer Dysregulation in Human Skin. *44th International Conference on Infrared, Millimeter, and Terahertz Waves (IRMMW-THz)*. Paris, France. September, 2019.
 2. Intensity-Dependent Suppression of Calcium Signaling in Human Skin Models. *43rd International Conference on Infrared, Millimeter, and Terahertz Waves (IRMMW-THz)*. Nagoya, Japan. September, 2018.
 3. Effects of Intense THz Pulses on Gene Expression Dynamics in Human Skin Models. *8th International THz-Bio Workshop*. ENEA Research Center, Frascati, Italy. October, 2017.

4. Biological Effects of Intense Terahertz Pulses on Human Skin Tissue Models. *42nd International Conference on Infrared, Millimeter, and Terahertz Waves (IRMMW-THz)*. Cancun, Mexico. September, 2017.
- Oral presentations
 1. Genomic Signature of Membrane Permeation Induced by Intense THz Pulses. *45th Infrared Millimeter and Terahertz Waves (IRMMW-THz)*, Buffalo, NY, 2020. (Presented remotely).
 2. Terahertz-Induced Cancer Signaling Dysregulation in Human Skin. *65th Annual Scientific Meeting – Canadian Association of Medical Physicists (COMP)*. Kelowna, BC, 2019.

Acknowledgements

Many mentors, collaborators, peers, family, and friends have provided essential support and guidance throughout the duration of this research project. First, I am incredibly grateful for the support and mentorship of my two supervisors, Drs. F. Hegmann and B. Warkentin. Dr. Hegmann has been a continual source of education, guidance, and support, and I sincerely appreciate the years of encouragement he has provided. In addition to valuable research guidance, Dr. Hegmann also provided a stimulating laboratory environment, with a culture of open inquiry and ample opportunity for collaboration. Dr. Warkentin, in addition to project oversight, provided a valuable clinical perspective, and ensured that the project direction has maintained alignment with my values of contributing meaningfully to the lives of cancer patients. Dr. Warkentin inspires a forward-thinking, clinically-progressive mindset towards medical science that I hope to emulate in my future as a researcher.

I am very thankful for the involvement of my supervisory committee. Drs. F. Hegmann, B. Warkentin, J. Tuszyński, D. Murray, and G. Fallone provided valuable feedback and guidance throughout the duration of the project. Gratitude is also extended to the internal examiners, Drs. K. Wachowicz and D. Robinson, and external examiner Dr. V. Wallace, for providing arms-length feedback and valuable assessment of the project directions and thesis.

A significant portion of this thesis project involved investigation and analysis of biological response mechanisms, and several mentors provided extremely valuable education on these topics. Drs. D. Murray and R. Mirzayans provided extensive discussions, literature material, and guidance in biology and experimental oncology that were essential for the success of this project. Drs. M. Kulka, J. Tuszyński, L. Titova, and O. Kovalchuk were primary collaborators, and additionally provided invaluable education in cell biology, molecular biophysics, genomics, and wet lab techniques.

I would like to thank my peers in the Hegmann laboratory: D. Purschke, Dr. M. Narreto, Dr. V. Jelic, P. Nguyen, C. Jensen, J. Calzada, H. Simpson, A. McDowell, N. Refvik, C. Strilet, J. Hernandez, Y. Luo, T. Wang, and N. Amer. Especial gratitude is extended to D. Purschke, who contributed to laser characterization, terahertz measurements, data analysis and interpretation, and provided valuable discussions on a wide variety of topics, from fundamental photonic theory to gene expression statistics. I would additionally like to thank B. Shi, G. Popowich, and J. Chaulk for technical assistance, and M. Reid for use of the pyroelectric imager.

At the Cross Cancer Institute (CCI), I would like to thank Dr. N. De Zanche, who introduced me to modern medical physics research during my undergraduate degree, and Dr. G. Fallone, who accepted my application for enrolment. I was subsequently introduced to the many knowledgeable instructors at CCI who shaped my approach to medical physics research. I would also like to thank and honour the life of Dr. John “Jack” Cunningham (January 5, 1927 – January 4, 2020). The opportunity to study under a great figure in the history of Canadian medical physics has been one of the greatest privileges of my academic journey thus far.

I would like to thank the past and present students in my time with the CCI medical physics program. I am very lucky to have enrolled in the 2014 cohort, where I met R. Barta, Dr. R. Yang, Dr. B. Cawston-Grant, S. Ferguson, and Dr. O. Zelyak. I am confident that these brilliant individuals will all accomplish amazing achievements in their chosen fields, and I am excited to witness their careers unfold.

I would like to thank the terahertz research community, and the International Society of Infrared, Millimetre, and Terahertz Waves, for valuable research interactions of all kinds. Particular gratitude is extended to Drs. P. Siegel, E. Pickwell-MacPherson, and G. P. Gallerano for generous invitations to visit their institutions and present my research at conferences. I would also like to thank and commemorate the life of Dr. Charles Schmuttenmaer (August 5, 1963 – July 26, 2020), a pioneer of the terahertz community who is sorely missed.

Administrative assistance was greatly appreciated from J. Martin, D. Howorko, and B. Sheen (Medical Physics, CCI), T. Schuetz-Zawaduk and C. Klein (Department of Oncology), and K. Robertson, T. Mish, and S. Hamilton (Departments of Physics).

I am very grateful for financial support that provided freedom to focus primarily on research. Thank you to the Canadian Institutes of Health Research (CIHR) and the Natural Sciences and Engineering Research Council (NSERC Discovery Grant program, NSERC CGSM and PGSD scholarship programs), as well as internal funding from U of A. Funding was also provided by the Canadian Foundation for Innovation (CFI), and Alberta Innovates Technology Futures (AITF).

Finally, I would like to thank my friends and family for their encouragement, support, and patience during the years of this project. I am especially thankful to my wife, Kayla Gaffney-Hough, without whom I would not have had the ability to pursue these scientific endeavours, and our daughter, Amalie Helena Hough, who we welcomed to the world on July 25, 2020, and to whom this work is dedicated.

Table of Contents

1	Introduction.....	1
1.1	Cancer in Canada	1
1.2	Therapeutic approaches to cancer	2
1.2.1	The hallmarks of cancer	2
1.3	Radiation in medicine	3
1.3.1	Modern radiation therapy.....	4
1.3.2	Other forms of medical radiation therapy	4
1.4	Terahertz radiation	6
1.4.1	Introduction to terahertz radiation.....	6
1.4.2	The “terahertz gap”	7
1.4.3	Growth of terahertz research.....	8
1.4.4	Non-biomedical terahertz applications	9
1.4.5	Biomedical applications of terahertz radiation	10
1.4.6	Challenges and limitations	13
1.4.7	Biological effects, safety considerations, and potential therapeutic applications	14
1.5	Thesis statement and outline	15
1.5.1	Thesis statement.....	15
1.5.2	Outline.....	16
1.6	References.....	18
2	Terahertz dynamics and interaction mechanisms in biological systems.....	27
2.1	Introduction.....	27
2.2	Terahertz biology	27
2.2.1	History and development.....	27
2.2.2	Ultrafast dynamics in biological systems.....	28
2.3	Mathematical models of terahertz dynamics and interactions in biological systems.....	30
2.3.1	Dielectric model of terahertz field exposure.....	31
2.3.2	Nonlinear energy transfer in biological systems: The Fröhlich condensate.....	34

2.3.3	Mechanical model of DNA breathing in a terahertz field.....	37
2.4	Biological effects of terahertz radiation.....	39
2.4.1	Thermal vs. non-thermal biological effects.....	39
2.4.2	Frequency-dependence of biological effects.....	41
2.5	Conclusion	41
2.6	References.....	41

3 Terahertz source development: Laser-based generation of intense terahertz pulses in lithium niobate48

3.1	Introduction.....	48
3.1.1	Lasers in terahertz science	48
3.2	Laser physics.....	50
3.2.1	Population inversion in an excitable laser gain medium.....	50
3.2.2	Ti:Sapphire Lasers	53
3.3	Nonlinear optics	54
3.3.1	The nonlinear wave equation	54
3.3.2	Nonlinear dynamics in materials and optical rectification.....	57
3.3.3	Terahertz pulse generation by optical rectification.....	60
3.3.4	Tilted-pulse-front optical rectification.....	61
3.4	Laser-based generation of intense terahertz pulses in lithium niobate.....	64
3.4.1	Modelocked oscillator.....	65
3.4.2	Regenerative amplifier.....	67
3.4.3	The terahertz source.....	71
3.5	Conclusion	75
3.6	References.....	75

4 Terahertz waveform analysis: Beam characterization and measurement of incoherent and coherent pulse parameters79

4.1	Introduction.....	79
4.2	Terahertz source summary	79
4.3	Detection of terahertz radiation.....	81

4.3.1	Coherent detection	81
4.3.2	Incoherent detection.....	84
4.4	Terahertz pulse measurements and beam characterization	88
4.4.1	Measuring the pulse energy, ϵ	88
4.4.2	Measuring the pulse duration, τ	89
4.4.3	Measuring the focused spot area, A	91
4.4.4	Measuring the electric field strength, E_{THz}	92
4.4.5	Summary of terahertz pulse parameters.....	93
4.5	Spectral decomposition of the terahertz beam	93
4.5.1	Bandpass terahertz waveform analysis	94
4.6	Terahertz field modulation in a focusing beam geometry.....	99
4.6.1	Carrier-envelope phase modulation and the Gouy phase shift.....	102
4.6.2	Significance of pulse phase modulation for exposure studies	105
4.7	Conclusion	106
4.8	References.....	106

5 A system for field-enhanced terahertz pulse exposure and real-time analysis of biological samples.....109

5.1	Introduction.....	109
5.1.1	Terahertz systems for biological exposure studies.....	109
5.2	Review of existing terahertz exposure systems	111
5.2.1	Continuous-wave terahertz exposures.....	112
5.2.2	Pulsed terahertz exposures.....	113
5.3	System design and characterization	115
5.3.1	Field enhancement with sharp metallic tips.....	118
5.3.2	Sample housing.....	120
5.3.3	Other sources used for biological exposure studies.....	123
5.4	Alignment procedure for sample exposures.....	123
5.5	Normal-incidence terahertz reflection spectroscopy.....	125
5.5.1	Quantitative calculation of field strength at the sample location.....	128
5.6	Conclusion	130
5.7	References.....	130

6 Terahertz dosimetry for biological exposure studies: Simulation of coherent spatiotemporal pulse dynamics in many optically thin materials135

6.1	Introduction.....	135
6.2	Terahertz dosimetry	136
6.2.1	Boundary dose modulations in terahertz exposures.....	136
6.2.2	Dose models inspired by coherent transfer function spectroscopy	140
6.3	Theoretical formalism of coherent pulse dosimetry in many optically thin materials	142
6.3.1	Spatiotemporal field dynamics in dissipative, dispersive, layered media.....	142
6.3.2	Modelling the transfer function with binary decision trees	146
6.3.3	Recursive decision tree construction.....	149
6.4	Terahertz pulse dose simulations	151
6.4.1	Comparison of dose model to transmission spectroscopy data.....	151
6.4.2	Simulation of terahertz biological exposure experiments	153
6.4.3	Transverse dose variation.....	155
6.5	Conclusion	156
6.6	References.....	156

7 Tissue-level effects: Dysregulation of cancer-related signaling pathways in human skin tissue models158

7.1	Introduction.....	158
7.2	Signaling pathways in cancer.....	159
7.2.1	Ras signaling in cancer	160
7.2.2	Calcium signaling in cancer	162
7.3	Differential gene expression and signaling pathway dysregulation in human skin tissue induced by intense terahertz pulses.....	162
7.3.1	Methods.....	162
7.3.2	Results.....	171
7.4	Discussion	178
7.4.1	Activation of pro-inflammatory signaling	178
7.4.2	Suppression of pro-mitotic signaling	179
7.4.3	Consideration of thermal effects	181
7.5	Conclusion	182

7.6 References..... 182

8 Cellular-level effects: Investigations of membrane permeabilization induced by intense terahertz pulses187

8.1 Introduction..... 187

8.2 The plasma membrane 189

 8.2.1 The membrane potential..... 190

 8.2.2 Membrane electroporation 190

 8.2.3 Pulse shape and field delivery..... 199

8.3 Intense terahertz pulse source and exposure system 199

8.4 Long-term effects of intense terahertz pulses to membrane permeability in A-431 epithelial carcinoma cells..... 200

 8.4.1 Methods..... 200

 8.4.2 Results..... 203

8.5 Real-time effects of intense terahertz pulses to membrane permeability in RBL-2H3 rat basophilic leukemia cells with tip-enhancement 205

 8.5.1 Methods..... 205

 8.5.2 Results..... 207

8.6 Discussion..... 208

 8.6.1 Relation to tissue-level effects 209

8.7 Conclusion 213

8.8 References..... 214

9 Molecular-level effects: Disassembly of microtubules by intense terahertz pulses220

9.1 Introduction..... 220

9.2 Biopolymers and the cytoskeleton 221

9.3 Terahertz-induced disassembly of polymerized and chemically stabilized microtubules.....223

 9.3.1 Methods..... 223

 9.3.2 Results..... 229

9.4 Discussion 234

 9.4.1 Intensity dependence..... 234

9.4.2	Frequency dependence.....	235
9.4.3	Considerations of thermal or shockwave interaction mechanisms	236
9.4.4	Relation to tissue-level biological effects	237
9.5	Conclusion	240
9.6	References.....	241

10 Summary and Conclusions246

10.1	Thesis summary and contribution.....	246
10.2	Proposed future directions	248
10.2.1	Targeted protein expression assays for “terahertz targets”	249
10.2.2	Terahertz spectroscopy of cell media solutions: Influence of media conductivity on biological response to intense terahertz pulses	249
10.2.3	Time-resolved, quantitative dielectric characterization of ionizing dose deposition in cells and tissue.....	250
10.2.4	Terahertz radiation as a sensitizing agent	251
10.2.5	Homogenizing the intensity and frequency distribution with raster-scan exposures.....	252
10.3	Concluding statements	253
10.4	References.....	254

Bibliography.....256

A. Appendix.....290

A.1	Fourier series expansion.....	290
A.1.1	The Fourier transform	291
A.2	Bioinformatics analysis of gene expression microarrays: Signal Pathway Perturbation Analysis (SPIA)	296
A.2.1	Pathway perturbation analysis in R.....	296
A.2.2	Details on transcript-level dysregulation of cancer-related signaling pathways	297
A.2.3	Conventional thresholds vs. cut-off free analysis (COFA).....	306
A.3	References.....	313

List of figures

Figure 1.1. **2019 percentage of new cancer cases, deaths and incidence/mortality rates in Canada by age.** Adapted from [1]. The percentage (bars, left axes) and rates (curves, right axes) of new cancer cases (a) and deaths (b)..... 1

Figure 1.2. **Energy deposition characteristics (percent-depth dose (PDD) curves) in water for various forms of medical radiation.** 10×10 cm² fields, 100 cm SAD/SSD, adapted from [46, 47]. Photons of varying beam energies are used for deep tissue irradiation, and normal tissues are spared by using multiple beams from varying angles and tumor-conforming beam filtration, or by modern radiotherapy modalities such as intensity-modulated or image-guided radiotherapy (IMRT, IGRT). Electrons are useful for treating surface lesions, although the Bremsstrahlung tail will deposit some dose in deep tissue. Proton beams deposit the majority of the beam energy in deep tissue, and are used for localized treatments of tumors near critical organ structures such as the eye or spine..... 5

Figure 1.3. **The terahertz (THz) band of the electromagnetic (EM) spectrum.** The frequency (f), wavelength (λ), wavenumber (k), and photon energy (E) of the electromagnetic spectrum (logarithmic scales). The THz band (highlighted) is non-ionizing radiation between the microwave and infrared bands, and is a relatively underexplored region at the interface of conventional electronic and photonic regimes. Natural oscillatory dynamics of biomolecules and cellular structures occur at THz frequencies, and external excitation with EM energy at similar frequencies couples to these dynamics. Typical energy ranges for diagnostic and therapeutic applications of ionizing radiation are labelled for reference. 7

Figure 1.4. **Principle of THz reflection spectroscopy and imaging for diagnosis of diseased tissue.** Adapted from [84]. (a) Schematic of THz pulsed imaging acquisition. A femtosecond infrared laser source (800 nm) generates and coherently detects THz pulses via photoconductive switching on a semiconductor substrate [62]. THz pulses are transmitted through a quartz window on the scan probe face. (b) The THz pulses are raster-scanned across the imaging area, and reflected pulses for each pixel are detected in the time domain via electro-optic sampling. The Fourier transform provides the amplitude and phase information in the measured pulses, which may be utilized to determine dielectric properties of the scanned tissue. There are often quantitative differences in dielectric properties (e.g., the refractive index, left) between diseased and normal tissue that provide diagnostic contrast without the need for additional contrast agents. Alternatively, the dielectric data may be converted into a spatial

representation for qualitative or quantitative THz imaging that provides high-contrast delineation of tumor margins..... 12

Figure 1.5. **Refractive index and absorption coefficient for liquid water in the THz band (0.1 – 10 THz).** Data were collected by Fourier transform spectroscopy, from [108]. (a) Water is highly dispersive. Low THz frequencies see a high index in liquid water, and therefore travel slower relative to high frequencies ($v = c/n$). (b) Water is highly absorptive, particularly for higher frequencies. At 1 THz, the absorption is 230 cm^{-1} , and has a corresponding characteristic penetration depth of $\delta=43 \text{ }\mu\text{m}$ 14

Figure 2.1. **Ultrafast processes in physical and biological systems.** Adapted from [6, 11, 12]. At top is a representative example of an energy landscape along a coordinate that characterizes the molecule’s conformational state (the “reaction coordinate” X). The fast dynamics associated with bond rotation and vibration may oscillate between microstates due to relatively low energy barriers in the highly frustrated ranges close to the ground state energy ΔE_G . Slower, larger-amplitude transport dynamics that occur on \sim ns timescales may require larger energies but do not result in a large-scale conformational change ($A \rightarrow A$ or $B \rightarrow B$). Energy transition events that correspond to conformation state change ($A \rightarrow B$, e.g., folding protein) require larger activation energies and occur on slower timescales ($\mu\text{s} - \text{ms}$). 29

Figure 2.2. **Relative dielectric permittivity and conductivity of biological tissues from RF to THz frequencies.** Adapted from [35, 36, 37, 38]. *Left:* An idealized diagram of dielectric relaxation of permittivity (red, left axes) and conductivity (blue, right axes). Biological tissues generally have 3 distinct relaxation bands, indicated by labels α , β , and γ . In the main plot, permittivity (red) and conductivity (blue) spectra of a selection of biological tissues (blood, bone, fat, gray matter, white matter, kidney, spleen, heart, liver, lung, muscle, and skin) are shown. Thick solid lines indicate the curve means of the different tissues. Dotted lines are for dry skin, highlighting the effect of tissue hydration. Data for skin from [36] and tissue water from [38] are appended to show these quantities extended into the shaded THz region. 32

Figure 2.3. **Fröhlich’s model of nonlinear energy transfer in biological systems.** Adapted from [47]. (a) Diagram of a Fröhlich system. A population of Z oscillators are in a heat bath to which the dynamics are coupled linearly (ϕ) and nonlinearly (χ). External energy is supplied to the oscillators (ξ) at a mean rate s . (b) Time evolution solution of a Fröhlich system, showing mode occupancy n_j of the first four energy levels. The majority of vibrational quanta of the oscillators

occupy the lowest energy mode, forming a low-frequency, long-lived, bulk oscillatory state. 35

Figure 2.4. Simulation of breathing dynamics and bubble formation of THz-exposed DNA. (a) The chemical structure of DNA, and an idealized Peyrard-Bishop-Dauxois (PBD) model of DNA, with amplitude, length, and position of DNA bubbles labelled [50, 51]. (b) The 2D power spectrum of the solution y_n to Equation (2.9) for $\Omega = 2.0$ THz, adapted from [49]. The driving force is present everywhere along the modelled DNA strand at 2.0 THz. A localized 1.0 THz “bubble” forms that is superposed on a localized DC separation at nucleotide (nt) 40. Breather modes induced by THz exposure create and amplify localized bubbles in the DNA strand, which is hypothesized to affect biological function by altering gene expression. 38

Figure 2.5. Time- and frequency-domain representations of intense THz pulses used for biological exposures. (a) Intense THz pulses are single-cycle, approximately picosecond-duration EM pulses reaching very high peak electric fields (~ 640 kV/cm in this example). The energy localization in time corresponds to a broad power spectrum in (b). The peak-power frequency for this pulse is $f_0=1.3$ THz, and the spectrum bandwidth is 1.8 THz (full width tenth max, FWTM). 40

Figure 3.1. Physics of laser operation. (a) Stimulated emission and feedback amplification in a reflective cavity oscillator. (1) An external energy source excites atoms in a gain medium to higher energy levels. (2) Population inversion is achieved when more atoms exist in high energy states (E_2) relative to the ground state (E_1). (3) Excited particles quickly relax to the upper lasing level E_2^* . (4) Stimulated transition to the ground level results in the emission of a photon in phase with the stimulating photon. (5) Photons are trapped in the oscillator cavity, and multiple round-trips stimulate similar emissions that provide photonic gain. (6) The cavity modes interfere to form a localized pulse that is trapped between the end mirrors of the reflective cavity (i.e., “modelocking”). (7) One end-mirror is partially transmissive, allowing a small fraction of pulse energy to form the laser emission. (b) The laser emission spectrum is a combination of the gain profile of the lasing medium and the oscillatory modes that the cavity can support. Constructive interference of the cavity modes produces modelocked pulse emission. 52

Figure 3.2. The energy landscape of a Ti:Sapphire laser gain medium. (a) Energy levels of $Ti:Al_2O_3$, adapted from [38, 39]. The primary lasing source is due to the cubic field from the neighbouring oxygen atoms that cause splitting Δ between an excited doublet (E) and a ground-

state triplet (T), with finer energy splitting given by V/δ . The electron distributions corresponding to the energy levels are depicted at right. (b) Electronic energy vs. displacement of the Ti^{3+} ion. (1) Initially, bound electrons are in the ground state. (2) Absorption of a blue-green photon raises the electron to the excited band E where it quickly relaxes into the upper lasing level (3). (4) Stimulated emission to the triplet ground state T results in the emission of a red photon. 53

Figure 3.3. **The dipole oscillator model of nonlinear material polarization response to an applied field.** Adapted from [7]. (a) At low intensities, electrons are in a harmonic potential, and oscillate symmetrically about their equilibria. At high intensities, higher-order displacements are significant, and result in asymmetric motion (gray). (b) The corresponding electron dynamics. In the linear regime (blue curve), electrons oscillate symmetrically about their equilibria. For sufficiently intense applied fields, the nonlinear contribution (red curve) causes asymmetric electron oscillation about their equilibrium, which can be expressed as a superposition of two nonlinear generation processes, SHG and OR..... 58

Figure 3.4. **Optical rectification in nonlinear media.** (a) A sufficiently intense Gaussian laser pulse incident on a nonlinear crystal will induce a DC polarization that is proportional to the input field amplitude. This behaves as a source of EM radiation that is proportional to the second-derivative of the polarization response, and produces frequencies that did not exist in the input field. (b) The nonlinear dipole model fit to a measured THz pulse, which accurately characterizes the main features of a real THz pulse generated by optical rectification..... 60

Figure 3.5. **The principle of tilted-pulse-front enhancement of THz wave generation.** In the generation crystal, the THz pulse exists as a Cherenkov cone with the laser pulse at its apex. For extended sources, tilting the pulse front along the cone edge results in constructive interference of the generated wave. 61

Figure 3.6. **Tilted-pulse-front beam geometry.** The pulse front of the infrared laser is tilted with respect to the phase front by isolating the first mode from a reflective diffraction grating. A 4f-imaging system is constructed with two plano-convex cylindrical lenses that image the pulse front and grating plane onto the output face of the LN prism. The tilted-pulse-front beam is described geometrically by right triangles with sides w and L , angles θ , and hypotenuses d , as labelled and described in the text. 62

Figure 3.7. **Box-diagram schematic of the entire experimental configuration.** Ultrafast infrared laser pulses from a Ti:Sapphire laser (Section 3.2.2 and 3.4.1) are amplified in a regenerative amplifier (Section 3.4.2) via chirped-pulse-amplification (CPA), and split such that ~80% of the beam is used for THz generation via tilted-pulse-front optical rectification (Section 3.3.4).

The remaining portion of the beam is utilized for laser diagnostics and THz detection via electro-optic sampling. Quadrature detectors monitor spatial symmetry of the laser mode, and an auto-correlator is utilized to characterize the compressed pulse duration (Section 3.4.2.1)

..... 65

Figure 3.8. **The Coherent Micra oscillator.** (a) Schematic representation of the Micra oscillator.

The Verdi input laser (532 nm CW, green path) pumps the gain medium (1), activating a lasing process that outputs energy (light red path) according to the Ti:Sapphire gain profile. The cavity will only support discrete lasing modes, assisted by active mode-locking methods such as a spring oscillator (2) to broaden the mode profiles. A pair of prisms (3) compensates pulse group velocity dispersion each round trip of the cavity. Kerr lensing spatially separates the modelocked region of the beam, which is isolated with a slit aperture at (4) and retro-reflected back through the optical components and gain medium (dark red path). A partially transmissive cavity end-mirror at (5) reflects most of the generated pulse train back through the system for additional passes. The small portion transmitted through this end-mirror forms the laser output.

(b) The measured spectrum for each Micra output pulse. The central wavelength is 804 nm and bandwidth is 27 nm (fit to Equation (3.34)). (c) Measurements of the Micra beam size as it exits the oscillator (blue curve), and 103 cm from the oscillator output (red curve). The beam divergence is 0.88 mrad (0.05°). (d) An oscilloscope waveform of the output pulse train detected by a photodetector at the output of the oscillator cavity. The pulse spacing is stable at 12.5 ns corresponding to the 80 MHz repetition rate. 66

Figure 3.9. **Chirping pulses with paired diffraction gratings disperses the frequency components in space and time, facilitating safe amplification via Chirped Pulse Amplification (CPA).**

A pulse centred at $\lambda_0 \pm \Delta\lambda$ will diffract at a wavelength-dependent angle (Equation (3.25)). The differential pathlengths disperse the wavelength components, which are re-collected by diffraction gratings into a compressed pulse..... 68

Figure 3.10. **The Coherent Legend regenerative amplifier.** (a) Schematic representation of the Legend regenerative amplifier, and (b) the corresponding pulse timing diagram, adapted from [41]. (Components are numbered consistently in (a) and (b)).

A stretched input pulse train (1) with s-polarization enters the amplifier and is reflected by a Brewster window towards a Pockel's cell (4) triggered at 1 kHz. When triggered, the cell converts the pulse to p-polarization, which allows the reflected pulse to now be transmitted through the Brewster window into the Ti:sapphire medium (3). At the same time, a pump laser (2) is used to induce population inversion in the Ti:sapphire, facilitating amplification of the input pulse in the cavity. The pulse is reflected through the cavity multiple times, resulting in a build-up of the

amplification (5). Once the final amplification is attained, the second Pockel's cell (6) is triggered, converting the pulse back to s-polarization, enabling a Brewster window to reflect the pulse out of the system (rather than transmitting it back into the cavity), becoming the amplified pulse output (7). (c) The measured spectrum for each output pulse. The central wavelength is 801 nm and the bandwidth is 12 nm. (d) Measurements of the amplified pulse beam size by the knife-edge method. (e) An oscilloscope waveform displaying the build-up of the selected pulse in the amplifier cavity (yellow trace) and the output amplified 1 kHz pulse train (blue trace) as measured by a photodetector at the amplifier output..... 69

Figure 3.11. **Single-shot autocorrelator for temporal characterization of amplified laser pulse.**

Modified from [41]. (a) The pulse is equally split into two beamlines, and non-collinearly propagated to intersect in a frequency-doubling KDP crystal. The second-harmonic signal generated is a temporal trace of the intensity distribution and is detected by a CCD array. (b) The width of the oscilloscope trace with the time axis calibrated to the optical delay time determines the pulse duration (50.4 fs FWHM). 71

Figure 3.12. **Intense THz pulse source.** (a) Schematic of the source of intense THz pulses that

occupies the “THz Source” module in the box diagram of Figure 3.7. The amplified pump pulse from the oscillator/amplifier is prepared in a tilted-pulse-front geometry as described in Section 3.3.4 and incident on a lithium niobate (LN) crystal with a 63° cut face. Gold off-axis parabolic mirrors (OAPMs) expand and refocus the emitted collimated THz beam. The position of the THz focus may be rotated in a 360° arc to convert the source between “exposure”, “detection”, or “spectroscopy” modes. (b) The electric field waveform of the intense THz pulse. The per-pulse energy is 1.5 μJ, and this is focused to a ~1 mm diameter spot to achieve a maximum field strength of 640 kV/cm. (c) The frequency spectrum for the pulse in (b). The peak frequency is 1.3 THz, with a bandwidth of 1.8 THz (full-width tenth max, FWTM). 72

Figure 3.13. **Spatial THz emission directly from the LN generation crystal.** (a) Normalized

pulse energy vs. space. Images of the THz spot were taken at a fixed height ($z = 6''$ (152.4 mm) from the bench surface) on-axis to characterize variation in the emitted THz spot size. (b) Average pulse energy decay vs. longitudinal distance from the crystal (y), for varying transverse locations (x). Energy growth near beam fringes is due to horizontal divergence. (c) THz spot size vs. longitudinal distance from the LN output. Note the change to abscissa values in (c) compared to (a) and (b)..... 73

Figure 3.14. **THz enhancement with anti-reflection coatings (ARCs) and pump laser filtration**

at the output of the lithium niobate prism. (a) Two layers of Kapton tape (total thickness 60 μm) secured to the output face of the crystal provides an anti-reflection coating (ARC) that

increases THz pulse energy by 9%. (b) Filtration of leakage of the infrared laser (red) by black polyethylene (top, attenuates THz energy) or a silicon wafer at Brewster's angle (bottom, lossless but induces vertical offset). 74

Figure 4.1. Source schematic and characteristics for intense THz pulses. (a) Diagram of optical rectification of tilted-pulse-front infrared laser pulses in lithium niobate (LN), and propagation of the THz beam through the exposure system with the rotating off-axis parabolic mirror (ROAPM) oriented for waveform detection via electro-optic sampling in gallium phosphide (GaP). The modulated sampling pulse is shifted and split by a quarter wave plate (QWP) and Wollaston prism (WP), respectively, and detected by a pair of balanced photo-detectors (BPD). A delay stage (DS) on a motorized linear track varies the relative position of the sampling pulse within the THz pulse for electro-optic sampling of the THz field. (b) A 1 kHz pulse train of ~picosecond-duration pulses, corresponding to a duty cycle = 10^{-9} . (c) A plot of the intense THz pulse waveform, a single-cycle EM pulse reaching peak field strengths of ~640 kV/cm. *Inset:* The THz spot at the beam focus, spot size = 1.12×1.32 mm². (d) THz pulse power spectrum. The peak frequency is 1.3 THz, with a 1.8 THz FWTM (full-width tenth max).... 80

Figure 4.2. Schematic representation of electro-optic (EO) sampling of a THz field with an optical sampling pulse in nonlinear media. (a) An electric field applied along the (110) normal vector induces a birefringence that shifts the relative phase between horizontal and vertical polarizations ($n_x \neq n_y$). (b) A THz pump pulse (blue) and optical sampling pulse (red) are colinearly incident normal to the (110) plane of a gallium phosphide (GaP) crystal. The thick substrate is index-matched to reduce reflection interference typical in thin EO crystals. (c) Diagram of EO sampling at zero THz amplitude (top) and max THz field (bottom) sampling locations. The modulation in the sampling pulse is amplified with a quarter-wave plate ($\lambda/4$) and spatially separated by a Wollaston prism (WP). The relative signal amplitudes are read via peak-detection of the signal integrated by a pair of balanced photo-detectors..... 82

Figure 4.3. Photos and diagrams of the pyroelectric technologies used for incoherent THz detection. (a) Single element large-area detectors are used for detecting the total THz pulse energy. Pyroelectric elements are instantaneously polarized by the thermal energy deposition on the absorber electrode, inducing a measurable current. (b) The pyroelectric imager houses a 320×240 array of 48.5 μ m square pyroelectric elements. A modulating chopper synchronized to the laser repetition rate provides an iteratively updating reference image in real time, increasing sensitivity to small thermal fluctuations. 85

- Figure 4.4. **Alignment of the sample holder with the ScienceTech pyroelectric detector.** A 1 mm custom-machined aperture holds the detector centred over the THz input window. Maximizing the pulse energy through the aperture locates the THz beam waist that is used as the reference point to align the other components of the bio-exposure system..... 86
- Figure 4.5. **Frequency linearity of pyroelectric detectors.** Total pulse energy measurements for each THz band (green labels in THz) are determined from the pyroelectric detector readout (SPJ-D-8), the total integrated camera pixel intensity (PV320), and the integrated power spectrum of EO-sampled waveforms. There is reasonable linearity between detectors, particularly for higher frequencies. The deviation for the 0.5 THz band is attributed to an underestimation of energy in the integrated power spectrum, since the two pyroelectric detectors with significantly different element pixel sizes (10 mm vs. 0.05 mm) are in agreement. 87
- Figure 4.6. **THz pulse energy detection with the SPJ-D-8 pyroelectric detector.** (a) Gold off-axis parabolic mirrors (effective focal length = 76.2 mm) focus the THz beam to the pyroelectric element, and the resulting current is displayed as an oscilloscope pulse. (b) The amplitude of the oscilloscope signal ΔV_{ab} is linearly proportional and calibrated to the THz pulse energy digital readout. (c) The relative uncertainty in detection vs. pulse energy from the detector count histograms..... 89
- Figure 4.7. **Two methods of defining the pulse duration.** (a) The magnitude of the Hilbert transform defines the envelope for an arbitrary field distribution. The width of this envelope, by convention the $1/e$ threshold (green), defines the THz pulse duration. Also shown are alternative pulse width metrics – FWHM and $1/e^2$. (b) Normalized cumulative integral of the noise-subtracted temporal energy distribution. Pulse durations may be defined as time to accumulate a given fraction of total energy. 90
- Figure 4.8. **Quantifying THz spot area with combined 1D Gaussian fits.** Data is extracted from the 2D image from horizontal and vertical line profiles drawn along the major/minor axes of the elliptical THz spot. By convention, the spot size in each dimension is reported as the $1/e^2$ width of the fit. 91
- Figure 4.9. **Windowed FFTs of the THz pulse highlighting coarse spectral variation in time.** (a) Time-domain waveforms, showing pulse separation into the two dominant components: The main THz pulse generated from the optically rectified Gaussian infrared laser pulse (green), and the positive-time oscillations (red) due to crystal ringing and water vapor-induced dispersion that causes high frequencies to travel faster than low frequencies in humid air. (b) The corresponding power spectra show that the main pulse captures the majority of the

broadband spectral shape, and the peaks in the positive-time ringing exactly overlap with THz water absorption lines.....	94
Figure 4.10. THz bandpass filters. Fields incident on the conductive mesh establish capacitance and inductance distributions that preferentially transmit single frequency bands dependent on the specific geometry of the cross-absent structure (top-right). <i>Bottom:</i> Stereoscope images of the bandpass filters at 0.5, 1.0, and 2.2 THz, showing cross-absent geometries tuned for desired wavelength transmission.	95
Figure 4.11. Time-domain waveforms for individual THz bands. (a) The set of normalized waveforms, labelled by nominal bandpass frequency and quality Q of the associated transmission profile. (b) Power spectra for all filters overlaid on the broadband spectrum (black). (c) Transmission spectra (power spectra ratios) for each bandpass filter. (d) Pulse energy for each THz band, as measured by the methods discussed in Section 4.3.2.2. (e) Peak (maximum absolute value) electric field of the associated bandpassed waveform.	96
Figure 4.12. Per-band THz pulse duration. The characteristic time of amplitude decay (example for 1.0 THz at left) agrees well with the pulse duration as determined from the Hilbert profile width (right).....	97
Figure 4.13. Per-band spatial intensity distributions. (a) Each spot image is a square with 2 mm side lengths. The top row has been globally normalized to the 0.86 THz pixel maximum, and the bottom row images are normalized to their own maxima. (b) The mean spot size (average of horizontal and vertical diameters), compared to the theoretical diffraction-limited spot size, assuming an initial beam size of 30 mm. (c) $1/e^2$ contour lines for each of the same bands, overlaid on the broadband spot image, highlighting the frequency distribution in space embedded within the broadband exposure. Thus, the centre of the beam contains the entire broadband spectrum, while the beam energy at the fringes are relatively low-frequency.	98
Figure 4.14. The average and peak intensities of individual THz bands. The trade-offs between energy, duration, and spot size in the intensity calculation of Equation (4.6) result in roughly flat intensity profiles across the THz pulse spectrum.....	99
Figure 4.15. Waveform modulation of a focusing beam. (a) Schematic of the THz source in reflection mode for focusing beam waveform detection. Reflections from an Si wafer at the sample locations are acquired, and the sample holder is translated longitudinally (z) to effectively shift the GaP detection plane through the sampled THz beam focus. (b) Field vs. time of the EO-sampled THz pulse waveforms, with vertical offsets for varying longitudinal locations for clarity. The secondary reflections are from the distal surface of the Si wafer. (c) Pulses aligned with their position in the focusing beam geometry, showing focusing-induced	

phase modulation. The red lines indicate the maximum and minimum field strength range. The locations of field maxima straddle the maximum intensity beam waist..... 100

Figure 4.16. Intensity and field variation for a focusing THz pulse. (a) A 3D plot showing the variation of the positive/negative (blue/red) field lobe amplitudes through the focus ($d = 0$ mm), with the intensity of the focusing beam shown on the vertical axis. The three 2D projections of this 3D space are shown in the bottom plots. (b) The intensity as measured by the integrated power spectra follows the functional form of a focusing Gaussian beam (Equation (4.10)), with $z_R = (8.0 \pm 0.2)$ mm representing an effective broadband Rayleigh range. (c) The field amplitude for each lobe of the THz waveform during focusing. The maximum field for each lobe straddles the location of maximum intensity. (d) Intensity vs. squared peak field strength. Far from the focus, the linear scaling of Equation (4.7) is valid. Within the effective Rayleigh range of the focus (highlighted band), the gradient directions reverse, due to the focusing-induced Gouy phase shift. 101

Figure 4.17. Carrier-envelope phase shifting, and field modulation due to the Gouy phase shift of a focusing THz beam. (a) A plot displaying the principle of carrier-envelope phase (CEP) modulation. When the relative phase between the envelope (red) and the carrier wave (blue) is shifted, such as during beam-focusing, the net pulse (black) is modulated. (b) The beam waist (black, left) and phase (red, right) of a focusing beam. The yellow circles at ± 4 mm indicate the Rayleigh range ($z_R = 8.0$ mm). (c) Temporal modulation of the THz pulse at the beam waist, and $d = \pm 4$ mm. (d) Power spectra of the waveforms in (c). Modulations are observed at 0.8 and 1.3 THz. (e) Off-focus power spectra normalized to the focused spectrum, highlighting the modulations in frequency space for sensing in the converging (red) or diverging (blue) region of the beam. 104

Figure 4.18. Gouy phase modulation spectra of a focusing THz beam, and determination of the frequency-dependent Rayleigh range. (a) Phase spectra vs. location through the THz focus ($d = 0$), corrected for linear phase propagation. (b) An example fit of $\phi_G(z)$ using the 0.62 THz column from the phase matrix (dotted square column). (c) The extracted Rayleigh range as a function of frequency, relative to the effective broadband Rayleigh range..... 105

Figure 5.1. The three components of a general system for investigations of THz-induced biological effects. (a) Sources used for bio-exposures may be continuous-wave or pulsed. The latter may be generated with a fixed repetition rate, or in more complex series of micropulses within a larger macropulse characterized by multiple repetition rates. (b) For the duration of

THz exposure, the sample should be in an environment with temperature and humidity monitored and regulated. The pH of the sample solution should be regulated with either CO₂ or pH-regulating buffer media. (c) Real-time analysis during THz exposure is performed for observation of transient or reversible effects. Here, examples of light and fluorescence microscopy of cancer cells are shown, though these methods may vary widely by experimental context and goals. 110

Figure 5.2. Schematic representation of intense THz pulse generation for exposure of biological systems. (a) A reflective diffraction grating (RDG) establishes a tilted-pulse-front geometry in the incident pump laser pulse that is imaged with a 4f-lens configuration to the output face of a LiNbO₃ (LN) crystal with a 63° cut face. The collimated THz beam is expanded and refocused with a series of off-axis parabolic mirrors (OAPMs). A fraction of pump energy (~20%) is aligned coincident with the focusing THz beam, with tunable power via a pulse attenuator (AT), for electro-optic sampling of the THz pulse as described in Section 4.3.1.1. The rotating OAPM provides a THz focus that moves in a 3” (76.2 mm) annulus about the y-axis, enabling multiple operational modes (see Figure 5.3). 116

Figure 5.3. The Beam’s Eye View (BEV) of the THz bio-exposure system following THz generation in LN. The THz pulse is incident on the programmable rotating 3” (76.2 mm) OAPM at the location indicated by . The mirror orientation adjusts the direction of the focused THz beam to operate the various system modes for different bio-exposure studies or for THz waveform detection via electro-optic sampling (left). Details on the various operation modes are provided in the main text. 117

Figure 5.4. Simulations of THz near-field enhancement in water with a sharp conductive tip. (a) The COMSOL geometry for tip-enhanced THz exposures, which consists of a free tip immersed in water, a polystyrene (-C₈H₈-) substrate, and port window located directly below the components. *Inset:* A zoomed image of the meshed tip apex region. (b) The horizontal (x) electric field component around the tip apex region at the time where the field peaks. (c) The field enhancement as a function of THz propagation distance through the tip apex at z=0 mm. The peak field enhancement is 35 with a FWHM of 0.38 μm. (d) A photo of the tip placed at the sample location. Silicon wedges are used to make a sample channel into which the tip is placed aligned with the THz field direction, as shown in the inset. 119

Figure 5.5. THz transmission spectroscopy for suitable substrate determination. (a) The schematic for operation of the THz source for transmission spectroscopy analysis. A sample is placed in the beam path, THz pulses are detected via EO sampling, and compared to reference pulses without the sample. (b) Power spectra comparison of a reference pulse (black) and a

pulse transmitted through 0.17 mm fused quartz (red). (c) Comparison of fused quartz transmission spectra to simulation. Oscillations in frequency correspond to reflections in the detected time window due to the thin substrate. (d) THz transmission (ratio of power spectra) of potential substrate candidates for bio-exposure experiments. The relatively low amplitude of modulations indicates reduced reflection amplitude for the Ibidi optical plastic wells and dishes..... 122

Figure 5.6. Alignment procedure for THz exposure and real-time analysis. The horizontal red dashed line indicates the focus of the THz beam. (1) The dish is levelled, and the THz beam focus is located by translating the holder/detector and maximizing pulse energy through a 1 mm pinhole aperture centred over the beam input window. (2) The microscope is centred (*x-y*) and longitudinally (*z*) aligned to the THz focus by bringing the alignment aperture used for THz energy measurements into focus in the FOV. (3) The sample plane for a given substrate is aligned to the THz focus by longitudinally (*z*) translating the sample holder until a test sample is in focus. 124

Figure 5.7. Schematic for real-time analysis of tip-enhanced THz exposure. Fluorescence microscopy of propidium iodide-labelled adherent cell cultures with long-working-distance, infinity-corrected objectives (optics schematic adapted from [40]) allows real-time characterization of biological effects and provides sufficient space for placement of a sharp conductive tip for local field enhancement in target regions. The fluorescence excitation line is focused through a 1 mm hole in the rotating OAPM and propagates colinearly with the focusing THz beam to illuminate the sample plane at the THz beam waist. The tip is estimated to locally enhance the 640 kV/cm incident field to a maximum of ~22.5 MV/cm in a ~0.4 μm (FWHM) region near the tip apex. A bright-field microscope image of the tip placed in a monolayer cell sample is shown at top-right. The THz pulse propagates out of the page, and the tip shaft is aligned parallel with the THz field direction..... 126

Figure 5.8. Operation of the THz source for normal-incidence reflection spectroscopy. (a) Schematic and photo of the modified THz source for normal-incidence THz reflection spectroscopy and field measurement at the sample location. The fused quartz beam splitter (BS2) is attached to the 4" (102 mm) OAPM and aligned as a single removable unit. Reference or sample materials are placed at the sample location and waveforms are acquired with a re-directed EO sampling line (beam splitter BS1). (b) Example waveform and power spectra for two different field strengths (blue and red) for time-domain THz reflection spectroscopy of an InGaAs crystal wafer. Pulses are offset in time due to varying thicknesses of Si wafers used for attenuating the THz beam. (c) The reflectance spectra of InGaAs (left) and GaP (right) for four

THz pulses of varying field strength, with linear interpolation applied. Differential reflectance with incident field strength is a result of nonlinear material responses that are modulated by the THz field itself..... 127

Figure 6.1. **Single-boundary modulation of coherent fields.** Single-cycle anti-symmetric THz pulse between air ($n = 1$) and a material with index $n = 1.5$. (a) Field modulation near material interfaces for a THz pulse propagating from low to high index (top) and high to low index (bottom). The leading lobe of the pulse will reflect and interfere with the tailing lobe, leading to field modulations within $\lambda/2n$ of the boundary. The dotted red lines indicate the incident field strength range, and interference modulates the incident field outside of this range. (b) Relative energy (left) and maximum field strengths of the positive and negative lobes of a pulse propagating from air to glass (low-to-high index) and then from glass to air (high-to-low index). The modulations of energy and field near the boundaries are in the highlighted yellow bands. 137

Figure 6.2. **Energy absorption and multiple-beam interference (MBI) in the sample region for varying sample thickness.** (a) Relative energy vs. propagation distance through a sample region modelled as pure water. Individual curves represent different sample thickness. Multiple beam interference in thin samples results in absorption that deviates from pure exponential decay. *Inset:* Pure exponential decay is observed in thick (1 mm) samples where MBI is negligible. The effective broadband field penetration depth in water is 75.3 μm . (b) The relative energies at the input and output face of the sample region as a function of sample thicknesses, and the absorbed dose. There is large variation of absorbed dose within typical cell sizes, and MBI effects induce further modulation for small thicknesses. (c) Isolated MBI energy modulation for varying sample thickness. These are the curves from (a) with the pure reference exponential subtracted. Modulations due to interference with the reflected waves in the sample region lead to an additional 5% – 10% energy modulation in the sample region. In (b) and (c), the gray shaded regions represent a typical range of animal cell diameters..... 139

Figure 6.3. **Effect of sample thickness.** (a) For thick samples, the multiple reflections in the reflected and transmitted pulse trains are distinguishable in the acquired waveform, and time-gating in post processing isolates the interactions with individual material boundaries. (b) For thin samples, many internal reflections interfere that cannot be gated and isolated. These many internal reflections must therefore be theoretically incorporated for accurate modelling of interactions in optically thin materials. 141

Figure 6.4. **Transfer functions determined by accumulation of spatial phase factors and reflection/transmission coefficients.** As an incident field, E_0 , propagates through layered media, it will accumulate phase and reflection/transmission coefficients according to Equations (6.7) and (6.8). These comprise the transfer function, TF, that maps the incident field to the simulated modulated field in each region. The TFs for the principal transmitted ($TF^{(3)}$) and reflected ($TF^{(1)}$) fields typically used for spectroscopy are shown at right for Regions 1 and 3, for which only the first few terms are typically needed (the spatial propagation terms (Equation (6.5)) are not included for clarity). For geometries with many optically thin materials, thousands or potentially millions of TF terms may be required for accurate simulation of field modulation over a reasonable interaction duration..... 144

Figure 6.5. **Demonstration of complete spatiotemporal simulation of coherent field variation for a generalized spectroscopy geometry.** (a) A 350 μm thick dispersive sample (green) is sandwiched between two 1 mm thick fused quartz windows (blue), with air regions on each side (gray). Plots show the spatial field variation in all five regions before ($t=-9.5$ ps) and after ($t=+6.6$ ps) interaction with the sample, with pulse reflection origins labelled. (b) Temporal field variation at different points in space. Interfering waves lead to a complex predicted field distribution in the sample region at 0 ps, and echo recombinations from secondary reflections at 15 ps and 30 ps. 145

Figure 6.6. **Decision tree representations of multiple beam interference through layered materials.** Nodes represent interaction at a material interface, and bifurcations of each node represent the reflected and transmitted fractions of the field. Red indicates the incident field, grey indicates terminal regions. (a) In the case of $N=3$ materials, all bifurcations have a terminal node. There is only one traversal through the decision tree representing internal beam interference, and the system is analytically solvable as a Fabry-Perot (FP) cavity with a finite number of infinite geometric series. (b) Multiple beam interference for $N=5$ materials. For $N>3$ materials, there are an infinite number of traversals of the corresponding decision tree that cannot be modelled as a finite set of FP cavities, and so a different approach is required.... 147

Figure 6.7. **Network step algorithm and pseudo-code for the recursion calculation that determines the set of all possible radiation paths from the decision tree model.** (a) Block diagram of the algorithm stepping rules that dictates how indices of a reflected ($x \equiv r$) or transmitted ($x \equiv t$) node is updated, and generally depends on wave direction (positive when $i>j$, negative when $i<j$). Additionally, each step accrues a phase factor $\exp(-\delta_i L_i)$ for propagation in the i^{th} region. This diagram forms a basis that can be used to recursively construct decision trees for propagation through an arbitrary set of materials. (b) Pseudocode

of recursive network determination. For a provided initial state array, `start`, the function `traverse_decision_tree()` generates two new tree branches according to the network stepping rules, and re-inserts the updated arrays as new inputs, which will each be updated again, etc. A given traversal is terminated when energy exits the system, or when a pre-defined cost function reaches a desired truncation threshold. 150

Figure 6.8. Comparison of simulations to THz spectroscopy data. (a) Comparison of simulated (dotted line) and measured (solid red line) THz pulses transmitted through 0.17 mm fused silica ($n=1.97$), with the measured incident pulse in black. The transmitted pulses are offset by $\Delta t = nd/c$ due to reduced wave speed in the quartz, $v = c/n$. (b) The simulated power spectrum is in good agreement with measurement, with slight discrepancy at higher frequencies with reduced SNR. (c) Transmission profiles are the ratio of the transmitted spectrum to the reference spectrum. The time and frequency domain representations are in good agreement, and the oscillation in the transmission profile due to interfering reflections is recovered. The blue data shows results of a manual fit to transmission data for the proprietary Ibidi optical plastic substrate to determine effective material parameters. 152

Figure 6.9. THz dosimetry simulation for exposure of cells through a 1 mm glass substrate, grown on a 0.17 mm fused silica coverslip, with aqueous media above. (a) The THz field in space before interaction with the biological sample (green), modelled as 100 μm thick epithelial cells with data from [5]. Below is the total energy in space over the entire simulation duration ($T_w=30$ ps), showing boundary modulations and THz energy decay. The zoomed sample region highlights the simulated energy in the sample region, compared to pure exponential decay (black dashed line) to highlight the effect of coherent field modulation due to optically thin samples in complex dielectric environments. (b) The THz energy (dashed line) and peak field strength (solid line) in the sample region during the interaction that begins at $t=0$ ps. 153

Figure 6.10. Scale comparison of 2D THz dose variation vs. human epithelial cell size. A-431 epithelial keratinocytes overlaid on a measured THz focus dose distribution. For a realistic exposure, dose adjustments presented in this chapter are accurate for cells near the centre of the focus, but an additional dose factor must be applied to account for intensity variation towards the fringes of the 2D dose distribution, given by the colourbar values. 155

Figure 7.1. Membrane-regulated Ras signaling activation and associated processes. Adapted from [16, 18, 19]. (a) The epidermal layer of skin tissue is comprised of stratified layers of

squamous epithelial keratinocytes (SC=stratum corneum, GL=granular layer, SL=squamous layer, BL=basal layer) latched to the basement membrane substrate for structural stability. Epidermal differentiation is partially regulated by the *Ras signaling* pathway, which is activated by a dimerized epidermal growth factor receptor (EGFR) binding to a growth factor ligand, inducing conformational change that provides binding sites for Ras activation via GTP binding. (b) Activated (GTP-bound) Ras regulates a diverse set of functions (green boxes) via binding to various downstream targets (circles). The canonical RAS-RAF-MEK-ERK axis (blue box) is one of the most well-characterized cellular differentiation and division pathways, and a popular target for anti-cancer therapy..... 161

Figure 7.2. Waveform and spectrum for the highest intensity THz pulse for skin tissue exposures (2.4 $\mu\text{J}/\text{pulse}$, 240 kV/cm, 74 MW/cm²). (a) THz pulse electric field waveform at the beam focus. *Inset:* Intensity profile at the beam focus. The cyan outline represents the $1/e^2$ boundary – 1.5 \times 2.6 mm². (b) Corresponding power spectrum of the THz pulse. The peak-power frequency is 0.6 THz and the bandwidth is 1.8 THz FWTM. 163

Figure 7.3. Measurement of global differential gene expression with cDNA microarrays. (a) Generalized steps in preparing the fluorescent DNA microarray. For illustration purposes, cells are shown with an artificially simplified genome – one chromatin fiber and 3 genes. Tissues are exposed to THz radiation, and altered gene expressions are activated to respond to the external stimulus. Messenger RNA (mRNA, i.e., gene transcripts) are extracted from the cells, labelled with a fluorescent molecule, and hybridized to an array of microbeads with probes that bind to all genes in the considered genome. A fluorescence image of the microbead array is acquired, and the intensity is related to the concentration of the corresponding mRNA transcript. Comparison of fluorescence signals between control and exposed populations is used to characterize the differential gene expression levels of the global genome. (b) A fluorescence image of a microbead array (vertical black bar) with ~47,000 human genome probes for transcript binding. The photo at top right shows a total of 36 microbead array (12 arrays each on 3 chips). Each gene is uniquely identified by its bead location, and the fluorescence intensity (see zoomed image) is related to the bound transcript concentration. 166

Figure 7.4. Signal Pathway Impact Analysis (SPIA) workflow for determining pathway-level dysregulation from gene-level expression measurements. (1) Measured global differential gene expression induced by intense THz pulses. (2) For each pathway, the KEGG database is used to filter the global data to include only the relevant genes. (3) Pathway topology information (node/edge interaction properties) is used to calculate the upstream accumulated

perturbation $A(g_i)$ for each gene, and is presented as a two-way plot (expression vs. perturbation). (4) The total accumulated perturbation $A_{tot} = \sum A(g_i)$ is determined (blue line) and compared to the simulated null distribution (black curve). If the accumulated perturbation is greater than the quantity corresponding to the pre-defined significance threshold determined from the null distribution (yellow circle), the calculated perturbation is considered statistically significant, and the pathway is predicted to be dysregulated by the relative magnitude A_{tot} . 170

Figure 7.5. **Intensity-dependent global differential gene expression induced by THz pulses in human skin tissue.** Dashed lines indicate conventional significance thresholds: $|\text{Log}_2(\text{Expression ratio})| > 0.58$ and $p < 0.05$. (a) Measured gene expression profiles for 5 THz pulse energies, showing intensity-dependent growth in expression magnitude and significance for THz-expressed genes. (b) Gene expression for the highest THz intensity. From 9311 total genes detectable in control tissues, conventional significance thresholds identify 1681 (1088 downregulated and 593 upregulated) significantly differentially expressed genes. 172

Figure 7.6. **Gene ontology (GO) terms significantly over-represented ($p < 0.01$) by THz-affected genes.** The odds-ratio (OR) is the magnitude of statistical over-representation of THz-affected genes compared to the total set of genes associated with each term, and the p-value (bars) is the associated statistical significance. 173

Figure 7.7. **THz-induced dysregulation to cancer-related signaling processes.** Dysregulation of 8 cancer-related signaling pathways, listed at left. The central bar plot shows the total accumulated perturbation (A_{tot}) as calculated by pathway perturbation analysis for each exposure condition. Associated p-values are shown at right, with points to the right of the shaded region indicating statistical significance ($p < 0.05$). 174

Figure 7.8. **Identification of the dominant transcript-level sources of pathway-level dysregulation by clustering the pathway edge matrix.** (a) Area plot indicating the number of genes involved in dysregulation of cancer-related signaling (88) relative to the total number of THz-affected (1681). (b) Venn diagram showing broad categorization of the 88 THz-affected cancer-related genes. The dysregulation of inflammatory processes is nearly entirely genomically distinct from the dysregulation to pro-mitotic pathways. (c) The pathway edge matrix, populated by the normalized number of edges extending from a node/gene (columns) in the corresponding pathway (rows). K-means clustering (dendrograms at top and right) identifies 42 THz-affected genes that predominantly drive cancer-associated signaling dysregulation (pink box). 176

Figure 8.1. **Structure and transport mechanisms of the plasma membrane (PM) in animal cells** [2]. The plasma membrane (PM, zoomed window) may be modelled as a fluid mosaic, a phospholipid bilayer embedded with biomolecules and peripheral/integral proteins that assist in regulating membrane function. The diagram outlines various membrane transport mechanisms that regulate biomolecular and ionic transport into or out of the cell. 188

Figure 8.2. **Mechanisms of field-induced permeabilization.** Adapted from [22]. (a) Mechanisms of membrane permeability changes induced by electric fields, with rows representing varying applied field strengths, indicated at right. For clarity, water is excluded from the membrane diagrams. (i) Electroporation: An applied field will induce water intrusion into the hydrophobic region of the bilayer, and lipids re-organize to form a meta-stable hydrophilic pore. (ii) Chemical alteration of membrane lipids, such as lipid peroxidation, that deform tails and increase bilayer permeability. (iii) Modulation of protein channel function. The open/close state of voltage-gated ion channels may be altered by an applied field. (b) Stages and timescales of electropore formation. The red curve indicates the applied step field, and the blue dashed curve indicates the induced change in TMV= ΔV_m . Within 1 ps of an applied field, water molecules penetrate into the hydrophobic region and rotationally align with the applied field [36]. Within ~ 1 ns, these protrusions form a water bridge that guide phosphate head groups into the interior. Within 1 μ s, the pore stabilizes, and continues to expand as long as the field is applied. For clarity, the lipid tail groups that form the membrane interior are excluded from the bottom diagram. 192

Figure 8.3. **Continuum model of membrane electroporation of a single cell.** (a) An external electric field is applied to the cell which is immersed in the extracellular dielectric medium (permittivity/conductivity $\epsilon_{ex}/\sigma_{ex}$), and comprised of two dielectric regions: The membrane (ϵ_m/σ_m) and intracellular cytoplasm ($\epsilon_{in}/\sigma_{in}$). *Right:* An equivalent circuit model for the electrical properties of the membrane, in terms of dielectric relaxation parameters discussed previously in this thesis (Chapter 2), adapted from [37]. (b) Examples of calculated membrane response (blue axes) for varying field inputs (red axes) for physiological (solid blue line) and low-conductivity (dotted blue line) extracellular environments, adapted from [38]. Potentials are for polar angle $\theta = 0^\circ$, and normalized to the cell radius R (see Equation (8.2)). (i) Extended pulses induce a saturation voltage of $\Delta V_m/R=1.5$. (ii) Pulses shorter than the membrane charging rise time will not reach the maximum potential. (iii) Trains of short pulses with sufficiently high duty cycles will accumulate potential in the membrane, then fluctuate about a stable average potential. (iv) Sinusoidal fields induce a potential that settles at a lagged sinusoidal potential variation. 194

Figure 8.4. **Broadband and bandpass exposures of A431 monolayer cell cultures.** (a) Schematic of parameter variation for different regions of the cellular growth area. White squares indicate the microscope FOV at low magnification (10x), and red dots indicate the relative THz spot size. Sample fluorescence images of the DAPI channel are shown at right, with the broadband THz spot size indicated by the red circle. (b) EO-sampled THz pulses (vertically shifted as labelled for clarity) and power spectra. The energy transmittance for bandpass spectra are labelled in the spectra plot. *Inset:* Power spectra on a logarithmic scale. 202

Figure 8.5. **Effect of free-space intense THz pulses to membrane permeability in A-431 epithelial carcinoma cells 24 hours post-exposure.** (a) Negative and positive cell death controls showing significant increase of the ZombieGreen (ZG) viability probe for chemically permeabilized membranes at low (10x, top) and high (40x, bottom) magnification. (b) Fluorescence images of THz-exposed cells for varying exposure times (number of pulses). The number of ZG+ cells increase with exposure time, indicating compromised cellular membranes. (c) Relative fraction of ZG+ cells compared to the DAPI reference image, with error bars propagated from standard Poisson counting uncertainty ($N \pm \sqrt{N}$). (d) Microscopy of bandpass exposures. No increase of ZG+ cells was observed. 204

Figure 8.6. **Results of tip-enhanced THz exposures to membrane integrity in target RBL-2H3 cells.** (a) Control brightfield images show a low-confluency population for single-cell targeting. The images at center and bottom show fluorescence images for sham-exposed and positive death controls, respectively. The positive death control shows a positive PI signal indicating compromised membranes immediately following the addition of 1 mL of cold methanol. (b) A zoomed FOV showing the tip apex positioned at the target cell. At 8 minutes of THz exposure, a small PI+ signal in the target cell is observed. Within 2 minutes of this initiating event, a dramatic increase in PI is detected, indicating a compromised membrane in the target cell. (c) The average pixel intensity (mean \pm SD) of raw images in the ROI surrounding the tip apex (dotted circle in (b)) over the THz exposure duration. The onset of PI fluorescence in the target cell occurs within 2 minutes of initiation, with relatively little further change up to 10 minutes later. 208

Figure 8.7. **The cellular structure of skin tissue, and calcium-regulated gene expression of epidermal differentiation.** Skin is an organ comprised of epithelial epidermal and connective dermal tissues. The epidermis is comprised of four stratified layers: Basal layer (BL), spinous layer (SL), granular layer (GL), and the stratum corneum (SC). Snapshot in time of gene expression in the cellular layers during epidermal differentiation, adapted from [61, 62]. A calcium spike in the basal layer triggers a switch that expresses keratin 1 and 10 instead of

keratin 5 and 14. A steep calcium gradient across the epidermis then regulates the sequential expression of genes that encode for structural proteins that provide mechanical stability of skin, as detailed in the text body. 210

Figure 8.8. Intense THz pulses significantly downregulate membrane-related genes that regulate epidermal differentiation in human skin. Volcano plots display: (a) Significant downregulation of all gene families of Figure 8.7 involved in epidermal differentiation. (b) and genes that encode for membrane-bound cell-cell contacts (desmosomes, tight junctions, or adherens junctions). (c) Results of Gene Ontology analysis. There is significant over-representation of THz-downregulated genes in membrane-regulated biological processes and cellular structures. At right are examples of high-significance (top) vs. high odds-ratio (bottom) gene expressions that achieved significant over-representations within processes and structures that regulate epidermal differentiation. 212

Figure 9.1. Microtubule structure and fluorescence microscopy image. (a) Bound $\alpha\beta$ -tubulin dimers comprise the hydrogen-bonded protofilaments [20]. 13 protofilaments laterally bind to form a hollow cylindrical polymer with a 25 nm diameter. (b) Fluorescence image of rhodamine-labelled polymerized microtubules. The average length is 10 μm 221

Figure 9.2. THz source generation and exposure schematics. (a) The intense THz pulse source for tilted-pulse-front optical rectification in lithium niobate (LN, LiNbO_3), using an 1800 mm^{-1} reflective diffraction grating (RDG) and a pair of 4f-imaging lenses (L1 and L2), as described in [32]. Cross-absent bandpass filters (BPF) are used to isolate individual frequency bands. The THz beam is focused to either the sample location (beam propagating in the $+z$ direction out of the page), or to the EO sampling system (beam in the $-x$ direction) with a rotating gold off-axis parabolic mirror (ROAPM). A fraction of the pump pulse energy from a beamsplitter (BS) is attenuated (AT) and propagated colinearly with the THz beam for EO sampling in gallium phosphide (GaP). (b) The ROAPM is set at 0° ($+z$, upwards) for through-substrate exposure of MTs in solution. The fluorescence excitation line is focused through the hole in the mirror and propagates to the sample colinearly with the focusing THz beam. The sample fluorescence emission is collected by long-working distance objectives, passed through a $578\pm 16\text{ nm}$ bandpass filter, and analyzed in real-time with a CCD camera. For EO sampling, the ROAPM is set to 90° 224

Figure 9.3. Waveforms and spot areas for the intense THz pulse beam. (a) Broadband and bandpass EO sampled THz waveforms, shifted vertically as labelled for clarity. The peak

broadband field and pulse energy is 409 kV/cm and 1.2 μJ , respectively. (b) The corresponding power spectra and total energy transmission factors. (c) Pyroelectric camera image of the focused THz spot. Gaussian fits to horizontal (top) and vertical (left) line profiles define the $1/e^2$ broadband spot size as $1.5 \times 1.5 \text{ mm}^2$. The contours (right) represent the $1/e^2$ boundaries corresponding to the labelled frequency bands. For diffraction limited broadband beams, individual frequency bands focus to different areas of space..... 226

Figure 9.4. **Real-time fluorescence images for real-time imaging of THz-exposed MTs.** At low concentration (C_{ub} , left), MTs are individually resolvable and are stabilized at $\sim 10 \mu\text{m}$ in length. At high C_{ub} (right), MTs form large aggregate structures and are not individually resolvable. 228

Figure 9.5. **Broadband MT exposure results.** (a) High magnification (40x) fluorescence images of low tubulin concentration (0.25 mg/mL) show detailed structural disassembly to individual MTs. A single motion-tracked MT disassembling within 11 minutes of THz exposure. The ImageJ hill-shade algorithm is utilized to enhance edge contrast. (b) Low magnification (10x) images of high tubulin concentration (5 mg/mL) show large-scale disassembly of MT aggregate structures in a varying intensity distribution. The three sets of time-series images correspond to three $100 \times 100 \mu\text{m}^2$ regions indicated in the THz spot image (right), having approximate energy densities of 80, 50, and 30 $\mu\text{J}/\text{cm}^2$. Greater disassembly is observed in the highest intensity central region. (c) High magnification (40x) and high tubulin concentration (5 mg/mL) show MT aggregates in a nearly uniform intensity FOV. Both time series are separate results with similar pulse energy (1.2 μJ) and peak field (409 kV/cm [top] and 400 kV/cm [bottom]). At larger THz energy and field strengths, significant MT disassembly is observed within 5 min. Red labels highlight regions of MT polymer breakage..... 230

Figure 9.6. **Fluorescence imaging of tip-enhanced MT exposures.** When the THz beam is off, the labelled MTs aggregate on the conductive tip. Within 1 minute of THz exposure, a dramatic ejection and disassembly of MTs (red circles) from the tip apex is observed..... 231

Figure 9.7. **Analysis and results of MT exposures with varying spectral content.** (a) An example image analysis of MT structural change. By converting quantitative fluorescence images (column 1) to a binary image with a common threshold (column 2), the disassembly of MTs over time may be quantified by the change of area fraction with rhodamine signal above a common intensity threshold. The area fractions are determined by algorithmic contours with the ImageJ plugin, "Analyze Particles". The reduction of area fractions follow an exponential decay curve. (b) Fractional MT area calculated using the procedure in (a) for varying THz bands, with dashed curves representing exponential fits, and τ is the associated characteristic

time. Each dataset was normalized to the initial relative MT area. The exponential fit qualities (R^2) are 0.99, 0.96, and 0.92 for the broadband, 0.5 THz, and 1.5 THz fits, respectively. An equivalent analysis on unexposed MTs is included for reference. *Top*: The total pixel intensity of the raw images. The total rhodamine signal of all images does not degrade significantly (<5%) over the exposure duration, indicating the MT area fraction decay is not due to photobleaching. (c) The MT area fraction vs. total dose (J/cm^2), which corrects for differences in pulse energy and focused spot area (see Table 9.1). D_x is the characteristic dose for the corresponding curve ($\exp(-D/D_x)$). The characteristic total dose for the low-frequency 0.5 THz band ($1.4 J/cm^2$) is significantly lower than both the broadband and high-frequency 1.5 THz band ($13 J/cm^2$ and $23 J/cm^2$, respectively), indicating frequency-dependence of THz-induced MT disassembly, with greater disassembly induced by low-frequency THz energy (~ 0.5 THz). 233

Figure 9.8. Intense THz pulses significantly downregulate several members of tubulin/MT gene families. (a) Volcano plot showing differential expression of the tubulin superfamily and other microtubule-associated genes induced by intense THz pulses in human skin. Dashed lines indicate conventional thresholds of expression significance ($|\text{Log}_2(I/I_0)| > 0.58, p < 0.05$). Genes that encode for structural α/β tubulin (TUBA/TUBB) subunits are significantly downregulated. (b) Gene Ontology (GO) analysis of the global expression dataset identifies significant over-representation in eight cytoskeleton-related processes, components, and functions. 238

Figure 10.1. Raster-scanning a gaussian THz spot uniform THz intensity/frequency distributions of arbitrary growth areas. (a) 1D superposition of gaussian pulses with a step size of $\Delta x = 0.5$ mm, showing the creation of an approximately uniform energy distribution (black curve) from a raster-scanned THz pulse at dimensions suitable for large cell populations. (b) 2D superposition of Gaussian THz pulses showing uniform energy coverage of the desired geometry, and an enhanced intensity relative to single-spot exposures. 253

Figure A.1. Plot legend to assist the following pathway discussions. *Left*: A bar plot displaying the expression magnitude of genes within the considered pathway determined to be significantly differentially expressed by the highest THz intensity. In the top-right corner of each plot is the ratio of THz-affected genes to the total number of genes in the pathway. *Right*:

A two-way plot, displaying expression levels of all genes in the pathway, and the resulting accumulated perturbation assigned to each gene. Blue datapoints indicate genes that were affected by intense THz pulses and did not receive additional perturbation from upstream genes, but may contribute to downstream perturbation. Green points are genes that were not affected by THz, but were affected by upstream perturbations in the relevant network (but cannot cause further downstream perturbation). Red points are genes that were both expressed by THz exposure (and so may contribute to downstream perturbation) and were further affected by upstream perturbations in the associated gene interaction network. 298

Figure A.2. **Transcript-level sources of THz-induced dysregulation to *Cytokine-cytokine receptor interaction signaling***. 299

Figure A.3. **Transcript-level sources of THz-induced dysregulation to *Proteoglycan signaling in cancer***. 300

Figure A.4. **Transcript-level sources of THz-induced dysregulation to *cGMP-PKG signaling***. 301

Figure A.5. **Transcript-level sources of THz-induced dysregulation to *Calcium signaling***. 302

Figure A.6. **Transcript-level sources of THz-induced dysregulation to the *Regulation of actin cytoskeleton* pathway**. 303

Figure A.7. **Transcript-level sources of THz-induced dysregulation to *Rap1 signaling***. 304

Figure A.8. **Transcript-level sources of THz-induced dysregulation to *Ras signaling***. 305

Figure A.9. **Transcript-level sources of THz-induced dysregulation to *Glioma* signaling**. .. 306

Figure A.10. **Correspondence between SPIA analysis using conventional thresholds compared to cut-off free analysis (COFA)**. The main plot shows comparisons of the total accumulated perturbation between 40 pathways identified using both of the two methods ($p < 0.05$). The activation/inhibition status are consistent, with the exception of one pathway (*Axon guidance*; see Table A.1). *Inset*: The Venn diagram shows near total overlap of pathways identified using COFA with those identified with conventional thresholds. 309

List of tables

Table 1.1. **Publication rates by field search term (Web of Science 2018)**. 9

Table 1.2. **Sensitivity and specificity by cancer type with THz medical imaging** 11

Table 1.3. Structural hierarchy of biological systems. Functions of lower-level systems regulate processes observed in higher-level systems. This thesis reports direct investigation of the highlighted scales.	16
Table 2.1. Debye relaxation parameters for water and epidermal skin tissue.	33
Table 3.1. Ranges of THz pulse parameters, and the pulse with the highest achieved field. ..	75
Table 4.1. Typical range of THz pulse parameters and the pulse with the highest achieved field	93
Table 4.2. Incident broadband THz pulse parameters (black pulse in Figure 4.11(a)).	95
Table 5.1. Peak field and energy transmission ratios for potential substrate candidates	121
Table 6.1. Results of simulation for varying bio-exposure geometries. Maximum field and energy seen by the sample region in real bio-exposure experimental configurations. Integrals are normalized to tissue values, in which all energy is absorbed by the sample, and MBI effects are negligible.	154
Table 7.1. THz pulse parameters for each exposure condition	163
Table 7.2. Contingency table for GO over-representation analysis. The symbols A, B, C, and D, represent number of genes in each category for a given GO term.	167
Table 7.3. Total accumulated perturbation in cancer-associated signaling pathways for the highest pulse energy. Green (red) text represents inhibition (activation) of the pathway for the highest THz intensity.....	177
Table 7.4. Transcript-level terahertz targets. THz-affected genes (top five clusters) that maximally drive cancer signaling dysregulation for the highest pulse energy. Green (red) text represents downregulation/inhibition (upregulation/activation) of the gene/pathway for the highest THz intensity.....	177
Table 8.1. Typical dielectric parameters for animal cells [16, 38, 40].....	195
Table 8.2. THz pulse parameters for A-431 exposures	201
Table 8.3. THz pulse parameters for RBL-2H3 exposures	207
Table 9.1. THz pulse parameters for MT exposures	225
Table A.1. Pathways identified using both Conventional Thresholds and Cut-off Free Analysis (COFA).	310
Table A.2. Pathways identified by Cut-off Free Analysis not identified using Conventional Thresholds	311
Table A.3. Pathways identified using Conventional Thresholds not identified using Cut-off Free Analysis.	311

1 Introduction

1.1 Cancer in Canada

In 2019, there were 220,400 new cancer cases diagnosed in Canada, resulting in 82,100 deaths [1]. This is a five-year increase from 191,300 cases and 76,600 deaths reported in 2014, although encouragingly the mortality rate decreased by 2.7% [2]. The distribution of cancer incidence by sex and age is shown in Figure 1.1(a), and the deaths and mortality rate distributions are shown in Figure 1.1(b).

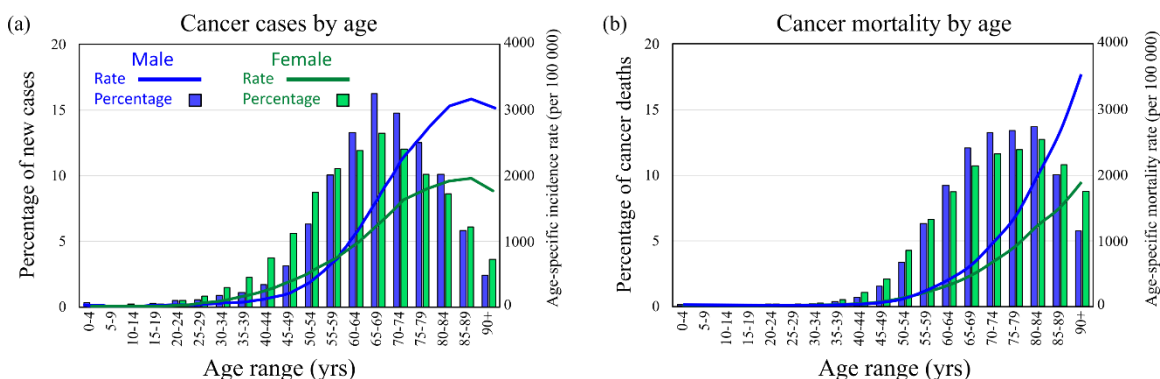


Figure 1.1. **2019 percentage of new cancer cases, deaths, and incidence/mortality rates in Canada by age.** Adapted from [1]. The percentage (bars, left axes) and rates (curves, right axes) of new cancer cases (a) and deaths (b).

It is estimated that roughly half of Canadians will receive a cancer diagnosis in their lifetime, and overall, cancer is the leading cause of death in Canada (29.6%) [1, 3]. The five-year net survival ratio in 2019 for all cancers was 63% (although this varies significantly by cancer type), representing an encouraging increase from 55% reported in the early 1990s, corresponding to an estimated 126,043 cancer deaths avoided by improvements in cancer technologies and patient care in that time.

The best opportunity for a positive prognosis is by early detection of pre-metastatic, localized malignant cells that may be surgically removed. Unfortunately, symptoms of cancer often do not present until advanced stages when simple resection is no longer possible. In these situations, cancer may be treated with pharmacological or radiation therapy approaches with various mechanisms of therapeutic action.

1.2 Therapeutic approaches to cancer

1.2.1 The hallmarks of cancer

Cancer is fundamentally a disease of the genome that manifests as dysregulation of normal biological function in service of sustaining cancer's life and amplifying its spread [4, 5]. In *The Emperor of All Maladies*, Siddhartha Mukherjee writes [6]:

“Cancer, in short, was not merely genetic in its origin; it was genetic in its entirety. Abnormal genes governed all aspects of cancer’s behavior. Cascades of aberrant signals, originating in mutant genes, fanned out within the cancer cell, promoting survival, accelerating growth, enabling mobility, recruiting blood vessels, enhancing nourishment, drawing oxygen – sustaining cancer’s life.”

While this passage predates modern understandings of epigenetic considerations for cancer [7], these words are a direct reference to a set of well-known principles in cancer science, the original “Six Hallmarks of Cancer” proposed by Hanahan & Weinberg in 2000 that provided a categorical framework with which to understand the diverse and complex set of processes that contribute to the initiation and progression of cancer [8]. These six distinct capabilities that enable tumor growth and metastatic invasion are:

1. Sustaining proliferative signaling
2. Evading growth suppressors
3. Activating invasion and metastasis
4. Enabling replicative immortality
5. Inducing angiogenesis
6. Resisting cell death

In 2011, Hanahan & Weinberg appended two additional hallmarks [9]:

7. Dysregulating cellular energetics
8. Avoiding immune destruction

that account for modern understandings of cancer-enabling characteristics such as genomic instability and tumor-promoting inflammation.

Importantly, these eight hallmarks are not merely descriptive, but rather prescriptive avenues along which anti-cancer therapies may be formulated. Successful therapeutic approaches for cancer involve direct counter-action of the cancer hallmarks, and commonly aim to inhibit proliferative signaling [10, 11, 12], amplify growth suppressors [13, 14], inhibit invasion and metastasis [15, 16], disable replicative immortality [17, 18], modulate tumor vasculature and oxygenation [19, 20], or activate cell death in tumor tissue [21]. Recent research in novel approaches to cancer therapy additionally seek to control cellular energetics [22, 23, 24], or activate immune responses [25, 26].

Cancer may arise and be treated through one or several of these mechanisms. Further, tumor tissue may acquire resistance to the therapeutic environment, and therefore a combined, adaptive approach is often utilized to maximize therapeutic effectiveness. Classically, the two non-surgical options for cancer therapies are chemotherapy or radiation therapy.

1.3 Radiation in medicine

While “radiation” is a general physical phenomenon encompassing all forms of transverse or longitudinal wave/particle emission and propagation, in medical contexts “radiation therapy” is more commonly understood as the use of ionizing particles or waves to destroy cancer cells. The historical origins of medical physics as a scientific discipline may be traced to seventeenth century Italy [27], however the use of ionizing radiation for medical application originates with Wilhelm Röntgen’s discovery of X-rays in 1895, followed by Henri Becquerel’s discovery of radioactivity in 1896. X-ray imaging applications were reported by 1895 and therapy applications with radioactive isotopes by 1896 [28, 29], although the interaction mechanisms and health consequences of ionizing radiation would not be discovered for some time. Indeed, while radiation is a powerful tool for anti-cancer therapies, the International Agency for Research on Cancer (IARC) has identified all types of ionizing radiation (including UVA) as a Group 1 carcinogen [30], and so balancing the therapeutic benefit with the risk of secondary malignancies that arise from the primary treatment is an important consideration [31, 32, 33].

The therapeutic mechanism of ionizing radiation therapies is the activation of cell death or permanent cell cycle arrest (senescence) in target tumor tissue [34]. Radiation-induced cell death may occur through several mechanisms, but the two dominant modes are apoptosis or mitotic catastrophe [35]. Apoptosis is a programmed cell death in response to irreparable radiation-induced DNA damage [21]. Most malignancies have inhibited pro-apoptotic activity (Hallmark #6), for example via impaired p53 function, and may acquire resistance to apoptosis activation [34]. In

these cases, mitotic catastrophe, or cell death activated by aberrant mitosis leading to formation of non-viable cells, is the dominant mode of radiation-induced cell-killing leading to increased tumor control [36].

1.3.1 Modern radiation therapy

Radiation may be delivered externally (external beam radiation therapy, EBRT) or with radioactive sources placed in or near the malignant tissue (brachytherapy). Modern advancements have produced a wide variety of radiotherapy modalities that primarily aim to improve therapeutic effectiveness of tumor-killing (increase tumor control probability, TCP), while reducing the necessary dose to incidental normal tissue structures (decreasing the normal tissue complication probability, NTCP) by more precise targeting of the treatment volume [37]. These treatment protocols are additionally assisted by developments in related areas such as machine learning [38], optimized dose fractionation [39], or development of pharmacological radiosensitizers [40].

Intensity-modulated radiation therapy (IMRT) is a 3D conformal adaptive approach that modulates the treatment beam intensity or shape during patient exposure to conform the dose distribution to the target treatment volume [41]. Volumetric modulated arc therapy (VMAT) is a popular form of IMRT that modulates the radiation beam during continuous gantry rotation [42]. Adaptive treatment modalities may also be combined with image-guided radiation therapy (IGRT) technologies, such as kV/MV projection, cone-beam CT (CBCT), or magnetic resonance imaging (MRI) modules integrated into the therapy gantry that utilize real-time imaging of the treatment volume during treatment to modulate the IMRT parameters in response to patient or tumor motion [43, 44]. Stereotactic radiosurgery (SRS) and stereotactic body radiation therapy (SBRT) provide even more dramatic levels of dose escalation in precisely contoured treatment volumes with the goal of ablation of deep-seated tumors [45].

1.3.2 Other forms of medical radiation therapy

Ionizing radiation therapies may also be in the form of particle beams such as electrons, protons, ions, or neutron beam therapies with varying energy deposition characteristics as shown in Figure 1.2. These modalities may be utilized for specific applications [46]. Electrons are used for treating surface lesions that do not require large penetration depths. Proton or ion beams deposit their energy in a highly localized deep-seated location, or Bragg peak, and are used for tumors close to critical organ structures such as spinal or ocular malignancies to spare essential structures.

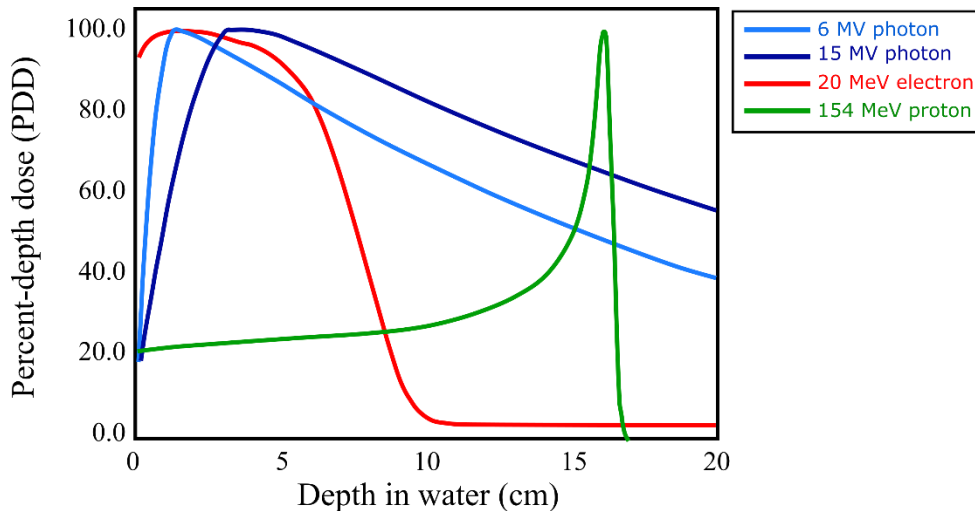


Figure 1.2. **Energy deposition characteristics (percent-depth dose (PDD) curves) in water for various forms of medical radiation.** $10 \times 10 \text{ cm}^2$ fields, 100 cm SAD/SSD, adapted from [46, 47]. Photons of varying beam energies are used for deep tissue irradiation, and normal tissues are spared by using multiple beams from varying angles and tumor-conforming beam filtration, or by modern radiotherapy modalities such as intensity-modulated or image-guided radiotherapy (IMRT, IGRT). Electrons are useful for treating surface lesions, although the Bremsstrahlung tail will deposit some dose in deep tissue. Proton beams deposit the majority of the beam energy in deep tissue, and are used for localized treatments of tumors near critical organ structures such as the eye or spine.

1.3.2.1 Therapeutic mechanisms of non-ionizing radiation

Emerging modalities for cancer therapy using various interaction mechanisms of non-ionizing radiation are also being investigated, as tissue interaction characteristics may avoid negative consequences of other therapies such as drug toxicity or radiation carcinogenesis [48]. Hyperthermal or nanoparticle-assisted radiofrequency ablation (HRFA/NP-RFA) of tumor tissue has demonstrated improved clinical outcome as an adjuvant therapy [49]. Photodynamic therapy utilizes visible light (400 – 700 nm) to generate reactive oxygen species in excited photosensitizers placed in tumor tissue, and has been successful as a therapy for recurrent surface lesions for nearly 40 years [50]. Electroporation, the use of electric pulses to target tissue to increase cellular uptake of drugs or dyes, may be combined with chemotherapy or immunotherapy to enhance the cytotoxic effect and increase tumor control [51, 52]. Tumor Treating Fields (TTFs) are continuously-applied low-power RF fields (100 – 300 kHz) that disrupt mitotic activity via frequency-dependent field-enhancement in the geometry of a dividing cell that induces aberrant mitosis, and therefore preferentially targets mitotically-active tissue [53]. TTFs have been recently approved by the FDA for astrocytoma glioblastoma multiforme [48, 54], and has shown therapeutic effectiveness for lung cancer in clinical trials [55].

One of the most interesting frequency bands for potential clinical application is the terahertz (THz) band, due to the high prevalence of natural oscillatory modes at several scales of biological structure that couple strongly to external excitations at similar frequencies, as discussed in the next section. Recent advances have dramatically increased the generation capabilities of THz radiation, and these have spurred a resurgence of research interest in the investigation of biological systems with THz radiation in recent decades. Several technologies now exist for diagnostic clinical use, and observations of non-thermal modulation of biological function induced by THz exposure suggest potential therapeutic mechanisms that may be exploited for novel clinical application.

1.4 Terahertz radiation

1.4.1 Introduction to terahertz radiation

Terahertz (THz) radiation is a non-ionizing form of electromagnetic (EM) energy that occupies a broad band between 0.1 and 10 THz ($3 - 300 \text{ cm}^{-1}$) at the interface of conventional microwave and infrared bands, as shown in the highlighted region of Figure 1.3. In the literature and media, “THz radiation” has also been popularly referred to as “sub-millimetre waves”, “far infrared”, “Tremendously High Frequency (THF)”, or “T-Rays”.

THz frequencies coincide with natural oscillatory dynamics of many physical phenomena, such as the rotational modes of gas molecules, low-frequency vibrational modes in solid molecules, and the vibrational/rotational modes of hydrogen bond networks [56, 57]. Additionally, vibrational dynamics of important biomolecules (e.g., all proteins, RNA/DNA, and membrane structures) occur on picosecond timescales, and therefore correspond to natural THz dynamics that may be externally coupled via EM THz excitation. The coupling to these modes suggests that THz radiation may be used as a sensitive modality to probe or excite natural dynamic behaviour in biological systems of interest. Further, intense pulses of THz radiation with high peak electric fields may non-thermally dysregulate the structural dynamics of biomolecules or cellular structures such that the associated biological function is compromised, and induce biological effects via an interaction mechanism that is unique to the THz band.

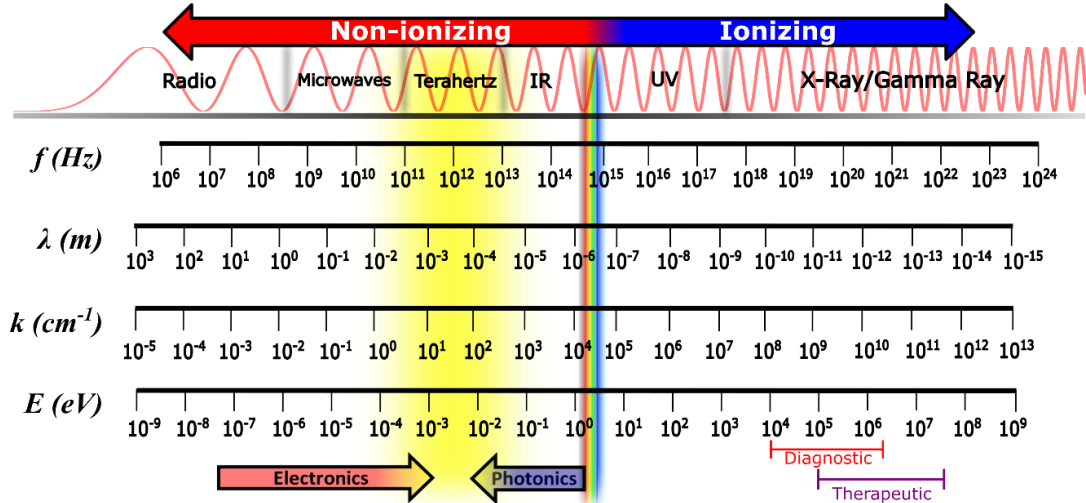


Figure 1.3. **The terahertz (THz) band of the electromagnetic (EM) spectrum.** The frequency (f), wavelength (λ), wavenumber (k), and photon energy (E) of the electromagnetic spectrum (logarithmic scales). The THz band (highlighted) is non-ionizing radiation between the microwave and infrared bands, and is a relatively underexplored region at the interface of conventional electronic and photonic regimes. Natural oscillatory dynamics of biomolecules and cellular structures occur at THz frequencies, and external excitation with EM energy at similar frequencies couples to these dynamics. Typical energy ranges for diagnostic and therapeutic applications of ionizing radiation are labelled for reference.

1.4.2 The “terahertz gap”

Non-ionizing radiation is typically classified by two distinct regimes of the EM spectrum [58]. Low frequencies (i.e., RF, microwave, $f < 100$ GHz) are the electronic regime, as the associated physics is fundamentally based on charge carrier transport (e.g., circuits, amplifiers, antennae, etc.). High frequencies (i.e., infrared, visible, $f > 10$ THz) are the photonic regime, which is understood by absorption and emission of photons due to discrete energy transitions in materials (e.g., lasers or semiconductors). In 1897, around the same time that ionizing radiation was first being applied for diagnostic and therapeutic purpose, Rubens & Nichols first acknowledged [59]:

“Since we have become accustomed to think of waves of electrical energy and light waves as forming component parts of a common spectrum, the attempt has often been made to extend our knowledge over the wide region which has separated the two phenomena, and to bring them closer together, either by cutting down the wave length of electric oscillations...or by the discovery and measurement of longer heat waves.”

This band at the interface between electronic and photonic regimes came to be known as the “terahertz gap”, due to the difficulties in generating and detecting THz waves by conventional methods and the lack of available technologies that operate in this intermediate range [60]. For this reason, progress in radiation research in the THz band relative to other EM bands has been hindered, particularly for research in biological systems, which require relatively high powers to penetrate and propagate in high-attenuation aqueous environments. Research and innovations over recent decades have bridged the THz gap, and today efficient sources and detectors for THz waves have been achieved from both the electronic and photonic sides of the THz band [61, 62, 63].

1.4.3 Growth of terahertz research

Representation of THz fields in research publications has increased significantly in recent decades. From 1993 – 2013, the number of research articles that relate to terahertz fields has increased exponentially with a doubling time (τ) of 3.8 years ($R^2=0.98$) [64]. For a breakdown by sub-discipline, the *Web of Science 2018* database was queried with field-specific keywords selected from reference [65], and the publication numbers from 1992 to 2018 were tabulated and fit to an exponential growth model. As shown in Table 1.1, these THz research fields fit reasonably well to this model, with the exception of defense (which may not be readily available from the searched database). THz-biomedical research is the smallest but fastest growing publication field ($\tau = 2.9$ yrs), followed by research in source technology ($\tau = 3.2$ yrs) and spectroscopy ($\tau = 3.4$ yrs) [64]. For relative context, similar data of articles related to sub-disciplines in Medical Physics are shown (radiation therapy, nuclear medicine, magnetic resonance imaging, and magnetic resonance spectroscopy), which show slower but more stable growth of a much larger volume of work in the same time frame.

Table 1.1. **Publication rates by field search term (Web of Science 2018).**

Field search term	Total Publications	Publication Doubling Time τ (yrs)	Exponential fit quality R^2
<i>Terahertz-related fields</i>			
Biomedical*	816	2.9	0.89
THz sources/detectors	1248	3.2	0.89
THz spectroscopy	3328	3.4	0.92
Communications	1889	3.5	0.97
Material science	6131	3.5	0.96
Terahertz*	7465	3.8	0.98
Space	2085	5.5	0.95
Defense/security	816	N/A	0.55
<i>Medical Physics</i>			
Magnetic resonance imaging	207711	8.5	0.99
Radiation therapy	107550	9.3	0.99
Nuclear medicine	14097	13.1	0.94
Magnetic resonance spectroscopy	40436	15.6	0.98

*=data from [64].

1.4.4 *Non-biomedical terahertz applications*

1.4.4.1 *Material science and spectroscopy*

As THz waves are non-ionizing, they may be used to non-destructively probe or modulate natural dynamics in systems of interest that occur on ultrafast timescales, such as photoexcited charge carrier dynamics in semiconductors [66] or natural vibrational or rotational dynamics in molecular structures [67]. Recent studies characterizing semiconductor surfaces utilizing THz-driven scanning tunneling microscopy (TD-STM) show that coupling the THz pulse to a sharp conductive tip leads to very large local THz field enhancement, and is capable of measuring electron tunneling dynamics and material conductivities on sub-picosecond timescales with atomic resolution [68].

1.4.4.2 *Astronomy and space physics*

Space is a highly active environment of THz radiation interactions: Roughly half of the energy radiated since the Big Bang has been absorbed by dust and re-emitted between 0.6 – 5 THz [69], and the cosmic microwave background spectrum is peaked at 0.16 THz [70, 71]. THz technologies are particularly well-suited for space and astronomy research due to the absence of attenuation and dispersion in vacuum [72]. The Herschel Space Observatory, a cosmic spectrometer that covers the

0.5 – 5 THz band [73], was formally proposed to the European Space Agency in 1982, construction commenced in 2001, and was launched in 2009 [72]. Herschel completed its mission in 2013, and data collected have been reported in hundreds of research publications that have significantly advanced knowledge on star formation, galaxy evolution, and water distribution in the Milky Way [69].

1.4.4.3 Communications

As demands for higher data rates and larger bandwidths for communication systems increase, accelerating data transfer will demand technologies that operate in the THz band (>100 of Gbit/s) [74]. Several suitable atmospheric windows have been identified and may be utilized for next-generation short-range high-speed wireless communication [75, 76]. For wired connections (e.g., fiber-optic or passive optical networks), expansion into THz data-transfer addresses a current technological bottle-neck and may provide real-time tele-conferencing with virtually no delay.

1.4.4.4 Defense and security

As THz waves transmit easily through most non-metallic and non-polar materials (plastics, ceramics, textiles), but are reflected and absorbed by skin, THz reflectance imaging is well-suited for detection of concealed objects [77, 78]. Further, dangerous or volatile materials such as explosives, illicit drugs, or chemical/biological agents often have quantifiable features in their THz dielectric spectrum that may be uniquely chemically identified and distinguished from non-hazardous items [79]. While Table 1.1 suggests that security is a relatively small THz specialization, it is also one of the most recognized in terms of commercial use, most popularly in airport scanners [78].

1.4.5 Biomedical applications of terahertz radiation

There are several motivating reasons for investigating biological interactions and medical capabilities of THz radiation [56, 64, 80]. THz photons are non-ionizing ($E \sim 4$ meV) with no risk of tissue damage at sufficiently low power. For diagnostic spectroscopy or imaging applications, coherent time-gated pulse detection provides very low noise levels and thus high SNR, and the strong absorption of THz radiation in aqueous environments results in highly localized interaction in the target tissue with very low scatter. Further, quantitative dielectric properties of the reflected

structures are encoded in the spectra of coherent time-domain waveforms, as outlined in Figure 1.4. Since these quantities often differ between diseased and healthy tissue, THz diagnostic probes often have inherent contrast without the need for additional contrast agents, allowing for quantitative diagnosis based on known dielectric properties of tissues of varying pathology. The interaction mechanisms between THz radiation and biological systems are discussed in more detail in the next chapter.

Advances in THz technologies have led to the development of clinical tools for diagnostic medical applications such as THz Pulsed Spectroscopy [81, 82, 83] and THz Pulsed Imaging [84, 85, 86, 87, 88, 89], for which the contrast mechanism is predominantly differential water content, cell density, and protein concentration [80, 90]. THz imaging for medical application has excellent soft tissue contrast, high SNR ($\sim 10^3 - 10^5$), reasonable resolution ($\sim 0.1 - 1$ mm features), and is often capable of diagnostic contrast between healthy and diseased (e.g., tumor) tissue, as well as discrimination between tumor sub-types [91]. Overviews of diagnostic THz applications over recent years are reviewed in references [56, 67, 80, 84, 92, 93, 94, 95].

1.4.5.1 *Diagnosis of cancer*

THz diagnostic technologies are capable of early detection of skin cancer, and have also been used as an intra-operative imaging tool during breast cancer surgery [81, 86]. Recent studies characterizing the current diagnostic capability of THz imaging indicate comparable or improved diagnostic capabilities relative to other emerging or conventional modalities [86, 96, 97, 98, 99, 100]. Table 1.2 summarizes ROC analysis results (sensitivities and specificities as calculated from diagnostic true-/false-positive ratios) that highlight the diagnostic capability of modern THz imaging technologies for three cancer types reported in the literature.

Table 1.2. Sensitivity and specificity by cancer type with THz medical imaging

Cancer Type	Sensitivity (%)	Specificity (%)	Reference
<i>Breast</i>	87 – 96	87 – 96	[86, 96, 97]
<i>Colon</i>	90 – 100	86 – 90	[98]
<i>Gastric</i>	96	84	[99]

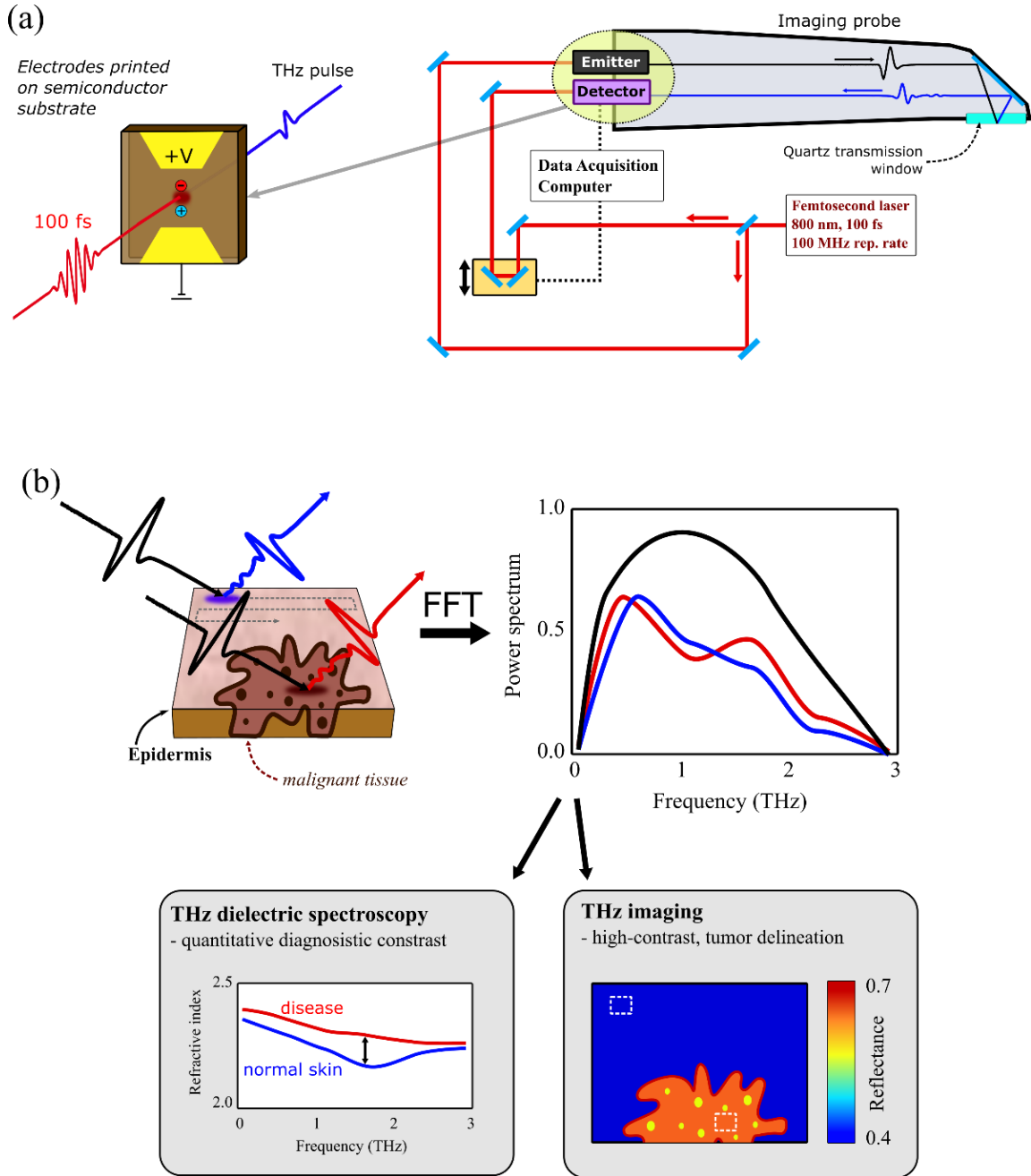


Figure 1.4. **Principle of THz reflection spectroscopy and imaging for diagnosis of diseased tissue.** Adapted from [84]. (a) Schematic of THz pulsed imaging acquisition. A femtosecond infrared laser source (800 nm) generates and coherently detects THz pulses via photoconductive switching on a semiconductor substrate [62]. THz pulses are transmitted through a quartz window on the scan probe face. (b) The THz pulses are raster-scanned across the imaging area, and reflected pulses for each pixel are detected in the time domain via electro-optic sampling. The Fourier transform provides the amplitude and phase information in the measured pulses, which may be utilized to determine dielectric properties of the scanned tissue. There are often quantitative differences in dielectric properties (e.g., the refractive index, left) between diseased and normal tissue that provide diagnostic contrast without the need for additional contrast agents. Alternatively, the dielectric data may be converted into a spatial representation for qualitative or quantitative THz imaging that provides high-contrast delineation of tumor margins.

1.4.5.2 *Tissue-water sensing for diagnosis and staging of wounds, burns, ocular disease, or diabetes*

Comparative studies tracking tissue water content (TWC) show that the THz reflection signal is linear with TWC concentration levels, and this correlation may be exploited as a quantitative metric for burn degree stage [89, 101, 102, 103], tissue damage status [104], or stage of wound healing [105].

THz sensing is also promising in ophthalmology due to sensitivity to corneal hydration levels [106]. This is an important diagnostic metric in characterizing several forms of ocular disease, such as corneal edema that may indicate underlying pathology. THz reflectivity measurements of corneal tissue are highly sensitive to small changes in hydration and may be applied in a clinical workflow for diagnosing corneal dystrophy, graft rejection, or refractive surgery staging.

THz imaging has also found niche application for non-invasive early diagnosis of diabetes by monitoring TWC of patient extremities [107]. Hernandez-Cardoso et al. have developed a THz imaging chamber that scans the sole of the foot of a seated patient through floor windows, and predicts the prevalence of diabetic foot syndrome by relative hydration levels [107]. Preliminary results suggest that THz characterization of extremity hydration may be utilized for early identification of potentially severe symptoms of advanced diabetes.

1.4.6 *Challenges and limitations*

The principal challenge in applying THz radiation to biological systems is the high absorption and dispersion of THz energy in aqueous environments. Figure 1.5 shows the refractive index and absorption coefficient as a function of THz frequency in liquid water, which are similar to measured values in biological media. Absorption and penetration (the depth at which energy falls to $1/e$) at 1 THz are about 230 cm^{-1} and $43\text{ }\mu\text{m}$, respectively. Therefore, applications are currently limited to those in which THz energy can be directly delivered, such as skin exposure, endoscopy, or during surgery [84]. Intense THz pulses with sufficiently low duty cycles and high peak intensities ($>\sim\text{MW}/\text{cm}^2$) can deliver appreciable energy to deeper regions, while maintaining low average intensities ($\sim\text{mW}/\text{cm}^2$) to minimize heating. It is important to note that these categories of “high and low” intensity are relative terms based on the possibility of inducing non-thermal biological effects in a given bio-system under study. The various types of THz sources, their exposure parameter ranges, and the biological effects that they have been observed to induce, are reviewed in Chapter 5, Section 5.2.

An additional limitation is the typical cost of commercial laser systems and THz source components for biomedical applications, ranging from \$50 000 to \$350 000, which may be above the typical price-point for technologies within the fields of immediate application.

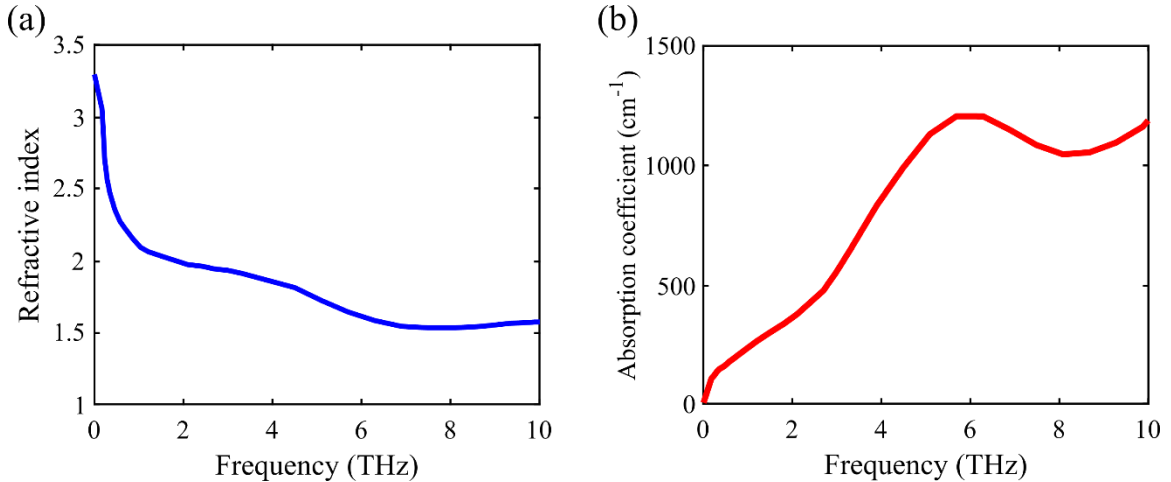


Figure 1.5. **Refractive index and absorption coefficient for liquid water in the THz band (0.1 – 10 THz).** Data were collected by Fourier transform spectroscopy, from [108]. (a) Water is highly dispersive. Low THz frequencies see a high index in liquid water, and therefore travel slower relative to high frequencies ($v = c/n$). (b) Water is highly absorptive, particularly for higher frequencies. At 1 THz, the absorption is 230 cm^{-1} , and has a corresponding characteristic penetration depth of $\delta=43 \text{ }\mu\text{m}$.

1.4.7 Biological effects, safety considerations, and potential therapeutic applications

Terahertz energy is absorbed strongly by tissue, and may induce biological effects by either thermal or non-thermal mechanisms. Continuous-wave (CW) THz beams, or pulsed beams with high duty cycles, induce significant heating in biological tissue characterized by the specific-absorption-rate (SAR) or average power density (i.e., intensity). However, Echchgadda et al. have shown that the response of cells heated by a CW THz beam relative to equivalent bulk-heated controls induced significantly different biological responses [109]. Moreover, heating cells with temperature-matched CW THz beams at different frequencies (1.4 THz, 2.52 THz, 3.11 THz) also induced differential biological responses, corroborating the hypothesized interaction mechanism of external EM energy coupling to natural oscillatory dynamics of biological systems, which is expected to be frequency-dependent [110]. While non-thermal interaction mechanisms of THz exposure are recognized by the International Committee for Non-ionizing Radiation Protection (ICNRP), the recommended safe exposure levels of THz radiation are extrapolated from thermal effects of microwaves [111]. However, several investigations, including collaborative global initiatives, have shown significant biological effects induced at absorbed power levels well below existing recommended levels, such as increased membrane permeability affecting signaling activity

in neurons, and several other indications of potentially significant biological effects [112, 113]. Further, recent investigations have established that single-cycle, picosecond duration THz pulses with high peak electric fields ($> \sim 500$ kV/cm) may induce dramatic modulation of biological function that is not explained by the estimated or measured temperature increase [114]. Various methods of characterizing the temperature rise induced by THz beams are detailed in Chapters 7 – 9.

Importantly, recent discoveries suggest several potential avenues for therapeutic application of THz radiation, such as inhibition of pro-mitotic signaling (Chapter 7) or disassembly of pro-mitotic structures (Chapter 9). Currently approved cancer therapies involve inhibition of proteins that are responsible for uncontrolled cell proliferation, or driving metastatic cells towards the apoptotic phenotype (e.g., by irreparably damaging DNA). However, many of these therapies include significant side effects, such as the absorption of ionizing radiation or systemic activity of anti-mitotic drugs in otherwise healthy tissue. Due to high absorption and very low scatter, non-ionizing THz exposures have a very high degree of conformality to the target region. Additionally, since applications are limited to areas of direct radiation delivery (skin, oral, endoscopic, intra-operative, etc.), exposure to normal tissue is minimal. Thus, THz exposures may be less susceptible to the disadvantages of current therapies. If a significant and predictable response can be shown to be therapeutically effective, it may offer a viable alternative for some cancers in the future.

1.5 Thesis statement and outline

1.5.1 Thesis statement


Natural oscillatory dynamics of important biomolecules occupy a wide band of THz frequencies (0.1 – 10 THz). Since structural dynamics are explicitly associated with biomolecular function, it is hypothesized that external excitation with EM energy at similar frequencies will couple to these dynamics, and sufficient field strength or pulse intensity may non-thermally dysregulate the structural dynamics to the point of affecting the associated function.

To investigate this hypothesis, two broad projects were pursued:

1. Design, construction, and characterization of a source of intense terahertz pulses dedicated to exposure and analysis of biological samples.
2. Performing THz exposures of protein complexes, cells, and skin tissue, and monitoring for structural or functional change induced by intense THz pulses.

This thesis reports investigations into the biological effects of intense THz pulses at three levels of biological organization highlighted in Table 1.3.

Table 1.3. **Structural hierarchy of biological systems.** Functions of lower-level systems regulate processes observed in higher-level systems. This thesis reports direct investigation of the highlighted scales.

 <p style="text-align: center;">Large/ complex</p> <p style="text-align: center;">Small/ fundamental</p>	Organism	<i>Human, dog, insect, fish, etc.</i>
	Organ system	<i>Integumentary, skeletal, circulatory, nervous, respiratory, endocrine, lymphatic, excretory, reproductive, digestive, muscular</i>
	Organs	<i>Brain, heart, lungs, skin, etc. (>79 total)</i>
	Tissues	<i>Epithelial, connective, nervous, muscular</i>
	Cells	<i>Fibroblast, keratinocyte, neuron, myocyte, etc. (~200 distinct types)</i>
	Molecules	<i>Proteins, membranes, DNA, microtubules, etc.</i>
	Atoms/ions	<i>Fundamental elements, charge carriers, messenger particles</i>

1.5.2 Outline

This introductory chapter began with recent statistics on the current state of cancer incidence and mortality in Canada, showing promising progress in recent years, but also highlighting the significant burden cancer continues to impose on Canadian and global health that motivate the continual search for novel diagnostic or therapeutic approaches to identify and treat cancer. General medical therapeutic approaches to cancer were described, including the role of ionizing radiation in modern cancer therapy. Background on THz radiation and its industrial and clinical applications were introduced. Current and future biomedical applications (including its potential role in cancer treatment) motivate our investigations of THz-induced biological effects.

Chapter 2 discusses THz dynamics in biological systems and theoretical interaction mechanisms of THz radiation that motivate the primary hypothesis: Intense THz pulses may non-thermally dysregulate biological function via coupling to natural oscillatory dynamics of important structures. Three mathematical models are outlined that characterize THz interactions from dielectric, energetic, and mechanical perspectives, and all posit significant modulations to biological structure or function via non-thermal interaction mechanisms. A review of biological effects induced by THz radiation reported in the literature is also presented.

Chapters 3 and 4 describe the theory, design, construction, and characterization of the THz radiation source used for biological exposures. Chapter 3 introduces the theory of nonlinear optics relevant to laser-based generation of intense THz pulses, and describes the operation principles of the laser systems and THz source. Chapter 4 provides a comprehensive guide for measuring THz pulse parameters and beam characteristics for accurate determination of THz exposure conditions. An explicit spectral decomposition of the broadband THz beam using bandpass filters provides a detailed analysis of the frequency distribution in space and time, and time-domain analysis of a focusing beam characterizes field changes that arise due to geometrical phase modulations.

Chapter 5 describes the integration of the THz source into the larger system dedicated for exposure and analysis of a variety of biological systems. This includes the design and construction of an environmentally-controlled sample holder, characterization of apposite substrates suitable for both sample growth and THz transmission, and real-time analysis of biological structure or function (light microscopy, fluorescence microscopy, or spectroscopy). Modification to the THz exposure system for normal-incidence THz reflection spectroscopy of biological samples is also presented.

Chapter 6 presents a theoretical formalism for coherent THz pulse simulation for dosimetry in common biological exposure configurations, and is the bridge between the constructed THz bio-exposure system described in the previous chapters to the biological exposure studies reported in the following chapters. A dose model inspired by coherent dielectric spectroscopy theory is presented, and limitations of standard THz bio-exposure geometries motivate a theory that accounts for coherent characterization in many optically thin samples that is not well-characterized by existing methods. A novel, quasi-analytic method of constructing a transfer function that characterizes the field dynamics and energy deposition in space and time is utilized to determine significant dose variations in THz exposures depending on the chosen exposure geometry. These results may then be applied to adjust dosimetric parameters reported in the exposure studies.

Chapters 7, 8, and 9 discuss experiments investigating the biological effects of intense THz pulses at the three scales of biological organization highlighted in Table 1.3. Experiments at the tissue level are the focus of Chapter 7. Bioinformatics analyses are applied to global gene expression profiles to predict the biological processes expected to be dysregulated by THz exposure, and gene-level sources of THz-induced signaling dysregulation are identified. From these data, intense THz pulses are predicted to inhibit proliferative signaling pathways in skin by direct downregulation of proto-oncogene transcripts. Chapter 8 discusses experiments at the cellular level, including THz-induced permeabilization of the plasma membrane in human and rat cell lines as detected by high-resolution and real-time fluorescence microscopy. Chapter 9 discusses the

molecular level, and describes observations of THz-induced disassembly of microtubules, a filamentous protein complex essential in mitosis, and a common target of conventional cancer therapies. These results are presented in the context of potential therapeutic mechanisms for clinical applications of intense THz pulses.

Finally, the appendix provides additional details on calculations, analyses, or discussions that were not included in the main text.

1.6 References

- [1] Canadian Cancer Society's Advisory Committee on Cancer Statistics, "Canadian Cancer Statistics 2019," Canadian Cancer Society, Statistics Canada, Toronto, ON, 2019.
- [2] Canadian Cancer Society's Advisory Committee on Cancer Statistics, "Canadian Cancer Statistics 2014 Special Topic: Skin cancers," Canadian Cancer Society, Statistics Canada, Toronto, ON, 2014.
- [3] D. R. Brenner, H. K. Weir, A. A. Demers, L. F. Ellison, C. Louzado, A. Shaw, D. Turner, R. R. Woods and L. M. Smith, "Projected estimates of cancer in Canada in 2020," *Canadian Medical Association Journal*, vol. 192, no. 9, pp. E199 - E205, 2020.
- [4] M. R. Stratton, P. J. Campbell and P. A. Futreal, "The cancer genome," *Nature*, vol. 458, no. 7239, pp. 719 - 724, 2009.
- [5] L. E. MacConaill and L. A. Garraway, "Clinical Implications of the Cancer Genome," *Journal of Clinical Oncology*, vol. 28, no. 35, pp. 5219 - 5228, 2010.
- [6] S. Mukherjee, *The Emperor of All Maladies: A Biography of Cancer*, New York, NY: Scribner, 2011.
- [7] H. Takeshima and T. Ushijima, "Accumulation of genetic and epigenetic alterations in normal cells and cancer risk," *Precision Oncology*, vol. 3, no. 7, pp. 1 - 8, 2019.
- [8] D. Hanahan and R. A. Weinberg, "The Hallmarks of Cancer," *Cell*, vol. 100, pp. 57 - 70, 2000.
- [9] D. Hanahan and R. A. Weinberg, "Hallmarks of Cancer: The Next Generation," *Cell*, vol. 144, pp. 646 - 674, 2011.
- [10] J. Baselga and C. L. Arteaga, "Critical Update and Emerging Trends in Epidermal Growth Factor Receptor Targeting in Cancer," *Journal of Clinical Oncology*, vol. 23, no. 11, pp. 2445 - 2459, 2005.
- [11] A. Takashima and D. Faller, "Targeting the RAS Oncogene," *Expert Opinion on Therapeutic Targets*, vol. 17, no. 5, pp. 507 - 531, 2013.

- [12] P. J. Roberts and C. J. Der, "Targeting the Raf-MEK-ERK mitogen-activated protein kinase cascade for the treatment of cancer," *Oncogene*, vol. 26, pp. 3291 - 3310, 2007.
- [13] T. Abbas and A. Dutta, "p21 in cancer: intricate networks and multiple activities," *Nature Reviews Cancer*, vol. 9, no. 6, pp. 400 - 414, 2009.
- [14] M. Ruas and G. Peters, "The p16INK4a/CDKN2A tumor suppressor and its relatives," *Biochimica et Biophysica Acta - Reviews on Cancer*, vol. 1378, pp. F115 - F177, 1998.
- [15] R. A. Parikh, P. Wang, J. H. Beumer, E. Chu and L. J. Appleman, "The potential roles of hepatocyte growth factor (HGF)-MET pathway inhibitors in cancer treatment," *OncoTargets and Therapy*, vol. 7, pp. 969 - 983, 2014.
- [16] G. V. Scagliotti, S. Novello and J. von Pawel, "The emerging role of MET/HGF inhibitors in oncology," *Cancer Treatment Reviews*, vol. 39, no. 7, pp. 793 - 801, 2013.
- [17] C. B. Harley, "Telomerase and cancer therapeutics," *Nature Reviews Cancer*, vol. 8, no. 3, pp. 167 - 179, 2008.
- [18] M. Ruden and N. Puri, "Novel anticancer therapeutics targeting telomerase," *Cancer Treatment Reviews*, vol. 39, no. 5, pp. 444 - 456, 2013.
- [19] M. Shibuya, "VEGF-VEGFR Signals in Health and Disease," *Biomolecules and Therapeutics*, vol. 22, no. 1, pp. 1 - 9, 2014.
- [20] D. W. Siemann and M. R. Horsman, "Modulation of the tumor vasculature and oxygenation to improve therapy," *Pharmacology & Therapeutics*, vol. 153, pp. 107 - 124, 2015.
- [21] I. M. Ghobrial, T. E. Witzig and A. A. Adjei, "Targeting Apoptosis Pathways in Cancer Therapy," *CA Cancer Journal for Clinicians*, vol. 55, no. 3, pp. 178 - 194, 2005.
- [22] M. G. Vander-Heiden, L. C. Cantley and C. B. Thompson, "Understanding the Warburg Effect: The Metabolic Requirements of Cell Proliferation," *Science*, vol. 324, no. 5930, pp. 1029 - 1033, 2009.
- [23] N. Hay, "Reprogramming glucose metabolism in cancer: can it be exploited for cancer therapy?," *Nature Reviews Cancer*, vol. 16, pp. 635 - 649, 2016.
- [24] B. J. Altman, Z. E. Stine and C. V. Dang, "From Krebs to clinic: glutamine metabolism in cancer therapy," *Nature Reviews Cancer*, vol. 16, pp. 619 - 634, 2016.
- [25] Z. Hu, P. A. Ott and C. J. Wu, "Towards personalized, tumour-specific therapeutic vaccines for cancer," *Nature Reviews Immunology*, vol. 18, no. 3, pp. 168 - 182, 2018.
- [26] A. D. Waldman, J. M. Fritz and M. J. Lenardo, "A guide to cancer immunotherapy: from T cell basic science to clinical practice," *Nature Reviews Immunology*, vol. 20, pp. 651 - 668, 2020.

- [27] F. A. Duck, "The origins of medical physics," *Physica Medica*, vol. 30, pp. 397 - 402, 2014.
- [28] M. Cohen and N. G. Trott, "Radiology, physical science, and the emergence of medical physics," *Medical Physics*, vol. 22, no. 11, pp. 1889 - 1897, 1995.
- [29] T. Bortfeld and R. Jeraj, "The physical basis and future of radiation therapy," *British Journal of Radiology*, vol. 84, no. 1002, pp. 485 - 498, 2011.
- [30] International Agency for Research on Cancer, "List of Classifications, Agents classified by the IARC Monographs, Volumes 1 - 124," IARC Monographs on the Evaluation of Risk to Humans, 2021.
- [31] E. J. Hall and C. -S. Wu, "Radiation-induced second cancers: the impact of 3D-CRT and IMRT," *International Journal of Radiation Oncology Biology Physics*, vol. 56, no. 1, pp. 83 - 88, 2003.
- [32] W. D. Newhauser and M. Durante, "Assessing the risk of second malignancies after modern radiotherapy," *Nature Reviews Cancer*, vol. 11, pp. 438 - 448, 2011.
- [33] D. Williams, "Radiation carcinogenesis: lessons from Chernobyl," *Oncogene*, vol. 27, pp. S9 - S18, 2009.
- [34] E. Hall, *Radiobiology for the Radiologist*, Philadelphia, PA: Lippincott, Williams & Wilkins, 2000.
- [35] D. Eriksson and T. Stigbrand, "Radiation-induced cell death mechanisms," *Tumor Biology*, vol. 31, no. 4, pp. 363 - 372, 2010.
- [36] I. B. Roninson, E. V. Broude and B. -D. Chang, "If not apoptosis, then what? Treatment-induced senescence and mitotic catastrophe in tumor cells," *Drug Resistance Updates*, vol. 4, no. 5, pp. 303 - 313, 2001.
- [37] L. B. Marks and J. Ma, "Challenges in the clinical application of advanced technologies to reduce radiation-associated normal tissue injury," *International Journal of Radiation Oncology Biology Physics*, vol. 69, no. 1, pp. 4 - 12, 2007.
- [38] S. Cui, H. -H. Tseng, J. Pakela, R. K. Ten Haken and I. E. Naqa, "Introduction to machine and deep learning for medical physicists," *Medical Physics*, vol. 47, no. 5, pp. e127 - e147, 2020.
- [39] K. A. Ahmed, C. R. Correa, T. J. Dilling, N. G. Rao, R. Shridhar, A. M. Trotti, R. B. Wilder and J. J. Caudell, "Altered fractionation schedules in radiation treatment: a review," *Seminars in Oncology*, vol. 41, no. 6, pp. 730 - 750, 2014.
- [40] H. Wang, X. Mu, H. He and X. -D. Zhang, "Cancer Radiosensitizers," *Trends in Pharmacological Sciences*, vol. 39, no. 1, pp. 24 - 48, 2018.
- [41] T. Bortfeld, "IMRT: a review and preview," *Physics in Medicine and Biology*, vol. 51, pp. R363 - R379, 2006.

- [42] K. Otto, "Volumetric modulated arc therapy: IMRT in a single gantry arc," *Medical Physics*, vol. 35, no. 1, pp. 310 - 317, 2008.
- [43] L. A. Dawson and D. A. Jaffray, "Advances in Image-Guided Radiation Therapy," *Journal of Clinical Oncology*, vol. 25, no. 8, pp. 938 - 946, 2007.
- [44] Canadian Agency for Drugs and Technologies in Health, "Magnetic Resonance Guided Radiotherapy: MR-simulation and MR-linac," *CADTH Issues in Emerging Health Technologies*, no. 181, pp. 1 - 14, 2020.
- [45] R. D. Timmerman, B. D. Kavanagh, C. Cho, L. Papiez and L. Xing, "Stereotactic Body Radiation Therapy in Multiple Organ Sites," *Journal of Clinical Oncology*, vol. 25, no. 8, pp. 947 - 952, 2007.
- [46] F. Khan, *The physics of radiation therapy*, Philadelphia, PA: Lippincott Williams & Wilkins, 2003.
- [47] W. D. Newhauser and R. Zhang, "The physics of proton therapy," *Physics in Medicine and Biology*, vol. 60, pp. R155 - R209, 2015.
- [48] M. -O. Mattsson and M. Simko, "Emerging medical applications based on non-ionizing electromagnetic fields from 0 Hz to 10 THz," *Medical Devices: Evidence and Research*, vol. 12, pp. 347 - 368, 2019.
- [49] H. P. Kok, P. Wust, P. R. Stauffer, F. Bardati, G. C. van Rhoon and J. Crezee, "Current state of the art of regional hyperthermia treatment planning: a review," *Radiation Oncology*, vol. 10, no. 196, pp. 1 - 14, 2015.
- [50] X. Li, J. F. Lovell, J. Yoon and X. Chen, "Clinical development and potential of photothermal and photodynamic therapies for cancer," *Nature Reviews Clinical Oncology*, vol. 17, pp. 657 - 674, 2020.
- [51] M. Belehradek, C. Domenge, B. Luboinski, S. Orłowski, J. Belehradek and L. M. Mir, "Electrochemotherapy, a new antitumor treatment. First clinical phase I-II trial," *Cancer*, vol. 72, no. 12, pp. 694 - 700, 1993.
- [52] C. Y. Calvet and L. M. Mir, "The promising alliance of anti-cancer electrochemotherapy with immunotherapy," *Cancer Metastasis Review*, vol. 35, pp. 165 - 177, 2016.
- [53] M. Giladi, R. S. Schneiderman, T. Voloshin, Y. Porat, M. Munster, R. Blat, S. Sherbo, Z. Bomzon, N. Urman, A. Itzhaki, S. Cahal, A. Shteingauz, A. Chaudhry, E. D. Kirson, U. Weinberg and Y. Palti, "Mitotic Spindle Disruption by Alternating Electric Fields Leads to Improper Chromosome Segregation and Mitotic Catastrophe in Cancer Cells," *Scientific Reports*, vol. 5, no. 18046, 2015.
- [54] K. D. Swanson, E. Lok and E. T. Wong, "An Overview of Alternating Electric Fields Therapy (NovoTTF Therapy) for the Treatment of Malignant Glioma," *Current Neurology and Neuroscience Reports*, vol. 16, no. 8, pp. 1 - 10, 2016.

- [55] M. Pless, C. Droege, R. von Moos, M. Salzberg and D. Betticher, "A phase I/II trial of Tumor Treating Fields (TTFields) therapy in combination with pemetrexed for advanced non-small cell lung cancer," *Lung Cancer*, vol. 81, pp. 445 - 450, 2013.
- [56] J.-H. Son, Terahertz Biomedical Science and Technology, Boca Raton, FL: CRC Press, 2014.
- [57] M. Hoffmann and J. Fülöp, "Intense ultrashort terahertz pulses: generation and applications," *Journal of Physics D: Applied Physics*, vol. 44, no. 8, p. 083001, 2011.
- [58] J. Chamberlain, R. Miles, C. Collins and D. Steenson, "Introduction to Terahertz Solid-state Devices," in *New Directions in Terahertz Technology*, Netherlands, Kluwer Academic Publishers, 1997, pp. 3-27.
- [59] H. Rubens and E. Nichols, "Heat rays of great wave-length," *Physical Review (Series I)*, vol. 4, no. 4, pp. 314 - 323, 1897.
- [60] J. Chamberlain, "Where optics meets electronics: recent progress in decreasing the terahertz gap," *Philosophical Transactions of the Royal Society*, vol. 362, pp. 199 - 213, 2004.
- [61] R. A. Lewis, "A review of terahertz sources," *Journal of Physics D: Applied Physics*, vol. 47, 2014.
- [62] Y. Lee, Principles of Terahertz Science and Technology, New York, NY: Springer, 2009.
- [63] F. Blanchard, G. Sharma, L. Razzari, X. Ropagnol, H. -C. Bandulet, F. Vidal, R. Morandotti, J. -C. Kieffer, T. Ozaki, H. Tiedje, H. Haugen, M. Reid and F. Hegmann, "Generation of Intense Terahertz Radiation via Optical Methods," *IEEE Journal of Selected Topic in Quantum Electronics*, vol. 17, no. 1, pp. 5 - 16, 2011.
- [64] S. Fan, Y. He, B. S. Ung and E. Pickwell-MacPherson, "The growth of biomedical terahertz research," *Journal of Physics D: Applied Physics*, vol. 47, pp. 1 - 11, 2014.
- [65] S. S. Dhillon, M. S. Vitiello, E. H. Linfield, A. G. Davies, M. C. Hoffmann, J. Booske, C. Paoloni, M. Gensch, P. Weightman, G. P. Williams, E. Castro-Camus, D. R. Cumming, F. Simoens, I. Escorcia-Carranza, J. Grant, S. Lucyszyn, M. Kuwata-Gonokami, K. Konishi, M. Koch, C. A. Schmuttenmaer, T. L. Cocker, R. Huber, A. G. Markelz, Z. D. Taylor, V. P. Wallace, J. A. Zeitler, J. Sibik, T. M. Korter, B. Ellison, S. Rea, P. Goldsmith, K. B. Cooper, R. Appleby, D. Pardo, P. G. Huggard, V. Krozer, H. Shams, M. Fice, C. Renaud, A. Seeds, A. Stöhr, M. Naftaly, N. Ridler, R. Clarke, J. E. Cunningham and M. B. Johnston, "The 2017 terahertz science and technology roadmap," *Journal of Physics D: Applied Physics*, vol. 50, no. 043001, pp. 1 - 49, 2017.
- [66] D. N. Purschke, M. Na, A. Longman, L. V. Titova and F. A. Hegmann, "Enhancement of hot-carrier photoluminescence with intense terahertz pulses," *Applied Physics Letters*, vol. 112, no. 072105, pp. 1 - 5, 2018.

- [67] P. Jepsen, D. Cooke and M. Koch, "Terahertz spectroscopy and imaging - Modern techniques and applications," *Laser and Photonics Reviews*, vol. 5, no. 1, pp. 124-166, 2011.
- [68] V. Jelic, K. Iwaszczuk, P. Nguyen, C. Rathje, G. Hornig, H. Sharum, J. Hoffman, M. Freeman and F. Hegmann, "Ultrafast terahertz control of extreme tunnel currents through single atoms on a silicon surface," *Nature Physics*, vol. 13, no. 6, pp. 591 - 598, 2017.
- [69] Eales, S. et al., "The Herschel ATLAS," *Publications of the Astronomical Society of the Pacific*, vol. 122, pp. 499 - 515, 2010.
- [70] National Aeronautics and Space Administration, "NASA Missions - Herschel," [Online]. Available: https://www.nasa.gov/mission_pages/Herschel/index.html.
- [71] J. C. Mather, E. S. Cheng, R. E. Eplee, R. B. Isaacman, S. S. Meyer, R. A. Shafer, R. Weiss, E. L. Wright, C. L. Bennett, N. W. Beggess, E. Dwek, S. Gulikis, M. G. Hauser, M. Janssen, T. Kelsall, P. M. Lubin, S. H. Moseley, T. L. Murdock, R. F. Silverberg, G. F. Smoot and D. T. Wilkinson, "A preliminary measurement of the cosmic microwave background spectrum by the Cosmic Background Explorer (COBE) satellite," *The Astrophysical Journal*, vol. 354, pp. L37 - L40, 1990.
- [72] G. L. Pilbratt, J. R. Riedinger, T. Passvogel, G. Crone, D. Doyle, U. Gageur, A. M. Heras, C. Jewell, L. Metcalfe, S. Ott and M. Schmidt, "Herschel Space Observatory: An ESA facility for far-infrared and submillimetre astronomy," *Astronomy and Astrophysics*, vol. 518, pp. 1 - 6, 2010.
- [73] "Herschel," European Space Agency, [Online]. Available: <https://sci.esa.int/web/herschel>.
- [74] T. Kleine-Ostmann and T. Nagatsuma, "A review on terahertz communication research," *Journal of Infrared, Millimeter, and Terahertz Waves*, vol. 32, no. 2, pp. 143 - 171, 2011.
- [75] J. Ma, R. Shrestha, L. Moeller and D. M. Mittleman, "Invited Article: Channel performance for indoor and outdoor terahertz wireless links," *APL Photonics*, vol. 3, no. 051601, 2018.
- [76] M. A. Salhi, T. Kleine-Ostmann and T. Schrader, "Propagation Channel Measurements in the mm- and Sub-mm Wave Range for Different Indoor Communication Scenarios," *Journal of Infrared, Millimeter, and Terahertz Waves*, vol. 42, pp. 357 - 370, 2021.
- [77] J. F. Federici, B. Schulkin, F. Huang, D. Gary, R. Barat, F. Oliveira and D. Zimdars, "THz imaging and sensing for security applications - explosives, weapons, and drugs," *Semiconductor Science and Technology*, vol. 20, pp. S266 - S280, 2005.
- [78] D. Woolard, E. Brown, M. Pepper and M. Kemp, "Invited Paper: Terahertz frequency sensing and imaging: A time of reckoning for future applications?," *Proceedings of IEEE*, vol. 93, no. 10, pp. 1722 - 1745, 2005.

- [79] J. B. Sleiman, J. -B. Perraud, B. Bousquet, J. -P. Guillet, N. Palka and P. Mounaix, "Identifying explosives by chemometrics with terahertz spectral imaging," *Proceedings of SPIE*, no. 10.1117, 2015.
- [80] E. Pickwell and V. P. Wallace, "Biomedical applications of terahertz technology," *Journal of Physics D: Applied Physics*, vol. 39, no. 17, pp. R301 - R310, 2006.
- [81] P. Ashworth, E. Pickwell-MacPherson, E. Provenzano, E. Pinder, S. Purushotham and M. Pepper, "Terahertz pulsed spectroscopy of freshly excised human breast cancer," *Optics Express*, vol. 17, no. 5, pp. 12444 - 12454, 2009.
- [82] V. P. Wallace, A. J. Fitzgerald, E. Pickwell, R. J. Pye, P. F. Taday, N. Flanagan and T. Ha, "Terahertz Pulsed Spectroscopy of Human Basal Cell Carcinoma," *Applied Spectroscopy*, vol. 60, no. 10, pp. 1127 - 1133, 2006.
- [83] C. B. Reid, G. Reese, A. P. Gibson and V. P. Wallace, "Terahertz Time-Domain Spectroscopy of Human Blood," *IEEE Journal of Biomedical and Health Informatics*, vol. 17, no. 4, pp. 774 - 778, 2013.
- [84] E. Pickwell-MacPherson and V. Wallace, "Terahertz pulsed imaging - A potential medical imaging modality?," *Photodiagnosis and Photodynamic Therapy*, vol. 6, no. 2, pp. 128 - 134, 2009.
- [85] V. Wallace, A. Fitzgerald, S. Shankar, N. Flanagan, R. Pye, J. Cluff and D. Arnone, "Terahertz pulsed imaging of basal cell carcinoma ex vivo and in vivo," *British Journal of Dermatology*, vol. 151, pp. 424-432, 2004.
- [86] A. Fitzgerald, V. Wallace, M. Jimenez-linan, L. Bobrow, R. Pye and A. Purushotham, "Terahertz Pulsed Imaging of human breast tumors," *Radiology*, vol. 239, no. 2, pp. 533 - 540, 2006.
- [87] R. M. Woodward, B. E. Cole, V. P. Wallace, R. J. Pye, D. D. Arnone, E. H. Linfield and M. Pepper, "Terahertz pulse imaging in reflection geometry of human skin cancer and skin tissue," *Physics in Medicine and Biology*, vol. 47, no. 21, pp. 3853 - 3863, 2002.
- [88] C. B. Reid, A. Fitzgerald, G. Reese, R. Goldin, P. Tekkis, P. S. O'Kelly, E. Pickwell-MacPherson, A. P. Gibson and V. P. Wallace, "Terahertz pulsed imaging of freshly excised human colonic tissues," *Physics in Medicine and Biology*, vol. 56, no. 14, 2011.
- [89] D. M. Mittleman, M. Gupta, R. Neelamani, R. G. Baraniuk, J. V. Rudd and M. Koch, "Recent advances in terahertz imaging," *Applied Physics B: Lasers and Optics*, vol. 68, pp. 1085 - 1094, 1999.
- [90] A. Panwar, A. Singh, A. Kumar and H. Kim, "Terahertz Imaging System for Biomedical Applications: Current Status," *International Journal of Engineering and Technology*, vol. 13, no. 2, pp. 33 - 39, 2013.
- [91] M. -A. Brun, F. Formanek, A. Yasuda, M. Sekine, N. Ando and Y. Eishii, "Terahertz imaging applied to cancer diagnosis," *Physics in Medicine and Biology*, vol. 55, no. 16, pp. 4615 - 4623, 2010.

- [92] O. Smolyanskaya, N. Chernomyrdin, A. Konovko, K. Zaytsev, I. Ozheredov, O. Cherkasova, M. Nazarov, J.-P. Guillet, S. Kozlov, Y. V. Kistenev, J.-L. Coutaz, P. Mounaix, V. Vaks, J.-H. Son, H. Cheon and V. Wallace, "Terahertz biophotonics as a tool for studies of dielectric and spectral properties of biological tissues and liquids," *Progress in Quantum Electronics*, vol. 62, pp. 1-77, 2018.
- [93] X. Yang, X. Zhao, K. Yang, Y. Liu, Y. Liu, W. Fu and Y. Luo, "Biomedical Applications of Terahertz Spectroscopy and Imaging," *Trends in Biotechnology*, vol. 34, no. 10, pp. 810 - 824, 2016.
- [94] A. I. Nikitkina, P. Y. Bikmulina, E. R. Gafarova, N. V. Kosheleva, Y. M. Efremov, E. A. Bezrukov, D. V. Butnaru, I. N. Dolganova, N. V. Chernomyrdin, O. P. Cherkasova, A. A. Gavdush and P. S. Timashev, "Terahertz radiation and the skin: a review," *Journal of Biomedical Optics*, vol. 26, no. 4, pp. 1 - 26, 2021.
- [95] P. H. Siegel, "Terahertz Technology in Biology and Medicine," *IEEE Transactions on Microwave Theory and Techniques*, vol. 4, pp. 1575 - 1578, 2004.
- [96] T. Bowman, T. Chavez, K. Khan, J. Wu, A. Chakraborty, N. Rajaram, K. Bailey and M. El-Shenawee, "Pulsed terahertz imaging of breast cancer in freshly excised murine tumors," *Journal of Biomedical Optics*, vol. 23, no. 2, pp. 1 - 13, 2018.
- [97] M. Grootendorst, A. J. Fitzgerald, S. G. Brouwer de Koning, A. Santaolalla, A. Portieri, M. Van Hemelrijck, M. R. Young, J. Owen, M. Cariati, M. Pepper, V. P. Wallace, S. E. Pinder and A. Purushotham, "Use of a handheld terahertz pulsed imaging device to differentiate benign and malignant breast tissue," *Biomedical Optics Express*, vol. 8, no. 6, 2017.
- [98] L. H. Eadie, C. Reid, A. Fitzgerald and V. Wallace, "Optimizing multi-dimensional terahertz imaging analysis for colon cancer diagnosis," *Expert Systems with Applications*, vol. 40, pp. 2043 - 2050, 2013.
- [99] Y. Cao, P. Huang, X. Li, W. Ge, D. Hou and G. Zhang, "Terahertz spectral unmixing based method for identifying gastric cancer," *Physics in Medicine and Biology*, vol. 63, no. 035016, pp. 1 - 10, 2018.
- [100] E. St. John, T. Athanasiou, D. Hadjiminias and D. Leff, "Diagnostic Accuracy of Intraoperative Techniques for Margin Assessment in Breast Cancer Surgery: A Meta-analysis," *Annals of Surgery*, vol. 265, no. 2, pp. 300 - 310, 2017.
- [101] N. Bajwa, S. Sung, D. B. Ennis, M. C. Fishbein, B. Nowroozi, D. Ruan, A. Maccabi, J. Alger, M. A. St. John, W. S. Grundfest and Z. D. Taylor, "Terahertz Imaging of Cutaneous Edema: Correlation with Magnetic Resonance Imaging in Burn Wounds," *IEEE Transactions of Biomedical Engineering*, vol. 64, no. 11, pp. 2682 - 2694, 2017.
- [102] O. B. Osman, T. J. Tan, S. Henry, A. Warsen, N. Farr, A. M. McClintic, Y. -N. Wang, S. Arbabi and M. H. Arbab, "Differentiation of burn wounds in an in vivo porcine model using terahertz spectroscopy," *Biomedical Optics Express*, vol. 11, no. 11, pp. 6528 - 6535, 2020.

- [103] M. H. Arbab, T. C. Dickey, D. P. Winebrenner, A. Chen, M. B. Klein and P. D. Mourad, "Terahertz reflectometry of burn wounds in a rat model," *Biomedical optics express*, vol. 2, no. 8, pp. 2339 - 2347, 2011.
- [104] M. H. Arbab, D. P. Winebrenner, T. C. Dickey, A. Chen, M. B. Klein and P. D. Mourad, "Terahertz spectroscopy for the assessment of burn injuries in vivo," *Journal of Biomedical Optics*, vol. 18, no. 7, 2013.
- [105] S. Fan, B. S. Y. Ung, E. P. J. Parrott, V. P. Wallace and E. Pickwell-MacPherson, "In vivo terahertz reflection imaging of human scars during and after the healing process," *Journal of Biophotonics*, vol. 10, no. 9, pp. 1143 - 1151, 2017.
- [106] D. B. Bennett, Z. D. Taylor, P. Tewari, R. S. Singh, M. O. Culjat, W. S. Grundfest, D. J. Sassoon, R. D. Johnson, J. -P. Hubschman and E. R. Brown, "Terahertz sensing in corneal tissues," *Journal of Biomedical Optics*, vol. 16, no. 5, 2011.
- [107] G. G. Hernandez-Cardoso, S. C. Rojas-Landeros, M. Alfaro-Gomez, A. I. Hernandez-Serrano, I. Salas-Gutierrez, E. Lemus-Bedolla, A. R. Castillo-Guzman, H. L. Lopez-Lemus and E. Castro-Camus, "Terahertz imaging for early screening of diabetic foot syndrome: A proof of concept," *Scientific Reports*, vol. 7, no. 42124, 2017.
- [108] M. N. Afsar and J. B. Hasted, "Measurements of the optical constants of liquid H₂O and D₂O between 6 and 450 cm⁻¹," *Journal of the Optical Society of America*, vol. 67, pp. 902 - 904, 1977.
- [109] I. Echchgadda, J. E. Grundt, C. Z. Cerna, C. C. Roth, J. A. Payne, B. L. Ibej and G. J. Wilmink, "Terahertz Radiation: A Non-contact Tool for Selective Stimulation of Biological Responses in Human Cells," *IEEE Transactions on Terahertz Science and Technology*, vol. 6, no. 1, pp. 54 - 68, 2016.
- [110] I. Echchgadda, C. Cerna, M. Sloan, D. Elam and B. Ibej, "Effects of different terahertz frequencies on gene expression in human keratinocytes," *Proceedings of the Society of Photo-Optical Instrumentation Engineers*, vol. 9321, pp. Q1 - Q9, 2015.
- [111] International Commission on Non-Ionizing Radiation Protection, "Exposure to high frequency electromagnetic fields, biological effects and health consequences," International Commission on Non-Ionizing Radiation Protection, Germany, 2009.
- [112] P. H. Siegel and V. Pukhov, "THz in Biology and Medicine: Towards Quantifying and Understanding the Interaction of Millimeter- and Submillimeter-Waves with Cells and Cell Processes," *Proc. of SPIE: Optical Interactions with Tissues and Cells XXI*, vol. 7562, no. 75620H, pp. 1 - 13, 2010.
- [113] "Tera-Hertz radiation in Biological Research, Investigations on Diagnostics and study on potential Genotoxic Effects (THz-BRIDGE), Final Report," [Online]. Available: <https://www.frascati.enea.it/THz-BRIDGE/>.
- [114] G. Wilmink and J. Grundt, "Invited Review Article: Current State of Research on Biological Effects of Terahertz Radiation," *Journal of Infrared, Millimeter, and Terahertz Waves*, vol. 32, no. 10, pp. 1074 - 1122, 2011.

2 Terahertz dynamics and interaction mechanisms in biological systems

“...living matter, while not eluding the ‘laws of physics’, ...is likely to involve ‘other laws of physics’ hitherto unknown, ... [which] will form just as integral a part of science as the former.”

– Erwin Schrödinger, in “What is Life?” (1944)

2.1 Introduction

The relatively recent availability of terahertz (THz) source and detector technologies that have bridged the “terahertz gap” has initiated a resurgence of research interest into the potential biological effects of THz radiation. In this chapter, interaction mechanisms between THz radiation and biological systems are discussed. These mechanisms elucidate why THz probes provide unique structural and chemical information for diagnostic applications, but additionally imply that intense THz radiation may induce biological effects. First, the history of research interest in THz dynamics in biological systems is presented, including a description of the ultrafast dynamics of biomolecules that may couple to external energy excitations at similar frequencies. Next, a selection of three physical models characterizing the nature of THz-biology interactions from dielectric, energetic, and mechanical perspectives are presented that highlight the response of complex biological systems to applied THz fields, and directly motivate the hypothesis that intense THz pulses may non-thermally dysregulate important biological processes. Finally, the biological effects of THz exposure reported in the literature are reviewed and discussed in the context of potential therapeutic mechanisms and clinical application of THz radiation.

2.2 Terahertz biology

2.2.1 History and development

In 1938, Herbert Fröhlich, a theoretical physicist by training but genuine polymath, learned that the potential across an active cell membrane (~ 100 mV across ~ 10 nm) corresponds to a very large electric field that would lead to dielectric breakdown in most non-biological material, and so surmised the existence of some unknown dielectric property exploited by biological systems [1]. A

back-of-the-envelope calculation¹ estimated that the natural oscillations corresponding to this field occur between 0.1 – 1 THz, and these dynamics may be important in regulating cellular function. At the time, efficient sources of radiation to probe these dynamics in the THz gap were not available, and the problem was not revisited until the late 1960s.

The first experiment on the biological effects of THz radiation was performed by Webb and Dodd at the University of Saskatchewan in 1968 [2, 3]. While irradiating *E. coli* cells using a microwave spectrometer operating at 136 GHz (0.136 THz), they noticed inhibited mitotic activity that was not explained by the estimated heating. Around the same time, Fröhlich was developing a model of nonlinear energy transfer in biological systems that may explain the coherent behaviour observed in complex macromolecules like proteins – this model is outlined in Section 2.3.2 [4]. Fröhlich later collaborated with Webb to validate this model in *E. coli* cells [5]. Today, modern understandings of structural dynamics in biological systems that occur on femtosecond-picosecond (i.e., “ultrafast”) timescales provide a framework with which to understand fundamental THz interactions in biological systems that assist in explaining these intriguing observations.

2.2.2 Ultrafast dynamics in biological systems

Figure 2.1 shows a selection of timescales associated with common processes that occur in physical and biological systems [6]. These natural oscillatory dynamics are fundamentally electromagnetic (EM) in nature, and may therefore be coupled to external EM excitations at similar frequencies. The explicit connection between structural dynamics and regulatory function in biomolecules has been recognized for decades [7, 8, 9]. Moreover, the knowledge that biomolecular vibrations and rotations occur on picosecond timescales has been similarly established [10], and together these set the stage for the key hypothesis advanced in this thesis: External excitation of THz radiation with sufficient intensity may couple to natural oscillatory dynamics of important biological structures and dysregulate structural dynamics such that the associated function is affected.

¹ This order-of-magnitude estimate is from the speed of longitudinal membrane oscillations: $v = (\lambda/2) \cdot f$, where wave speed in a lipid bilayer is $v \sim 10^5 - 10^6$ cm/s and the fundamental mode wavelength λ is twice the membrane thickness ($d \sim 10$ nm). This was the initial impetus behind Fröhlich’s investigations of THz dynamics in biological systems, and his later model of nonlinear energy transfer.

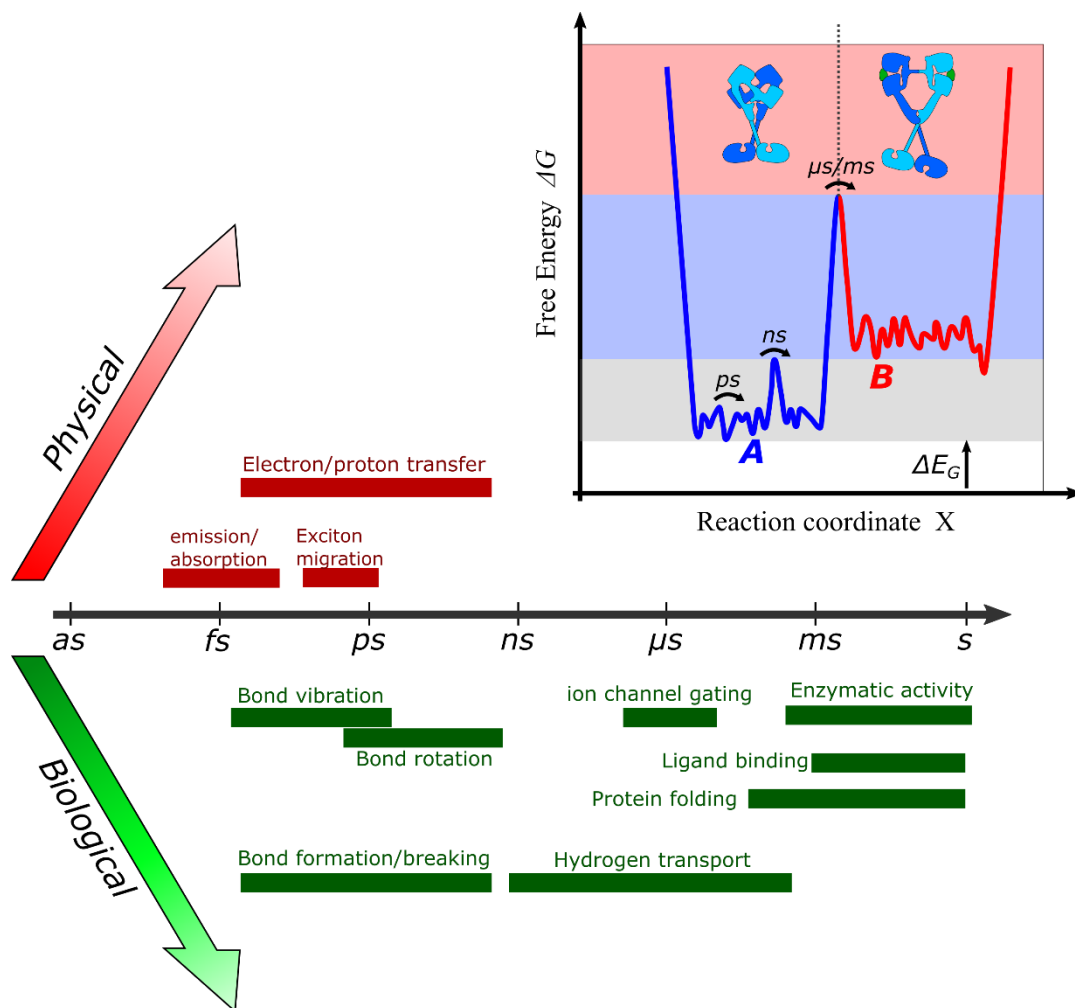


Figure 2.1. **Ultrafast processes in physical and biological systems.** Adapted from [6, 11, 12]. At top is a representative example of an energy landscape along a coordinate that characterizes the molecule’s conformational state (the “reaction coordinate” X). The fast dynamics associated with bond rotation and vibration may oscillate between microstates due to relatively low energy barriers in the highly frustrated ranges close to the ground state energy ΔE_G . Slower, larger-amplitude transport dynamics that occur on \sim ns timescales may require larger energies but do not result in a large-scale conformational change ($A \rightarrow A$ or $B \rightarrow B$). Energy transition events that correspond to conformation state change ($A \rightarrow B$, e.g., folding protein) require larger activation energies and occur on slower timescales (μ s – ms).

The femtosecond/picosecond ranges of Figure 2.1 are the “ultrafast” regime, and in biological systems correspond to a highly frustrated region in typical energy landscapes [6, 13]. In physiological environments, biomolecules will rapidly transition between low-energy-cost barriers, which manifests as vibration or rotation on picosecond timescales and thus corresponds to natural oscillatory dynamics at THz frequencies. In principle, these oscillations may be externally coupled via EM excitation at similar frequencies.

The formation, rotation, and vibration of intermolecular hydrogen bond (H-bond) networks occupy a wide band of THz frequencies [14, 15]. H-bonds are ubiquitous in biological systems: All biomolecular interactions occur in a water environment, and water often takes an active regulatory role in mediating these interactions (e.g., lowering the energy barrier to facilitate ligand-binding) [16, 17]. All proteins are comprised of secondary structures, either alpha-helices or beta-sheets, and these are stabilized by H-bonds between adjacent residues [18]. Further, proteins undergo folding into a functional conformational state, and these folding dynamics are predominantly dictated by H-bonding with the surrounding water environment [19].

The low-frequency vibrational dynamics of amino acids, peptides, and proteins have been measured across the THz band [9, 20, 21, 22, 23], and these oscillatory dynamics are thought to be dominant factors that influence biomolecular reaction and transport efficiencies [24]. In the DNA molecule, H-bonds between neighbouring base pairs stabilize the DNA molecule in its double-helix configuration [25]. In spectroscopy studies of both proteins and nucleic acids, narrow THz absorption bands characteristic of resonant interaction are observed in lyophilized (dried) systems [26, 27].

Simulation work provides further insight into the structural properties that influence the measured THz spectra [28, 29]. THz dynamics correspond to the low-frequency motion of the global atomic population, and its interaction with the surrounding molecular environment. Spectral signatures are predominantly influenced by intermolecular dynamics (e.g., H-bond between neighbouring molecules), and these are only predictable when H-bonding with an external water environment is properly accounted for.

2.3 Mathematical models of terahertz dynamics and interactions in biological systems

Three selected formalisms of THz dynamics in biological systems are now presented from a dielectric, energetic, and mechanical perspective. These models posit significant modulations to biological systems via non-thermal mechanisms that may in turn dysregulate biological functions that rely on properly-regulated structural dynamics.

2.3.1 Dielectric model of terahertz field exposure

Linear dielectric analysis describes the response of materials in an external electric field $\vec{E}(t)$ for the RF, microwave, and THz bands. The precise nature of response is dictated by the complex dielectric function $\tilde{\epsilon}(\omega)$ that characterizes an induced displacement field, \vec{D} ,

$$\vec{D} = \epsilon \vec{E} = \tilde{\epsilon}(\omega) \epsilon_0 \vec{E} \quad (2.1)$$

where $\epsilon_0 = 8.85 \times 10^{-12}$ F/m is the vacuum permittivity, $\omega = 2\pi f$ is the angular frequency, and $\tilde{\epsilon} = \epsilon_1 - i\epsilon_2$ is the complex permittivity function related to the complex conductivity $\tilde{\sigma} = \sigma_1 + i\sigma_2$ as

$$\begin{aligned} \tilde{\epsilon}(\omega) &= 1 + i \frac{\tilde{\sigma}}{\epsilon_0 \omega} \\ \epsilon_1(\omega) &= 1 - \frac{\sigma_2}{\epsilon_0 \omega} \\ \epsilon_2(\omega) &= \frac{\sigma_1}{\epsilon_0 \omega}. \end{aligned} \quad (2.2)$$

In dielectric spectroscopy, biological tissue may be modeled as inhomogenous, anisotropic, polydomain, dispersive solutions [30, 31]. Their spectra are generally characterized by a superposition of three sigmoidal transition bands labelled α , β , and γ as in Figure 2.2, representing polarization relaxations each with an associated time constant τ [32]. For tissues, $\tilde{\epsilon}(\omega)$ may be modelled by a summation of Debye dispersions with a static conductivity component ($\sigma_0 = \sigma_1$), or multiple Cole-Cole dispersion [32]:

$$\tilde{\epsilon}(\omega) = \epsilon_\infty + \sum_n \frac{\Delta\epsilon_n}{1 + (i\omega\tau_n)^{1-k_n}} + \frac{\sigma_0}{i\omega\epsilon_0} \quad (2.3)$$

where $\Delta\epsilon = \epsilon_s - \epsilon_\infty$ is the dispersion magnitude (with low and high frequency permittivities surrounding the relaxation band given by ϵ_s and ϵ_∞ , respectively), τ is the relaxation time constant, and k is the distribution parameter, a measure of dispersion-broadening. In general, α -relaxation is

attributed to dispersion of cellular ion flow (e.g., calcium waves), β -dispersion arises due to membrane charge build-up, and γ -dispersion is due to dipolar water rotation [33, 34].

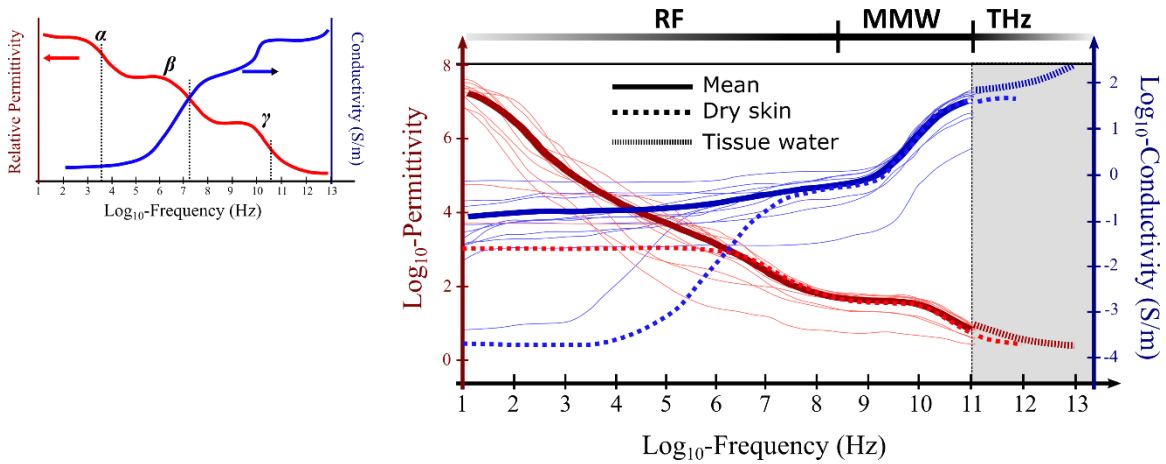


Figure 2.2. **Relative dielectric permittivity and conductivity of biological tissues from RF to THz frequencies.** Adapted from [35, 36, 37, 38]. *Left:* An idealized diagram of dielectric relaxation of permittivity (red, left axes) and conductivity (blue, right axes). Biological tissues generally have 3 distinct relaxation bands, indicated by labels α , β , and γ . In the main plot, permittivity (red) and conductivity (blue) spectra of a selection of biological tissues (blood, bone, fat, gray matter, white matter, kidney, spleen, heart, liver, lung, muscle, and skin) are shown. Thick solid lines indicate the curve means of the different tissues. Dotted lines are for dry skin, highlighting the effect of tissue hydration. Data for skin from [36] and tissue water from [38] are appended to show these quantities extended into the shaded THz region.

Gabriel et al. have comprehensively characterized the dielectric function of a variety of biological tissue (blood, bone, fat, grey matter, white matter, kidney, spleen, heart, liver, lung, muscle, and skin) across the low-RF ($\sim 10^7$ Hz) to microwave (~ 10 GHz, millimeter-wave, MMW) bands [31, 32, 35]. These data were fit to Equation (2.3) from which the real permittivities/conductivities were determined as the thin red/blue curves in Figure 2.2, with the corresponding means of all tissues represented by the thick curves. Permittivity in biological tissue generally starts high for RF frequencies ($\sim 10^7$) and decreases to ~ 10 approaching the THz band, while conductivity starts relatively low in the RF band (~ 0.1 S/m), and increases to ~ 100 S/m at THz frequencies.

The dotted lines indicate permittivity and conductivity for dry skin, and highlights the effect of tissue hydration. Dry tissue has unusually low permittivity and conductivity at low frequencies (~ 10 Hz – 10 MHz) relative to other tissues, but are roughly consistent with mean tissue values at higher frequencies approaching the THz band. Data from THz spectroscopy experiments of skin and tissue water from references [36] and [38] are appended in the shaded THz region of Figure

2.2. While the qualitative features of the dielectric function are similar for different tissue types, the values can differ by orders of magnitude.

Pickwell et al. have extended the theoretical dielectric characterization of skin tissue permittivity to the 0.1 – 2.0 THz band as a double Debye process [39]:

$$\tilde{\epsilon}(\omega) = \epsilon_{\infty} + \frac{\epsilon_S - \epsilon_2}{1 + i\omega\tau_1} + \frac{\epsilon_2 - \epsilon_{\infty}}{1 + i\omega\tau_2} \quad (2.4)$$

where ϵ_2 is an intermediate permittivity parameter, and τ_1 and τ_2 are the slow and fast relaxation time constants attributed to bond-breaking and dipole reorientation, respectively. Parameter values for THz dielectric relaxation for water and skin are provided in Table 2.1. Several other forms of dielectric models for tissue have been developed, particularly for skin tissue [40, 41]. Comparisons of time-domain simulations accurately predict THz pulse interaction in biological tissue. Therefore, dielectric parameters determined by THz spectroscopy accurately characterize THz pulse interaction in biological tissue for the frequencies utilized in this thesis.

Table 2.1. **Debye relaxation parameters for water and epidermal skin tissue.**

	ϵ_S	ϵ_2	ϵ_{∞}	τ_1 (ps)	τ_2 (ps)
Skin [39]	60.0	3.6	3.0	10.0	0.20
Water [39]	78.8	6.6	4.1	10.6	0.18
Water [42]	80.5	-	4.11 ± 0.05	10.0 ± 0.18	0.57 ± 0.04

Dielectric dispersion in cellular and tissue environments is the mechanism underlying the diagnostic contrast in medical imaging and spectroscopy applications [39, 43, 44]. Tumor tissues often correspond to disparate dielectric properties across a wide band of THz frequencies relative to normal tissue, and these dielectric differences may be exploited for clinical diagnostic advantage for the identification and diagnosis of diseased tissue. Further, observations of non-thermal biological effects induced by intense THz pulses may be understood from a dielectric perspective: The coupling of THz excitations to water dynamics that influence membrane structure explains field-induced permeabilization of cellular membranes, as investigated in Chapter 8.

2.3.2 Nonlinear energy transfer in biological systems: The Fröhlich condensate

In 1968, Herbert Fröhlich devised a model of energy transfer in biological systems that predicted long-lived and long-range coherent energy states that explained the complex large-scale organization observed in even the simplest biological systems (e.g., a protein) [4]. In the formalism, a macromolecule is modelled as a population of coupled dipole oscillators in a thermal environment fed by an external energy source, and predicts that energy exchange will channel quanta into the lowest frequency mode via mechanisms similar to the well-characterized Bose-Einstein condensation, as long as the external energy rate is above a critical threshold [45]. While high-temperature Bose-type condensations have been observed in atomic gas systems [46], the existence of Fröhlich condensates in physiological conditions remains controversial.

In the original formulation, Fröhlich utilized balanced rate equations in which the terms were informed by assumed thermal distributions [4]. In 1978, Wu and Austin introduced a microscopic formalism utilizing an interaction Hamiltonian and showed that Fröhlich's *ansatz* was sound: Bose-Einstein condensation at biological temperatures, a “Fröhlich condensate”, is a predicted outcome of the nonlinear energy-exchange model as follows [45]:

A Fröhlich system is modelled by three interacting components as in Figure 2.3(a):

1. Z interacting dipole oscillators representing the macromolecule, described by creation/annihilation operators a_i^\dagger/a_i for normal modes ω_i
2. A thermal environment (heat bath) described by b_k^\dagger/b_k for normal modes Ω_k
3. External energy source supplied at mean rate s described by P_p^\dagger/P_p for normal modes $\bar{\Omega}_p$

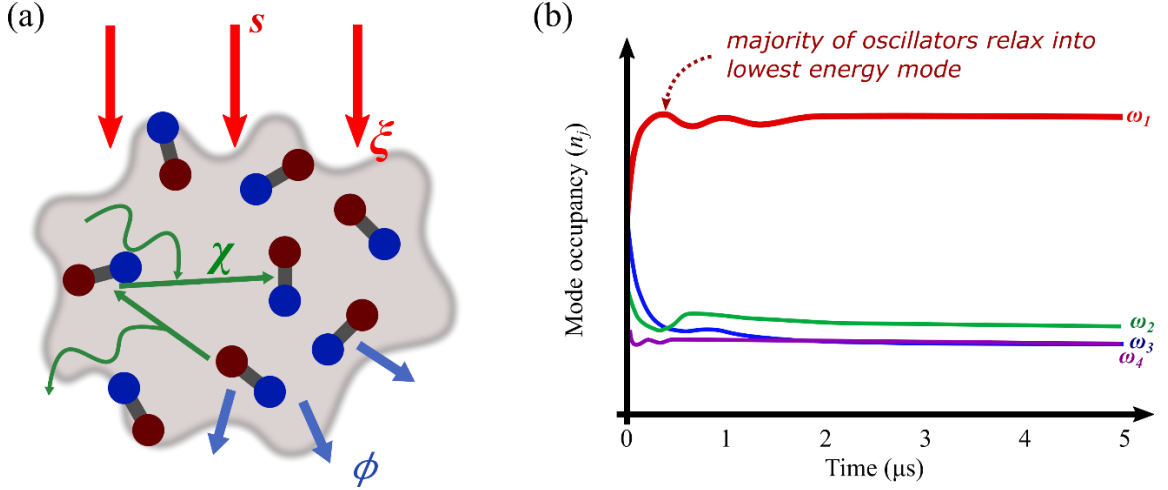


Figure 2.3. **Fröhlich's model of nonlinear energy transfer in biological systems.** Adapted from [47]. (a) Diagram of a Fröhlich system. A population of Z oscillators are in a heat bath to which the dynamics are coupled linearly (ϕ) and nonlinearly (χ). External energy is supplied to the oscillators (ξ) at a mean rate s . (b) Time evolution solution of a Fröhlich system, showing mode occupancy $\langle n_j \rangle$ of the first four energy levels. The majority of vibrational quanta of the oscillators occupy the lowest energy mode, forming a low-frequency, long-lived, bulk oscillatory state.

These components are energetically coupled linearly and nonlinearly by coupling constants ϕ , χ , and ξ for 1-quantum, 2-quanta, and external processes, respectively. From these, the Hamiltonian is constructed as

$$\begin{aligned}
 H = & \sum_i \hbar \omega_i a_i^\dagger a_i + \sum_k \hbar \Omega_k b_k^\dagger b_k + \sum_p \hbar \bar{\Omega}_p P_p^\dagger P_p + \sum_{i,k} (\phi b_k^\dagger a_i + \phi^* b_k a_i^\dagger) \\
 & + \sum_{p,l} (\xi P_p a_i^\dagger + \xi^* P_p^\dagger a_i) + \sum_{i,j,k} (\chi a_j^\dagger a_i b_k^\dagger + \chi^* a_j a_i^\dagger b_k).
 \end{aligned} \quad (2.5)$$

The first three terms are the non-interaction terms, and represent the total energy for each of the three system components separately. The fourth and fifth terms represent linear energy exchange between the oscillators/bath and oscillators/energy source, respectively. The final term is the nonlinear interaction term, and describes 2-quanta exchange between the oscillators and the thermal environment. Of interest is the number of oscillators in the j^{th} mode, $n_j = a_j^\dagger a_j$, which may be obtained from the differential equation

$$\langle \dot{n}_j \rangle = \frac{1}{i\hbar} \langle [n_j, H] \rangle. \quad (2.6)$$

Numerical approaches obtain an approximate solution of the time-course of mode occupancy by mode energy level, and predict fast relaxation of the majority of oscillators into the lowest energy mode as depicted in Figure 2.3(b).

To show where this preferential energy flow to low-frequency modes arises, Equation (2.6) may be solved analytically in the steady-state condition ($\langle \dot{n}_j \rangle = 0$) as [45]

$$\langle n_j \rangle = \left[1 + \frac{s}{\phi + \chi N} \right] \cdot \frac{1}{e^{(\hbar\omega_j - \mu)/kT} - 1} \quad (2.7)$$

where $\mu \geq 0$ is a minimum energy parameter defined by the model parameters as

$$e^{-\mu/kT} = 1 - \frac{\chi}{\phi + \chi N} \cdot \frac{S(T)}{\phi} \leq 1 \quad (2.8)$$

where $N = \sum_j n_j$ and $S(T) = s \cdot \sum_j \exp(\hbar\omega_j/kT)$.

When $s = 0$ (i.e., no external energy supply), the j^{th} mode occupancy of Equation (2.7) reduces to the thermal equilibrium distribution. The condition $\langle n_i \rangle \geq 0$ implies $\hbar\omega_0 > \mu \geq 0$. Therefore, Equations (2.7) and (2.8) show that the j^{th} mode occupancy $\langle n_j \rangle$ is maximized for $\hbar\omega_j \rightarrow \mu$, which occurs for the minimum value of $\hbar\omega_j$. This is bosonic condensation into the lowest energy mode, termed “Fröhlich condensation”, and describes emergence of large-scale, low-frequency, long-lived coherent oscillations of the bulk system at arbitrarily high temperature that arise via nonlinear energy coupling. Importantly, if the external energy rate is below a threshold s_0 , or if nonlinear 2-quanta processes are neglected ($\chi = 0$), $\langle n_j \rangle$ reduces to the Planck distribution describing thermal equilibrium, and no condensation occurs [4, 45].

From this model, Fröhlich predicted that Coulombic forces in biological systems establish [4]

“...several branches of longitudinal modes probably in a frequency range of 10^{11} - 10^{12} sec⁻¹. ...A certain fraction of the supplied energy, therefore, is not thermalized but stored in a single mode which then exhibits long-range phase correlations.”

Originally, Fröhlich envisioned the energy source (s in Equations (2.6) – (2.8)) as endogenous, for example hydrogen bond or non-localized electron oscillations locally exciting nearby dipoles [4]. He hypothesized that this may explain the observed coherent behaviour of complex biomolecules such as proteins, which do not behave as hundreds of individual oscillators, but as single entities with directed function, and may even influence functions of higher complexity such as cell division. The search for the existence of Fröhlich condensates has been an active field of research since the original model was proposed. Fröhlich himself published experiments claiming to verify his model using Raman spectra of *E. coli* cultures, and observations of Fröhlich condensates in protein crystals have been reported as recently as 2015 [5, 48]. While it may be unlikely that Fröhlich condensates can possibly exist in physiological conditions, this model provides a framework to understand nonlinear, non-thermal energy transfer that may influence biological dynamics prior to thermalization, and is a milestone in the history of THz-biology research.

2.3.3 Mechanical model of DNA breathing in a terahertz field

More recently, modern understanding of structural biology and the growth of computational capabilities have allowed for simulation of more sophisticated structural models of THz dynamics in biological systems. Here, a mechanical model of DNA breathing proposed by Alexandrov et al. is outlined [49]. Consider the force balance equation characterizing the separation distance between the n^{th} base pair along a DNA strand, y_n , as a function of time and location

$$m\ddot{y}_n + m\gamma\dot{y}_n + U'(y_n) + [W'(y_{n+1}, y_n) + W'(y_n, y_{n-1})] = A \cdot \cos(\Omega t) \quad (2.9)$$

where $U(y_n)$ is the Morse potential² for hydrogen-bonding between complementary base pairs of the DNA molecule and W is the quadratic stacking potential³ of adjacent bases (see Figure 2.4(a)). $m\gamma\dot{y}_n$ is the energy dissipation term due to the aqueous environment, and the right-hand side is the external THz field, modelled as a pure sinusoid with amplitude A and frequency Ω .

² $U(y_n) = D_n(e^{-a_n y_n} - 1)^2$, where D_n and a_n are base-pair-dependent [51].

³ $W(y_n, y_{n-1}) = \frac{1}{2}\chi[y_n, y_{n-1}](y_n - y_{n-1})^2$, where $\chi[y_n, y_{n-1}] = k(1 + \rho \cdot e^{-\beta(y_n - y_{n-1})})$ [51].

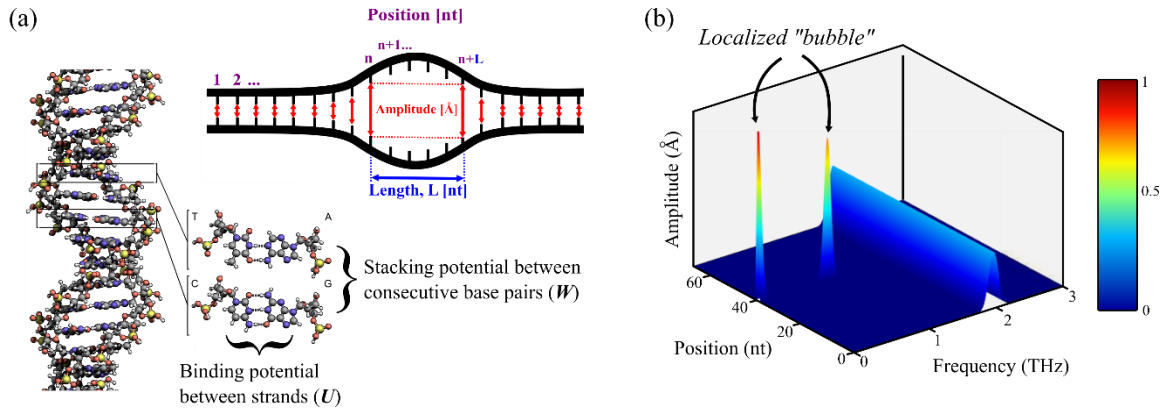


Figure 2.4. **Simulation of breathing dynamics and bubble formation of THz-exposed DNA.** (a) The chemical structure of DNA, and an idealized Peyrard-Bishop-Dauxois (PBD) model of DNA, with amplitude, length, and position of DNA bubbles labelled [50, 51]. (b) The 2D power spectrum of the solution y_n to Equation (2.9) for $\Omega = 2.0$ THz, adapted from [49]. The driving force is present everywhere along the modelled DNA strand at 2.0 THz. A localized 1.0 THz “bubble” forms that is superposed on a localized DC separation at nucleotide (nt) 40. Breather modes induced by THz exposure create and amplify localized bubbles in the DNA strand, which is hypothesized to affect biological function by altering gene expression.

Figure 2.4(b) shows the power spectrum of the solution y_n . The signature of the 2.0 THz drive is present along the entire DNA strand. Interestingly, localized unbindings, or “bubbles”, in the DNA strand are observed, termed “breather modes”. These manifest as a localized DC separation, with a period-doubled ($\Omega/2=1$ THz) oscillation superposed. Investigation of the origins of these localized separations found that a minimum external energy was required, consistent with the existence of a minimum energy threshold observed in the Fröhlich system in Section 2.3.2.

Importantly, the nature of the solution has direct biological relevance: Formation of localized strand separations, or “bubbles”, in DNA is an important event in recognition of gene promoter regions in transcription by increasing the probability of RNA polymerase II binding to the transcription start site [52, 53]. Normally, bubbles arise due to endogenous thermal fluctuations that occur on picosecond timescales, and so the function of gene recognition and transcription initiation corresponds to natural oscillations at THz frequencies. Outcomes from this model explicitly posit that THz exposure could modulate gene expression via non-thermal, nonlinear interactions by creating and amplifying localized separations in the DNA molecule. In measurements with mouse mesenchymal cells, Alexandrov et al. have shown that upregulated gene expression is correlated with propensity for DNA breathing, and differential gene expression is a common observation in THz exposure studies [54]. This hypothesis is explored in this thesis in Chapter 7.

2.4 Biological effects of terahertz radiation

Historically, studies into the biological effects induced by THz radiation have been hindered by: (1) The limited availability of generation and detection technologies in the THz band, and (2) the prohibitive absorptive properties of aqueous media at THz frequencies. Increasing the energy of THz exposure is one method of overcoming absorption limitations, but this typically corresponds to significant heating, and any non-thermal biological effects are obscured by the heat shock response [55, 56]. Early studies investigating potential biological effects were restricted to low-intensity, continuous-wave (CW) sources, for which thermal effects were dominant [2]. However, with recent advances in development of highly intense, single-cycle THz pulses, it is now possible to excite biological systems at THz frequencies with very high peak powers (\sim MW/cm² – GW/cm²) that can propagate within high-attenuation aqueous environments, but sufficiently low average powers (\sim mW/cm²) to minimize heating and avoid inducing thermal effects. For comprehensive reviews of biological effects induced by THz radiation, see references [2, 57, 58, 59].

Several studies have reported a variety of THz-induced phenotypic changes at all levels of biological organization: THz exposures have been shown to increase membrane permeability [60, 61], non-thermally induce differential gene expression in human stem cells, keratinocytes, and skin models [62, 63, 64, 65], affect cellular differentiation in mammalian stem cells [66], activate acute inflammatory responses at the cellular [62], tissue [63, 64], and organism [66] level, and induce aneuploidy in human fibroblasts [67].

2.4.1 *Thermal vs. non-thermal biological effects*

Echchgadda et al. have investigated the thermal effects of 2.52 THz exposure at the highest reported CW intensity (636 mW/cm²) in human keratinocytes with well-matched uniformly-heated thermal controls [56]. Interestingly, significant differences in global differential gene expression and associated signaling pathways were observed between cells heated by a CW THz beam and bulk-heated controls. These effects additionally depended significantly on the narrow-band THz frequency (1.4 THz, 2.52 THz, and 3.11 THz), although these latter experiments were at reduced average intensity in order to match exposure conditions (44.2 mW/cm²) [62]. These results lend important insight into the compelling distinction between thermal and non-thermal effects of THz radiation, and motivate experiments utilizing pulsed THz beams for which non-thermal effects can be isolated and characterized.

Conversely, THz bio-exposure systems that utilize pulsed, often single-cycle, THz sources may be implemented to induce only minimal (biologically negligible) heating, and effects observed may be attributed to non-thermal coupling to natural oscillatory dynamics. Figure 2.5(a) shows a representative waveform of an intense THz pulse utilized in this thesis work, and the corresponding power spectrum is shown in Figure 2.5(b). The temporal localization of single-cycle pulsed sources correspond to broad power spectra peaked in the THz band, and so a wide range of oscillatory dynamics are excited in bio-systems of interest. Intense pulses of THz radiation (\sim MW/cm² – GW/cm²) have been shown to disassemble biopolymers like actin [68] and microtubules [69], dysregulate cancer-related signaling pathways in human skin [64, 65, 70], activate several proteins of the DNA damage response, and induce phosphorylation of the H2AX histone in skin tissue models [71]. The latter is an indication of severe genotoxic stress often used as a correlative marker for double-strand breaks, a form of DNA damage that often results in cell death [72]. THz exposure has also been observed to induce epigenetic alterations such as genome-wide demethylation, although these results are controversial [73, 74].

As radiation-induced DNA damage is a known therapeutic mechanism for several genetic disorders including cancer, these data and observations led to the speculation that intense THz pulses may find application in a therapeutic capacity via wholly distinct interaction characteristics with biological systems compared to conventional radiotherapy sources. Thus, further investigation into the potential effects and clinical uses of THz radiation is warranted.

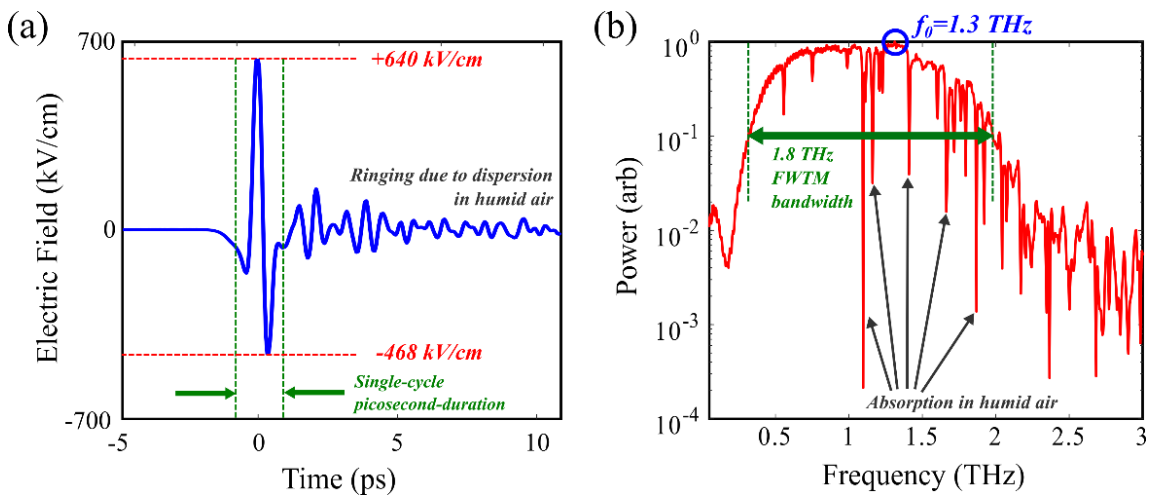


Figure 2.5. **Time- and frequency-domain representations of intense THz pulses used for biological exposures.** (a) Intense THz pulses are single-cycle, approximately picosecond-duration EM pulses reaching very high peak electric fields (\sim 640 kV/cm in this example). The energy localization in time corresponds to a broad power spectrum in (b). The peak-power frequency for this pulse is $f_0=1.3$ THz, and the spectrum bandwidth is 1.8 THz (full width tenth max, FWTM).

2.4.2 Frequency-dependence of biological effects

One of the most interesting hypotheses that may be inferred from the proposed interaction mechanisms is that biological effects may be expected to depend strongly on spectral content, or the frequency distribution of the incident THz radiation. For each pulse in Figure 2.5(a) that is absorbed in a biological system, the biomolecular dynamics within the frequency band in Figure 2.5(b) are excited. Therefore, it is expected that varying the spectral content of the THz pulse may influence the biological response [62, 75]. While it was an early hope that THz exposures may precisely excite target resonant modes in biomolecules that are critical for cellular function, the broad spectra that arise in realistic physiological conditions due to the high-temperatures and non-ordered/-oriented samples make this challenging [76]. However, differences in biological response have been observed for varying spectral content, and this effect is also investigated in this thesis.

2.5 Conclusion

Since the low-frequency vibrational and rotational modes of biomolecular systems occupy a wide band of THz frequencies, external EM excitations at similar frequencies efficiently couple to these dynamics, and sufficient intensities may dysregulate the structural dynamics to the point of affecting the associated function. The physical models presented outline how THz may modulate biological function from a dielectric, energetic, and mechanical perspective, and characterization of effects via these mechanisms may lead to the development of novel THz technologies that may be exploited clinically. These effects must be characterized to establish safe exposure levels of existing THz technologies, such as airport security scanners and medical imaging systems, or to develop potential therapeutic technologies.

2.6 References

- [1] G. J. Hyland, "Herbert Frohlich, FRS (1905 - 1991) - A Physicist Ahead of His Time," *Electromagnetic Biology and Medicine*, vol. 24, no. 3, pp. 161 - 182, 2005.
- [2] G. Wilmink and J. Grundt, "Invited Review Article: Current State of Research on Biological Effects of Terahertz Radiation," *Journal of Infrared, Millimeter, and Terahertz Waves*, vol. 32, no. 10, pp. 1074 - 1122, 2011.
- [3] S. Webb and D. Dodds, "Inhibition of Bacterial Cell Growth by 136 gc Microwaves," *Nature*, vol. 218, pp. 374 - 375, 1968.

- [4] H. Fröhlich, "Long-Range Coherence and Energy Storage in Biological Systems," *International Journal of Quantum Chemistry*, vol. 2, pp. 641 - 649, 1968.
- [5] S. Webb, M. Stoneham and H. Fröhlich, "Evidence for Non-thermal Excitation of Energy Levels in Active Biological Systems," *Physics Letters*, vol. 63A, no. 3, pp. 407 - 408, 1977.
- [6] M. Chergui, "Ultrafast structural dynamics of biological systems," *Comprehensive Biophysics*, vol. 1, pp. 398 - 424, 2012.
- [7] N. Citri, "Conformational adaptability in enzymes," *Advances in Enzymology and Related Areas of Molecular Biology*, vol. 37, pp. 397 - 648, 1973.
- [8] W. P. Jencks, "Binding energy, specificity, and enzymic catalysis: the circe effect," *Advances in Enzymology and Related Areas of Molecular Biology*, vol. 43, pp. 219 - 410, 1975.
- [9] A. Carpinteri, G. Lacidogna, G. Piana and A. Bassani, "Terahertz mechanical vibrations in lysozyme: Raman spectroscopy vs modal analysis," *Journal of Molecular Structure*, vol. 1139, pp. 222 - 230, 2017.
- [10] J. A. McCammon, P. G. Wolynes and M. Karplus, "Picosecond Dynamics of Tyrosine Side Chains in Proteins," *Biochemistry*, vol. 18, no. 6, pp. 927 - 942, 1979.
- [11] J.-H. Son, *Terahertz Biomedical Science and Technology*, Boca Raton, FL: CRC Press, 2014.
- [12] R. Milo and R. Phillips, "Cell biology by the numbers," [Online]. Available: <http://book.bionumbers.org/>.
- [13] F. O. Tzul, D. Vasilchuk and G. I. Makhatadze, "Evidence for the principle of minimal frustration in the evolution of protein folding landscapes," *Proceedings of the National Academy of Science*, vol. 114, no. 9, pp. E1627 - E1632, 2017.
- [14] D. F. Plusquellic, K. Siegrist, E. J. Heilweil and O. Esenturk, "Applications of Terahertz Spectroscopy in Biosystems," *ChemPhysChem*, vol. 8, pp. 2412 - 2431, 2007.
- [15] M. Heyden and M. Havenith, "Combining THz spectroscopy and MD simulations to study protein-hydration coupling," *Methods*, vol. 52, pp. 74 - 83, 2010.
- [16] D. Laage, T. Elsaesser and J. Hynes, "Water Dynamics in the Hydration Shells of Biomolecules," *Chemical Reviews*, vol. 117, no. 16, pp. 10694 - 10725, 2017.
- [17] K. Mazur, I. A. Heisler and S. R. Meech, "Ultrafast Dynamics and Hydrogen-Bond Structure in Aqueous Solutions of Model Peptides," *Journal of Physics Chemistry B*, vol. 114, no. 32, pp. 10684 - 10691, 2010.
- [18] B. Alberts, A. Johnson, J. Lewis, M. Raff, K. Roberts and P. Walter, *The Molecular Biology of the Cell*, 4th Edition, New York, NY: Garland Science, 2002.
- [19] L. Lins and R. Brasseur, "The hydrophobic effect in protein folding," *FASEB Journal*, vol. 9, pp. 535 - 540, 1995.

- [20] T. M. Korter, R. Balu, M. B. Campbell, M. C. Beard, S. K. Gregurick and E. J. Heilweil, "Terahertz spectroscopy of solid serine and cysteine," *Chemical Physics Letters*, vol. 418, pp. 65 - 70, 2006.
- [21] R. J. Falconer and A. G. Markelz, "Terahertz Spectroscopic Analysis of Peptides and Proteins," *Journal of Infrared and Millimeter Waves*, vol. 33, pp. 973 - 988, 2012.
- [22] J. R. Knab, J. -Y. Chen, H. Yunfen and A. G. Markelz, "Terahertz Measurements of Protein Relaxational Dynamics," *Proceedings of the IEEE*, vol. 95, no. 8, pp. 1605 - 1610, 2007.
- [23] A. Markelz, S. Whitmire, J. Hillebrecht and R. Birge, "THz time domain spectroscopy of biomolecular conformational modes," *Physics in Medicine and Biology*, vol. 47, pp. 3797 - 3805, 2002.
- [24] A. Charkhesht, C. K. Regmi, K. R. Mitchell-Koch, S. Cheng and N. Q. Vinh, "High-Precision Megahertz-to-Terahertz Dielectric Spectroscopy of Protein Collective Motions and Hydration Dynamics," *The Journal of Physical Chemistry B*, vol. 122, pp. 6341 - 6350, 2018.
- [25] R. Philips, J. Kondev, J. Theriot and H. Garcia, *Physical Biology of the Cell*, New York, NY: Garland Science, 2013.
- [26] B. Fischer, M. Walther and P. Jepsen, "Far-infrared vibrational modes of DNA components studied by terahertz time-domain spectroscopy," *Physics in Medicine and Biology*, vol. 47, no. 21, pp. 3807 - 3814, 2002.
- [27] G. Acbas, K. Niessen, E. Snell and A. Markelz, "Optical measurements of long-range protein vibrations," *Nature Communications*, vol. 5, no. 3076, pp. 1 - 7, 2014.
- [28] T. Ding, T. Huber, A. P. J. Middelberg and R. J. Falconer, "Characterization of Low-Frequency Modes in Aqueous Peptides Using Far-Infrared Spectroscopy and Molecular Dynamics Simulation," *Journal of Physical Chemistry A*, vol. 115, pp. 11559 - 11565, 2011.
- [29] O. Sushko, R. Dubrovka and R. S. Donnan, "Terahertz Spectral Domain Computational Analysis of Hydration Shell of Proteins with Increasingly Complex Tertiary Structure," *Journal of Physical Chemistry B*, vol. 117, pp. 16486 - 16492, 2013.
- [30] S. Romanenko, R. Begley, A. H. Harvey, L. Hool and V. P. Wallace, "The interaction between electromagnetic fields at megahertz, gigahertz and terahertz frequencies with cells, tissues and organisms: risks and potential," *Journal of the Royal Society Interface*, vol. 14, no. 137, pp. 1 - 22, 2017.
- [31] C. Gabriel, S. Gabriel and E. Corthout, "The dielectric properties of biological tissues: I. Literature survey," *Physics in Medicine and Biology*, vol. 41, pp. 2231 - 2249, 1996.
- [32] S. Gabriel, R. W. Lau and C. Gabriel, "The dielectric properties of biological tissues: III. Parametric models for the dielectric spectrum of tissues," *Physics in Medicine and Biology*, vol. 41, pp. 2251 - 2269, 1996.

- [33] H. P. Schwan, "Electrical Properties of Tissue and Cell Suspensions," *Advances in Biological and Medical Physics*, vol. 5, pp. 147 - 209, 1957.
- [34] N. Nasir and M. A. Ahmad, "Cells Electrical Characterization: Dielectric Properties, Mixture, and Modeling Theories," *Journal of Engineering*, vol. 2020, no. 9475490, pp. 1 - 17, 2020.
- [35] S. Gabriel, R. W. Lau and C. Gabriel, "The dielectric properties of biological tissues: II. Measurements in the frequency range 10 Hz to 20 GHz," *Physics in Medicine and Biology*, vol. 41, pp. 2251 - 2269, 1996.
- [36] B. C. Truong, H. D. Tuan, H. H. Kha and H. T. Nguyen, "Debye Parameter Extraction for Characterizing Interaction of Terahertz Radiation With Human Skin Tissue," *IEEE Transactions on Biomedical Engineering*, vol. 60, no. 6, pp. 1528 - 1537, 2013.
- [37] M. Grandolfo, S. M. Michaelson and A. Rindi, *Biological Effects and Dosimetry of Nonionizing Radiation*, New York, NY: NATO Scientific Affairs & Plenum Press, 1983.
- [38] A. Lajevardipour, A. W. Wood, R. L. McIntosh and S. Iskra, "Estimation of Dielectric Values for Tissue Water in the Terahertz Range," *Bioelectromagnetics*, vol. 37, pp. 563 - 567, 2016.
- [39] E. Pickwell, B. E. Cole, A. J. Fitzgerald, V. P. Wallace and M. Pepper, "Simulation of terahertz pulse propagation in biological systems," *Applied Physics Letters*, vol. 84, no. 12, pp. 2190 - 2192, 2004.
- [40] B. C. Q. Truong, H. D. Tuan, A. J. Fitzgerald, V. P. Wallace and H. T. Nguyen, "A Dielectric Model of Human Breast Tissue in Terahertz Regime," *IEEE Transactions on Biomedical Engineering*, vol. 62, no. 2, pp. 699 - 707, 2015.
- [41] J. Wang, H. Lindley-Hatcher, X. Chen and E. Pickwell-MacPherson, "THz Sensing of Human Skin: A Review of Skin Modeling Approaches," *Sensors*, vol. 21, no. 3624, pp. 1 - 26, 2021.
- [42] P. Jepsen and H. Merbold, "Terahertz Reflection Spectroscopy of Aqueous NaCl and LiCl Solutions," *Journal of Infrared, Millimeter, and Terahertz Waves*, vol. 31, no. 4, pp. 430-440, 2010.
- [43] O. Smolyanskaya, N. Chernomyrdin, A. Konovko, K. Zaytsev, I. Ozheredov, O. Cherkasova, M. Nazarov, J.-P. Guillet, S. Kozlov, Y. V. Kistenev, J.-L. Coutaz, P. Mounaix, V. Vaks, J.-H. Son, H. Cheon and V. Wallace, "Terahertz biophotonics as a tool for studies of dielectric and spectral properties of biological tissues and liquids," *Progress in Quantum Electronics*, vol. 62, pp. 1-77, 2018.
- [44] E. Pickwell-MacPherson and V. Wallace, "Terahertz pulsed imaging - A potential medical imaging modality?," *Photodiagnosis and Photodynamic Therapy*, vol. 6, no. 2, pp. 128 - 134, 2009.
- [45] T. Wu and S. Austin, "Bose-Einstein condensation in biological systems," *Journal of Theoretical Biology*, vol. 71, pp. 209 - 214, 1978.

- [46] A. A. Serga, V. S. Tiberkevich, C. W. Sandweg, V. I. Vasyuchka, D. A. Bozhko, A. V. Chumak, T. Neumann, B. Obry, G. A. Melkov, A. N. Slavin and B. Hillebrands, "Bose-Einstein condensation in an ultra-hot gas of pumped magnons," *Nature communications*, vol. 5, no. 3452, 2014.
- [47] J. Reimers, L. McKemmish, R. McKenzie, A. Mark and N. Hush, "Weak, strong, and coherent regimes of Fröhlich condensation and their applications to terahertz medicine and quantum consciousness," *Proceedings of the National Library of Science*, vol. 106, no. 11, pp. 4219 - 4224, 2009.
- [48] I. V. Lundholm, H. Rodilla, W. Y. Wahlgren, A. Duelli, G. Bourenkov, J. Vukusiv, R. Friedman, J. Stake, T. Schneider and G. Katona, "Terahertz radiation induces non-thermal structural changes associated with Fröhlich condensation in a protein crystal," *Structural Dynamics*, vol. 2, no. 054702, pp. 1 - 12, 2015.
- [49] B. S. Alexandrov, V. Gelev, A. R. Bishop, A. Usheva and K. Ø. Rasmussen, "DNA breathing dynamics in the presence of a terahertz field," *Physics Letters A*, vol. 374, pp. 1214 - 1217, 2010.
- [50] R. Wheeler, Artist, *DNA Structure*. [Art]. Wikimedia Commons, 2019.
- [51] T. Dauxois, M. Peyrard and A. R. Bishop, "Entropy-driven DNA denaturation," *Physical Review E*, vol. 47, pp. R44 - R47, 1993.
- [52] B. S. Alexandrov, V. Gelev, S. W. Yoo, A. R. Bishop, K. Ø. Rasmussen and A. Usheva, "Toward a Detailed Description of the Thermally Induced Dynamics of the Core Promoter," *Public Library of Science*, vol. 5, no. 3, pp. 1 - 10, 2009.
- [53] B. S. Alexandrov, V. Gelev, S. W. Yoo, L. B. Alexandrov, Y. Fukuyo, A. R. Bishop, K. O. Rasmussen and A. Usheva, "DNA dynamics play a role as a basal transcription factor in the positioning and regulating of gene transcription initiation," *Nucleic Acids Research*, vol. 38, no. 6, pp. 1790 - 1795, 2009.
- [54] B. S. Alexandrov, M. L. Phipps, L. B. Alexandrov, L. G. Booshehri, A. Erat, J. Zabolotny, C. H. Mielke, H. -T. Chen, G. Rodriguez, K. O. Rasmussen, J. M. Martinez, A. R. Bishop and A. Usheva, "Specificity and Heterogeneity of Terahertz Radiation Effect on Gene Expression in Mouse Mesenchymal Stem Cells," *Scientific Reports*, vol. 3, pp. 1 - 8, 2013.
- [55] I. Echchgadda, C. C. Roth, C. Z. Cerna and G. J. Wilmink, "Temporal Gene Expression Kinetics for Human Keratinocytes Exposed to Hyperthermic Stress," *Cells*, vol. 2, no. 2, pp. 224 - 243, 2013.
- [56] I. Echchgadda, J. E. Grundt, C. Z. Cerna, C. C. Roth, J. A. Payne, B. L. Ibey and G. J. Wilmink, "Terahertz Radiation: A Non-contact Tool for Selective Stimulation of Biological Responses in Human Cells," *IEEE Transactions on Terahertz Science and Technology*, vol. 6, no. 1, pp. 54 - 68, 2016.
- [57] O. P. Cherkasova, D. S. Serdyukov, A. S. Ratushnyak, E. F. Nemova, E. N. Kozlov, Y. V. Shidlovskii, K. I. Zaytsev and V. V. Tuchin, "Effects of Terahertz Radiation on Living Cells: a Review," *Optics and Spectroscopy*, vol. 128, no. 6, pp. 855 - 866, 2020.

- [58] M. Mattsson, O. Zeni and M. Simko, "Is there a biological basis for therapeutic applications of millimeter waves and THz waves?," *Journal of Infrared, Millimeter, and Terahertz Waves*, vol. 39, pp. 863 - 878, 2018.
- [59] L. V. Titova, F. A. Hegmann and O. Kovalchuk, "Biological Effects of Broadband Terahertz Pulses," in *Terahertz Biomedical Science and Technology*, Boca Raton, FL, CRC Press, 2014, pp. 241 - 263.
- [60] "Tera-Hertz radiation in Biological Research, Investigations on Diagnostics and study on potential Genotoxic Effects (THz-BRIDGE), Final Report," [Online]. Available: <https://www.frascati.enea.it/THz-BRIDGE/>.
- [61] A. Ramundo-Orlando, G. P. Gallerano, P. Stano, A. Doria, E. Giovenale, G. Messina, M. Cappelli, M. D'Arienzo and I. Spassovsky, "Permeability Changes Induced by 130 GHz Pulsed Radiation on Cationic Liposomes Loaded With Carbonic Anhydrase," *Bioelectromagnetics*, vol. 28, no. 8, pp. 587 - 598, 2007.
- [62] I. Echchgadda, C. Cerna, M. Sloan, D. Elam and B. Ibey, "Effects of different terahertz frequencies on gene expression in human keratinocytes," *Proceedings of the Society of Photo-Optical Instrumentation Engineers*, vol. 9321, pp. Q1 - Q9, 2015.
- [63] L. Titova, A. Ayesheshim, A. Golubov, R. Rodriguez-Juarez, R. Woycicki, F. Hegmann and O. Kovalchuk, "Intense THz pulses down-regulate genes associated with skin cancer and psoriasis: a new therapeutic avenue?," *Scientific Reports*, vol. 3, no. 2363, pp. Q1 - Q10, 2013.
- [64] C. M. Hough, D. N. Purschke, C. Huang, L. V. Titova, O. V. Kovalchuk, B. J. Warkentin and F. A. Hegmann, "Topology-based prediction of pathway dysregulation induced by intense terahertz pulses in human skin tissue models," *Journal of Infrared, Millimeter, and Terahertz Waves*, vol. 39, pp. 887 - 898, 2018.
- [65] C. M. Hough, D. N. Purschke, C. Huang, L. V. Titova, O. V. Kovalchuk, B. J. Warkentin and F. A. Hegmann, "Intense Terahertz Pulses Inhibit Ras Signaling and Other Cancer-associated Signaling Pathways in Human Skin Models," *Journal of Physics: Photonics*, vol. 3, no. 034004, pp. 1 - 14, 2021.
- [66] K. -T. Kim, J. Park, S. J. Jo, S. Jung, O. S. Kwon, G. P. Gallerano, W. -Y. Park and G. -S. Park, "High-power femtosecond-terahertz pulse induces a wound response in mouse skin," *Scientific Reports*, vol. 3, no. 2296, pp. 1 - 7, 2013.
- [67] A. Amicis, S. D. Sanctis, S. D. Cristofaro, V. Franchini, F. Lista, E. Regalbuto, E. Giovenale, G. P. Gallerano, P. Nenzi, R. Bei, M. Fantini, M. Benvenuto, L. Masuelli, E. Coluzzi, C. Cicia and A. Sgura, "Biological effects of in vitro THz radiation exposure in human foetal fibroblasts," *Mutation Research/Genetic Toxicology and Environmental Mutagenesis*, vol. 793, pp. 150 - 160, 2015.
- [68] S. Yamazaki, M. Harata, Y. Ueno, M. Tsubouchi, K. Konagaya, Y. Ogawa, G. Isoyama, C. Otani and H. Hoshina, "Propagation of THz irradiation energy through aqueous layers: Demolition of actin filaments in living cells," *Scientific Reports*, vol. 10, no. 9008, pp. 1 - 10, 2020.

- [69] C. M. Hough, D. N. Purschke, C. Bell, A. P. Kalra, P. J. Oliva, C. Huang, J. A. Tuszyński, B. J. Warkentin and F. A. Hegmann, "Disassembly of microtubules by intense terahertz pulses," *Accepted by Biomedical Optics Express*, 2021.
- [70] C. M. Hough, D. N. Purschke, C. Huang, L. V. Titova, O. V. Kovalchuk, B. J. Warkentin and F. A. Hegmann, "Invited Paper: Global gene expression in human skin tissue induced by intense terahertz pulses," *Terahertz Science and Technology*, vol. 11, no. 1, pp. 28 - 33, 2018.
- [71] L. Titova, A. Ayesheshim, A. Golubov, D. Fogen, R. Rodriguez-Juarez, F. Hegmann and O. Kovalchuk, "Intense THz pulses cause H2AX phosphorylation and activate DNA damage response in human skin tissue," *Biomedical Optics Express*, vol. 4, no. 4, pp. 559 - 568, 2013.
- [72] E. Hall, *Radiobiology for the Radiologist*, Philadelphia, PA: Lippincott, Williams & Wilkins, 2000.
- [73] H. Cheon, H.-j. Yang, S.-H. Lee, Y. A. Kim and J.-H. Son, "Terahertz molecular resonance of cancer DNA," *Scientific Reports*, vol. 6, no. 37103, pp. 1 - 10, 2016.
- [74] Y. H. Tao, S. I. Hodgetts, A. R. Harvey and V. P. Wallace, "Reproducibility of Terahertz Peaks in a Frozen Aqueous Solution of 5-Methylcytidine," *Journal of Infrared, Millimeter, and Terahertz Waves*, vol. 42, pp. 588 - 606, 2021.
- [75] T. Kawasaki, K. Tsukiyama and A. Irizawa, "Dissolution of a fibrous peptide by terahertz free electron laser," *Scientific Reports*, vol. 9, no. 1, pp. 1 - 8, 2019.
- [76] A. Markelz and Z. Taylor, "The 2017 terahertz science and technology roadmap - Biological applications of THz technology," *Journal of Physics D: Applied Physics*, vol. 50, 2017.

3 Terahertz source development: Laser-based generation of intense terahertz pulses in lithium niobate

“Since we have become accustomed to think of waves of electrical energy and light waves as forming component parts of a common spectrum, the attempt has often been made to extend our knowledge over the wide region which has separated the two phenomena, and to bring them closer together, ...”

– H. Rubens & E. F. Nichols, in “Heat Rays of Great Wavelength.” (1897)

3.1 Introduction

In Chapter 1, the “terahertz gap” was introduced, a conspicuous lack of sources and detectors that operate efficiently in the intermediate band between conventional electronic and photonic regimes [1, 2]. Technological advances over recent decades have bridged the THz gap, and a wide variety of sources are now available with multiple operational principles [3, 4, 5, 6, 7].

An important class of THz generation techniques is the utilization of nonlinear material dynamics to down-convert the frequency spectrum of amplified laser pulses [8]. Lasers are capable of generating highly intense, coherent, and directional electromagnetic (EM) energy via positive feedback in a resonating reflective cavity. Ultrafast laser pulses with envelope durations on the order of $\sim 10 - 100$ fs, and intensities sufficient to induce nonlinear dynamics in materials, may be used to generate and coherently detect intense pulses of THz radiation.

3.1.1 Lasers in terahertz science

Lasers facilitate amplification of light by stimulated emission, first theoretically formalized by Albert Einstein in 1916 – 1917 [9, 10]. The first laser was developed by Theodore Maiman in 1960 [11], and over the subsequent six decades, lasers have become a ubiquitous research tool in the fields of imaging [12], spectroscopy [13], medicine [14], optogenetics [15, 16], and particle acceleration [17]. In 1981, the colliding-pulse ring dye laser was developed by Bell Labs, leading to the emergence of “ultrafast phenomena” as a field of scientific inquiry [18, 19]. This allowed researchers to use fast pulses of laser light to study material processes that occur on very short timescales (femtosecond/picosecond) such as carrier dynamics in semiconductors [20], photochemical processes (e.g., fluorescence) [21], or molecular vibrational spectroscopy [22].

The most popular laser-based method of generating THz radiation is optical rectification (OR), a nonlinear material process that produces THz pulses via rectification of an intense AC input laser field to a DC polarization (discussed in detail in Section 3.3.2). The first demonstration of OR was reported in 1973 for generation of single-cycle THz pulses in lithium niobate (LiNbO_3 , LN) as measured by a far-infrared Michelson interferometer [23]. In 1984, Auston et al. characterized the emission geometry of the THz pulse during the OR generation process inside a lithium tantalate crystal, including direct characterization of the Cherenkov cone formation, an optical phenomenon that manifests as a photonic “shockwave” induced by a light source traveling faster than its emitted wave in a material [24, 25]. Further measurements were performed with a delayed ultrafast optical pulse modulated by the birefringence induced by the THz pulse, representing an early application of time-domain pump-probe detection techniques that would later be termed “electro-optic (EO) sampling”. The first coherent detection of a THz pulse in free space with EO sampling was performed in 1995, providing detailed sub-picosecond resolution of the temporal variation of the THz field [26]. These coherent generation and detection methods set the stage for time-domain spectroscopy in biological analysis [27, 28] and medical imaging [29, 30, 31].

In 2002, Hebling et al. proposed a theoretical method for dramatically increasing the generation efficiency of OR by modulating the propagation geometry of the incident pump pulse, and further demonstrated the technique in a gallium phosphide (GaP) crystal [32]. By establishing a pump pulse with an angle between the pulse front and the phase front equal to the Cherenkov cone angle, THz generation is concentrated to a line source along the cone edge. This results in constructive interference of the generated THz wave as the tilted laser pulse propagates through the crystal. This method of generating intense THz pulses by OR of tilted-pulse-front (TPF) infrared lasers is a popular laser-based method of modern THz generation.

The first demonstration of THz generation by tilted-pulse-front optical rectification (TPFOR) in LiNbO_3 was reported in 2004 [33], and by 2007 these sources had reached capabilities of generating intense THz pulses with energy and field strength up to 10 μJ and 250 kV/cm , respectively, with peak intensities of $\sim 10 \text{ MW/cm}^2$. TPFOR is the THz generation method utilized in this thesis project for biological exposure studies, as has been successfully implemented in other THz bio-exposure systems [34, 35].

In this chapter, theoretical and experimental discussions of THz generation using ultrafast laser pulses are presented. First, the theory of laser physics is outlined, specifically focusing on titanium-doped sapphire gain media used for THz generation and detection in this project. Next, unusual dielectric response in materials that may be induced by sufficiently intense laser excitation, known

as “nonlinear optics”, is introduced. The nonlinear wave equation is derived from Maxwell’s equations, and it is shown that OR is a consequence of including nonlinear material responses in the derivation of the wave equation. The theory of THz generation by OR is then outlined, with considerations of velocity-matching for TPFOR. In Section 3.4, the laser oscillator and amplifier systems, as well as ancillary systems used in this project, are described in detail. Finally, Section 3.4.3 summarizes these descriptions in the operation of the source of intense THz pulses used for biological exposures.

3.2 Laser physics

For lasing to be possible, three components are required: The first is a lasing gain medium capable of population inversion of excited energy levels (i.e., more atoms in high energy state than low energy ground state). The second is an external energy pump source for creating population inversion in the gain medium. Finally, a resonating cavity with reflective end-mirrors provide positive feedback for photonic gain.

3.2.1 Population inversion in an excitable laser gain medium

Consider a photon beam with flux F and cross-sectional area A , incident on a 2-level material with N_1 atoms in the ground state, E_1 , and N_2 in the excited state, E_2 [36]. The transition rate for stimulated emission ($2 \rightarrow 1$) is governed by

$$\frac{dN_2}{dt} = -W_{21}N_2 \quad (3.1)$$

where $W_{21} = \sigma_{21}F$ is the stimulated emission rate constant, and σ_{21} is the interaction cross-section. Similarly, the absorption rate ($1 \rightarrow 2$) is

$$\frac{dN_1}{dt} = -W_{12}N_1 \quad (3.2)$$

where $W_{12} = \sigma_{12}F$ for an absorption cross-section σ_{12} . Assuming levels 1 and 2 have degeneracy g_1 and g_2 , respectively, then

$$\begin{aligned}
g_2 W_{21} &= g_1 W_{12} \\
g_2 \sigma_{21} &= g_1 \sigma_{12}.
\end{aligned}
\tag{3.3}$$

A material interaction length dz changes the number of photons by $A dF$. Setting this equal to the difference between stimulated emission and absorption gives

$$dF = \sigma_{21} F \left[N_2 - \left(\frac{g_2 N_1}{g_1} \right) \right] dz. \tag{3.4}$$

From Equation (3.4), $dF/dz > 0$ when $N_2 > g_2 N_1 / g_1$, and the beam is amplified by the interaction. This condition is generally not satisfied in two-level systems at thermal equilibrium, since the relative population at temperature T is given by the Boltzmann distribution

$$\frac{N_2}{N_1} = \exp\left(-\frac{E_2 - E_1}{kT}\right) \tag{3.5}$$

where $k = 1.37 \times 10^{-23}$ J/K is the Boltzmann constant. Therefore, under thermal equilibrium, $N_2 < N_1$, and materials act as absorbers. To achieve population inversion ($N_2 > g_2 N_1 / g_1$) required for amplification, an external energy source (the ‘‘pump’’) is connected to the lasing medium, which may be in the form of chemical (e.g., a battery), electric (e.g., diode circuit), or photonic (e.g., another laser) techniques. At least three energy levels (i.e., $g_1 + g_2 > 2$) are required for population inversion to be possible, as the emission and absorption rates of two-level systems are exactly balanced (i.e., the material becomes transparent at $g_2 N_2 = g_1 N_1$, known as two-level saturation) [36].

A schematic of laser operation is depicted in Figure 3.1. Photonic amplification is achieved by trapping EM energy from stimulated emission in a reflective cavity that makes many round-trips through the active gain medium, stimulating similar transitions and emission of other photons that are in phase and constructively interfere, resulting in compounding amplification and coherent emission of laser light. The laser output is determined by both the gain profile of the lasing medium and the modes f_n that the cavity may support, determined by the cavity length L as

$$f_n = \frac{nc}{2L} \tag{3.6}$$

for positive integers n as shown in Figure 3.1(b). The net interference of the modes of Equation (3.6) produce a single localized pulse that reflect between the cavity end-mirrors, known as “modelocking”. One end-mirror is slightly transmissive, and this allows pulse ejection at a repetition rate equal to the inverse round-trip time of the cavity pulse.

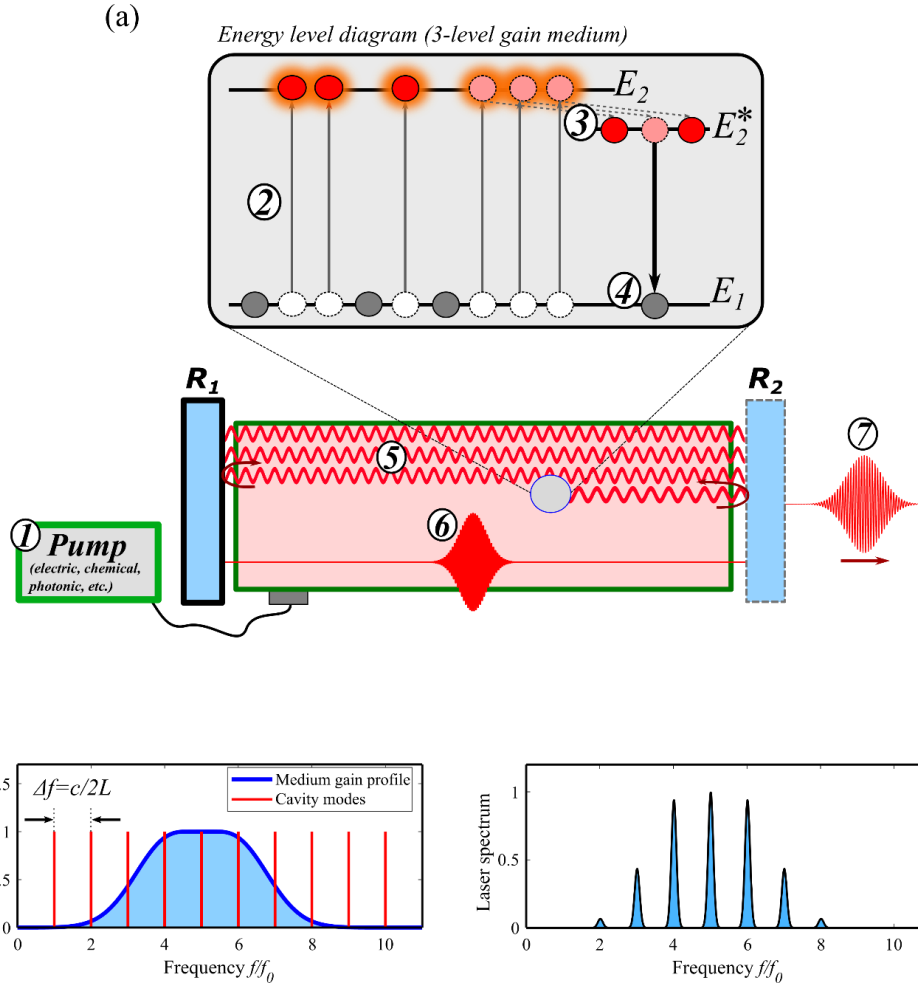


Figure 3.1. Physics of laser operation. (a) Stimulated emission and feedback amplification in a reflective cavity oscillator. (1) An external energy source excites atoms in a gain medium to higher energy levels. (2) Population inversion is achieved when more atoms exist in high energy states (E_2) relative to the ground state (E_1). (3) Excited particles quickly relax to the upper lasing level E_2^* . (4) Stimulated transition to the ground level results in the emission of a photon in phase with the stimulating photon. (5) Photons are trapped in the oscillator cavity, and multiple round-trips stimulate similar emissions that provide photonic gain. (6) The cavity modes interfere to form a localized pulse that is trapped between the end mirrors of the reflective cavity (i.e., “modelocking”). (7) One end-mirror is partially transmissive, allowing a small fraction of pulse energy to form the laser emission. (b) The laser emission spectrum is a combination of the gain profile of the lasing medium and the oscillatory modes that the cavity can support. Constructive interference of the cavity modes produces modelocked pulse emission.

3.2.2 Ti:Sapphire Lasers

In this thesis project, the generation and detection of intense THz pulses rely specifically on laser technologies that utilize titanium-doped sapphire (Ti:Sapphire, or $\text{Ti:Al}_2\text{O}_3$) as a gain medium, first characterized by Moulton in 1986 [37]. The development of Ti:Sapphire crystals with low loss and attractive mechanical, thermal, and optical properties contribute to excellent modelocking capabilities; consequently, Ti:Sapphire laser technologies have become one of the most popular laser technologies for modern laboratory application due to relative ease of use and wide tunability [38]. The widespread availability of Ti:Sapphire laser technology for THz generation has spurred rapid development particularly in the field of THz time-domain spectroscopy (TDS) [8].

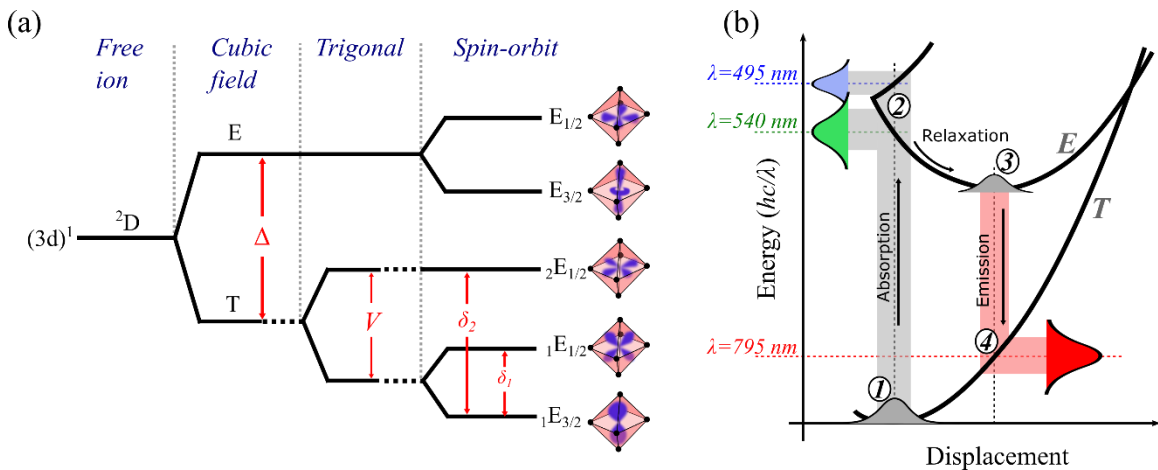


Figure 3.2. **The energy landscape of a Ti:Sapphire laser gain medium.** (a) Energy levels of $\text{Ti:Al}_2\text{O}_3$, adapted from [38, 39]. The primary lasing source is due to the cubic field from the neighbouring oxygen atoms that cause splitting Δ between an excited doublet (E) and a ground-state triplet (T), with finer energy splitting given by V/δ . The electron distributions corresponding to the energy levels are depicted at right. (b) Electronic energy vs. displacement of the Ti^{3+} ion. (1) Initially, bound electrons are in the ground state. (2) Absorption of a blue-green photon raises the electron to the excited band, E, where it quickly relaxes into the upper lasing level (3). (4) Stimulated emission to the triplet ground state, T, results in the emission of a red photon.

A depiction of the energy diagram of $\text{Ti:Al}_2\text{O}_3$ is shown in Figure 3.2(a). The titanium dopant replaces aluminum at the lattice binding site where it binds to six neighbouring oxygen atoms, and effectively exists as a Ti^{3+} ion [38]. A single d -electron is in the outermost shell, and a total of 5 free energy levels exist as an excited doublet (E in Figure 3.2(a)) and ground state triplet (T in Figure 3.2(a)) that arise from the cubic field distribution. The electron distribution for each level is depicted schematically at right of the energy diagram.

The Ti:Sapphire gain medium has a pump absorption band peaked in the blue-green at roughly 490 nm with a ~ 75 nm bandwidth (FWHM) [38]. The finer structure in energy splitting (V and δ

in Figure 3.2(a)) are typically ignored relative to Δ ($\sim 20000 \text{ cm}^{-1}$; 2.5 eV) [38, 39]. The emission band is peaked at 790 nm, and has wide tunability between $\sim 650 \text{ nm}$ up to 1200 nm. Figure 3.2(b) is a schematic of the electron energy as a function of Ti^{3+} ion displacement. In the ground state, the $3d$ electron may be excited by green/blue photon absorption, which quickly relaxes into the upper lasing level. Another relaxation to the ground state results in photon emission contributing to the stimulated emission laser output. These emissions may be photonically amplified by the lasing process outlined in Section 3.2.1.

Ti:Sapphire laser technologies are used in the commercial oscillator and regenerative amplifier technologies from the Coherent company used for this thesis project [40, 41]. Schematics, descriptions, and characterizations of these laser systems are presented in detail in Section 3.4. Importantly, these systems produce sufficiently intense pulses of ultrafast infrared laser pulses capable of driving nonlinear polarization responses in many materials of interest. Material dynamics in this intensity regime are described by the field of nonlinear optics [42].

3.3 Nonlinear optics

“Nonlinear” optical phenomena refer to the aspects of a material response to an applied optical field that do not scale linearly with the strength of the field [42]. Fundamentally, this arises from materials driven far enough from equilibrium that their optical properties are altered by the presence of the incident light field itself [43]. Typically, this regime of material response requires high intensities, such as those attainable by laser technologies as described in the previous section. Shortly following the discovery of the ruby laser by Theodore Maiman in 1960, the first demonstration of second-harmonic generation (a nonlinear optical phenomenon) was performed by Franken et al. in 1961, and is considered the birth of the field of nonlinear optics [11, 43].

3.3.1 *The nonlinear wave equation*

To explicate the origin of the nonlinear response of materials to a sufficiently intense applied field, we begin by outlining the derivation of the wave equation, which in turn begins with a definition of Maxwell’s Equations in continuous polarizable media [42]:

$$\nabla \cdot \vec{D} = \rho \quad \text{Gauss' law for electric fields}$$

$$\begin{aligned}
\nabla \cdot \vec{B} &= 0 && \text{Gauss' law for magnetic fields} \\
\nabla \times \vec{E} &= -\frac{\partial \vec{B}}{\partial t} && \text{Faraday's law of induction} \\
\nabla \times \vec{H} &= \frac{\partial \vec{D}}{\partial t} + \vec{j} && \text{Ampere's circuit law (with displacement} \\
&&& \text{current term)}
\end{aligned} \tag{3.7}$$

where $\vec{D} = \epsilon \vec{E} = \epsilon_0 \vec{E} + \vec{P}$ is the displacement field proportional to the electric field \vec{E} , $\epsilon = \epsilon_r \epsilon_0$ is the total permittivity (where ϵ_r is the material-dependent relative permittivity and $\epsilon_0 = 8.85 \times 10^{-12}$ F/m is the vacuum permittivity), and \vec{P} is the induced polarization that depends nonlinearly on \vec{E} in general. In the linear regime, $\vec{P} = \vec{P}_L = \epsilon_0 \chi \vec{E}$, where χ is the electric susceptibility, and therefore $\epsilon_r = 1 + \chi$.

Assuming non-magnetic media, the net magnetization is zero, and the magnetic field \vec{B} is related to the H -field as $\vec{B} = \mu_0 \vec{H}$ for a vacuum permeability $\mu_0 = 1/(\epsilon_0 c^2) = 4\pi \times 10^{-7}$ H/m. It is also assumed that there are no free charges or currents ($\rho = \vec{j} = 0$). To derive the electric field wave equation, the curl of Faraday's law is taken and inserted into Ampere's circuit law to eliminate the magnetic field dependence. Using the identity $\nabla \times \nabla \times \vec{A} = \nabla(\nabla \cdot \vec{A}) - \nabla^2 \vec{A}$, and assuming negligible variation in electric field divergence (i.e., $\nabla(\nabla \cdot \vec{E}) \approx 0$), the wave equation is derived as

$$\nabla^2 \vec{E} - \frac{1}{c^2} \frac{\partial^2 \vec{E}}{\partial t^2} = \frac{1}{\epsilon_0 c^2} \frac{\partial^2 \vec{P}}{\partial t^2}. \tag{3.8}$$

The term on the RHS is a source term, and represents the mathematical statement that accelerating charges generate EM radiation. For linear media with electric susceptibility χ , $\vec{P}_L = \epsilon_0 \chi \vec{E}$ (i.e., the induced polarization scales linearly with the applied electric field). Inserting this into Equation (3.8) results in the wave equation for linear media

$$\nabla^2 \vec{E} - \frac{1}{v^2} \frac{\partial^2 \vec{E}}{\partial t^2} = 0. \tag{3.9}$$

The net effect is a description of a new wave propagating at reduced speed $v = c/n$ where $n = \sqrt{\epsilon_r}$ is the refractive index, and reduced wavelength $\lambda = \lambda_0/n$ for a vacuum wavelength λ_0 .

3.3.1.1 Including nonlinear polarization in the wave equation

To incorporate nonlinear media responses, the induced polarization is Taylor-expanded for higher-order terms of the applied E -field

$$\vec{P} = \vec{P}_L + \vec{P}_{NL} = \epsilon_0 \left(\chi^{(1)} \vec{E} + \frac{1}{2!} \chi^{(2)} \vec{E} \vec{E} + \frac{1}{3!} \chi^{(3)} \vec{E} \vec{E} \vec{E} + \frac{1}{4!} \chi^{(4)} \vec{E} \vec{E} \vec{E} \vec{E} + \dots \right) \quad (3.10)$$

where $\chi^{(n)}$ is the n^{th} -order susceptibility [42]. With this substitution in Equation (3.8), the nonlinear wave equation is

$$\nabla^2 \vec{E} - \frac{1}{v^2} \frac{\partial^2 \vec{E}}{\partial t^2} = \mu_0 \frac{\partial^2 \vec{P}_{NL}}{\partial t^2}. \quad (3.11)$$

Thus, the inclusion of nonlinear effects results in a time-varying nonlinear polarization response of the medium, \vec{P}_{NL} , that is an additional source term for EM radiation not present in the linear case (Equation (3.9)).

The consequences of this modification in terms of radiation generation may be seen by considering an input E -field expressed as a sum of its Fourier components:

$$\vec{E}(t) = \sum_n \vec{E}_n e^{-i\omega_n t} + CC_n \quad (3.12)$$

where \vec{E}_n , ω_n , and CC_n are the n^{th} amplitude, frequency, and complex conjugate, respectively. Consider a field comprised of two frequencies, ω_1 and ω_2 , that induces a nonlinear polarization response in the material to second-order:

$$\vec{P}_{NL} \propto E^2 = (E_1 e^{-i\omega_1 t} + E_2 e^{-i\omega_2 t} + CC)^2. \quad (3.13)$$

The terms that arise from squaring the expression in brackets are:

Nonlinear term	Corresponding Generation Mode
$E_1^2 e^{-i2\omega_1 t} + E_2^2 e^{-i2\omega_2 t}$	Second harmonic generation (SHG)
$2E_1 E_2 e^{-i(\omega_1 + \omega_2)t}$	Sum-Frequency generation (SFG)
$2E_1 E_2^* e^{-i(\omega_1 - \omega_2)t}$	Difference Frequency Generation (DFG)
$2(E_1 ^2 + E_2 ^2)$	Optical Rectification (OR)

where the asterisk denotes a complex conjugate. Since time-varying nonlinear polarization, \vec{P}_{NL} , is a source term in Equation (3.11), these material responses result in the generation of EM radiation at new frequencies that did not exist in the input field. While the above example considers an input field comprised of only two frequencies, the argument may be generalized for an arbitrary field with any number of Fourier components.

The capability of utilizing nonlinear materials to generate frequencies that did not exist in the input field is the key characteristic of nonlinear optics that allows THz generation from highly intense laser radiation, even though they occupy vastly different regions of the photon energy spectrum. Of particular interest are those terms in which the frequency dependence cancels, leading to a DC polarization induced in the material that depends only on field amplitude, termed optical rectification (OR).

3.3.2 Nonlinear dynamics in materials and optical rectification

To formalize how these nonlinear processes may be utilized to generate THz radiation, consider an applied EM field $E(t) = E_0 e^{-i\omega t}$ that induces electron oscillations about their equilibria according to Newton's Second Law:

$$\ddot{x} + \gamma \dot{x} + \omega_0^2 x + \alpha x^2 = -\frac{q}{m} E(t) \quad (3.14)$$

where q/m is the electron charge/mass, γ is the linear damping coefficient, ω_0 is the resonant frequency, and α is a constant that captures the second-order displacement. The solution $x(t)$ is the net electron motion as a function of time.

In the linear optical regime, second-order effects are negligible ($\alpha \approx 0$). Using the *ansatz* $x(t) = x_0 e^{-i\omega t}$, the differential equation is solved as

$$x(t) = -\frac{q}{m} \cdot \frac{E_0 e^{-i\omega t}}{\omega_0^2 - \omega^2 - i\omega\gamma} + C.C. \quad (3.15)$$

The electron motions are proportional to the applied field, and oscillate in phase at frequency ω with amplitude

$$x_0 = \left| \frac{qE_0}{m} \cdot \frac{1}{\omega_0^2 - \omega^2 - i\omega\gamma} \right| \quad (3.16)$$

corresponding to the symmetric quadratic potential $U(x) = \frac{1}{2}m\omega_0^2 x^2$ (Figure 3.3(a), blue curve) and symmetric electron motion at a frequency ω (Figure 3.3(b), blue curve). The induced linear polarization is

$$P(t) = -N \cdot q \cdot x(t) = \frac{Nq^2}{m} \cdot \frac{E_0 e^{-i\omega t}}{\omega_0^2 - \omega^2 - i\omega\gamma} = \epsilon_0 \chi(\omega) E_0 e^{-i\omega t} \propto E(t) \quad (3.17)$$

where N is the electron number of the material.

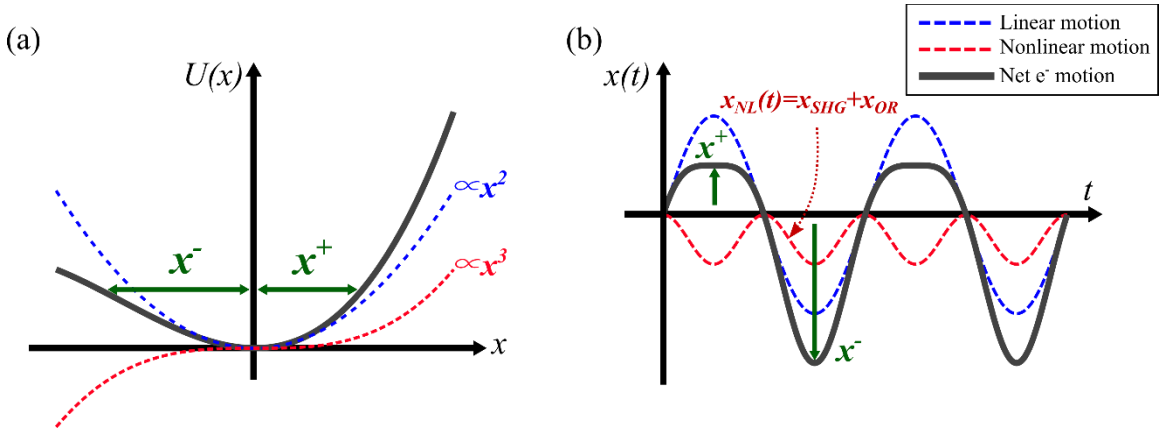


Figure 3.3. **The dipole oscillator model of nonlinear material polarization response to an applied field.** Adapted from [7]. (a) At low intensities, electrons are in a harmonic potential, and oscillate symmetrically about their equilibria. At high intensities, higher-order displacements are significant, and result in asymmetric motion (gray). (b) The corresponding electron dynamics. In the linear regime (blue curve), electrons oscillate symmetrically about their equilibria. For sufficiently intense applied fields, the nonlinear contribution (red curve) causes asymmetric electron oscillation about their equilibria, which can be expressed as a superposition of two nonlinear generation processes, SHG and OR.

For the nonlinear optical regime ($\alpha > 0$ in Equation (3.14)), the electrons are in an uneven net potential due to higher-order perturbations, shown by the gray curve of Figure 3.3(a), and motions about their equilibria are not symmetric, as shown in Figure 3.3(b). A solution to the nonlinear case

is obtained by a perturbative approach assuming $\alpha x^2 \ll \omega_0^2 x$, and expanding the electron displacement as $x(t) = \sum_{n=1}^{\infty} x^{(n)}(t)$. The first-order solution $x^{(1)}(t)$ is the linear case solved above that oscillates in phase with the applied field. The second-order term is obtained by equating terms of similar frequency-dependence:

$$\ddot{x}^{(2)} + \gamma \dot{x}^{(2)} + \omega_0^2 x^{(2)} = -\alpha [x^{(1)}]^2. \quad (3.18)$$

Inserting Equation (3.15) for $x^{(1)}$, we find

$$x^{(2)}(t) = -\alpha \left[\frac{qE_0}{m} \right]^2 \frac{e^{-i2\omega t}}{(\omega_0^2 - \omega^2 - i\omega\gamma)^2 \cdot (\omega_0^2 - (2\omega)^2 - i2\omega\gamma)} \\ - 2\alpha \left[\frac{q}{m\omega_0} \right]^2 \frac{|E_0|^2}{(\omega_0^2 - \omega^2)^2 + (\omega\gamma)^2} + C.C. \quad (3.19)$$

The second-order electron displacement $x^{(2)}$ is recognized as a superposition of second-harmonic generation (SHG) at frequency 2ω and DC optical rectification (OR)

$$x^{(2)} = x_{SHG}^{(2)} + x_{OR}^{(2)} \quad (3.20)$$

shown by the red curve in Figure 3.3(b). The bulk polarization induced by OR in the nonlinear dipole model is:

$$P_{OR} = -Nq x_{OR}^{(2)} = \frac{2\alpha q^2 N}{m\omega_0^2 [(\omega_0^2 - \omega^2)^2 + (\omega\gamma)^2]} \cdot |E_0|^2 \quad (3.21)$$

$$P_{OR} = 2\epsilon_0 \chi^{(2)} |E_0|^2$$

where

$$\chi^{(2)}(\omega) = \frac{\alpha q^2 N}{\epsilon_0 m \omega_0^2 [(\omega_0^2 - \omega^2)^2 + (\omega\gamma)^2]} \quad (3.22)$$

is the frequency-dependent second-order susceptibility expressed in terms of dipole parameters. Therefore, the AC input field is “rectified” into a DC material polarization, P_{OR} , that depends only on $\chi^{(2)}$ and the input field amplitude.

3.3.3 Terahertz pulse generation by optical rectification

Now, consider a laser pulse with a time-varying Gaussian amplitude with sufficient intensity to induce OR in a nonlinear crystal as depicted in Figure 3.4(a). By the nonlinear wave equation derived in Section 3.3.1 (Equation (3.11)), the time-varying optically-rectified polarization, $P_{OR}(t) = P_0 \exp(-2t^2/\tau^2)$, acts as a source of EM radiation, and generates frequencies that did not exist in the input wave. Theoretically, according to Equation (3.11), the emitted pulse in the far-field is characterized by the second derivative of $P_{OR}(t)$

$$E_{THz} = \frac{4P_0}{\tau^2} \exp\left(-\frac{2t^2}{\tau^2}\right) \left(1 - 4\left(\frac{t}{\tau}\right)^2\right)$$

shown by the blue waveform in Figure 3.4(a).

Figure 3.4(b) shows a comparison of an ideal EM pulse calculated by the nonlinear dipole model to a measured THz pulse generated by OR in lithium niobate. The main features of a real THz pulse are well-characterized by the second-order nonlinear dipole model, although it does not capture the oscillations for $t > 0$ that arise due to crystal ringing and dispersion in humid air, or the phase-modulations due to detecting a focusing THz beam (i.e., the ‘‘Gouy phase shift’’, see Chapter 4).

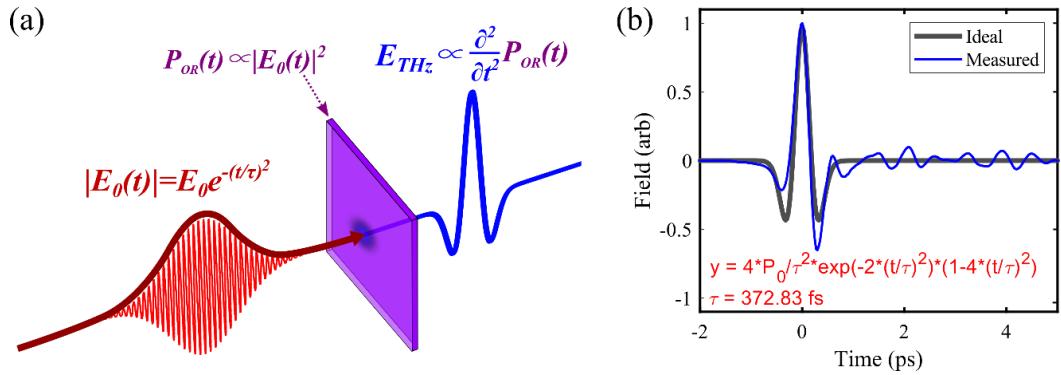


Figure 3.4. **Optical rectification in nonlinear media.** (a) A sufficiently intense Gaussian laser pulse incident on a nonlinear crystal will induce a DC polarization that is proportional to the input field amplitude. This behaves as a source of EM radiation that is proportional to the second-derivative of the polarization response, and produces frequencies that did not exist in the input field. (b) The nonlinear dipole model fit to a measured THz pulse, which accurately characterizes the main features of a real THz pulse generated by optical rectification.

3.3.4 Tilted-pulse-front optical rectification

A significant limitation in efficient THz generation by optical rectification is the disparate speeds at which the laser pump pulse travels in the crystal relative to the THz wave it is generating in many otherwise suitable nonlinear media [32]. For many materials, the refractive index seen by the THz wave is significantly larger than the optical refractive index (e.g., in LN, $n_{THz} = 5$ and $n_{opt} = 2.25$). When a wave source travels faster than the generated wave, a Cherenkov cone (the optical analogue of a “sonic boom”) is generated by the superposition of the lagging spherical wavefronts, as shown in Figure 3.5. The THz pulse therefore exists as a Cherenkov cone in the generation medium prior to free-space emission. In reality, the pump pulse will have some spatial extent, which may be modeled as a superposition of many interfering Cherenkov cones. By tilting the laser pulse front along the Cherenkov cone edge, constructive interference of the generated THz wave is achieved.

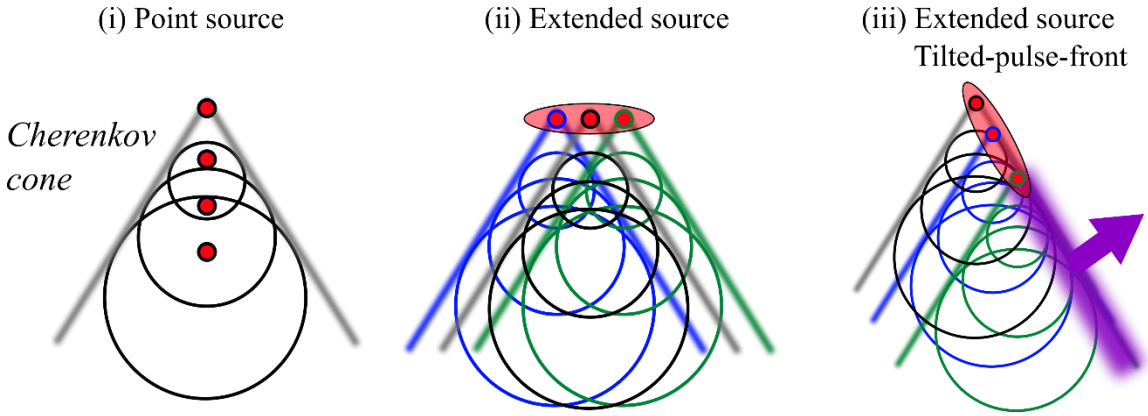


Figure 3.5. **The principle of tilted-pulse-front enhancement of THz wave generation.** In the generation crystal, the THz pulse exists as a Cherenkov cone with the laser pulse at its apex. For extended sources, tilting the pulse front along the cone edge results in constructive interference of the generated wave.

Constructive interference between a source and a generated wave is satisfied by altering the propagation geometry such that the waves are phase-/velocity-matched, or, equivalently, the pulse front lies along the Cherenkov cone edge [32]. Velocity-matching between the optical pump pulse and generated THz wave is achieved under the condition

$$\vec{v}_{opt}^{gr} = \vec{v}_{THz}^{ph} \quad (3.23)$$

where \vec{v}_{opt}^{gr} is the group velocity of the optical pulse, and \vec{v}_{THz}^{ph} is the phase velocity of the THz wave. Adjusting the wave propagation geometry such that Equation (3.23) is satisfied is achieved

by tilting the pulse front of the optical beam with respect to its phase front, allowing constructive interference along the Cherenkov cone with angle γ calculated as

$$\cos \gamma = \frac{v_{THZ}^{ph}}{v_{opt}^{gr}} = \frac{n_{opt}^{gr}}{n_{THZ}^{ph}}. \quad (3.24)$$

For LN, the Cherenkov cone angle is calculated to be $\gamma=63^\circ$.

Tilting a pulse front is fundamentally achieved by angular dispersion of the optical pulse using a diffraction grating, as shown in Figure 3.6 [32]. This method provides constructive interference for the THz wavefront along the Cherenkov cone edge for frequencies below the crystal phonon frequency, and produces collimated THz beam output with scalable THz power by increasing the pump power or beam area.

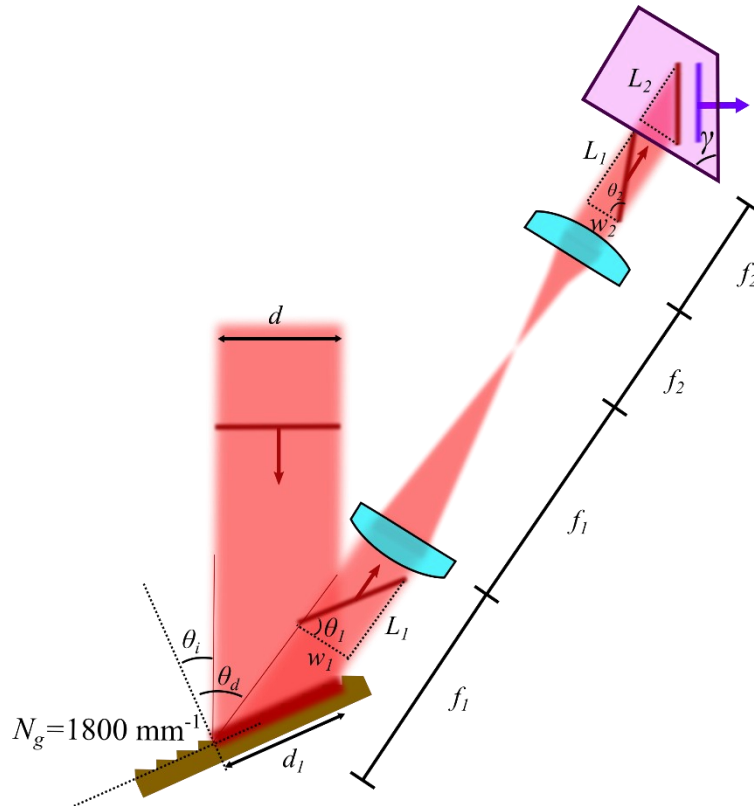


Figure 3.6. **Tilted-pulse-front beam geometry.** The pulse front of the infrared laser is tilted with respect to the phase front by isolating the first mode from a reflective diffraction grating. A 4f-imaging system is constructed with two plano-convex cylindrical lenses that image the pulse front and grating plane onto the output face of the LN prism. The tilted-pulse-front beam is described geometrically by right triangles with sides w and L , angles θ , and hypotenuses d , as labelled and described in the text.

3.3.4.1 Derivation of the tilted-pulse-front equation

The diffracted beam angle necessary to achieve the desired pulse-front tilt in the LN crystal ($\gamma = 63^\circ$ for LN) is calculated from ray geometry, with variables as defined in Figure 3.6. There are three components in the beam path that modify the propagation geometry: These are the grating itself, the lens' imaging system, and the LN crystal medium. The contribution of each is considered separately.

First, a collimated beam impinges on a reflective diffraction grating at an incident angle θ_i , and the first-order mode is diffracted at an angle θ_d according to the grating equation [19]

$$N_g \lambda = \sin \theta_i + \sin \theta_d \quad (3.25)$$

where N_g is the grating number (line frequency, inverse of slit spacing) for wavelength λ . From similar triangles in the diffraction geometry, $d/w_1 = \cos \theta_i / \cos \theta_d$. The free-space pulse-front angle is characterized as $\tan \theta_1 = L_1/w_1$, and the optical path difference induced along the pulse-front (L_1 in Figure 3.6) is expressed geometrically as

$$L_1 = d_1 \cdot (\sin \theta_i + \sin \theta_d) \quad (3.26)$$

and

$$\tan \theta_1 = \frac{1}{\cos \theta_d} \cdot (\sin \theta_i + \sin \theta_d) = \frac{N_g \lambda}{\cos \theta_d}. \quad (3.27)$$

In the lens' imaging system, a demagnification factor is defined as a ratio of beam widths:

$$D = \frac{w_2}{w_1} = \frac{\tan \theta_1}{\tan \theta_2}. \quad (3.28)$$

In the crystal, using $\tan \gamma = L_2/w_2$ and $\tan \theta_2 = L_1/w_2$, the cut angle is geometrically related to the longitudinal path differences as

$$L_2 \cdot \tan \theta_2 = L_1 \cdot \tan \gamma. \quad (3.29)$$

The optical pulse sees a refractive index n_{opt} in the crystal, defined as

$$L_1 = n_{opt} L_2. \quad (3.30)$$

Inserting into Equation (3.29),

$$\tan \theta_2 = n_{opt} \cdot \tan \gamma. \quad (3.31)$$

Inserting into Equation (3.28),

$$\tan \theta_1 = n_{opt} \cdot D \cdot \tan \gamma. \quad (3.32)$$

Finally, this is inserted into Equation (3.27) to obtain the expression describing the relationship between γ and θ_d in terms of experimental parameters:

$$n_{opt} \cdot D \cdot \tan \gamma = \frac{N_g \lambda}{\cos \theta_d}. \quad (3.33)$$

As an example calculation, consider an optical pulse with central wavelength $\lambda=800$ nm and $n_{opt}=2.25$. The demagnification factor D may also be expressed in terms of the focal lengths of the imaging lenses, $D = f_2/f_1$. This demagnification factor is chosen such that, with the choice of the grating, N_g , and calculated diffracted angle, θ_d , the surface of the diffraction grating is imaged to the output face of the LN [44]. For $N_g = 1800 \text{ mm}^{-1}$, a magnification of 0.6 corresponds to $\theta_d = 57^\circ$, and is satisfied by lens focal lengths of $f_1 = 100$ mm and $f_2 = 60$ mm.

3.4 Laser-based generation of intense terahertz pulses in lithium niobate

The theory outlined above was implemented in the design and construction of a laser-based source of intense THz pulses, integrated into an exposure system dedicated to biological studies. A schematic of all components of the experimental configuration is shown in Figure 3.7. The modelocked oscillator, regenerative amplifier, auto-correlator, and THz source are described in more detail in the following subsections.

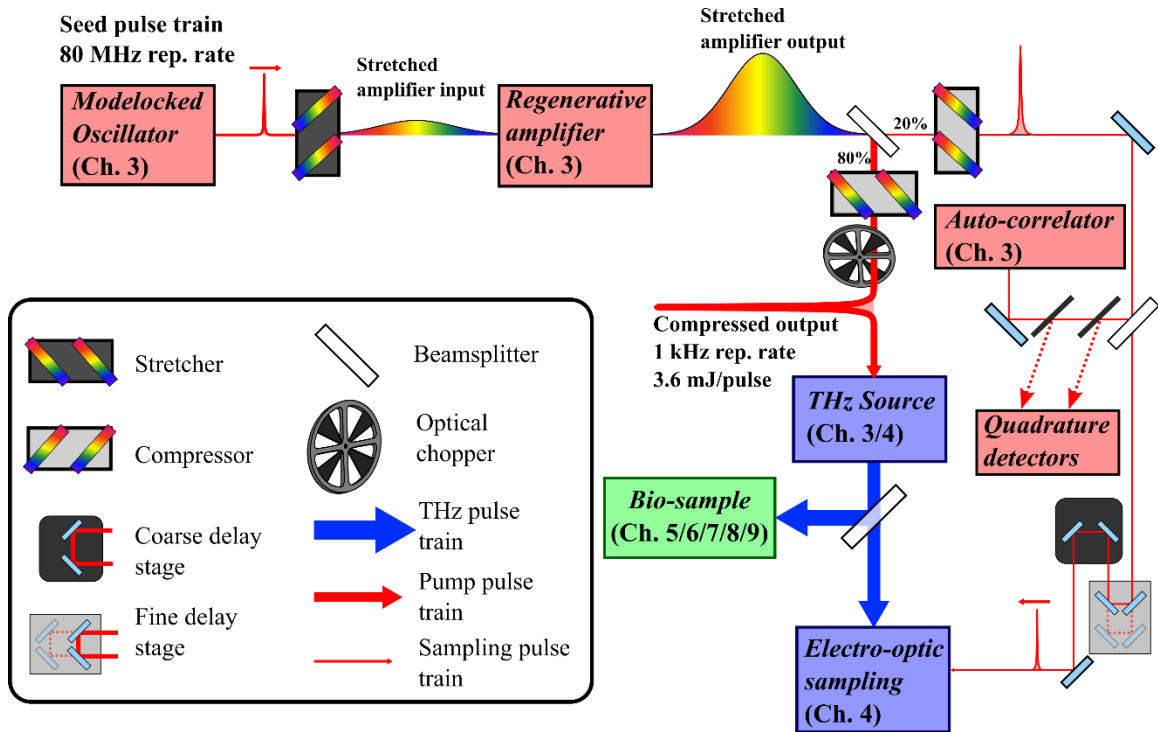


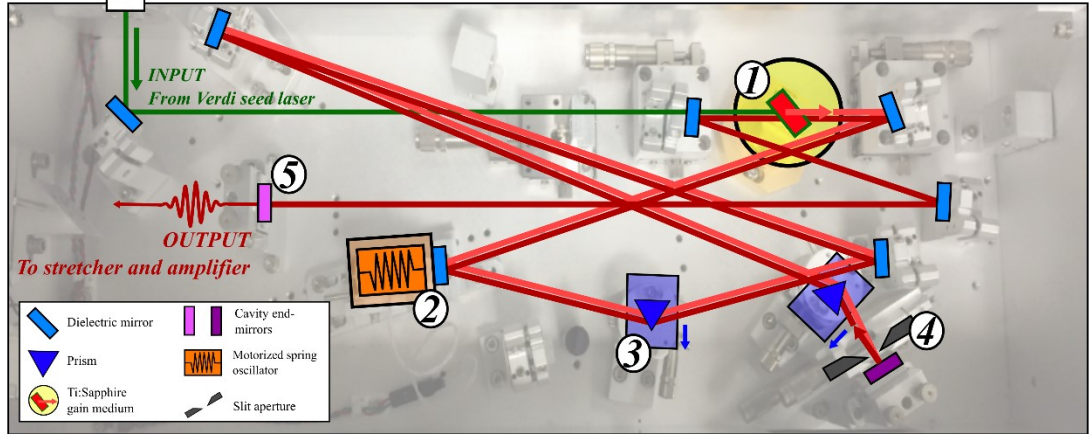
Figure 3.7. **Box-diagram schematic of the entire experimental configuration.** Ultrafast infrared laser pulses from a Ti:Sapphire laser (Section 3.2.2 and 3.4.1) are amplified in a regenerative amplifier (Section 3.4.2) via chirped-pulse-amplification (CPA), and split such that ~80% of the beam is used for THz generation via tilted-pulse-front optical rectification (Section 3.3.4). The remaining portion of the beam is utilized for laser diagnostics and THz detection via electro-optic sampling. Quadrature detectors monitor spatial symmetry of the laser mode, and an optical auto-correlator characterizes the compressed pulse duration (Section 3.4.2.1).

3.4.1 Modelocked oscillator

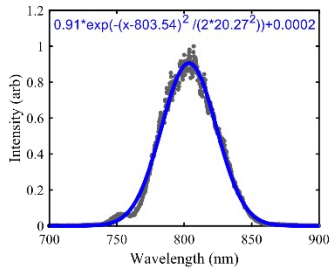
The THz pulse train utilized for bio-exposure studies begins as an optical pulse train, as generated by a Micra modelocked Ti:sapphire commercial laser oscillator (Coherent, Inc., Santa Clara, CA) as shown in Figure 3.8(a) [40]. The gain medium is externally pumped by a diode-pumped Nd:YVO₄ laser (Coherent Verdi, 5W, 532 nm CW). Modelocking, or the constructive interference of cavity mode oscillations for single-pulse generation, is achieved by both passive and active methods. The former is via Kerr lensing, a nonlinear optical effect that induces an intensity-dependent increase of the local refractive index, establishing an effective lens structure via radial variation of optical path length ($OPL(r) = n(r)L$) [40]. This spatially separates the constructively-interfered, high-intensity, mode-locked portion of the beam, which may then be isolated with a slit aperture (shown at label 4 in Figure 3.8(a)). Active mode-locking is achieved by mounting a cavity mirror to a motorized spring that varies the cavity length, broadening the cavity mode profiles that contribute to constructive interference (shown at label 2 in Figure 3.8(a)).

As the refractive index is wavelength-dependent, each cavity mode comprising the laser pulse will see a slightly different index, leading to differential phase velocities that contribute to group velocity dispersion (GVD) and spatiotemporal pulse broadening. Per-pulse coherence is maintained with a pair of prisms (position 3 in Figure 3.8(a)) that apply tunable levels of frequency dispersion (“chirp”) by creating wavelength-dependent path-length differences that exactly compensate the GVD accumulation on each round trip within the oscillator cavity.

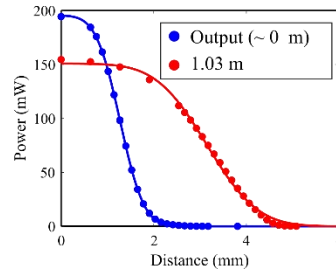
(a) Micra oscillator schematic



(b) Spectrum



(c) Knife-edge beam size



(d) 80 MHz pulse train

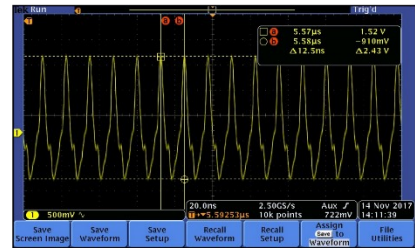


Figure 3.8. The Coherent Micra oscillator. (a) Schematic representation of the Micra oscillator. The Verdi input laser (532 nm CW, green path) pumps the gain medium (1), activating a lasing process that outputs energy (light red path) according to the Ti:Sapphire gain profile. The cavity will only support discrete lasing modes, assisted by active mode-locking methods such as a spring oscillator (2) to broaden the mode profiles. A pair of prisms (3) compensates pulse group velocity dispersion each round trip of the cavity. Kerr lensing spatially separates the modelocked region of the beam, which is isolated with a slit aperture at (4) and retro-reflected back through the optical components and gain medium (dark red path). A partially transmissive cavity end-mirror at (5) reflects most of the generated pulse train back through the system for additional passes. The small portion transmitted through this end-mirror forms the laser output. (b) The measured spectrum for each Micra output pulse. The central wavelength is 804 nm and bandwidth is 27 nm (fit to Equation (3.34)). (c) Measurements of the Micra beam size as it exits the oscillator (blue curve), and 103 cm from the oscillator output (red curve). The beam divergence is 0.88 mrad (0.05°). (d) An oscilloscope waveform of the output pulse train detected by a photodetector at the output of the oscillator cavity. The pulse spacing is stable at 12.5 ns corresponding to the 80 MHz repetition rate.

The pulse spectrum, measured with an infrared spectrometer (Ocean Optics Inc., FL), is shown in Figure 3.8(b). These data are fit to Gaussian distributions of the form

$$I(\lambda) = I_0 \cdot \exp\left[\frac{1}{2}\left(\frac{\lambda - \lambda_0}{\sigma}\right)^2\right] + I_{BG}. \quad (3.34)$$

The central wavelength and bandwidth of the Micra oscillator is $\lambda_0 \pm \sigma = 804 \pm 27$ nm, as determined from the fit.

The beam size is characterized by the knife-edge method: Power is monitored with an infrared energy detector, and a vertical razor-blade is linearly translated to block the beam. The maximum average power of the unblocked beam is 195 mW at the oscillator output. The power variation as a function of blade position, $P(x)$, is fit to the equation

$$P(x) = \frac{P_0}{2} \cdot \left[1 - \operatorname{erf}\left(\sqrt{2} \cdot \frac{x - x_0}{w_0}\right)\right] \quad (3.35)$$

from which the beam waist, w_0 , is extracted. The beam size was measured to be 0.81 mm at the output of the Micra (blue curve in Figure 3.8(c)), and 1.73 mm at the input of the stretcher/amplifier (red curve) that is 103.2 cm further down the beam path, corresponding to a beam divergence angle of 0.88 mrad, or 0.05°.

3.4.2 Regenerative amplifier

The pulse train emitted from the Micra oscillator is directed towards a Coherent Legend regenerative amplifier (Coherent, Inc.), which utilizes a chirped-pulse amplification (CPA) scheme [41]. CPA is a popular laser-amplification method commonly used to achieve previously unattainable peak laser powers by spatiotemporally dispersing the pulse frequency components, and thus lowering the pulse intensity; this enables pulse amplification without damaging amplifier components, while maintaining the pulse spectrum¹. Prior to reaching the amplification cavity, the pulses from the Micra are “stretched” (i.e., frequencies spatiotemporally dispersed) by diffraction gratings, as shown in Figure 3.9.

¹ In 2018, Drs. Donna Strickland and Gerard Mourou shared 50% of the Nobel Prize in physics for their discovery of chirped pulse amplification in 1985 [47, 48].

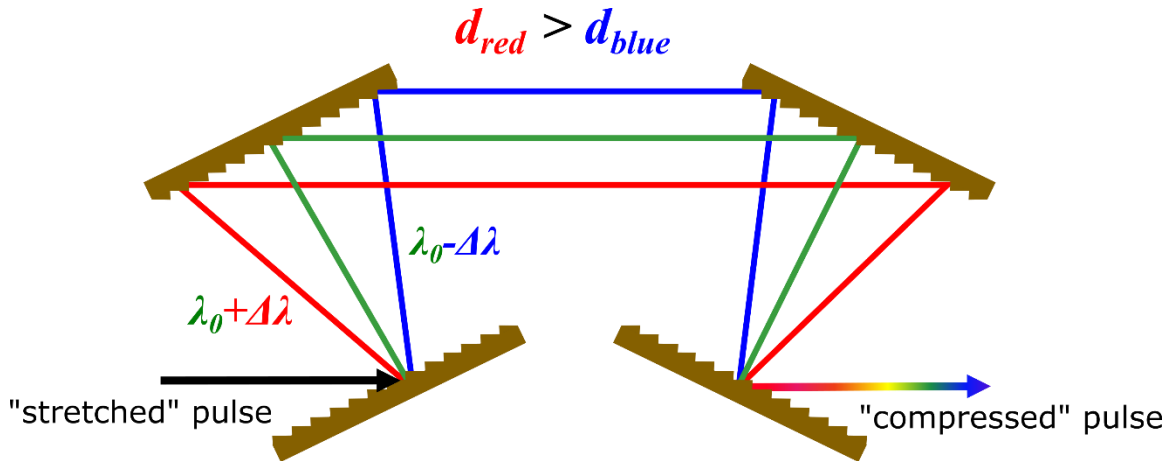
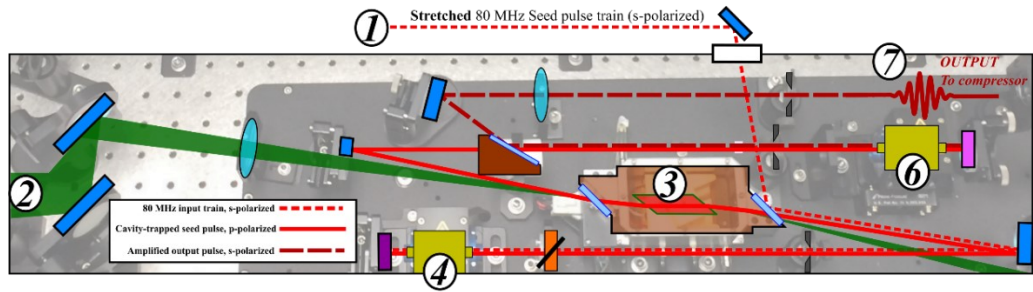


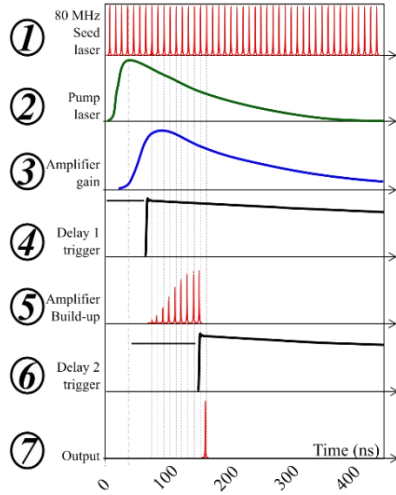
Figure 3.9. **Chirping pulses with paired diffraction gratings disperses the frequency components in space and time, facilitating safe amplification via Chirped Pulse Amplification (CPA).** A pulse centred at $\lambda_0 \pm \Delta\lambda$ will diffract at a wavelength-dependent angle (Equation (3.25)). The differential pathlengths disperse the wavelength components, which are re-collected by diffraction gratings into a compressed pulse.

A schematic and pulse-timing diagram outlining the operating principles of regenerative amplification are shown in Figure 3.10 [41]. The stretched 80 MHz pulse train from the oscillator enters the amplifier cavity *s*-polarized (i.e., perpendicular to the plane of incidence), and is reflected away from the amplification cavity by a polarization-selective Brewster window. A single pulse is selected at a 1 kHz sampling rate to enter the cavity by applying a delayed-triggered quarter-wave voltage to a Pockel's cell (#4 in Figure 3.10(a)), resulting in a round-trip half-wave shift that converts the pulse from *s*-polarized to *p*-polarized (i.e., parallel to the plane of incidence). This is then transmitted by the Brewster window and trapped in the amplification cavity, while the remainder of the 80 MHz pulse train is retro-reflected back out of the amplifier unit.

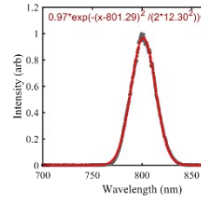
(a) Legend regenerative amplifier schematic



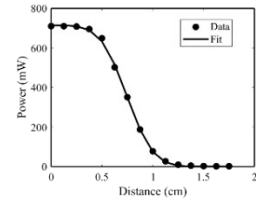
(b) Pulse timing diagram



(c) Spectrum



(d) Knife-edge beam size



(e) 1 kHz amplified output pulse train

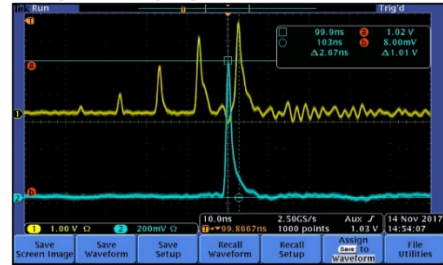


Figure 3.10. **The Coherent Legend regenerative amplifier.** (a) Schematic representation of the Legend regenerative amplifier, and (b) the corresponding pulse timing diagram, adapted from [41]. (Components are numbered consistently in (a) and (b)). A stretched input pulse train (1) with s-polarization enters the amplifier and is reflected by a Brewster window towards a Pockel's cell (4) triggered at 1 kHz. When triggered, the cell converts the pulse to p-polarization, which allows the reflected pulse to now be transmitted through the Brewster window into the Ti:sapphire medium (3). At the same time, a pump laser (2) is used to induce population inversion in the Ti:sapphire, facilitating amplification of the input pulse in the cavity. The pulse is reflected through the cavity multiple times, resulting in a build-up of the amplification (5). Once the final amplification is attained, the second Pockel's cell (6) is triggered, converting the pulse back to s-polarization, enabling a Brewster window to reflect the pulse out of the system (rather than transmitting it back into the cavity), becoming the amplified pulse output (7). (c) The measured spectrum for each output pulse. The central wavelength is 801 nm and the bandwidth is 12 nm. (d) Measurements of the amplified pulse beam size by the knife-edge method. (e) An oscilloscope waveform displaying the build-up of the selected pulse in the amplifier cavity (yellow trace) and the output amplified 1 kHz pulse train (blue trace) as measured by a photodetector at the amplifier output

Once trapped in the cavity, the *p*-polarized pulse makes $\sim 15 - 17$ round trips through the Ti:Sapphire gain medium, which has been gain-activated (atomic states excited to achieve population inversion) by an external pump laser (Coherent Verdi, 20W pulse, 532 nm. #2 in the pulse timing diagram). Each trip increases the total pulse energy for a total amplification factor of $\sim 10^6$ [41]. When amplification is complete, the cavity Pockel cell (#6 in Figure 3.10(a)) is activated with a quarter-wave voltage, inducing another round-trip half-wave shift of the pulse, and is

reflected out of the amplifying cavity by a Brewster window. An oscilloscope connected to a pair of photodetectors monitors the build-up (yellow trace in Figure 3.10(e)) and the amplified output (blue trace in Figure 3.10(e)). The stretched pulses are then compressed by gratings that establish the opposite spatiotemporal dispersions as the stretcher, and reverts the safely-amplified pulses to the original duration. A beamsplitter (see Figure 3.7) transmits ~80% of the amplifier output towards the external pump compressor, while ~20% is directed towards the internal sampling compressor. The former is utilized for THz generation, while the latter is used for coherent THz detection, and these fractions may be adjusted to optimize laser power distribution, if desired.

As with the oscillator seed output, the spectrum and beam size of the amplified pulse train were characterized via fits to Equations (3.34) and (3.35), shown in Figure 3.10(c – d). The central wavelength and bandwidth is $\lambda_0 = 801 \pm 12$ nm, and the beam size is 4.1 ± 0.2 mm. The 20%-split beam is actively monitored by an infrared detector during laser operation, and the average power of the 1 kHz pulse train is measured to be 715 mW. Therefore, the total amplified average laser power is 3.6 W, or 3.6 mJ per pulse at a 1 kHz ($T=1$ ms) repetition rate.

3.4.2.1 *Measurement of ultrafast laser pulse duration with an optical auto-correlator*

The temporal duration of the amplified, compressed pump pulse is characterized with a single-shot optical auto-correlator, as shown in Figure 3.11(a). The amplified pulsed beam is split into two that intersect noncollinearly in a KDP (monopotassium phosphate) crystal for frequency-doubling via second-harmonic generation [41]. The relative difference between the path length of the two pulses produces a spatial delay in the doubled signal, producing an autocorrelation of the pulse's intensity profile. The autocorrelated signal is detected by an array of CCD diodes sent to an oscilloscope, from which the data in Figure 3.11(b) was extracted. The FWHM of the Gaussian autocorrelation was measured to be 50.4 fs, corresponding to a single-Gaussian pulse duration of $\tau=50.4/\sqrt{2}=35.6$ fs. Therefore, the pulse intensity of the amplified laser pulse is calculated to be $I = E/(A\tau)=0.8$ TW/cm².

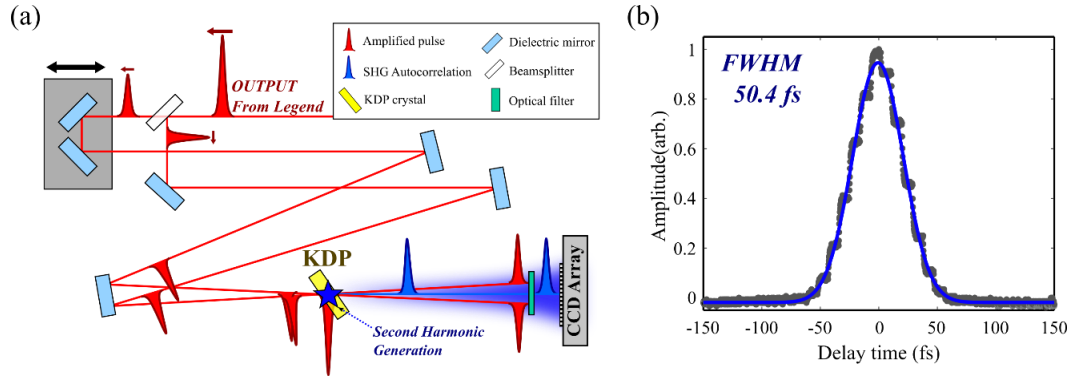


Figure 3.11. **Single-shot autocorrelator for temporal characterization of amplified laser pulse.** Modified from [41]. (a) The pulse is equally split into two beamlines, and non-collinearly propagated to intersect in a frequency-doubling KDP crystal. The second-harmonic signal generated is a temporal trace of the intensity distribution and is detected by a CCD array. (b) The width of the oscilloscope trace with the time axis calibrated to the optical delay time determines the autocorrelation width (50.4 fs FWHM), related to the single-Gaussian pulse duration as $50.4/\sqrt{2}=35.6$ fs.

3.4.3 The terahertz source

The amplified pulse train characterized in Section 3.4 is partitioned with a beamsplitter such that 80% of the energy is utilized for THz generation, while a small amount of the remaining power is used as the probe for coherent THz detection as shown in Figure 3.12(a). The collimated pump beam is magnified or demagnified with a zoom lens (a pair of cylindrical plano-convex ultrafast lenses positioned with coincident foci), and incident on a reflective diffraction grating (RDG) at an angle of $\theta_i = 37^\circ$, which, by Equation (3.25), produces first-order diffraction modes propagating with a tilted pulse front of $\theta_d = 57^\circ$ relative to the phase front.

Two plano-convex cylindrical lenses (L1 and L2 in Figure 3.12(a)) with focal lengths $f_1=10$ cm and $f_2=6$ cm are positioned in a 4f-imaging configuration as follows (see Figure 3.6): L1 is mounted f_1 from the grating plane center, and L2 is mounted f_1+f_2 from L1 such that their focal points are coincident. The crystal output face is positioned f_2 away from L2, forming a system that images the grating plane to the crystal plane as discussed in [44]. The total path length from grating to crystal is $2f_1+2f_2=32$ cm.

Upon propagation through the 4f-lens imaging system and crystal, this pulse-front angle will match the $\gamma = 63^\circ$ Cherenkov cone angle produced in a LN crystal. The LN output face is cut with an equivalent angle as described in Section 3.3.4 to maximize efficient THz emission to free space.

(a) Source schematic

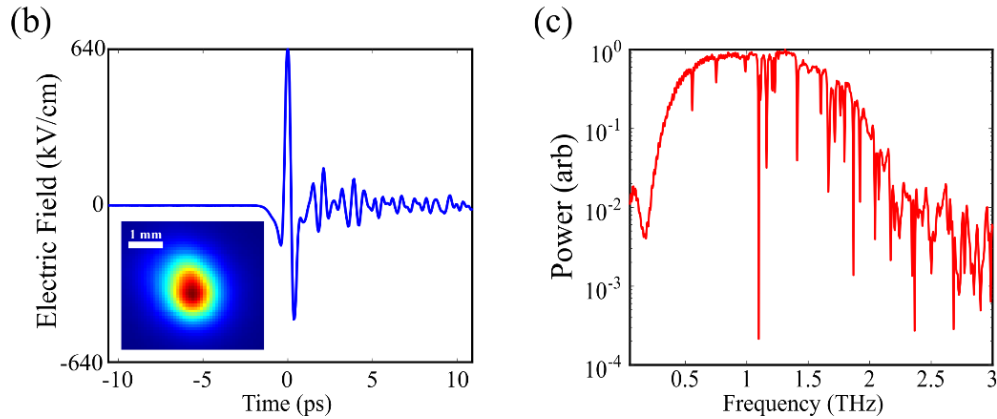
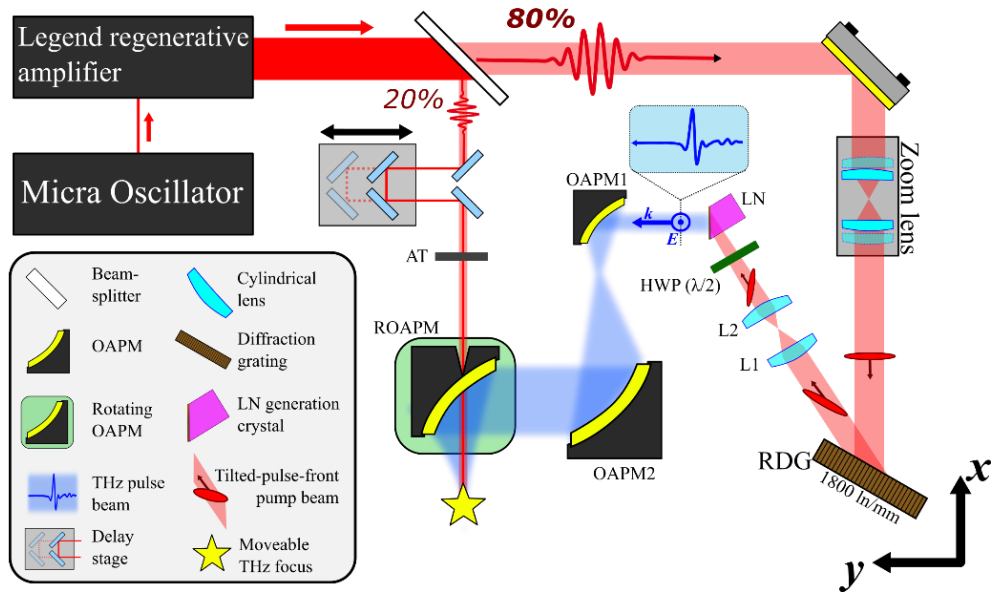


Figure 3.12. **Intense THz pulse source.** (a) Schematic of the source of intense THz pulses that occupies the “THz Source” module in the box diagram of Figure 3.7. 80% of the amplified pump pulse from the oscillator/amplifier is prepared in a tilted-pulse-front geometry as described in Section 3.3.4 and incident on a lithium niobate (LN) crystal with a 63° cut face. Gold off-axis parabolic mirrors (OAPMs) expand and refocus the emitted THz beam. The position of the THz focus may be rotated in a 360° arc to convert the source between “exposure”, “detection”, or “spectroscopy” modes. The remaining $\sim 20\%$ is sent through a delay stage and propagated colinearly with the THz beam for detection via electro-optic (EO) sampling. (b) The electric field waveform of the intense THz pulse. The per-pulse energy is $1.5 \mu\text{J}$, and this is focused to a ~ 1 mm diameter spot to achieve a maximum field strength of 640 kV/cm . (c) The frequency spectrum for the pulse in (b). The peak frequency is 1.3 THz , with a bandwidth of 1.8 THz (full-width tenth max, FWTM).

3.4.3.1 Terahertz emission from lithium niobate

The train of amplified laser pulses produces a beam of intense THz pulses with a 1 kHz repetition rate. The THz emission from the crystal output face was collimated by maximizing energy detected far ($\sim 30 \text{ cm}$) from the crystal output axis by adjusting the incident pump pulse

using the imaging lens' and grating position. Fixed-height (z) measurements of the pulse energy were taken at 3 cm longitudinal (y) intervals and ± 0.2 cm transverse (x) intervals to spatially characterize the collimated THz emission profile directly from the crystal output, as shown in Figure 3.13(a). On-axis spot images were acquired to monitor the 2D (xz) intensity distribution of the emitted THz, shown above the corresponding longitudinal position. Figure 3.13(b) are line projections from the data in (a), showing on-/off-axis energy loss in ambient laboratory conditions.

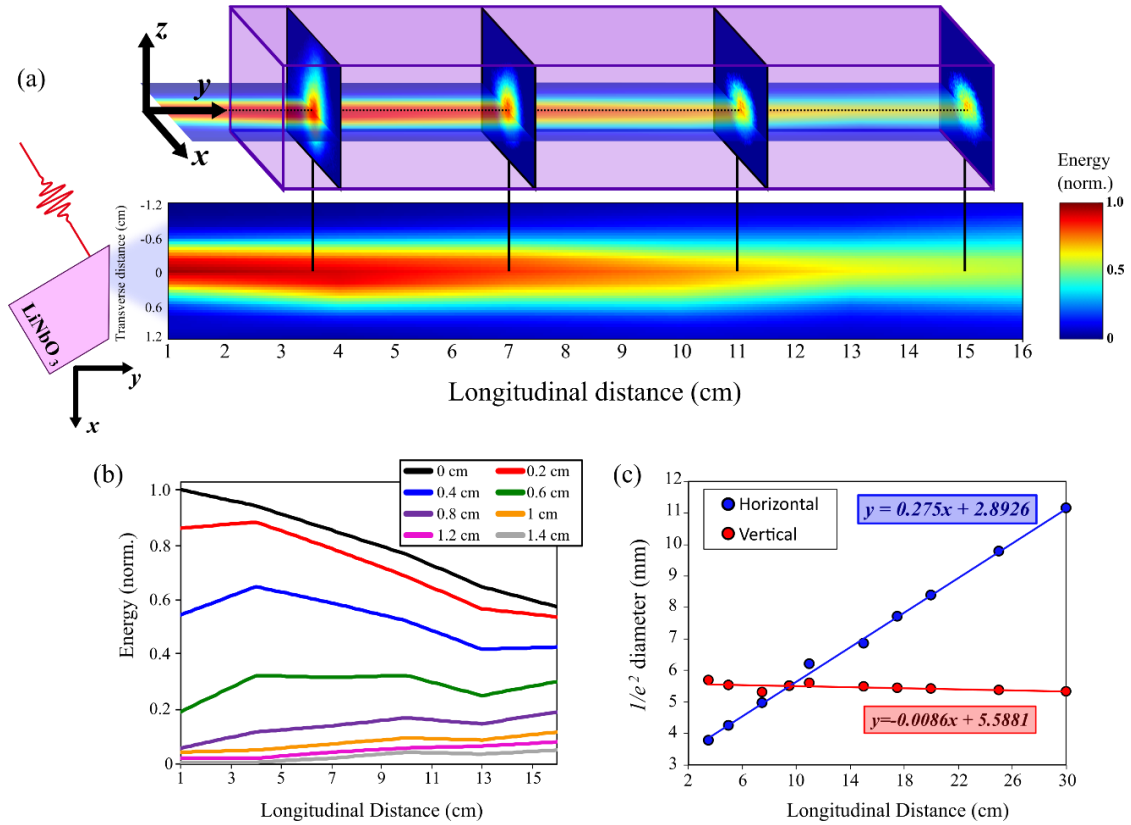
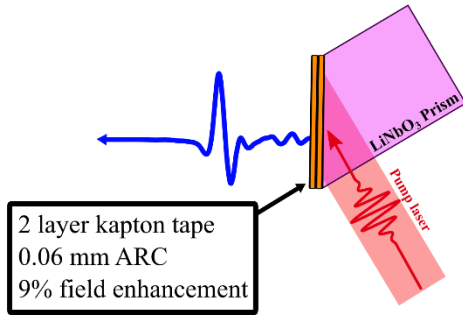


Figure 3.13. **Spatial THz emission directly from the LN generation crystal.** (a) Normalized pulse energy vs. space. Images of the THz spot were taken at a fixed height ($z = 6$ " (152.4 mm) from the bench surface) on-axis to characterize variation in the emitted THz spot size. (b) Average pulse energy decay vs. longitudinal distance from the crystal (y), for varying transverse locations (x). Energy growth near beam fringes is due to horizontal divergence. (c) THz spot size vs. longitudinal distance from the LN output. Note the change to abscissa values in (c) compared to (a) and (b).

From the on-axis energy decay, the effective absorption coefficient of the ambient environment is 20.8 cm^{-1} . The fringes of the beam grow in energy for increasing longitudinal distance due to horizontal beam divergence (1.6° , 27 mrad), shown in Figure 3.13(c). This divergence is likely due to the spatial dispersion of the pump pulse's image on the crystal output face, which is an angularly dispersed tilted-pulse-front in the "horizontal" (xy) plane.

(a) Kapton tape anti-reflection coating



(b) Pump/scatter filtration

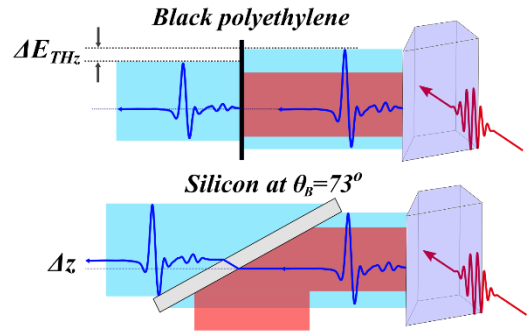


Figure 3.14. **THz enhancement with anti-reflection coatings (ARCs) and pump laser filtration at the output of the lithium niobate prism.** (a) Two layers of Kapton tape (total thickness $60\ \mu\text{m}$) secured to the output face of the crystal provides an anti-reflection coating (ARC) that increases THz pulse energy by 9%. (b) Filtration of leakage of the infrared laser (red) by black polyethylene (top, attenuates THz energy) or a silicon wafer at Brewster's angle (bottom, lossless but induces vertical offset).

To increase the emission efficiency of the THz beam from the LN crystal, two layers of kapton tape were adhered to the crystal output face as in Figure 3.14(a), creating an anti-reflection coating (ARC) that increases the coupling efficiency to free-space propagation, resulting in a 9% increase of the THz pulse energy [45]. Following emission from the kapton+crystal output, a 3" (76.2 mm) diameter silicon (Si, $n=3.41$, $d=1\ \text{mm}$) wafer is mounted at Brewster's angle (73° for Si) relative to the p -polarized THz beam, as shown in Figure 3.14(b) [46]. This allows reflectionless THz beam transmission, while blocking infrared light from the pump from propagating to the sample or detector locations. The Si Brewster window results in a further 7% energy enhancement relative to filtration with black polyethylene. While the THz enhancement is significant, refraction in Si alters the typically fixed height of the THz beam by an amount $\Delta z = d(\tan \theta_1 - \tan \theta_2)$, where $\theta_1 = \theta_B = 73^\circ$ and $\theta_2 = 16^\circ$ are the incident and transmitted beam angles, respectively, and d is the thickness of the Si wafer. Therefore a vertical re-alignment of either the pump or THz optics is required. Alternatively, propagation through a second inverted Si wafer may be used to correct the refraction offset to maintain the vertical pulse position.

3.4.3.2 Terahertz beam exposure parameters

For completeness, Table 3.1 shows a summary of typical parameters of the THz exposure beam, as well as the maximum fields achieved under optimal generation and alignment conditions. The 'mean pulse' reports parameter ranges determined from the average of many pulses generated from this source over several years, and represents the typical ranges achievable on a given day.

Details on measurements and analyses to characterize these beam parameters are discussed in the next chapter.

Table 3.1. Ranges of THz pulse parameters, and the pulse with the highest achieved field

	Mean pulse	Max. field pulse
Peak field (kV/cm)	332±140	640.3
Pulse energy (μJ)	1.2±0.4	1.45
*Spot size ($w_H \times w_V$ mm ²)	1.6 × 1.9	1.12 × 1.32
†Duration (ps)	1.0±0.3	0.93
Peak frequency (THz)	0.7±0.3	1.3
Bandwidth (FWTM THz)	1.2±0.5	1.1
Average intensity (mW/cm ²)	67±28	125.0
Pulse intensity (MW/cm ²)	54±40	134.5

*Spot sizes are reported as the major/minor axes' diameters (l/e^2) of the elliptical THz focus.

†Pulse durations reported as the $1/e$ width of the Hilbert pulse envelope.

FWTM = full-width tenth max

3.5 Conclusion

This chapter discussed theoretical aspects and experimental implementation of laser-based generation of intense THz pulses by tilted-pulse-front optical rectification in lithium niobate. This source of intense THz pulses was integrated into a larger bio-exposure system with a novel design that allows wide versatility of operation for exposure and analysis of several types of biological samples, with a relatively small table footprint. Methods of measuring and characterizing the THz beam are addressed in Chapter 4, and the integration into the larger THz bio-exposure system is discussed in Chapter 5.

3.6 References

- [1] J. Chamberlain, R. Miles, C. Collins and D. Steenson, "Introduction to Terahertz Solid-state Devices," in *New Directions in Terahertz Technology*, Netherlands, Kluwer Academic Publishers, 1997, pp. 3-27.
- [2] J. Chamberlain, "Where optics meets electronics: recent progress in decreasing the terahertz gap," *Philosophical Transactions of the Royal Society*, vol. 362, pp. 199 - 213, 2004.
- [3] S. S. Dhillon, M. S. Vitiello, E. H. Linfield, A. G. Davies, M. C. Hoffmann, J. Booske, C. Paoloni, M. Gensch, P. Weightman, G. P. Williams, E. Castro-Camus, D. R. Cumming, F. Simoens, I. Escorcia-Carranza, J. Grant, S. Lucyszyn, M. Kuwata-Gonokami, K. Konishi, M. Koch, C. A. Schmuttenmaer, T. L. Cocker, R. Huber, A. G. Markelz, Z. D. Taylor, V. P. Wallace, J. A. Zeitler, J. Sibik, T. M. Korter, B. Ellison, S. Rea, P. Goldsmith, K. B. Cooper, R. Appleby, D. Pardo, P. G. Huggard, V. Krozer, H. Shams, M. Fice, C. Renaud, A. Seeds, A. Stöhr, M. Naftaly, N. Ridler, R. Clarke, J. E.

- Cunningham and M. B. Johnston, "The 2017 terahertz science and technology roadmap," *Journal of Physics D: Applied Physics*, vol. 50, no. 043001, pp. 1 - 49, 2017.
- [4] M. D. Thomson, M. Kress, T. Löffler and H. G. Roskos, "Broadband THz emission from gas plasmas induced by femtosecond optical pulses: From fundamentals to applications," *Laser & Photonics Review*, vol. 1, no. 4, pp. 349 - 368, 2007.
- [5] I. Hosako, N. Sekine, M. Patrashin, S. Saito, K. Fukunaga, Y. Kasai, P. Baron, T. Seta, J. Mendrok, S. Ochiai and H. Yasuda, "At the Dawn of a New Era in Terahertz Technology," *Proceedings of the IEEE*, vol. 95, no. 8, pp. 1611 - 1623, 2007.
- [6] A. J. Lee, D. J. Spence and H. M. Pask, "Terahertz sources based on stimulated polariton scattering," *Progress in Quantum Electronics*, vol. 71, pp. 1 - 23, 2020.
- [7] Y. Lee, *Principles of Terahertz Science and Technology*, New York, NY: Springer, 2009.
- [8] M. Hoffmann and J. Fülöp, "Intense Ultrashort terahertz pulses: generation and applications," *Journal of Physics D: Applied Physics*, vol. 44, no. 8, p. 083001, 2011.
- [9] A. Einstein, "Translated: On the quantum theory of radiation," *Physikalische Zeitschrift*, vol. 18, pp. 121 - 128, 1917.
- [10] A. Einstein, "Translated: Radiation emission and absorption according to quantum theory," *Verhandlungen der Deutschen Physikalischen Gesellschaft*, vol. 18, pp. 318 - 323, 1916.
- [11] T. H. Maiman, "Stimulated Optical Radiation in Ruby," *Nature*, vol. 187, no. 4736, pp. 493 - 494, 1960.
- [12] K. König, "Multiphoton microscopy in life sciences," *Journal of Microscopy*, vol. 200, no. 2, pp. 83 - 104, 2000.
- [13] M. Baudalet, *Laser Spectroscopy for Sensing: Fundamentals, Techniques, and Applications*, Woodhead Publishing, 2014.
- [14] S. G. Brown, "Clinical review: Science, medicine, and the future. New techniques in laser therapy," *British Medical Journal*, vol. 316, pp. 754 - 757, 1998.
- [15] H. Schneckeburger, "Laser-assisted optoporation of cells and tissues - a mini-review," *Biomedical Optics Express*, vol. 10, no. 6, pp. 2883 - 2888, 2019.
- [16] S. Hosseinpour and L. J. Walsh, "Laser-assisted nucleic acid delivery: A systematic review," *Journal of Biophotonics*, vol. 14, pp. 1 - 17, 2020.
- [17] K. Krushelnick and V. Malka, "Laser wakefield plasma accelerators," *Laser & Photonics Review*, vol. 4, no. 1, pp. 42 - 52, 2010.
- [18] R. L. Fork, B. I. Greene and C. V. Shank, "Generation of optical pulses shorter than 0.1 psec by colliding pulse mode locking," *Applied Physics Letters*, vol. 38, no. 9, pp. 671 - 672, 1981.

- [19] E. Hecht, *Optics*, Reading, MA: Addison Wesley Longman, 1998.
- [20] V. Buschmann, H. Hempel, A. Knigge, C. Kraft, M. Roczen, M. Weyers, T. Siebert and F. Koberling, "Characterization of semiconductor devices and wafer materials via sub-nanosecond time-correlated single-photon counting," *Journal of Applied Spectroscopy*, vol. 80, pp. 449 - 457, 2013.
- [21] M. Vengris, I. H. van Stokkum, X. He, A. F. Bell, P. J. Tonge, R. van Grondelle and D. S. Larsen, "Ultrafast excited and ground-state isomerization dynamics of the green fluorescent protein chromophore in solution," *Journal of Physical Chemistry A*, vol. 108, no. 4587, 2004.
- [22] L. He, Q. Zhang, P. Lan, W. Cao, X. Zhu, C. Zhai, F. Wang, W. Shi, M. Li, X. -B. Bian, P. Lu and A. D. Bandrauk, "Monitoring ultrafast vibrational dynamics of isotopic molecules with frequency modulation high-order harmonics," *Nature Communications*, vol. 9, no. 1108, 2018.
- [23] K. H. Yang, P. L. Richards and S. Y. R., "Generation of Far-Infrared Radiation by Picosecond Light Pulses in LiNbO₃," *Applied Physics Letters*, vol. 19, no. 9, 1971.
- [24] D. H. Auston, K. P. Cheung, J. A. Valdmanis and D. A. Kleinman, "Cherenkov Radiation from Femtosecond Optical Pulses in Electro-Optic Media," *Physical Review Letters*, vol. 53, no. 16, 1984.
- [25] Z. Wang, "Ultrafast Imaging of Terahertz Pulses," PhD Thesis, University of Alberta, Edmonton, AB, 2013.
- [26] Q. Wu and X.-C. Zhang, "Free-space electro-optic sampling of terahertz beams," *Applied Physics Letters*, vol. 67, no. 3523, 1995.
- [27] P. Jepsen, D. Cooke and M. Koch, "Terahertz spectroscopy and imaging - Modern techniques and applications," *Laser and Photonics Reviews*, vol. 5, no. 1, pp. 124-166, 2011.
- [28] P. Jepsen and H. Merbold, "Terahertz Reflection Spectroscopy of Aqueous NaCl and LiCl Solutions," *Journal of Infrared, Millimeter, and Terahertz Waves*, vol. 31, no. 4, pp. 430-440, 2010.
- [29] E. Pickwell-MacPherson and V. Wallace, "Terahertz pulsed imaging - A potential medical imaging modality?," *Photodiagnosis and Photodynamic Therapy*, vol. 6, no. 2, pp. 128 - 134, 2009.
- [30] J.-H. Son, *Terahertz Biomedical Science and Technology*, Boca Raton, FL: CRC Press, 2014.
- [31] X. Yang, X. Zhao, K. Yang, Y. Liu, Y. Liu, W. Fu and Y. Luo, "Biomedical Applications of Terahertz Spectroscopy and Imaging," *Trends in Biotechnology*, vol. 34, no. 10, pp. 810 - 824, 2016.
- [32] J. Hebling, G. Almasi and I. Kozma, "Velocity matching by pulse front tilting for large-area THz-pulse generation," *Optics express*, vol. 10, no. 21, pp. 1161 - 1166, 2002.

- [33] J. Hebling, A. G. Stepanov, G. Almasi, B. Bartal and J. Kuhl, "Tunable THz pulse generation by optical rectification of ultrashort laser pulses with tilted pulse fronts," *Applied Physics B: Lasers and Optics*, vol. 78, no. 5, pp. 593 - 599, 2004.
- [34] L. Titova, A. Ayeshehshim, A. Golubov, D. Fogen, R. Rodriguez-Juarez, F. Hegmann and O. Kovalchuk, "Intense THz pulses cause H2AX phosphorylation and activate DNA damage response in human skin tissue," *Biomedical Optics Express*, vol. 4, no. 4, pp. 559 - 568, 2013.
- [35] H. Cheon, H.-j. Yang, S.-H. Lee, Y. A. Kim and J.-H. Son, "Terahertz molecular resonance of cancer DNA," *Scientific Reports*, vol. 6, no. 37103, pp. 1 - 10, 2016.
- [36] O. Svelto, *Principles of Lasers*, New York, NY: Springer, 2010.
- [37] P. Moulton, "Spectroscopic and laser characteristics of Ti:Al₂O₃," *Journal of Optical Society B*, vol. 3, no. 1, pp. 125 - 133, 1986.
- [38] K. F. Wall and A. Sanchez, "Titanium Sapphire Lasers," *The Lincoln Laboratory Journal*, vol. 3, no. 3, pp. 447 - 462, 1990.
- [39] B. Wong and Schawlow, "Far-infrared spectrum of Al₂O₃:V⁴⁺," *The Journal of Chemical Physics*, vol. 49, no. 2, pp. 835 - 842, 1968.
- [40] "Operator's Manual: Micra Modelocked Ti:Sapphire Laser," Coherent, Inc., Santa Clara, CA.
- [41] "Operator's Manual: Legend Laser System - Kilohertz, Diode-Pumped, Ultrafast Ti:Sapphire Amplifier," Coherent, Inc., Santa Clara, CA.
- [42] R. W. Boyd, *Nonlinear Optics*, 3rd Ed., Orlando, FL: Academic Press Inc., 2008.
- [43] P. A. Franken, A. E. Hill, C. W. Peters and G. Weinreich, "Generation of Optical Harmonics," *Physical Review Letters*, vol. 7, pp. 118 - 119, 1961.
- [44] H. Hirori, A. Doi, F. Blanchard and K. Tanaka, "Single-cycle terahertz pulses with amplitudes exceeding 1 MV/cm generated by optical rectification in LiNbO₃," *Applied Physics Letters*, vol. 98, no. 9, 2011.
- [45] X. -J. Wu, J. -L. Ma, B. -L. Zhang, S. -S. Chai, Z. -J. Fang, C. -Y. Xia, D. -Y. Kong, J. -G. Wang, H. Liu, C. -Q. Zhu, X. Wang, C. -J. Ruan and Y. -T. Li, "Highly efficient generation of 0.2 mJ terahertz pulses in lithium niobate at room temperature with sub-50 fs chirped Ti:sapphire laser pulses," *Optics Express*, vol. 26, no. 6, pp. 7107 - 7116, 2018.
- [46] M. Naftaly, "An international intercomparison of THz time-domain spectrometers," in *International Conference on Infrared, Millimeter, and Terahertz Waves*, Copenhagen, Denmark, 2016.
- [47] The Nobel Foundation, "The Nobel Prize in Physics 2018," Nobel Prize Outreach, [Online]. Available: <https://www.nobelprize.org/prizes/physics/2018/summary/>.
- [48] D. Strickland and G. Mourou, "Compression of amplified chirped optical pulses," *Optics Communications*, vol. 56, no. 3, pp. 219 - 221, 1985.

4 Terahertz waveform analysis: Beam characterization and measurement of incoherent and coherent pulse parameters

“One can Fourier transform anything – often meaningfully.”

– John Tukey

4.1 Introduction

In this chapter, a comprehensive overview of important measurements for characterizing the exposure parameters of a terahertz (THz) beam are detailed. This will provide a useful reference guide for future operation of the THz source and biological exposure system housed in the Ultrafast Nanotools laboratory at the University of Alberta, or similar systems. These measurements are important aspects of accurate quantitative characterization of THz exposure parameters, and are necessary inputs for dosimetry calculations (Chapter 6). First, the THz source introduced in Chapter 3 is summarized, and the general principles of THz detection are outlined. Section 4.4 provides a comprehensive guide to measuring and calculating THz pulse parameters of interest, including energy, field strength, pulse duration, focused spot size, average or peak intensity, and frequency distribution. Next, a spectral decomposition analysis is performed using THz bandpass filters to characterize the frequency distribution of the broadband THz pulse in space and time. Finally, an analysis of field modulation in a focusing beam geometry is presented, and the contribution of carrier-envelope phase shift to the THz field calculations is described.

4.2 Terahertz source summary

Our THz system utilizes optical rectification of tilted-pulse-front infrared laser pulses ($\lambda = 800$ nm, 35 fs, 3.6 mJ) generated by a Ti:Sapphire oscillator (Coherent Micra) and regeneratively amplified (Legend), as introduced in Chapter 3 and shown schematically in Figure 4.1(a). A tilted-pulse-front is established in this input pump beam by isolating the first diffraction mode from an 1800 ln/mm reflective diffraction grating (RDG), and imaged with a 4f cylindrical lens system ($f_1=100$ mm, $f_2=60$ mm) to the output face of a lithium niobate (LiNbO_3 , LN) crystal [1, 2]. The LiNbO_3 prism is manufactured with a 63° cut angle for efficient coupling of the THz pulse propagating in the crystal to free-space. Following generation, a pyroelectric detector (SPJ-D-8, Spectrum Detector, Inc.) and camera (PV320, Electrophysics) are used to measure the pulse energy and beam profile, respectively, at the location labelled “Pyro” in Figure 4.1(a).

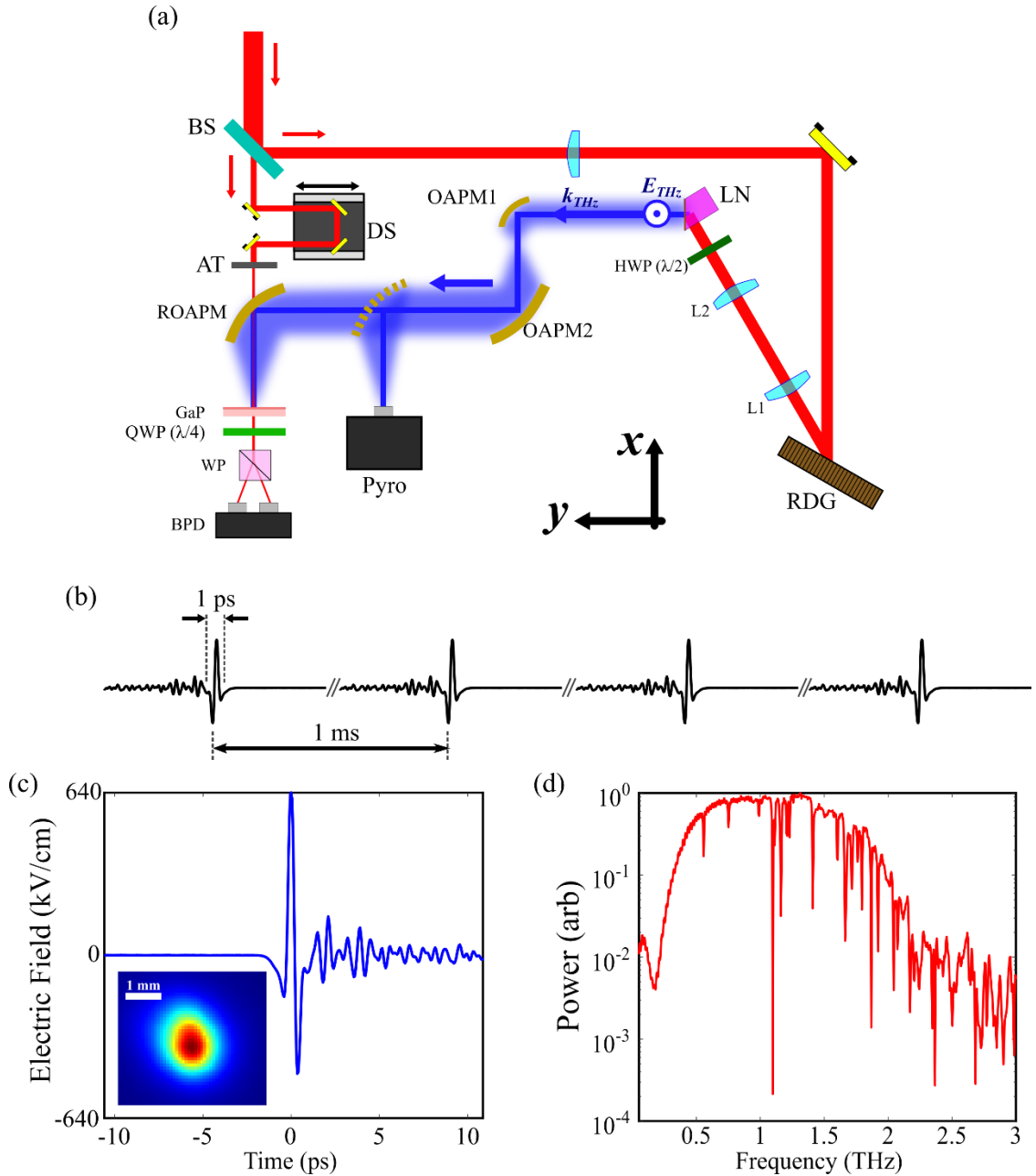


Figure 4.1. **Source schematic and characteristics for intense THz pulses.** (a) Diagram of optical rectification of tilted-pulse-front infrared laser pulses in lithium niobate (LN), and propagation of the THz beam through the exposure system with the rotating off-axis parabolic mirror (ROAPM) oriented for waveform detection via electro-optic sampling in gallium phosphide (GaP). The modulated sampling pulse is shifted and split by a quarter wave plate (QWP) and Wollaston prism (WP), respectively, and detected by a pair of balanced photo-detectors (BPD). A delay stage (DS) on a motorized linear track varies the relative position of the sampling pulse within the THz pulse for electro-optic sampling of the THz field. (b) A 1 kHz pulse train of ~picosecond-duration pulses, corresponding to a duty cycle = 10^{-9} . (c) A plot of the intense THz pulse waveform, a single-cycle EM pulse reaching peak field strengths of ~640 kV/cm. *Inset:* The THz spot at the beam focus, spot size = $1.12 \times 1.32 \text{ mm}^2$. (d) THz pulse power spectrum. The peak frequency is 1.3 THz, with a 1.8 THz FWTM (full-width tenth max).

The 1 kHz train of \sim picosecond-duration pulses is shown in Figure 4.1(b), corresponding to a duty cycle of $\sim 10^{-9}$. A single THz pulse waveform with a pulse duration of 0.93 ps is shown in Figure 4.1(c). The pulse energy and peak electric field in optimal alignment conditions is 1.5 μ J and 640 kV/cm, respectively. The corresponding power spectrum is computed by the Fast Fourier Transform (FFT), shown in Figure 4.1(d), and is broadly peaked at 1.3 THz. The beam focus spot size is an ellipse with axis diameters $1.12 \times 1.32 \text{ mm}^2$, corresponding to average (peak) intensity of 125.0 mW/cm² (134.5 MW/cm²). The methods of measuring and calculating these pulse parameters is now described in detail.

4.3 Detection of terahertz radiation

There are two broad categories of radiation detection [3]: Incoherent detection utilizes direct sensing technology for signal amplitude detection. Coherent detection refers to electromagnetic sensing that is sensitive to the signal phase in addition to amplitude.

4.3.1 Coherent detection

4.3.1.1 Electro-optic sampling of intense terahertz pulses in gallium phosphide

Electro-optic (EO) sampling is a pump-probe (THz pump, optical probe) detection technique that characterizes the electric field of the THz pulse in the time domain by exploiting the second-order Pockel's effect [4]. The principle of electro-optic sampling is outlined in Figure 4.2. The THz field is focused normally to the (110) plane of a gallium phosphide (GaP) crystal, inducing an optical birefringence via the Pockel's effect in the asymmetric GaP lattice. This effect is depicted by the index ellipsoid in Figure 4.2(a), indicating a differential refractive index seen by a vertically polarized field relative to a horizontally polarized field. An ultrafast optical sampling pulse split from the incident amplified beam is propagated colinearly through the GaP crystal, and a relative phase shift between the horizontal and vertical polarization components is induced that is proportional to the THz-induced birefringence magnitude, Δn . A quarter-wave plate ($\lambda/4$, QWP) induces a further 90° phase shift between horizontal and vertical polarizations, and a Wollaston prism (WP) spatially separates the vertical and horizontal polarizations into two beams. These are each separately detected by a pair of balanced photodetectors (BPD), which send signals via BNC to an oscilloscope, as depicted in Figure 4.2(c).

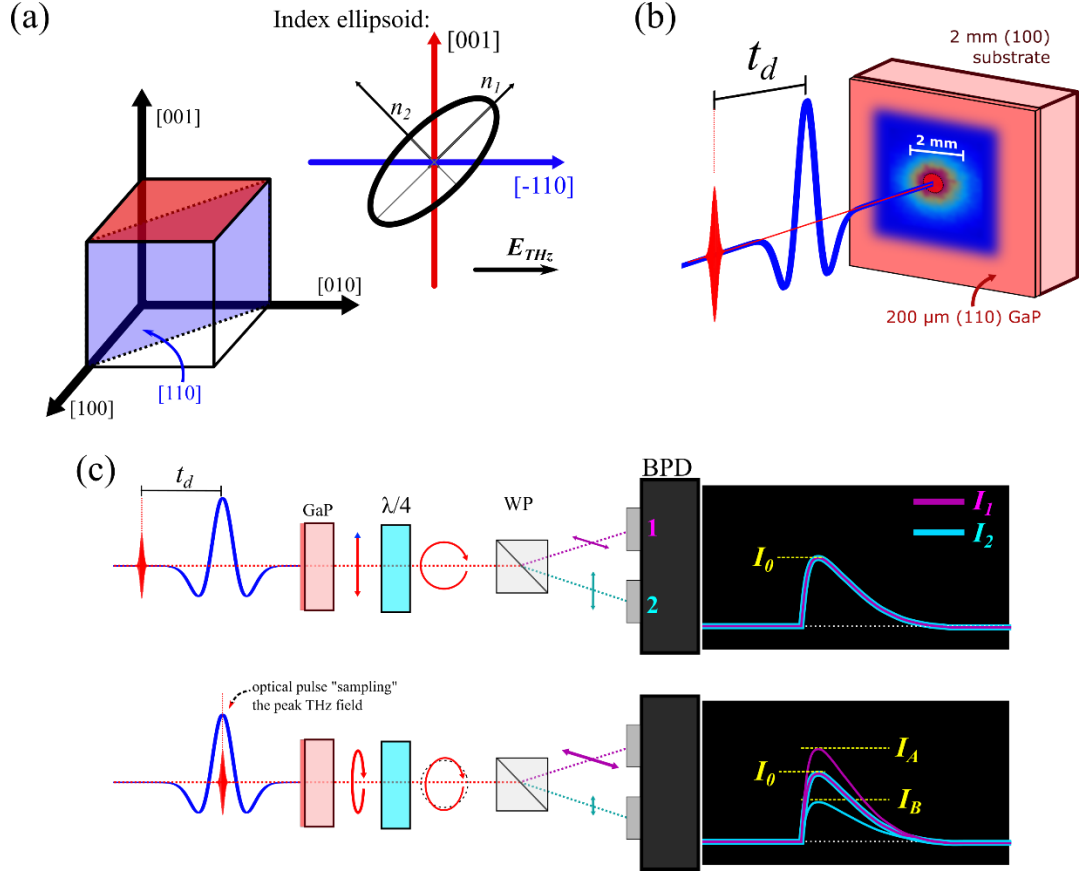


Figure 4.2. **Schematic representation of electro-optic (EO) sampling of a THz field with an optical sampling pulse in nonlinear media.** (a) An electric field applied along the (110) normal vector induces a birefringence that shifts the relative phase between horizontal and vertical polarizations ($n_x \neq n_y$). (b) A THz pump pulse (blue) and optical sampling pulse (red) are colinearly incident normal to the (110) plane of a gallium phosphide (GaP) crystal. The thick substrate is index-matched to reduce reflection interference typical in thin EO crystals. (c) Diagram of EO sampling at zero THz amplitude (top) and max THz field (bottom) sampling locations. The modulation in the sampling pulse is amplified with a quarter-wave plate ($\lambda/4$) and spatially separated by a Wollaston prism (WP). The relative signal amplitudes are read via peak-detection of the signal integrated by a pair of balanced photo-detectors.

The EO signal induced by the THz field is measured as a relative change to oscilloscope trace amplitudes. Each signal split from the Wollaston prism produces a unique trace, labelled I_1 and I_2 , with corresponding peaks I_A and I_B . The normalized EO signal, I_{EO} , is calculated as

$$I_{EO} = \frac{I_A - I_B}{I_A + I_B} = \frac{\Delta I}{2I_0} \quad (4.1)$$

where $\Delta I = I_A - I_B$ is the total signal difference, and I_0 is the reference signal amplitude with no THz field present.

An absolute determination of the THz electric field strength, E_{THZ} , may be determined directly from the measured I_{EO} , as long as the nominal index (n_0), electro-optic coefficient (r_{ij}), amplitude transmission coefficient (t), and thickness (L) of the detection crystal are known. As the optical sampling pulse propagates through the crystal, components polarized horizontally see a refractive index n_x , while components polarized vertically see an index n_y , given by [5]

$$\begin{aligned} n_x &= n_0 - \frac{1}{2} n_0^3 r_{ij} E_{THZ} \\ n_y &= n_0 + \frac{1}{2} n_0^3 r_{ij} E_{THZ}. \end{aligned} \quad (4.2)$$

Due to the polarization-dependent refractive index, as EM fields propagate through a distance L in the detection crystal, the orthogonal components will accumulate a relative phase difference $\Delta\phi$

$$\Delta\phi = \Delta k L = (n_y - n_x) \cdot \frac{2\pi}{\lambda} \cdot L = \frac{2\pi L}{\lambda} n_0^3 r_{ij} t E_{THZ} \quad (4.3)$$

where $\Delta k = \Delta n \omega / c$ is the difference in wavenumber between the orthogonal polarization states and λ is the central wavelength of the modulated sampling pulse. The sine of the phase shift in Equation (4.3) is proportional to the modulation of the signal amplitude:

$$I_{EO} = \sin(\Delta\phi). \quad (4.4)$$

E_{THZ} is then related to the measured EO signal from Equations (4.3) and (4.4) as

$$I_{EO} = \sin\left(\frac{2\pi L}{\lambda} n_0^3 r_{ij} t E_{THZ}\right). \quad (4.5)$$

Therefore for small signals, the measured EO modulation is approximately proportional to the THz field strength. Measurement of this value for varying delay times, t_d , between the THz pump pulse and optical probe pulse traces the THz field strength as a function of time with sub-picosecond resolution. Shifting the relative phase between the THz and sampling pulse is achieved by increasing or decreasing the path length of the sampling beam with a programmable motorized delay stage (DS in Figure 4.1(a)).

4.3.2 *Incoherent detection*

Incoherent detection refers to amplitude measurements of scalar parameters such as pulse energy or intensity. Several methods of incoherent infrared and far-infrared detection are available that mostly exploit the known thermal properties of given absorber materials. These include bolometers [6, 7] or Golay cells [8]. In this project, detectors that exploit the physics of pyroelectric materials are utilized for energy and intensity detection [9].

4.3.2.1 *Pyroelectricity for terahertz detection*

Pyroelectricity is a material property that refers to a spontaneous polarization response to thermal stimulus. Radiation is incident on an absorbing material that acquires a net charge upon absorption, which in turn establishes a surface charge distribution in the nearby pyroelectric material, or a material near a ferroelectric phase transition that is sensitive to small thermal fluctuation [5]. The net change of polarization changes the dielectric constant, and thus capacitance, of the sensor, which registers as a transient current in an external circuit that is proportional to the total absorbed energy.

There are three pyroelectric detectors used for various energy characterizations of the THz pulse, shown in Figure 4.3. The total pulse energy is measured with a single-element large-area pyroelectric detector (Spectrum Detector Inc., SPJ-D-8), shown in Figure 4.3(a). This detector has a single 7.8×7.8 mm element (the material is a proprietary metallic composite) that integrates all thermal energy in the nominal wavelength range of $0.1 - 1000 \mu\text{m}$ ($0.3 - 300$ THz) [10, 11]. The resulting current may be monitored by an oscilloscope via BNC connection, or the digital readout in the proprietary software via USB connection. The input area may be fitted with various filtration components such as a silicon wafer (to block stray light) or an iris. The detector is bolted to a removable magnetic mount such that it may be reproducibly placed and removed from the THz beam path.

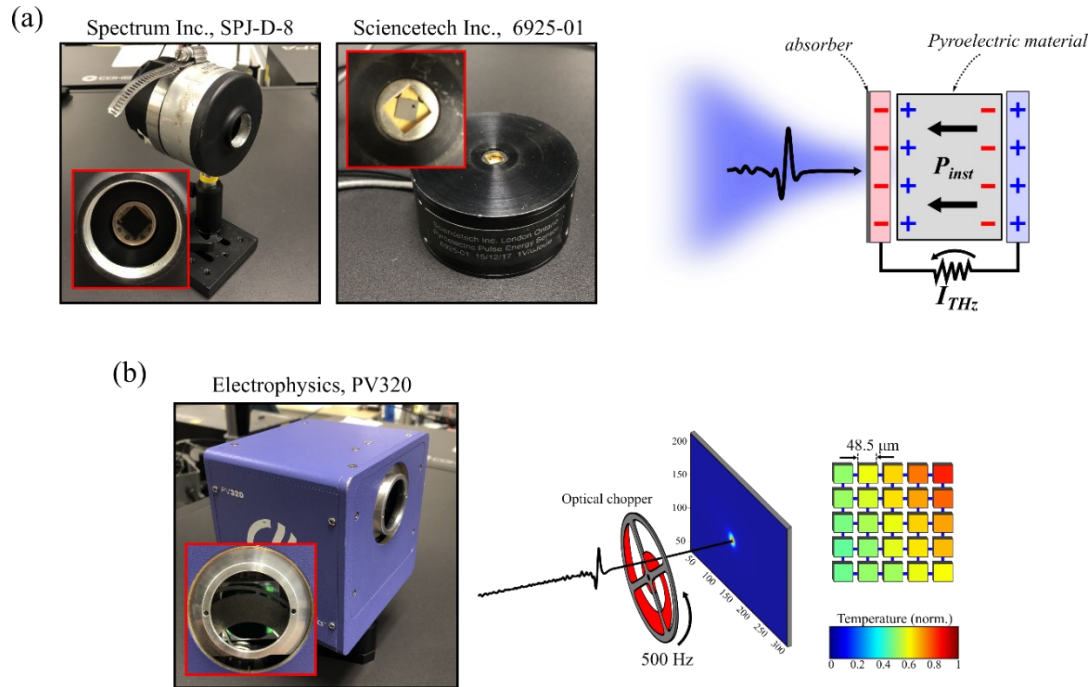


Figure 4.3. **Photos and diagrams of the pyroelectric technologies used for incoherent THz detection.** (a) Single element large-area detectors are used for detecting the total THz pulse energy. Pyroelectric elements are instantaneously polarized by the thermal energy deposition on the absorber electrode, inducing a measurable current. (b) The pyroelectric imager houses a 320×240 array of $48.5 \mu\text{m}$ square pyroelectric elements. A modulating chopper synchronized to the laser repetition rate provides an iteratively updating reference image in real time, increasing sensitivity to small thermal fluctuations.

The second pyroelectric detector (ScienceTech, 6925-01), shown at right in Figure 4.3(a), is a smaller single-element pyroelectric detector used for alignment of the bio-exposure system. A custom holder was designed to fit in the sample area, and centre the detector over a 1 mm diameter pinhole aperture, as shown in Figure 4.4. Maximizing signal amplitude to this alignment module by adjusting the holder position with a 3D linear translation stage places the pinhole at the THz focus. This provides a point of reference to align all other components of the THz bio-exposure system, similar to the concept of “isocentre” in medical radiation gantries [12].

The third pyroelectric detection technology is a pyroelectric infrared imager shown in Figure 4.3(b) (Electrophysics, PV320), and is used to acquire the spatial THz energy distribution (i.e., images of the THz beam cross-section) [13]. The sensitive area of the detector is an array of ferroelectric BST ceramic composites (nominally $\text{Ba}_{0.66}\text{Sr}_{0.34}\text{TiO}_3$), with polarization that depends strongly on temperature in ambient conditions, and is highly sensitive to small thermal fluctuations. When the input is modulated with a chopper synchronized to the imaging rate, and the sensor is

maintained at a temperature near the ferroelectric phase transition, a 2D map of the temperature fluctuations due to EM energy absorption is acquired in real-time.

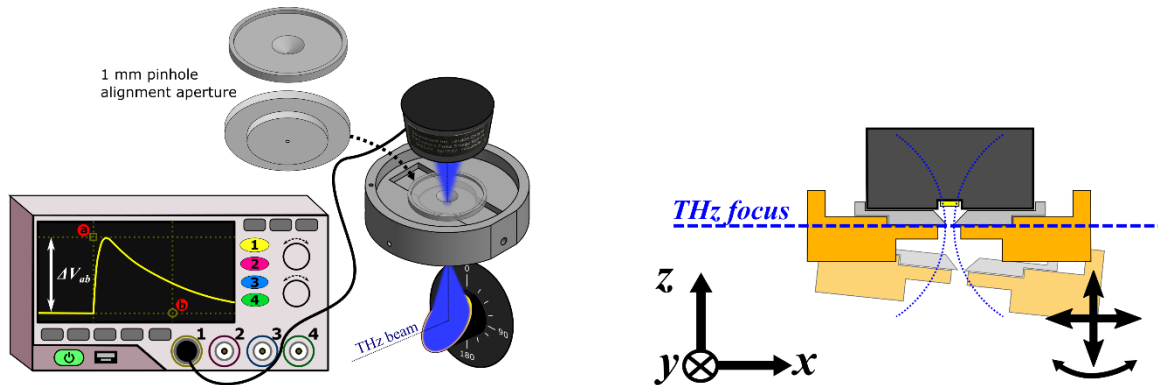


Figure 4.4. **Alignment of the sample holder with the ScienceTech pyroelectric detector.** A 1 mm custom-machined aperture holds the detector centred over the THz input window. Maximizing the pulse energy through the aperture locates the THz beam waist that is used as the reference point to align the other components of the bio-exposure system.

The modulation from the chopper intermittently blocks the input thermal irradiance allowing a uniformly averaged reference signal on the sensor array to be collected for real-time background correction in the integrated circuitry (in addition to the thermal background correction at longer time scales employed in practical THz spot imaging). The geometry of the chopper, an Archimedes spiral shown at right in Figure 4.3(b), performs this modulation with equivalent area fractions of the incident intensity in a radially symmetric fashion [14]. The sensitive area of the detector array is 320×240 pixels. Each element is $48.5 \mu\text{m}$ square for a $15.5 \times 11.6 \text{ mm}^2$ field-of-view (FOV). This camera is connected via USB to proprietary software (Electrophysics, Velocity) for real-time visualization of the imaged beam. A global thermal background with the THz beam blocked is additionally acquired to characterize the background and detector non-uniformities, and this is subtracted from an equivalent image with the THz beam unblocked. The nominal wavelength range for the PV320 imager is $3 - 20 \mu\text{m}$ ($15 - 100 \text{ THz}$), which is significantly higher than the THz band utilized in this thesis. Therefore, a per-band linearity analysis was performed to quantify the detector responsivity for frequency bands that comprise the broadband THz pulse [13].

4.3.2.2 Frequency response of pyroelectric detectors from 0.5 – 2.5 THz

Three methods of measuring the total pulse energy for individual THz bands were performed (see Section 4.5.1 for further discussion): (1) Calibrated voltage readout from the SPJ-D-8 pyroelectric detector, (2) Total pixel intensity from the PV320 pyroelectric imager, and (3) Integral

of the EO-sampled pulse power spectrum. By quantifying the pulse energy for each band, the linearity and potential frequency-dependence of these detectors can be directly compared. This is important for measurements of broadband THz pulses, as an ideal detector would detect all frequencies in the pulse with uniform sensitivity. A comparison of energy measurements for varying frequency bands is shown in Figure 4.5, plotted in the 3D energy parameter space as the black datapoints, labelled by the relevant band in green. The data traces a monotonically increasing curve, with the exception of the 0.5 THz band, which has a significantly lower power spectrum integral. This is likely due to the integrated power spectrum underestimating the THz pulse energy in this lowest frequency band, which corresponds to the largest focused spot size, and a relatively lower fraction of the total pulse energy seen by the optical sampling beam.

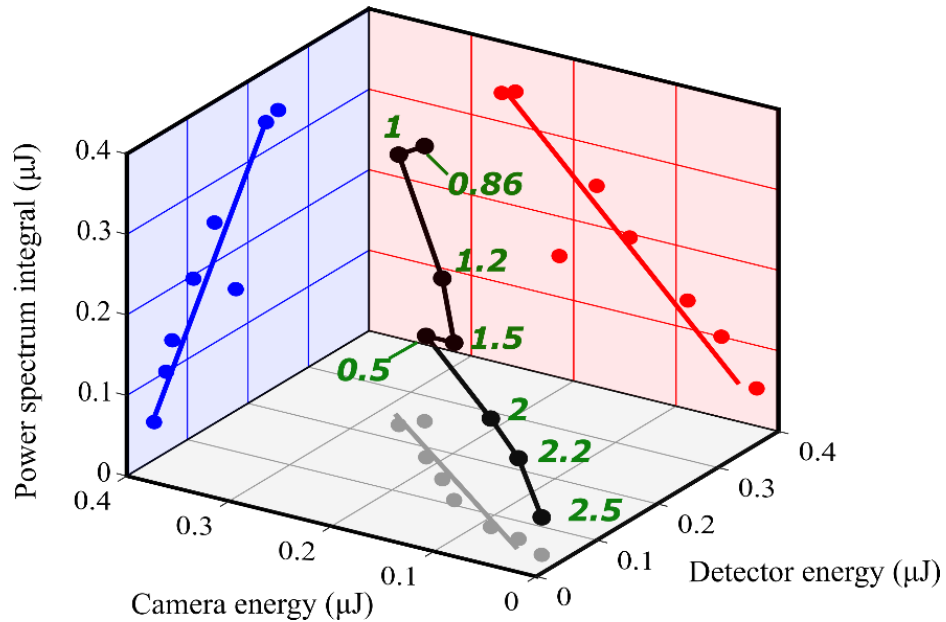


Figure 4.5. **Frequency linearity of pyroelectric detectors.** Total pulse energy measurements for each THz band (green labels in THz) are determined from the pyroelectric detector readout (SPJ-D-8), the total integrated camera pixel intensity (PV320), and the integrated power spectrum of EO-sampled waveforms. There is reasonable linearity between detectors, particularly for higher frequencies. The deviation for the 0.5 THz band is attributed to an underestimation of energy in the integrated power spectrum, since the two pyroelectric detectors with significantly different element pixel sizes (10 mm vs. 0.05 mm) are in agreement.

In particular, the PV320 imager response is limited by pixel size, and is intended for application in the 3 – 20 μm range (15 – 100 THz) [13]. However, it is shown to reasonably quantify energy in the broadband THz pulse used in this thesis (0.1 – 3 THz \rightarrow 0.1 – 3 mm) when compared to the large-element SPJ-D-8, which is designed for the 0.3 – 300 THz range [11], although there is some disagreement as seen in the gray projection of Figure 4.5.

4.4 Terahertz pulse measurements and beam characterization

Measurement of scalar properties such as pulse energy (ε), spot size (A), and duration (t) allow for quantification of power P or intensity I as

$$I = \frac{P}{A} = \frac{\varepsilon}{At}. \quad (4.6)$$

Using $t = \tau$ (where $\tau \sim 1$ ps is the single-cycle pulse duration) results in the peak power or intensity, while using $t = T$ (where $T = 1$ ms is the period of the 1 kHz pulse train) gives the average power or intensity. Since this project investigates the biological effects of intense THz pulses, the goal of maximizing intensity is achieved by generating pulses that maximize ε , minimize A by focusing the THz beam to the smallest possible spot size, and minimize τ by utilizing single cycles of picosecond-duration EM oscillations. Measurements of the pulse energy, spot size, and pulse duration are now described.

4.4.1 *Measuring the pulse energy, ε*

The measurement of the THz pulse energy, ε , is obtained directly using the SPJ-D-8 detector, as shown in Figure 4.6(a). A removable off-axis parabolic mirror (OAPM) is placed against pre-aligned stops bolted to the table in the collimated region of the THz beam in the position labelled “Pyro” in the source schematic of Figure 4.1(a). The beam is focused to the detector element and the energy is read from the digital readout in the proprietary software, or from the amplitude of a calibrated oscilloscope trace, as shown in Figure 4.6(b). Aluminum foil in contact with the detector housing reduces electronic noise, and a ~ 1 mm layer of black polyethylene filters ambient thermal energy. The relative uncertainty of THz pulse energy detection is shown in Figure 4.6(c), calculated from the standard deviation of the count histograms in the proprietary energy detection software.

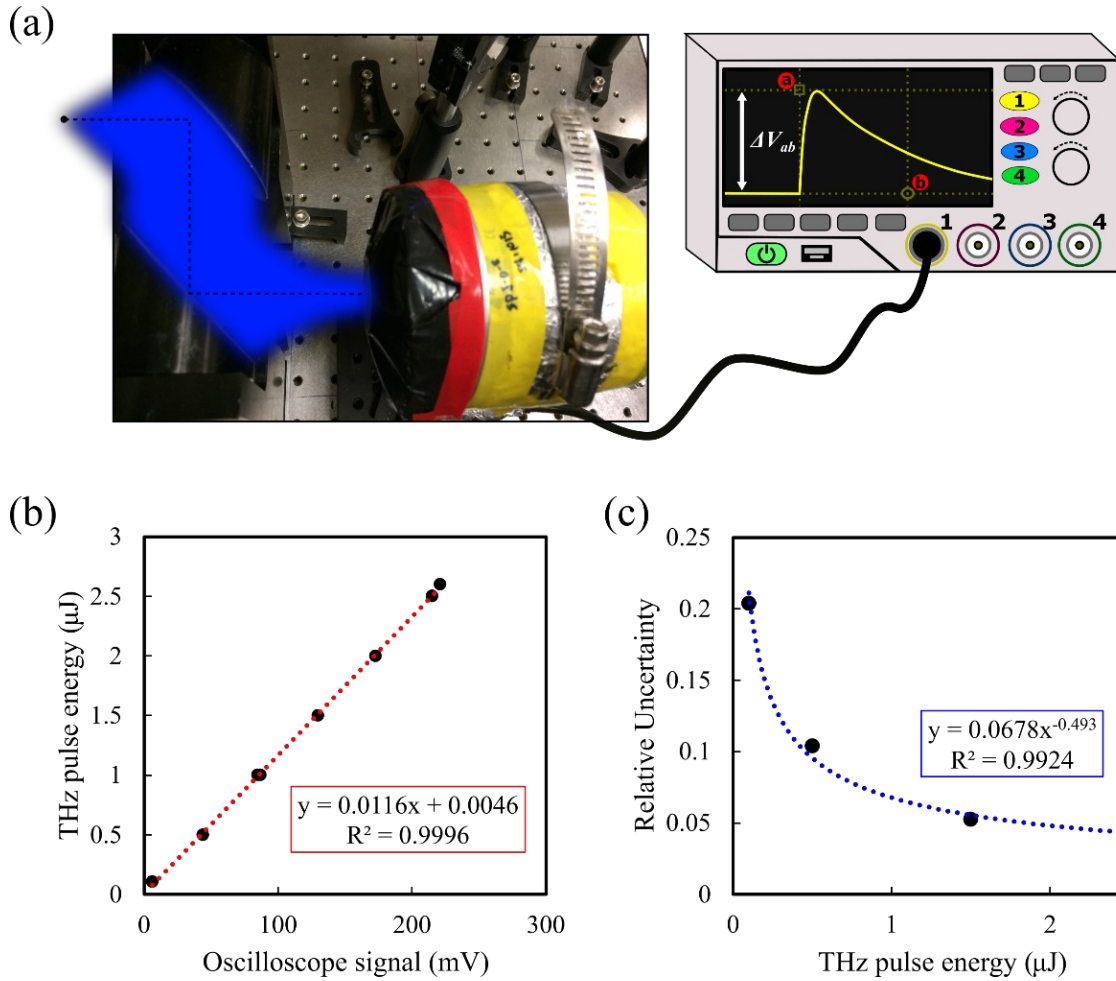


Figure 4.6. **THz pulse energy detection with the SPJ-D-8 pyroelectric detector.** (a) Gold off-axis parabolic mirrors (effective focal length = 76.2 mm) focus the THz beam to the pyroelectric element, and the resulting current is displayed as an oscilloscope pulse. (b) The amplitude of the oscilloscope signal ΔV_{ab} is linearly proportional and calibrated to the THz pulse energy digital readout. (c) The relative uncertainty in detection vs. pulse energy from the detector count histograms.

4.4.2 Measuring the pulse duration, τ

The pulse duration is an important parameter in ultrafast physics. In general, faster pulses correspond to broader spectra peaked at higher frequencies. There are several methods of characterizing the THz pulse duration. In the literature, it is typically defined using the pulse envelope calculated from the Hilbert transform [15]. To compute a Hilbert envelope, the pulse is summed in quadrature with a copy of itself shifted by $\pi/2$ rad (90°). The width of the distribution resulting from the transformation (e.g., FWHM, FWTM, $1/e$, $1/e^2$, etc.) is taken as the pulse duration. The logic for this may be understood by considering the pulse decomposed into constituent sinusoids, with associated phases $\phi(\omega)$ and amplitudes $A(\omega)$ given by the Fourier

transform. For a given frequency ω_0 , the Fourier component is $A \cdot \sin(\omega_0 t + \phi_0)$. Summing the root sum-of-squares of this wave with a 90° -shifted copy is equivalent to

$$A \cdot \sqrt{\sin^2(\omega_0 t + \phi_0) + \cos^2(\omega_0 t + \phi_0)} = A$$

which is the “envelope” of a monochromatic sinusoid. Extending this concept for all frequencies and phases that exist in the pulse therefore defines the envelope for an arbitrary field distribution. An example of a Hilbert envelope and extracted durations for a measured THz pulse are shown in Figure 4.7(a).

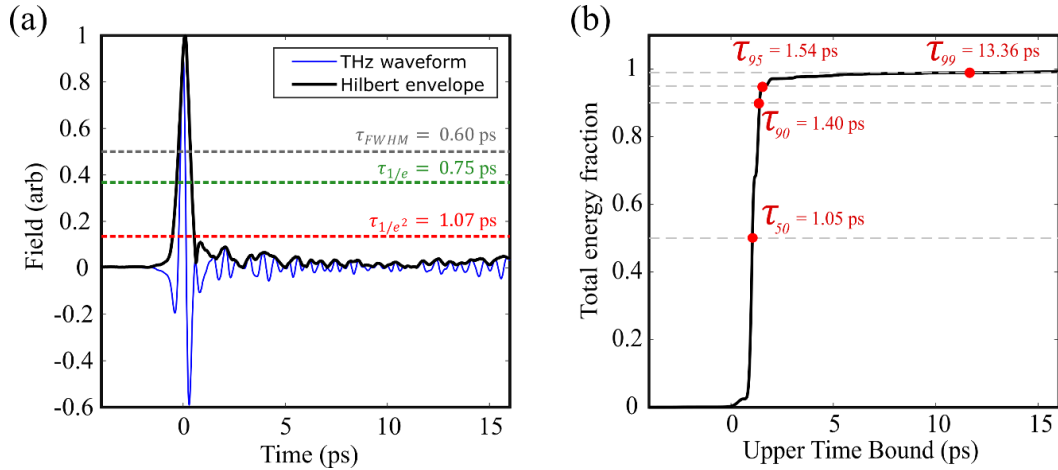


Figure 4.7. **Two methods of defining the pulse duration.** (a) The magnitude of the Hilbert transform defines the envelope for an arbitrary field distribution. The width of this envelope, by convention the $1/e$ threshold (green), defines the THz pulse duration. Also shown are alternative pulse width metrics – FWHM and $1/e^2$. (b) Normalized cumulative integral of the noise-subtracted temporal energy distribution. Pulse durations may be defined as time to accumulate a given fraction of total energy.

Another method of quantifying the pulse duration is by fractional energy arrival time as shown in Figure 4.7(b). Here, a cumulative energy integral $\varepsilon^*(t) = \int_0^t E^2(t') dt'$ is computed, resulting in a curve representing energy growth of the pulse as a function of time up to a maximum given by the total pulse energy $\varepsilon = \max(\varepsilon^*)$. Pulse durations may then be extracted by defining an energy fraction threshold $X\%$, for which the associated time duration τ_X is the time to reach the chosen threshold. To eliminate the influence of measurement noise, a linear function is fit to the cumulative integral in the negative time ($t < 0$ ps) field region. Assuming noise energy is roughly constant, this line is extrapolated to the positive time domain and subtracted from the total integral. The remainder of the cumulative integral represents the noise-subtracted THz energy in time. The widths of the Hilbert transform in Figure 4.7(a) can be compared to energy growth times in Figure 4.7(b). It is typical to see the $1/e$ width used in the THz literature (green line in Figure 4.7a). In

this example, the pulse duration is determined to be $\tau_{1/e} = 0.75$ ps, which is equivalent to roughly 40% of the total pulse energy.

4.4.3 Measuring the focused spot area, A

To measure the spot size, image data of the THz focus is acquired by the PV320 imager in Figure 4.3(b). A silicon wafer is mounted on the detector input to filter residual infrared pump leakage. The imager is placed at the “Pyro” location in Figure 4.1(a) and manually shifted until the smallest spot is achieved (the THz beam may need to be attenuated with crossed wire-grid polarizers or silicon wafers to avoid camera saturation). A second image with the THz beam blocked is used for background subtraction in post-analysis.

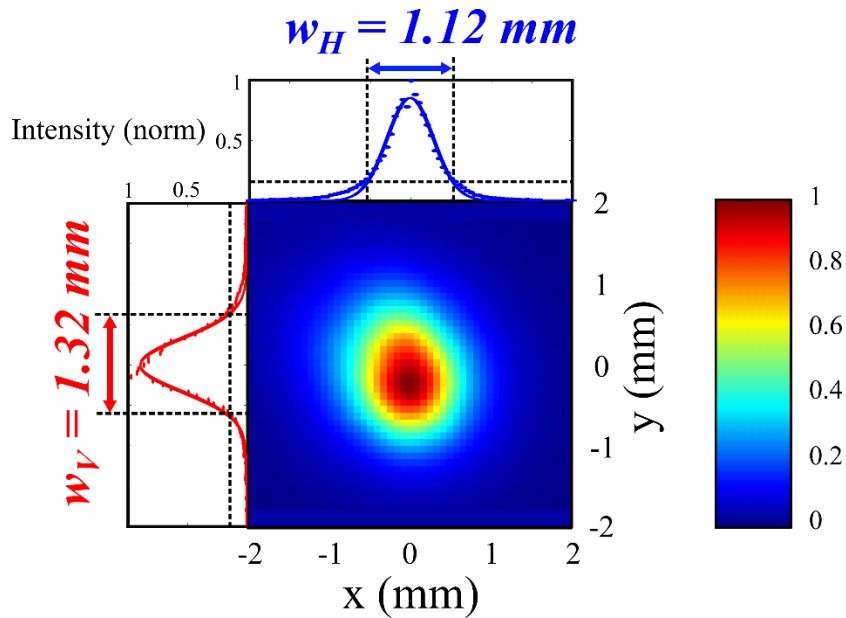


Figure 4.8. **Quantifying THz spot area with combined 1D Gaussian fits.** Data is extracted from the 2D image from horizontal and vertical line profiles drawn along the major/minor axes of the elliptical THz spot. By convention, the spot size in each dimension is reported as the $1/e^2$ width of the fit.

The measured THz focus for the beam under optimal alignment conditions (the “max field pulse” in Table 4.1) is shown in Figure 4.8. Horizontal and vertical line projections are plotted through a reference point in the image data, typically the maximum pixel intensity, or the maximum average local intensity if noise is high, and fit to a Gaussian function $G(x; x_i) = x_1 \exp\left(-\frac{(x-x_2)^2}{2x_3^2}\right) + x_4$ for fitting parameters x_i . The spot diameter is extracted from the fitted width x_3 , conventionally reported as the width at $1/e^2$ of the peak value. These measurements may

then be utilized in Equation (4.6) in defining the intensities of the THz pulse, or for calculation of the peak electric field discussed presently.

4.4.4 *Measuring the electric field strength, E_{THz}*

The field strength need only be quantitatively determined at a single point (typically t_0 , the timepoint of the “peak” or maximum field), and this is used to scale the relative waveform acquired by EO sampling to determine the electric field as a function of time. In general, two methods are commonly employed:

4.4.4.1 *Field calculation from classical electric energy density*

The first method utilizes the classical relationship $u = \frac{1}{2}\epsilon_0 E_{THz}^2$, where $u = \epsilon/V$ is the energy density in a region of space $V = Az = A\tau c$, A is the transverse spot area, τ is the pulse duration, c is the vacuum speed of light (2.9979×10^8 m/s) and ϵ_0 is the permittivity of free space (8.85×10^{-12} F/m) [16]. Re-arranging to solve for the field strength, E_{THz} , gives

$$E_{THz} = \sqrt{2Z_0 I_p} = \sqrt{\frac{2Z_0 \epsilon}{A\tau}} \quad (4.7)$$

where $Z_0 = (\epsilon_0 c)^{-1} = 377 \Omega$ is the impedance of free space. This method is useful for estimates of the field magnitude from the measured pulse energy (Section 4.4.1), pulse duration (Section 4.4.2), and spot size (Section 4.4.3). Other definitions for τ have also been employed, such as waveform integrals, as in references [17, 18]. However, as the initial expression for energy density is derived from a time-average of a plane-wave over many field cycles, this relationship is not valid in general for single-cycle field oscillations in a focusing geometry, as relevant to our bio-exposure studies [16].

4.4.4.2 *Field calculation directly from the electro-optic signal*

The preferred method of calculating field strength for this thesis is directly from the measured normalized EO signal, I_{EO} , discussed in Section 4.3.1.1. Rearranging Equation (4.5) [19]:

$$E_{THz} = \arcsin(I_{EO}) \cdot \frac{\lambda}{2\pi L n_0^3 r_{41} t_{GaP}} \quad (4.8)$$

where $L=200 \mu\text{m}$, $n_0=3.18$, $r_{41}=0.88 \text{ pm/V}$, $t_{GaP} = 0.46$ is the GaP thickness, index, EO coefficient, and amplitude transmission coefficient, respectively, and $\lambda=800 \text{ nm}$ is the sampling beam wavelength.

4.4.5 Summary of terahertz pulse parameters

A Matlab GUI was designed to automate the calculations described in Sections 4.4.1 – 4.4.4 from raw data: EO sampled waveform, THz spot image, and pulse energy measurement. These logged calculations were queried in order to establish a distribution of THz pulse parameters, and report typical ranges of these parameters utilized in this project. Table 4.1 reports a summary for 35 measured THz pulses utilized for various experimental contexts over the duration of this thesis project. The Max Field Pulse is the pulse measured with the highest peak field strength (640.3 kV/cm), and represents the THz generation capabilities under optimal efficiency and alignment conditions.

Table 4.1. **Typical range of THz pulse parameters and the pulse with the highest achieved field**

	<u>Mean parameters</u>	<u>Max. field pulse</u>
Peak field (kV/cm)	332±140	640.3
Pulse energy (μJ)	1.2±0.4	1.45
*Spot size ($w_H \times w_V$ mm ²)	1.6 × 1.9	1.12 × 1.32
†Duration (ps)	1.0±0.3	0.93
Peak frequency (THz)	0.7±0.3	1.3
Bandwidth (FWTM THz)	1.2±0.5	1.1
Average intensity (mW/cm ²)	67±28	125.0
Peak intensity (MW/cm ²)	54±40	134.5

†Pulse durations reported as the $1/e$ -width of the Hilbert envelope

*Spot sizes reported as major/minor axis $1/e^2$ -diameters of elliptical THz focus.

FWTM=full-width tenth max

4.5 Spectral decomposition of the terahertz beam

The distribution of spectral energy in time and space for a THz pulse is an important consideration for biological exposure studies, as the interaction mechanism implies that frequency may be a key control parameter for THz-induced biological effects, and so must be properly

characterized. Figure 4.9 shows the coarse spectral differences between the principal single-cycle pulse (green) and the small-amplitude ringing that follows (red), comprising 94% and 6% of the total THz pulse energy, respectively. The corresponding power spectra show significant frequency dispersion, with the energy of the positive-time ringing predominantly contained in the water absorption bands, and is a spectral signature of free-space propagation in humid air.

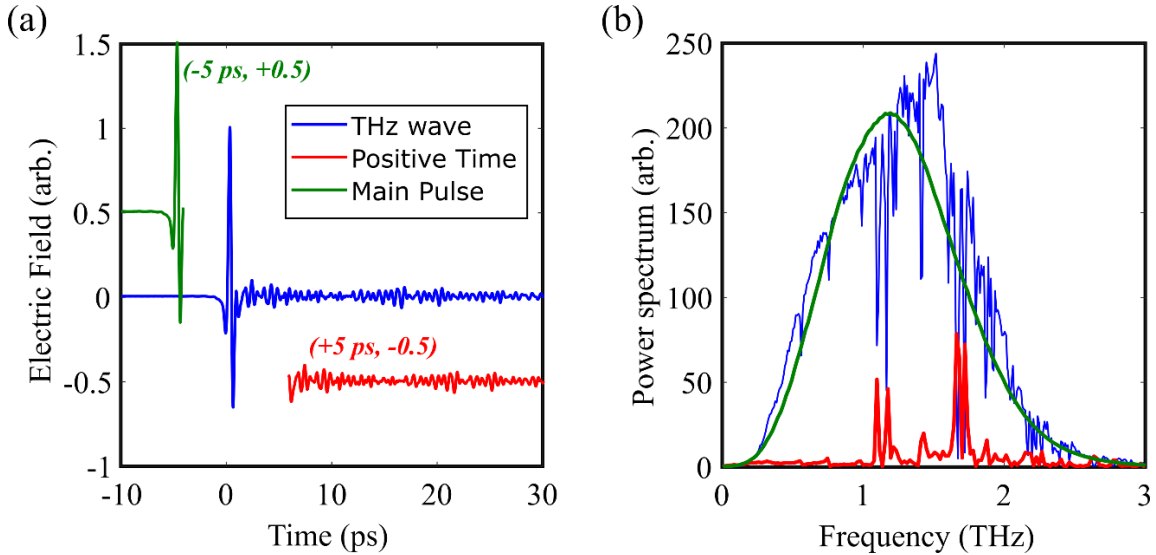


Figure 4.9. **Windowed FFTs of the THz pulse highlighting coarse spectral variation in time.** (a) Time-domain waveforms, showing pulse separation into the two dominant components: The main THz pulse generated from the optically rectified Gaussian infrared laser pulse (green), and the positive-time oscillations (red) due to crystal ringing and water vapor-induced dispersion that causes high frequencies to travel faster than low frequencies in humid air. (b) The corresponding power spectra show that the main pulse captures the majority of the broadband spectral shape, and the peaks in the positive-time ringing exactly overlap with THz water absorption lines.

4.5.1 Bandpass terahertz waveform analysis

The single-cycle, broadband pulse can be thought of as containing many non-visible “colours” of THz energy, and the Fourier transform provides the continuous (window-limited) frequency distribution that exists in the pulse. The frequency bands that comprise the total broadband pulse correspond to their own temporal waveforms that may be individually measured via electro-optic sampling, with associated peak field, energy, pulse duration, spot size, and intensity characterized as described in Sections 4.3 and 4.4. These waveforms are obtained by filtering the broadband THz pulse with bandpass filters that preferentially transmit narrow energy bands from the incident broadband spectrum, as shown in Figure 4.10. Filtering the THz pulse prior to biological exposure provides the best method of investigating frequency-dependent biological effects.

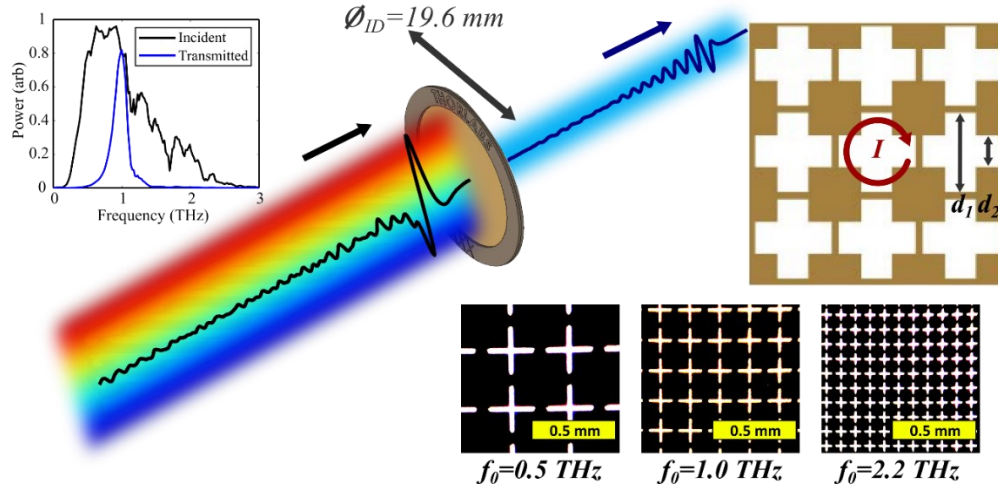


Figure 4.10. **THz bandpass filters.** Fields incident on the conductive mesh establish capacitance and inductance distributions that preferentially transmit single frequency bands dependent on the specific geometry of the cross-absent structure (top-right). *Bottom:* Stereoscope images of the bandpass filters at 0.5, 1.0, and 2.2 THz, showing cross-absent geometries tuned for desired wavelength transmission.

To characterize the properties for the individual frequency bands that comprise the THz pulse, 8 bandpass filters were acquired for the $\{0.5, 0.86, 1.0, 1.2, 1.5, 2.0, 2.2, 2.5\}$ THz bands (Thorlabs FB19M λ , where λ is the central wavelength of the filter in μm). These filters are $1 \mu\text{m}$ thick gold mesh in a cross-absent pattern, and are a photonic analog of a resonant LC circuit. The conductive grid pattern establishes field-driven charge separations (capacitance, C) and current loops (inductance, L) that reject out-of-band radiation by reflection and destructive interference, and preferentially transmit the desired frequency band [20, 21, 22]. The normalized EO-sampled waveforms for each bandpass filter are shown in Figure 4.11(a) and the associated power spectra are in Figure 4.11(b). The incident broadband parameters are given in Table 4.2.

Table 4.2. **Incident broadband THz pulse parameters (black pulse in Figure 4.11(a)).**

Pulse Energy (μJ)	1.6
Peak field (kV/cm)	567
Peak frequency (THz)	0.6
Bandwidth FWHM (THz)	0.7
Spot size ($w_H \times w_V$ mm ²)	2.0×1.7
Pulse duration (ps)	0.83

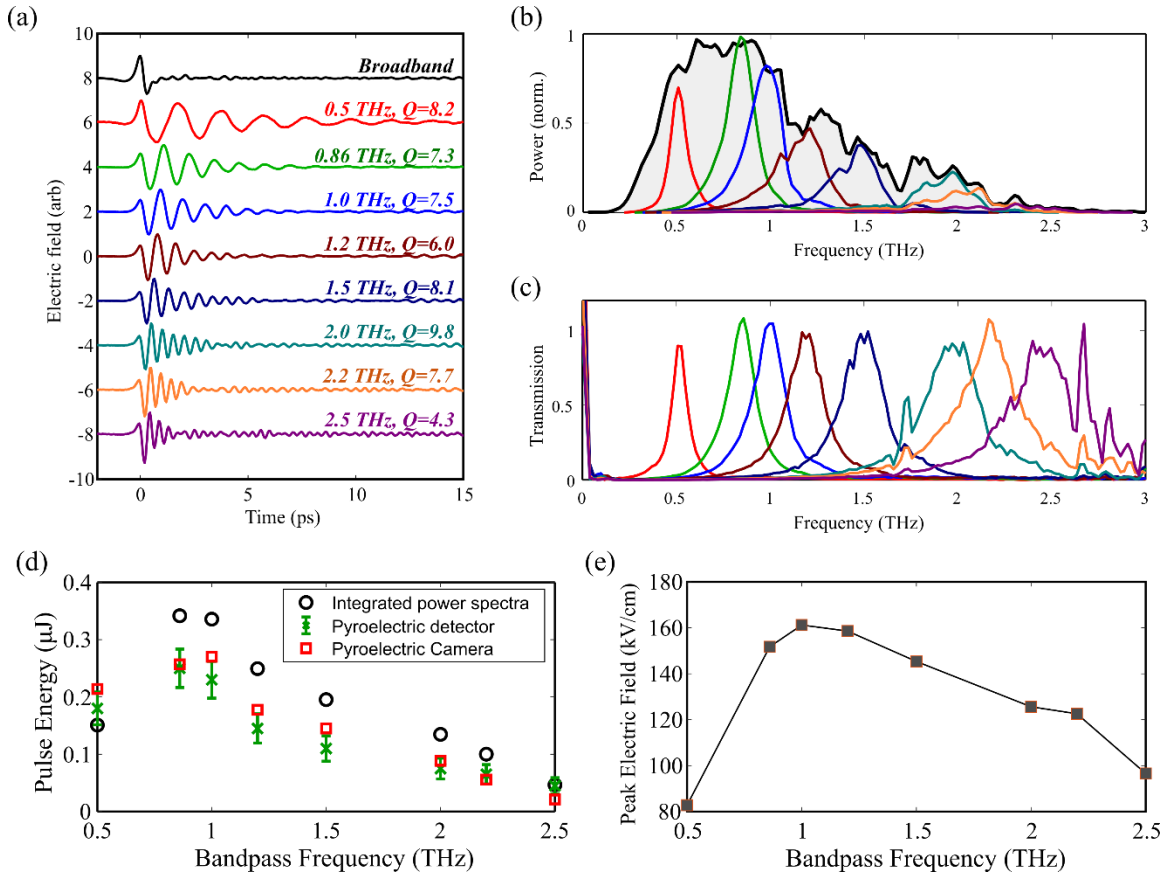


Figure 4.11. **Time-domain waveforms for individual THz bands.** (a) The set of normalized waveforms, labelled by nominal bandpass frequency and quality Q of the associated transmission profile. (b) Power spectra for all filters overlaid on the broadband spectrum (black). (c) Transmission spectra (power spectra ratios) for each bandpass filter. (d) Pulse energy for each THz band, as measured by the methods discussed in Section 4.3.2.2. (e) Peak (maximum absolute value) electric field of the associated bandpassed waveform.

The labelled Q -value for each waveform represents the quality, $Q = f_0/\Delta f$, of the associated transmission profile (Figure 4.11(c), calculated from the ratio of power spectra), where f_0 is the peak frequency and Δf is the FWHM width. The total pulse energy for each band was measured by three methods as discussed in Section 4.4.1, and approximately trace the power spectrum of the broadband pulse as in Figure 4.11(d). The peak electric field amplitudes for each waveform are shown in Figure 4.11(e).

4.5.1.1 Per-band pulse duration

Qualitatively, the temporal waveforms of Figure 4.11(a) are clearly faster for higher frequency bands, as expected, and field amplitudes appear to follow an exponential decay. Therefore, the peaks of the temporal field were fit to an equation $y = y_0 e^{-t/\tau}$ to determine a characteristic decay

time τ . An example of this fit is shown in Figure 4.12 for the 1.0 THz band. The associated linear frequency $f = 2\pi/\tau$ is plotted against the bandpass frequency f_0 , and compared to durations as determined from the Hilbert envelope (Section 4.4.2). Pulse durations for the 2.0 and 2.2 THz bands are slower than the expected linear trend, but may be due to fitting error in low-SNR bands.

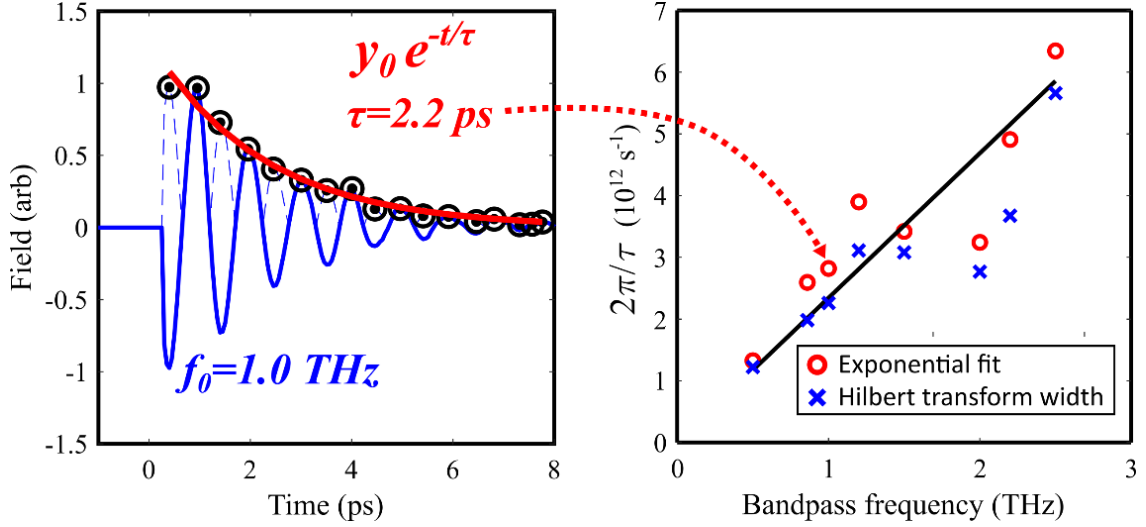


Figure 4.12. **Per-band THz pulse duration.** The characteristic time of amplitude decay (example for 1.0 THz at left) agrees well with the pulse duration as determined from the Hilbert profile width (right).

4.5.1.2 Per-band beam size and frequency distribution in space

Free-space THz pulses are diffraction-limited, and the minimum beam radius, w_0 , is frequency-dependent. Therefore, each frequency band will focus to different sizes in potentially different regions of space, with high frequencies generally capable of tighter focusing. The theoretical diffraction limit for Gaussian beams is given by [23]

$$2w_0 = \frac{4c}{\pi f_0} \cdot \frac{F}{d} \quad (4.9)$$

where $c=2.9979 \times 10^8$ m/s is the speed of light, $F=76.2$ mm is the mirror focal length, and $d=30$ mm is the mirror aperture.

Images of the THz focus for individual frequency bands provides the spatial frequency distribution present in the total broadband pulse, as shown in Figure 4.13(a). The images in the top row are globally normalized to the max intensity of the highest energy pulse (0.86 THz), and the images in the bottom row are each individually normalized to their own maxima. Together, these

show the dependence of total energy and focused spot size for varying frequency bands within the broadband pulse. Figure 4.13(b) shows the mean spot sizes (average of horizontal and vertical diameters), compared to the diffraction limit from Equation (4.9). Contour lines for the region encompassing the $1/e^2$ intensity of each image are shown in Figure 4.13(c).

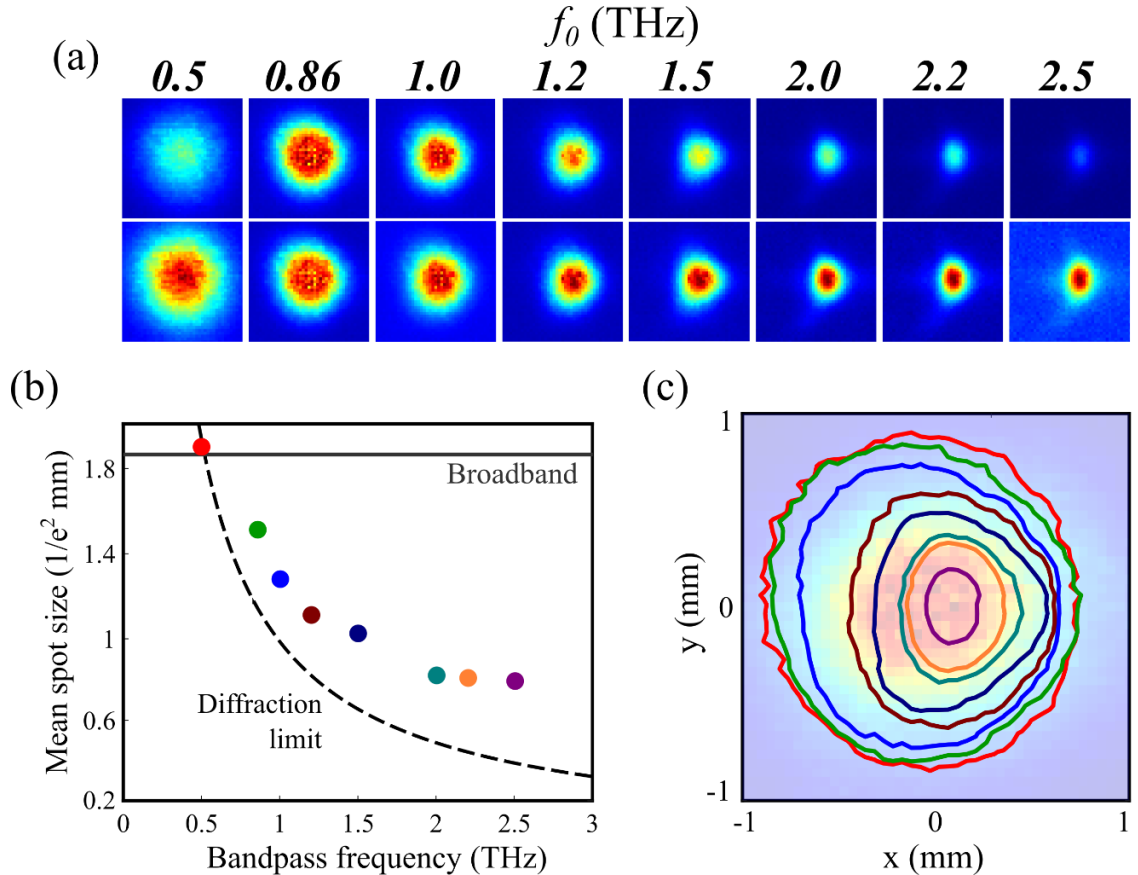


Figure 4.13. **Per-band spatial intensity distributions.** (a) Each spot image is a square with 2 mm side lengths. The top row has been globally normalized to the 0.86 THz pixel maximum, and the bottom row images are normalized to their own maxima. (b) The mean spot size (average of horizontal and vertical diameters), compared to the theoretical diffraction-limited spot size, assuming an initial beam size of 30 mm. (c) $1/e^2$ contour lines for each of the same bands, overlaid on the broadband spot image, highlighting the frequency distribution in space embedded within the broadband exposure. Thus, the centre of the beam contains the entire broadband spectrum, while the beam energy at the fringes are relatively low-frequency.

This frequency-dependent characterization of the spatial distribution is important for a focused broadband beam used for biological exposure studies, as an exposed sample sees an altered spectrum depending on the location within the THz spot. For typical human cell sizes (10 – 100 μm diameter), anywhere from 1000 to 100,000 confluent cells may exist in the broadband THz spot ($2.02 \times 1.68 \text{ mm}^2$). The cells near the centre of the focus see the full spectrum, while cells near the fringes see a higher fraction of low-frequency energy (i.e., as if a low-pass filter is applied from the beam centre to the edges).

4.5.1.3 Per-band peak and average intensities

Finally, Figure 4.14 shows the average and peak intensity for each THz band, calculated by Equation (4.6) from the measured pulse energy (pyroelectric detector, Figure 4.11(d)), duration (Figure 4.12), and spot size (Figure 4.13). While the pulse energy generally decreases for higher frequencies, the decreases in pulse duration and spot size compensate, and high-frequency peak intensities are comparable or even greater than the maximum-energy frequency bands.

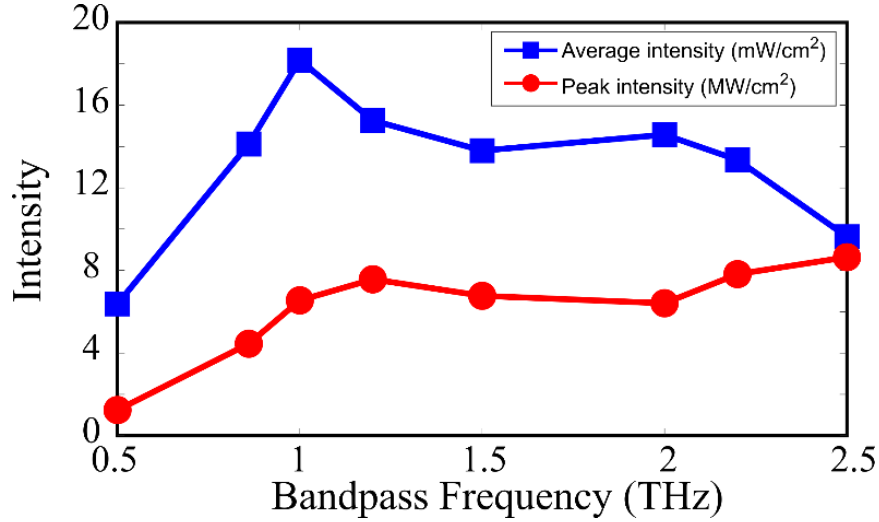
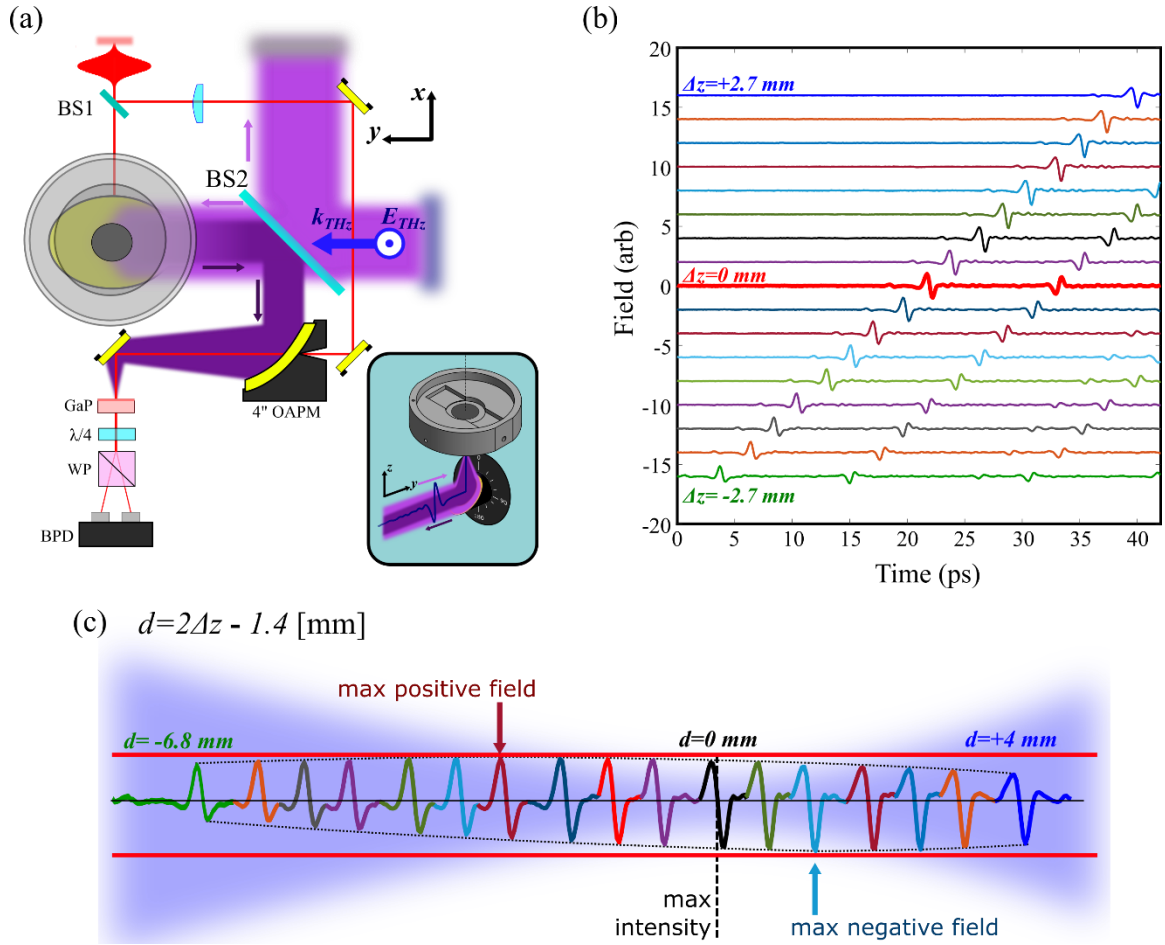


Figure 4.14. **The average and peak intensities of individual THz bands.** The trade-offs between energy, duration, and spot size in the intensity calculation of Equation (4.6) result in roughly flat intensity profiles across the THz pulse spectrum.

4.6 Terahertz field modulation in a focusing beam geometry

To maximize THz intensity, a focusing beam is utilized that deviates from simplified plane-wave characterizations. To investigate modulation of the THz pulse in a focusing geometry, a THz waveform was acquired for varying longitudinal locations through the beam focus. In practice, the THz source was prepared in reflection mode, as shown schematically in Figure 4.15(a) (see Chapter 5 for details), with a 0.5 mm thick silicon (Si) wafer placed at the sample location. A series of 17 waveforms, shown in Figure 4.15(b), were acquired by EO sampling with the sample stage shifted by $\Delta z \in [-2.7, +2.7]$ mm on either side of the location of the initial reference at $\Delta z = 0$. This effectively shifts the detection plane of the GaP crystal to locations $z \in [-5.4, +5.4]$ mm due to the return trip in reflection mode. The location of maximum intensity was determined to be at $z = z_0 = +2.8$ mm, and is intermediate to the locations of the maximum/minimum positive/negative field lobes as shown in Figure 4.15(c). Therefore, the pulse propagation distance variable, d , is defined as $d = 2\Delta z - 1.4$ [mm], so that the data are symmetric about the beam waist at $d=0$ mm.



$$(c) \quad d = 2\Delta z - 1.4 \text{ [mm]}$$

Figure 4.15. **Waveform modulation of a focusing beam.** (a) Schematic of the THz source in reflection mode for focusing beam waveform detection. Reflections from an Si wafer at the sample locations are acquired, and the sample holder is translated longitudinally (z) to effectively shift the GaP detection plane through the sampled THz beam focus. (b) Field vs. time of the EO-sampled THz pulse waveforms, with vertical offsets for varying longitudinal locations for clarity. The secondary reflections are from the distal surface of the Si wafer. (c) Pulses aligned with their position in the focusing beam geometry, showing focusing-induced phase modulation. The red lines indicate the maximum and minimum field strength range. The locations of field maxima straddle the maximum intensity beam waist.

For each waveform, the field values of the maximum and minimum pulse lobes were extracted. These are plotted for as a function of space and intensity in Figure 4.16(a), and each of the 2D projections of these data are shown in Figure 4.16(b – d). In Gaussian optics, longitudinal variation of the beam waist $w(z)$ is given by [23]

$$w(z) = w_0 \sqrt{1 + \left(\frac{z - z_0}{z_R}\right)^2} \quad (4.10)$$

where w_0 is the minimum beam waist (i.e., the focus' radius, Equation (4.9)) and $z_R = \pi w_0^2/\lambda$ is the Rayleigh range (half the depth of focus) for a monochromatic wavelength, λ . The average intensity for each location is quantified from the integrated power spectra of the associated waveform for varying positions through the focus, and this variation as the THz pulse is focused is shown in Figure 4.16(b). Using Equation (4.10) the measured values were fit to a function $F = 1/w^2$ (black curve), and the extracted fit parameters were $w_0 = 0.9 \pm 0.1$ mm, consistent with the measured spot size, and $z_R = 8.0 \pm 0.2$ mm is an effective broadband Rayleigh range. Using these to solve for λ in the above expression for z_R gives a corresponding effective monochromatic wavelength of 0.32 mm, or 0.94 THz.

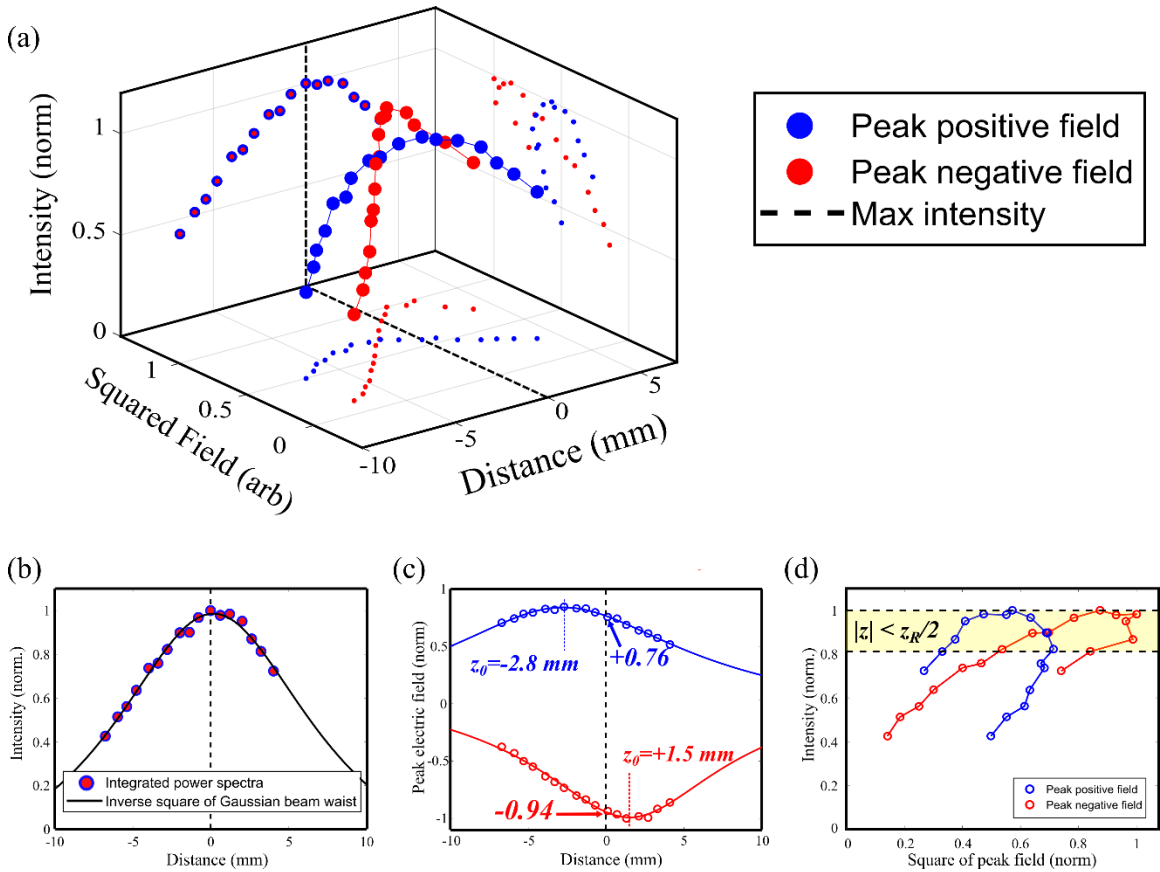


Figure 4.16. **Intensity and field variation for a focusing THz pulse.** (a) A 3D plot showing the variation of the positive/negative (blue/red) field lobe amplitudes through the focus ($d=0$ mm), with the intensity of the focusing beam shown on the vertical axis. The three 2D projections of this 3D space are shown in the bottom plots. (b) The intensity as measured by the integrated power spectra follows the functional form of a focusing Gaussian beam (Equation (4.10)), with $z_R = (8.0 \pm 0.2)$ mm representing an effective broadband Rayleigh range. (c) The field amplitude for each lobe of the THz waveform during focusing. The maximum field for each lobe straddles the location of maximum intensity. (d) Intensity vs. squared peak field strength. Far from the focus, the linear scaling of Equation (4.7) is valid. Within the effective Rayleigh range of the focus (highlighted band), the gradient directions reverse, due to the focusing-induced Gouy phase shift.

The maximum and minimum field values are plotted vs. distance in Figure 4.16(c). Of note is the 4.3 mm gap between the maximum positive field and the minimum negative field lobes, which straddle either side of the maximum intensity focus at $d=0$ mm.

Figure 4.16(d) shows the intensity vs. the squared-field extracted from the waveforms during focusing. The linear proportionality predicted by Equation (4.7) is satisfied for points far from the focus relative to the effective broadband Rayleigh range. However, within $\pm z_R/2$ of the beam waist (highlighted band), the linear trend undergoes a reversal due to a focusing-induced π -phase shift. This phenomenon is known as the Gouy phase shift, first characterized by Louis Georges Gouy in 1890 [24].

4.6.1 Carrier-envelope phase modulation and the Gouy phase shift

The field modulation in Figure 4.15 and Figure 4.16 is due to a carrier-envelope phase (CEP) shift of the focusing THz pulse, and fundamentally arises due to the finite spatial extent of the THz beam in space [25].

4.6.1.1 Physical origin of the Gouy phase shift

Mathematical descriptions of a propagating wave often utilize the plane-wave approximation, which assumes that there is no transverse curvature of the EM field vectors (i.e., the vectors lie on a 2D plane of infinite extent). In reality, THz fields are not plane waves, but are approximately $\{0,0\}$ Gaussian mode distributions with non-zero transverse momentum $k_{x/y}$ related to the total wavevector k as

$$\bar{k}_z \equiv \frac{\langle k_z^2 \rangle}{k} = k - \frac{\langle k_r^2 \rangle}{k} \quad (4.11)$$

where the bra-ket notation indicates the expectation value of the wavevector, $k_r^2 = k_x^2 + k_y^2$, and radial symmetry is assumed. Longitudinal propagation is governed by $\bar{k}_z \equiv \partial\phi(z)/\partial z$. Therefore, the first term of Equation (4.11) gives a linear phase term, kz , for an infinite plane wave, and the second term represents the Gouy phase shift, or the expectation value of the axial phase shift:

$$\phi_G = -\frac{1}{k} \int_0^z \langle k_r^2 \rangle dz'. \quad (4.12)$$

A radially finite THz field, $E(r, z)$, is modeled as a transverse $\{0,0\}$ Gaussian distribution

$$E(r, z) = \sqrt{\frac{2}{\pi}} \cdot \frac{1}{w(z)} \cdot \exp\left\{-\frac{r^2}{w^2(z)}\right\} \quad (4.13)$$

where $w(z)$ is the beam waist given by Equation (4.10). The Fourier transform of Equation (4.13) gives the transverse wavevector distribution, and is also Gaussian in k -space centred at $k_r = 0$:

$$\tilde{E}(k_r) = \frac{w(z)}{2\pi} \cdot \exp\left\{-\frac{w^2(z)}{4} k_r^2\right\}. \quad (4.14)$$

As ϕ_G relies on the expectation value, we find via Equation (4.14)

$$\langle k_r^2 \rangle = \int_0^\infty k_r^2 |\tilde{E}(k_r)|^2 dr = \frac{2}{w^2(z)}. \quad (4.15)$$

Inserting into Equation (4.12):

$$\phi_G = -\frac{2}{k} \int_0^z \frac{dz'}{w^2(z')}. \quad (4.16)$$

Substituting Equation (4.10) into Equation (4.16) and integrating, the Gouy phase shift of a Gaussian beam as it propagates through the focal plane, z_0 , is

$$\phi_G(z) = -\arctan\left(\frac{z - z_0}{z_R}\right). \quad (4.17)$$

4.6.1.2 Gouy phase modulation of the focusing terahertz pulse

The principle of CEP modulation is shown in Figure 4.17(a), depicting the effect to the net pulse due to relative phase shifts between the envelope (red) and carrier (blue) waves. Equations (4.17) and (4.10) are plotted in Figure 4.17(b), displaying the CEP reversal for a focusing beam

geometry at the minimum beam waist. Figure 4.17(c – d) show the modulations to the measured THz waveform and spectrum in the converging ($d=-4$ mm), focused ($d=0$ mm), and diverging ($d=+4$ mm) beam regions. The pulse durations, t_{hil} , and peak-power frequencies, f_0 , were also determined. As the pulses approach the focal plane, both t_{hil} and f_0 increase to maxima of 1.18 ps and 0.78 THz, respectively, and decrease to 1.11 ps and 0.62 THz when sampled 4 mm from the focus.

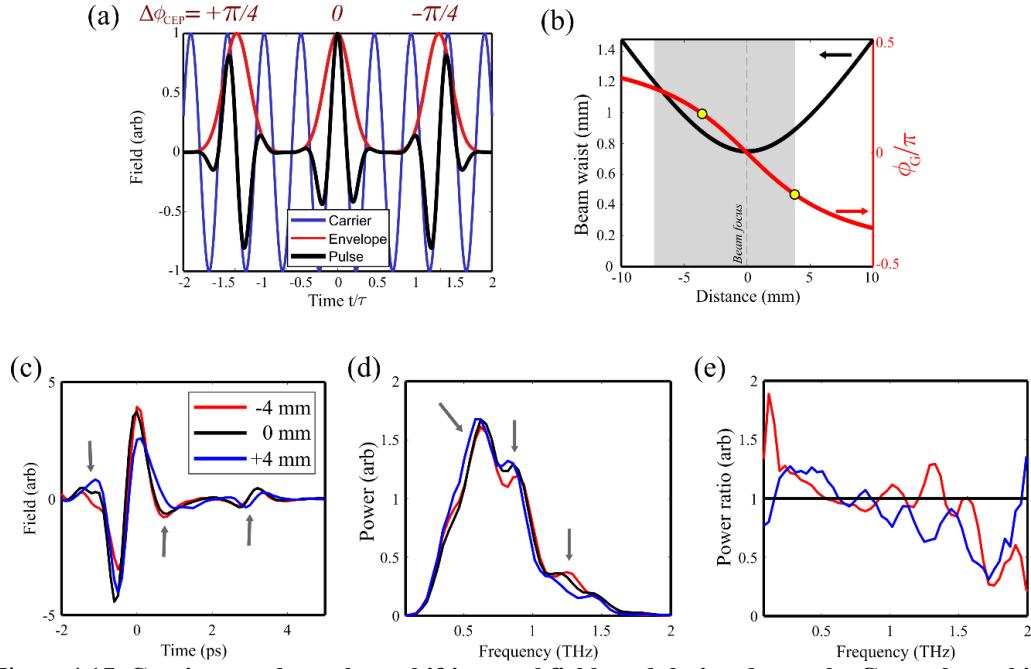


Figure 4.17. Carrier-envelope phase shifting, and field modulation due to the Gouy phase shift of a focusing THz beam. (a) A plot displaying the principle of carrier-envelope phase (CEP) modulation. When the relative phase between the envelope (red) and the carrier wave (blue) is shifted, such as during beam-focusing, the net pulse (black) is modulated. (b) The beam waist (black, left) and phase (red, right) of a focusing beam. The yellow circles at ± 4 mm indicate the Rayleigh range ($z_R = 8.0$ mm). (c) Temporal modulation of the THz pulse at the beam waist, and $d = \pm 4$ mm. (d) Power spectra of the waveforms in (c). Modulations are observed at 0.8 and 1.3 THz. (e) Off-focus power spectra normalized to the focused spectrum, highlighting the modulations in frequency space for sensing in the converging (red) or diverging (blue) region of the beam.

Interestingly, the effect to the frequency content of the pulse appears to be an energy trade-off between, predominantly, the 0.8 THz band behind the focus ($z = -4$ mm) and the 1.3 THz band ahead of the focus ($z = +4$ mm). Figure 4.17(e) plots the ratios of the off-focus spectra to the focused spectrum, and shows that these energy trades are features of periodic modulations from 0 – 2 THz.

The phase spectra from the complex FFT for each windowed waveform of Figure 4.15(b) were fit to a linear function, and these were subtracted to correct for linear phase (the first term of

Equation (4.11)). The corrected phase spectra shown in Figure 4.18(a) show the isolated Gouy phase modulation vs. distance, and the matrix columns were fit to Equation (4.17), with z_0 and z_R as fitting parameters. Figure 4.18(b) shows an example fit from the phase matrix using $\phi_G(z)$ at 0.62 THz, and Figure 4.18(c) shows the frequency-dependent Rayleigh range $z_R(f)$ extracted from each column. The lower-frequency bands dominate the broadband focusing geometry, while the higher frequency bands have relatively smaller focused lengths around $\sim 4 - 5$ mm.

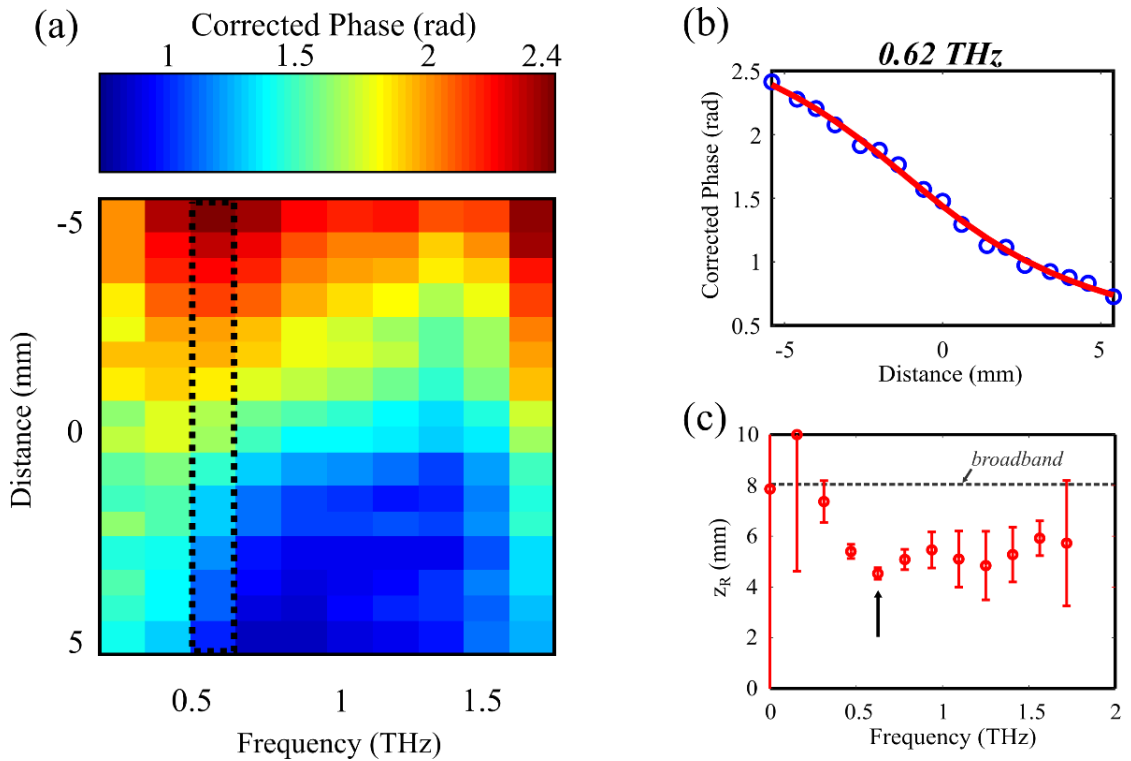


Figure 4.18. **Gouy phase modulation spectra of a focusing THz beam, and determination of the frequency-dependent Rayleigh range.** (a) Phase spectra vs. location through the THz focus ($d = 0$), corrected for linear phase propagation. (b) An example fit of $\phi_G(z)$ using the 0.62 THz column from the phase matrix (dotted square column). (c) The extracted Rayleigh range as a function of frequency, relative to the effective broadband Rayleigh range.

4.6.2 Significance of pulse phase modulation for exposure studies

Often, the THz generation and source component alignment will be optimized for either maximum pulse energy or maximum field strength. These data show that the location of the maximum beam intensity does not coincide with the locations of maximum field strength, which were significantly far from the beam waist (-2.8 mm and $+1.5$ mm, see Figure 4.16(c)). This range

is very large relative to the typical thickness of exposed samples, and these results aid in the alignment of the sample within the desired region of the focusing beam.

4.7 Conclusion

In this chapter, practical detection, measurement, and characterization methods were presented to provide a complete description of a pulsed THz beam. Following a summary of the THz source and pulse parameters to contextualize the present chapter's discussion, general properties of coherent and incoherent THz sensing principles were introduced, specifically focusing on EO sampling and pyroelectricity-based methods utilized in this project. Section 4.4 provides a guide for practical THz parameter measurement, and may be used as a reference for researchers using similar systems for comprehensive beam characterization. A Matlab GUI is available on the laboratory workstation that automates most of the calculations outlined in this chapter from raw measurements of the THz waveform, spot size, and pulse energy. Sections 4.5 and 4.6 provide results of two additional analyses, characterizing the THz pulse decomposed into individual frequency bands, and field modulation in a focusing beam geometry.

These investigations are of direct relevance for biological exposure studies. Accurate THz detection influences proper alignment of the exposure system, and measurement of THz pulse exposure parameters are necessary for accurate dosimetry. THz bandpass exposures provide the best method of investigating frequency-dependence of biological response, and the band-level characterizations of Section 4.5.1 provide direct measurement of the frequency distribution of the THz pulse in time and space for these studies. The characterization of field modulation in a focusing beam geometry provided further insight into the optimal placement of a biological sample in the focusing beam. In particular, it was found that the depth of focus for a THz beam (~8 mm) is large relative to most samples' thickness (~10 – 100 μm), and varying locations within this range correspond to significant modulations of field strength and spectral content that are important considerations in understanding variations of biological response induced by exposure to intense THz pulses.

4.8 References

- [1] J. Hebling, G. Almasi and I. Kozma, "Velocity matching by pulse front tilting for large-area THz-pulse generation," *Optics express*, vol. 10, no. 21, pp. 1161 - 1166, 2002.

- [2] K.-L. Yeh, M. Hoffmann and K. Nelson, "Generation of 10 uJ ultrashort terahertz pulses by optical rectification," *Applied Physics Letters*, vol. 90, no. 171121, pp. 1 - 3, 2007.
- [3] M. Naftaly, *Terahertz Metrology*, Boston, MA: Artech House, 2015.
- [4] R. W. Boyd, *Nonlinear Optics*, 3rd Ed., Orlando, FL: Academic Press Inc., 2008.
- [5] Y. Lee, *Principles of Terahertz Science and Technology*, New York, NY: Springer, 2009.
- [6] A. W. M. Lee, Q. Qin, S. Kumar, B. S. Williams and Q. Hu, "Real-time terahertz imaging over a standoff distance (>25 meters)," *Applied Physics Letters*, vol. 89, no. 141125, 2006.
- [7] P. L. Richards, "Bolometers for infrared and millimeter waves," *Journal of Applied Physics*, vol. 76, no. 1, 1994.
- [8] N. Karpowicz, H. Zhong, J. Xu, K.-I. Lin, J.-S. Hwang and X.-C. Zhang, "Non-destructive sub-THz CW imaging," *Proceedings of SPIE*, vol. 5727, 2005.
- [9] A. Dobroiu, M. Yamashita, Y. N. Ohshima, Y. Morita, C. Otani and K. Kawase, "Terahertz imaging system based on a backward-wave oscillator," *Applied Optics*, vol. 43, no. 30, pp. 5637 - 5646, 2004.
- [10] Spectrum/Gentec-DO, "Cross-reference product list," QC, Canada, 2014.
- [11] Gentec-EO, "Energy detectors: QE-I-USB v1.02," QC, Canada, 2011.
- [12] M. Zhang, S. -M. Zhou and T. Qu, "What Do We Mean When We Talk About Linac Isocenter?," *International Journal of Medical Physics, Clinical Engineering and Radiation Oncology*, vol. 4, pp. 233 - 242, 2015.
- [13] Electrophysics, *PV-320 Operating Manual*, Fairfield, New Jersey, 2006.
- [14] A. L. Kormos and C. M. Hanson, "Semi-opaque chopper for thermal imaging system and method". United States Patent 6034371, 7 March 2000.
- [15] S. Hahn, "Hilbert transforms," in *The Transforms and Applications Handbook*, Boca Raton, FL, CRC Press, 1996.
- [16] D. J. Griffiths, *Introduction to Electrodynamics*, Glenview, IL: Pearson Education, Inc., 2013.
- [17] G. Sharma, I. Al-Naib, H. Hafez, R. Morandotti, D. G. Cooke and T. Ozaki, "Carrier density dependence of the nonlinear absorption of intense THz radiation in GaAs," *Optics Express*, vol. 20, no. 16, pp. 18016 - 18024, 2012.
- [18] M. D. Thomson, M. Kreß, T. Löffler and H. G. Roskos, "Broadband THz emission from gas plasmas induced by femtosecond optical pulses: From fundamentals to applications," *Laser and Photonics Reviews*, vol. 1, no. 4, pp. 349 - 368, 2007.

- [19] H. Hirori, A. Doi, F. Blanchard and K. Tanaka, "Single-cycle terahertz pulses with amplitudes exceeding 1 MV/cm generated by optical rectification in LiNbO₃," *Applied Physics Letters*, vol. 98, no. 9, 2011.
- [20] "THz Bandpass Filters: 10 um - 590 um Center Wavelength," Thorlabs, 2018. [Online]. Available: <https://www.thorlabs.com/catalogpages/obsolete/2018/FB19M10.pdf>.
- [21] B. A. Munk, *Frequency Selective Surfaces: Theory and Design*, John Wiley & Sons, Inc., 2000.
- [22] A. M. Melo, A. L. Gobbi, M. H. Piazzetta and A. M. P. A. da Silva, "Cross-Shaped Terahertz Metal Mesh Filters: Historical Review and Results," *Advances in Optical Techniques*, vol. 2012, no. 530512, pp. 1 - 12, 2012.
- [23] E. Hecht, *Optics*, Reading, MA: Addison Wesley Longman, 1998.
- [24] L. G. Gouy, Translated: *On a new property of light waves*, Paris, France: Gauthier-Villars, 1890.
- [25] S. Feng and H. G. Winful, "Physical origin of the Gouy phase shift," *Optics Letters*, vol. 26, no. 8, pp. 485 - 487, 2001.

5 A system for field-enhanced terahertz pulse exposure and real-time analysis of biological samples

5.1 Introduction

In this chapter, design and implementation considerations for integrating a terahertz (THz) source into a larger system for biological exposure investigations are outlined. First, a summary and review of these systems that have been reported in the literature is presented, and a distinction between investigations utilizing continuous-wave (CW) vs. pulsed THz beams is emphasized in the context of thermal and non-thermal biological effects. Next, the design of the THz bio-exposure system constructed for this thesis project is described. This system allows for multiple source operation modes with a small table footprint, and capability of local field-enhancement in biological samples that is quantitatively characterized by finite-element simulation. Potential substrate candidates are analyzed via THz transmission measurements to determine the optimal materials for both sample growth (e.g., cell culture) and THz transmission, and an alignment procedure is outlined that defines a global reference point in space for an arbitrary substrate that ensures the beam focus, sample, and image planes are coincident in space. Finally, modifications of the bio-exposure system to facilitate normal-incidence reflection spectroscopy measurements are outlined, and performance is demonstrated with THz reflectance datasets in semiconductor materials (InGaAs and GaP). Additionally, reflection mode provides a method of quantitative field calculation at the bio-sample location, which is an important consideration to ensure that the exposed sample sees the expected THz field.

5.1.1 Terahertz systems for biological exposure studies

There are three necessary components for any general THz bio-exposure system, as shown in Figure 5.1. These are the THz source, the sample housing, and the analysis system that is dependent on the biological assays employed.

The “source” refers to any components for the generation, manipulation (i.e., steering, attenuating, filtering, etc.), and detection of THz waves, and is dependent on the chosen method for THz generation. In general, a source capable of inducing non-thermal biological effects should produce intense pulses of THz radiation with high generation efficiency and peak electric field strength. The repetition rate of the pulse train should be chosen such that THz power is maximized

while maintaining negligible levels of average steady-state temperature increase in the exposed system. The pulse spectrum should be peaked in the THz band, and ideally tunable. The chosen THz generation technique is typically the limiting factor in exploring biological effects for varying exposure parameters, as many source types efficiently produce only a limited energy profile. Table-top laser-based sources that satisfy the above criteria are the most popular technology in recent reported literature.

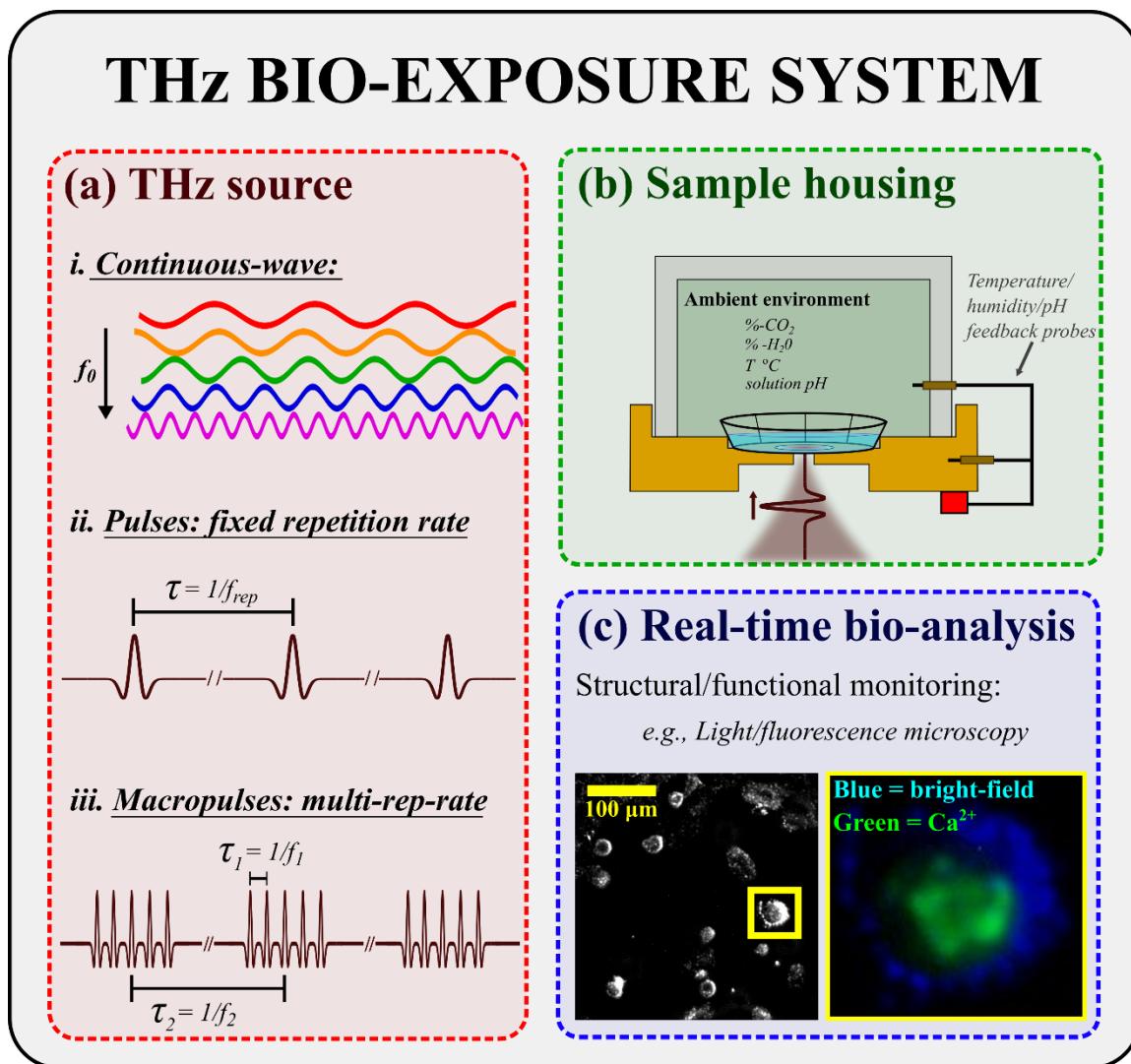


Figure 5.1. **The three components of a general system for investigations of THz-induced biological effects.** (a) Sources used for bio-exposures may be continuous-wave or pulsed. The latter may be generated with a fixed repetition rate, or in more complex series of micropulses within a larger macropulse train characterized by multiple repetition rates. (b) For the duration of THz exposure, the sample should be in an environment with temperature and humidity monitored and regulated. The pH of the sample solution should be regulated with either CO₂ or pH-regulating buffer media. (c) Real-time analysis during THz exposure is performed for observation of transient or reversible effects. Here, examples of light and fluorescence microscopy of cancer cells are shown, though these methods may vary widely by experimental context and goals.

The “sample housing” refers to any container and environment of the biological sample during THz exposure, including the growth substrate and sample chamber. The housing accommodates a variety of biological samples at multiple scales of biological organization (e.g., molecular, cellular, or tissue). Since experiments often require extended exposure times (greater than a few minutes), care is taken to ensure that important environmental parameters like temperature and humidity are regulated. When necessary, the media pH is regulated, either by maintaining ambient CO₂ concentrations at appropriate levels (typically 5% – 10% for most cell lines), or by use of pH-regulating media buffers such as HEPES. For substrates, many materials that are commonly employed in standard biological assays are not optimal for use in THz exposure studies. For example, simple borosilicate glass is one of the most commonly used materials for substrates in cell biology due to mechanical stability, support for cell growth, and transparency to relevant wavelengths used in visible light and fluorescence microscopy, or other types of radiation exposure studies (e.g., X-rays). However, glass substrates have undesirable absorption characteristics across the THz band, and so specialized substrates suitable for the THz source are a key consideration. A discussion and characterization of various substrate options is provided in Section 5.3.2.2.

The “analysis system” refers to any components that characterize the potentially transient or reversible effects induced by THz radiation in real-time during exposure. This may include standard equipment such as a light microscope, thermal imager, or systems for specific assays such as fluorescence microscopy of target fluorophores introduced into the sample, or spectroscopy systems to monitor changes in dielectric parameters during exposure. Analyses of irreversible or fixed effects that may be performed outside of exposure conditions do not influence the larger system design, and so are not considered here.

5.2 Review of existing terahertz exposure systems

While the sample housing and analysis technologies may be designed and implemented with flexibility, development of widely-tunable THz generation technologies that achieve sufficient powers is challenging. Experimentation is often limited to the THz parameter ranges of available and practical sources, and any observed effects are not necessarily generalizable outside of these ranges. Ideally, there would be a sufficient number of similar THz sources in the research community for reproducing and verifying reported observations in different cellular systems or laboratory environments, and a sufficient number of dissimilar sources to cover the relevant THz

parameter space (field, energy, peak/average intensity, spectral power density, and pulse repetition rate).

Investigation of THz-induced effects in biological systems may be performed with either continuous-wave (CW) or pulsed THz radiation beams. Pulsed sources may have a fixed repetition rate, or deliver THz energy in more complex “macropulse trains”, such as those generated by free-electron laser facilities. Here, a selection of a variety of THz sources as applied to biological exposure studies are summarized.

5.2.1 *Continuous-wave terahertz exposures*

Narrow-band CW sources are interesting for biological exposures as they are capable of approximately single-mode excitation. However, these sources often induce significant heating¹ in bio-systems at moderate power levels that must be controlled for. While it was an early hope that THz exposures were capable of precise excitation of target resonant modes in biomolecules that are critical for biological function, this is not feasible for samples in realistic physiological conditions due to the broad spectra that arise in high-temperature (37 °C), non-ordered/-oriented samples [1, 2], as well as the biological heat-shock response that obscures non-thermal effects.

The majority of CW THz exposure studies in the reported literature were performed using optically pumped far-infrared gas lasers. These utilize an external laser to optically excite the rotational modes of low pressure gasses such as methanol [3, 4, 5, 6, 7, 8] or ammonia [9] that produce THz beams with intensities $<1 \text{ W/cm}^2$. CW biological exposure experiments have also been performed, although at comparatively low intensities ($0.03 - 5.7 \text{ mW/cm}^2$), using backward wave oscillators [10], frequency-multiplied microwave waveguides [11, 12], millimetre-wave printed circuitboards [13], or gyrotrons with extended ($\sim 10 \text{ ms}$) pulse emissions [14]. While a variety of THz-induced effects were reported, such as frequency-dependent differential gene expression [5], activation of actin polymerization [14], spindle disturbances in human-hamster hybrid cells [11], or increased genomic instability in human lymphocytes [12] (in addition to various negative results), the differences in the exposure conditions and bio-samples investigated across studies limit the general conclusions that can be made.

¹ What constitutes “significant” heating depends on the biological system under study. In organisms, less than a degree change of internal temperature induces physiological stress. In many animal cell lines, an increase of a few degrees is required to activate a heat shock response. Isolated proteins in solution may withstand even greater temperature increases ($>10^\circ\text{C}$) before denaturing.

5.2.2 Pulsed terahertz exposures

5.2.2.1 Fixed pulse repetition rate

THz bio-exposure systems that utilize pulsed, often single-cycle, THz sources are implemented to induce only minimal (biologically negligible) heating, and effects observed may be attributed to non-thermal mechanisms. Further, the temporal localization of pulsed sources correspond to broad power spectra, and so a wider range of oscillatory dynamics may be excited in bio-systems of interest. The majority of pulsed THz bio-exposure studies in the reported literature were performed with laser-based THz generation technologies, as high powers achievable from commercial laser amplifier systems offset the low conversion efficiencies in THz-generating media. As a result, intense THz pulses with sufficiently high pulse energies and peak electric fields may be generated with practical table-top laboratory technologies. Laser-based pulse generation methods in the literature include optical rectification in inorganic crystals (e.g., ZnTe, LiNbO₃, GaP) [15, 16, 17, 18, 19] or organic crystals (e.g., DAST, OH1) [20], laser-induced ionization in gas plasmas [7, 21, 22], or laser-activated photoconductive antennae [22, 23, 24].

Laser-induced plasma ionization sources are capable of generating pulses with very broad spectra (~30 THz) peaked at high frequencies (~10 THz) [7, 21]. While the field strength, energy, and intensity of these pulses may reach significant levels above what has been seen to induce significant biological effect, the low spectral density is also an important consideration, as the biological effect is thought to depend significantly on frequency. The relatively high frequencies associated with these technologies couple correspondingly fast biological dynamics, but the low power at low THz frequencies may be insufficient to drive the slower, large-scale global oscillatory dynamics that may play important regulatory roles. Therefore, pulsed THz sources with increased spectral density at lower frequencies, such as optical rectification in inorganic or organic crystals, occupy complementary ranges of the THz parameter space.

Optical rectification in nonlinear (i.e., $\chi^{(2)} \neq 0$) media is another laser-based method of intense THz pulse generation (as described in Chapter 4), in which the asymmetric dielectric response induces a static polarization in the crystal that is proportional to the envelope of the input laser pulse. The time-varying polarization results in the emission of a single-cycle, picosecond-duration, THz pulse that is proportional to the second derivative of the incident laser pulse envelope [25]. Organic crystals (e.g., DAST, OH1) are capable of generating high pulse energies and peak electric fields (>10 μJ , >1 MV/cm) at intermediate frequencies (~1 – 10 THz), but are limited to relatively low repetitions of the input pump laser (~1 – 100 Hz) to satisfy stringent damage thresholds. In

contrast, inorganic crystals (e.g., LiNbO₃, ZnTe, GaP) are also capable of generating high peak fields and energies (>1 μ J, >100 kV/cm) in lower THz bands (\sim 0.1 – 2 THz), and may additionally be pumped at much higher repetition rates (\sim MHz). In general, it is preferable to maximize THz power to the bio-system while maintaining biologically negligible heating. Previous investigations have empirically found that for these sources, pulse repetition rates of about \sim 1 kHz provide high peak powers (\sim MW/cm²) to propagate in high-attenuation biological media, but low average powers (\sim mW/cm²) to minimize heating. Titova et al. showed that intense THz pulses generated by tilted-pulse-front optical rectification in LiNbO₃ at 1 kHz repetition rate are capable of activating signaling cascades and protein expression of the DNA damage response and dysregulation of epidermal differentiation pathways in human skin, and this effect was largely distinct from similar exposure at UVA frequencies [17]. The latter effect has been corroborated by our previous investigations [15]. Using a similar source with comparable THz fields and energies, Cheon et al. have observed genome-wide demethylation in lung cancer cells [19].

5.2.2.2 *Multiple pulse repetition rates: Macro-pulse trains*

Another popular type of source for pulsed THz bio-exposures are macropulse trains, characterized by multiple repetition rates and associated power levels for each rate level: A slow pump rate for the burst of energy (the macropulse) that is comprised of closely-spaced micropulses at a second fast repetition rate, as in Figure 5.1(a). THz beams of intense macropulse trains may be generated by THz free electron lasers (FELs), and are commonly found at large research facilities such as the Compact FEL at ENEA-Frascati [26, 27, 28, 29], the NovoFEL at Novosibirsk [30, 31], or the FIR-FEL at Osaka University [32, 33].

The THz-BRIDGE collaboration reported several investigations using the Compact FEL at ENEA-Frascati [26]. This source outputs a macropulse at a slow rep-rate of 2 Hz, and these are comprised of 50 ps THz micropulses centered at 0.12 THz at a fast rep-rate of 3 GHz. The power within a 4 μ s macropulse is 1.5 kW. These investigations reported significant induction of micronuclei (MN) in whole blood. Utilizing this THz source, Amicis et al. have investigated a wide variety of genotoxicity assays in human fibroblasts, and have reproduced the observation of increased MN frequency in human fibroblasts [28]. This indicates severe genotoxic stress at the chromosome level, corroborating the similar observations of genotoxic stress at the DNA level made by Titova et al. [17] and Cheon et al. [19]. However, Zeni et al. have used this FEL source to conduct a pilot study of the cytogenetic effects in human blood leukocytes, but found no significant induction of DNA or chromosome damage, or change to proliferation [27].

The NovoFEL has been used for bio-exposures to investigate GFP (green fluorescent protein) expression in *E. coli*, and genotoxic effects in human fibroblasts [30, 31]. This source outputs a CW 2.3 THz burst that is intermittently blocked by a manually-controlled two-disk shutter to form the macropulse train. The averaged power intensity is 0.5 W and the peak power is 15 kW. These investigations observed altered GFP expression levels in *E. coli* cells, but found no change to the DNA damage response or gene expression in human embryonic stem cells, although these latter studies utilized a raster-scanned THz beam that reduces the total dose seen by the sample.

Frequency-dependent investigations using the FIR-FEL at Osaka University have investigated molecular level effects of THz macropulse trains on amyloid fibrils with varying centre frequencies from 3.1 THz to 5 THz [32]. These studies observed structural changes and dissociation of the β -sheet in the fibril, while the opposite effect was observed in thermal controls. Further, using this source, Yamazaki et al. observed dramatic structural change to polymerized actin filaments in cells, and this effect was attributed to a THz-induced shockwave in the liquid medium [33]. This is particularly interesting, as it introduces a wholly new interaction mechanism for THz-induced biological change separate from coupling to natural oscillatory dynamics.

5.3 System design and characterization

The THz source to be integrated into a bio-exposure system is shown schematically in Figure 5.2. The collimated THz beam emitted from the LN generation crystal is first expanded and re-collimated with two gold off-axis parabolic mirrors (OAPMs, effective focal lengths 15 mm and 101.6 mm for a total magnification factor of 6.8).

The filtered, expanded, collimated THz beam is then directed towards a 3" (76.2 mm) OAPM that is mounted to a programmable rotation stage (Thorlabs PRM1Z8), indicated by the green box in Figure 5.2. The THz focus may then be directed in a 360° annular ring about the y -axis for varying experimental configurations, as shown in Figure 5.3, which shows the beams-eye-view (BEV) from the perspective of the expanded collimated region of the THz source.

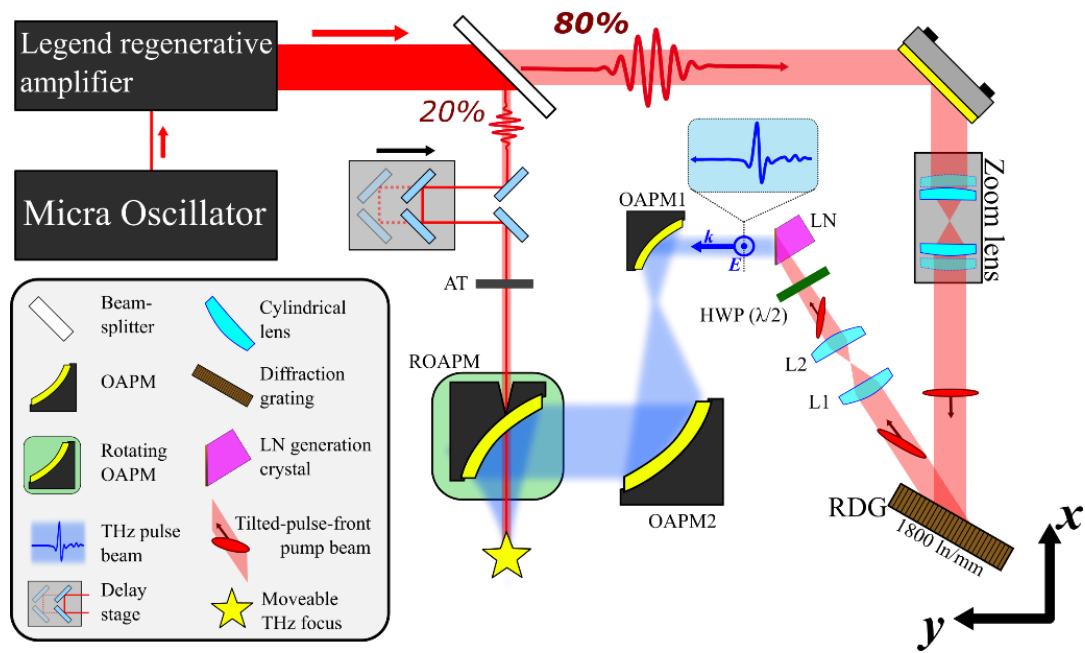


Figure 5.2. **Schematic representation of intense THz pulse generation for exposure of biological systems.** (a) A reflective diffraction grating (RDG) establishes a tilted-pulse-front geometry in the pump laser pulse that is imaged with a 4f-lens configuration to the output face of a LiNbO₃ (LN) crystal with a 63° cut face. The collimated THz beam is expanded and refocused with off-axis parabolic mirrors (OAPMs). A fraction of pump energy (~20%) is aligned coincident with the focusing THz beam, with tunable power via a pulse attenuator (AT), for electro-optic sampling of the THz pulse as described in Section 4.3.1.1. The rotating OAPM provides a THz focus that moves in a 3" (76.2 mm) annulus about the *y*-axis, enabling multiple operational modes (see Figure 5.3)

Currently, there are four modes of operation dependent on the orientation of the rotating OAPM:

1. 0° orientation (upwards) is for through-substrate exposure studies of bio-samples grown in aqueous media, such as monolayer cell cultures, or for THz-reflection spectroscopy of biological samples as described in Section 5.5. This operation mode has environmental regulatory control as described in Section 5.3.2, and real-time analysis of biological systems via light and fluorescence microscopy. The imaging system has an imaging plane coincident with both the sample plane and the THz beam waist, and the use of long-working-distance (LWD) objectives provide ample space for a variety of sample types, as well as field-enhancement with conductive tips (Section 5.3.1).
2. 90° orientation (left) is for electro-optic (EO) sampling of the THz waveform as described in Chapter 4. The sampling beam is focused through a 1 mm hole in the ROAPM, and propagated colinearly with the THz beam for EO sampling in gallium phosphide. The THz pulse, associated power spectrum, and focused spot image are shown under optimal conditions at left of Figure 5.3.

3. 180° orientation (down) is for top-down exposure studies of bio-samples exposed to air, such as tissue samples that are media-fed from below (e.g., organisms or 3D tissue models).
4. 270° orientation (right) is for laser-assisted bio-exposure studies, pump-probe experiments using the tunable EO sampling line, or characterization of THz-induced effects via UV fluorescence spectroscopy (data not shown).

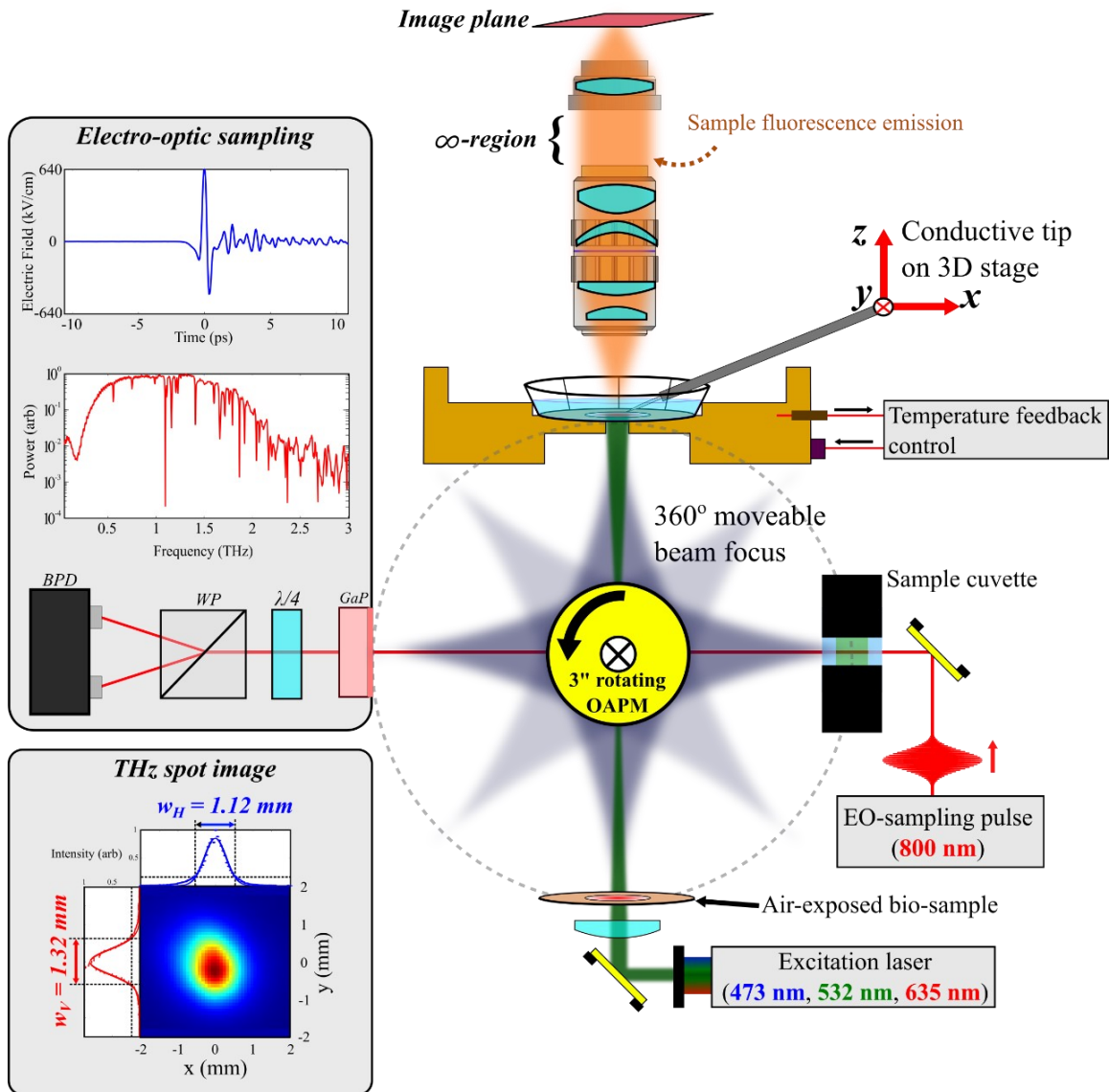


Figure 5.3. **The Beam's Eye View (BEV) of the THz bio-exposure system following THz generation in LN.** The THz pulse is incident on the programmable rotating 3" (76.2 mm) OAPM at the location indicated by \otimes . The mirror orientation adjusts the direction of the focused THz beam to operate the various system modes for different bio-exposure studies or for THz waveform detection via electro-optic sampling (left). Details on the various operation modes are provided in the main text.

5.3.1 *Field enhancement with sharp metallic tips*

The use of long-working distance objectives with the analysis microscope allows sufficient space to mount a sharp conductive tip into the THz beam path while still preserving the real-time light and fluorescence microscopy analysis capabilities, as shown in the upwards orientation of Figure 5.3. The tip provides dramatic field-enhancement due to field-induced plasma oscillations that may be localized to a region of the tip apex much smaller than is possible with free-space focusing, as discussed in the following sections [34]. In this configuration, the tip is mounted to a 3D linear translation stage by a custom holder, and positioned such that the tip apex is coincident with both the THz beam focus and the microscope imaging plane, and the tip shaft is aligned parallel to the THz field direction.

5.3.1.1 *Electrochemical etching of conductive tips*

Conductive tungsten tips for THz field enhancement are electrochemically etched, as outlined in [35]. The clean, unsharpened tungsten wire is lightly submerged ~ 2 mm in a 2M NaOH solution and centred inside a conductive wire loop. A DC voltage of 4.6 V is established between the loop and tip, and the current is monitored via a custom LabVIEW VI. As the electrolysis process erodes the wire end into a sharpened tip, the DC current falls roughly linearly. A sharp decrease in current is observed when etching is complete. Sharpened tips are removed, washed in hot (90°C) water, and inspected manually under a microscope to verify the sharpening procedure.

5.3.1.2 *Simulations of terahertz field enhancement with conductive tips in water*

Finite-element method time-domain COMSOL simulations were performed to characterize the expected field enhancement that is possible in this experimental configuration, as shown in Figure 5.4(a) and (b). The simulation geometry consists of a 2 mm long tapered tungsten wire with a shaft diameter of 0.25 mm, full taper cone angle of 32° , and apex radius of curvature of 100 nm, resting above the sample at a $1 \mu\text{m}$ separation distance, d . The tip shaft axis is inclined at an angle of 18° relative to the substrate surface. To simulate a free-space THz pulse propagating from the port window to the tip, the Wave-Optics module [36] is implemented to first solve the wave equation for the electromagnetic field components in the time domain. Material constants, such as the conductivity and relative permittivity, are appropriately set for the conducting tungsten tip, water, and the dielectric polystyrene [37] at room temperature. The geometry is meshed with sizes of order $100 \mu\text{m}$ for the far-field regions, while the gap region mesh size (Figure 5.4(a), inset) is of order 10

nm, thus making a mesh size composition ranging up to 4 orders of magnitude. The mesh is designed strategically such that mesh sizes around the tip apex are a fraction of the $d=1\ \mu\text{m}$ tip-substrate distance ($d/20 \sim 50\ \text{nm}$), and the outer domain mesh sizes are a fraction of the THz wavelength corresponding to spectrum peaked at 0.5 THz ($\lambda_{\text{THz}}/5 \sim 120\ \mu\text{m}$). Numerical stability was verified by using finer mesh sizes and smaller time-steps, for which results do not differ from the original settings.

The results from these simulations show a maximum field enhancement factor of 35 at the sample location, and the longitudinal FWHM of the enhancement profile is $0.4\ \mu\text{m}$. For context, the typical diameter of human cells is in the range of $10 - 100\ \mu\text{m}$, and so the tip apex must be in very close proximity to the sample for it to see the enhanced THz field. Figure 5.4(d) show a photograph and diagram (inset) of the tip mounted in a cellular sample aligned with the THz field direction.

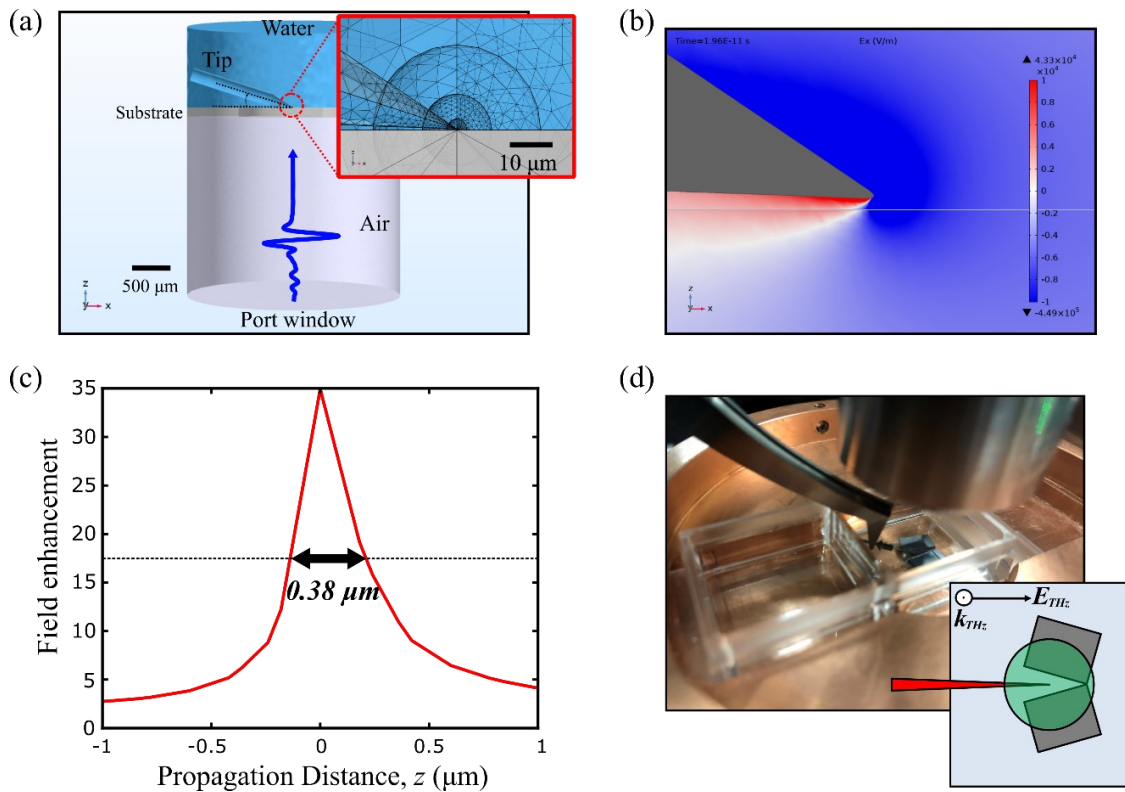


Figure 5.4. Simulations of THz near-field enhancement in water with a sharp conductive tip. (a) The COMSOL geometry for tip-enhanced THz exposures, which consists of a free tip immersed in water, a polystyrene ($-\text{C}_8\text{H}_8-$) substrate, and port window located directly below the components. *Inset*: A zoomed image of the meshed tip apex region. (b) The horizontal (x) electric field component around the tip apex region at the time where the field peaks. (c) The field enhancement as a function of THz propagation distance through the tip apex at $z=0\ \text{mm}$. The peak field enhancement is 35 with a FWHM of $0.38\ \mu\text{m}$. (d) A photo of the tip placed at the sample location. Silicon wedges are used to make a sample channel into which the tip is placed aligned with the THz field direction, as shown in the inset.

5.3.2 *Sample housing*

5.3.2.1 *Sample holder*

THz bio-exposures often require extended exposure times, from several minutes to tens of hours [12, 16, 21], during which time the bio-sample may be outside of the regulated environment of the storage incubator. While it is possible to put control samples through identical environmental agitation, complex biological processes may still deviate from expected variation. For example, the difference between treated and control samples at room temperature may not be the same as the difference between treated and control samples at physiological temperatures (37°C), even though environments were controlled for. Some exposure systems direct the THz beam into an environment-regulating incubator [8, 38]. While this is ideal to ensure minimal environmental agitation, it may not be practical for many laboratory configurations with commercial incubators. Instead, we have designed a sample holder that may monitor and tune the relevant environmental parameters, such as temperature and solution pH, that are typically incubator-regulated.

The sample holder is a thick copper dish, seen in the photo of Figure 5.4(d), fitted with a bracket for mounting to a 3D linear translation stage for precise sample positioning. Notched cut-outs accommodate culture dishes, wells, or slides centered over a 5 mm hole through which the THz beam is focused through the culture substrate from the rotating OAPM. Temperature regulation is performed via a feedback circuit to a resistor in thermal contact with the sample dish. Two probes on opposite sides of the holder monitor the temperature to ensure thermal uniformity. If the temperature readout falls below the set point, a current is delivered to the resistor until the desired temperature is reached.

Bio-incubators additionally regulate the pH of the sample media by maintaining a set ambient concentration of CO₂, typically 5 – 10 %. In this system, this function is replaced by use of standard pH-regulating media buffers, such as HEPES, while samples are outside of the incubator environment [39].

5.3.2.2 *Substrate transmission measurements*

A suitable substrate for THz bio-exposure studies must satisfy three criteria: (1) Supportive of cellular growth and adherence, (2) Transmissive to visible wavelengths for standard microscopy or fluorescence characterization, and (3) Transmissive to THz frequencies, with minimal dispersion. The latter is particularly important, as many standard substrates used in biological studies (such as

borosilicate glass) have poor transmission and large index changes across the relevant THz frequencies.

Table 5.1 shows the peak field and energy transmission ratios through potential substrate candidates, including a standard glass slide, fused quartz and silica wafers (readily available in-lab), and proprietary optical plastic wells (Cat. 80286) and low-walled grid dishes (Cat. 80156) from the Ibidi company. From these data, the optimal transmission properties are best satisfied by the proprietary optical plastic material from the Ibidi company.

Table 5.1. **Peak field and energy transmission ratios for potential substrate candidates**

Substrate	Energy transmission	Peak field transmission
1.00 mm glass slide	0.19	0.38
0.17 mm fused quartz	0.78	0.86
0.16 mm fused silica	0.77	0.86
0.18 mm Ibidi μ slide	0.92	0.96
0.18 mm Ibidi Grid500 dish	0.89	0.94

Figure 5.5 shows the results of in-air transmission spectroscopy measurements for the five substrates in Table 5.1. The bio-exposure system is operated with the ROAPM at 90° for EO sampling (left in Figure 5.3), shown schematically in Figure 5.5(a). A THz pulse is transmitted through the test substrate, and the spectrum is computed and compared to the reference spectrum, as in the fused quartz example in Figure 5.5(b). The transmission spectrum is then calculated as the ratio of the sample to reference spectra. Ideally, a substrate that is visibly transparent and supportive of cell growth would have a flat THz transmission profile close to unity.

Figure 5.5(c) shows a comparison of the measured transmission for fused quartz relative to simulation (see Chapter 6), and Figure 5.5(d) shows a comparison of all transmission measurements. A 1 mm glass slide often used for exposure experiments is unsuitable for through-substrate THz exposure, due to large absorption, particularly at high frequencies. All thin substrates correspond to periodic oscillations in frequency space, indicating that a THz pulse reflection was contained within the analysis window at time $t = 2d/c$, where d is the substrate thickness. This is to be expected, as the limitations of gating the main signal to reject this reflection results in inadequate frequency resolution in the transmission spectra. However, the reduced amplitude of these oscillations for the Ibidi substrates indicate the amplitude of the reflection is reduced relative to the quartz and silica wafers, and thus has an index closer to that of air. From simulation, a material of thickness $d=0.195$ mm and index $n=1.5$ reproduces the measured transmission spectra,

It is important to note that these transmission measurements were performed in air. In realistic exposure scenarios, the incident THz pulses see a liquid medium following penetration through the substrate and interaction with the adherent bio-sample that may have complex dielectric or conductive properties. Theoretically, this significantly alters the THz field and energy deposition dynamics in the substrate and sample regions in complex ways, and therefore these measurements should be interpreted in this context. A method of simulating per pulse THz interactions in common bio-exposure geometries and materials, accounting for loss, dispersion, and internal reflection interference in these environments, is discussed in Chapter 6 to aid in accurate THz dose calculations.

5.3.3 Other sources used for biological exposure studies

Some biological exposure studies reported in this thesis were performed while the bio-exposure system described in this chapter was being designed and constructed. Therefore, during this time, a different source of intense THz pulses available in the laboratory was used for the tissue exposures in Chapter 7, and some microtubule exposures in Chapter 9. The generation technique of both sources are equivalent (optical rectification in lithium niobate of tilted-pulse-front infrared laser pulses), and utilize the same oscillator and amplifier systems for the pump and sampling beams. The intense THz pulses produced by both sources are similar, and measured waveforms and pulse parameters for all exposure studies are reported in the individual relevant sections.

5.4 Alignment procedure for sample exposures

For exposure and real-time fluorescence analysis, the various components of the THz bio-exposure system must all be aligned for each experiment that uses a new substrate, as variable thickness substrates will not coincide with a previously aligned configuration. Accurate alignment maximizes the likelihood of achieving sufficient pulse energy and field strength to induce significant biological effect, and additionally ensures that the sample under study sees the characterized pulse determined dosimetrically as closely as possible. In particular, the THz focus, sample plane, and microscope object plane must all be set coincident in space. For tip-enhanced exposures, the tip must be positioned with the apex at the THz focus and the shaft parallel to the field direction, with minimal obscuration of the microscope image FOV.

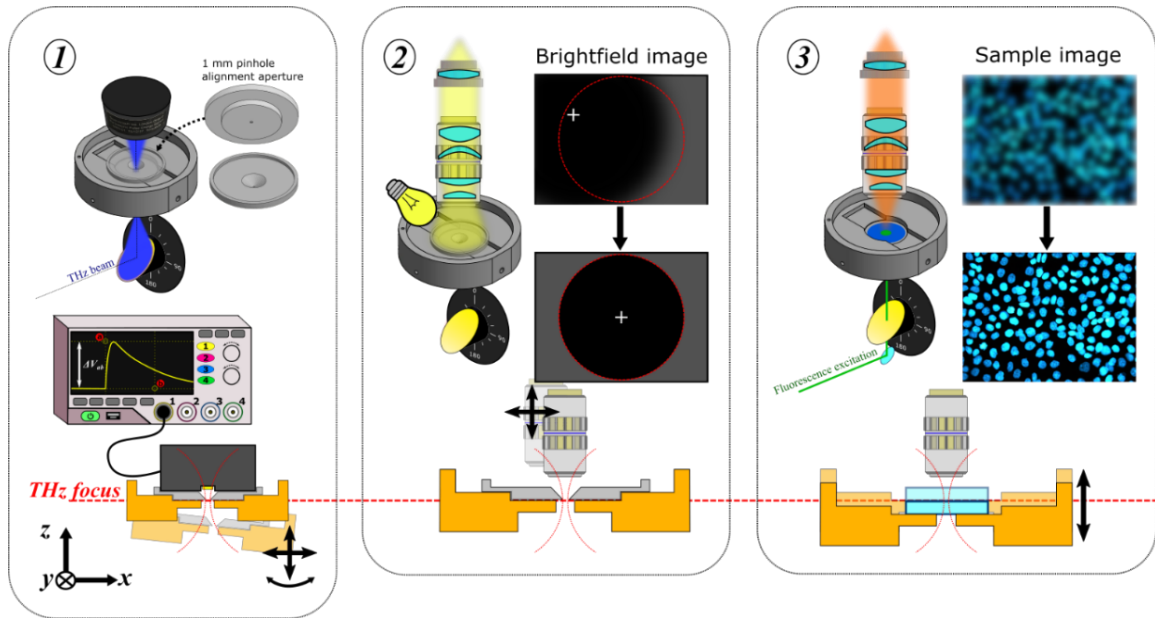


Figure 5.6. **Alignment procedure for THz exposure and real-time analysis.** The horizontal red dashed line indicates the focus of the THz beam. (1) The dish is levelled, and the THz beam focus is located by translating the holder/detector and maximizing pulse energy through a 1 mm pinhole aperture centred over the beam input window. (2) The microscope is centred (x-y) and longitudinally (z) aligned to the THz focus by bringing the alignment aperture used for THz energy measurements into focus in the FOV. (3) The sample plane for a given substrate is aligned to the THz focus by longitudinally (z) translating the sample holder until a test sample is in focus.

To satisfy these conditions, the following alignment procedure is employed, as outlined schematically in Figure 5.6. For the steps relying on microscope images, a 5x objective (Mitutoyo, 378-802-6) and 2x tube lens (Edmund Optics, MT-2, 56-863) provide a reasonably large field-of-view (FOV) with sufficient precision to finely position translation stages.

1. Aligning the THz focus to the sample holder

An alignment tool (the 1 mm pinhole alignment aperture shown in Figure 5.6) was designed to fit in the sample holder such that a 1 mm pinhole aperture is centred over the THz transmission window. Using a pyroelectric detector (Sciencetech Inc., 6925-01) centred above the pinhole, and ensuring the sample holder is level, the THz pulse energy is maximized by 3D-translation of the sample holder to locate the longitudinal focus region.

2. Aligning the imaging plane to the THz focus

Next, the detector is removed, and the microscope is translated such that the 1 mm pinhole of the alignment aperture is brought into the brightfield focus. This centres the imaging FOV over the 2D THz spot, and longitudinally aligns the imaging plane to the THz focus plane.

3. Aligning the sample plane to the imaging plane and THz focus

As various substrates have different thicknesses, the sample plane may shift relative to the housing, and must be aligned separately. To ensure that a loaded sample is coincident with the THz focus and imaging plane, a sham sample using the relevant substrate is loaded into the sample housing, and the sample holder is translated longitudinally (not transversely!) until the substrate surface is in focus. This ensures the THz focus, imaging plane, and sample plane are aligned and centered.

4. Aligning the tip (for local tip-enhanced exposure scenarios only)

If local field-enhancement with a sharp conductive tip is desired, the tip apex must be coincident with the THz focus, and the tip shaft must be aligned parallel to the THz field direction. The tip is loaded into a custom tip holder mounted to a 3D translation stage. The shaft is aligned to the THz field direction, and the tip apex is centred and focused to the microscope image plane to ensure it is coincident with the THz focus. COMSOL simulations predict that for an optimally-aligned incident THz peak field of 640 kV/cm, the maximum enhanced field in water is 22.5 MV/cm in a localized region about the tip apex, with an enhancement FWHM of $\sim 0.4 \mu\text{m}$ (from the profile in Figure 5.7).

5.5 Normal-incidence terahertz reflection spectroscopy

In addition to bio-exposure experiments, the THz exposure system in Figure 5.3 may also be used for normal-incidence reflection spectroscopy analysis with relatively simple modifications. Reflection spectroscopy operation mode may be used for explicit characterizations of the quantitative dielectric THz spectra of biological samples and substrate materials, or to monitor the change to the reflected THz waveform for the duration of a bio-exposure. These characterizations over extended exposures may be utilized to provide additional understanding of the structural or functional changes that may occur during exposure within the system under study.

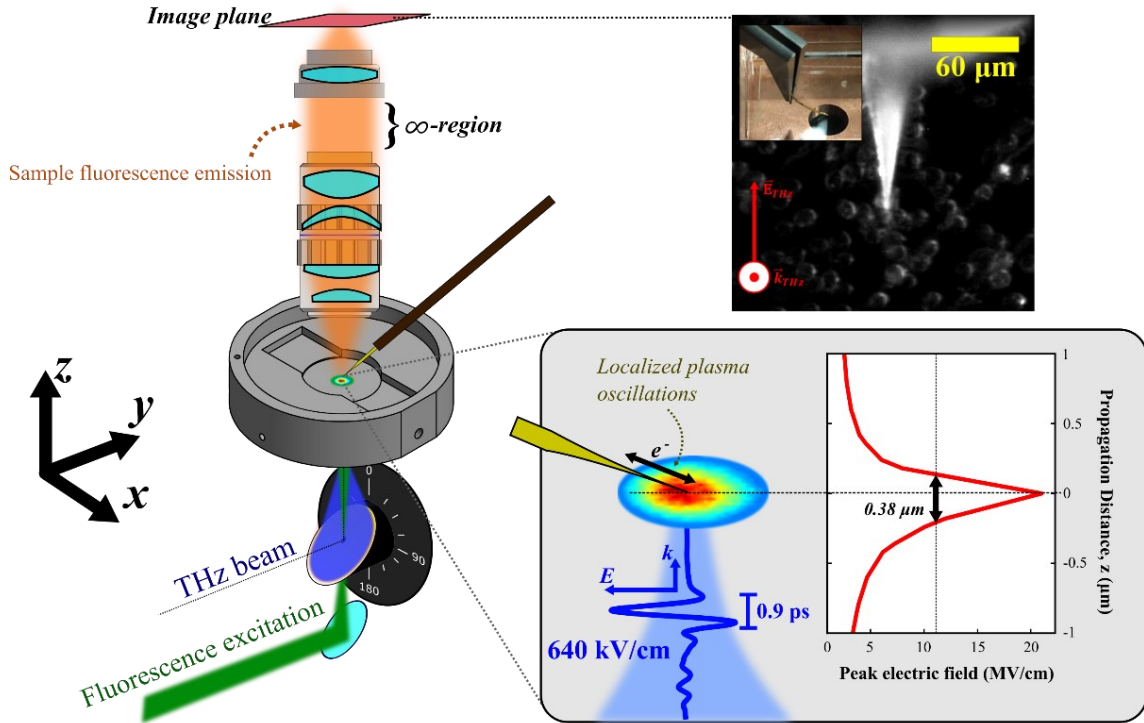


Figure 5.7. **Schematic for real-time analysis of tip-enhanced THz exposure.** Fluorescence microscopy of propidium iodide-labelled adherent cell cultures with long-working-distance, infinity-corrected objectives (optics schematic adapted from [40]) allows real-time characterization of biological effects and provides sufficient space for placement of a sharp conductive tip for local field enhancement in target regions. The fluorescence excitation line is focused through a 1 mm hole in the rotating OAPM and propagates colinearly with the focusing THz beam to illuminate the sample plane at the THz beam waist. The tip is estimated to locally enhance the 640 kV/cm incident field to a maximum of ~ 22.5 MV/cm in a ~ 0.4 μm (FWHM) region near the tip apex. A bright-field microscope image of the tip placed in a monolayer cell sample is shown at top-right. The THz pulse propagates out of the page, and the tip shaft is aligned parallel with the THz field direction.

A 4" (102 mm) diameter fused quartz plate ($n=1.96$, 2 mm thickness) was mounted in the collimated section at a 45° angle to the incident THz Poynting vector, forming a THz beamsplitter (BS2 in Figure 5.8(a)) that transmits $\sim 80\%$ of the THz energy to the sample at normal incidence. The rotating OAPM is set to 0° (upwards in Figure 5.3) such that the THz beam is focused and is retro-reflected from the sample back to the beamsplitter and re-focused with a gold OAPM to the EO sampling module, along with a re-directed sampling beamline (BS1). Reference scans are acquired with a gold mirror (assumed to be a perfect THz reflector) placed face-down at the sample location, which is replaced with a sample of interest for analysis scans.

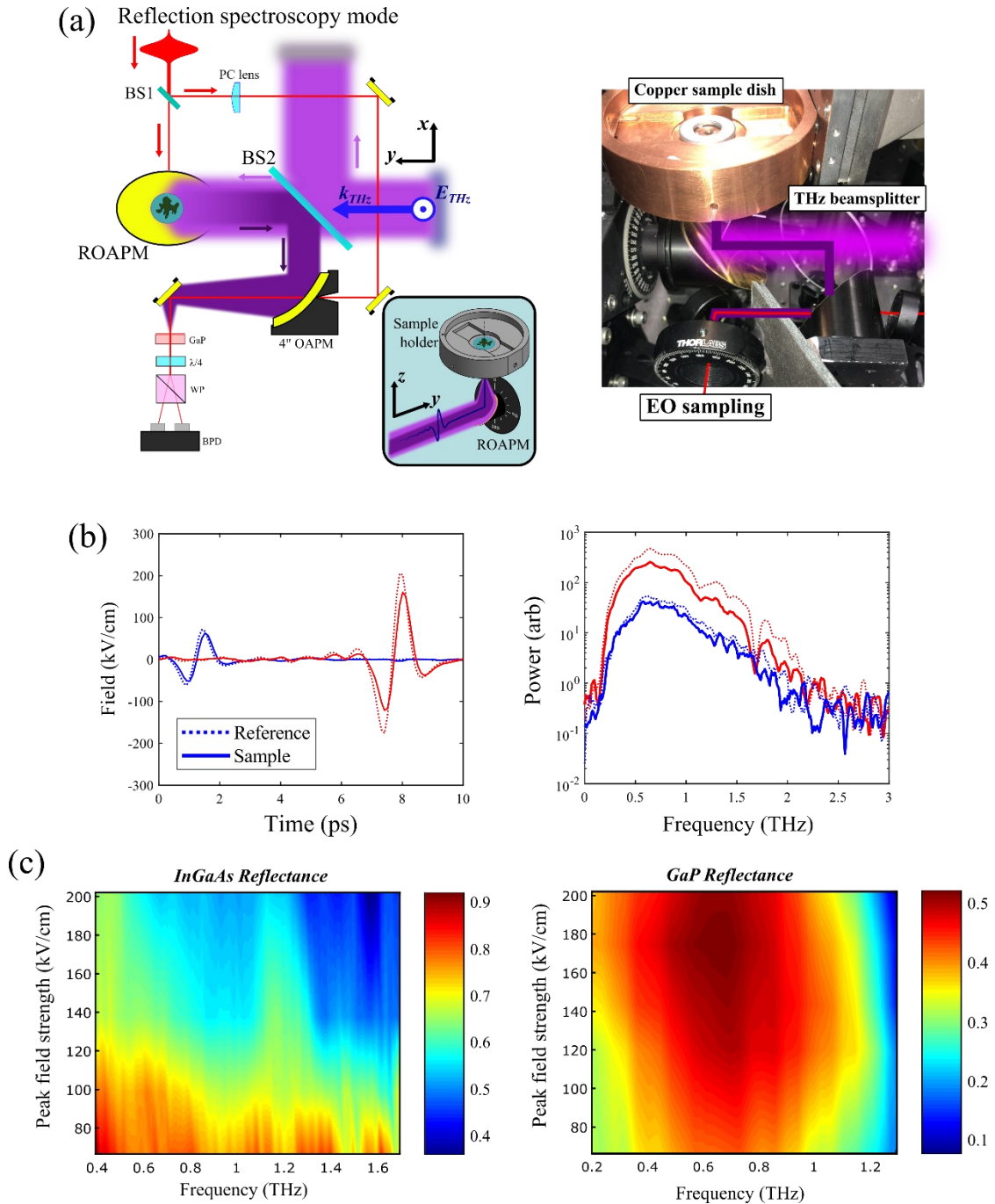


Figure 5.8. **Operation of the THz source for normal-incidence reflection spectroscopy.** (a) Schematic and photo of the modified THz source for normal-incidence THz reflection spectroscopy and field measurement at the sample location. The fused quartz beam splitter (BS2) is attached to the 4" (102 mm) OAPM and aligned as a single removable unit. Reference or sample materials are placed at the sample location and waveforms are acquired with a re-directed EO sampling line (beam splitter BS1). (b) Example waveform and power spectra for two different field strengths (blue and red) for time-domain THz reflection spectroscopy of an InGaAs crystal wafer. Pulses are offset in time due to varying thicknesses of Si wafers used for attenuating the THz beam. (c) The reflectance spectra of InGaAs (left) and GaP (right) for four THz pulses of varying field strength, with linear interpolation applied. Differential reflectance with incident field strength is a result of nonlinear material responses that are modulated by the THz field itself.

As an example, reflected waveforms and corresponding power spectra were acquired for InGaAs and GaP crystals (the low and high field scans for InGaAs are shown in Figure 5.8(b)). A total of four scans were acquired for varying degrees of THz attenuation, and the power reflectance spectra (ratio of sample to reference power spectra) for varying incident THz field strengths is determined as shown in Figure 5.8(c). These reflectance measurements show indications of nonlinear effects, due to the differential reflectance properties for varying THz field strength. In the InGaAs reflectance spectra, there is an enhanced reflection at high fields near 1.2 THz. In GaP, the reflectance spectra sees a broad maximum at high fields in the 0.7 THz band. These examples for InGaAs and GaP show simple power spectra ratios, however the complete time-domain information allows any level of sophistication in time-domain spectroscopy that may be applied in dedicated spectroscopy analysis systems, such as quantitative permittivity or conductivity determination, as reviewed in [41].

5.5.1 Quantitative calculation of field strength at the sample location

Operating the THz source for normal incidence reflection spectroscopy (Figure 5.8(a)) enables quantitative measurement of the THz pulse waveform and field strength at the actual sample location. This allows verification of the field measurements performed when the rotating OAPM is positioned for EO sampling (left, 90° in Figure 5.3), at the location that is physically occupied by the sample under study.

To determine the field at the sample location with the THz exposure system in reflection mode, a gold mirror (assumed a perfect THz reflector) is placed in the sample holder at the THz focus and a waveform is electro-optically sampled. Recall from Chapter 4, the THz field strength may be calculated directly from the measured EO signal (I_{EO}) in $L=200\ \mu\text{m}$ GaP ($n_0=3.18$, $r_{41}=0.88\ \text{pm/V}$, $t_{GaP}=0.46$) as

$$E_{THZ} = \arcsin(I_{EO}) \cdot \frac{\lambda}{2\pi L n_0^3 r_{41} t_{GaP}} \quad (5.1)$$

where $\lambda=800\ \text{nm}$ is the sampling pulse central wavelength.

Quantitative determination of the THz field from Equation (5.1) is modified to account for the losses introduced by the 45° fused quartz beamsplitter (BS2) according to Snell's law [42]

$$n_1 \sin \theta_1 = n_2 \sin \theta_2 \quad (5.2)$$

where n_k/θ_k is the index/angle for the ray in the k^{th} material, and the Fresnel equations for s-polarized waves are

$$r_s = \frac{n_1 \cos \theta_i - n_2 \cos \theta_t}{n_1 \cos \theta_i + n_2 \cos \theta_t}$$

$$t_s = \frac{2n_1 \cos \theta_i}{n_1 \cos \theta_i + n_2 \cos \theta_t} \quad (5.3)$$

where r_s and t_s are the amplitude reflection and transmission coefficients for the s-polarized THz beams with incident/transmitted angle θ_i/θ_t .

The THz pulse accumulates Fresnel reflection and transmission coefficients as it propagates through the BS, from the sample, and back to the EO sampling crystal as indicated by the light and dark purple beam paths in Figure 5.8(a). Using Equations (5.2) and (5.3), the refractive indices of air ($n_1=1$) and fused quartz ($n_2=1.96$), and neglecting absorption in the BS, the incident THz field is calculated to be modulated by [43]:

1. Transmission through BS2 face 1 (air to quartz) at $\theta_i = 45^\circ$

$$t_{s,1} = 0.68$$

2. Transmission through BS2 face 2 (quartz to air) at $\theta_i = 21.1^\circ$

$$t_{s,2} = 1.44$$

3. Reflection from BS2 face 2 (air to quartz) at $\theta_i = 45^\circ$

$$r_{s,1} = -0.44.$$

Thus, the THz pulse seen at the EO crystal is modulated by a total factor of $t_{s,1}t_{s,2}r_{s,1} = -0.43$ relative to a direct EO signal measurement with no BS. Therefore, a peak field calculated by Equation (5.1) with the EO signal in this configuration may be scaled by an absolute factor of $1/0.43=2.33$ to quantitatively determine the incident THz field strength that is physically seen by the sample under study.

5.6 Conclusion

In this chapter, considerations for the integration of a source of intense THz pulses with suitable sample housing and real-time analysis capabilities was presented. A review of existing THz bio-exposure systems was discussed, and various experiments using continuous-wave and pulsed generation technologies were outlined. The design of a new THz bio-exposure system in the Ultrafast Nanotools laboratory at the University of Alberta was detailed. A key innovation of this design is the rotating focusing mirror, allowing 360° control over the direction of the THz focus, and wide versatility for THz exposure operation with a relatively small table footprint. The operation modes currently in use were outlined, including through-substrate bio-exposures, direct in-air bio-exposures, and electro-optic sampling and energy detection of the THz beam. In the following chapters, dosimetry considerations and results of bio-exposure studies will be presented and analyzed.

5.7 References

- [1] A. Markelz and Z. Taylor, "The 2017 terahertz science and technology roadmap - Biological applications of THz technology," *Journal of Physics D: Applied Physics*, vol. 50, 2017.
- [2] G. Acbas, K. Niessen, E. Snell and A. Markelz, "Optical measurements of long-range protein vibrations," *Nature Communications*, vol. 5, no. 3076, pp. 1 - 7, 2014.
- [3] I. Echchgadda, J. E. Grundt, C. Z. Cerna, C. C. Roth, J. A. Payne, B. L. Ibey and G. J. Wilmink, "Terahertz Radiation: A Non-contact Tool for Selective Stimulation of Biological Responses in Human Cells," *IEEE Transactions on Terahertz Science and Technology*, vol. 6, no. 1, pp. 54 - 68, 2016.
- [4] G. J. Wilmink, B. D. Rivest, C. C. Roth, B. L. Ibey, J. A. Payne, L. X. Cundin, J. E. Grundt, X. Peralta, D. G. Mixon and W. P. Roach, "In Vitro Investigation of the Biological Effects Associated With Human Dermal Fibroblasts Exposed to 2.52 THz Radiation," *Lasers in Surgery and Medicine*, vol. 43, no. 2, pp. 152 - 163, 2011.
- [5] I. Echchgadda, C. Cerna, M. Sloan, D. Elam and B. Ibey, "Effects of different terahertz frequencies on gene expression in human keratinocytes," *Proceedings of the Society of Photo-Optical Instrumentation Engineers*, vol. 9321, pp. Q1 - Q9, 2015.
- [6] G. J. Wilmink, B. L. Ibey, C. L. Roth, R. L. Vincelette, B. D. Rivest, C. B. Horn, J. Bernhard, D. Roberson and W. P. Roach, "Determination of Death Thresholds and Identification of Terahertz (THz)-Specific Gene Expression Signatures," *Proceedings of the Society of Photo-Optical Instrumentation Engineers*, vol. 7562, pp. K1 - K8, 2010.

- [7] B. S. Alexandrov, M. L. Phipps, L. B. Alexandrov, L. G. Booshehri, A. Erat, J. Zabolotny, C. H. Mielke, H. -T. Chen, G. Rodriguez, K. O. Rasmussen, J. M. Martinez, A. R. Bishop and A. Usheva, "Specificity and Heterogeneity of Terahertz Radiation Effect on Gene Expression in Mouse Mesenchymal Stem Cells," *Scientific Reports*, vol. 3, pp. 1 - 8, 2013.
- [8] C. Z. Cerna, D. P. Elam, I. Echchgadda, M. A. Sloan and G. J. Wilmsink, "State-of-the-art Exposure Chamber for Highly Controlled and Reproducible THz Biological Effects Studies," *Proceedings of SPIE*, vol. 8941, pp. H1 - H9, 2014.
- [9] O. P. Cherkasova, V. I. Fedorov, E. F. Nemova, S. S. Popova, A. S. Pogodin and A. G. Khamoyan, "Terahertz radiation influence on peptide conformation," *Proceedings of SPIE*, vol. 6727, pp. 1 - 5, 2007.
- [10] H. Hintzsche, C. Jastrow, B. Heinen, K. Baaske, T. Kleine-Ostmann, M. Schwerdtfeger, M. K. Shakfa, U. Karst, M. Koch, T. Schrader and H. Stopper, "Terahertz Radiation at 0.380 THz and 2.520 THz Does Not Lead to DNA Damage in Skin Cells In Vitro," *Radiation Research*, vol. 179, no. 1, pp. 38 - 45, 2013.
- [11] H. Hintzsche, C. Jastrow, T. Kleine-Ostmann, H. Stopper, E. Schmid and T. Schrader, "Terahertz Radiation Induces Spindle Disturbances in Human-Hamster Hybrid Cells," *Radiation Research*, vol. 175, no. 5, pp. 569 - 574, 2011.
- [12] A. Korenstein-Ilan, A. Barbul, P. Hasin, A. Eliran, A. Gover and R. Korenstein, "Terahertz Radiation Increases Genomic Instability in Human Lymphocytes," *Radiation Research*, vol. 170, pp. 224 - 234, 2008.
- [13] S. Koyama, E. Narita, Y. Shimizu, T. Shiina, M. Taki, N. Shinohara and J. Miyakoshi, "Twenty Four-Hour Exposure to a 0.12 THz Electromagnetic Field Does Not Affect the Genotoxicity, Morphological Changes, or Expression of Heat Shock Protein in HCE-T Cells," *International Journal of Environmental Research and Public Health*, vol. 13, no. 793, pp. 1 - 9, 2016.
- [14] S. Yamazaki, M. Harata, T. Idehara, K. Konagaya, G. Yokoyama, H. Hoshina and Y. Ogawa, "Actin polymerization is activated by terahertz irradiation," *Scientific Reports*, vol. 8, no. 9990, pp. 1 - 7, 2018.
- [15] C. M. Hough, D. N. Purschke, C. Huang, L. V. Titova, O. V. Kovalchuk, B. J. Warkentin and F. A. Hegmann, "Topology-based prediction of pathway dysregulation induced by intense terahertz pulses in human skin tissue models," *Journal of Infrared, Millimeter, and Terahertz Waves*, vol. 39, pp. 887 - 898, 2018.
- [16] K. -T. Kim, J. Park, S. J. Jo, S. Jung, O. S. Kwon, G. P. Gallerano, W. -Y. Park and G. -S. Park, "High-power femtosecond-terahertz pulse induces a wound response in mouse skin," *Scientific Reports*, vol. 3, no. 2296, pp. 1 - 7, 2013.
- [17] L. Titova, A. Ayesheshim, A. Golubov, D. Fogen, R. Rodriguez-Juarez, F. Hegmann and O. Kovalchuk, "Intense THz pulses cause H2AX phosphorylation and activate DNA damage response in human skin tissue," *Biomedical Optics Express*, vol. 4, no. 4, pp. 559 - 568, 2013.

- [18] L. Titova, A. Ayesheshim, A. Golubov, R. Rodriguez-Juarez, R. Woycicki, F. Hegmann and O. Kovalchuk, "Intense THz pulses down-regulate genes associated with skin cancer and psoriasis: a new therapeutic avenue?," *Scientific Reports*, vol. 3, no. 2363, pp. Q1 - Q10, 2013.
- [19] H. Cheon, H.-j. Yang, S.-H. Lee, Y. A. Kim and J.-H. Son, "Terahertz molecular resonance of cancer DNA," *Scientific Reports*, vol. 6, no. 37103, pp. 1 - 10, 2016.
- [20] D. S. Sitnikov, I. V. Ilina and A. A. Pronkin, "Experimental system for studying bioeffects of intense terahertz pulses with electric field strength up to 3.5 MV/cm," *Optical Engineering*, vol. 59, no. 6, pp. 1 - 10, 2020.
- [21] J. Bock, Y. Fukuyo, S. Kang, M. L. Phipps, L. B. Alexandrov, K. O. Rasumussen, A. R. Bishop, E. D. Rosen, J. S. Martinez, H. -T. Chen, G. Rodriguez, B. S. Alexandrov and A. Usheva, "Mammalian Stem Cells Reprogramming in Response to Terahertz Radiation," *Public Library of Science (PLoS) ONE*, vol. 5, no. 12, pp. 1 - 6, 2010.
- [22] A. A. Angeluts, A. B. Gapeyev, M. N. Esaulkov, O. G. Kosareva, S. N. Matyunin, M. M. Nazarov, T. N. Pashovkin, P. M. Solyankin, O. P. Cherkasova and A. P. Shkurinov, "Study of terahertz-radiation-induced DNA damage in human blood leukocytes," *Quantum Electronics*, vol. 44, no. 3, pp. 247 - 251, 2014.
- [23] M. V. Duka, L. N. Dvoretzkaya, N. S. Balbekin, M. K. Khodzitskii, S. A. Chivilikhin and O. A. Smolyanskaya, "Numerical and experimental studies of mechanisms underlying the effect of pulsed broadband terahertz radiation on nerve cells," *Quantum Electronics*, vol. 44, no. 8, pp. 707 - 712, 2014.
- [24] I. A. Geyko, O. A. Smolyanskaya, M. I. Sulatskiy, S. E. Parakhuda, E. A. Sedykh, E. L. Odlyanitskiy, M. K. Khodzitskiy and A. G. Zabolotniy, "Impact of terahertz radiation on the epithelialization rate of scarified cornea," *Proceedings of SPIE*, vol. 9542, pp. 1 - 7, 2015.
- [25] R. W. Boyd, *Nonlinear Optics*, 3rd Ed., Orlando, FL: Academic Press Inc., 2008.
- [26] "Tera-Hertz radiation in Biological Research, Investigations on Diagnostics and study on potential Genotoxic Effects (THz-BRIDGE), Final Report," [Online]. Available: <https://www.frascati.enea.it/THz-BRIDGE/>.
- [27] O. Zeni, G. P. Gallerano, A. Perrotta, M. Romano, A. Sannino, M. Sarti, M. D'Arienzo, A. Doria, E. Giovenale, A. Lai, G. Messina and M. R. Scarfi, "Cytogenetic observations in human peripheral blood leukocytes following in vitro exposure to THz radiation: a pilot study," *Health Physics*, vol. 92, no. 4, pp. 349 - 357, 2007.
- [28] A. Amicis, S. D. Sanctis, S. D. Cristofaro, V. Franchini, F. Lista, E. Regalbuto, E. Giovenale, G. P. Gallerano, P. Nenzi, R. Bei, M. Fantini, M. Benvenuto, L. Masuelli, E. Coluzzi, C. Cicia and A. Sgura, "Biological effects of in vitro THz radiation exposure in human foetal fibroblasts," *Mutation Research/Genetic Toxicology and Environmental Mutagenesis*, vol. 793, pp. 150 - 160, 2015.

- [29] G. Gallerano, A. Doria, E. Giovenale and I. Spassovsky, "High power THz sources and applications at ENEA-Frascati," *Journal of Infrared Millimeter and Terahertz Waves*, vol. 35, pp. 17 - 24, 2014.
- [30] A. N. Bogomazova, E. M. Vassina, T. N. Goryachkovskaya, V. M. Popik, A. S. Sokolov, N. A. Kolchanov, M. A. Lagarkova, S. L. Kiselev and S. E. Peltek, "No DNA damage response and negligible genome-wide transcriptional changes in human embryonic stem cells exposed to terahertz radiation," *Scientific Reports*, vol. 5, no. 7749, pp. 1 - 6, 2015.
- [31] E. V. Demidova, T. N. Goryachkovskaya, T. K. Malup, S. V. Bannikova, A. I. Semenov, N. A. Vinokurov, V. M. Popik and S. E. Peltek, "Studying the Non-Thermal Effects of Terahertz Radiation on *E. coli*/pKatG-gfp Biosensor Cells," *Bioelectromagnetics*, vol. 34, pp. 15 - 21, 2013.
- [32] T. Kawasaki, K. Tsukiyama and A. Irizawa, "Dissolution of a fibrous peptide by terahertz free electron laser," *Scientific Reports*, vol. 9, no. 1, pp. 1 - 8, 2019.
- [33] S. Yamazaki, M. Harata, Y. Ueno, M. Tsubouchi, K. Konagaya, Y. Ogawa, G. Isoyama, C. Otani and H. Hoshina, "Propagation of THz irradiation energy through aqueous layers: Demolition of actin filaments in living cells," *Scientific Reports*, vol. 10, no. 9008, pp. 1 - 10, 2020.
- [34] V. Jelic, K. Iwaszczuk, P. Nguyen, C. Rathje, G. Hornig, H. Sharum, J. Hoffman, M. Freeman and F. Hegmann, "Ultrafast terahertz control of extreme tunnel currents through single atoms on a silicon surface," *Nature Physics*, vol. 13, no. 6, pp. 591 - 598, 2017.
- [35] W. -T. Chang, I. -S. Hwang, M. -T. Chang, C. -Y. Lin, W. -H. Hsu and J. -L. Hou, "Method of electrochemical etching of tungsten tips with controllable profiles," *Review of Scientific Instruments*, vol. 83, no. 083704, pp. 1 - 6, 2012.
- [36] COMSOL, Inc., *Introduction to the Wave Optics Module*, COMSOL 5.1 Documentation, 2015.
- [37] N. Sultanova, S. Kasarova and I. Nikolov, "Characterization of optical properties of optical polymers," *Optical and Quantum Electronics*, vol. 45, pp. 221 - 232, 2013.
- [38] R. Williams, A. Schofield, G. Holder, J. Downes, D. Edgar, P. Harrison, M. Siggel-King, M. Surman, D. Dunning, S. Hill, D. Holder, F. Jackson, J. Jones, J. McKenzie, Y. Saveliev, N. Thomsen, P. Williams and P. Weightman, "The influence of high intensity terahertz radiation on mammalian cell adhesion, proliferation and differentiation," *Physics in Medicine and Biology*, vol. 58, pp. 373 - 391, 2013.
- [39] J. Michl, K. C. Park and P. Swietach, "Evidence-based guidelines for controlling pH in mammalian live-cell culture systems," *Communications Biology*, vol. 2, no. 144, pp. 1 - 12, 2019.
- [40] Edmund Optics, "Understanding Microscopes and Objectives," Edmund Optics, 2021. [Online]. Available: <https://www.edmundoptics.com/knowledge-center/application-notes/microscopy/understanding-microscopes-and-objectives/>.

- [41] P. Jepsen, D. Cooke and M. Koch, "Terahertz spectroscopy and imaging - Modern techniques and applications," *Laser and Photonics Reviews*, vol. 5, no. 1, pp. 124-166, 2011.
- [42] E. Hecht, *Optics*, Essex: Pearson Education, 2017.
- [43] M. Naftaly and R. Miles, "Terahertz Time-Domain Spectroscopy for Material Characterization," *Proceedings of the IEEE*, vol. 95, no. 8, pp. 1658 - 1665, 2007.

6 Terahertz dosimetry for biological exposure studies: Simulation of coherent spatiotemporal pulse dynamics in many optically thin materials

6.1 Introduction

In Medical Physics, “dose” is a physical quantity defined in terms of ionizing energy absorbed per unit mass of tissue [1, 2]. For non-ionizing beams, biological effects are typically discussed in terms of the specific absorption rate (SAR) in a volume V formally defined as

$$\text{SAR} = \frac{1}{V} \int \frac{\sigma(\mathbf{r})|\mathbf{E}(\mathbf{r})|^2}{\rho(\mathbf{r})} d\mathbf{r} \quad (6.1)$$

where σ is the tissue conductivity, E is the electric field, and ρ is the sample density. SAR is used for frequencies in the range 100 kHz – 10 GHz [3]. According to the International Commission on Non-Ionizing Radiation Protection (ICNIRP), at frequencies greater than this range, SAR is not a good measure due to the small absorption volume, and incident power density (or average intensity), is a more appropriate dosimetric quantity.

Therefore, for the non-ionizing terahertz (THz) beam, “dose” (u_A) is used as a shorthand for the THz energy absorbed in the exposed region as pulse energy per unit area. Assuming all energy, ε , is absorbed in the exposed area, A , the THz dose rate (i.e., average intensity) is

$$\dot{u}_A = \frac{\varepsilon}{A} \cdot f_{rep} \quad (6.2)$$

where $f_{rep} = 1/T$ is the repetition rate of a pulsed source with period T . For a 1 kHz train using the measured energy and spot size of our THz source (Table 1 of Chapter 4), the dose rate of the THz beam in optimal conditions is 125 mW/cm², or 7.5 J/cm²/min, and the total absorbed dose, u_A , is determined by scaling by the total exposure time.

In this chapter, considerations for accurate dose modelling of biological THz exposures are discussed, and methods for incorporating non-thermal, gradient, and field-induced biological effects into dose modelling that are not considered by Equation (6.2) are presented. Limitations of coherent pulse modelling when THz beams propagate through many optically thin materials affect

accurate dose characterizations, which motivates an adjusted simulation framework. A novel method of constructing a frequency-space transfer function by modelling radiation propagation with binary decision trees is presented, and results in THz dose simulations that are quasi-analytic up to causal constraints.

6.2 Terahertz dosimetry

For the THz exposure experiments described in Chapters 7 – 9, accurate characterization of the electric field strength and energy absorbed in the sample region is essential for a quantitative framework with which to contextualize observed biological effects. However, since Equation (6.2) only utilizes average energy associated with thermal effects, it is insufficient to capture the hypothesized non-thermal interaction mechanisms of coupling to natural oscillatory dynamics of biological structures, which may generally depend on the electric field strength/direction, gradient effects, or frequency content of the incident EM pulse. Therefore, a theoretical formalism for simulation of coherent pulse propagation was pursued to capture these relevant exposure parameters in dose simulations.

6.2.1 *Boundary dose modulations in terahertz exposures*

With coherent THz pulses, complications arise in dose calculations due to the comparable size of the pulse wavelength relative to interaction lengths in typical bio-exposure configurations. Recall, the 0.1 – 10 THz band corresponds to a 30 – 3000 μm wavelength range that is on the order of typical animal cell diameters ($\sim 10 - 100 \mu\text{m}$), epidermal tissue thickness ($\sim 1 \text{ mm}$), and many standard substrate thicknesses ($\sim 0.1 - 1 \text{ mm}$) [4]. Interactions in these conditions modulate THz energy deposition due to self-interference near material boundaries, as shown in Figure 6.1(a). Field lobes on the leading edge of the pulse reflect and interfere with the incoming trailing edge, and since these distances are on the order of material thickness, this modulation will affect the propagation characteristics and energy deposition in the region of dosimetric interest.

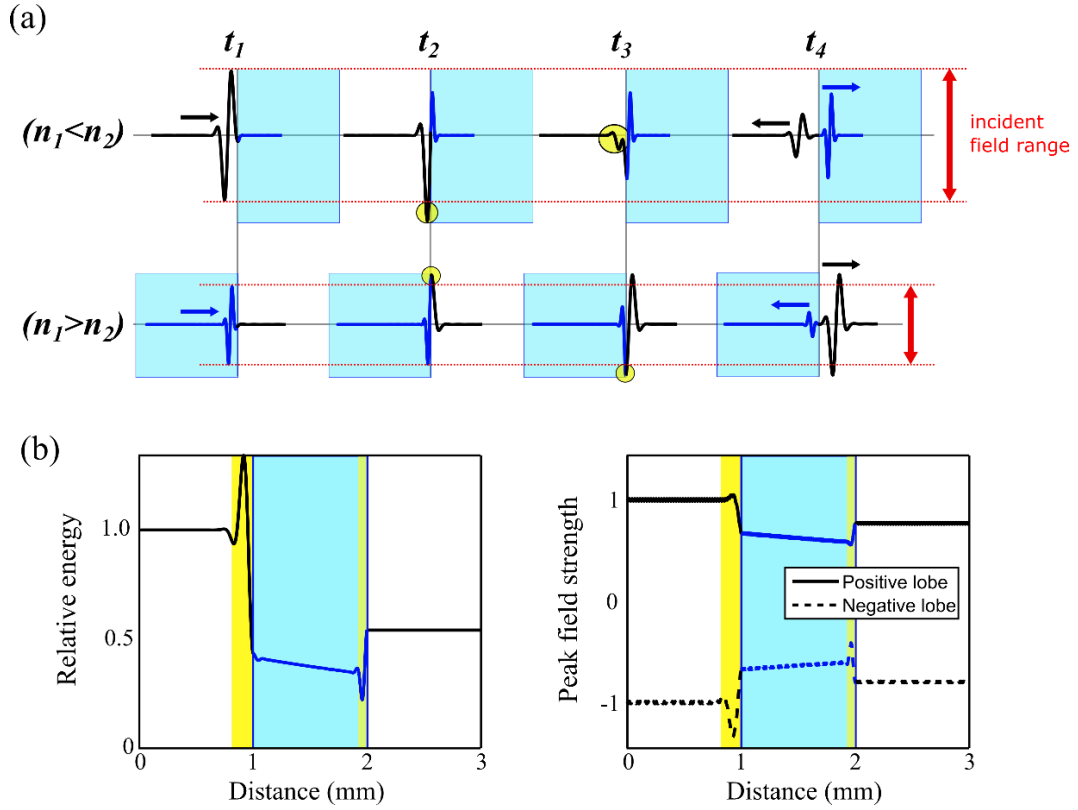


Figure 6.1. **Single-boundary modulation of coherent fields.** Single-cycle anti-symmetric THz pulse between air ($n = 1$) and a material with index $n = 1.5$. (a) Field modulation near material interfaces for a THz pulse propagating from low to high index (top) and high to low index (bottom). The leading lobe of the pulse will reflect and interfere with the tailing lobe, leading to field modulations within $\lambda/2n$ of the boundary. The dotted red lines indicate the incident field strength range, and interference modulates the incident field outside of this range. (b) Relative energy (left) and maximum field strengths of the positive and negative lobes of a pulse propagating from air to glass (low-to-high index) and then from glass to air (high-to-low index). The modulations of energy and field near the boundaries are in the highlighted yellow bands.

When propagating from low to high index (Figure 6.1(a), top row), there is an energy enhancement a distance $\sim \lambda/(2n_1)$ from the boundary that decreases to a “cold spot” at the surface, as highlighted in the yellow band of Figure 6.1(b). Conversely, when propagating from high to low index (Figure 6.1(a), bottom row) the effect is reversed: a field/energy enhancement is observed at the boundary surface, with a diminution a distance $\sim \lambda/(2n_2)$ away.

6.2.1.1 Effect of sample thickness on boundary modulations

It is evident from the single-boundary example above that the presence of thin materials with closely spaced boundaries will result in complex interference. To see this, imagine reducing the thickness of the high-index material in Figure 6.1(b), such that both types of modulations are occurring simultaneously in the same region of space. Further, this effect is exacerbated as the

number of materials increases, each with potentially different dielectric properties, and therefore different reflection/transmission/attenuation/dispersion characteristics that will alter the precise nature of boundary effects. Importantly, these complex modulations occur in the region occupied by the sample in most standard THz exposure configurations. Therefore, accurate determination of the field, energy, and dose that is actually seen by the exposed sample requires accurate characterization of complex coherent pulse propagation through many layers of optically thin materials that accounts for these effects.

Figure 6.2(a) shows the energy of a THz pulse as a function of distance in epidermis (data from [5]), calculated for varying sample thicknesses from 10 μm to 1 mm, and additionally accounts for reflections from both a glass substrate and aqueous/water media surrounding the sample region to simulate realistic exposure materials. Sample thickness affects the absorbed energy in two ways: First, the interaction length dictates the absorbed energy according to the absorption coefficient as $e^{-\alpha(\omega)L}$. Second, for sufficiently thin samples, interfering reflections cause the energy profile to deviate from a simple exponential decay. For the thickest sample case (1 mm), multiple beam interference (MBI) is negligible, and results in pure exponential decay, as shown in the inset of Figure 6.2(a). The total energy in this thick 1 mm sample was fit to an exponential function, yielding an effective broadband decay length of $z_0 = 75.3 \mu\text{m}$; this is used as a reference for the modulated energy profiles in thin samples.

Figure 6.2(b) shows the entrance, exit, and absorbed energy in the sample region for varying thickness. Interference of the back-reflected waves when samples are sufficiently thin modulates the entrance energy as shown in the blue curve. The total dose absorbed is shown by the black curve, and typical animal cell diameters occupy the shaded region. The interaction length in the sample is the dominant influence of absorbed dose, and is additionally modulated in thin samples by MBI effects. Figure 6.2(c) shows the energy dose profiles with the thick-sample reference subtracted, and isolates only the contribution of MBI dose modulation. For samples $\leq 40 \mu\text{m}$, destructive interference of the initial pulse lobe reduces the electric field energy profiles in the sample region by an additional $\sim 5\% - 10\%$. If sufficient space is allowed for the reflection of the initial lobe to constructively interfere with the second lobe, this valley is shifted to larger distances, and an enhancement is seen at the boundary as shown for $L > 40 \mu\text{m}$. As the sample thickness increases, the modulation decreases to zero.

These large variations of energy absorption in the sample region are important considerations when investigating dose-/field-dependent THz-induced biological effects. Therefore, a formalism that accounts for interference effects in many thin materials was necessary.

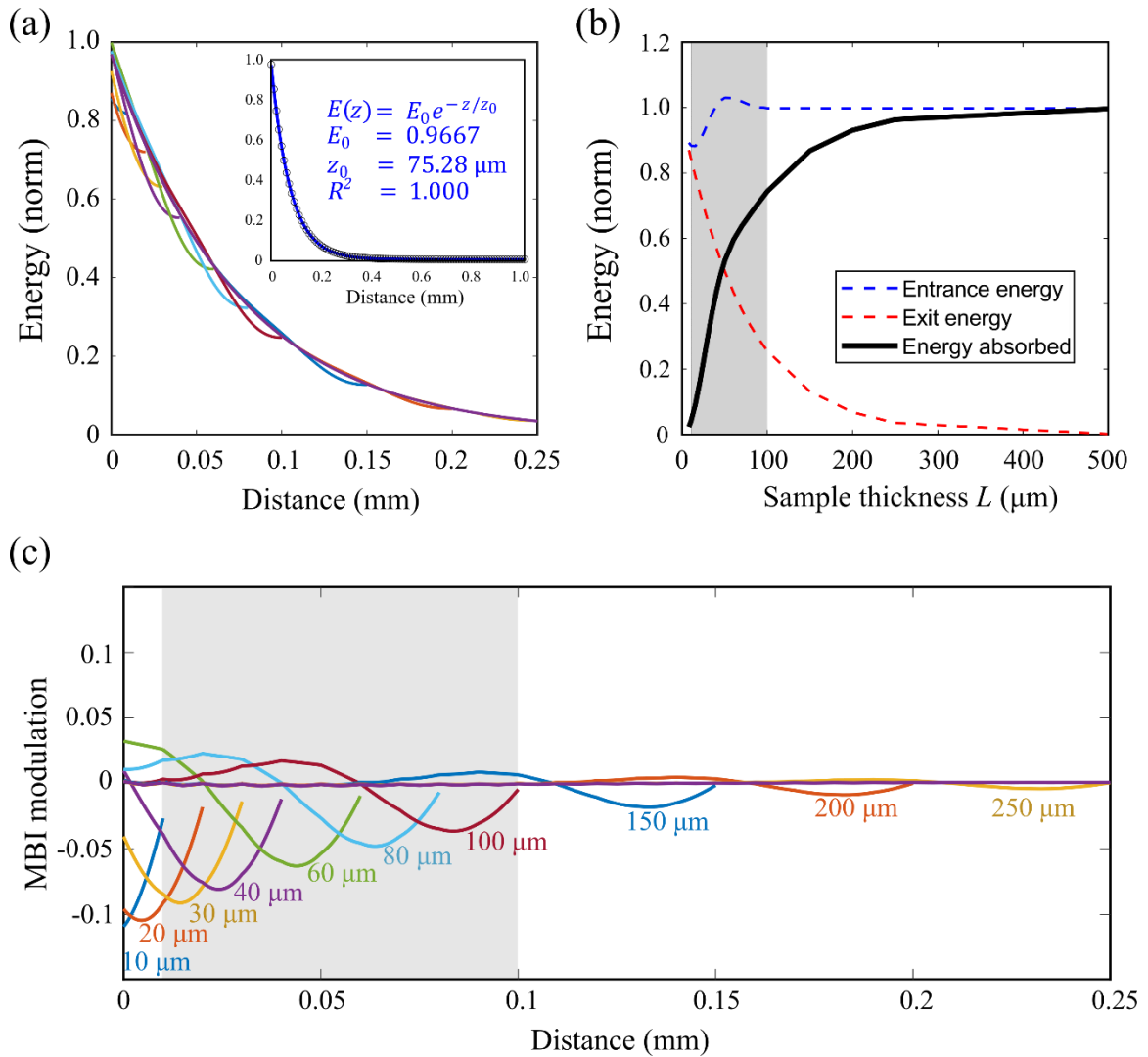


Figure 6.2. **Energy absorption and multiple-beam interference (MBI) in the sample region for varying sample thickness.** (a) Relative energy vs. propagation distance through a sample region modelled as pure water. Individual curves represent different sample thickness. Multiple beam interference in thin samples results in absorption that deviates from pure exponential decay. *Inset:* Pure exponential decay is observed in thick (1 mm) samples where MBI is negligible. The effective broadband field penetration depth in water is 75.3 μm . (b) The relative energies at the input and output face of the sample region as a function of sample thicknesses, and the absorbed dose. There is large variation of absorbed dose within typical cell sizes, and MBI effects induce further modulation for small thicknesses. (c) Isolated MBI energy modulation for varying sample thickness. These are the curves from (a) with the pure reference exponential subtracted. Modulations due to interference with the reflected waves in the sample region lead to an additional 5% – 10% energy modulation in the sample region. In (b) and (c), the gray shaded regions represent a typical range of animal cell diameters.

6.2.2 Dose models inspired by coherent transfer function spectroscopy

In THz spectroscopy, the purpose of theoretical pulse interaction models is to fit measured pulse data and extract dielectric parameters [6]. In generalized time-domain spectroscopy, a reference waveform, E_{ref} , is incident on a sample whose dielectric properties are to be determined. The modulated (reflected or transmitted) field is measured, and a transfer function is determined that relates the modulated field, E_{mod} , to the reference field as

$$E_{mod}(\omega, \vec{r}) = TF(\omega, \vec{r}) \cdot E_{ref}(\omega, \vec{r}) \quad (6.3)$$

where $TF(\omega, \vec{r})$ is a frequency-domain transfer function at a point \vec{r} , that generally depends on the dielectric parameters [7]. Optimization techniques determine the dielectric parameters in the theoretical model that minimize the deviation from the experimental result.

For dosimetry, the goal of modelling is the inverse to that of spectroscopy: TF is calculated from material dielectric properties that are known *a priori*, and the THz field propagation and energy deposition characteristics are calculated in complex geometries relevant for realistic biological exposure experiments. Biological responses observed in THz exposure experiments may be related to the simulated field dynamics in the sample region that may arise by non-thermal interaction mechanisms not considered by Equation (6.2), such as field strength or direction, gradient effects, or frequency content. Details on mathematical characterizations of transfer functions are presented in Section 6.3.1.

6.2.2.1 Approximation regimes of transfer function models

It is common to design experimental configurations for which approximations of the transfer function model may be applied [6]. Figure 6.3(a) shows one type of approximation for thick samples, for which only the first few terms of a transfer function are necessary in describing the modulated field within the acquired time window [8, 9]. Boundary reflections are separated in time by

$$\Delta t = \frac{2dn}{c} \quad (6.4)$$

where d is the sample thickness, n is the refractive index, and $c=3 \times 10^8$ m/s is the speed of light. Therefore, a localized pulse with $\Delta t = 1$ ps requires $nd > 0.15$ mm for distinguishable reflections,

where $OPL = nd$ is the optical path length. These samples will produce pulse trains that are well-separated in time and can be easily gated in the acquired waveforms. However, for thin samples with $OPL \ll 0.15$ mm, many interfering reflections will not be distinguishable and cannot be gated and analyzed separately, as shown in Figure 6.3(b). These many internal reflections must be theoretically incorporated for accurate dose modelling.

(a) Thick sample

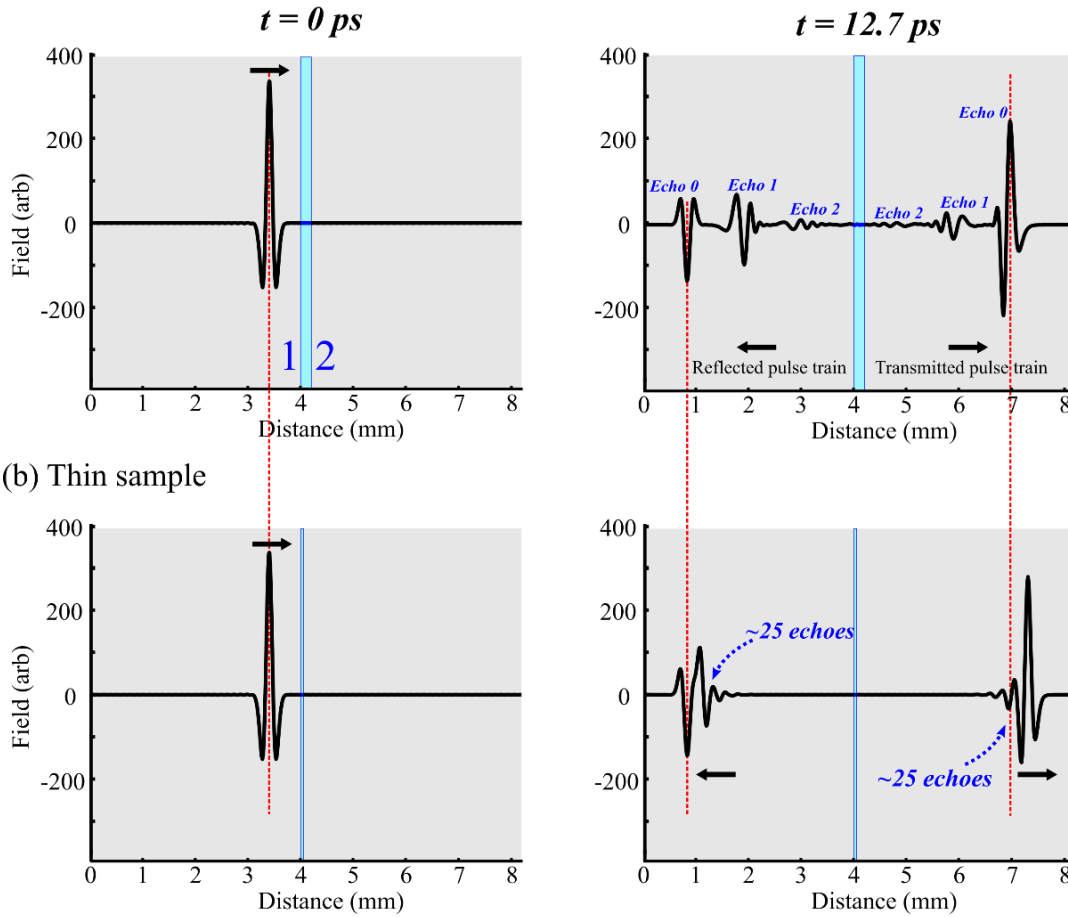


Figure 6.3. **Effect of sample thickness.** (a) For thick samples, the multiple reflections in the reflected and transmitted pulse trains are distinguishable in the acquired waveform, and time-gating in post processing isolates the interactions with individual material boundaries. (b) For thin samples, many internal reflections interfere that cannot be gated and isolated. These many internal reflections must therefore be theoretically incorporated for accurate modelling of interactions in optically thin materials.

One approach to model optically thin ($OPL \ll \lambda$) samples for configurations with no more than $N = 3$ propagation regions is to treat the internal region as a Fabry-Perot (FP) cavity [9, 10, 11]. This 3-region geometry is solvable because it reduces to solving a finite number of convergent sums. However, the addition of one or more regions/boundaries cannot be treated modularly with

a set of finite FP cavities, as these geometries are instead modelled by an infinite number of infinite sums (more on this in Section 6.3.2).

Exposure experiments are often limited to the samples and substrates utilized in standard biological assays, and adjusting experimental parameters like the number of regions or sample thickness is not feasible. Moreover, even the simplest bio-exposure configuration, such as an adherent cell line in a culture dish, requires simulating at least 4 regions (and often more), including multiple regions that are thin relative to THz wavelengths. This will lead to boundary modulations and interfering reflections discussed in Section 6.2.1 and Figure 6.3. These conditions are not consistent with the assumptions made in existing models, and therefore an adjusted framework for accurate characterization of coherent pulse propagation through many optically thin materials is necessary.

6.3 Theoretical formalism of coherent pulse dosimetry in many optically thin materials

Pickwell et al. have shown that THz interactions with biological tissue are well-modelled by their dielectric parameters in the THz band, as introduced in Chapter 2 [12]. Therefore, calculations of THz interactions with materials defined by dielectric parameter values from THz spectroscopy measurements are used to calculate the coherent pulse propagation within the sample region of interest. From these simulations, the field variation and energy deposition characteristics are determined for THz dose calculations in exposure geometries used in this thesis.

6.3.1 Spatiotemporal field dynamics in dissipative, dispersive, layered media

The theoretical formalism begins with a general spatiotemporal description of a wave propagating in a dielectric material [13]. A separable solution to Maxwell's equations describing a monochromatic electric field is given by $\vec{E}(\vec{r}, t) = \vec{E}_0(\vec{r})e^{i\omega t}$, where the spatially-dependent field amplitude (taking $\vec{r} = z$ as the propagation direction) is

$$\vec{E}_0(z) = E_0 e^{-\delta(\omega)z} \quad (6.5)$$

and $\delta(\omega)$ is the spatial phase factor describing propagation and attenuation of a wave at frequency ω :

$$\delta(\omega) = \frac{\omega}{c} [\kappa(\omega) + in(\omega)] \quad (6.6)$$

where $\tilde{n} = n + i\kappa$ is the complex refractive index, n is the conventional refractive index, and κ is the extinction coefficient, related to the energy absorption coefficient from Beer's Law as $\alpha(\omega) = 2\kappa\omega/c$.

Consider an electric field propagating through N regions of different \tilde{n} , where the thickness of the k^{th} region is given by L_k , and the material-dependent phase factor (Equation(6.6)) is δ_k . In each region, Equation (6.5) can be decomposed into positive/negative (forward/backward) propagation directions, given by:

$$E_{0,+}^{(k)}(z, \omega) = E_0(\omega) \cdot \exp\left(-\delta_k(\omega) \left[z - \sum_{s=1}^{k-1} L_s \right]\right) \quad (6.7)$$

$$E_{0,-}^{(k)}(z, \omega) = E_0(\omega) \cdot \exp\left(-\delta_k(\omega) \left[\sum_{s=1}^k L_s - z \right]\right)$$

where the sums in the exponential arguments initialize the phase in the k^{th} region of interest, and $E_0^{(k)}(z, \omega) = E_{0,+}^{(k)} + E_{0,-}^{(k)}$ are the frequency-domain incident field amplitudes at each point in space. For a signal in the time domain, the amplitudes, $E_0(\omega)$, and phases, $\phi(\omega)$, of the monochromatic plane-wave components are given by the Fourier transform: $F\{E(z, t)\} = E_0(z, \omega)e^{i\phi(\omega)}$.

In addition to dispersion and attenuation, a p -polarized wave impinging normally on an interface between regions of differing \tilde{n} will undergo frequency-dependent reflection and transmission, described by [13]

$$\left(\frac{\tilde{E}_{0,ref}}{\tilde{E}_{0,inc}}\right) \equiv \tilde{r}_{ij} = \frac{\tilde{n}_j - \tilde{n}_i}{\tilde{n}_j + \tilde{n}_i} \quad (6.8)$$

$$\left(\frac{\tilde{E}_{0,trans}}{\tilde{E}_{0,inc}}\right) \equiv \tilde{t}_{ij} = \frac{2\tilde{n}_j}{\tilde{n}_j + \tilde{n}_i}$$

where \tilde{r}_{ij} (\tilde{t}_{ij}) is the complex amplitude reflection (transmission) coefficient for a wave propagating in region i from region j . Defining indices in this way establishes a coordinate system and encodes propagation direction: forward (+ z) when $i > j$ and backward ($-z$) when $i < j$.

Together, Equations (6.5) – (6.8) provide a complete spatial description of modulation to the incident field, E_{inc} , as a function of frequency. As the component waves propagate, they will accumulate phase (Equation (6.7)) and reflection/transmission factors (Equation (6.8)) dependent on frequency and location, z , in the region of interest. These are used to construct the transfer function TF for all regions of interest from the materials' dielectric properties, as depicted in Figure 6.4. The transfer function for a given geometry is applied to the incident field distribution in the complex frequency domain, and the material-modulated spatiotemporal field, E_{mod} , is recovered via the inverse Fourier transform:

$$\vec{E}_{mod}(z, t) = F^{-1}\{TF(z, \omega) \cdot E_{inc}(\omega) \cdot e^{i(\omega t + \phi(\omega))}\} \quad (6.9)$$

where the complex exponential factor contains the temporal and phase information from the incident field's Fourier transform.

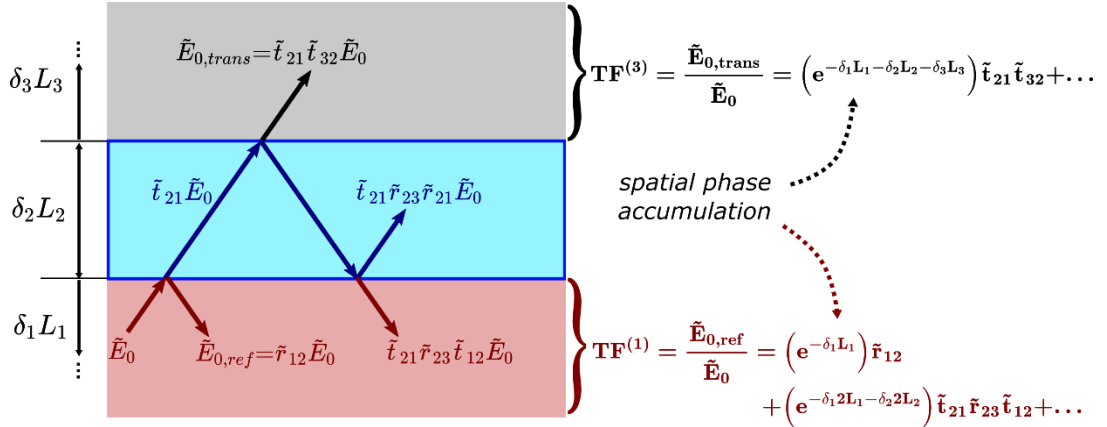


Figure 6.4. **Transfer functions determined by accumulation of spatial phase factors and reflection/transmission coefficients.** As an incident field, \tilde{E}_0 , propagates through layered media, it will accumulate phase and reflection/transmission coefficients according to Equations (6.7) and (6.8). These comprise the transfer function, TF , that maps the incident field to the simulated modulated field in each region. The TFs for the principal transmitted ($TF^{(3)}$) and reflected ($TF^{(1)}$) fields typically used for spectroscopy are shown at right for Regions 1 and 3, for which only the first few terms are typically needed (the spatial propagation terms (Equation (6.5)) are not included for clarity). For geometries with many optically thin materials, thousands or potentially millions of TF terms may be required for accurate simulation of field modulation over a reasonable interaction duration.

Accurate determination of $TF(z, \omega)$ is therefore of critical importance in simulations of modulated field distributions. Of interest is the explicit determination of how the electric field and energy vary in time and space in the simulated configuration. Computationally, Equation (6.9) results in a 2D matrix of complex field values, $E_{mod}(z, t)$, for which the temporal (spatial) variation comprises the row (column) space. Conversion of the complex field to real amplitude or energy values is straightforward, and integration along the rows (columns) results in a 1D distribution of energy or field amplitude with respect to space (time).

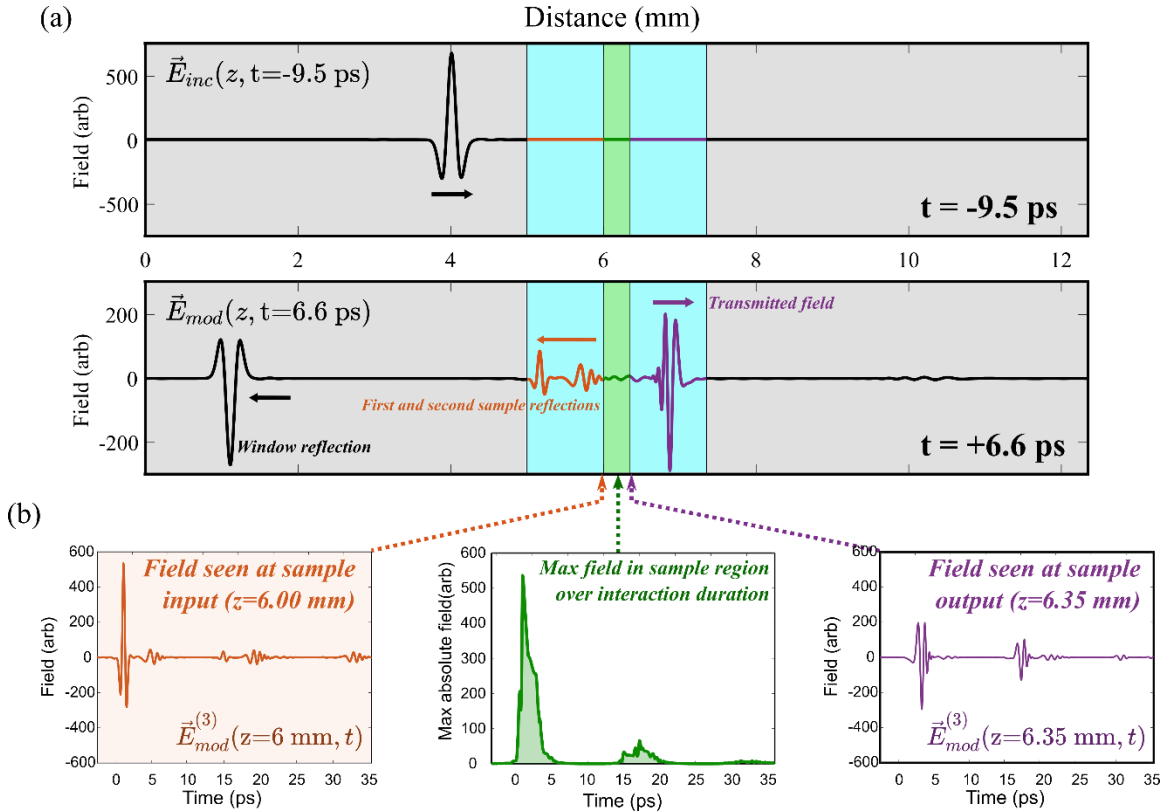


Figure 6.5. Demonstration of complete spatiotemporal simulation of coherent field variation for a generalized spectroscopy geometry. (a) A 350 μm thick dispersive sample (green) is sandwiched between two 1 mm thick fused quartz windows (blue), with air regions on each side (gray). Plots show the spatial field variation in all five regions before ($t=-9.5$ ps) and after ($t=+6.6$ ps) interaction with the sample, with pulse reflection origins labelled. (b) Temporal field variation at different points in space. Interfering waves lead to a complex predicted field distribution in the sample region at 0 ps, and echo recombinations from secondary reflections at 15 ps and 30 ps.

An example demonstrating a complete spatiotemporal description of $E_{mod}(z, t)$ in Equation (6.9) for a general spectroscopy geometry is shown in Figure 6.5. A 350 μm thick dispersive sample is sandwiched between two 1 mm thick fused quartz windows, with air comprising the incident/reflected and transmitted regions. Figure 6.5(a) shows the spatial field distribution at two points in time before ($t=-9.5$ ps) and after ($t=+6.6$ ps) sample interactions, while Figure 6.5(b)

shows the temporal variation at the input and output of the sample region (green, Region 3). From these simulations, complex field variation due to frequency dependent interaction and propagation, as well as interference with back-reflected waves inducing boundary modulations, are accurately modelled in all regions of interest. The maximum field in the sample region is shown in the middle plot of Figure 6.5(b), highlighting sub-picosecond determination of field dynamics.

6.3.2 *Modelling the transfer function with binary decision trees*

The propagation of radiation through layered media can be modelled as the sum of the set of traversals of a binary decision tree, as shown in Figure 6.6. Each node of the tree represents an interaction at a material interface, and bifurcation of each node represents the reflected and transmitted fraction of the incident wave. Each traversal of the tree represents a unique path an incident wave will take through the materials (e.g., the blue trajectory in Figure 6.6b), and the whole tree represents the set of all possible paths. By identifying all possible wave trajectories through the material (which becomes a question of identifying the set of all traversals of the decision tree), and applying relevant propagation, phase accumulation, and reflection/transmission factors at each node, all TF terms are obtained and summed to form the total transfer function.

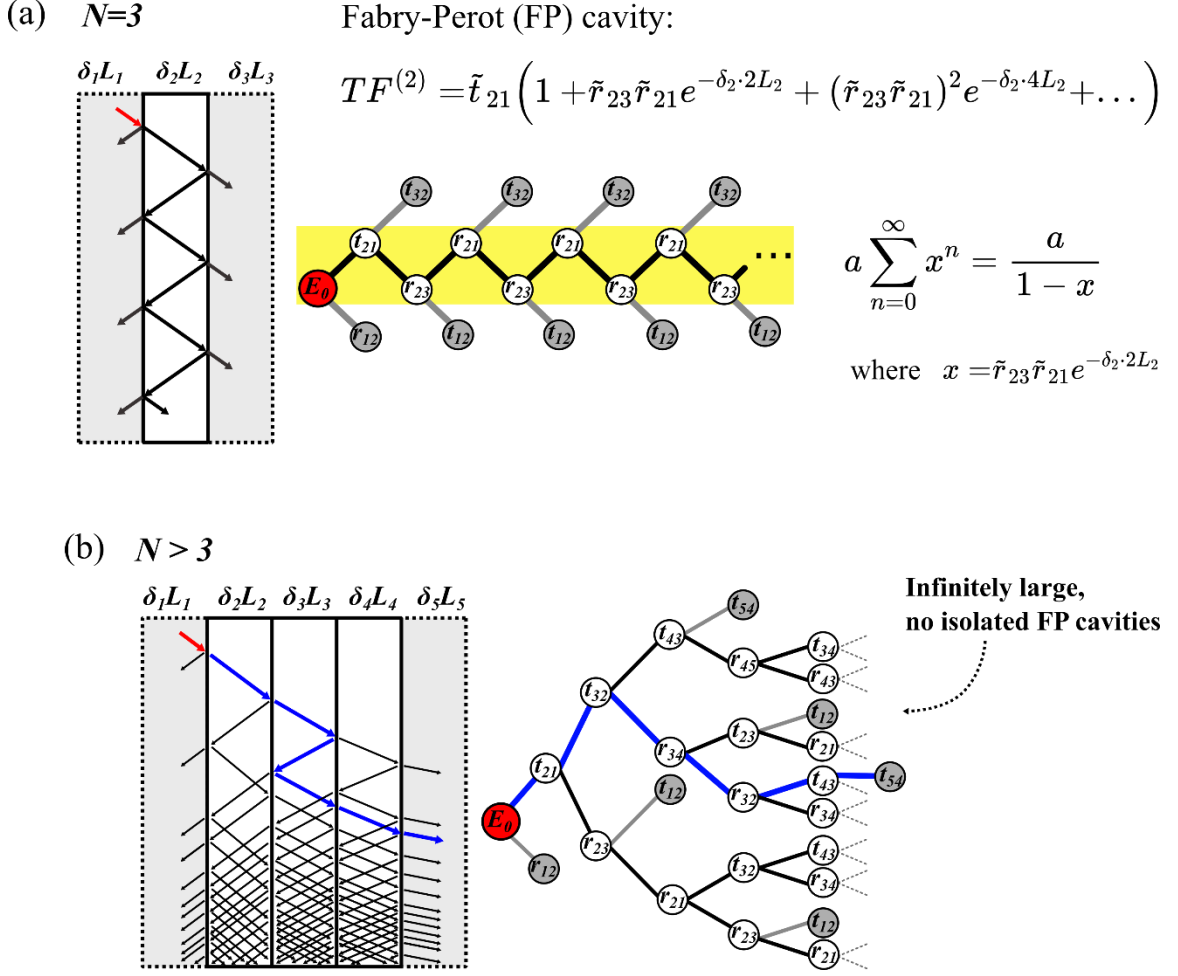


Figure 6.6. **Decision tree representations of multiple beam interference through layered materials.** Nodes represent interaction at a material interface, and bifurcations of each node represent the reflected and transmitted fractions of the field. Red indicates the incident field, grey indicates terminal regions. (a) In the case of $N=3$ materials, all bifurcations have a terminal node. There is only one traversal through the decision tree representing internal beam interference, and the system is analytically solvable as a Fabry-Perot (FP) cavity with a finite number of infinite geometric series. (b) Multiple beam interference for $N=5$ materials. For $N>3$ materials, there are an infinite number of traversals of the corresponding decision tree that cannot be modelled as a finite set of FP cavities, and so a different approach is required.

As above, consider a field propagating through N regions, where the thickness and phase factor of the k^{th} region are given by L_k and δ_k , and assume no energy is reflected back into the system from the first or N^{th} regions. For an incident field impinging normally from the first region, all possible trajectories begin with \tilde{t}_{21} (for simplicity in computation, the principal reflection term \tilde{r}_{12} is dropped, and is manually added later). Following entry, this wave will accumulate phase in region 2 ($e^{-\delta_2 L_2}$) before bifurcating into a reflected (\tilde{r}_{23}) and transmitted (\tilde{t}_{32}) branch. Each of these branches will then accumulate phase in regions 2 and 3, respectively, before both bifurcating further ($\tilde{r}_{23} \rightarrow \{\tilde{r}_{21}, \tilde{t}_{12}\}$ and $\tilde{t}_{32} \rightarrow \{\tilde{r}_{34}, \tilde{t}_{43}\}$). These new trajectories will accumulate phase and

bifurcate once more at the following interfaces, and so on. With each step, the decision tree grows exponentially larger (the tree size scales as 2^p for the p^{th} step, neglecting terminal nodes). Trajectories are terminated when energy exits and cannot be reflected back into the system, which occurs at terminal nodes $\{\tilde{t}_{12}, \tilde{t}_{N,N-1}\}$. The product of amplitude coefficients, phase factors, and propagation terms for the m^{th} traversal form a single term of the transfer function, TF_m , and the sum of all M traversals form the total transfer function for the k^{th} region:

$$TF_m^{(k)} = \text{Pr}_k \cdot \prod_{p=1}^P (\text{Ph}_p) \cdot (\tilde{c}_p) \quad (6.10)$$

$$TF^{(k)} = \sum_{m=1}^M TF_m^{(k)}$$

where Ph_p , Pr_k and \tilde{c}_p are the phase accumulation, propagation, and reflection/transmission coefficients for the p^{th} step of the m^{th} sequence in the k^{th} region given by Equations (6.6) – (6.8).

Equation (6.10) is the generalized form of TF computation. As an example, consider the blue trajectory of Figure 6.6(b) that terminates in Region 5. From Equation (6.10), tracing this trajectory through the corresponding traversal of the decision tree results in a single term of the transfer function for the final step of:

$$TF_m^{(5)} = e^{-\delta_5 \cdot [z - (L_1 + L_2 + L_3 + L_4)]} \cdot (e^{-\delta_1 L_1}) \cdot (\tilde{t}_{21} e^{-\delta_2 L_2}) \cdot (\tilde{t}_{32} e^{-\delta_3 L_3}) \cdot (\tilde{r}_{34} e^{-\delta_3 L_3})$$

$$\cdot (\tilde{r}_{32} e^{-\delta_3 L_3}) \cdot (\tilde{t}_{43} e^{-\delta_4 L_4}) \cdot (\tilde{t}_{54} e^{-\delta_5 L_5}).$$

Repeating this calculation stepwise for all traversals and for all N regions results in a transfer function characterizing the field modulation over the entire spatial domain of interest. For completeness, the incident and principal reflection terms that were previously neglected can then be manually added to the TF in the same format as Equation (6.10), as a zeroth term in Region 1

$$TF_0^{(1)} = e^{-\delta_1 z} + e^{-\delta_1 (L_1 - z)} \cdot (\tilde{r}_{12} e^{-\delta_1 L_1}).$$

In general, a binary decision tree is infinitely large. For $N = 3$, a significant simplification occurs: all tree bifurcations result in a terminal node (either \tilde{t}_{12} or \tilde{t}_{32}), as shown in Figure 6.6(a). and there exists only a single non-terminating trajectory representing multiple beam interference in the $k = 2$ region. There is then a finite number of traversals allowing one to model this region as a

Fabry-Perot (FP) cavity, as discussed in Section 6.2.2. This model utilizes the geometric series to obtain an analytic solution of the field distribution in all 3 regions, as outlined in [13].

When considering more than 3 regions, there are an infinite number of trajectories within the diverging decision tree, and the FP cavity model breaks down as shown in Figure 6.6(b). An arbitrary global time window, T_w , of sufficient length relative to the interaction duration, serves to truncate the number of steps and traversals of the decision tree by rejecting terms that fall outside of the causal window (i.e., waves that originate at time $t > T_w$ are not considered). This treatment is therefore quasi-analytic; While not formally analytic, the computational results are identical to an analytic treatment, as all waves that could possibly contribute to the transfer function are accounted for. The only discrepancies are terms that violate causality, and so these rejections are of no consequence.

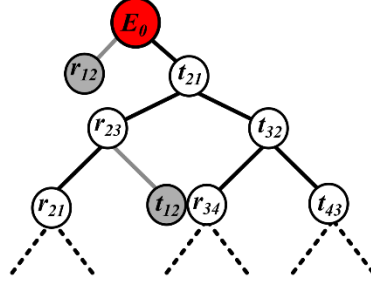
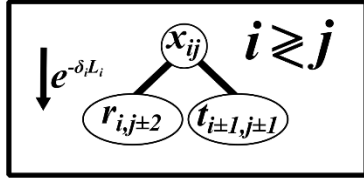
6.3.3 Recursive decision tree construction

All tree bifurcations can be constructed from summation of the basis “unit tree”, shown in Figure 6.7(a). The unit tree is a generalized node bifurcation according to the network’s stepping rules: Depending on wave propagation direction ($i > j$ or $i < j$), indices of the reflected branch update as $\{i, j\} \rightarrow \{i, j \pm 2\}$, and indices of the transmitted branch update as $\{i, j\} \rightarrow \{i \pm 1, j \pm 1\}$. Additionally, each step of a given traversal accumulates phase in the i^{th} region, given by $e^{-\delta_i L_i}$. With these stepping rules, the total set of tree traversals is generated recursively, as outlined in the pseudo-code of Figure 6.7(b).

Each step of a given traversal is represented by a state array $\{C, i, j, t_{d,i}\}$, where $C = R$ or T (branch type identifier), and $t_{d,i} = \text{Re}(\tilde{n}_i) \cdot L_i/c$ is the time debt associated with that step. All traversals are initialized with the array $\{T, 2, 1, 0\}$, representing energy transmitting into the system from Region 1. A function accepts this initial state as an input and creates two new state arrays, representing the reflected and transmitted branches as outputs. These updated states are logged, then re-inserted into the function as new inputs to be updated again into new reflected and transmitted tree branches. This recursion continues until the termination criteria are met, which occurs when energy exits the system at terminal nodes $\{\tilde{t}_{12}, \tilde{t}_{N,N-1}\}$ or when $\sum_i t_{d,i} > T_w$. The resulting finite set of sequences represents all possible waves traveling within the causal window T_w . The product of terms corresponding to the steps of a given sequence results in a single term of the transfer function, and the sum of terms from all sequences is the total transfer function for the corresponding region, as in Equation (6.10).

(a)

Network stepping algorithm



(b)

```

start = {T, 2, 1, 0} %initialize with energy entering system (t21)

All_sequences = traverse_decision_tree(start)

%recursive function:
function Sequences = traverse_decision_tree(sequence)

    if (i > j) %forward traveling

        seq{1} = traverse_decision_tree({R, i, j+2, cost}) %reflected branch
        seq{2} = traverse_decision_tree({T, i+1, j+1, cost}) %transmitted branch

    elseif (i < j) %backward traveling

        seq{1} = traverse_decision_tree({R, i, j-2, cost}) %reflected branch
        seq{2} = traverse_decision_tree({T, i-1, j-1, cost}) %transmitted branch

    end

    Sequences = [{sequence}, seq] %update network with new steps

end

```

Figure 6.7. Network step algorithm and pseudo-code for the recursion calculation that determines the set of all possible radiation paths from the decision tree model. (a) Block diagram of the algorithm stepping rules that dictates how indices of a reflected ($x \equiv r$) or transmitted ($x \equiv t$) node is updated, and generally depends on wave direction (positive when $i > j$, negative when $i < j$). Additionally, each step accrues a phase factor $\exp(-\delta_i L_i)$ for propagation in the i^{th} region. This diagram forms a basis that can be used to recursively construct decision trees for propagation through an arbitrary set of materials. (b) Pseudocode of recursive network determination. For a provided initial state array, `start`, the function `traverse_decision_tree()` generates two new tree branches according to the network stepping rules, and re-inserts the updated arrays as new inputs, which will each be updated again, etc. A given traversal is terminated when energy exits the system, or when a pre-defined cost function reaches a desired truncation threshold.

6.4 Terahertz pulse dose simulations

6.4.1 Comparison of dose model to transmission spectroscopy data

The dose model developed above can be validated by comparing measured sample-modulated pulse data from THz spectroscopy to the simulation predictions. Figure 6.8 shows a comparison of the simulated modulation to a measured THz pulse transmitted through two substrate materials introduced in Chapter 5 (0.17 mm fused silica with $n = 1.97$, and the Ibidi proprietary optical plastic with unknown properties) [14]. The black waveform in Figure 6.8(a) is the electro-optically sampled reference pulse with no material in the beam path, and the solid red is the measured pulse transmitted through the substrate. The corresponding power spectra are shown in Figure 6.8(b). While there is some discrepancy at lower SNR for $f > 1.5$ THz, the main features of the modulated pulse are well-characterized, including the temporal shift due to propagating through a higher-index material and the oscillations in frequency space due to pulse reflections in the acquired window. Figure 6.8(c) shows the simulated and measured transmission spectra (ratio of modulated to reference power spectra), highlighting the capability to capture the multiply-interfering waves that arise from the thin material. The blue transmission curves are a comparison to data for the proprietary Ibidi optical plastic slide (Cat. 80286), whose dielectric information was not known before-hand. Although the nominal thickness of the substrate is 0.18 mm [15], a manual fit to the oscillation period and amplitude of the transmission spectra determines a calculated thickness of 0.195 mm, with an effective refractive index of $n=1.5$ for the broadband THz pulse.

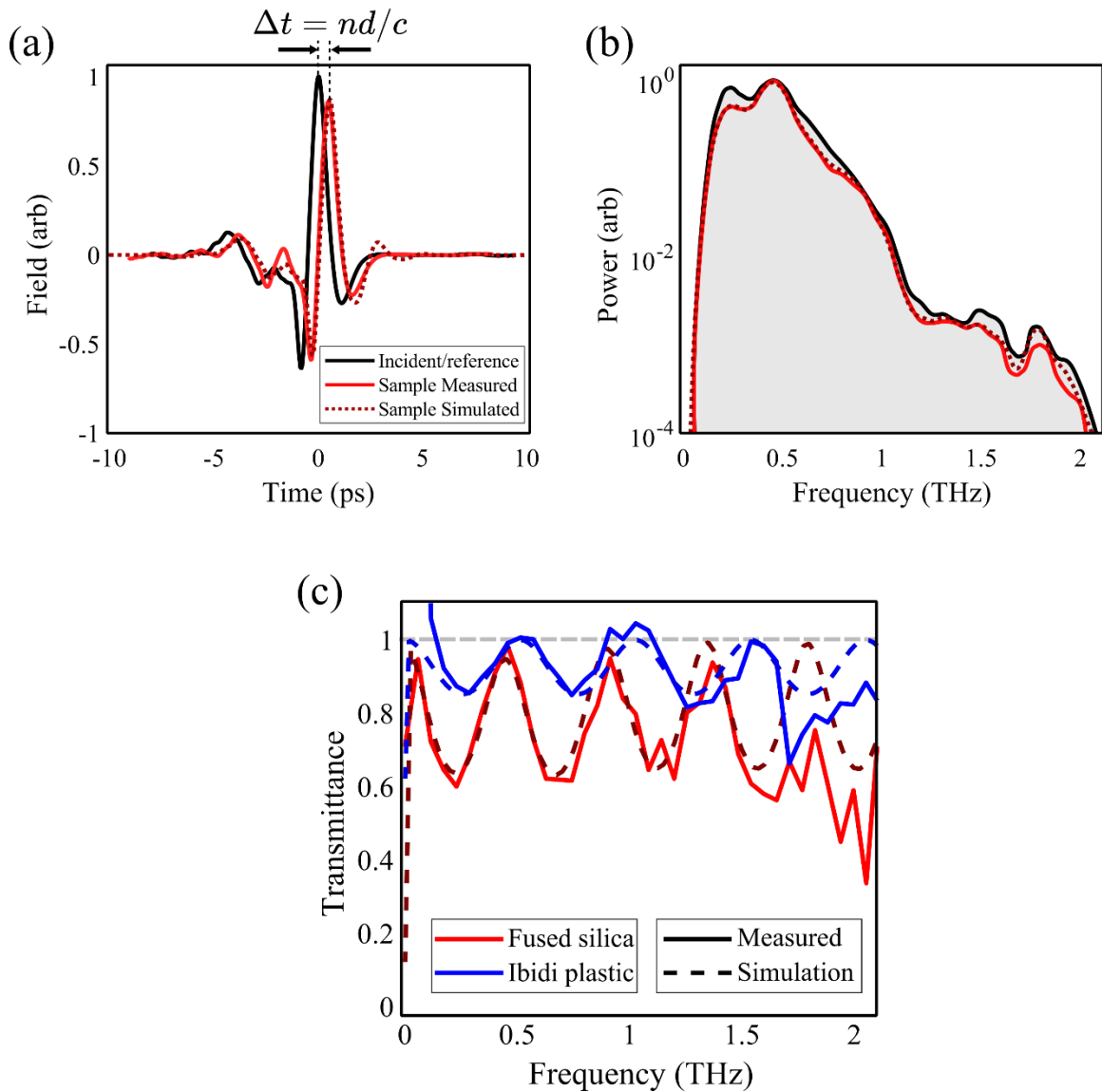


Figure 6.8. **Comparison of simulations to THz spectroscopy data.** (a) Comparison of simulated (dotted line) and measured (solid red line) THz pulses transmitted through 0.17 mm fused silica ($n=1.97$), with the measured incident pulse in black. The transmitted pulses are offset by $\Delta t = nd/c$ due to reduced wave speed in the quartz, $v = c/n$. (b) The simulated power spectrum is in good agreement with measurement, with slight discrepancy at higher frequencies with reduced SNR. (c) Transmission profiles are the ratio of the transmitted spectrum to the reference spectrum. The time and frequency domain representations are in good agreement, and the oscillation in the transmission profile due to interfering reflections is recovered. The blue data shows results of a manual fit to transmission data for the proprietary Ibidi optical plastic substrate to determine effective material parameters.

6.4.2 Simulation of terahertz biological exposure experiments

Three geometries were simulated that are commonly utilized in THz-biology exposure experiments: (1) Monolayer cells grown on a 0.195 mm transmissive plastic well (Ibidi, Cat. 80286) with aqueous media above; (2) Monolayer cells grown on a 0.17 mm fused silica coverslip and placed on a 1 mm thick glass microscope slide, with aqueous media above; and (3) Direct exposure of 1 mm thick tissue (multi-cellular layers), with aqueous media below. For the former two cases, the THz field must propagate through substrate materials before interacting with the thin sample region. In the latter case, the field is directly incident on the cellular population that is thick relative to the radiation wavelength.

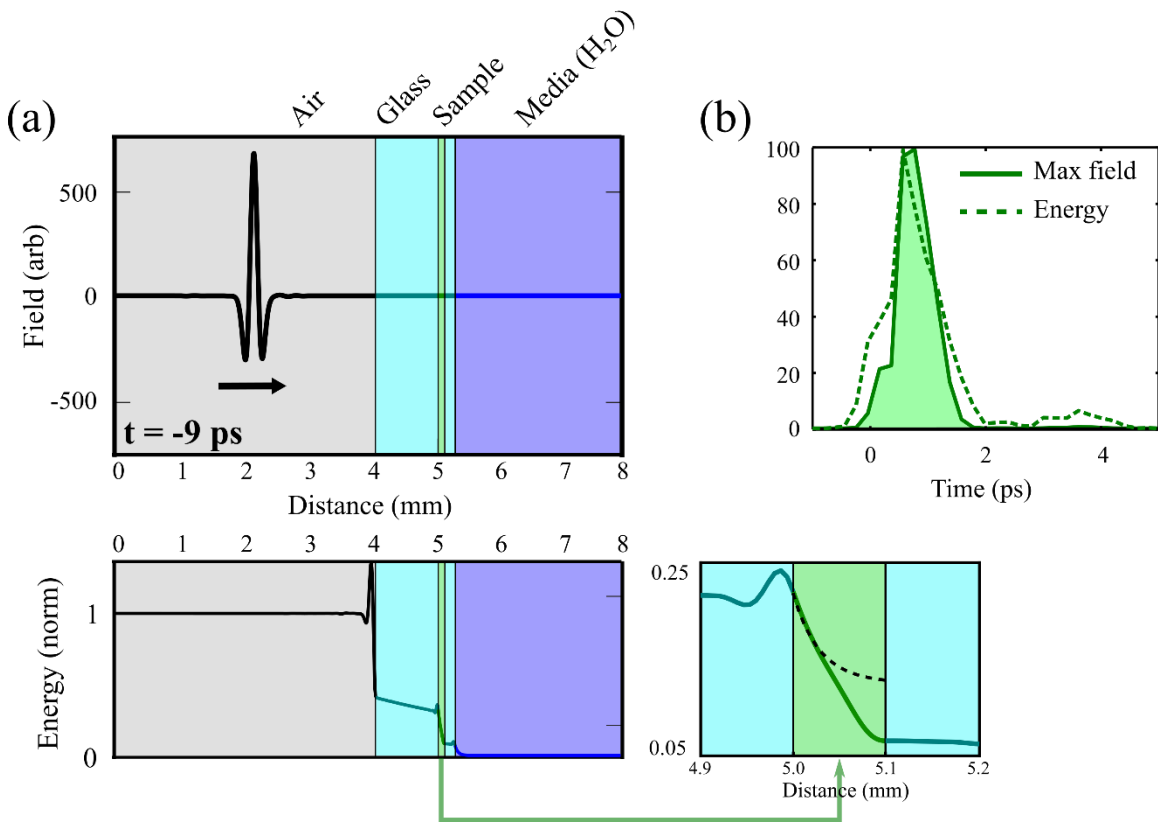


Figure 6.9. THz dosimetry simulation for exposure of cells through a 1 mm glass substrate, grown on a 0.17 mm fused silica coverslip, with aqueous media above. (a) The THz field in space before interaction with the biological sample (green), modelled as 100 μ m thick epithelial cells with data from [5]. Below is the total energy in space over the entire simulation duration ($T_H=30$ ps), showing boundary modulations and THz energy decay. The zoomed sample region highlights the simulated energy in the sample region, compared to pure exponential decay (black dashed line) to highlight the effect of coherent field modulation due to optically thin samples in complex dielectric environments. (b) The THz energy (dashed line) and peak field strength (solid line) in the sample region during the interaction that begins at $t=0$ ps.

Figure 6.9(a) shows an example simulation for geometry #2 listed above, with the THz exposure of cells (100 μm thick) through a 1 mm glass slide substrate, grown on a 0.17 mm coverslip with aqueous media above. For the sample region (green), the complex refractive index data of epidermis as measured in reference [5] are used. The aqueous media is assumed to have similar dielectric parameters as water. The total energy vs. space over the entire simulated duration is shown in the bottom plot, with emphasis placed on the sample region in the zoomed plot. THz pulse modulation in the sample region due to the surrounding materials significantly alters the THz pulse energy absorbed in the sample region, relative to a pure exponential decay (black dashed curve). Figure 6.9(b) shows the THz energy and maximum field strength in the sample region over the sample interaction duration. Results from similar simulations for all relevant exposure geometries in the sample regions ($L_{\text{sample}} = 100 \mu\text{m}$) are summarized in Table 6.1.

Table 6.1. **Results of simulation for varying bio-exposure geometries.** Maximum field and energy seen by the sample region in real bio-exposure experimental configurations. Integrals are normalized to tissue values, in which all energy is absorbed by the sample, and MBI effects are negligible.

Simulated geometry	Tree size	Interaction time	Peak field	Field integral	Energy integral
		(FWTM ps)		$\int E(t) dt$	$\int E(t)^2 dt$
3D tissue models	21	2.7	0.6695	1.000	1.0000
Monolayer cells in dish	643113	1.9	0.5970	0.6953	0.5634
Monolayer cells on glass slide	79418	1.9	0.5728	0.4356	0.4366

For the 3D tissue case, as the optical path length of the sample is large, only a small number of TF terms (i.e., the decision tree size) are relevant in the simulated window. This geometry absorbs virtually all of the transmitted THz pulse energy, and is therefore used as a reference for the two more complex geometries. For monolayer cell exposure cases, with thinner and more materials to consider, much larger decision trees (and thus more transfer function terms) are required to characterize the multiple interfering waves. The highest field is for the tissue case where the cells are directly exposed, seeing 67% of the incident field at the surface due to principal reflection loss. In addition to higher field and energy in the sample region, the thicker sample also corresponds to a larger interaction time and length in the sample region, which increases the total energy deposition (i.e., the “dose”) as shown in the last column of Table 6.1.

From these results, it is shown that the field and dose in the sample is modulated significantly from the expected values due to the geometry of surrounding materials during exposure. For monolayer cells in a plastic dish, the sample absorbed 56% of the estimated energy for each pulse, with a maximum field that is 60% of incident. For the glass slide substrate, the dose per pulse is

only 44% of nominal measurement, and the maximum field seen by the sample is 57% of incident. These results may be used to adjust the dosimetric parameters measured for biological exposure studies to accurately correlate observed biological effects to THz radiation exposure parameters. For example, when exposing monolayer cell samples on a plastic slide, the nominal average intensity (Equation (6.2)) should be scaled by 0.56, and the nominal peak field strength scaled by 0.60, to accurately characterize the THz field and dose in the sample region for this exposure configuration.

6.4.3 Transverse dose variation

An additional consideration is the variation of dose within the 2D Gaussian THz spot. The simulations presented above utilize either idealized functional forms of a THz pulse, or real THz pulse data as acquired by electro-optic sampling, and therefore represent the electric field variation and energy deposition characteristics near the center of the THz beam. However, for a realistic biological exposure experiment, a typical animal cell population will see a large variation in THz dose in space, as shown in the scaled overlay in Figure 6.10. Therefore, cells occupying the central region of the THz focus will be characterized by the dose adjustments discussed in Section 6.4.2, but the dose toward the edges of the THz spot must be adjusted by an additional dose factor given by the colourbar in Figure 6.10.

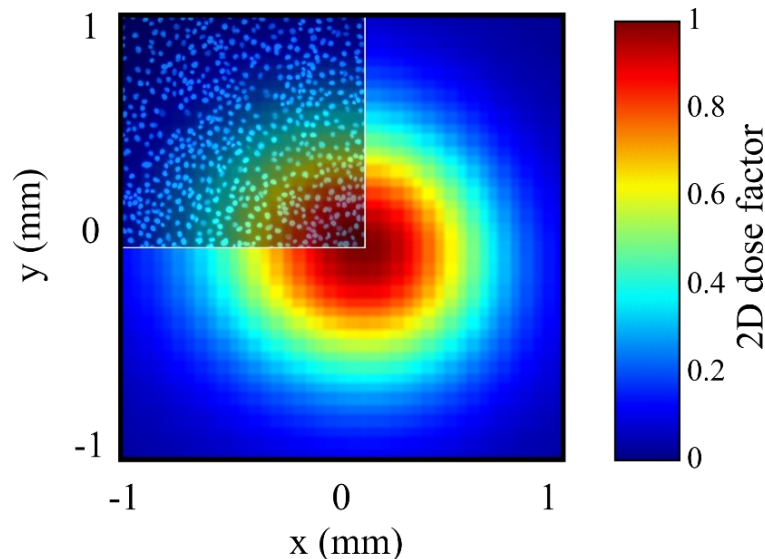


Figure 6.10. **Scale comparison of 2D THz dose variation vs. human epithelial cell size.** A-431 epithelial keratinocytes overlaid on a measured THz focus dose distribution. For a realistic exposure, dose adjustments presented in this chapter are accurate for cells near the centre of the focus, but an additional dose factor must be applied to account for intensity variation towards the fringes of the 2D dose distribution, given by the colourbar values.

6.5 Conclusion

In this chapter, THz interaction characteristics in typical biological exposure configurations were highlighted that render conventional non-ionizing dosimetry insufficient to capture the relevant interaction mechanisms. Further, boundary modulations in many optically thin materials were insufficiently treated by standard coherent models utilized in THz spectroscopy. Therefore, a simulation method inspired by coherent dielectric spectroscopy that captured the relevant THz interaction properties in many optically thin materials relevant for typical biological exposure studies was formulated. By modelling radiation propagation as a recursively-generated binary decision tree, a quasi-analytic transfer function is obtained that bypasses conventional limitations of optically thin samples, or many layers that are not simply modelled by cavity theory. Further, these simulations provide a guide for methods of controlling THz doses for free-space bio-exposure configurations of interest. For example, dose-enhancement in the sample region may be achieved with higher conductivity electrolytic media or gold-coated coverslips that increase reflected energy back into the sample region. Conversely, dose-diminution may be achieved by selecting materials of matched refractive indices to reduce back-reflected energy into the sample region. A table of dose adjustment factors was obtained (Table 6.1) for the exposure configurations utilized in this thesis project.

While the formalism presented was specifically applied to THz exposure dose modelling, the mathematical principles utilized and the results obtained are general, and may be equivalently applied to any type of coherent spatiotemporal field dynamics, as long as the relevant material properties are known. For example, this formalism may be applied for theoretical modeling of B1 transmit fields in magnetic resonance imaging/spectroscopy, or mechanical waves in ultrasound imaging, as long as the magnetic or acoustic impedances (respectively) are known.

6.6 References

- [1] F. H. Attix, Introduction to Radiological Physics and Radiation Dosimetry, New York, NY: John Wiley and Sons, Inc, 1986.
- [2] F. Khan, The physics of radiation therapy, Philadelphia, PA: Lippincott Williams & Wilkins, 2003.
- [3] International Commission on Non-Ionizing Radiation Protection, "ICNIRP Guidelines for limiting exposure to time-varying electric, magnetic and electromagnetic fields (up to 300 GHz)," *Health Physics*, vol. 74, no. 4, pp. 494 - 522, 1998.

- [4] B. Dörschel, D. Hermsdorf, S. Pieck, S. Starke and H. Thiele, "Thickness measurements on cell monolayers using CR-39 detectors," *Nuclear Instruments and Methods in Physics Research B*, vol. 187, no. 4, pp. 525 - 534, 2002.
- [5] E. Pickwell, B. Cole, A. Fitzgerald, M. Peppe and V. Wallace, "In vivo study of human skin using pulsed terahertz radiation," *Physics in Medicine and Biology*, vol. 49, no. 9, pp. 1595-1607, 2004.
- [6] J. Neu and C. A. Schmuttenmaer, "Tutorial: An introduction to terahertz time domain spectroscopy (THz-TDS)," *Journal of Applied Physics*, vol. 124, no. 23, 2018.
- [7] K. I. Zaytsev, I. N. Dolganova, N. V. Chernomyrdin, G. M. Katyba, A. A. Gavidush, O. P. Cherkasova, G. A. Komandin, M. A. Shchedrina, A. N. Khodan, D. S. Ponomarev, I. V. Reshetov, V. E. Karasik, M. Skorobogatiy, V. N. Kurlov and V. V. Tuchin, "The progress and perspectives of terahertz technology for diagnosis of neoplasms: a review," *Journal of Optics*, vol. 22, no. 013001, pp. 1 - 44, 2020.
- [8] P. Jepsen and H. Merbold, "Terahertz Reflection Spectroscopy of Aqueous NaCl and LiCl Solutions," *Journal of Infrared, Millimeter, and Terahertz Waves*, vol. 31, no. 4, pp. 430-440, 2010.
- [9] P. Jepsen, D. Cooke and M. Koch, "Terahertz spectroscopy and imaging - Modern techniques and applications," *Laser and Photonics Reviews*, vol. 5, no. 1, pp. 124-166, 2011.
- [10] J. Sun and S. Lucyszyn, "Extracting Complex Dielectric Properties From Reflection-Transmission Mode Spectroscopy," *IEEE Access.*, vol. 6, pp. 8302-8321, 2018.
- [11] L. Duvillaret, F. Garet and J. -L. Coutaz, "Highly precise determination of optical constants and sample thickness in terahertz time-domain spectroscopy," *Applied Optics*, vol. 38, no. 2, pp. 409 - 415, 1999.
- [12] E. Pickwell, B. E. Cole, A. J. Fitzgerald, V. P. Wallace and M. Pepper, "Simulation of terahertz pulse propagation in biological systems," *Applied Physics Letters*, vol. 84, no. 12, pp. 2190 - 2192, 2004.
- [13] E. Hecht, *Optics*, Essex: Pearson Education, 2017.
- [14] M. Naftaly and R. Miles, "Terahertz Time-Domain Spectroscopy for Material Characterization," *Proceedings of the IEEE*, vol. 95, no. 8, pp. 1658 - 1665, 2007.
- [15] The Ibidi Company, "Instructions u-Slide 2 Well (PDF) V3.1," Ibidi, 2020.

7 Tissue-level effects: Dysregulation of cancer-related signaling pathways in human skin tissue models

“What we lack in knowledge, we make up for in data.”

– Ethem Alpaydin

A version of this chapter has been published in two articles:

C. M. Hough, D. N. Purschke, C. Huang, L. V. Titova, O. V. Kovalchuk, B. J. Warkentin, and F. A. Hegmann, “Topology-Based Prediction of Pathway Dysregulation Induced by Intense Terahertz Pulses in Human Skin Tissue Models,” *Journal of Infrared, Millimeter, and Terahertz Waves*. vol. 39, no. 034004, pp. 887 – 898, 2018.

C. M. Hough, D. N. Purschke, C. Huang, L. V. Titova, O. V. Kovalchuk, B. J. Warkentin, and F. A. Hegmann, “Intense terahertz pulses inhibit *Ras signaling* and other cancer-associated signaling pathways in human skin tissue models,” *Journal of Physics: Photonics*. vol. 3, no. 034004, pp. 1 – 14, 2021.

7.1 Introduction

It is useful to begin the discussion of biological effects in skin by establishing the tissue scale of structure within the larger hierarchy of biological organization that was introduced in Table 1.3 in Chapter 1 [1, 2]. *Molecules* refers to systems of atoms or ions, and in biological contexts may be simpler molecular structures, such as water or guanosine triphosphate (GTP), or more complex macromolecular structures, such as proteins or DNA, that form the structural underpinnings of complex *cells*, recognized as the fundamental unit of a “living” system. Interacting *cellular* systems comprise *tissues*, which are the structural components of *organs*, and in turn *organisms*. In general, processes in lower-level structural systems regulate function observed in higher-level systems. This thesis reports investigations of the three highlighted levels in Table 1.3, and this chapter begins with the largest scale investigating effects in human skin tissue.

In this chapter, tissue-level biological effects of intense terahertz (THz) pulses in skin are investigated via bioinformatics “big data” approaches. Genomics databases such as the Kyoto

Encyclopedia of Genes and Genomes (KEGG) and the Gene Ontology (GO) Consortium are used to analyze differential gene expression measurements induced by THz exposure [3, 4], and modern algorithms for statistical over-representation and signal pathway perturbation analyses are applied to determine the cancer-related signaling processes that are likely to be dysregulated [5]. Importantly, several pathways that are commonly implicated in the initiation, development, and progression of cancer are predicted to be dysregulated by exposure to intense THz pulses. Downregulation of important oncogenes (e.g., Ras) and predicted suppression of pro-mitotic signaling are discussed in the context of potential therapeutic mechanisms of THz radiation.

First, general descriptions of signaling pathways as regulators of cellular function are provided. Processes regulated by the *Ras* and *Calcium signaling* pathways in human skin are discussed in anticipation of THz-induced signaling dysregulation to these networks. Section 7.3 describes our experiments of 3D human skin tissue exposed to extended trains of intense THz pulses. Global differential gene expression profiles are measured with fluorescent microarrays for varying THz intensities, and from these data, signaling pathways that are likely to be dysregulated are identified by utilizing known gene/protein interaction characteristics from the queried database information. Particular attention is paid to pro-mitotic and pro-inflammatory signaling pathways that are often implicated in human cancer. Genes that predominantly drive THz-induced dysregulation are identified, and transcript-level (i.e., mRNA) sources of dysregulation to cancer-related processes in skin are reduced from 1681 potential candidates to a subset of only 88. Results from these analyses provide a list of specific targets for designing investigative assays for mechanistic studies that are more practical than global transcriptomics; such studies represent the best candidates for understanding the biological mechanisms underlying THz-induced dysregulation of pro-mitotic and pro-inflammatory signaling in human skin.

7.2 Signaling pathways in cancer

In cellular systems, signaling pathways are a series of biochemical interactions that serve to communicate changes to or within the cellular environment in order to regulate higher-level biological function [6, 7]. For example, extracellular ligands such as growth factors may bind to a receptor protein in the cell membrane, initiating a conformational change that facilitates protein binding/activation through the intracellular space that eventually activates transcription factors in the nucleus. Abnormal activity of signaling pathways is associated with diseases such as cancer, and controlled modulation of signaling pathways is an effective method of treatment for certain genetic disorders [8, 9, 10].

Signaling pathways can be represented as network graphs, in which each node represents a gene/protein, and the edges represent the empirically determined interaction characteristics between relevant signaling proteins [11, 12]. This representation allows for prediction of the pathways and processes likely to be affected by an external agent (e.g., THz irradiation) from measurement of changes to the cellular system's gene expression profile [3, 13]. As demonstrative examples, two pathways of particular relevance to cancer research and therapy are described, the *Ras signaling* and *Calcium signaling* pathways.

7.2.1 *Ras signaling in cancer*

The *Ras signaling* network is a ubiquitous and highly conserved pathway in almost all eukaryotic cells, and regulates proliferation, survival, growth, migration, and differentiation [10, 14, 15]. The Ras protein, a membrane-bound small GTPase of which there are three dominant forms (KRAS, NRAS, and HRAS), is a central node that regulates mitotic signal transduction by acting as a binary molecular switch to regulate *Ras signaling* activity.

The process of Ras activation is shown in Figure 7.1(a) [16, 17]. An extracellular growth factor (e.g., epidermal growth factor [EGF], or tumor growth factor α [TGF α]) binds to an epidermal growth factor receptor (EGFR), inducing a conformational change in the membrane protein structure, allowing trans-phosphorylation of intracellular EGFR domains that create a binding site for the Gab protein at the inner leaflet of the cell membrane. Son-of-sevenless (SOS) may then bind and convert inactive RAS-GDP to active RAS-GTP, which may then recruit downstream signaling targets, and initiate biochemical regulation of a wide variety of processes as shown in Figure 7.1(b).

Due to this pathway's generalized mitotic function, it is one of the most commonly implicated pathways in the development of many human cancers [14]. Approximately 30% of all human cancers and 25% of melanomas are associated with a mutation in the central Ras protein [10, 14]. These mutations allow Ras to acquire resistance to hydrolysis by GTPase-activating proteins (the switch's "off" signal), leading to perpetual pro-mitotic signaling that is a key feature in malignant transformation and metastatic invasion. For this reason, Ras and the related signaling components have been a key focus of cancer drug discovery research, with an emphasis on identifying and characterizing agents that inhibit the proliferative activity of Ras and the pathway's related signaling molecules [10, 14, 15].

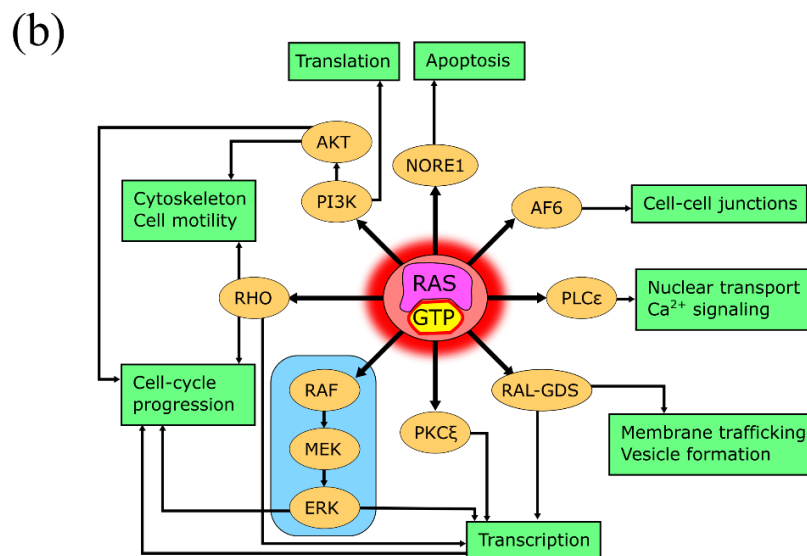
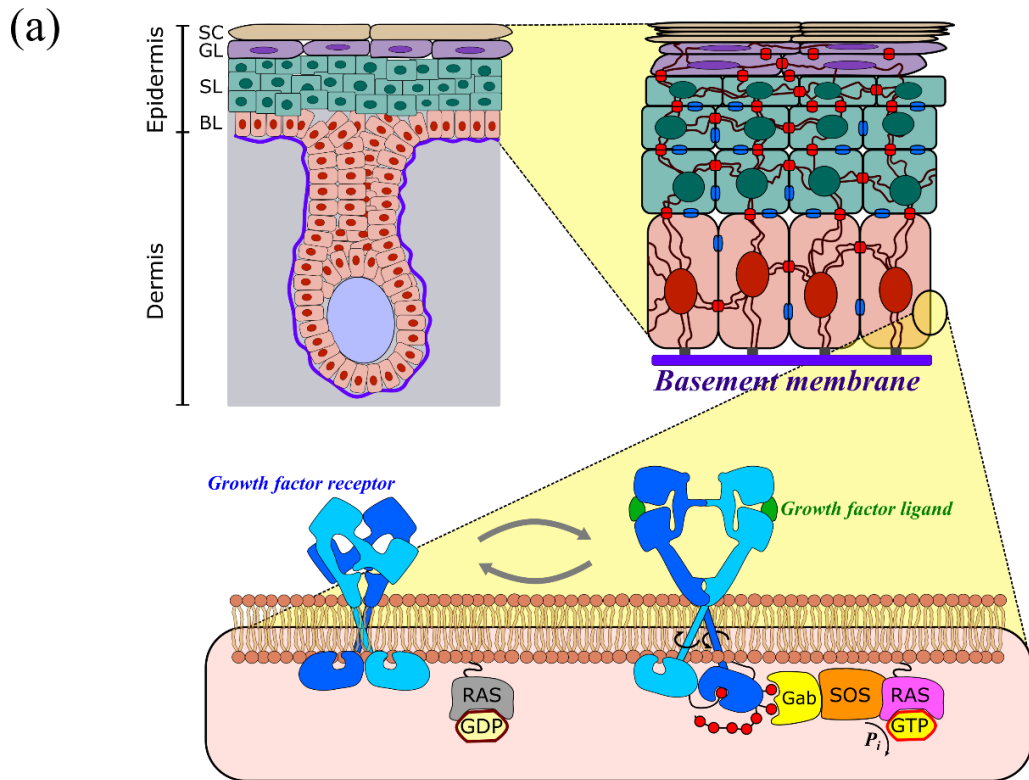


Figure 7.1. **Membrane-regulated Ras signaling activation and associated processes.** Adapted from [16, 18, 19]. (a) The epidermal layer of skin tissue is comprised of stratified layers of squamous epithelial keratinocytes (SC=stratum corneum, GL=granular layer, SL=squamous layer, BL=basal layer) latched to the basement membrane substrate for structural stability. Epidermal differentiation is partially regulated by the *Ras signaling* pathway, which is activated by a dimerized epidermal growth factor receptor (EGFR) binding to a growth factor ligand, inducing conformational change that provides binding sites for Ras activation via GTP binding. (b) Activated (GTP-bound) Ras regulates a diverse set of functions (green boxes) via binding to various downstream targets (circles). The canonical RAS-RAF-MEK-ERK axis (blue box) is one of the most well-characterized cellular differentiation and division pathways, and a popular target for anti-cancer therapy.

7.2.2 *Calcium signaling in cancer*

Of additional interest is the THz effect on the *Calcium signaling* pathway, as calcium ions (Ca^{2+}) are one of the most potent second messenger particles in biological systems. In this pathway, Ca^{2+} binds and activates calcium-binding proteins (CBPs) that regulate a diverse set of general cellular functions, including protein signaling, metabolism, enzyme function, cytoskeletal dynamics, proliferation, and apoptosis [20, 21]. In skin, epidermal differentiation is tightly regulated by a strong calcium gradient across the epidermis that triggers sequential expression of structural/binding proteins for stability and formation of the skin barrier. However, Ca^{2+} ions may also bind and activate CBPs that drive tumor growth and metastasis through oncogene activation or dysregulated proliferation, apoptosis, adhesion, or morphology. Control of calcium signaling dynamics has therefore attracted significant interest as a potential target for novel cancer therapies [21, 22].

The following experiments report intense-THz-pulse-induced gene expressions in human skin tissue that are predicted to suppress the signaling dynamics of these, and related, signaling pathways. The predicted suppression of pro-mitotic pathways that are often mutated or over-active in human cancer implies a potential therapeutic mechanism of THz radiation.

7.3 **Differential gene expression and signaling pathway dysregulation in human skin tissue induced by intense terahertz pulses**

7.3.1 *Methods*

7.3.1.1 *Generation and detection of intense THz pulses*

As introduced in Chapter 4, a 1 kHz train of single-cycle, picosecond-duration THz pulses was generated by optical rectification of infrared laser light ($\lambda_0 = 800$ nm) in lithium niobate [23], followed by black polyethylene to filter residual infrared/visible wavelengths. The pulse energy and spatial intensity distribution were measured with a pyroelectric detector (Spectrum Detector, SPJ-D-8) and camera (Electrophysics, PV320), respectively. The temporal waveform was detected by free-space electro-optic sampling in GaP. The peak electric field was calculated by calibration to dielectric properties of the $L = 200$ μm GaP detection crystal ($n_0 = 3.18$, $r_{41} = 0.88 \times 10^{-12}$ m/V) as [24]

$$E_{THz} = \frac{\lambda_0}{2\pi n_0^3 r_{41} t_{GaP}} \cdot \sin^{-1} \left(\frac{\Delta I}{2I_0} \right) \quad (7.1)$$

where $t_{GaP}=0.46$ is the GaP transmission coefficient and $\Delta I/2I_0$ is the measured peak modulation of the electro-optic signal, as described in Chapter 3. Equation (7.1) was used for the highest field calculation before the system was aligned for biological exposure, and lower field strengths were determined by scaling as the square root of the pulse energy, which was verified to be accurate for these studies. Five exposure conditions were used by attenuating THz transmission through crossed wire-grid polarizers, resulting in pulse energies of 0.03 – 2.4 μJ , peak electric fields of 27 – 240 kV/cm, and a measured spot size ($1/e^2$) of $1.6 \times 2.7 \text{ mm}^2$ (additional details are provided in Table 7.1). The THz pulse and spatial intensity distribution for the highest intensity pulse are shown in Figure 7.2(a), and the corresponding frequency spectrum is shown in Figure 7.2(b).

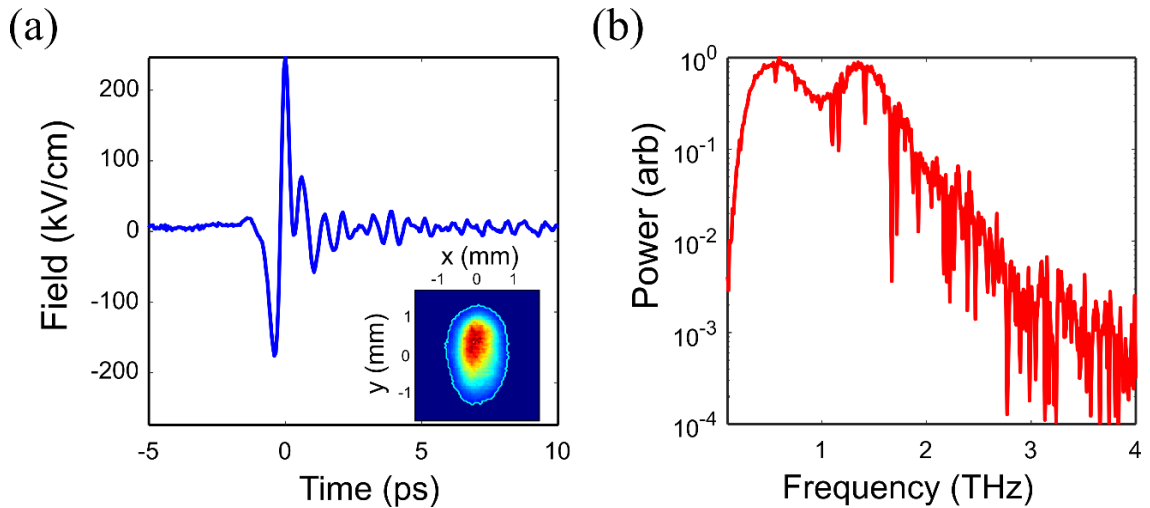


Figure 7.2. **Waveform and spectrum for the highest intensity THz pulse for skin tissue exposures (2.4 $\mu\text{J}/\text{pulse}$, 240 kV/cm, 74 MW/cm^2).** (a) THz pulse electric field waveform at the beam focus. *Inset:* Intensity profile at the beam focus. The cyan outline represents the $1/e^2$ boundary – $1.5 \times 2.6 \text{ mm}^2$. (b) Corresponding power spectrum of the THz pulse. The peak-power frequency is 0.6 THz and the bandwidth is 1.8 THz FWTM.

Table 7.1. **THz pulse parameters for each exposure condition**

Index	Pulse Energy (μJ)	Peak Field (kV/cm)	Average Intensity (mW/cm^2)	Pulse Intensity (MW/cm^2)	Total Dose (J/cm^2)
1	0.03	26.9	0.9	0.9	0.6
2	0.10	49.1	3.1	3.1	1.8
3	0.94	150.5	28.9	28.9	17.4
4	1.45	186.9	44.6	44.6	26.8
5	2.40	240.5	73.8	73.8	44.3

7.3.1.2 *Preparation of skin tissue samples*

Full-thickness 3D human skin tissue models were acquired from the MatTek Corporation (EpidermFT, <https://www.mattek.com/products/epidermft>). These are a stratified co-culture of normal epidermal keratinocytes and dermal fibroblasts in a collagen matrix, and interact to form a mitotically and metabolically active 3D model of human skin. 3D tissue models have significant advantages over 2D cell monolayers as they allow the study to probe effects that arise due to more realistic intercellular interaction, cell-extracellular matrix interaction, and the impact of the micro-environment [25]. Upon delivery, tissue wells were transferred to 2.5 mL of pre-warmed media (DMEM, 10% FBS, 1X penicillin/streptomycin). The proprietary wells allow the tissue to absorb media from below through a porous membrane, leaving the epidermal layer exposed to air. This is particularly advantageous for THz exposure experiments, as this system allows for direct tissue exposure and bypasses constraints of attenuation losses when exposing through substrates or cell media. Tissues were incubated in this state for 16 hours for re-equilibration.

Tissue wells were removed from the incubator and placed vertically in a custom sample holder. To ensure precision of sample placement, the sample holder was first fit with a 1 mm alignment aperture and translated with a 3D linear stage such that THz energy was maximized, as described in Chapter 5. The tissue well was then mounted into the holder such that the epidermal surface was coincident with the pinhole, ensuring the centre of the tissue surface was repeatably coincident with the THz focus, allowing accurate determination of the exposed region.

7.3.1.3 *Terahertz exposure of skin tissue wells*

The THz beam was focused to the centre of the epidermal layer for 10 minutes. The average temperature increase in the irradiated region on the surface of these samples as measured with a thermal imager (Reed Instruments, R2100) was less than 1 K, and these are benchmarked with similar measurements in a pure water reference environment. Following exposure, wells were transferred to fresh, pre-warmed media, and returned to the incubator for 30 minutes to allow for acute (early) response of THz-induced gene expression. To isolate the variation of THz pulse energy as the sole independent variable, similar exposure and fixing times as previous investigations were chosen [26, 27]. The biochemical indicators of this response were fixed via snap-freezing in liquid nitrogen and transferring on dry ice to -80°C storage. This process was repeated for five different sets of THz pulse parameters (Table 7.1) and one identical sham-exposed

condition with the THz beam fully blocked. Each condition (5 exposed + 1 sham) was performed in quadruplicate for a total of 24 tissue samples.

7.3.1.4 Whole-genome expression profiling

The exposed region of the frozen tissue samples was excised with a 1.5 mm diameter sterile punch tool aligned to the centre of the tissue wells to ensure only the THz-exposed cells were analyzed. The workflow for measuring global differential gene expression is outlined in Figure 7.3. Total RNA was isolated (Zymo Research, Irvine), and UV spectroscopy quantified RNA quality and integrity, as per the manufacturers' instructions (NanoDrop, Wilmington, DE; Agilent 2100 Bioanalyzer, Santa Clara, CA). Amplified cDNA was labelled (Encore Biotin, IL) and hybridized to the HumanHT-12_v4 Whole Genome Expression BeadChip Arrays (Illumina). Differential gene expression and corresponding *p*-values were determined from the fluorescence measurements (iScan & BeadStudio, Illumina). *P*-values were corrected for multiple hypothesis testing via the false discovery rate (FDR) method. Data was corrected for batch effects via the ComBat algorithm [28]. Significantly differentially expressed genes were identified by conventional significance thresholds ($|\text{Log}_2(\text{Expression ratio})| > 0.58$ and $p < 0.05$). These data are used as inputs for the over-representation and pathway level analyses, described in the following sections.

7.3.1.5 Over-representation analysis – Gene Ontology

Gene ontology (GO) analysis attempts to utilize differential gene expression data to answer three questions: (1) What *biological processes* are THz-affected genes associated with? (2) What *molecular functions* are responsible for these processes? (3) What *cellular components* are involved? Lists of gene sets that regulate known biological processes, cellular components, and molecular functions were obtained from the Gene Ontology Consortium [4], a database of GO terms that contains nested sets of genes for given processes, structures, and functions.

Each GO term is uniquely identified by its GO ID, and contains the corresponding gene set that regulates the associated process, function, or component. The goal of GO analysis is to identify statistical over-representation of THz-affected genes within various biological processes, cellular components, and molecular functions, relative to the expected global background. Thus, all gene sets available from the GO consortium are checked against the genes that were identified by the microarray measurements as being significantly differentially expressed by intense THz pulses.

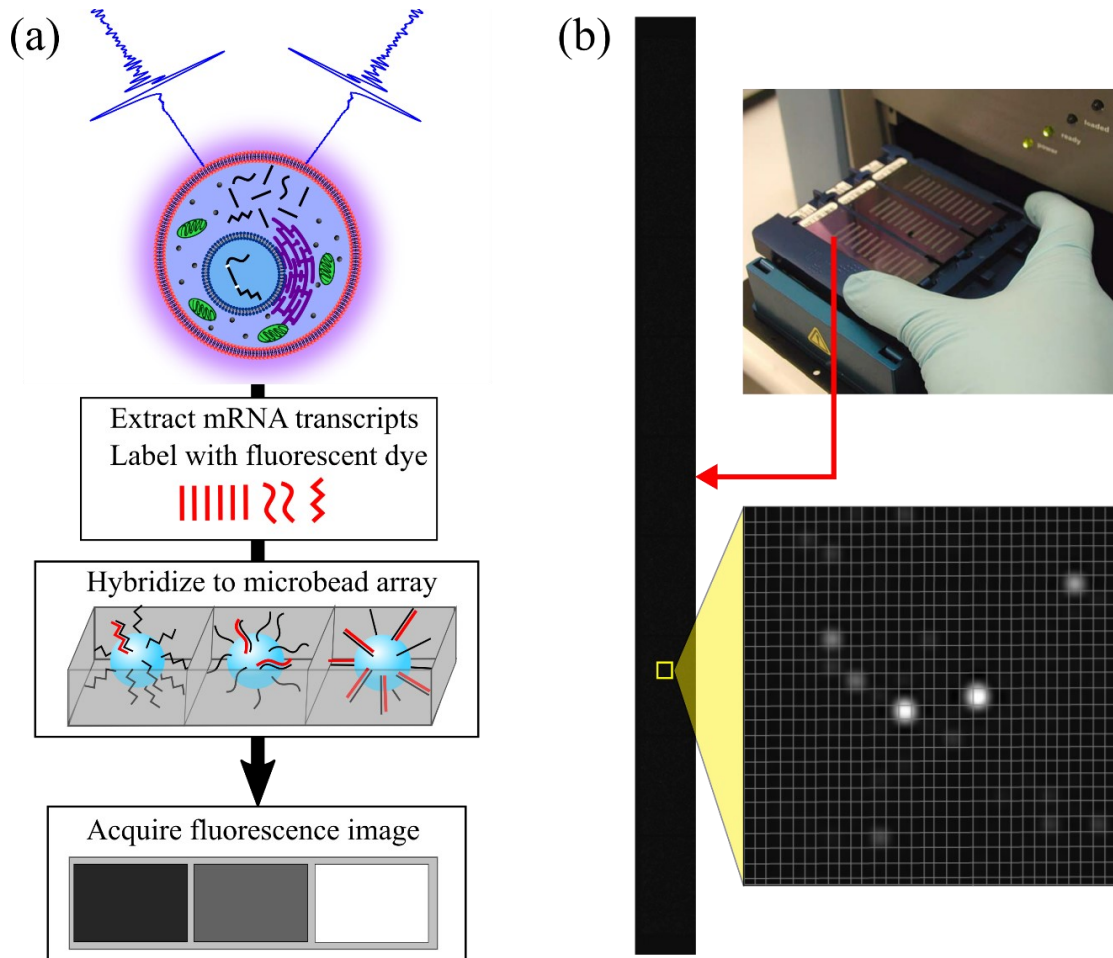


Figure 7.3. **Measurement of global differential gene expression with cDNA microarrays.** (a) Generalized steps in preparing the fluorescent DNA microarray. For illustration purposes, cells are shown with an artificially simplified genome – one chromatin fiber and 3 genes. Tissues are exposed to THz radiation, and altered gene expressions are activated to respond to the external stimulus. Messenger RNA (mRNA, i.e., gene transcripts) are extracted from the cells, labelled with a fluorescent molecule, and hybridized to an array of microbeads with probes that bind to all genes in the considered genome. A fluorescence image of the microbead array is acquired, and the intensity is related to the concentration of the corresponding mRNA transcript. Comparison of fluorescence signals between control and exposed populations is used to characterize the differential gene expression levels of the global genome. (b) A fluorescence image of a microbead array (vertical black bar) with ~47,000 human genome probes for transcript binding. The photo at top right shows a total of 36 microbead array (12 arrays each on 3 chips). Each gene is uniquely identified by its bead location, and the fluorescence intensity (see zoomed image) is related to the bound transcript concentration.

To perform the GO analysis, a contingency table is first constructed for each GO term, as demonstrated in Table 7.2.

Table 7.2. **Contingency table for GO over-representation analysis.** The symbols A, B, C, and D, represent number of genes in each category for a given GO term.

	In GO term	Not in GO term	Row total
THz-affected	A	B	A+B
THz-unaffected	C	D	C+D
Column total	A+C	B+D	A+B+C+D

Statistical over-representation may be expressed in terms of the odds-ratio, *OR*, calculated as

$$OR = \frac{A/B}{C/D} \quad (7.2)$$

where the numerator represents the odds of finding a THz-affected gene in the given GO term, and the denominator represents the odds of finding a THz-unaffected gene (i.e., a gene that did not meet significance criteria). The *p*-value associated with each *OR* is calculated from binomial coefficients

$$p = \frac{\binom{A+B}{A} \binom{C+D}{C}}{\binom{A+B+C+D}{A+C}} \quad (7.3)$$

and are adjusted for multiple hypothesis testing via the FDR method. GO terms for which $OR > 1$ and adjusted $p < 0.01$ are considered significantly over-represented within the set of THz-affected genes, and represent biological processes, structures, or functions that may be expected to be dysregulated, based on THz-induced gene expression measurements.

Gene set databases for biological processes, cellular components, and molecular functions are queried with an R-script using the R/BioConductor platform [29]. Upregulated and downregulated genes are analyzed separately, which increases the statistical power of GO associations [30]. Terms that are obsolete or did not contain any similar genes as the global THz dataset in control probes were removed, and the above statistical analysis was performed by applying Fisher's exact one-sided test to each contingency table constructed as in Table 7.2 for each GO term, via the R function `fisher.test(Table, alternative = "greater")`.

7.3.1.6 Signal pathway perturbation analysis – *ROntoTools*

While GO analyses provide broad associations based on significant genes, they do not account for direction of gene expression (i.e., upregulated vs. downregulated), nor interactions with other related genes. For these characterizations, signaling pathway models, such as Signal Pathway Impact Analysis (SPIA) may be used. These analyze gene expression data in the context of interactions within a specified signaling process, accounting for known interactions between related signaling proteins.

Pathway IDs, associated gene lists, and pathway topology information (i.e., interaction characteristics) were obtained from the Kyoto Encyclopedia of Genes and Genomes (KEGG) [3]. Pathways were filtered for relevance to human cancer (KEGG categories include *Environmental Information Processing*, *Cellular Processes*, *Organismal Systems*, and *Human Diseases*). Signal pathway perturbation analysis was performed with the R/Bioconductor package *ROntoTools* [5, 31]. This algorithm combines conventional over-representation analysis with modern topology-based analyses that additionally account for the magnitude and direction of gene expression (upregulation vs. downregulation), as well as how genes interact within a given signaling network. This results in a prediction of the perturbation status (activation vs. inhibition) of considered pathways, and provides information regarding potential phenotypic endpoints likely to be induced by intense THz pulses based on the gene expression measurements.

The workflow of Signal Pathway Impact Analysis (SPIA) is outlined in Figure 7.4. Initial perturbations as measured by gene expression profiles are propagated through signaling networks that regulate known biological functions, taking into account the interactions (edges) between each gene (node). For each gene, g_i , in the network, a perturbation factor $PF(g_i) = \alpha \cdot \Delta E(g_i) + A(g_i)$ is assigned, where $\Delta E(g_i)$ is the measured differential gene expression ratio (log-transformed), and the accumulated perturbation is estimated from upstream perturbation factors as

$$A(g_i) = \sum_{j < i} \beta_{ij} \cdot \frac{PF(g_j)}{N_{ds}} \quad (7.4)$$

where β_{ij} describes the interaction direction between the i^{th} and j^{th} gene in the network (+1 for activation/anti-inhibition, -1 for inhibition/anti-activation, or 0 for no interaction), N_{ds} is the number of genes downstream of g_j , and the sum index of ' $j < i$ ' indicates that signaling perturbation

may only come from upstream nodes. α is a p -value-based weighting factor that allows for cut-off free analysis (COFA) as discussed in the Appendix [32]. All network nodes are sequentially assigned a value of $A(g_i)$, and from this, a total accumulated perturbation score $A_{tot} = \sum_i A(g_i)$ is determined for the considered pathway, along with associated p -values adjusted for multiple hypothesis testing. Significantly perturbed pathways ($p < 0.05$) are considered dysregulated by the relative magnitude, A_{tot} . Positive (negative) values of A_{tot} imply the associated pathway activity is increased (decreased) by intense THz pulses.

7.3.1.7 Identification of “terahertz targets”

Not all genes differentially regulated by THz pulses (or any agent) affect a pathway uniformly. For example, in a given pathway, a node with many downstream effectors (i.e., a greater number of edges extending *from* the node) is more “important” for signal proliferation, and induced perturbation, $A(g_i)$, of the node will contribute to the total accumulated perturbation, A_{tot} , more so than genes with relatively few downstream effectors [5, 31]. Moreover, a single gene may have distinct regulatory roles across multiple pathways. Hence, signaling pathways in nature are rarely separate closed systems, but rather there is a potentially large degree of cross-talk between sets of pathways that share common signaling proteins. It is therefore of interest to identify the genes that are both differentially expressed by THz and also significantly drive pathway dysregulation, accounting for inter-pathway crosstalk between signaling systems containing common nodes. These represent genes that most significantly drive THz-induced changes of signaling processes in human skin, and are the best candidates for determining the gene-level mechanisms that lead to the predicted THz-induced effects to cancer-related signaling. These provide a convenient roadmap to motivate future hypotheses and experiments in THz-cancer research.

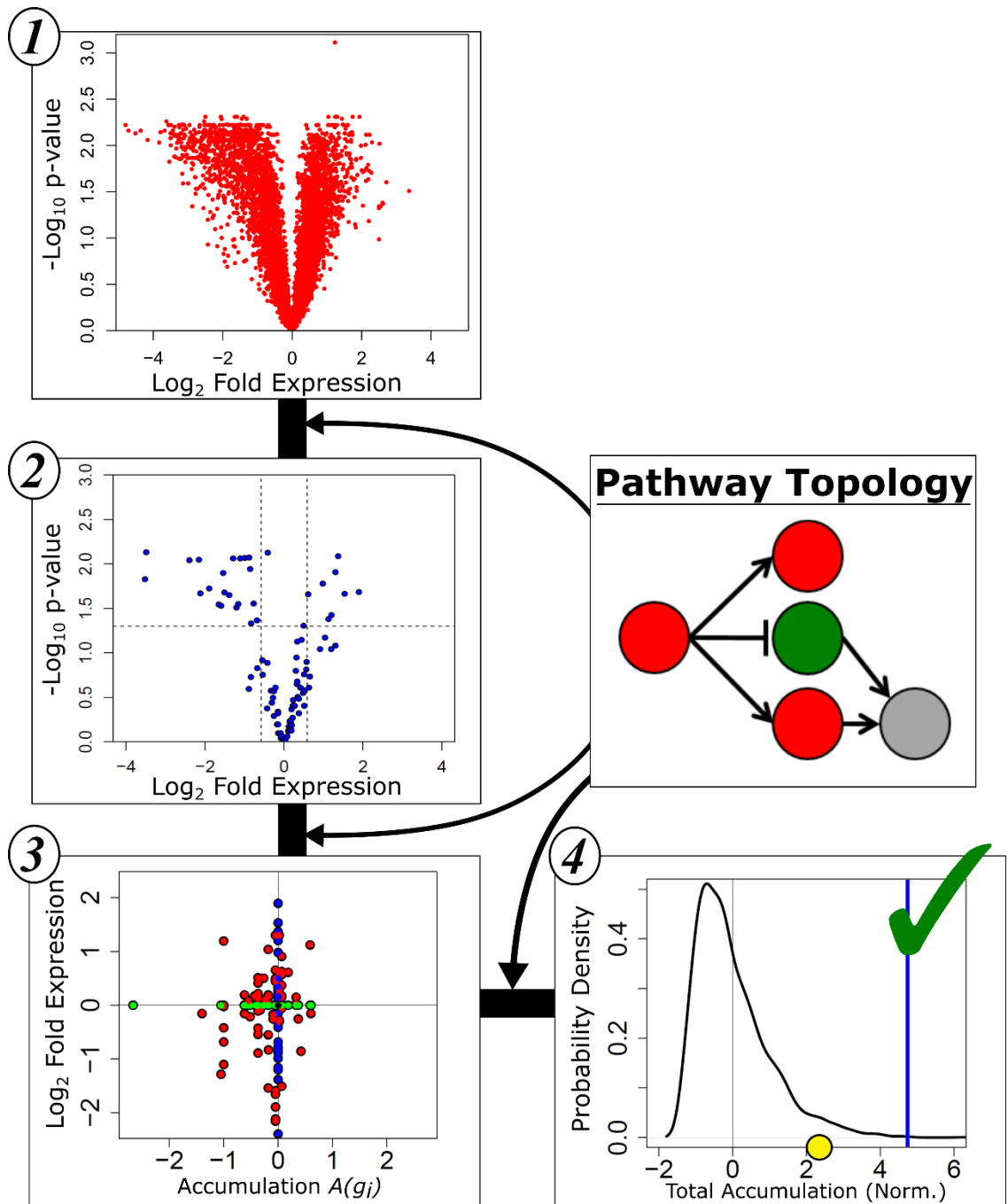


Figure 7.4. **Signal Pathway Impact Analysis (SPIA) workflow for determining pathway-level dysregulation from gene-level expression measurements.** (1) Measured global differential gene expression induced by intense THz pulses. (2) For each pathway, the KEGG database is used to filter the global data to include only the relevant genes. (3) Pathway topology information (node/edge interaction properties) is used to calculate the upstream accumulated perturbation $A(g_i)$ for each gene, and is presented as a two-way plot (expression vs. perturbation). (4) The total accumulated perturbation, $A_{tot} = \sum A(g_i)$, is determined (blue line) and compared to the simulated null distribution (black curve). If the accumulated perturbation is greater than the quantity corresponding to the pre-defined significance threshold determined from the null distribution (yellow circle), the calculated perturbation is considered statistically significant, and the pathway is predicted to be dysregulated by the relative magnitude, A_{tot} .

To achieve this, the “pathway edge matrix” is constructed, for which the identified networks/pathways comprise the row-space, and the nodes/genes occupy the column-space. The matrix is populated by the number of edges extending *from* the node, normalized to the total number of edges in the corresponding network. Since nodes with a larger number of downstream effectors have greater potential to propagate node-level perturbation through the network, this is a measure of the relative importance of that node. Standard k -means clustering ($k=2$) is performed across rows/columns to group genes/pathways by matrix similarity [33]. This algorithm iteratively bisects each dimension by maximizing the difference of group means. Since the metric in the matrix is a measure of gene significance in regulating cancer processes, the resulting ordered gene list represents the dominant transcript-level sources of the predicted pathway dysregulation, and provides the best candidates for understanding mechanisms of the changes to cancer signaling dynamics induced by intense THz pulses.

7.3.2 Results

7.3.2.1 Intensity-dependent global gene expression and signaling pathway dysregulation

The global differential gene expression profiles for varying THz pulse intensities are shown in Figure 7.5(a). In general, expression magnitudes and statistical significance increases for increasing pulse energy. Figure 7.5(b) indicates the genes from the highest THz intensity ($2.4 \mu\text{J/pulse}$, 74 MW/cm^2) that meet conventional thresholds for significant gene expression. Of 9311 total genes detectable in control tissues, 1681 genes are identified as significantly differentially expressed, with 1088 downregulated and 593 upregulated.

7.3.2.2 Gene ontology analysis: Processes, structures, and functions statistically over-represented by terahertz-affected genes

Figure 7.6 shows the odds-ratio (OR) and corresponding p -values (negative log-transformed) of the GO terms found to be significantly over-represented in the set of THz-affected genes (Figure 7.5(b)), as calculated by Equations (7.2) and (7.3). These terms are categorized as biological processes, cellular components, or molecular functions, and are an indication of the processes that THz exposure may dysregulate based on the gene expression profiles.

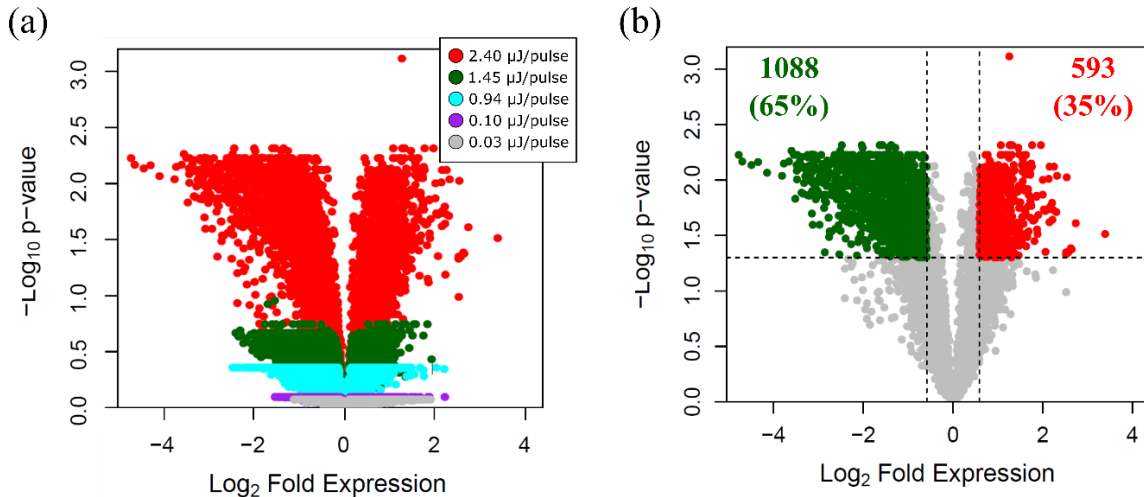


Figure 7.5. **Intensity-dependent global differential gene expression induced by THz pulses in human skin tissue.** Dashed lines indicate conventional significance thresholds: $|\text{Log}_2(\text{Expression ratio})| > 0.58$ and $p < 0.05$. (a) Measured gene expression profiles for 5 THz pulse energies, showing intensity-dependent growth in expression magnitude and significance for THz-expressed genes. (b) Gene expression for the highest THz intensity. From 9311 total genes detectable in control tissues, conventional significance thresholds identify 1681 (1088 downregulated and 593 upregulated) significantly differentially expressed genes.

Of the 58 significant GO terms identified, 57 are due to the profile of THz-downregulated genes, while 1 (*cytokine activity* – a molecular function) is over-represented by upregulated genes. As expected, many of the GO terms are directly related to functional activity observed in skin. Many terms that broadly describe processes that take place in the multiple layers of skin (e.g., *skin development*, *establishment of skin barrier*, *regulation of water loss via skin*, *multicellular organismal water homeostasis*) were among the most significant GO terms identified. Specialized processes that only occur in the epidermal keratinocytes (e.g., *keratinocyte differentiation*, *keratinization*, *epidermal cell differentiation*, *epidermis morphogenesis*) were also significantly over-represented, which may be due to the majority of energy being absorbed in the superficial layers in the highly attenuating aqueous environment. Additionally, processes that specifically regulate the epidermal differentiation processes (e.g., *peptide cross-linking*, *regulation of peptidase activity*, *intermediate filament-based process*, *hemidesmosome assembly*) were identified. These are consistent with the previously observed effects of THz exposure to skin, which localized the effect to the “epidermal differentiation complex” [26].

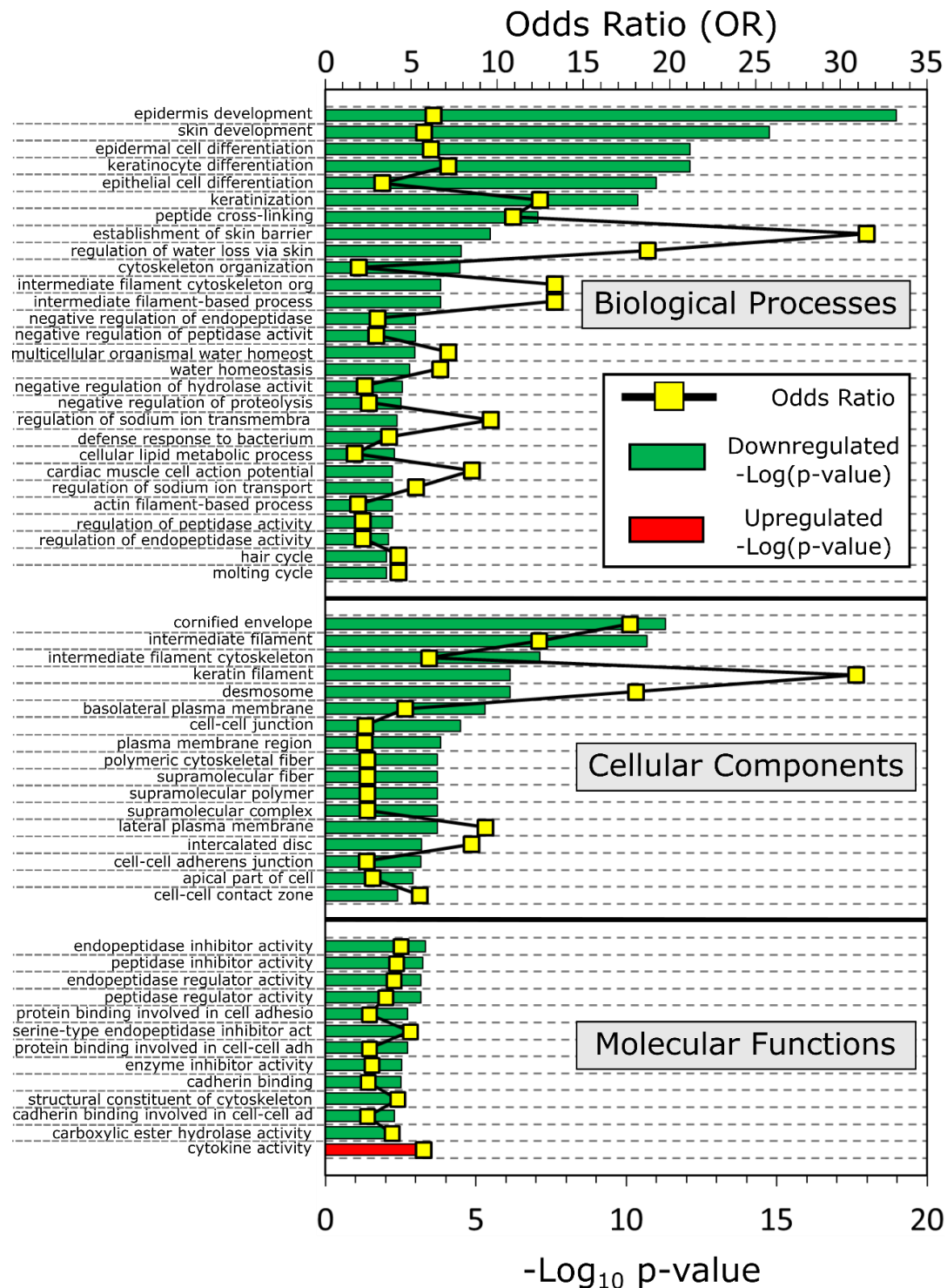


Figure 7.6. Gene ontology (GO) terms significantly over-represented ($p < 0.01$) by THz-affected genes. The odds-ratio (OR) is the magnitude of statistical over-representation of THz-affected genes compared to the total set of genes associated with each term, and the p-value (bars) is the associated statistical significance.

7.3.2.3 Signal pathway impact analysis: Dysregulation of cancer-related signaling networks

From the measured gene expression profiles (Figure 7.5), pathway-level dysregulation was predicted as described in Section 7.3.1.6. Of the 184 pathways available in the KEGG database, 54 were found to be significantly dysregulated by at least the highest THz pulse energy ($p < 0.05$). Of these, 8 are involved in regulating initiation, development, or progression of human cancer. These pathways are listed at left in Figure 7.7, and the magnitude, direction, and significance of the pathway-level dysregulation are displayed by plots at centre and right. These results indicate that intense THz pulses are predicted to dysregulate many important cancer-related signaling pathways, and generally depends on pulse energy.

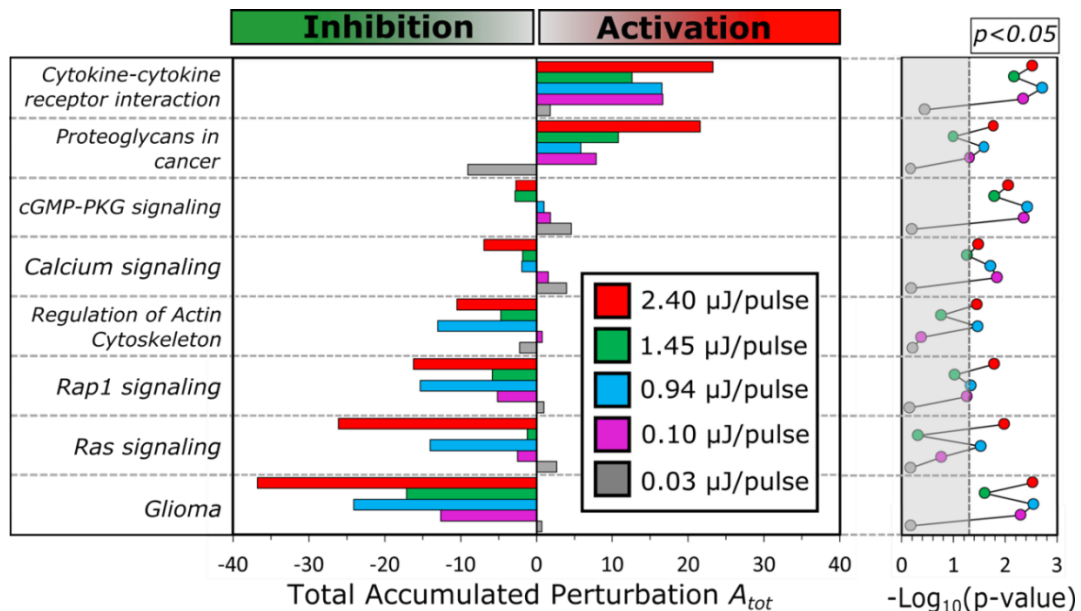


Figure 7.7. **THz-induced dysregulation to cancer-related signaling processes.** Dysregulation of 8 cancer-related signaling pathways, listed at left. The central bar plot shows the total accumulated perturbation (A_{tot}) as calculated by pathway perturbation analysis for each exposure condition. Associated p-values are shown at right, with points to the right of the shaded region indicating statistical significance ($p < 0.05$).

7.3.2.4 Transcript-level sources of terahertz-induced signaling dysregulation

Figure 7.8 summarizes the results of identifying the most significant genes in THz-induced cancer signaling dysregulation, as described in Section 7.3.1.7. As shown in Figure 7.8(a), of the 1681 differentially expressed genes that meet significance thresholds, all dysregulation related to cancer signaling processes is due to a subset of only 88. These can be broadly categorized as “pro-mitotic”, “cancer-specific”, and “pro-inflammatory” (Figure 7.8(b)), for which the latter is seen to

be nearly entirely genomically distinct. The pathway edge matrix (Figure 7.8(c)) shows the relative importance of the 88 genes within the 8 cancer-related pathways predicted to be dysregulated. Since the matrix is populated by a measure of nodes' perturbative capacities, clustering these values leads to ordered grouping of genes based on relative importance across pathways.

The pathways are not independent signaling systems, but rather are regulated by many common genes/proteins. This crosstalk is evident in the discrete blocks that emerge in the structure seen in the clustered matrix: Blocks along rows indicate groups of genes that significantly regulate a given pathway, and blocks along columns indicate individual genes that regulate function across multiple pathways. In Figure 7.8(c), these groups are qualitatively indicated by the dendrograms at right (for pathways) and above (for genes). Due to these complex interactions, standard methods that identify dysregulatory sources within an individual pathway are insufficient: The effect to other unconsidered pathways are not easily predictable but may dominate the overall phenotypic response. Therefore, the complete analysis accounting for complex inter-pathway crosstalk as described in Section 7.3.1.7 is a statistical approach that allows one to identify an ordered list of primary sources of pathway-level dysregulation, taking inter-pathway signaling contexts into account.

For row-clustering (pathways), there are three broad pathway categories that emerge as expected from the Venn diagram in Figure 7.8(b): Pro-mitotic, pro-inflammatory, and cancer-specific. These categories, the corresponding pathways, and predicted total accumulated perturbation at the highest THz intensity (A_{tot} from Figure 7.7) are listed in Table 7.3.

For column-clustering (genes), several discrete structures emerge in the clustered edge matrix. The pink box in Figure 7.8(c) are the genes with the largest clustering index, and indicate the genes that are both significantly differentially expressed by THz exposure, and significantly drive cancer signaling dysregulation in the associated pathways. Table 7.4 shows the top five gene clusters (containing 23 of the 88 genes), as well as associated processes and THz-induced expression measurements at the highest THz intensity. In Table 7.3 and Table 7.4, green (red) text represents downregulation/inhibition (upregulation/activation) of the gene/pathway for the highest THz intensity.

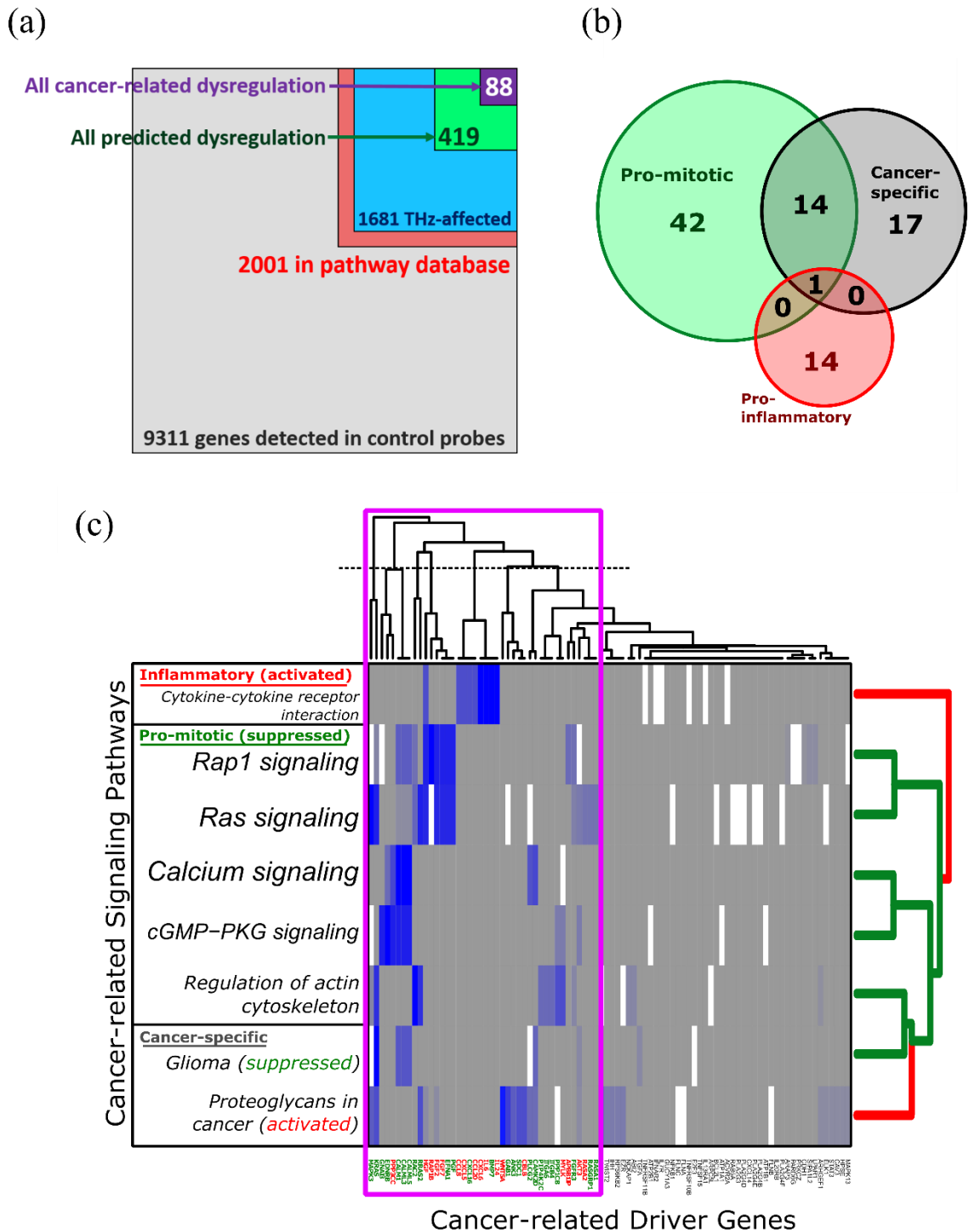


Figure 7.8. **Identification of the dominant transcript-level sources of pathway-level dysregulation by clustering the pathway edge matrix.** (a) Area plot indicating the number of genes involved in dysregulation of cancer-related signaling (88) relative to the total number of THz-affected (1681). (b) Venn diagram showing broad categorization of the 88 THz-affected cancer-related genes. The dysregulation of inflammatory processes is nearly entirely genomically distinct from the dysregulation to pro-mitotic pathways. (c) The pathway edge matrix, populated by the normalized number of edges extending from a node/gene (columns) in the corresponding pathway (rows). K-means clustering (dendrograms at top and right) identifies 42 THz-affected genes that predominantly drive cancer-associated signaling dysregulation (pink box).

Table 7.3. **Total accumulated perturbation in cancer-associated signaling pathways for the highest pulse energy.** Green (red) text represents inhibition (activation) of the pathway for the highest THz intensity.

Category	Pathway Name	Total Accumulated Perturbation A_{tot}	p-value $\times 10^{-2}$
<i>Pro-inflammatory</i>	Cytokine-cytokine receptor interaction	+23.27	0.41
<i>Pro-mitotic</i>	Ras signaling	-26.08	2.3
	Rap1 signaling	-16.22	2.3
	Regulation of actin cytoskeleton	-10.45	4.8
	Calcium signaling	-6.91	4.7
	cGMP-PKG signaling	-2.70	1.2
<i>Cancer-specific</i>	Glioma	-36.76	4.1
	Proteoglycans in cancer	+21.63	1.6

Table 7.4. **Transcript-level terahertz targets.** THz-affected genes (top five clusters) that maximally drive cancer signaling dysregulation for the highest pulse energy. Green (red) text represents downregulation/inhibition (upregulation/activation) of the gene/pathway for the highest THz intensity.

Gene Cluster	Gene Name	Log2-fold Expression	p-value $\times 10^{-2}$	Associated Pathways
1	KRAS	-1.10	0.86	Ras signaling pathway
	MAPK3	-0.83	4.7	Rap1 signaling pathway Glioma Regulation of actin cytoskeleton Proteoglycans in cancer
2	CALML5	-3.49	0.73	Ras signaling pathway
	CALML3	-3.52	1.5	Rap1 signaling pathway
	CALM1	-0.88	0.84	Calcium signaling pathway
	GNAI3	-1.04	1.4	cGMP-PKG signaling pathway
	EDNRB	+1.52	3.1	Glioma
	PPP3CC	+1.33	2.8	
3	RAC2	-1.29	0.86	Ras signaling pathway
	RRAS2	-0.69	4.3	Rap1 signaling pathway Regulation of actin cytoskeleton Proteoglycans in cancer
4	HGF	+1.37	0.82	Ras signaling pathway
	RAP1B	+0.61	2.2	Rap1 signaling pathway
	FGF2	+1.90	2.1	Cytokine-cytokine receptor interaction
	FGF7	+1.54	2.2	Proteoglycans in cancer
	EFNA1	-2.39	0.90	
	PGF	-0.77	2.8	
5	CXCL16	-1.08	3.6	Cytokine-cytokine receptor interaction
	BMP7	-2.08	0.90	
	CCL8	+3.39	3.1	
	CXCL5	+2.73	2.5	
	CCL20	+2.21	1.6	
	IL6	+2.57	4.5	
	IL24	+2.23	1.9	

7.4 Discussion

In earlier studies using similar skin models, THz exposure parameters, and biological assays as those discussed in this study, Titova et al. observed differential expression of 442 genes induced by intense THz pulses [26]. Subsequent analysis showed a downregulation of genes in the epidermal differentiation complex (EDC) and predicted activation of an acute inflammatory response. The present study verifies both observations in the relevant tissue system (human skin) and further characterizes specific pathways, associated biological processes, and the THz-affected genes that most significantly drive the predicted dysregulation to important cancer signaling processes.

The predicted THz-induced dysregulation can be broadly categorized as activation of pro-inflammatory processes (positive A_{tot} of the *Cytokine-cytokine receptor interaction* pathway) and suppression of pro-mitotic processes (negative A_{tot} of the *Glioma, Ras signaling, Rap1 signaling, Regulation of actin cytoskeleton, Calcium signaling, and cGMP-PKG signaling* pathways). The suppression of pro-mitotic pathways, particularly within the *Ras signaling* and *Calcium signaling* networks, implies a potential therapeutic mechanism of intense THz pulses.

7.4.1 Activation of pro-inflammatory signaling

Cytokines are extracellular ligands that are released following inflammatory stimuli and participate in inter-cellular communication to regulate the growth, differentiation, and activation of immune cells [34]. Specific responses are triggered upon cytokines binding to cytokine receptors in the membranes of target cells. In addition to regulating the general inflammatory response in normal tissue, cytokines have an important role in the development of the tumor microenvironment, and have been observed to both suppress and drive the metastatic phenotype, dependent on the cytokines involved, or the type/stage of the cancer [34]. Emerging evidence shows that cytokines are involved in regulating tumor formation, and controlled modulation of this regulatory function may be exploited for cancer therapy [34, 35]. Early phase clinical trials investigating multiple components of the immune system as therapeutic targets have shown success in effective tumor response in neural tissue, as reviewed in reference [36].

7.4.1.1 Stimulation of cytokine/cytokine receptor interaction

The *Cytokine-cytokine receptor interaction* pathway is predicted to be the most strongly dysregulated by intense THz pulses, and is consistent with previous observations of a THz-induced inflammatory response [26, 27, 37, 38, 39, 40, 41]. 18 of 76 genes considered in this pathway are differentially expressed at the highest THz pulse energy, and these are largely localized to differential expression of the chemokine and inflammatory cytokine families (CCL, CXCL), interleukins (IL6), and interferons (IL24), as shown in Cluster 5 of Table 7.4. The predicted activation at the pathway level is due to accumulated perturbation at downstream nodes, which predominantly include the corresponding receptors of these ligand families (CCR, CXCR, ILR). Therefore, the dominant sources of pathway activation were not due to genes directly affected by THz exposures, but rather due to downstream targets of directly affected genes. This indicates that from a biological perspective, the extended exposure of skin tissue to intense THz pulses is recognized and responded to as an acute immune response. Kim et al. have compared the tissue response of mouse skin to varying inflammatory stimuli, and show that this inflammatory response to THz exposures is most genomically similar to a wound response, and dissimilar to responses stimulated by burns or exposure to other types of radiation (UV, neutrons) [37]. In our dataset, the activation of the inflammatory response is nearly entirely genomically distinct from the suppression of pro-mitotic signaling, evident in Figure 7.8(b) and (c).

7.4.2 Suppression of pro-mitotic signaling

The *Glioma* pathway is predicted to be the most strongly suppressed in Figure 7.7 and Table 7.3 ($A_{tot}=-36.8$, $p=0.004$ at highest THz pulse energy). This pathway is categorized as “cancer-specific”, and the predicted dysregulation is due to the distinct effect on sub-networks, in particular the *Ras signaling* and *Calcium signaling* pathway. As shown in Table 7.4, the most significant THz-affected genes driving predicted cancer signaling dysregulation are central signaling molecules in these pathways (most significantly KRAS, MAPK3, and calcium-binding proteins). The most strongly affected non-specific cancer pathway is the *Ras signaling* network.

7.4.2.1 Suppression of Ras signaling activity

The *Ras signaling* pathway, in particular the canonical RAS-RAF-MEK-ERK axis, is one of the most well-characterized signaling cascades in molecular biology, due to its ubiquity in nearly all eukaryotic cell types. As this pathway regulates general division, differentiation, and

proliferation processes, it is often implicated in many human cancers and is therefore a target of modern cancer therapy research.

Of the 100 genes considered in this network, 29 were significantly expressed at the highest THz pulse energy. THz-affected genes in the Ras superfamily include members of the Ras (KRAS, RAP1B, RRAS2), Rap (RAP1B), and Rho (RAC2) families. Associated Ras-dependent families (RASA1, RASA2, RASGRP1) additionally regulate the binding and activity of Ras-related proteins. Expression changes of these genes (KRAS and MAPK3) are the most significant sources of cancer-related dysregulation and predicted suppression of mitotic signaling. Many of the gene clusters associated with the *Ras signaling* pathway are also responsible for the predicted suppression of several other networks in the pro-mitotic group (*Rap1 signaling*, *Calcium signaling*, *cGMP-PKG signaling*, and *Regulation of actin cytoskeleton*), indicating the nested nature of these signaling processes that interact with significant crosstalk. Processes that this group of pathways regulate, such as division, differentiation, motility, and apoptosis, are all involved in various aspects of mitotic activity. The THz-downregulation of the KRAS oncogene, associated signaling genes, and subsequent prediction of inhibition of Ras signaling activity ($A_{tot}=-26.1$, $p=0.01$) indicates that intense THz pulses may find potential therapeutic application for some cancers, with the goal of targeted inhibition of pro-mitotic signaling in diseased tissue.

7.4.2.2 *Suppression of calcium signaling activity*

11 of 54 genes in this pathway were significantly expressed at the highest THz pulse energy, and these are largely represented by downregulation of calmodulin and calmodulin-like genes that encode for calcium binding proteins (CBPs; CALM, CALML, CAMK2D families, see Cluster 2 of Table 7.4). The genes affected in the pro-mitotic category are directly related: Many Ras-related proteins encoded by THz-affected genes are in turn calcium-regulated, and their proper function relies on regulatory activity of the listed CBPs [42]. Since calcium influx may be expected to dysregulate division and differentiation pathways that are closely correlated to calcium signaling, inhibition of associated signaling may be a genomic response to field-induced membrane permeabilization, as discussed subsequently in Chapter 8. As differential gene expression profiles represent the tissue response to the applied stimulus, expressing genes to attenuate calcium signaling is a feasible homeostasis-seeking response to increased calcium influx. This hypothesis is additionally corroborated by the pathway analysis in Figure 7.8(c), since the pro-mitotic pathways identified are also largely calcium regulated. For example, RAS activity is sensitive to changes in Ca^{2+} concentration, since several Ras-activators (e.g., Rap1) are in turn calcium-

activated via binding of RASGRP [43]. In addition, studies investigating gene expression in skin following electroporation have reported activation of a local inflammatory response, including increased expression of the cytokine-related gene families upregulated by intense THz pulses (CCL and CXCL families), as discussed in Section 7.4.1 [44].

7.4.3 Consideration of thermal effects

An important consideration is the possibility of thermal effects in biological systems induced by THz radiation [38, 39, 45, 46, 47, 48]. While recent studies have shown that thermal effects from relatively low powers of CW THz exposure is genomically distinct from general bulk heating processes [49], care has been taken in these experiments to ensure that the observed biological response is non-thermal by limiting the pulse train's duty cycle (1 kHz train of picosecond-duration pulses). This minimizes the average power of the THz beam such that thermal effects are negligible, while maintaining high peak power for THz energy to propagate in high-attenuation aqueous environments [46].

Two effects are occurring: (1) Each pulse will cause some amount of temperature increase in a volume of space, and (2) the thermal energy is dissipated from this volume at a rate dependent on the sample's thermal conductivity. These two contributions for the 1 kHz pulse train will reach a steady state of average heating. An estimate of the per-pulse temperature increase is ~ 4 mK, using $\Delta Q = mc\Delta T$, where ΔT is the temperature change due to a THz pulse with total energy ΔQ in a volume of water of mass $m = \rho V$ [$\rho = 1$ g/cm³]; volume, V , is calculated using the measured THz spot size and penetration depth; and $c=4.2$ J/g/K is the specific heat capacity of water. The average steady-state heating due to the 1 kHz pulse train was measured with a thermal imager in water to be less than 1°C. This measurement is consistent with heating measurements induced in similar THz exposure systems when scaled by average power [47, 49, 50]. In terms of biological response, the heat shock factor (HSF, regulator of the heat shock response) was not differentially expressed, and other heat shock proteins were not upregulated [6]. No biological processes related to thermal stress or heat response were significantly identified by pathway or gene ontology analyses. It is therefore unlikely that the observed gene expression induced by intense THz pulses is thermal in origin. At minimum, intense THz pulses were not recognized biologically as a normal thermal stimulus.

An additional possibility that should be explored in future work is dependence on the pulse train's repetition rate (1 kHz for this study). As argued above, both the per-pulse and train-averaged

temperature increase are biologically negligible. However, a small thermal energy input, while generally biologically insignificant, may induce a frequency-dependent effect by coupling to and altering structural or chemical dynamics. In addition to intense THz wave interaction with fast biomolecular motions, additional thermal kHz-coupling to slower dynamics may be another important interaction mechanism to explore.

7.5 Conclusion

In this chapter, it was shown that intense THz pulses cause significant changes in gene expression patterns in human skin. The expression magnitude and statistical significance generally increase with THz pulse intensity. From these data, intensity-dependent dysregulation of epidermal differentiation processes and cancer-related signaling pathways are predicted. Pro-inflammatory processes are predicted to be activated due to upregulation of common inflammatory cytokines, interleukins, and interferons, and is consistent with previous studies' observations. Pro-mitotic pathways are predicted to be inhibited, largely due to downregulation of genes in the Ras superfamily or genes that encode for calcium binding proteins. Pathway topology information was used to identify 88 genes (of 1681 possible candidates) responsible for all predicted cancer-related dysregulation, with 42 genes dominantly responsible. The top clusters, containing the top 23 THz-affected genes that predominantly drive cancer signaling dysregulation, are presented as an ordered list in Table 7.4, along with their associated signaling pathways. These genes and associated processes represent the strongest candidates for future specific mechanistic studies in characterizing THz-induced dysregulation of the signaling processes of interest. Moreover, suppression of the *Ras signaling* and *Calcium signaling* pathways are of particular significance, as these are commonly implicated pathways in human cancers, and popular targets for existing and emerging cancer therapies.

7.6 References

- [1] F. H. Martini, J. L. Nath and E. F. Bartholomew, *Fundamentals of Anatomy and Physiology* 9th Ed., Benjamin Cummings, 2012.
- [2] R. Philips, J. Kondev, J. Theriot and H. Garcia, *Physical Biology of the Cell*, New York , NY: Garland Science, 2013.
- [3] M. Kanehisa and S. Goto, "KEGG: Kyoto Encyclopedia of Genes and Genomes," *Nucleic Acids Research*, vol. 28, no. 1, pp. 27 - 30, 2000.

- [4] S. Carbon, A. Ireland, C. J. Mungall, S. Shu, B. Marshall and S. Lewis, "AmiGO: Online access to ontology and annotation data," *Bioinformatics*, vol. 25, no. 2, pp. 288 - 289, 2009.
- [5] A. L. Tarca, S. Draghici, P. Kahtri, S. S. Hassan, P. Mittal, J. -S. Kim, C. J. Kim, J. P. Kusanovic and R. Romero, "A novel signaling pathway impact analysis," *Bioinformatics*, vol. 25, no. 1, pp. 75 - 82, 2009.
- [6] B. Alberts, A. Johnson, J. Lewis, M. Raff, K. Roberts and P. Walter, *The Molecular Biology of the Cell*, 4th Edition, New York, NY: Garland Science, 2002.
- [7] R. A. Bradshaw and E. A. Dennis, *Handbook of Cell Signaling*, Amsterdam, Netherlands: Academic Press, 2010.
- [8] P. Sebastian-Leon, E. Vidal, P. Minguez, A. Conesa, S. Tarazona, A. Amadoz, C. Armero, F. Salavert, A. Vidal-Puig, D. Montaner and J. Dopazo, "Understanding disease mechanisms with models of signaling pathway activities," *BMC Systems Biology*, vol. 8, no. 121, pp. 1 - 19, 2014.
- [9] R. J. Akhurst and A. Hata, "Targeting the TGFB signalling pathway in disease," *Nature Reviews Drug Discovery*, vol. 11, pp. 790 - 811, 2012.
- [10] P. J. Roberts and C. J. Der, "Targeting the Raf-MEK-ERK mitogen-activated protein kinase cascade for the treatment of cancer," *Oncogene*, vol. 26, pp. 3291 - 3310, 2007.
- [11] R. Albert, "Scale-free networks in cell biology," *Journal of cell science*, vol. 118, no. 21, pp. 4947 - 4957, 2005.
- [12] E. Almaas, "Biological impacts and context of network theory," *Journal of Experimental Biology*, vol. 210, no. 9, pp. 1548 - 1558, 2007.
- [13] S. A. Ochsner, D. Abraham, K. Martin, W. Ding, A. McOwiti, W. Kankanamge, Z. Wang, K. Andreano, R. A. Hamilton, Y. Chen, A. Hamilton, M. L. Gantner, M. Dehart, S. Qu, S. G. Hilsenbeck, L. B. Becnel, D. Bridges, A. Ma'ayan, J. M. Huss, F. Stossi, C. E. Foulds, A. Kralli, D. P. McDonnell and N. J. McKenna, "The Signaling Pathways Project, an integrated 'omics knowledgebase for mammalian cellular signaling pathways," *Scientific data*, vol. 6, no. 252, pp. 1 - 21, 2019.
- [14] A. Takashima and D. Faller, "Targeting the RAS Oncogene," *Expert Opinion on Therapeutic Targets*, vol. 17, no. 5, pp. 507 - 531, 2013.
- [15] National Institutes of Health: National Cancer Institute, "The Ras Initiative," 2020. [Online]. Available: <https://www.cancer.gov/research/key-initiatives/ras>.
- [16] M. Drosten, C. G. Lechuga and M. Barbacid, "Ras in epidermal proliferation," *Oncotarget*, vol. 5, no. 14, pp. 5194 - 5195, 2014.
- [17] J. Downward, "Targeting ras signalling pathways in cancer therapy," *Nature Reviews Cancer*, vol. 3, pp. 11 - 22, 2003.
- [18] E. Fuchs and S. Raghavan, "Getting Under the Skin of Epidermal Morphogenesis," *Nature Reviews Genetics*, vol. 3, no. 3, pp. 199 - 209, 2002.

- [19] E. R. Purba, E. -I. Saita and I. N. Maruyama, "Activation of the EGF Receptor by Ligand Binding and Oncogenic Mutations: The "Rotation Model", " *Cells*, vol. 6, no. 2, 2017.
- [20] D. Clapham, "Calcium Signaling," *Cell*, vol. 131, no. 6, pp. 1047 - 1058, 2007.
- [21] G. Sherbet, Calcium signaling in cancer, Boca Raton, FL: CRC Press, 2001.
- [22] C. Cui, R. Merritt, L. Fu and Z. Pan, "Targeting calcium signaling in therapy," *Acta Pharmaceutica Sinica B*, vol. 7, no. 1, pp. 3 - 17, 2017.
- [23] Y. Lee, Principles of Terahertz Science and Technology, New York, NY: Springer, 2009.
- [24] H. Hirori, A. Doi, F. Blanchard and K. Tanaka, "Single-cycle terahertz pulses with amplitudes exceeding 1 MV/cm generated by optical rectification in LiNbO₃," *Applied Physics Letters*, vol. 98, no. 9, 2011.
- [25] A. Acheva, A. Aerts, C. Rombouts, S. Baatout, S. Salomaa, K. Manda, G. Hildebrandt and M. Kamarainen, "Human 3-D tissue models in radiation biology: current status and future perspectives," *International Journal of Radiation Research*, vol. 12, no. 2, 2014.
- [26] L. Titova, A. Ayesheshim, A. Golubov, R. Rodriguez-Juarez, R. Woycicki, F. Hegmann and O. Kovalchuk, "Intense THz pulses down-regulate genes associated with skin cancer and psoriasis: a new therapeutic avenue?," *Scientific Reports*, vol. 3, no. 2363, pp. Q1 - Q10, 2013.
- [27] L. Titova, A. Ayesheshim, A. Golubov, D. Fogen, R. Rodriguez-Juarez, F. Hegmann and O. Kovalchuk, "Intense THz pulses cause H2AX phosphorylation and activate DNA damage response in human skin tissue," *Biomedical Optics Express*, vol. 4, no. 4, pp. 559 - 568, 2013.
- [28] W. E. Johnson, C. Li and A. Rabinovic, "Adjusting batch effects in microarray expression data using empirical Bayes methods," *Biostatistics*, vol. 8, no. 1, pp. 118 - 127, 2007.
- [29] M. E. Ritchie, M. J. Dunning, M. L. Smith, W. Shi and A. G. Lynch, "BeadArray Expression Analysis Using Bioconductor," *PLoS Computational Biology*, vol. 7, no. 12, pp. 1 - 6, 2011.
- [30] G. Hong, W. Zhang, H. Li, X. Shen and Z. Guo, "Separate enrichment analysis of pathways for up- and downregulated genes," *Journal of the Royal Society Interface*, vol. 11, no. 92, pp. 1 - 11, 2014.
- [31] C. Voichita, S. Ansari and S. Draghici, "ROntoTools: R Onto-Tools suite," *R Package version 2.6.0*, 2017.
- [32] C. Voichita, M. Donato and S. Draghici, "Incorporating gene significance in the impact analysis of signaling pathways," *11th International Conference on Machine Learning and Applications. ICMLA 2012*, pp. 126 - 131, 2012.

- [33] A. Likas, N. Vlassis and J. Verbeek, "The global k-means clustering algorithm," *Pattern Recognition*, vol. 36, no. 2, pp. 451 - 461, 2003.
- [34] G. Dranoff, "Cytokines in Cancer Pathogenesis and Cancer Therapy," *Nature Reviews Cancer*, vol. 4, no. 1, pp. 11 - 22, 2004.
- [35] A. Christofides, M. Kosmopoulos and C. Piperi, "Pathophysiological mechanisms regulated by cytokines in gliomas," *Cytokine*, vol. 71, pp. 377 - 384, 2015.
- [36] V. F. Zhu, J. Yang, D. G. LeBrun and M. Li, "Understanding the role of cytokines in Glioblastoma Multiforme pathogenesis," *Cancer Letters*, vol. 316, no. 2, pp. 139 - 150, 2012.
- [37] K. -T. Kim, J. Park, S. J. Jo, S. Jung, O. S. Kwon, G. P. Gallerano, W. -Y. Park and G. -S. Park, "High-power femtosecond-terahertz pulse induces a wound response in mouse skin," *Scientific Reports*, vol. 3, no. 2296, pp. 1 - 7, 2013.
- [38] G. Wilmink and J. Grundt, "Invited Review Article: Current State of Research on Biological Effects of Terahertz Radiation," *Journal of Infrared, Millimeter, and Terahertz Waves*, vol. 32, no. 10, pp. 1074 - 1122, 2011.
- [39] G. J. Wilmink, B. L. Ibey, C. L. Roth, R. L. Vincelette, B. D. Rivest, C. B. Horn, J. Bernhard, D. Roberson and W. P. Roach, "Determination of Death Thresholds and Identification of Terahertz (THz)-Specific Gene Expression Signatures," *Proceedings of the Society of Photo-Optical Instrumentation Engineers*, vol. 7562, pp. K1 - K8, 2010.
- [40] Y. Hwang, J. Ahn, J. Mun, S. Bae, Y. U. Jeong, N. A. Vinokurov and P. Kim, "In vivo analysis of THz wave irradiation induced acute inflammatory response in skin by laser-scanning confocal microscopy," *Optics Express*, vol. 22, no. 10, pp. 11465 - 11475, 2014.
- [41] G. J. Wilmink, B. D. Rivest, C. C. Roth, B. L. Ibey, J. A. Payne, L. X. Cundin, J. E. Grundt, X. Peralta, D. G. Mixon and W. P. Roach, "In Vitro Investigation of the Biological Effects Associated With Human Dermal Fibroblasts Exposed to 2.52 THz Radiation," *Lasers in Surgery and Medicine*, vol. 43, no. 2, pp. 152 - 163, 2011.
- [42] S. J. Cook and P. J. Lockyer, "Recent advances in Ca²⁺-dependent Ras regulation and cell proliferation," *Cell Calcium*, vol. 39, pp. 101 - 112, 2006.
- [43] J. C. Stone, "Regulation and Function of the RasGRP Family of Ras Activators in Blood Cells," *Genes and Cancer*, vol. 2, no. 3, pp. 320 - 334, 2011.
- [44] A. -K. Roos, F. Eriksson, J. A. Timmons, J. Gerhardt, U. Nyman, L. Gudmundsdotter, A. Brave, B. Wahren and P. Pisa, "Skin Electroporation: Effects on Transgene Expression, DNA Persistence and Local Tissue Environment," *PLoS One*, vol. 4, no. 9, pp. 1 - 10, 2009.
- [45] T. Kleine-Ostmann, C. Jastrow, K. Baaske, B. Heinen, M. Schwerdtfeger, U. Karst, H. Hintzsche, H. Stopper, M. Koch and T. Schrader, "Field Exposure and Dosimetry in the THz Frequency Range," *IEEE Transactions on Terahertz Science and Technology*, vol. 4, no. 1, pp. 12 - 25, 2014.

- [46] P. Weightman, "Prospects for the study of biological systems with high power sources of terahertz radiation," *Physical Biology*, vol. 9, pp. 1 - 10, 2012.
- [47] D. R. Dalzell, J. McQuade, R. Vincelette, B. Ibey, J. Payne, R. Thomas, W. P. Roach, C. L. Roth and G. J. Wilmink, "Damage thresholds for terahertz radiation," in *Proceedings of SPIE: Optical Interactions with Tissues and Cells XI*, San Francisco, California, 2010.
- [48] O. Bottauscio, M. Chiampi and L. Zilberti, "Thermal Analysis of Human Tissues Exposed to Focused Beam THz Radiations," *IEEE Transactions on Magnetics*, vol. 51, no. 3, pp. 1 - 4, 2015.
- [49] I. Echchgadda, J. E. Grundt, C. Z. Cerna, C. C. Roth, J. A. Payne, B. L. Ibey and G. J. Wilmink, "Terahertz Radiation: A Non-contact Tool for Selective Stimulation of Biological Responses in Human Cells," *IEEE Transactions on Terahertz Science and Technology*, vol. 6, no. 1, pp. 54 - 68, 2016.
- [50] T. Tachizaki, R. Salagicjo, S. Terada, K. -I. Kamei and H. Hirori, "Terahertz pulse-altered gene networks in human induced pluripotent stem cells," *Optics Letters*, vol. 45, no. 21, pp. 6078 - 6081, 2020.

8 Cellular-level effects: Investigations of membrane permeabilization induced by intense terahertz pulses

“...there is nothing so small as to escape our inquiry; hence there is a new visible World discovered to the understanding.”

– Robert Hooke, “Micrographia” (1665), in which the term ‘cell’ was coined.

8.1 Introduction

As in the previous chapter, it is again useful to begin by establishing cellular-level structure within the larger hierarchy of biological organization: *Organisms* are networks of interacting *organ systems*, and *organs* are comprised of systems of *tissues*, which are in turn comprised of interacting *cellular* systems. This classification schema also holds well for structural components like membranes, which is the cellular target of focus for our investigations of THz-induced biological effect in this chapter. Membrane structures provide protective barriers and regulate environmental sensing and chemical transport: Skin is a membranous *organ* that envelopes biological systems at the *organism* level, and epithelia are membranous *tissues* that envelop *organ* structures such as the heart or lungs [1]. At the *cellular* level, the plasma membrane establishes a mechanical boundary between the cell and its external environment, and smaller interior membranes envelope intracellular organelles such as the nucleus, mitochondria, or endoplasmic reticula, labelled in Figure 8.1.

In this chapter, cellular-level effects induced by THz radiation are considered, with a particular focus on the cellular plasma membrane (PM) as a key target of THz interaction. First, the structure and function of the PM is introduced, and a selection of biophysical models that relate structural dynamics of membrane components to regulatory biological activity are described. Next, the effects of external electric fields on membranes are discussed, and a theoretical formalism of field-induced electroporation is outlined. A selection of previous experimental investigations of membrane permeabilization by radiofrequency (RF), millimeter wave (MMW), and low-THz exposure are highlighted that motivate the key hypothesis of this chapter: Intense THz pulses may dysregulate cellular function via field-induced increase of membrane permeability. Finally, our experiments investigating this hypothesis in rat and human cancer cell lines are presented. Results indicate that the intense, broadband THz pulses utilized in these studies induce a small dose-dependent increase to membrane permeability, while bandpass exposures to isolate effects of individual frequency

bands were inconclusive. These investigations further the understanding of the physical interaction mechanisms between THz radiation and biological systems that may underlie observed phenotypic responses, and are important considerations in the design and implementation of biomedical and clinical THz technologies.

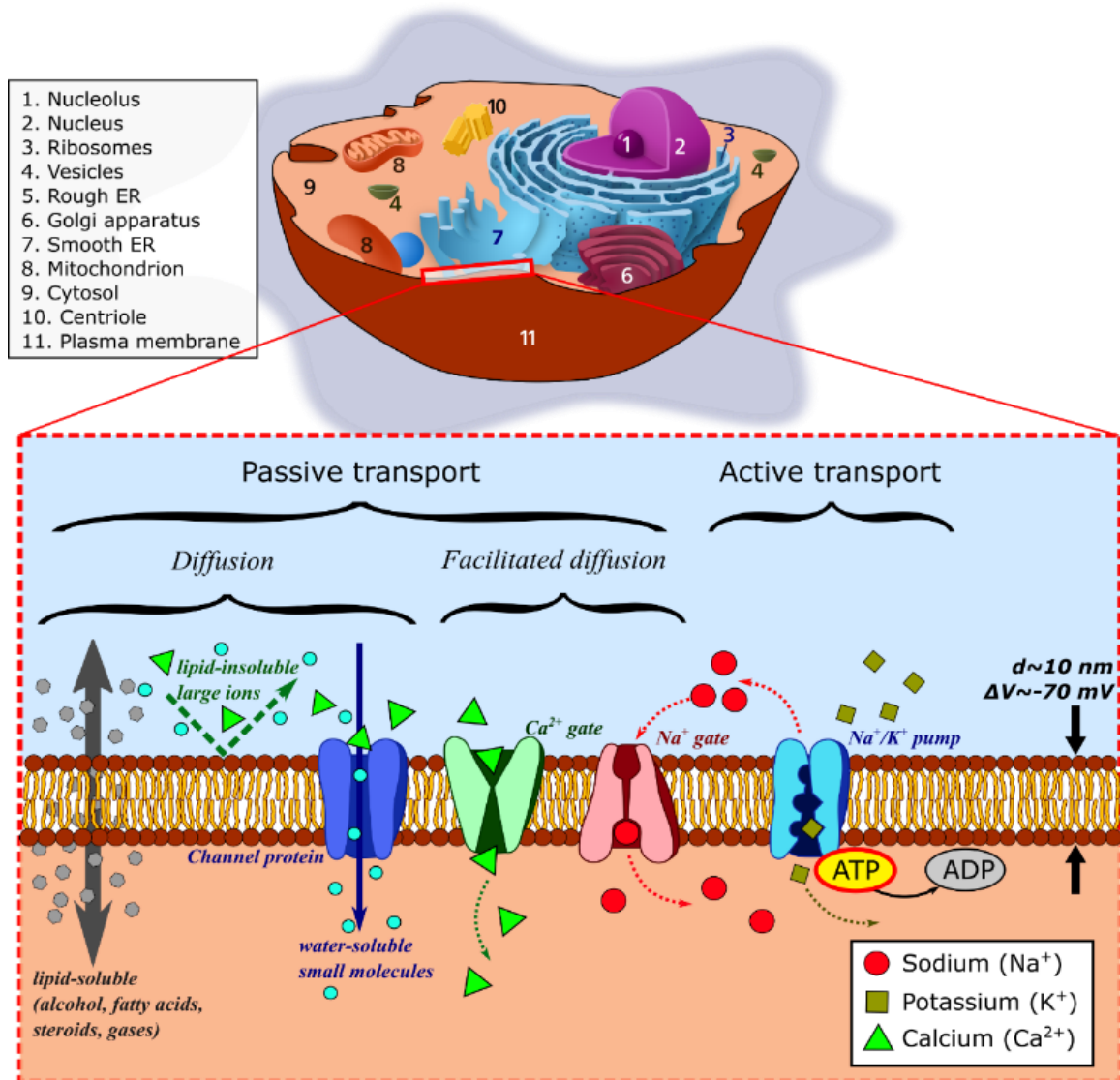


Figure 8.1. **Structure and transport mechanisms of the plasma membrane (PM) in animal cells** [2]. The plasma membrane (PM, zoomed window) may be modelled as a fluid mosaic, a phospholipid bilayer embedded with biomolecules and peripheral/integral proteins that assist in regulating membrane function. The diagram outlines various membrane transport mechanisms that regulate biomolecular and ionic transport into or out of the cell.

8.2 The plasma membrane

Several formulations for biophysical models of membrane structures have been developed that have informed our understanding of structurally-regulated membrane function, and these have been greatly aided by recent improvements in computational techniques [3, 4, 5, 6, 7, 8, 9, 10]. Classically, cellular membranes are most simply modeled by a fluid mosaic structure, a 2D sheet of bound phospholipids in the lamellar phase that provide a solvent for various membrane proteins and biomolecules, as shown in the zoomed window of Figure 8.1 [11, 12, 13]. Phospholipids are amphipathic (i.e., contain both hydrophobic and hydrophilic domains) molecules that form a dominant component of cellular membrane structures. In the presence of water, these molecules self-assemble into membranous structures in either a columnar or lamellar phase that minimizes free energy by sequestering the hydrophobic lipid tails in the structure's interior [14, 15]. For the lamellar phase, a “phospholipid bilayer” forms that is characterized by phosphate head groups in the hydrophilic exterior, and fatty tails in the hydrophobic interior.

The phospholipid bilayer forms a 2D protective barrier around the entire cell (the “plasma membrane”, PM), as well as interior organelles such as mitochondria, lysosomes, rough and smooth endoplasmic reticula, Golgi apparatus, or the nucleus (Figure 8.1). In addition to structural support and environmental protection, these regulate chemical transport via membrane proteins or vesicle budding, and provide a sensory structure for external mechanical, thermal, or electrical stimuli [16]. The interior of the plasma membrane is anchored to the exterior of the nuclear membrane by the cytoskeleton network (including microtubules), described in Chapter 9.

A key regulatory property of the PM is selective permeability, which facilitates controlled transport of molecules or ions via several passive and active diffusion mechanisms dependent on particle size, charge, solubility, relative concentration, and energy availability, as depicted in the zoomed window of Figure 8.1 [17]. Small, lipid-soluble molecules (alcohols, fatty acids, steroids, gases [e.g., O₂, CO₂], etc.) may traverse the membrane directly via passive diffusion. Lipid-insoluble molecules must utilize transport proteins that provide unfacilitated (i.e., channel proteins) or facilitated (i.e., carrier proteins) diffusion across the PM, and may require external stimuli for mechanical, thermal, or voltage-gated channels [1, 16, 17]. In some cases, the membrane must transport molecules against their net electrochemical gradient, and this requires utilizing intracellular energy stores and active transport mechanisms such as ATP-regulated ion pumps (e.g., the sodium-potassium ion pump) to maintain the homeostatic resting potential, the trans-membrane voltage (TMV).

8.2.1 *The membrane potential*

In physiological conditions, a net voltage exists across the PM due to a slight excess of cations in the extracellular space and an excess of negatively charged species (predominantly intracellular proteins) in the cell interior [1, 17]. In animal cells¹, this is typically around -70 mV, but may range from -10 mV to -100 mV [16, 17, 18]. The TMV is maintained by a system of channels and ion pumps in the PM that provide selective passive and active chemical transport, as described above.

Three dominant ion species that are particularly important for cellular function, and whose intra-/extra-cellular concentrations are regulated by PM protein pumps, are sodium (Na⁺), potassium (K⁺), and calcium (Ca²⁺). The PM is a mechanical barrier that establishes large ionic concentration gradients of these species between intra-/extra-cellular space, and this is an important mechanism of cellular signaling regulation. For example, Ca²⁺ is a ubiquitous second-messenger signaling particle that influences virtually all biological processes via protein activation, cytoskeletal modification, or regulation of division and differentiation pathway activities [19, 20, 21].

In the presence of an external electric field, a phenomenon known as “electroporation” (or more generally, “electropermeabilization”) occurs, in which the permeability of the PM increases, and biomolecules or ions may bypass the membrane’s regulatory structures and flow along their electrochemical gradients unimpeded [22]. Due to the large influence on biological function, and the universality of this effect across all cell types (animal, plant, and bacteria), this suggests that the membrane may be an important cellular target for THz-induced biological effects observed at the cell and tissue level.

8.2.2 *Membrane electroporation*

External fields induce a TMV that superimposes on the existing transmembrane resting potential, and is maintained as long as the external field is present [23]. Sufficient field strength and durations can establish non-physiological membrane potentials (~0.25 – 1 V) that trigger dramatic structural rearrangement of the membrane lipids and bound water, and results in stable

¹ As a historical aside: A TMV on the order of 100 mV across a $d \sim 10$ nm gap corresponds to a field of ~100 kV/cm, far greater than the static dielectric breakdown field in most materials. This back-of-the-envelope calculation was the impetus that led Herbert Fröhlich to explore the as-yet unknown dielectric properties of biological systems, and develop the early biophysical models and experiments investigating THz dynamics in biological systems [68, 69].

formation of discrete nanoscopic pores [24, 25]. This phenomenon has found wide applicability in microbiology and medicine to increase cellular uptake of drugs, dyes, or genetic material in a localized target region [26, 27, 28, 29]. It is also a topic of recent research interest investigating the cell membrane as an important cellular target responsible for observed biological effects induced by RF, MMW, and THz waves [30, 31, 32, 33, 34, 35, 36].

8.2.2.1 *Mechanism of membrane pore formation*

Membrane electroporation arises due to structural or chemical modification of membrane lipids, or modulation of protein function, that lead to electrical breakdown of the membrane region, as illustrated in Figure 8.2(a) [22]. Pore formation is initiated when the field-induced TMV reaches a critical value, ΔV_C , dependent on cell type, intra-/extra-cellular electrochemical environments, and local membrane structure, and is reversible if the field strength is below a second upper-limit sufficient to induce cellular damage.

Physically, electropores form in an external field due to re-established energy minimization demands in the altered electrochemical environment [36]. These manifest as intrusions of water into the membrane interior within ~ 1 ps, and subsequent re-ordering of the lipid bilayer structure into hydrophilic, conductive, permeable structures within ~ 1 μ s. Generally, a $TMV > \Delta V_C$ will detectably decrease the membrane permittivity and increase the electrical conductivity, facilitating ion transport across the membrane.

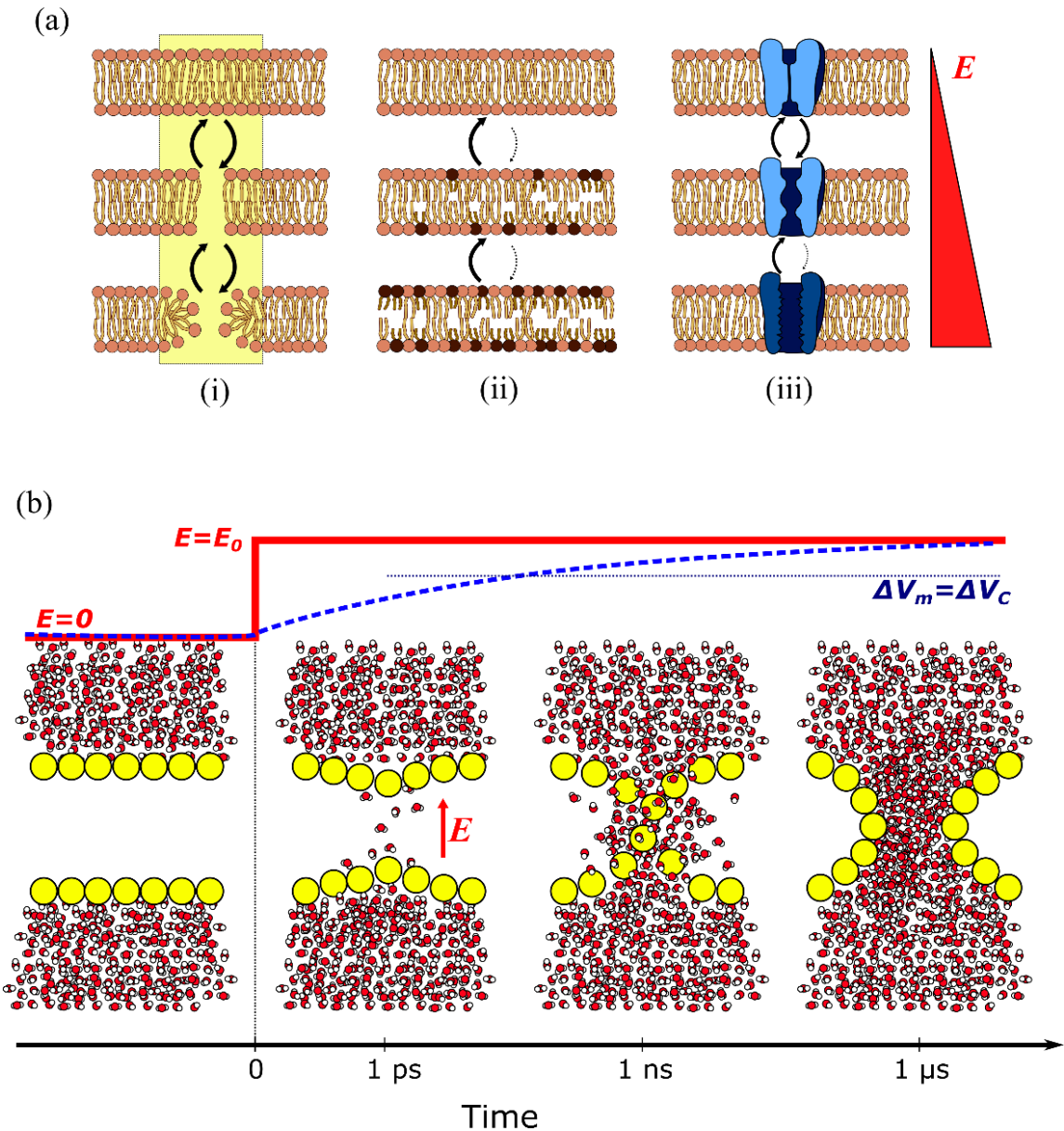


Figure 8.2. **Mechanisms of field-induced permeabilization.** Adapted from [22]. (a) Mechanisms of membrane permeability changes induced by electric fields, with rows representing varying applied field strengths, indicated at right. For clarity, water is excluded from the membrane diagrams. (i) Electroporation: An applied field will induce water intrusion into the hydrophobic region of the bilayer, and lipids re-organize to form a meta-stable hydrophilic pore. (ii) Chemical alteration of membrane lipids, such as lipid peroxidation, that deform tails and increase bilayer permeability. (iii) Modulation of protein channel function. The open/close state of voltage-gated ion channels may be altered by an applied field. (b) Stages and timescales of electropore formation. The red curve indicates the applied step field, and the blue dashed curve indicates the induced change in $TMV = \Delta V_m$. Within 1 ps of an applied field, water molecules penetrate into the hydrophobic region and rotationally align with the applied field [36]. Within ~ 1 ns, these protrusions form a water bridge that guide phosphate head groups into the interior. Within 1 μ s, the pore stabilizes, and continues to expand as long as the field is applied. For clarity, the lipid tail groups that form the membrane interior are excluded from the bottom diagram.

There are five steps in the initiation, formation, and decay of field-induced pores, each with associated timescales (the first two are depicted in Figure 8.2(b)) [18, 22]:

1. **Trigger (ns – μ s)** – Pore formation initiates once the TMV reaches the critical value ΔV_C . The electrical conductivity of the membrane increases detectably.
2. **Expansion (\sim pulse duration, ps – ms)** – Pores continue to grow provided $TMV > \Delta V_C$, and so is dependent on the applied field strength and shape. Conductivity and permeability continue to increase.
3. **Partial recovery (μ s – s)** – When $TMV < \Delta V_C$, membrane conductivity ($\sim \mu$ s) and permeability (\sim ms) decrease rapidly, but stabilizes at slightly elevated levels.
4. **Re-sealing (s – min)** – Original levels of permeability are eventually recovered, unless the cell was irreversibly damaged.
5. **Memory (hours)** – Some effects such as altered cytosolic ion concentration or hyperactive environmental stress responses persist for long periods following electropermeabilization [36].

8.2.2.2 Theory of membrane electroporation

For a model of electropermeabilization, consider a spherical cell in a homogenous external electric field that is immersed in an extracellular dielectric medium with permittivity and conductivity of ϵ_{ex} and σ_{ex} , respectively (Figure 8.3(a)) [22]. The cell is comprised of two regions: A spherical shell membrane (ϵ_m, σ_m) with thickness d , and an intracellular cytoplasm ($\epsilon_{in}, \sigma_{in}$) with radius R . Typical values in the literature for these parameters are provided in Table 8.1. An equivalent circuit that reproduces the frequency-response of the membrane electrical dynamics is shown in the inset of Figure 8.3(a). For sufficiently low membrane conductivity, the circuit is well-approximated by a charging/discharging parallel RC circuit.

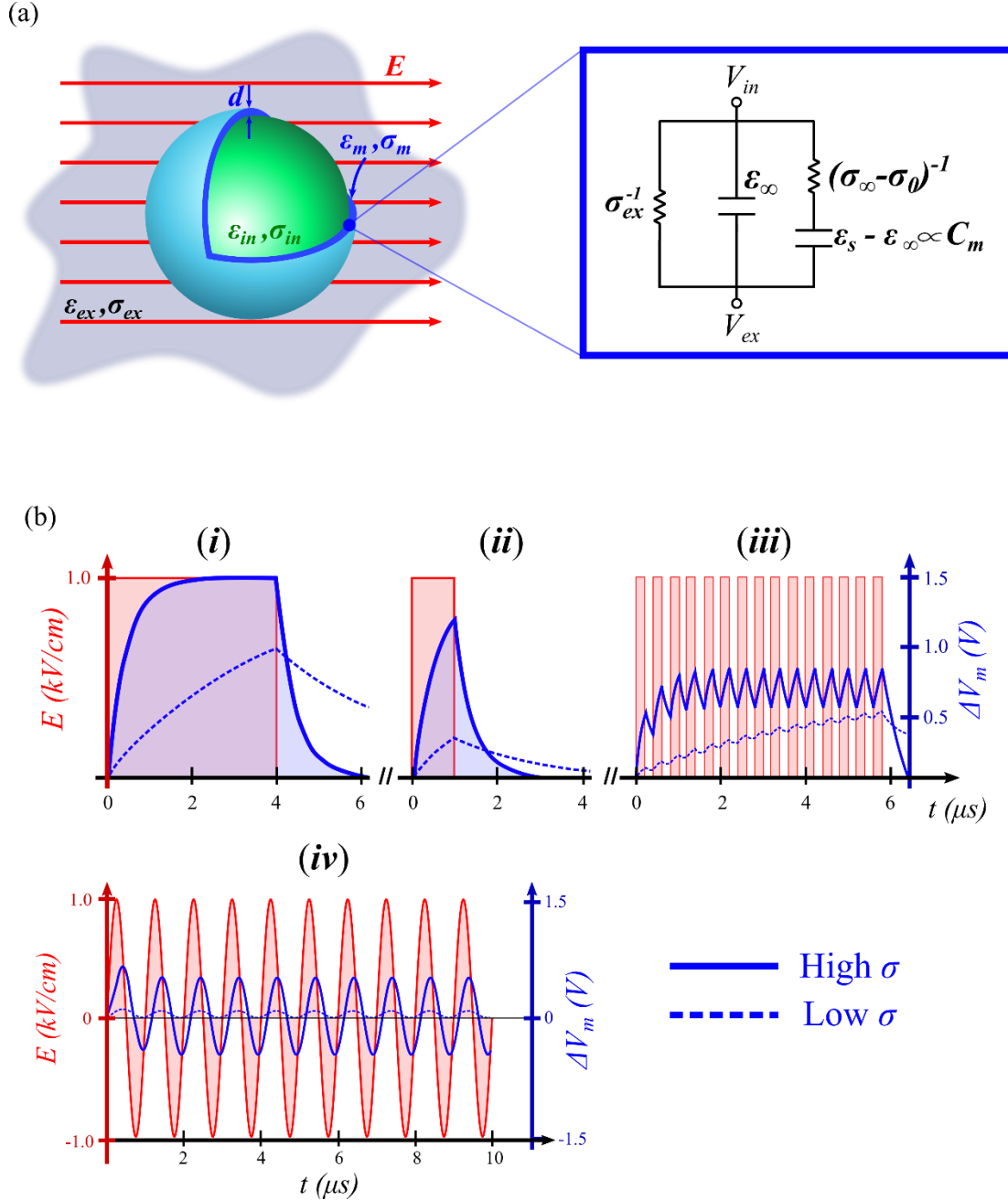


Figure 8.3. **Continuum model of membrane electroporation of a single cell.** (a) An external electric field is applied to the cell which is immersed in the extracellular dielectric medium (permittivity/conductivity $\epsilon_{ex}/\sigma_{ex}$), and comprised of two dielectric regions: The membrane (ϵ_m/σ_m) and intracellular cytoplasm ($\epsilon_{in}/\sigma_{in}$). *Right:* An equivalent circuit model for the electrical properties of the membrane, in terms of dielectric relaxation parameters discussed previously in this thesis (Chapter 2), adapted from [37]. (b) Examples of calculated membrane response (blue axes) for varying field inputs (red axes) for physiological (solid blue line) and low-conductivity (dotted blue line) extracellular environments, adapted from [38]. Potentials are for polar angle $\theta = 0^\circ$, and normalized to the cell radius R (see Equation (8.2)). (i) Extended pulses induce a saturation voltage of $\Delta V_m/R=1.5$. (ii) Pulses shorter than the membrane charging rise time will not reach the maximum potential. (iii) Trains of short pulses with sufficiently high duty cycles will accumulate potential in the membrane, then fluctuate about a stable average potential. (iv) Sinusoidal fields induce a potential that settles at a lagged sinusoidal potential variation.

For each region, there are two voltage components: The conductive component that is proportional to the electric field, and the dielectric component proportional to the field derivative. Expressing the vector electric field in terms of its potential gradient ($\vec{E} = -\nabla V$), the induced electric potential, V , is described by the Ampere-Maxwell equation [24, 38]:

$$\nabla \cdot \left(\left(\sigma + \epsilon \frac{\partial}{\partial t} \right) \nabla V(x, y, z, t) \right) = 0. \quad (8.1)$$

Equation (8.1) is solved for the desired geometry and boundary conditions that enforce continuity of the potential and current density at interfaces [39]. The membrane voltage, ΔV_m , is determined by computing the difference between intracellular (V_{in}) and extracellular (V_{ex}) environments: $\Delta V_m = V_{in} - V_{ex}$ [38]. From this solved potential difference, the time-evolution or frequency-dependence of the membrane response in terms of its dielectric parameters may be understood from models like the equivalent circuit in Figure 8.3(a).

Table 8.1. **Typical dielectric parameters for animal cells** [16, 38, 40]

	Symbol	Value	Units
Extracellular conductivity	σ_{ex}	3.0×10^{-1}	S/m
Membrane conductivity	σ_m	3.0×10^{-7}	S/m
Cytoplasm conductivity	σ_{in}^*	3.0×10^{-1}	S/m
Extracellular permittivity	ϵ_{ex}	7.1×10^{-10}	F/m
Membrane permittivity	ϵ_m	4.4×10^{-11}	F/m
Cytoplasm permittivity	ϵ_{in}	7.1×10^{-10}	F/m
Membrane capacitance	C_m	1.0×10^{-2}	F/m ²
Cell radius	R	10 – 100	μm
Membrane thickness	d	5 – 10	nm

*Intracellular conductivity σ_{in} set at a standardized value by convention [40].

For static fields, Equation (8.1) reduces to Laplace's equation: $\nabla^2 V = 0$, and the induced TMV in the membrane for spherical non-interacting cells is the steady-state Schwan equation [38]

$$\Delta V_m = fER \cos \theta \quad (8.2)$$

where R is the cell radius, θ is the polar angle in spherical coordinates with respect to the field direction, and $f = f(\sigma_{in}, \sigma_{ex}, \sigma_m; d, R)$ is a dimensionless factor related to the geometric and

electrical properties. In the non-conductive membrane regime ($\sigma_m \ll \sigma_{in/ex}$, cf., Table 8.1), $f \approx 3/2$.

The response to a step-change of a field in the low- σ_m regime may be represented as an RC circuit [38]

$$\Delta V_m = fER \cos \theta [1 - e^{-t/\tau_m}] \quad (8.3)$$

where E is a step function in time, and τ_m is the membrane relaxation time (~ 100 ns in physiological conditions for animal cells) [35]. Experimental validation of this model for long-duration step-inputs has been established for decades [41, 42].

To describe the membrane response to more complex environments or field distributions, the time-dependent Equation (8.1) is used, and an admittivity operator, Σ , is defined for each cellular region as [38]

$$\Sigma(t) = \sigma + \epsilon \frac{\partial}{\partial t}. \quad (8.4)$$

The Laplace transform converts the time-derivative operator to algebraic expressions of a complex frequency parameter, s

$$\mathcal{L}\{\Sigma(t)\} = \Sigma(s) = \sigma + \epsilon s. \quad (8.5)$$

The frequency-space geometric/dielectric factor $\mathcal{L}\{f\} = F$, which is now additionally a function of the regions' permittivities, is

$$F(\Sigma_{in}, \Sigma_{ex}, \Sigma_m) = \mathcal{L}\{f(\sigma_{in}, \sigma_{ex}, \sigma_m, \epsilon_{in}, \epsilon_{ex}, \epsilon_m)\} = \frac{a_1 s^2 + a_2 s + a_3}{b_1 s^2 + b_2 s + b_3} \quad (8.6)$$

where a_i and b_i are functions of the intracellular, extracellular, and membrane conductivities and permittivities, as detailed in the Appendix [38]. Therefore, provided the Laplace transform $E(s) = \mathcal{L}\{E(t)\}$ of the input field exists, the inverse Laplace transform

$$\frac{\Delta V_m(t)}{R} = \mathcal{L}^{-1} \left\{ \frac{\Delta V_m(s)}{R} \right\} = \mathcal{L}^{-1} \{ F(\Sigma_{in}, \Sigma_m, \Sigma_{ex}; s) E(s) \} \quad (8.7)$$

returns $\Delta V_m(t)$ normalized to the cell radius at $\theta = 0^\circ$. Scaling by R and $\cos \theta$ (cf. Equation (8.2)) describes the spatial distribution of the induced TMV for arbitrary fields, $E(t)$.

Examples of calculated membrane responses to varying field inputs using Equation (8.7) are shown for single square pulses, pulse trains, and sinusoidal waveforms in Figure 8.3(b), where the red curves are the input field waveform and the blue curves are the induced TMV (dotted lines are for low extracellular conductivity, $\sigma_{ex} \ll \sigma_{in}$). Interestingly, lower extracellular conductivity significantly decreases the induced TMV amplitude, and increases the membrane relaxation time [40]. Empirical data suggests that the membrane relaxation rate is inversely proportional to environmental conductivity, and may increase up to ~ 1 ms (cf. $\sim 0.1 - 10$ μ s in physiological conditions) [35, 42]. Cell electroporation is therefore expected to depend significantly on the conductive properties of its environment, and local conductivity variations in real cellular samples may significantly influence the dynamics of field-induced permeabilization.

For a 1 kHz train of picosecond-duration pulses as used in this thesis, the THz pulse may be approximated as an impulse function ($E(t) \approx \delta(t)$). Since typical decays of ΔV_m are exponential with $\sim \tau \sim 0.1 - 1$ μ s, each new pulse will see a fully relaxed environment in most experimental and physiological conditions [42]. This implies that for a 1 kHz train of intense THz pulses, each individual pulse must have sufficient field to achieve $\Delta V_m > \Delta V_C$. As shown in statistical and molecular dynamics simulations, physical triggering of pore formation or general permeabilization is entirely stochastic, with the probability of pore formation increasing linearly with field strength and exponentially with number of pulses [36, 43, 44, 45]. However, as indicated by the dashed lines in Figure 8.3(b), the conductivity of the extracellular medium plays an important role in the relaxation dynamics of the induced TMV [46]. If the relaxation time increases to ~ 1 ms, close to the repetition rate of the THz pulse train, a TMV build-up effect is feasible.

8.2.2.3 Membrane effects of picosecond/terahertz pulse exposure

Picosecond-duration pulses, while too short to allow appreciable ionic redistribution, may still increase the TMV and perturb membrane integrity, provided sufficient field strength and pulse numbers are applied, by similar mechanisms as those described above [18, 36]. An important characteristic of this regime is that the applied fields additionally induce TMVs on interior

organelle membranes, such as those enveloping the nucleus, mitochondria, endoplasmic reticula, and vesicles. With longer pulses, these structures are typically electronically screened by ionic redistribution in the PM, and the induced TMV on interior membranes with sub-nanosecond pulses may even exceed that of the cell PM [18, 46]. Therefore, the potential biological effects triggered by electropermeabilization in this regime are extended to the set of cellular processes regulated by these additional membrane structures' permeabilities.

Using 500 ps, 190 kV/cm field pulses, Vernier et al. observed dose-dependent Ca^{2+} transient spikes in rat glioma hybrid cells, but required thousands of pulses. This corroborates a stochastic mechanism having a probability of pore formation that depends on both field strength and number of pulses [25, 35, 36]. Interestingly, cytosolic Ca^{2+} levels remained elevated for ~ 100 s post-exposure, a biochemical "memory" of the compromised membrane that is not explained by the purely physical field interactions [36].

Utilizing the ^2H -NMR spectrum that is sensitive to water order at pore formation sites, Beneduci et al. observed reversible membrane permeabilization induced by low-power 50 – 70 GHz MMWs in phosphatidylcholine membrane models [30]. These were attributed to non-thermal coupling to bound water relaxation, while interaction with slower dynamics such as membrane fluctuations or water diffusion were excluded. The increase of permeability from these water dynamics is consistent with an isothermal gel-fluid phase transition, a known property of membrane permeability, and indicates additional dependence on the environmental influence of the systems' phase transition points [31, 47].

Ramundo et al. have investigated the effects of 0.13 THz macropulse trains (50 ps micropulses separated by 330 ps within a 4 μs macropulse) at low macro-repetition rates (5 – 10 Hz) as generated by a free electron laser (see Chapter 5) [31, 34]. Significant increase of permeability was detected as measured by increased intravesicular catalytic activity, but no permeability changes were observed for dose-matched 0.15 THz CW exposures, indicating significant dependence on field delivery, pulse shape, and coupling to structural dynamics of membrane components that is not explained by thermal mechanisms.

The theory outlined in Section 8.2.2.2, and the experimental results observed in the RF, MMW, and low-THz bands outlined above, motivate the hypothesis that picosecond-duration THz pulses may induce similar electropermeabilizations, provided sufficiently high field strength and exposure time. Further, this may be a key interaction mechanism underlying the observed biological effects induced by intense THz pulses, such as observations of THz-induced alteration of membrane-

regulated signaling processes [48], or direct measurements of THz-induced increases of membrane permeability [31, 49], action potential firing rate [32], and ion flow [36]. It should be noted, however, that field-induced modulation of membrane-regulated biological function may occur through mechanisms other than electroporation, such as lipid peroxidation or modulation of membrane protein function, as shown in Figure 8.2(a) [46].

8.2.3 Pulse shape and field delivery

In most experiments investigating electroporation, square/trapezoidal voltage pulses are delivered by direct electrical stimulation with electrodes in contact with the biological sample, which may induce spurious electrolytic or mechanical effects [18, 50]. Approaches to avoid these effects include utilization of AC magnetic fields, which may induce strong intracellular electric fields in deep tissue that induce electroporation [51, 52] or free-space electromagnetic pulses, potentially coupled to antennae structures. As discussed in [18, 53], large-antennae-coupled field exposures are feasible for the sub-nanosecond duration range, as tissue may be targeted with sufficiently small resolution.

In the picosecond regime in particular, simulations suggest that the field strength required to permeabilize the cell membrane depends significantly on pulse frequency and shape [33, 36, 54]. Further, due to the stochastic nature of interaction, potentially due to low duty cycles as argued above, the probability of pore formation additionally depends on exposure time, or the total number of pulses. In the experiments to be discussed, the hypothesis that intense THz pulses induce detectable levels of membrane permeabilization is investigated. Long-term effects in human epithelial cancer cells are investigated 24 hours following extended exposures (1 – 30 minutes), and potentially transient/reversible changes of membrane permeability are investigated via real-time fluorescence microscopy in rat cancer cells during exposure. Results indicate that broadband exposures induce long-term changes to membrane permeability that scale with total THz dose. Utilization of a conductive tip to locally enhance the peak electric field for a target cell further corroborates the hypothesis of field-strength-dependence of electropermeabilization.

8.3 Intense terahertz pulse source and exposure system

Here, the general aspects of cellular exposure studies are introduced, and experiment-specific details are provided in the relevant sections.

The THz bio-exposure system described in Chapter 5 is operated with the THz beam focused in the vertical orientation (rotational off-axis parabolic mirror (OAPM) set at 0°) for through-substrate exposures in the temperature-regulated sample holder. Samples were adherent monolayer cell lines, as in principle these minimize absorption losses to the aqueous extracellular medium, although small sample interaction lengths in flat monolayer cell cultures may detrimentally decrease the absorbed energy (see the dosimetry analysis of Chapter 6). Analyses of THz-induced effects were performed with fluorescence microscopy of labelled molecules whose positive fluorescence detection indicates compromised cell membranes. These analyses were either in real-time with long-working distance objectives, or following fixation with high-resolution contact objectives, as specified in the individual experiments.

8.4 Long-term effects of intense terahertz pulses to membrane permeability in A-431 epithelial carcinoma cells

8.4.1 Methods

8.4.1.1 Growing and passaging A-431 cells

A-431 cells (ATCC, CRL-1555) are an adherent human epithelial epidermoid carcinoma grown in Dulbecco's Modified Eagle Media (DMEM) supplemented with 10% fetal bovine serum (FBS) and 1X penicillin/streptomycin according to the distributors' instructions. Cells were thawed from liquid nitrogen, transferred to 10 mL of culture medium, and centrifuged (500g, 5 min) at room temperature. The supernatant was removed, cells resuspended in 10 mL media, and used to seed T75 flasks. Re-passaging was required every 2 – 3 days. Media was removed and cells were washed with 5 mL PBS (phosphate-buffered saline). To cleave the adherence molecules, 1 mL of 0.05% trypsin-EDTA was added to uniformly cover the growth surface, and incubated for 5 minutes at 37°C. Once all cells had detached, the trypsin-EDTA was neutralized with 5 mL of media and removed. 0.6 mL was transferred to a new flask and topped up with 12.5 mL of fresh media.

For exposure experiments, during passage a diluted volume of cells was plated in optical plastic tissue culture dishes (Ibidi μ -slide, 80281) and incubated overnight to allow the cells to adhere and re-equilibrate. Cell concentration and viability were determined with a hemocytometer and 0.4% trypan blue (Gibco, 15250061). The estimated concentration for confluency of the growth area (0.6 cm²) is estimated to be ~500 000 cells/mL. It was empirically determined that an initial seeding concentration of 200 000 cells/mL resulted in adequate confluency of 80-90% for exposure the

following day. Before exposure, cell media was removed and replaced with fresh media supplemented with 15 mM HEPES buffer to maintain physiological pH while cells are outside of the CO₂-regulated incubator environment.

8.4.1.2 Terahertz exposure of A-431 cells

Multiple THz exposures are performed in the double-well dishes to explore dependence on THz frequency and dose, as shown in Figure 8.4(a). One well is used to investigate frequency-dependence by filtering the broadband THz beam with bandpass filters (0.5, 1.5, 2.0 THz) directed towards different regions along the center of the well growth area. The total exposure times are adjusted as indicated to match the total dose and maximize exposure time, and was equivalent to 0.6 minutes of broadband exposure.

For broadband exposures, dose-response was investigated by varying the total exposure time from 1 – 30 minutes. The exposure parameters for each condition are summarized in Table 8.2. For the 2.0 THz band, the peak is at 1.3 THz due to side-leakage of the relatively small-amplitude spectrum seen on a log-scale in the inset of Figure 8.4(b).

Table 8.2. THz pulse parameters for A-431 exposures

	Broadband	0.5 THz band	1.5 THz band	2.0 THz band
Pulse Energy (nJ)	1000	66.5	71.3	16.8
Peak field (kV/cm)	430	49	92	65
Peak frequency (THz)	0.7	0.53	1.4	1.3
Bandwidth FWHM (THz)	0.7	0.07	0.3	0.8
Pulse duration (ps)	1.1	6.0	2.5	0.9

From the broadband pulse energy (1.0 μ J), measured circular spot diameter (1.3 mm), and THz pulse repetition rate (1 kHz), the average dose rate was 4.5 J/cm²/min. Thus, for exposure times of 1, 5, 10, and 30 minutes, the corresponding deposited energy density was 4.5, 22.5, 45, and 135 J/cm². Each broadband pulse had a peak intensity of 68.5 MW/cm². When exposures were complete, cells were placed in the incubator for 24 hours prior to fixing and staining (described next) to investigate the long-term effects to membrane integrity of extended THz pulse exposures.

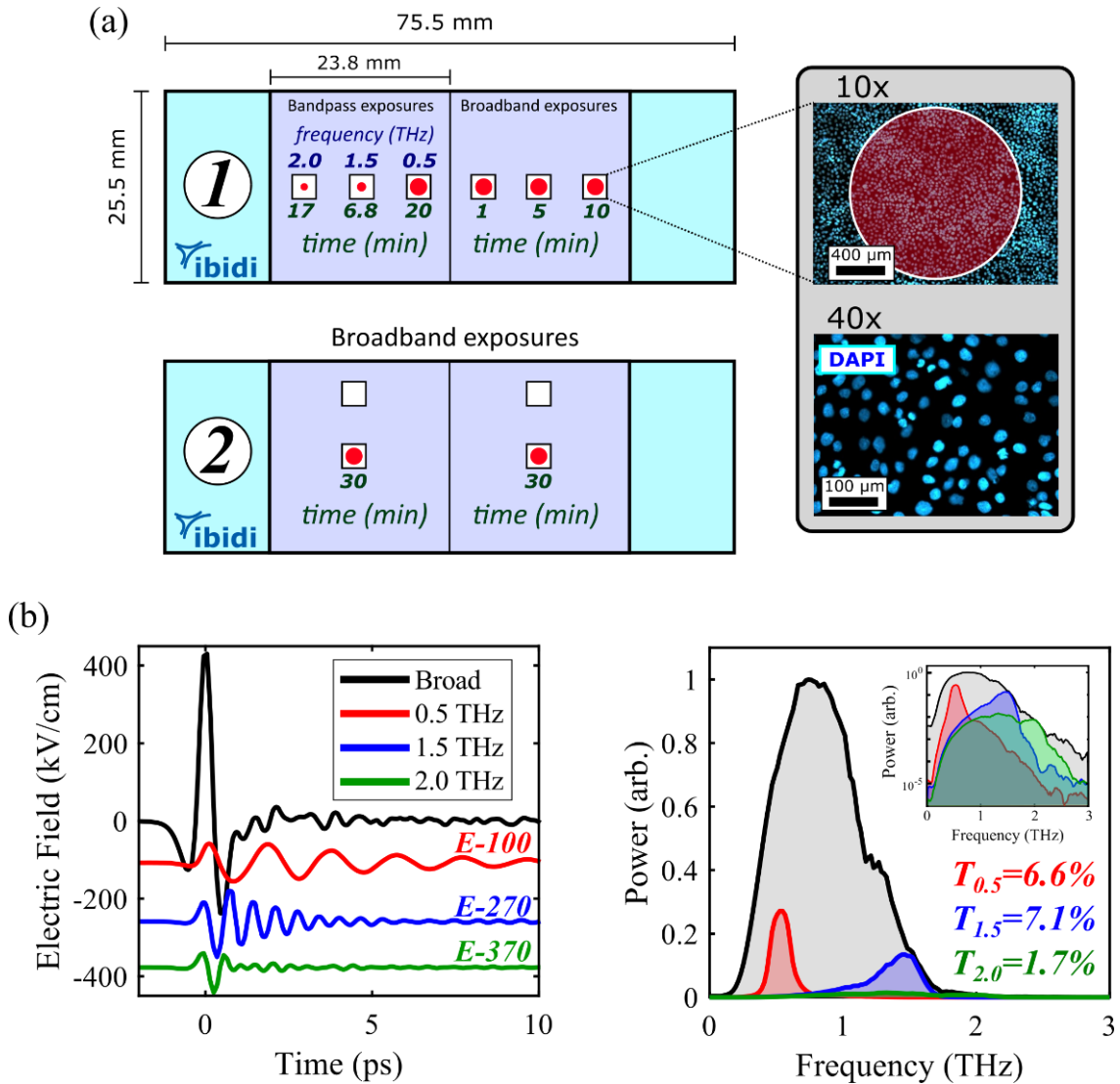


Figure 8.4. **Broadband and bandpass exposures of A431 monolayer cell cultures.** (a) Schematic of parameter variation for different regions of the cellular growth area. White squares indicate the microscope FOV at low magnification (10x), and red dots indicate the relative THz spot size. Sample fluorescence images of the DAPI channel are shown at right, with the broadband THz spot size indicated by the red circle. (b) EO-sampled THz pulses (vertically shifted as labelled for clarity) and power spectra. The energy transmittance for bandpass spectra are labelled in the spectra plot. *Inset:* Power spectra on a logarithmic scale.

8.4.1.3 DNA and viability staining of A-431 cells

Following exposure and incubation for the desired fixing time, cells were labelled with fluorescent DNA (4',6-diamidino-2-phenylindole, DAPI) and viability (Zombie Green, ZG, BioLegend 423111) stains. The former binds to AT-rich regions of DNA in the nucleus and is utilized for cellular localization, while the latter is an amine-reactive fluorescent dye that is permeable to compromised cell membranes. Cells were removed from the incubator, washed in PBS, and incubated in 1:1500 ZG viability stain (0.5 mL PBS + 0.33 μ L ZG) for 30 minutes at room temperature. The solution was then removed, cells washed again in PBS, and incubated in 1:2000 DAPI (0.5 mL PBS + 0.5 μ L – 1 mg/mL DAPI) for 10 minutes at room temperature. Labelled cells were mounted with \sim 5 μ L SlowFade and coverslip, and sealed with clear nail polish. Control dishes (positive and negative, shown in Figure 8.5(a)) were treated equivalently to THz-exposed cells. For the positive death controls, the cells were fixed with 1 mL 10% formalin for 30 minutes at room temperature prior to fluorescent staining.

8.4.1.4 Fluorescence imaging and analysis of A-431 cells

Labelled cells were imaged with an Olympus IX81 fluorescence microscope and Q-Capture Pro 7 software. The ZG excitation wavelength was 488 nm, and the emission, peaked at 520 ± 50 nm, was collected through a standard FITC fluorescence filter set. Analysis was performed with the open source image analysis software, ImageJ (<https://imagej.nih.gov/ij/>). The fraction of ZG-positive (ZG+) cells were identified by converting the image data to binary images, and using the cell counting plug-in “Analyze Particles”.

8.4.2 Results

Membrane permeable dyes are often utilized for apoptosis assays in which a key characteristic is a compromised membrane structure [55]. Here we are investigating THz-induced effects to membrane structure regardless of other biomolecular characteristics associated with cell death, such as annexin V expression or caspase activation [56], although future experiments correlating the membrane integrity to cell viability would be valuable. Figure 8.5 summarizes the results of the broadband and bandpass exposures outlined above. The DAPI channel (blue) indicates cell location, and the green channel indicates membrane integrity status as calibrated by the positive and negative death control images in Figure 8.5(a) used to set the fluorescence intensity scale of the microscope. Figure 8.5(b) shows the results of broadband THz dose-dependence for varying

exposure times. Cell counting algorithms applied to these image data were used to calculate the fraction of ZG+ cells, and is shown for increasing THz dose/exposure time in Figure 8.5(c), with error bars representing standard Poisson counting error. A small but significant increase in the fraction of hyperintense cells are observed relative to sham-exposed controls, indicating compromised membranes that increases with total dose. Interestingly, this curve saturates at $\sim 2\%$ in approximately 10 minutes, with very little change up to 30 minutes of subsequent exposure (discussed further in Section 8.6). An exponential model was fit to the data in Figure 8.5(c) to extract a characteristic time for this saturation behaviour, and was found to be 3.5 min.

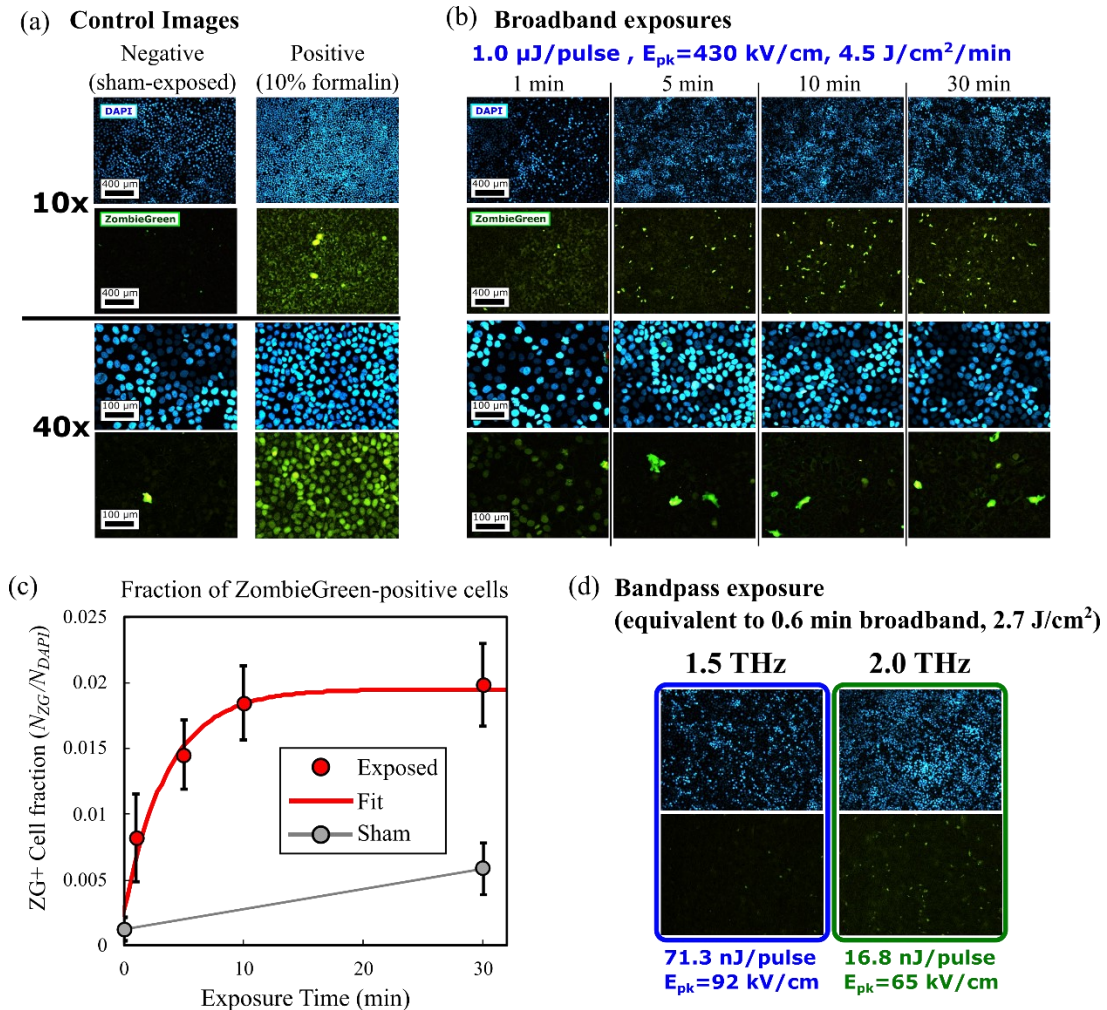


Figure 8.5. Effect of free-space intense THz pulses to membrane permeability in A-431 epithelial carcinoma cells 24 hours post-exposure. (a) Negative and positive cell death controls showing significant increase of the ZombieGreen (ZG) viability probe for chemically permeabilized membranes at low (10x, top) and high (40x, bottom) magnification. (b) Fluorescence images of THz-exposed cells for varying exposure times (number of pulses). The number of ZG+ cells increase with exposure time, indicating compromised cellular membranes. (c) Relative fraction of ZG+ cells compared to the DAPI reference image, with error bars propagated from standard Poisson counting uncertainty ($N \pm \sqrt{N}$). (d) Microscopy of bandpass exposures. No increase of ZG+ cells was observed.

For the bandpass exposures, during imaging it was found that the 0.5 THz, 20-minute exposure (see Figure 8.4(a)) was in a region close to the well wall with very sparse cellular population, and so only the 1.5 THz and 2.0 THz bands were analyzed. However, significant variation from the background fluorescence is not observed for either analyzed frequency band. As discussed in Section 8.6, this may be due to the relatively low field strength or total dose, as even the extended exposure times were equivalent to only 0.6 minutes of broadband exposure (2.7 J/cm^2).

8.5 Real-time effects of intense terahertz pulses to membrane permeability in RBL-2H3 rat basophilic leukemia cells with tip-enhancement

In Section 8.4, results were presented that characterized membrane integrity changes induced by intense THz pulses 24 hours post-exposure for varying dose. However, evidence from simulations suggests that membrane integrity may be a transient, reversible effect, and so a real-time investigation characterizing membrane permeability during exposure to intense THz pulses was performed. In these studies, propidium iodide (PI) was utilized to probe membrane integrity. PI-permeable cells have been shown to recover viability when the membrane-porating stimuli are removed and the membrane is repaired, although this effect should be verified to ensure this property is non-specific with cell type [57].

The hypothesis of THz-induced membrane permeabilization is tested on Rat Basophilic Leukemia (RBL-2H3, ATCC CRL-2256) cells, a histamine-releasing cell line that activates a release of large granule stores that contain pro-inflammatory mediators. Since THz exposures have been shown to induce recruitment of inflammatory markers across multiple cell types, these cells were chosen to investigate THz-induced effects, including alterations to membrane structure and integrity. These cells offer other advantages, such as adherent growth, which minimizes attenuation loss in the surrounding aqueous medium.

8.5.1 Methods

8.5.1.1 Growing and passaging RBL-2H3 cells

RBL-2H3 cells are an adherent rat blood basophilic leukemia cell line grown in Essential Modified Eagle's Media (EMEM) supplemented with 15% FBS and 1X penicillin/streptomycin. Cells were thawed from liquid nitrogen, transferred to 10 mL of culture medium, and centrifuged (200g, 5 min) at room temperature. The supernatant was removed, cells resuspended in 10 mL of

media, and used to seed T75 flasks. Re-passaging was required every 2 – 3 days. Media was removed and cells were washed with 5 mL PBS. 1 mL of 0.25% trypsin-EDTA was added to uniformly cover the growth surface, and incubated for 5 minutes at 37°C to detach the cells. Trypsin-EDTA was neutralized with 5 mL of media and removed. 0.6 mL was transferred to a new flask, and topped up with 12.5 mL of fresh media.

For exposure experiments, cells were plated in optical plastic tissue culture dishes (Ibidi μ -Dish, 35 mm low-wall Grid-500) and incubated overnight to allow the cells to adhere and re-equilibrate. Similar to the previous study, cell concentration and viability were determined with a hemocytometer and 0.4% trypan blue (Gibco, 15250061), and an initial seeding concentration of 200 000 cells/mL was empirically determined to result in adequate confluency of 80-90% for exposure the following day.

8.5.1.2 Fluorescence staining of RBL-2H3 cells

Cells were labelled immediately prior to THz exposure for real-time live-cell fluorescence monitoring of membrane integrity. Dishes were removed from the incubator, media removed, and cells washed twice in PBS. A 1:3000 propidium iodide (PI) staining solution was diluted with PBS from 1 mg/mL stock (Invitrogen, P3566). For the THz-exposed dishes, 0.33 μ L PI was added to each well with 1 mL PBS, incubated for 5 minutes at room temperature, and stored in the incubator until exposure. Positive death controls were fixed with cold methanol and incubated at -20°C for 5 minutes, washed three time with PBS, and labelled with equivalent PI+PBS solution to calibrate the microscope fluorescence signal. Before exposure, cell media was removed and replaced with fresh media supplemented with 15 mM HEPES buffer to maintain physiological pH while cells are outside of the CO₂ incubator environment.

8.5.1.3 Terahertz exposure and real-time fluorescence imaging of RBL-2H3 cells

The set of THz pulse exposure parameters for these exposures are summarized in Table 8.3. From the broadband pulse energy (0.55 μ J), circular spot diameter (1.7 mm), and THz pulse repetition rate (1 kHz), the average dose rate was 1.5 J/cm²/min. Each broadband pulse had a peak intensity of 17.5 MW/cm². For tip-enhanced exposures, a tip is loaded into a custom tip holder mounted to a 3D translation stage, as discussed in Chapter 5. The shaft is aligned to the THz field direction, and the tip apex is centred and focused to the microscope image plane to ensure it is coincident with the THz focus. COMSOL simulations predict that for an incident THz peak field

of 186 kV/cm, the enhanced field in water will be 6.5 MV/cm, localized to a FWHM region of 0.4 μm about the tip apex.

Table 8.3. THz pulse parameters for RBL-2H3 exposures

Pulse Energy (μJ)	0.55
Peak field (kV/cm)	186 (6500*)
Peak frequency (THz)	0.5
Bandwidth FWHM (THz)	0.3
Spot diameter (mm)	1.7
Pulse duration (ps)	1.4

*local tip-enhanced peak field

In the real-time exposure and analysis configuration, the THz beam propagates colinearly with the fluorescence excitation beam. Bright-field images were taken initially for cell localization. For real-time fluorescence imaging, the blue (473 nm) excitation laser line was used, and a 610 nm long-pass filter isolated the PI-emission peaked at 620 nm [58]. Images were taken every 2 minutes. For each timepoint, the fluorescence excitation laser exposed the samples for ~ 5 s per image set and a series of 15 images were averaged, each with an exposure time of no greater than 300 ms each.

8.5.2 Results

For free-space broadband exposures, no significant changes to PI fluorescence was observed up to 30 minutes of THz exposure. For tip-enhanced exposures, an increase in fluorescence is detected at the 8 minute timepoint, followed by a large increase within the following 2 minutes, as shown in Figure 8.6(b).

The mean pixel intensity from the raw image data in a region of interest (ROI) about the tip apex is shown in Figure 8.6(c). The ramp increase in PI fluorescence intensity indicates a sudden onset of compromised membrane structure.

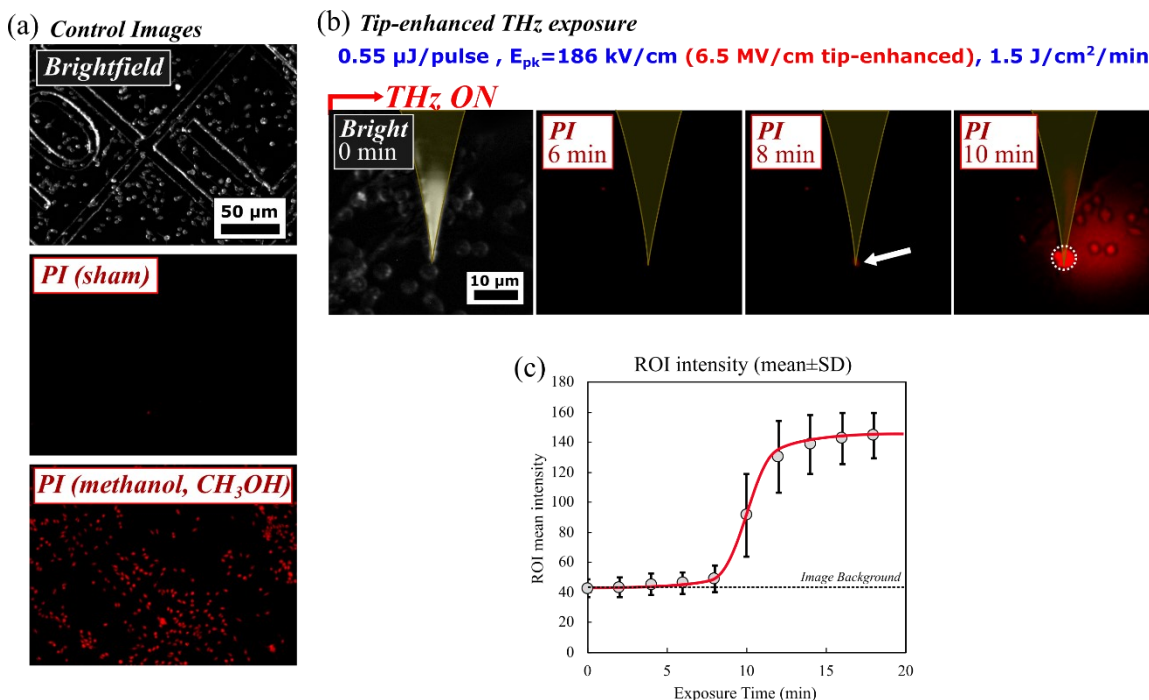


Figure 8.6. **Results of tip-enhanced THz exposures to membrane integrity in target RBL-2H3 cells.** (a) Control brightfield images show a low-confluency population for single-cell targeting. The images at center and bottom show fluorescence images for sham-exposed and positive death controls, respectively. The positive death control shows a positive PI signal indicating compromised membranes immediately following the addition of 1 mL of cold methanol. (b) A zoomed FOV showing the tip apex positioned at the target cell. At 8 minutes of THz exposure, a small PI+ signal in the target cell is observed. Within 2 minutes of this initiating event, a dramatic increase in PI is detected, indicating a compromised membrane in the target cell. (c) The average pixel intensity (mean±SD) of raw images in the ROI surrounding the tip apex (dotted circle in (b)) over the THz exposure duration. The onset of PI fluorescence in the target cell occurs within 2 minutes of initiation, with relatively little further change up to 10 minutes later.

8.6 Discussion

Molecular fluorescence probes (Zombie Green (ZG) and Propidium iodide (PI)) were used to assess the permeability status of the cell membrane. PI in particular binds to DNA, and so must traverse both the PM and the two concentric inner and outer nuclear membranes. Therefore, a positive fluorescence signal in these studies additionally indicates that intense THz pulses interact with interior membrane structures, as hypothesized in Section 8.2.2.3.

Measurement of a THz dose dependence was observed 24 hours following broadband exposure of A-431 cells (Figure 8.5). At the 1-minute exposure timepoint (4.5 J/cm² total dose), a small increase of ZG+ cell fraction is observed relative to sham controls. Interestingly, the fraction of permeabilized cells increases with time, but saturates at approximately 10 minutes of exposure (45 J/cm²), with relatively little additional effect observed up to 30 minutes (135 J/cm²). A potential

explanation for this in the context of the hypothesized mechanisms is the influence of cell geometry and extracellular dielectric environment that influence both the critical voltage necessary for electroporation (ΔV_C), as well as the dynamics and magnitude of the induced TMV for a given input field strength and duration (ΔV_m) [35, 42, 46]. Due to large variability of geometric characteristics of individual cells, and the interaction with complex environments leading to local variations of extracellular conductivity, it may be that only a subset of the entire cellular population meets the criteria for which the THz pulse could possibly induce a TMV that exceeds ΔV_C , either with variations that accommodate a relatively large TMV, or a relatively small ΔV_C . If so, this may be reflected in the saturation behaviour seen in Figure 8.5(c). Once the membranes of these cells were compromised, since the field strength and duration of each subsequent pulse was fixed, no further cell permeabilization was observed, as the pulse was insufficient to achieve $\text{TMV} > \Delta V_C$ in the remaining cells.

An investigation of frequency dependence using bandpass-filtered exposures did not see any indication of THz-induced permeabilization of A-431 cells at equivalent fixing time, although this may be due to the low total dose (2.7 J/cm² total dose, equivalent to 0.6 minutes of broadband exposure) or insufficient field strengths (92 kV/cm and 65 kV/cm for 1.5 THz and 2.0 THz band, respectively). This is additionally corroborated by the study of Section 8.5, which similarly did not see compromised membrane integrity, even for extended exposure times with broadband fields of relatively lower strength (186 kV/cm, 0.55 $\mu\text{J}/\text{pulse}$), while tip-enhanced fields (6.5 MV/cm) quickly compromised membrane integrity in the target cell (Figure 8.6). It is possible that the broadband field strengths utilized in the A-431 study (430 kV/cm, 1.0 $\mu\text{J}/\text{pulse}$) are close to the minimum necessary parameters to induce membrane permeabilization. In the exposures of PI-labelled RBL-2H3 cells (Section 8.5), while no significant effect was observed for free-space exposures, in the tip-enhanced configuration the membrane integrity of the target cell at the tip apex was compromised within 10 minutes, as in Figure 8.6.

8.6.1 Relation to tissue-level effects

These *cellular*-level results may also be discussed in terms of THz-induced effects observed at a higher *tissue*-level of biological structure. In Chapter 7, measurements of global differential gene expression profiles induced by THz pulses in human skin were reported [48, 59]. In those investigations, 3D human skin tissue models were exposed to a 1 kHz train of intense THz pulses with similar exposure parameters (2.4 $\mu\text{J}/\text{pulse}$, $E_{\text{peak}} = 240 \text{ kV}/\text{cm}$, $I_{\text{pulse}} = 74 \text{ MW}/\text{cm}^2$) as used here for the permeability studies, and the changes to global gene expression relative to unexposed

tissues were measured with cDNA microarrays. Several features of these data indicate that the measured global differential gene expression profiles represent a genomic response to compromised membrane permeability status, corroborating the hypothesis that the cell membrane is an important target in the initiation of THz-induced biological effects.

Since the theory of cell-level THz interactions outlined in Section 8.2.2.2 assumes non-interacting cells in a dielectric medium, observation of tissue-level electroporation effects may deviate significantly from such simplistic models. While the electroporation dynamics of each cell are chemically coupled via cytosolic leakage that modifies the conductivity of the extracellular environment seen by the population, experimental results suggest that as long as the local electric field distribution is properly characterized, cells in a large assembly behave approximately consistently with individual cells. As a result, the qualitative aspects of theoretical electroporation may still be applicable to the tissue scale as well [18, 60].

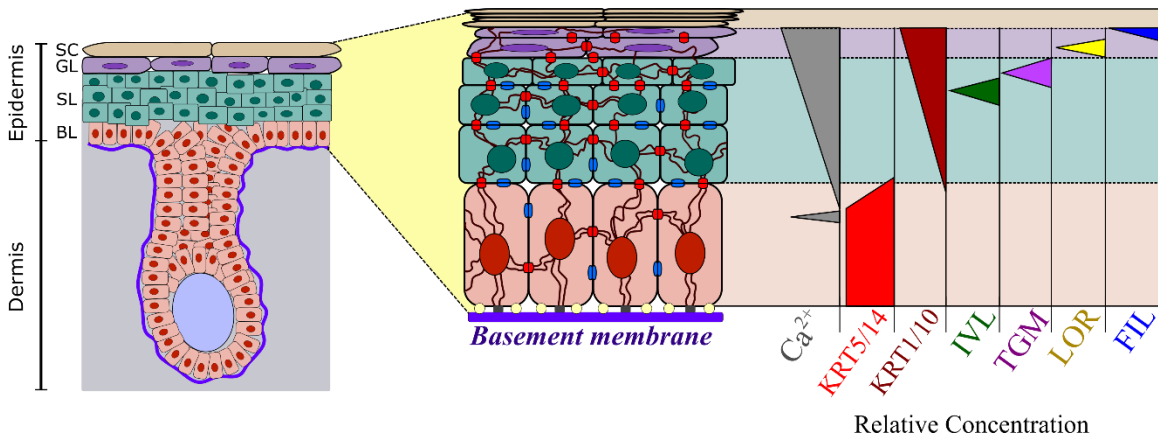


Figure 8.7. **The cellular structure of skin tissue, and calcium-regulated gene expression of epidermal differentiation.** Skin is an organ comprised of epithelial epidermal and connective dermal tissues. The epidermis is comprised of four stratified layers: Basal layer (BL), spinous layer (SL), granular layer (GL), and the stratum corneum (SC). Snapshot in time of gene expression in the cellular layers during epidermal differentiation, adapted from [61, 62]. A calcium spike in the basal layer triggers a switch that expresses keratin 1 and 10 instead of keratin 5 and 14. A steep calcium gradient across the epidermis then regulates the sequential expression of genes that encode for structural proteins that provide mechanical stability of skin, as detailed in the text body.

The epidermis is an epithelial tissue structure comprised of four stratified layers of squamous epithelial keratinocytes: basal layer (BL), spinous layer (SL), granular layer (GL), and stratum corneum (SC), as labelled in Figure 8.7 [63, 64]. During epidermal differentiation, the proliferating cells in the basal layer exit the cell cycle as they move to suprabasal regions where they begin to express genes that encode for the enzymes and substrates required for differentiation and construction of the epidermal barrier. A snapshot of the spatiotemporal gene expression dynamics that are regulated by a steep calcium (Ca^{2+}) gradient across the epidermis is shown at right in Figure

8.7. These dynamics are responsible for the continual differentiation, stratification, and turnover of the epidermal layer. Some of the important genes are:

- Keratin (KRT5, KRT14, KRT1, KRT10)
 - A type of intermediate filament that provides rigidity and structural stability to the cytoskeleton of keratinocytes
- Transglutaminase (TGM1, TGM3, TGM5)
 - Cross-linking enzymes that act on target substrates (IVL, LOR, FLG, SPR) and anchor them to the cornified envelope
- Involucrin (IVL), Loricrin (LOR), and Filaggrin (FLG)
 - Substrates for transglutaminase (TGM) and major component of the cornified envelope

At low calcium concentrations near the basal layer, cells proliferate, but do not differentiate [64]. Differentiation is initiated by a sudden release of intracellular calcium stores in the basal layer, causing rapid morphological change, upward motility, stratification in higher layers, and initiation of expression of genes that encode for proteins that form cytoskeletal components and cell-cell contacts required for differentiation [65].

Increasing calcium concentration towards the suprabasal layers triggers sequential expression of KRT1/10, IVL, TGM1, LOR, and FLG in the spinous and granular layers. The cornified layer contains the enucleated, terminally differentiated keratinocytes (“corneocytes”) that have undergone keratinization. Keratinization (or “cornification”) is a form of programmed cell death in which keratinocytes release lipids and proteases required for impermeability and desquamation (respectively), and the crosslinking enzymes TGM1/3/5 act on substrates (LOR, SPR, IVL) by anchoring them to the cornified envelope (highly cross-linked proteins and lipids), which forms the outer mechanical barrier of skin tissue [63, 65, 66].

Out of 1681 genes significantly differentially expressed by exposure to intense THz pulses, the greatest expression magnitude (fold-change, FC) was downregulation of CLCA2 ($\text{Log}_2(\text{FC}) = -4.78$, $p < 0.006$), a gene that encodes for a calcium-activated membrane chloride channel subunit that transports chloride across the PM [67]. Other genes that were significantly expressed include SCNN1A (encodes for a nonvoltage-gated sodium channel) and CLIC3 (an intracellular chloride channel) [67]. Moreover, all gene families that regulate epidermal differentiation discussed above, including membrane-dependent junction proteins, are downregulated by THz exposure, as shown in Figure 8.8(a – b).

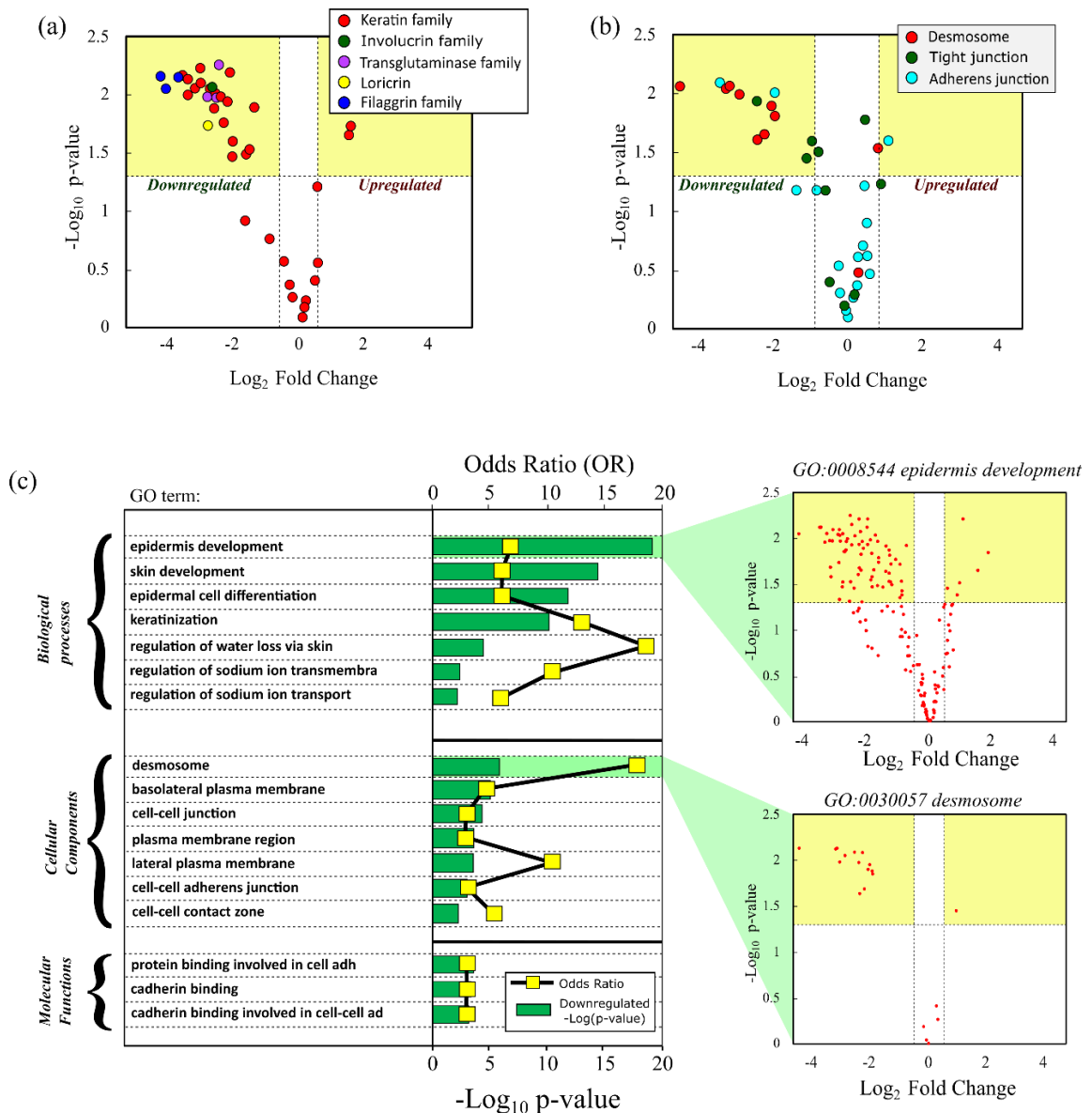


Figure 8.8. **Intense THz pulses significantly downregulate membrane-related genes that regulate epidermal differentiation in human skin.** Volcano plots display: (a) Significant downregulation of all gene families of Figure 8.7 involved in epidermal differentiation. (b) Genes that encode for membrane-bound cell-cell contacts (desmosomes, tight junctions, or adherens junctions). (c) Results of Gene Ontology analysis. There is significant over-representation of THz-downregulated genes in membrane-regulated biological processes and cellular structures. At right are examples of high-significance (top) vs. high odds-ratio (bottom) gene expressions that achieved significant over-representations within processes and structures that regulate epidermal differentiation.

Gene Ontology (GO) analysis, introduced in Chapter 7, was performed on the global gene expression dataset to identify statistical over-representation of all THz-affected genes within gene sets that regulate known biological processes, cellular components, and molecular functions [68]. 58 GO terms were identified as over-represented by the set of THz-affected genes, and a subset of

17 that are related to membrane-regulated processes and structures are summarized in Figure 8.7(c). GO terms significantly identified are predominantly related to membrane transport processes, membrane-embedded cell-cell contact structures, and cellular adhesion functions.

The formation of nanopores in the membranes of high-cellularity populations (e.g., in skin tissue) can be expected to dysregulate processes, components, and functions related to cell adhesion and binding, since these are dependent on membrane integrity. The downregulation of genes in stratified multi-cellular structures, and the over-representation of GO terms associated with membrane structural integrity, is consistent with this expectation. Further, ionic influx may also be expected to dysregulate pathways that are ion-regulated. As discussed in Chapter 7, bioinformatics analyses of the global differential expression data predict a significant inhibition of *Calcium* and *Ras signaling* pathways, pathways that are membrane-regulated. Since the processes identified in Figure 8.7(c) are also largely calcium-regulated, the predicted inhibition is again consistent with increased calcium influx as a potential initiating event. Taken together, these measurements may indicate a genomic response to ion influx, and are consistent with direct measurements of compromised membrane integrity as reported in Sections 8.4 and 8.5.

8.7 Conclusion

These data show that intense THz pulses are capable of permeabilizing membranes in large cellular populations. Comparison to exposure data in skin tissue indicates that similar mechanisms may be a dominant interaction underlying THz-induced biological effects, however more work establishing reproducibility for varying THz pulse parameters is necessary to understand the precise nature of the effect. In this chapter, data from investigations characterizing the prolonged and real-time (potentially transient) alteration of membrane integrity in cancer cells were presented. These data indicate that broadband intense THz pulses with fields exceeding 430 kV/cm are capable of permeabilizing membranes in cellular populations, while field strengths of 186 kV/cm were insufficient. These results are consistent with the stochastic interpretation of this regime discussed in Section 8.2.2, which predicts that the probability of pore formation scales with field strength and the number of applied pulses. While we did not observe any indication of frequency-dependence, this may be due to the relatively low field strength and total dose of the bandpass exposures. Future studies investigating frequency-dependence with larger field strengths is necessary to establish variation with spectral content, which may be expected to influence the membrane response.

In the experiments described, dose-dependence was investigated by varying the total exposure time. Future experiments with fixed exposure times that vary total dose by adjusting the pulse train repetition rate would assist in decoupling the dose-dependence observed from potential thermal effects, which may have relaxation times comparable to ionic relaxation. Additionally, experiments investigating specificity in regards to interior membranes with assays that probe specific organelle function (e.g., mitochondrial vs. nuclear) would assist in establishing the feasibility of the picosecond regime for biomedical applications that manipulate interior membranes, something that is typically not possible with longer pulses due to ionic screening [46]. Finally, we propose future experimentation correlating THz membrane effects to cell viability via multi-wavelength fluorescent labelling of a biochemical indicator of apoptosis (or other modes of cell death), in addition to membrane integrity probes.

The controlled modulation of membrane permeability has become a standard technique in microbiology to regulate cellular activity via the controlled uptake of microscopic material in target cells [26]. This mechanism is also of interest from a therapeutic standpoint: Electroporation leading to large Ca^{2+} influx leads to ATP depletion as cells work to re-establish chemical equilibrium, which increases the sensitivity to subsequent cytotoxic agents [69]. Electropermeabilized tissue has shown therapeutic efficacy in cells and mice, by increasing sensitivity to pharmacological agents in target cancer tissue. These THz-induced effects to cellular membrane structures therefore suggest a potential therapeutic mechanism of intense THz pulses, in addition to the interaction with the cytoskeleton (particularly microtubules), which is discussed in the next chapter.

8.8 References

- [1] F. H. Martini, J. L. Nath and E. F. Bartholomew, *Fundamentals of Anatomy and Physiology* 9th Ed., Benjamin Cummings, 2012.
- [2] K. Ma, Artist, *Animal Cell*. [Art]. Wikimedia Commons, 2012.
- [3] S. H. White and W. C. Wimley, "Membrane Protein Folding and Stability," *Annual Review of Biophysical and Biomolecular Structure*, vol. 28, pp. 319 - 365, 1999.
- [4] E. Evans and A. Yeung, "Hidden dynamics in rapid changes of bilayer shape," *Chemistry and Physics of Lipids*, vol. 73, pp. 39 - 56, 1994.
- [5] Y. Schweitzer, A. D. Lieber, K. Keren and M. M. Kozlov, "Theoretical Analysis of Membrane Tension in Moving Cells," *Biophysical Journal*, vol. 106, pp. 84 - 92, 2014.

- [6] A. P. Lyubartsev and A. L. Rabinovich, "Recent development in computer simulations of lipid bilayers," *Soft Matter*, vol. 7, pp. 25 - 39, 2011.
- [7] H. T. McMahon and J. L. Gallop, "Membrane curvature and mechanisms of dynamic cell membrane remodelling," *Nature*, vol. 438, pp. 590 - 596, 2005.
- [8] T. Rog, K. Murzyn and M. Pasenkiewicz-Gierula, "The dynamics of water at the phospholipid bilayer surface: a molecular dynamics simulation study," *Chemical Physics Letters*, vol. 3523, pp. 323 - 327, 2002.
- [9] M. Roark and S. E. Feller, "Molecular Dynamics Simulation Study of Correlated Motions in Phospholipid Bilayer Membranes," *Journal of Physical Chemistry B*, vol. 113, pp. 13229 - 13234, 2009.
- [10] M. Tokman, J. H. Lee, Z. A. Levine, M. -C. Ho, M. E. Colvin and P. T. Vernier, "Electric Field-Driven Water Dipoles: Nanoscale Architecture of Electroporation," *PLoS One*, vol. 8, no. 4, pp. 1 - 9, 2013.
- [11] S. Singer and G. Nicolson, "The Fluid Mosaic Model of the Structure of Cell Membranes," *Science*, vol. 175, no. 4027, pp. 1208 - 1215, 1972.
- [12] K. Simons and E. Ilkonen, "Functional rafts in cell membranes," *Nature*, vol. 387, pp. 569 - 572, 1997.
- [13] G. L. Nicolson, "The Fluid-Mosaic Model of Membrane Structure: Still relevant to understanding the structure, function and dynamics of biological membranes after more than 40 years," *Biochimica et Biophysica Acta*, vol. 1838, pp. 1451 - 1466, 2014.
- [14] P. -A. Monnard and D. W. Deamer, "Membrane self-assembly processes: Steps toward the first cellular life," *Anatomical Record*, vol. 268, no. 3, pp. 196 - 207, 2002.
- [15] N. Kimizuka, T. Kawasaki and T. Kunitake, "Self-Organization of Bilayer Membranes from Amphiphilic Networks of Complementary Hydrogen Bonds," *Journal of the American Chemical Society*, vol. 115, no. 10, pp. 4387 - 4388, 1993.
- [16] R. Philips, J. Kondev, J. Theriot and H. Garcia, *Physical Biology of the Cell*, New York, NY: Garland Science, 2013.
- [17] B. Alberts, A. Johnson, J. Lewis, M. Raff, K. Roberts and P. Walter, *The Molecular Biology of the Cell*, 4th Edition, New York, NY: Garland Science, 2002.
- [18] L. Rems and D. Miklavcic, "Tutorial: Electroporation of cells in complex materials and tissue," *Journal of Applied Physics*, vol. 119, no. 201101, pp. 1 - 21, 2016.
- [19] D. Clapham, "Calcium Signaling," *Cell*, vol. 131, no. 6, pp. 1047 - 1058, 2007.
- [20] L. B. Rosen, D. D. Ginty, M. J. Weber and M. E. Greenberg, "Membrane Depolarization and Calcium Influx Stimulate MEK and MAP Kinase via Activation of Ras," *Neuron*, vol. 12, pp. 1207 - 1221, 1994.
- [21] G. Sherbet, *Calcium signaling in cancer*, Boca Raton, FL: CRC Press, 2001.

- [22] T. Kotnik, L. Rem, M. Tarek and D. Miklavcic, "Membrane Electroporation and Electropermeabilization," *Annual Review of Biophysics*, vol. 48, pp. 63 - 91, 2019.
- [23] P. T. Vernier, Y. Sun and M. A. Gundersen, "Nanoelectropulse-driven membrane perturbation and small molecule permeabilization," *BMC Cell Biology*, vol. 7, no. 37, pp. 1 - 16, 2006.
- [24] T. Kotnik, G. Pucihar and D. Miklavcic, "Induced Transmembrane Voltage and Its Correlation with Electroporation-Mediated Molecular Transport," *Journal of Membrane Biology*, vol. 236, no. 3, pp. 3 - 13, 2010.
- [25] Z. L. Levine and P. T. Vernier, "Life Cycle of an Electropore: Field-Dependent and field-Independent Steps in Pore Creation and Annihilation," *Journal of Membrane Biology*, vol. 236, pp. 27 - 36, 2010.
- [26] M. L. Yarmush, A. Golberg, G. Sersa, T. Kotnik and D. Miklavcic, "Electroporation-Based Technologies for Medicine: Principles, Applications, and Challenges," *Annual Review of Biomedical Engineering*, vol. 16, pp. 295 - 320, 2014.
- [27] Z. Wang, J. Lu, W. Huang, Z. Wu, J. Gong, Q. Wang, Q. Liu, C. Wang, Y. Zhu, X. Ding and Z. Wang, "A retrospective study of CT-guided percutaneous irreversible electroporation (IRE) ablation: clinical efficacy and safety," *BMC Cancer*, vol. 21, no. 1, pp. 1 - 8, 2021.
- [28] R. Heller and L. C. Heller, "Gene Electrotransfer Clinical Trials," *Advances in Genetics*, vol. 89, pp. 235 - 262, 2015.
- [29] A. Gothelf, L. M. Mir and J. Gehl, "Electrochemotherapy: results of cancer treatment using enhanced delivery of bleomycin by electroporation," *Cancer Treatment Reviews*, vol. 29, pp. 371 - 387, 2003.
- [30] A. Beneduci, K. Cosentino, S. Romeo, R. Massa and G. Chidichimo, "Effect of millimetre waves on phosphatidylcholine membrane models: a non-thermal mechanism of interaction," *Soft Matter*, vol. 10, pp. 5559 - 5567, 2014.
- [31] A. Ramundo-Orlando, G. P. Gallerano, P. Stano, A. Doria, E. Giovenale, G. Messina, M. Cappelli, M. D'Arienzo and I. Spassovsky, "Permeability Changes Induced by 130 GHz Pulsed Radiation on Cationic Liposomes Loaded With Carbonic Anhydrase," *Bioelectromagnetics*, vol. 28, no. 8, pp. 587 - 598, 2007.
- [32] S. Romanenko, P. Siegel, D. A. Wagenaar and V. Píkov, "Effects of millimeter wave irradiation and equivalent thermal heating on the activity of individual neurons in the leech ganglion," *Journal of Neurophysiology*, vol. 112, pp. 2423 - 2431, 2014.
- [33] J. Tang, H. Yin, J. Ma, W. Bo, Y. Yang, J. Xu, Y. Liu and Y. Gong, "Terahertz Electric Field-Induced Membrane Electroporation by Molecular Dynamics Simulation," *Journal of Membrane Biology*, vol. 251, pp. 681 - 693, 2018.
- [34] "Tera-Hertz radiation in Biological Research, Investigations on Diagnostics and study on potential Genotoxic Effects (THz-BRIDGE), Final Report," [Online]. Available: <https://www.frascati.enea.it/THz-BRIDGE/>.

- [35] S. Xiao, S. Guo, V. Nesin, R. Heller and K. H. Schoenbach, "Subnanosecond Electric Pulses Cause Membrane Permeabilization and Cell Death," *IEEE Transactions on Biomedical Engineering*, vol. 58, no. 5, pp. 1239 - 1245, 2011.
- [36] P. Vernier, Z. Levine, M.-C. Ho, S. Xiao, I. Semenov and A. Pakhomov, "Picosecond and Terahertz Perturbation of Interfacial Water and Electropermeabilization of Biological Membranes," *Journal of Membrane Biology*, vol. 248, no. 5, pp. 837 - 848, 2015.
- [37] M. Grandolfo, S. M. Michaelson and A. Rindi, *Biological Effects and Dosimetry of Nonionizing Radiation*, New York, NY: NATO Scientific Affairs & Plenum Press, 1983.
- [38] T. Kotnik, D. Maklavcic and T. Slivnik, "Time course of transmembrane voltage induced by time-varying electric fields - a method for theoretical analysis and its application," *Bioelectricity and Bioenergetics*, vol. 45, pp. 3 - 16, 1998.
- [39] C. Grosse and H. P. Schwan, "Cellular membrane potentials induced by alternating fields," *Biophysical Journal*, vol. 63, no. 6, pp. 1632 - 1642, 1992.
- [40] T. Kotnik, F. Bobanovic and D. Maklavcic, "Sensitivity of transmembrane voltage induced by applied electric fields - a theoretical analysis," *Bioelectrochemistry and Bioenergetics*, vol. 43, pp. 285 - 291, 1997.
- [41] D. Gross, L. M. Loew and W. W. Webb, "Optical Imaging of Cell Membrane Potential Changes Induced by Applied Electric Fields," *Biophysical Journal*, vol. 50, no. 2, pp. 339 - 348, 1986.
- [42] Z. Lojewska, D. L. Farkas, B. Ehrenberg and L. M. Loew, "Analysis of the effect of medium and membrane conductance on the amplitude and kinetics of membrane potentials induced by externally applied electric fields," *Biophysical Journal*, vol. 56, no. 1, pp. 121 - 128, 1989.
- [43] I. P. Sugar and E. Neumann, "Stochastic model for electric field-induced membrane pores electroporation," *Biophysical Chemistry*, vol. 19, no. 3, pp. 211 - 225, 1984.
- [44] D. Popescu, C. Rucareanu and G. H. Victor, "A model for the appearances of statistical pores in membranes due to self-oscillations," *Bioelectrochemistry and Bioenergetics*, vol. 25, no. 1, pp. 91 - 103, 1991.
- [45] R. A. Bockmann, B. L. de Groot, S. Kakorin, E. Neumann and H. Grubmuller, "Kinetics, Statistics, and Energetics of Lipid Membrane Electroporation Studied by Molecular Dynamics Simulations," *Biophysical Journal*, vol. 95, no. 4, pp. 1837 - 1850, 2008.
- [46] T. Kotnik and D. Maklavcic, "Theoretical Evaluation of Voltage Inducement on Internal Membranes of Biological Cells Exposed to Electric Fields," *Biophysical Journal*, vol. 90, no. 2, pp. 480 - 491, 2006.
- [47] H. H. Mantsch and R. N. McElhaney, "Phospholipid phase transitions in model and biological membranes as studied by infrared spectroscopy," *Chemistry and Physics of Lipids*, vol. 57, pp. 213 - 226, 1992.

- [48] C. M. Hough, D. N. Purschke, C. Huang, L. V. Titova, O. V. Kovalchuk, B. J. Warkentin and F. A. Hegmann, "Intense Terahertz Pulses Inhibit Ras Signaling and Other Cancer-associated Signaling Pathways in Human Skin Models," *Journal of Physics: Photonics*, vol. 3, no. 034004, pp. 1 - 14, 2021.
- [49] P. H. Siegel and V. Pikov, "THz in Biology and Medicine: Towards Quantifying and Understanding the Interaction of Millimeter- and Submillimeter-Waves with Cells and Cell Processes," *Proc. of SPIE: Optical Interactions with Tissues and Cells XXI*, vol. 7562, no. 75620H, pp. 1 - 13, 2010.
- [50] T. Kotnik, D. Milavcic and L. M. Mir, "Cell membrane electroporation by symmetrical bipolar rectangular pulses. Part II. Reduced electrolytic contamination," *Bioelectrochemistry*, vol. 54, pp. 91 - 95, 2001.
- [51] Z. Shankayi and S. M. P. Firoozabadi, "The Effect of Pulsed Magnetic Field on the Molecular Uptake and Medium Conductivity of Leukemia Cell," *Cell Biochemistry and Biophysics*, vol. 65, pp. 211 - 216, 2013.
- [52] C. Chen, J. A. Evans, M. P. Robinson, S. W. Smye and P. O'Toole, "Electroporation of cells using EM induction of ac fields by a magnetic stimulator," *Physics in Medicine and Biology*, vol. 55, pp. 1219 - 1229, 2010.
- [53] F. Guo, C. Yao, C. Bajracharya, S. Polisetty, K. H. Schoenbach and S. Xiao, "Simulation Study of Delivery of Subnanosecond Pulses to Biological Tissues With an Impulse Radiating Antenna," *Bioelectromagnetics*, vol. 35, pp. 145 - 159, 2014.
- [54] J. Tang, J. Ma, L. Guo, K. Wang, Y. Yang, W. Bo, L. Yang, Z. Wang, H. Jiang, Z. Wu, B. Zeng and Y. Gong, "Interpretation of the molecular mechanism of the electroporation induced by symmetrical bipolar picosecond pulse trains," *BBA - Biomembranes*, vol. 1862, no. 183213, pp. 1 - 9, 2020.
- [55] G. Kroemer, L. Galluzzi, P. Vandenabeele, J. Abrams, E. S. Alnemri, E. H. Baehrecke, M. V. Blagosklonny, W. S. El-Deiry, P. Golstein, D. R. Green, M. Hengartner, R. A. Knight, S. Kumar, S. A. Lipton, W. Malorni, G. Nunez, M. E. Peter, J. Tschopp, J. Yuan, M. Piacentini, B. Zhivotovsky and G. Melino, "Classification of cell death: recommendations of the Nomenclature Committee on Cell Death 2009," *Cell Death and Differentiation*, vol. 16, pp. 3 - 11, 2009.
- [56] I. Vermes, C. Haanen and C. Reutelingsperger, "Flow cytometry of apoptotic cell death," *Journal of Immunological Methods*, vol. 243, pp. 167 - 190, 2000.
- [57] Y. Yang, Y. Xiang and M. Xu, "From red to green: the propidium iodide-permeable membrane of *Shewanella decolorationis* S12 is repairable," *Scientific Reports*, vol. 5, no. 18583, pp. 1 - 5, 2015.
- [58] BD Biosciences, "Spectrum Viewer," BD Biosciences, [Online]. Available: <https://www.bdbiosciences.com/en-us/applications/research-applications/multicolor-flow-cytometry/product-selection-tools/spectrum-viewer>.
- [59] C. M. Hough, D. N. Purschke, C. Huang, L. V. Titova, O. V. Kovalchuk, B. J. Warkentin and F. A. Hegmann, "Topology-based prediction of pathway dysregulation

- induced by intense terahertz pulses in human skin tissue models," *Journal of Infrared, Millimeter, and Terahertz Waves*, vol. 39, pp. 887 - 898, 2018.
- [60] M. Pavlin, V. Leven and D. Miklavcic, "Electroporation in dense cell suspension - Theoretical and experimental analysis of ion diffusion and cell permeabilization," *Biochimica et Biophysica Acta*, vol. 1770, pp. 12 - 23, 2007.
- [61] M. Drostén, C. G. Lechuga and M. Barbacid, "Ras in epidermal proliferation," *Oncotarget*, vol. 5, no. 14, pp. 5194 - 5195, 2014.
- [62] E. Fuchs and S. Raghavan, "Getting Under the Skin of Epidermal Morphogenesis," *Nature Reviews Genetics*, vol. 3, no. 3, pp. 199 - 209, 2002.
- [63] M. S. Rogers, T. Kobayashi, M. R. Pittelkow and E. E. Strehler, "Human Calmodulin-like Protein Is an Epithelial-Specific Protein Regulated during Keratinocyte Differentiation," *Experimental Cell Research*, vol. 267, no. 2, pp. 216 - 224, 2001.
- [64] E. -Y. Seo, J. -H. Namkung, K. -M. Lee, W. -H. Lee, M. Im, S. -H. Hee, G. T. Park, J. -M. Yang, Y. -J. Seo, J. -K. Park, C. D. Kim and J. -H. Lee, "Analysis of calcium-inducible genes in keratinocytes using suppression subtractive hybridization and cDNA microarray," *Genomics*, vol. 86, no. 5, pp. 528 - 538, 2005.
- [65] D. D. Bikle, Z. Xie and C.-L. Tu, "Calcium regulation of keratinocyte differentiation," *Expert Review of Endocrinology and Metabolism*, vol. 7, no. 4, pp. 461 - 472, 2013.
- [66] L. Galluzzi et al., "Essential versus accessory aspects of cell death: recommendations of the NCCD 2015," *Cell Death and Differentiation*, vol. 22, pp. 58 - 73, 2015.
- [67] G. Stelzer, N. Rosen, I. Plaschkes, S. Zimmerman, M. Twik, S. Fishilevich, T. I. Stein, R. Nudel, I. Lieder, Y. Mazor, S. Kaplan, D. Dahary, D. Warshawsky, Y. Guan-Golan, A. Kohn, N. Rappaport, M. Safran and D. Lancet, "The GeneCards Suite: From Gene Data Mining to Disease Genome Sequence Analysis," *Current Protocols in Bioinformatics*, vol. 54, pp. 1.30.1 - 1.30.33, 2016.
- [68] S. Carbon, A. Ireland, C. J. Mungall, S. Shu, B. Marshall and S. Lewis, "AmiGO: Online access to ontology and annotation data," *Bioinformatics*, vol. 25, no. 2, pp. 288 - 289, 2009.
- [69] S. K. Frandsen, H. Gissel, P. Hojman, T. Tramm, J. Eriksen and J. Gehl, "Direct Therapeutic Applications of Calcium Electroporation to Effectively Induce Tumor Necrosis," *Cancer Research*, vol. 72, no. 6, pp. 1336 - 1341, 2012.
- [70] H. Fröhlich, "Long-Range Coherence and Energy Storage in Biological Systems," *International Journal of Quantum Chemistry*, vol. 2, pp. 641 - 649, 1968.
- [71] S. Webb, M. Stoneham and H. Fröhlich, "Evidence for Non-thermal Excitation of Energy Levels in Active Biological Systems," *Physics Letters*, vol. 63A, no. 3, pp. 407 - 408, 1977.

9 Molecular-level effects: Disassembly of microtubules by intense terahertz pulses

“If you want to understand function, study structure.”

– Francis Crick

A version of this chapter has been accepted for publication:

C. M. Hough, D. N. Purschke, C. Bell, A. P. Kalra, P. J. Oliva, C. Huang, J. A. Tuszynski, B. J. Warkentin, and F. A. Hegmann, “Disassembly of microtubules by intense terahertz pulses,” Accepted by *Biomedical Optics Express*, August 2021.

9.1 Introduction

THz radiation has been observed to induce significant effects at multiple scales of biological structure [1, 2, 3]. While the specific nature of the fundamental interactions is not yet understood, these phenotypic effects may be attributable to interaction with sub-cellular macromolecular structures such as DNA [4, 5, 6, 7] or cellular membranes [8, 9, 10]. However, experimental investigation of THz exposure effects to cytoskeletal protein complexes (actin, intermediate filaments, and microtubules) is still at a preliminary stage. Studies with actin show that THz exposures of relatively low intensity ($\sim 0.6 \text{ W/cm}^2$) can stimulate polymerization, while highly intense THz pulses ($\sim 3 \text{ GW/cm}^2$) resulted in actin disassembly [11, 12]. To date, no studies have investigated the structural changes to microtubules (MTs) irradiated by THz pulses, although there is some experimental precedent that motivates the hypothesis that MTs may be an important target of THz-induced biological effects [13, 14, 15, 16]. Hintzche et al. observed disturbance to the spindle apparatus (a mitotic structure comprised of microtubules) in hybrid animal cells [13], and Amicis et al. observed significant increase of micronuclei in irradiated human epithelial cells, which arise due to abnormal mitotic activity forming multiple nuclear envelopes in non-viable daughter cells [14].

In this chapter, evidence of intensity-dependent THz-induced disassembly of polymerized and chemically stabilized MTs within minutes of exposure to a train of broadband intense THz pulses is presented. Further, bandpass-filtered exposures suggest additional frequency-dependence. The results of these investigations are analyzed in the context of signaling dysregulation observed at the tissue scale of organization, for which structural modulation of the cytoskeleton may be the

underlying cause. Disruption of cytoskeletal dynamics may be a fundamental interaction mechanism underlying observed phenotypic response, and additionally suggests a potential molecular-level therapeutic mechanism of intense THz pulses with the goal of inhibition of pro-mitotic intracellular dynamics.

9.2 Biopolymers and the cytoskeleton

In animal cells, the cytoskeleton is a cytoplasmic network of interlinking filamentous protein polymers of three main types: intermediate filaments, actin, and microtubules (MTs) [17, 18]. These complexes form a dynamic structure that connect the cell physically and biochemically to the extracellular and intranuclear environments, facilitates chemical transport, provides mechanical stability, and regulates morphology and motility. MTs are the most mechanically rigid of the cytoskeletal polymers, and form the dominant component of the mitotic spindle, providing the structural framework and force-generation necessary to carry out mitosis [18]. General MT function depends on a dynamic instability between states of polymerization and rapid depolymerization known as treadmilling [17, 19].

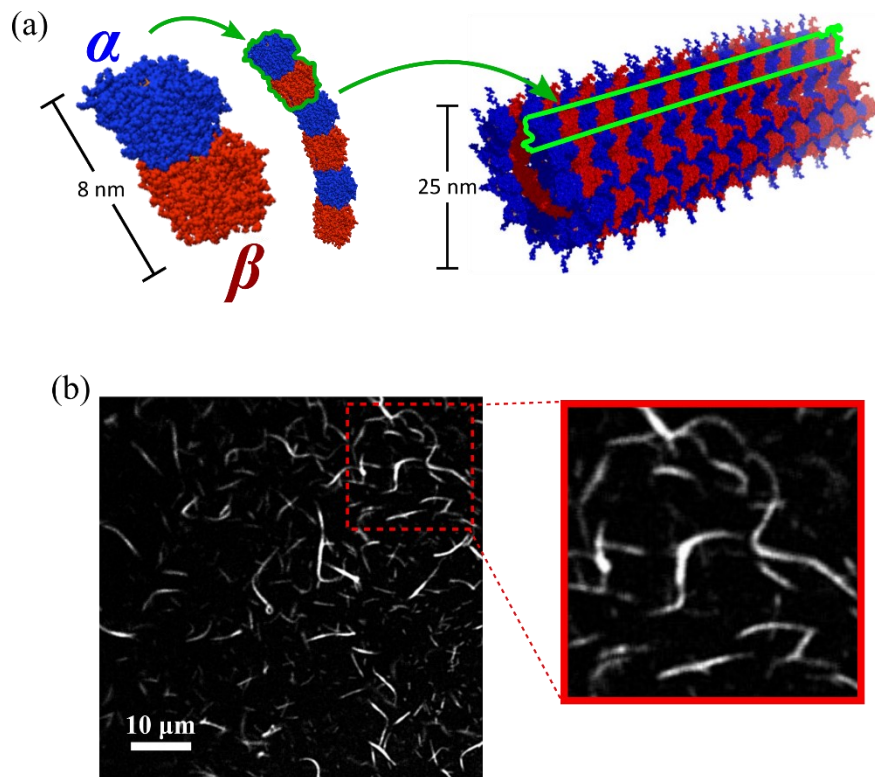


Figure 9.1. **Microtubule structure and fluorescence microscopy image.** (a) Bound $\alpha\beta$ -tubulin dimers comprise the hydrogen-bonded protofilaments [20]. 13 protofilaments laterally bind to form a hollow cylindrical polymer with a 25 nm diameter. (b) Fluorescence image of rhodamine-labelled polymerized microtubules. The average length is 10 μm .

MTs are comprised of tubulin dimer subunits, which are themselves a complex of bound α and β tubulin proteins, as shown in Figure 9.1(a). Structurally, $\alpha\beta$ -tubulin dimers spontaneously polymerize to form thirteen 1D protofilaments that bind laterally to form cylindrical MTs; they depolymerize via GTP (guanosine tri-phosphate) hydrolysis of tubulin dimers on the positive end [21]. Importantly, dimers and protofilaments bind via hydrogen-bonding, for which the natural oscillatory frequencies occupy a broad region of the THz band (0.1 – 10 THz), as discussed in Chapter 2 [21, 22, 23, 24]. External excitation of MTs with intense THz pulses may efficiently couple to these oscillations and dysregulate structural dynamics, which may in turn affect important MT functions such as polymerization and de-polymerization.

Simulation studies investigating MT structure in nanosecond-duration pulsed electric fields have been reported, and show significant structural dysregulation for field strengths in the range of 50 – 750 kV/cm [25, 26, 27]. These studies predict reduction of MT stability proportional to field strength through conformational changes to key loops involved in lateral protofilament contact (Figure 9.1 (a)), or alteration of local electrostatic properties at the GTP binding site. These results theoretically motivate the hypothesis that intense picosecond-duration pulses may also induce similar field-induced structural effects; however, more work simulating tubulin/MT response specifically to intense picosecond-duration fields is necessary. Simulation studies of THz fields for other macromolecular structures, such as membranes, offer insight into the expected interaction with intracellular environments [8]. For long-duration pulses ($>\sim 10$ ns), membrane interactions are predominantly due to ionic redistribution, as the field variations allow sufficient time for these motions to occur [28, 29]. In contrast, for fast, short-duration pulses ($<\sim 1$ ns), the interaction is predominantly dielectric, arising from faster dipole reorientation dynamics. Importantly, this suggests that picosecond-duration pulses with sufficient field strength may interact with interior cellular structures, since the electronic screening effect in the membrane does not occur [28].

9.3 Terahertz-induced disassembly of polymerized and chemically stabilized microtubules

9.3.1 Methods

9.3.1.1 Growth of fluorescently labelled microtubules

Rhodamine-labelled fluorescent tubulin (excitation/emission at 543/590 nm) was obtained from Cytoskeleton Inc. (Denver, USA), and MTs were polymerized according to the manufacturers' instructions [30]. One aliquot of rhodamine tubulin (Cytoskeleton, TL590M) was resuspended to 5 mg/mL (45.5 μ M) in 4.0 μ L of general tubulin buffer (Cytoskeleton, BST01) supplemented with 0.01 volumes of 100 mM GTP (Cytoskeleton, BST06) and 1 μ L of MT cushion buffer (Cytoskeleton, BST05) to facilitate polymerization. This solution was mixed with 70 μ L of an equivalent solution using unlabeled tubulin (Cytoskeleton, T240) for a final labelling ratio of 1:15. Aliquots were placed in an incubator at 37°C for 20 minutes to allow the tubulin to polymerize to MTs of appropriate length (average \sim 10 μ m). Upon polymerization, the MTs were removed from the incubator and stabilized with 100 μ L of taxol/MT buffer solution (20 μ M taxol in general tubulin buffer). These were stored at room temperature as recommended, and the MTs were verified to be stable in this state for several hours. Further dilutions of this stock solution with taxol/MT buffer were performed as experimentally required. A fluorescence image of rhodamine-labelled polymerized MTs is shown in Figure 9.1(b).

9.3.1.2 Generation and detection of intense THz pulses

Intense THz pulses were generated by optical rectification of tilted-pulse-front laser pulses in lithium niobate (LiNbO₃), as introduced in Chapter 3, and schematically shown in Figure 9.2(a). An oscillator/amplifier (Coherent Micra/Legend, Santa Clara, USA) generated a 1 kHz train of 800 nm, 50 fs, 3.6 mJ infrared laser pulses. An 1800 mm⁻¹ reflective diffraction grating (RDG) established a pulse-front-tilt in the pump laser to satisfy velocity-matching conditions in the LiNbO₃ generation crystal with a 63° cut output face [31]. Two cylindrical focusing lenses ($f_1=100$ mm, $f_2=60$ mm) in a 4f configuration imaged both the laser pulse front and grating surface onto the crystal output for optimal THz emission, as described in [32].

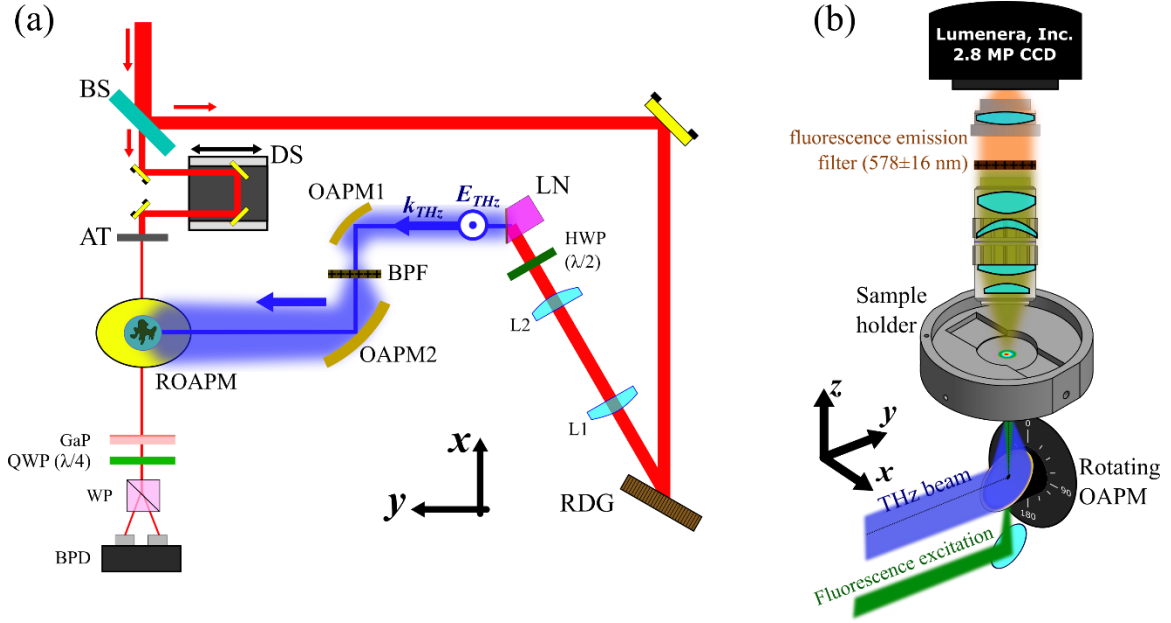


Figure 9.2. **THz source generation and exposure schematics.** (a) The intense THz pulse source for tilted-pulse-front optical rectification in lithium niobate (LN, LiNbO_3), using an 1800 mm^{-1} reflective diffraction grating (RDG) and a pair of 4f-imaging lenses (L1 and L2), as described in [32]. Cross-absent bandpass filters (BPF) are used to isolate individual frequency bands. The THz beam is focused to either the sample location (beam propagating in the $+z$ direction out of the page), or to the EO sampling system (beam in the $-x$ direction) with a rotating gold off-axis parabolic mirror (ROAPM). A fraction of the pump pulse energy from a beamsplitter (BS) is attenuated (AT) and propagated colinearly with the THz beam for EO sampling in gallium phosphide (GaP). (b) The ROAPM is set at 0° ($+z$, upwards) for through-substrate exposure of MTs in solution. The fluorescence excitation line is focused through the hole in the mirror and propagates to the sample colinearly with the focusing THz beam. The sample fluorescence emission is collected by long-working distance objectives, passed through a $578 \pm 16 \text{ nm}$ bandpass filter, and analyzed in real-time with a CCD camera. For EO sampling, the ROAPM is set to 90° .

The collimated THz emission from the LN crystal was filtered with black polyethylene to remove pump leakage. The beam was magnified and re-collimated by a pair of gold off-axis parabolic mirrors (OAPM) with focal lengths of $f_{\text{OAPM1}}=15 \text{ mm}$ and $f_{\text{OAPM2}}=101.6 \text{ mm}$ for a total magnification of 6.8. The expanded, collimated beam is directed towards a 76.2 mm focal length OAPM mounted to a programmable rotation stage (Thorlabs, PRM1Z8) as shown in Figure 9.2(b). This provided 360° control of the THz focus in a 76.2 mm radius annulus to focus to either the sample location (0°), or to the electro-optic (EO) sampling module for waveform detection (90°).

Temporal waveforms were detected by free-space EO sampling in a $200 \mu\text{m}$ (110) gallium phosphide (GaP) crystal mounted to a 2 mm (100) GaP substrate. Peak electric fields, E_{THz} , were calculated directly from the normalized EO signal, $\Delta I/2I_0$, from balanced photodetectors (BPD) according to the equation,

$$\frac{(\Delta I/2)}{I_0} = \sin\left(\frac{2\pi L}{\lambda_0} n_0^3 r_{41} t_{GaP} E_{THz}\right) \quad (9.1)$$

where $\lambda_0=800$ nm is the vacuum wavelength, and $L=200$ μm , $n_0=3.18$, $r_{41}=0.88$ pm/V, and $t_{GaP}=0.46$ are the thickness, nominal index, EO coefficient, and amplitude transmission coefficient for GaP, respectively [32].

The pulse energy and transverse intensity distribution were measured with a pyroelectric detector (Spectrum Detector, SPJ-D-8) and camera (Electrophysics, PV320), respectively. Focused spot sizes were calculated as the $1/e^2$ width of the Gaussian fits to 1D line profiles, and pulse durations were determined as the $1/e$ width of the waveform Hilbert transform. For investigations of frequency dependence, THz bandpass filters (Thorlabs, FB19M590/FB19M200, 19.6 mm inner diameter) were used as additional filtration to isolate the 0.5 THz and 1.5 THz bands. The broadband and bandpass waveforms, power spectra, and spatial intensity distributions at the focus are shown in Figure 9.3. Details on the quantitative parameters for representative THz pulses are summarized in Table 9.1.

Table 9.1. THz pulse parameters for MT exposures

	Broadband	0.5 THz band	1.5 THz band
Pulse Energy (μJ)	1.20 \pm 0.07	0.10 \pm 0.03	0.14 \pm 0.02
Peak field (kV/cm)	409	37	100
Peak frequency (THz)	1.0	0.52	1.5
Bandwidth FWHM (THz)	0.6	0.07	0.2
Pulse duration \dagger (ps)	1.0	6.3	2.9
Spot size* (mm)	1.5	2.1	1.0
Avg. intensity (mW/cm 2)	68 \pm 4	3.0 \pm 0.9	18 \pm 3
Peak intensity (MW/cm 2)	68 \pm 4	0.5 \pm 0.1	6.2 \pm 0.9

\dagger Pulse durations are the $1/e$ -width of the Hilbert envelope

*Spot sizes are the $1/e^2$ -diameter of the circular THz focus.

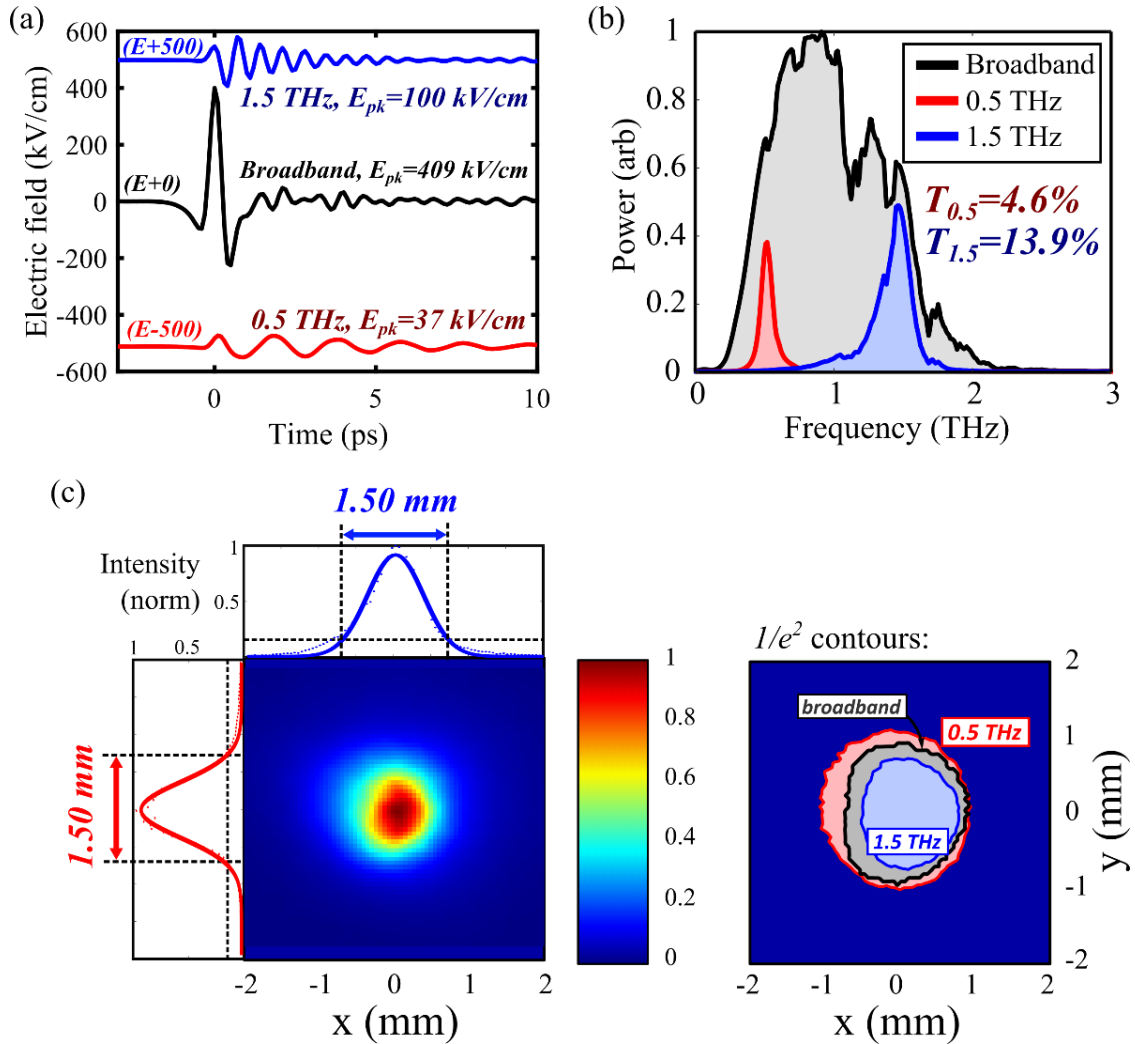


Figure 9.3. **Waveforms and spot areas for the intense THz pulse beam.** (a) Broadband and bandpass EO sampled THz waveforms, shifted vertically as labelled for clarity. The peak broadband field and pulse energy is 409 kV/cm and 1.2 μJ , respectively. (b) The corresponding power spectra and total energy transmission factors. (c) Pyroelectric camera image of the focused THz spot. Gaussian fits to horizontal (top) and vertical (left) line profiles define the $1/e^2$ broadband spot size as $1.5 \times 1.5 \text{ mm}^2$. The contours (right) represent the $1/e^2$ boundaries corresponding to the labelled frequency bands. For diffraction limited broadband beams, individual frequency bands focus to different areas of space.

9.3.1.2.1 Alignment procedure for real-time analysis

To ensure the THz focus, sample location, and microscope imaging plane were coincident in space, the following alignment procedure outlined in Chapter 5 was employed. Briefly, the THz pulse energy was first maximized through a 1 mm pinhole alignment aperture placed at the sample location with a pyroelectric detector (ScienceTech Inc., 6925-01) centered above. Once this signal was maximized, the detector was removed, and the microscope field-of-view (FOV) was focused to the pinhole to ensure the imaging plane and THz focus were longitudinally aligned and centered.

Next, a sham sample was loaded into the holder and longitudinally translated until the sample was in focus. This achieves coincidence of the sample and image planes with the THz beam focus for the real-time fluorescence analysis of MTs.

9.3.1.3 *Microtubule exposures*

MT solutions were loaded onto double-well microscope slides of optical plastic that were verified to be transmissive ($T=0.92$) to THz wavelengths (Ibidi μ -slide, Cat. 80281), with sufficient volume to fully cover the focused THz spot once compressed with a coverslip (1 – 3 μ L). The MTs were left for several minutes to 1 hour to settle to the substrate and ensure stability. For exposure, the THz beam was focused through a 5 mm diameter hole in the sample holder with the rotating OAPM to one of the wells, and the second well provided matched, unexposed control solutions. Similar to the recommended MT stock storage conditions, exposures were carried out at room temperature.

9.3.1.3.1 *Tip-enhanced exposure*

For local field enhancement with a sharp tip as described in Chapter 5, a tip is loaded into a custom tip holder mounted to a 3D translation stage aligned to the THz field direction, and the tip apex is centred and focused to the microscope image plane to ensure it is coincident with the THz focus. For these exposures, the free-space THz pulse energy was 0.5 μ J, with a peak field strength of 191 kV/cm. From COMSOL simulations, the tip-enhanced field in water is estimated to be 6.7 MV/cm in a 0.4 μ m FWHM region about the tip apex.

9.3.1.4 *Real-time fluorescence imaging and image analysis*

THz-exposed rhodamine-MTs were imaged in real-time with a fluorescence microscope aligned to the beam focus. The fluorescence excitation laser (532 nm CW diode-pumped solid-state laser) was focused from below through a 1 mm hole in the rotating OAPM, and uniformly excites the sample growth area. Short pass filters eliminated any residual 805 nm and 1064 nm emissions, and a neutral density filter wheel tuned the incident power. A programmable shutter connected to the imaging camera via USB blocked the laser and allowed fluorescence excitation to be controlled within the imaging software. Fluorescence emission (\sim 590 nm) from the sample plane was collected by long-working distance 5x/20x objectives (Mitutoyo, 378-802-6/378-804-3) and a 2x

tube lens (Edmund Optics, MT-2, 56-863), passed through a 578 ± 16 nm bandpass filter, and collected by a 2.8 MP monochrome CCD microscopy camera (Lumenera, Infinity 3-3URFM).

For each timepoint acquired during THz exposure, a series of 15 images were averaged with an exposure time of no greater than 300 ms each. The excitation laser therefore exposed the samples for no more than ~ 5 s for each image set. Excitation control images were acquired, and a photobleach calibration curve was experimentally determined. It was verified that the timescale for the fluorescent label to experience significant levels of photobleaching was much greater than the excitation exposure times utilized in this study. For imaging, auto-exposure control (AEC) was enabled when investigating general structural effects. In cases where the pixel intensity values were utilized for quantitative calculations (Section 9.3.2.2), AEC was disabled. Sample fluorescence images for low and high tubulin concentrations are shown in Figure 9.4. Low initial tubulin concentrations result in individually resolvable MTs, while large tubulin concentrations form large aggregate structures.

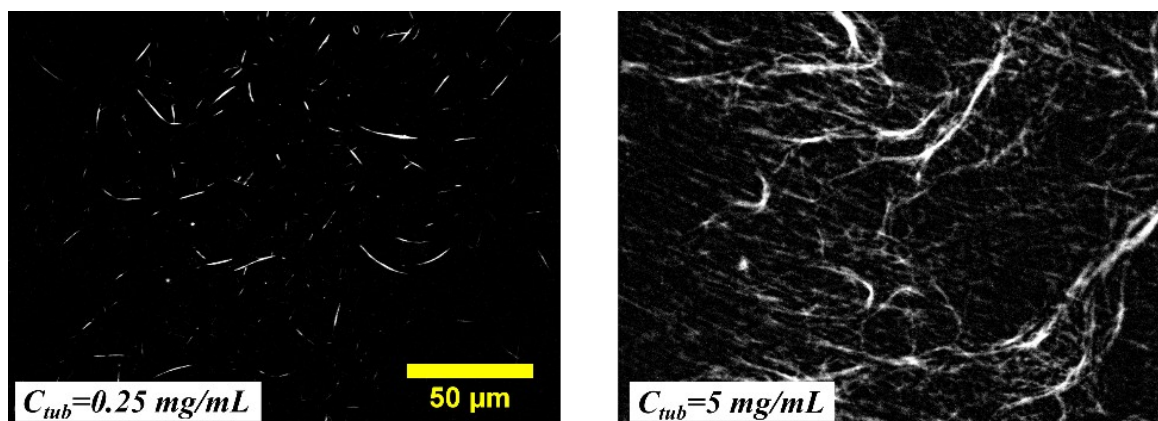


Figure 9.4. **Real-time fluorescence images for real-time imaging of THz-exposed MTs.** At low concentration (C_{tub} , left), MTs are individually resolvable and are stabilized at ~ 10 μm in length. At high C_{tub} (right), MTs form large aggregate structures and are not individually resolvable.

Image processing and analysis was performed using the open-source software, ImageJ (<https://imagej.net>). Fluorescence images were background-subtracted with a rolling-ball algorithm. For the frequency-dependent studies, the structural change to MTs were quantified by the area fraction of the image space occupied by MTs. MT area fractions were determined by first creating a binary image mask for each timepoint with a common pixel intensity threshold. As MTs disassemble, intensity per unit area reduces, which reduces the total fraction of fluorescence intensity above the chosen threshold for a given imaging region. The MT area fractions were determined with the ImageJ plugin “Analyze Particles” applied to the masked images, which

algorithmically contours the masked MTs and determines the enclosed areas. Each set of MT area fractions were normalized to the initial timepoint.

9.3.2 Results

9.3.2.1 Intensity-dependence of broadband THz pulses on microtubule structure

Figure 9.5 shows three sets of time-series images from broadband THz exposures for varying exposure conditions. Differing combinations of imaging magnification (M) and tubulin concentration (C_{tub}) were utilized to analyze either single or aggregate MT structures in either uniform or non-uniform intensity distributions.

High- M and low- C_{tub} experiments (40x, 0.25 mg/mL) provide detailed structural resolution to individual MTs. As shown in Figure 9.5(a), disassembly of a single MT is shown to occur within 11 minutes with 0.8 μ J pulses and 230 kV/cm peak field strength.

Low- M and high- C_{tub} (10x, 5 mg/mL) experiments with similar exposure parameters show the large-scale effects to MT aggregates (Figure 9.5(b)). The large FOV allows analysis of intensity-dependence within a single exposure: By analyzing structural effects to MTs for varying distances from the center of the THz focus, differential effects to MT structure for varying energy densities are investigated. From within the total imaging FOV of $870 \times 655 \mu\text{m}^2$, three $100 \times 100 \mu\text{m}^2$ FOVs were selected for analysis, corresponding to different regions of the THz intensity distribution (shown at right in Figure 9.5(b)). In the central region, the energy density reaches $80 \mu\text{J}/\text{cm}^2$, and the largest qualitative change to MT structure is observed. Near the beam edge ~ 0.5 mm from center, the energy density falls to $\sim 30 \mu\text{J}/\text{cm}^2$, and no significant structural change is observed.

High- M and high- C_{tub} (40x, 5 mg/mL) experiment shows structural effects to MT aggregates in a nearly uniform THz intensity profile at higher THz energy (1.2 μ J) and field strength (400 kV/cm and 409 kV/cm), depicted in Figure 9.5(c). In both time-series, MT disassembly and aggregate destruction occurs significantly faster than the previous exposure cases, within ~ 5 minutes, further corroborating the evidence for intensity-dependence that was indicated in the differential effects seen in the low-magnification images.

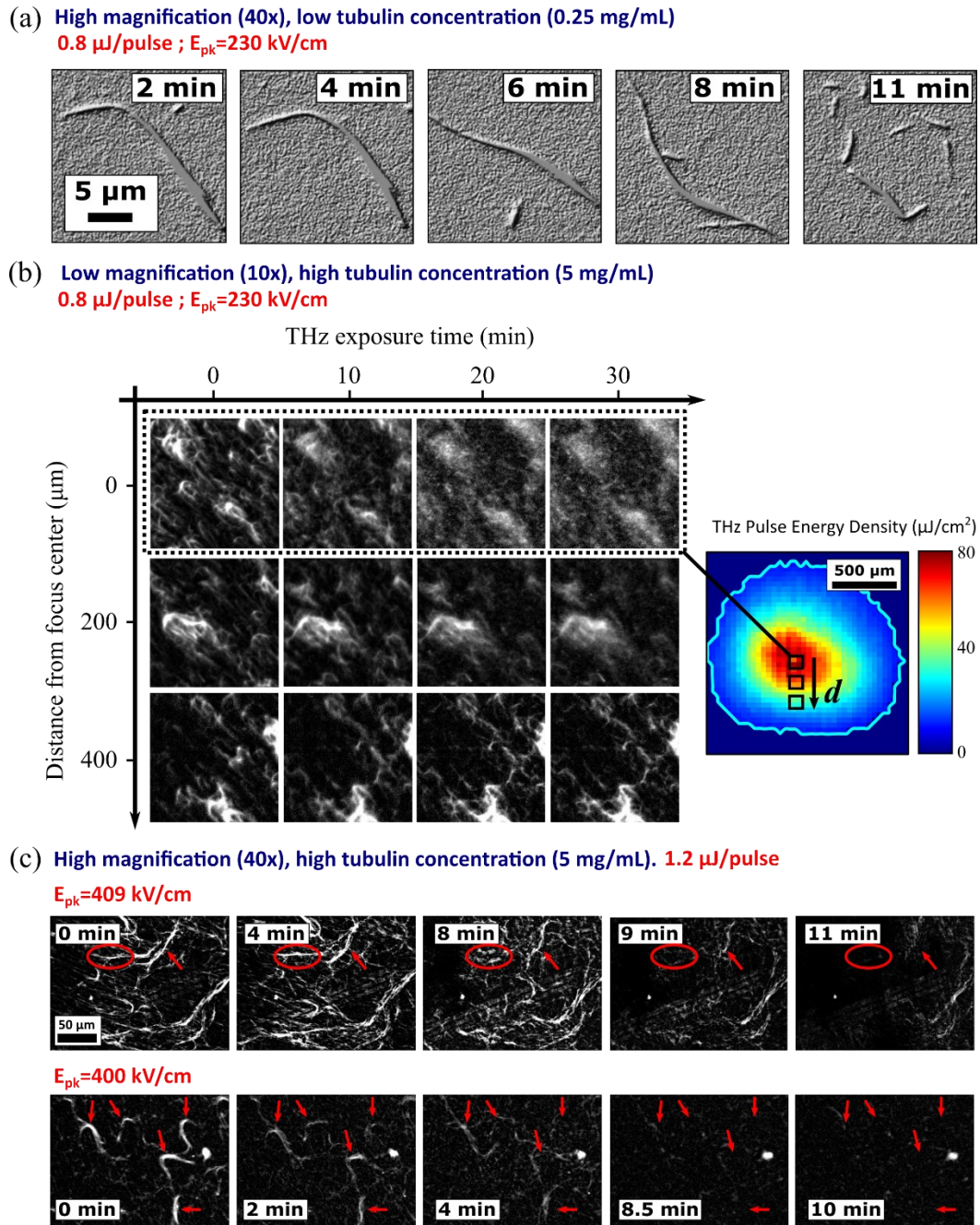


Figure 9.5. **Broadband MT exposure results.** (a) High magnification (40x) fluorescence images of low tubulin concentration (0.25 mg/mL) show detailed structural disassembly to individual MTs. A single motion-tracked MT disassembling within 11 minutes of THz exposure. The ImageJ hill-shade algorithm is utilized to enhance edge contrast. (b) Low magnification (10x) images of high tubulin concentration (5 mg/mL) show large-scale disassembly of MT aggregate structures in a varying intensity distribution. The three sets of time-series images correspond to three $100 \times 100 \mu\text{m}^2$ regions indicated in the THz spot image (right), having approximate energy densities of 80, 50, and $30 \mu\text{J/cm}^2$. Greater disassembly is observed in the highest intensity central region. (c) High magnification (40x) and high tubulin concentration (5 mg/mL) show MT aggregates in a nearly uniform intensity FOV. Both time series are separate results with similar pulse energy ($1.2 \mu\text{J}$) and peak field (409 kV/cm [top] and 400 kV/cm [bottom]). At larger THz energy and field strengths, significant MT disassembly is observed within 5 min. Red labels highlight regions of MT polymer breakage.

9.3.2.1.1 Tip-enhanced microtubule exposures

While the above parameters are sufficient to induce MT disassembly within $\sim 5 - 10$ minutes, higher-intensity regimes may be investigated by locally enhancing the THz field strength with a sharp conductive tip to an estimated $E_{THz} = 6.7$ MV/cm in a region $\sim 0.4 \mu\text{m}$ about the tip apex. Figure 9.6 shows a time-series of fluorescent images of tip-enhanced THz-exposed MTs. Images were acquired with the THz beam off for 10 minutes, during which time the MTs appeared to migrate to the conductive tip leading to fluorescence intensity increase, particularly near the tip apex. The THz beam was turned on at $t = 10$ min as indicated. Within 1 minute of intense THz pulse excitation, the aggregated MTs were dramatically ejected up to $20 \mu\text{m}$ from the tip apex.

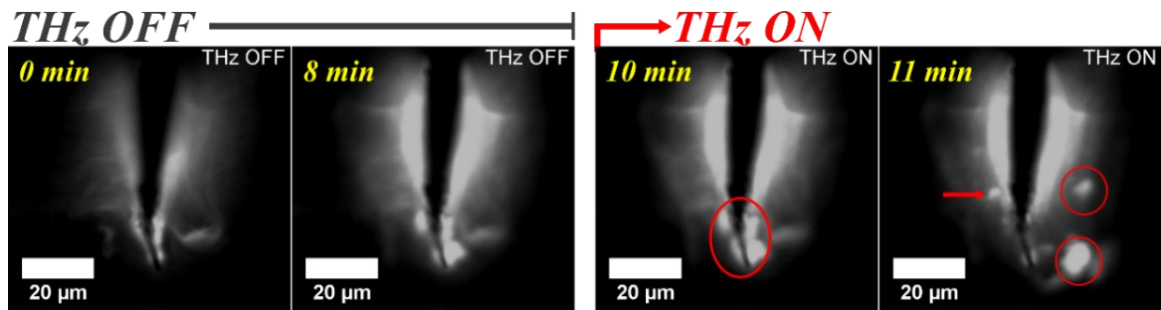


Figure 9.6. **Fluorescence imaging of tip-enhanced MT exposures.** When the THz beam is off, the labelled MTs aggregate on the conductive tip. Within 1 minute of THz exposure, a dramatic ejection and disassembly of MTs (red circles) from the tip apex is observed.

9.3.2.2 Exposures with terahertz bandpass filters

From the broadband exposure results in Sections 9.3.2.1, it is not possible to conclude that the observed effects are strictly only intensity-dependent, since wavelength-dependent focusing induces spatial variation in frequency for the broadband pulse, in addition to the power-density variation. The central intense region of the beam contains a larger fraction of high frequency energy relative to the low-intensity beam regions, and so the differential effect to large MT aggregates for varying location in the THz focus may additionally be influenced by the frequency distribution associated with the region of space under consideration.

To isolate the potential effects for varying spectral content, THz bandpass filters are used to transmit narrow 0.5 THz and 1.5 THz bands, and compared to broadband exposure, adjusted for intensity differences. For these analyses, THz-induced MT disassembly is quantified using the MT area fraction. As shown in Figure 9.7(a), contours determined with the analysis algorithm (Section 9.3.1.4) define this area fraction, which decreases over time as the fluorescence signal from disassembled MTs falls below the mask threshold. The results in Figure 9.7(b) show that the

decrease in MT area generally follows an exponential decay. For comparison, an equivalent analysis with images of unexposed MTs is included. The curves are labelled with characteristic times from fitting these data to an exponential function to establish quantitative timescales of THz-induced effect for varying spectral content. The top plot of Figure 9.7(b) shows the total pixel intensity of the images for each timepoint. The maximum loss of total fluorescence signal was ~5%, and so the decrease in MT area fraction of THz-exposed samples is not due to photobleaching of the rhodamine label, but rather to MT disassembly, as illustrated in the second column of Figure 9.7(a).

While there is a large range of characteristic times for varying spectral content from the fits in Figure 9.7(b), this could be due to differences in pulse energy and focused spot area between the separate THz pulses (Figure 9.3, Table 9.1). To correct for these differences, the MT area fraction is plotted as a function of the total dose, $D = I_{avg}t$, as shown in Figure 9.7(c). The total dose is reported in units of J/cm^2 , and is distinct from the per-pulse energy density ($\mu\text{J}/\text{cm}^2$) in Figure 9.5. The difference in characteristic doses indicate that THz-induced disassembly of MTs is significantly influenced by the pulse frequency content, as discussed in the following section.

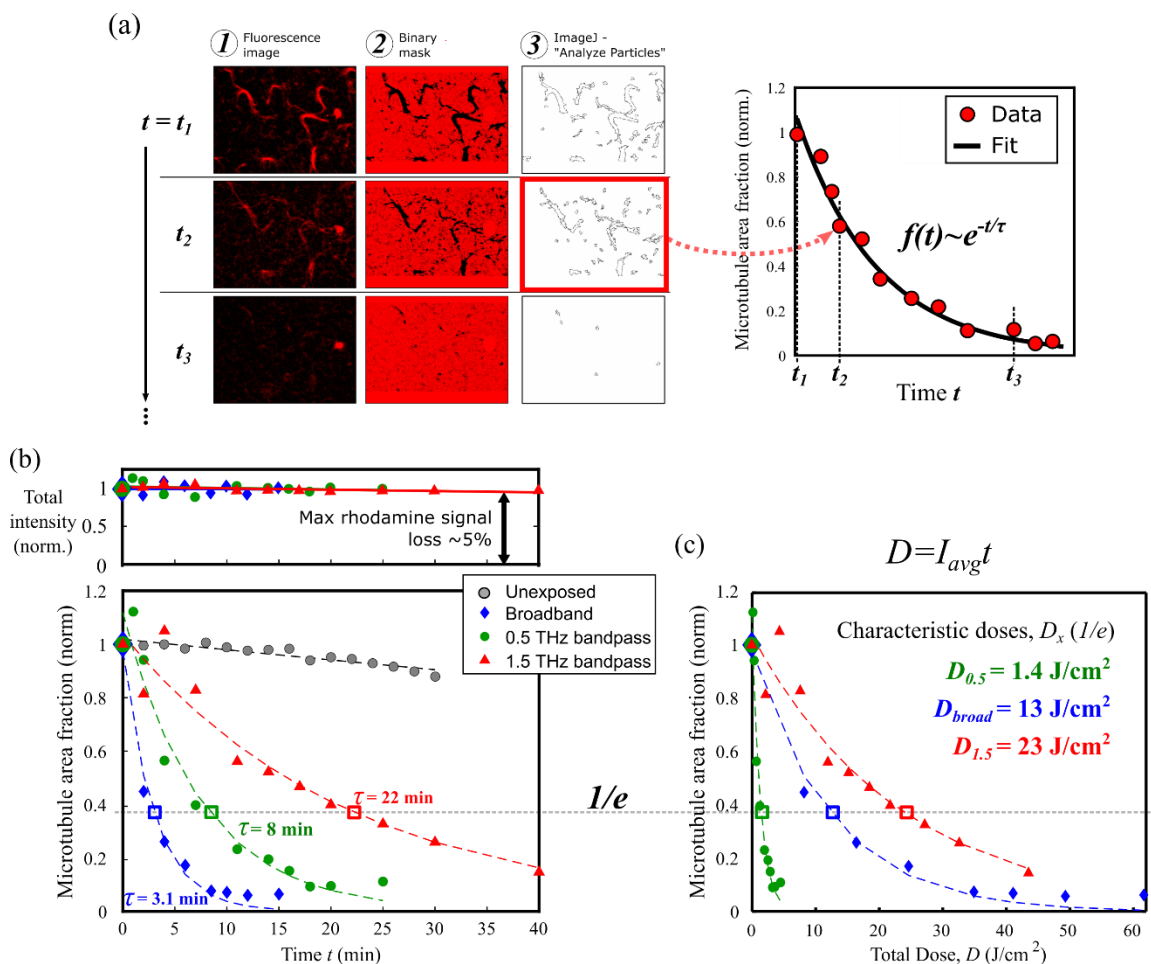


Figure 9.7. **Analysis and results of MT exposures with varying spectral content.** (a) An example image analysis of MT structural change. By converting quantitative fluorescence images (column 1) to a binary image with a common threshold (column 2), the disassembly of MTs over time may be quantified by the change of area fraction with rhodamine signal above a common intensity threshold. The area fractions are determined by algorithmic contours with the ImageJ plugin, “Analyze Particles”. The reduction of area fractions follow an exponential decay curve. (b) Fractional MT area calculated using the procedure in (a) for varying THz bands, with dashed curves representing exponential fits, and τ is the associated characteristic time. Each dataset was normalized to the initial relative MT area. The exponential fit qualities (R^2) are 0.99, 0.96, and 0.92 for the broadband, 0.5 THz, and 1.5 THz fits, respectively. An equivalent analysis on unexposed MTs is included for reference. *Top:* The total pixel intensity of the raw images. The total rhodamine signal of all images does not degrade significantly (<5%) over the exposure duration, indicating the MT area fraction decay is not due to photobleaching. (c) The MT area fraction vs. total dose (J/cm^2), which corrects for differences in pulse energy and focused spot area (see Table 9.1). D_x is the characteristic dose for the corresponding curve (e^{-D/D_x}). The characteristic total dose for the low-frequency 0.5 THz band ($1.4 \text{ J}/\text{cm}^2$) is significantly lower than both the broadband and high-frequency 1.5 THz band ($13 \text{ J}/\text{cm}^2$ and $23 \text{ J}/\text{cm}^2$, respectively), indicating frequency-dependence of THz-induced MT disassembly, with greater disassembly induced by low-frequency THz energy ($\sim 0.5 \text{ THz}$).

9.4 Discussion

9.4.1 Intensity dependence

Exposures at higher magnification (40x) and low tubulin concentration (0.25 mg/mL) provide an opportunity to observe detailed effects resolvable to single MTs (Figure 9.5a). Conversely, analysis of low-magnification (10x), high-concentration (5 mg/mL) MT samples provides an opportunity to investigate intensity-dependence in a single exposure by analyzing separate regions of the imaging FOV for varying locations in the Gaussian intensity distribution (Figure 9.5(b)). In the former case, disassembly of a single MT polymer is observed to occur within 11 minutes of THz exposure. In the latter configuration, significant variation in THz-induced change to MT structure is observed for varying locations within the THz focus. The strongest effect is observed in the central region with the highest intensity (top row of Figure 9.5(b)), in which the blurring of large aggregate structures is attributed to single MTs disassembling, as in Figure 9.5(a). As the analysis window moves to the outer fringe of the beam, the magnitude of this differential effect over the 30-minute exposure diminishes. While low magnification exposures provide an opportunity to observe intensity-dependent effects in a single exposure, it sacrifices specificity of identifying structural effects to individual MTs, and only broad effects to aggregate structure are visible.

The above cases were exposed with a relatively attenuated THz beam (0.8 $\mu\text{J}/\text{pulse}$, 230 kV/cm), and the disassembly to MTs occurred in 11 minutes. Figure 9.5(c) shows high-concentration exposures with higher pulse energy (1.2 $\mu\text{J}/\text{pulse}$) and field strength (400 kV/cm and 409 kV/cm), and at high magnification such that the THz intensity profile is roughly uniform across the imaging FOV. Here, MT structure changes are observed to initiate within 4 – 6 minutes, further supporting the intensity-dependence observed above.

Tip-enhancement provides a higher-intensity exposure in a localized region, and the dramatic ejection of aggregate structures near the tip apex within 1 minute is consistent with the intensity-dependence of THz-induced MT disassembly. Due to the aggregation of fluorescently-labelled protein at the tip apex saturating the signal at the region of maximal field enhancement, analyzing the change to the finer structure of the MTs that comprise the aggregates is challenging. Future experiments utilizing reduced labelling ratios in anticipation of fluorescence amplification due to tip aggregation are suggested.

9.4.2 Frequency dependence

Exposures at high magnification (40x) and high tubulin concentration (5 mg/mL) with THz bandpass filters investigated coarse frequency-dependence within an approximately uniform intensity distribution across the imaging FOV. The characteristic times for MT disassembly extracted from the exponential fits in Figure 9.7(b) are 8 ± 2 min ($R^2=0.9626$) and 22 ± 6 min ($R^2=0.9223$) for the 0.5 THz and 1.5 THz bands, respectively. While these are significantly longer than the broadband reference case ($\tau=3.1\pm 0.6$ minutes, $R^2=0.9854$), they also correspond to significantly lower pulse energy, intensity, and peak electric field, as summarized in Table 9.1.

Figure 9.7(c) shows the MT area fraction curves in terms of dose delivered (J/cm^2), which corrects for differences in pulse energy and area (but not peak electric field). If effects depended only on intensity, the corrected curves are expected to overlap. However, the characteristic dose for the 0.5 THz band is 1.4 ± 0.3 J/cm^2 , relative to 23 ± 6 J/cm^2 for the 1.5 THz band. Additionally, the field strength of the 0.5 THz band (37 kV/cm) is significantly lower than the 1.5 THz field strength (100 kV/cm). Since the 0.5 THz disassembly occurs faster not only at a lower dose, but also a lower peak field strength, these data indicate that MT disassembly is significantly influenced by frequency content. The broadband curve corresponds to a characteristic dose of 13 ± 3 J/cm^2 , intermediate to the curves for the low and high frequency bands. This suggests that the observed broadband MT disassembly is predominantly due to low-frequency energy, while much of the high-frequency content is not utilized for MT disassembly, but is likely instead absorbed by the media or thermalized.

Other effects may potentially explain the observed frequency dependence as well, such as differential absorption in the aqueous media environment prior to MT interaction. In water, the absorption coefficients at 0.5 THz and 1.5 THz are approximately 159.4 cm^{-1} and 295.3 cm^{-1} , respectively, and so more of the high-frequency band will be absorbed in aqueous media rather than the MTs [33]. Additionally, in MTs the calculated absorbed energy at 1.5 THz is also roughly twice the energy absorbed at 0.5 THz, and so these competing effects obscure one another experimentally [22]. Future studies investigating concentration dependence (i.e., varying probabilities of THz absorption in MT structures relative to surrounding media) or variation of aqueous media layer thickness (i.e., varying interaction distance in the MT solution) will assist in contextualizing these apparent frequency-dependent effects to better understand the precise nature of this interaction.

9.4.3 Considerations of thermal or shockwave interaction mechanisms

An important consideration is the potential for other interaction mechanisms, such as thermal effects or field-induced shockwaves, to influence the biological response in THz exposure studies [1, 12]. In our experiments, the duty cycle is limited (1 kHz train of picosecond-duration pulses) to ensure negligible heating in the biological media. An estimate of the maximum per-pulse temperature increase from the broadband THz pulse is roughly 5 mK, using $\Delta Q = mc\Delta T = \rho Vc\Delta T$, where ΔT is the temperature change due to a pulse energy ΔQ , and assuming similar properties to water (density $\rho=1$ g/cm³, specific heat capacity $c=4.2$ J/g/K). The volume $V=Az$ is calculated from the THz spot area and penetration depth. The average steady-state heating due to the 1 kHz pulse train is measured with a thermal imager (Reed Instruments, R2100) to be less than 1°C in water, and is consistent with measurements of other similar THz exposure systems [34, 35, 36]. These are also consistent with the THz-water heating model from Kristensen et al., which predicts a maximum temperature change at the beam center of 2°C for our broadband beam parameters [37].

In addition to the measurements above, experiments with taxol-stabilized MTs inherently control for thermal effects, as they are verified to be stable for several hours at room temperature, and higher temperatures assist MT polymerization (indeed, it is the mechanism exploited to polymerize MTs from tubulin by placing them into a 37°C incubator, as described in Section 9.3.1.1). Therefore, disassembly by THz represents the opposite effect to that expected from increasing sample temperature. This implies that the dominant interaction mechanism is non-thermal and may instead be explained by coupling to natural oscillatory dynamics of MT structures.

Using intense THz pulses generated by a free electron laser, Yamazaki et al. induced dramatic disassembly of actin polymers that was attributed to an acoustic shockwave formed in the aqueous medium that penetrates significantly deeper than EM THz energy [12]. While this represents an exciting new interaction mechanism to explore that may play a significant role in THz-induced biological effects, we cannot claim with confidence that similar shockwave phenomena are occurring in the present study. Tsubouchi et al. show that the acoustic shockwave amplitude is expected to scale linearly with the product of absorption coefficient and fluence, αF , with significant shockwave amplitude requiring αF on the order of $\sim 0.1 - 1$ J/cm³ [38]. The relatively lower values in our work ($\alpha F \sim 0.02$ J/cm³) may not be sufficient to produce acoustic waves with significant amplitude, although this should be explored as a potential mechanism in future

investigations. Nevertheless, we observed MT disassembly within minutes at similar fluence, but with lower acoustic generation efficiency.

9.4.4 *Relation to tissue-level biological effects*

In Chapter 7, differential gene expression induced by intense THz pulses in human skin, and identified biological processes predicted to be dysregulated were reported [39, 40]. In these experiments, 3D human skin tissue models were exposed using similar beam parameters (2.4 $\mu\text{J}/\text{pulse}$, $E_{\text{peak}} = 240 \text{ kV}/\text{cm}$, $I_{\text{pulse}} = 74 \text{ MW}/\text{cm}^2$) as those outlined in Section 9.3.1.2. Here, we emphasize features of these data that are consistent with the MT exposure data presented in Section 9.3.2, and provide insight into the higher-level processes that may be dysregulated by THz interaction with MTs. Specifically, these are the THz-induced gene expression of microtubule-associated genes in human skin, and the predicted dysregulation of cytoskeleton-related processes at the tissue-level of biological organization.

Figure 9.8(a) shows the differential gene expression induced by intense THz pulses of all genes in the tubulin superfamily and genes that encode for microtubule-associated proteins (MAPs). Intense THz pulses largely downregulate expression of tubulin and other genes related to MT structure and function. There is a particularly large suppression of genes in the α and β subfamilies (TUBA and TUBB), which encode for the principal structural components of MTs as described in Section 9.2. Gamma and delta tubulin, which play critical roles in MT nucleation, were unaffected. In the context of the significant disassembly of MTs induced by THz pulses presented in this study, this differential gene expression may represent the cell's genomic response to a disassembled and disrupted cytoskeletal network.

Downregulation of TUBA and TUBB following chemical disassembly of MTs in human cells has been established for decades [41, 42, 43, 44], further corroborating the significance of THz-induced MT disassembly as a key mechanism driving the tissue-level biological response in skin in Figure 9.8(a). However, more work needs to be done to elucidate the precise nature of this potential THz interaction mechanism. Among the other microtubule-regulating genes affected by THz are the microtubule-associated protein (MAP) family that regulate MT growth, and PLK4, a serine/threonine kinase that regulates mitotic centriole dynamics [45]. With the exception of TTL, a cytosolic enzyme responsible for post-translational modifications of alpha tubulin, all significant THz-induced effects on MT-associated gene expression were inhibitory.

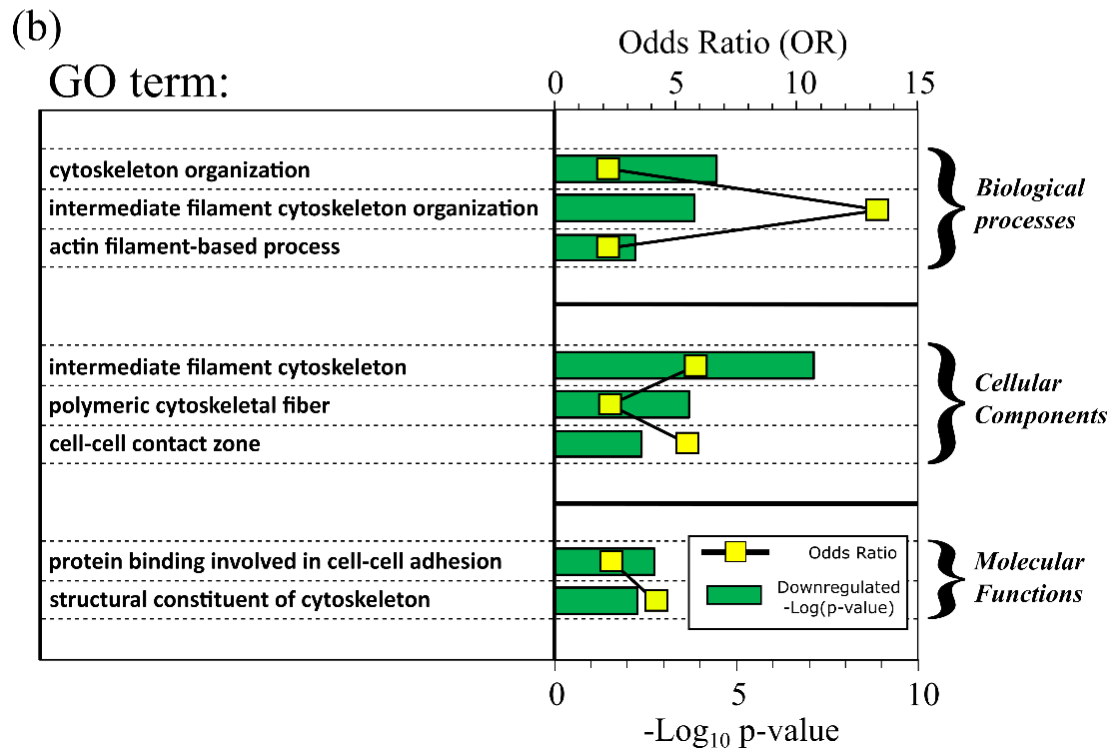
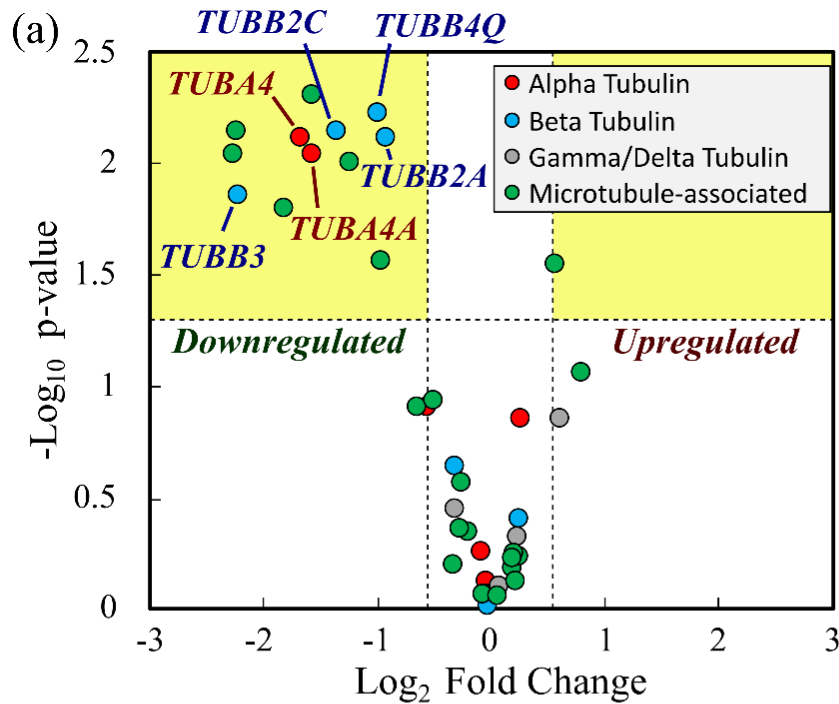


Figure 9.8. **Intense THz pulses significantly downregulate several members of tubulin/MT gene families.** (a) Volcano plot showing differential expression of the tubulin superfamily and other microtubule-associated genes induced by intense THz pulses in human skin. Dashed lines indicate conventional thresholds of expression significance ($|\text{Log}_2(I/I_0)| > 0.58$, $p < 0.05$). Genes that encode for structural α/β tubulin (TUBA/TUBB) subunits are significantly downregulated. (b) Gene Ontology (GO) analysis of the global expression dataset identifies significant over-representation in eight cytoskeleton-related processes, components, and functions.

Some of these THz-affected genes have also been investigated for therapeutic application in gene therapy: Knockdown of class II, III, or IV β -tubulin family genes (TUBB2A, TUBB2C, TUBB4Q, and TUBB3 in Figure 9.8(a)) has been shown to enhance the effectiveness of tubulin-binding pharmacological agents via suppression of MT dynamics and sensitization to apoptosis induction [46, 47]. These data motivate the hypothesis that intense THz pulses may enhance the sensitivity of diseased cells to similar drugs via interaction with MTs and potentially other cytoskeletal structures.

Gene Ontology (GO) analysis was performed on the measured expression dataset to identify statistical over-representations of biological processes, cellular components, and molecular functions among the set of significantly differentially expressed genes, relative to expected global background rates [48]. 58 total GO terms were identified as over-represented by the THz-induced expression profile ($p < 0.01$). These were largely related to epidermal processes (as the sample under study was skin), however, 8 GO terms were associated with general or specific cytoskeletal processes, components, and functions. The GO terms, odds-ratios (OR), and p-values are shown in Figure 9.8(b), and include over-representation of THz-affected genes in several important cytoskeleton-regulated processes. Thus, intense THz pulses may dysregulate these cytoskeletal-related functions leading to phenotypic changes observed at cellular or tissue levels. Future studies that explicitly investigate the correlation between THz-induced disassembly of MTs and the corresponding gene expression profiles will assist in clarifying the precise nature of the cellular response to THz-MT interactions.

These data show that intense THz pulses are capable of dissociating cellular concentrations of polymerized, taxol-stabilized MTs within minutes of application, and are consistent with differential gene expression measured in cellular systems. The onset of MT disassembly is dramatic and clearly triggered by THz power input, as seen in repeated, controlled experiments. Nonetheless, several exposures have also been performed in which no effect to MT structure was observed, even in similar exposure conditions that had previously induced disassembly. Since MTs are verified to be stable at room temperature for hours, spontaneous disassembly in controlled exposure studies is likely not occurring. The most likely explanation is that our current THz sources, while sufficient to induce MT disassembly under optimal conditions, are close to the levels necessary for detectable MT disassembly, as suggested by the diminished effect near the outer regions of the beam, but still within the defined THz focus (Figure 9.5(b)). Small variations in the MT environment may significantly affect the THz energy and field such that the pulse seen by the sample is rendered insufficient for significant MT disassembly. These data suggest that THz-induced disassembly

requires pulse energy density in the range of 30 – 80 $\mu\text{J}/\text{cm}^2$, total dose on the order of $\sim 1 - 10$ J/cm^2 , a peak-field strength > 37 kV/cm , and a further dependence on spectral content of the THz pulse, with faster disassembly for low-frequency THz bands (~ 0.5 THz). More research investigating the THz parameter space for differential structural change is necessary.

The inhibition of MT dynamics is a standard mechanism of action for several types of pharmacological agents used in chemotherapy. Paclitaxel (also known as taxol, the MT stabilizing agent used in these experiments) is an early chemotherapy drug that inhibits MT dynamics by stabilizing polymerized filaments such that necessary cycles of polymerization/depolymerization (“treadmilling”) are suppressed [19, 49]. Similarly, colchicine is an experimental anti-cancer (and anti-inflammatory) drug that inhibits tubulin dimers from polymerizing into MT filaments [50]. Several other types of tubulin-binding pharmacological agents such as vinblastine, demecolcine, or nocodazole, similarly inhibit MT dynamics and reduce polymer mass [51].

9.5 Conclusion

In this chapter, microtubule disassembly by intense THz pulses was investigated. Significant disassembly of MTs is observed within several minutes of THz power input, and these effects are not explained by heating or shockwave formation. Significant intensity dependence was observed in the rate of MT disassembly. Moreover, exposures using THz bandpass filters suggest that the frequency content has a significant influence on the detected structural changes. However, more work is required to isolate confounding variables in exposure experiments, such as the reduction in THz energy transmitted through aqueous media, relative to the increased absorption in MTs at higher frequencies. Our results were analyzed in the context of our previous THz exposures performed in skin tissue, introduced in Chapter 7, and suggest that MT disassembly by intense THz pulses may be a key interaction mechanism driving the biological response observed in higher-level systems like multicellular tissue.

As MTs are essential mitotic structures and popular targets of anti-cancer therapies, the THz-induced effects to MT structure reported in this paper suggest a potential therapeutic mechanism of intense THz pulses, possibly in combination with existing pharmacological interventions. Future research investigating these effects in higher-level cellular and tissue systems is necessary to establish the prospective clinical feasibility.

9.6 References

- [1] G. Wilmink and J. Grundt, "Invited Review Article: Current State of Research on Biological Effects of Terahertz Radiation," *Journal of Infrared, Millimeter, and Terahertz Waves*, vol. 32, no. 10, pp. 1074 - 1122, 2011.
- [2] M. Mattsson, O. Zeni and M. Simko, "Is there a biological basis for therapeutic applications of millimeter waves and THz waves?," *Journal of Infrared, Millimeter, and Terahertz Waves*, vol. 39, pp. 863 - 878, 2018.
- [3] T. Kleine-Ostmann, C. Jastrow, K. Baaske, B. Heinen, M. Schwerdtfeger, U. Karst, H. Hintzsche, H. Stopper, M. Koch and T. Schrader, "Field Exposure and Dosimetry in the THz Frequency Range," *IEEE Transactions on Terahertz Science and Technology*, vol. 4, no. 1, pp. 12 - 25, 2014.
- [4] B. S. Alexandrov, V. Gelev, A. R. Bishop, A. Usheva and K. Ø. Rasmussen, "DNA breathing dynamics in the presence of a terahertz field," *Physics Letters A*, vol. 374, pp. 1214 - 1217, 2010.
- [5] L. Titova, A. Ayesheshim, A. Golubov, D. Fogen, R. Rodriguez-Juarez, F. Hegmann and O. Kovalchuk, "Intense THz pulses cause H2AX phosphorylation and activate DNA damage response in human skin tissue," *Biomedical Optics Express*, vol. 4, no. 4, pp. 559 - 568, 2013.
- [6] L. Titova, A. Ayesheshim, A. Golubov, R. Rodriguez-Juarez, R. Woycicki, F. Hegmann and O. Kovalchuk, "Intense THz pulses down-regulate genes associated with skin cancer and psoriasis: a new therapeutic avenue?," *Scientific Reports*, vol. 3, no. 2363, pp. Q1 - Q10, 2013.
- [7] H. Cheon, H.-j. Yang, S.-H. Lee, Y. A. Kim and J.-H. Son, "Terahertz molecular resonance of cancer DNA," *Scientific Reports*, vol. 6, no. 37103, pp. 1 - 10, 2016.
- [8] J. Tang, J. Ma, L. Guo, K. Wang, Y. Yang, W. Bo, L. Yang, Z. Wang, H. Jiang, Z. Wu, B. Zeng and Y. Gong, "Interpretation of the molecular mechanism of the electroporation induced by symmetrical bipolar picosecond pulse trains," *BBA - Biomembranes*, vol. 1862, no. 183213, pp. 1 - 9, 2020.
- [9] A. Ramundo-Orlando, G. P. Gallerano, P. Stano, A. Doria, E. Giovenale, G. Messina, M. Cappelli, M. D'Arienzo and I. Spassovsky, "Permeability Changes Induced by 130 GHz Pulsed Radiation on Cationic Liposomes Loaded With Carbonic Anhydrase," *Bioelectromagnetics*, vol. 28, no. 8, pp. 587 - 598, 2007.
- [10] "Tera-Hertz radiation in Biological Research, Investigations on Diagnostics and study on potential Genotoxic Effects (THz-BRIDGE), Final Report," [Online]. Available: <https://www.frascati.enea.it/THz-BRIDGE/>.
- [11] S. Yamazaki, M. Harata, T. Idehara, K. Konagaya, G. Yokoyama, H. Hoshina and Y. Ogawa, "Actin polymerization is activated by terahertz irradiation," *Scientific Reports*, vol. 8, no. 9990, pp. 1 - 7, 2018.

- [12] S. Yamazaki, M. Harata, Y. Ueno, M. Tsubouchi, K. Konagaya, Y. Ogawa, G. Isoyama, C. Otani and H. Hoshina, "Propagation of THz irradiation energy through aqueous layers: Demolition of actin filaments in living cells," *Scientific Reports*, vol. 10, no. 9008, pp. 1 - 10, 2020.
- [13] H. Hintzsche, C. Jastrow, T. Kleine-Ostmann, H. Stopper, E. Schmid and T. Schrader, "Terahertz Radiation Induces Spindle Disturbances in Human-Hamster Hybrid Cells," *Radiation Research*, vol. 175, no. 5, pp. 569 - 574, 2011.
- [14] A. Amicis, S. D. Sanctis, S. D. Cristofaro, V. Franchini, F. Lista, E. Regalbuto, E. Giovenale, G. P. Gallerano, P. Nenzi, R. Bei, M. Fantini, M. Benvenuto, L. Masuelli, E. Coluzzi, C. Cicia and A. Sgura, "Biological effects of in vitro THz radiation exposure in human foetal fibroblasts," *Mutation Research/Genetic Toxicology and Environmental Mutagenesis*, vol. 793, pp. 150 - 160, 2015.
- [15] X. G. Peralta, J. C. Cantu, C. Z. Cerna and I. Echchgadda, "Impact of Sub-Millimeter Waves on the Assembly Kinetic of Microtubules," in *43rd International Conference on Infrared, Millimeter, and Terahertz Waves (IRMMW-THz)*, Nagoya, Japan, 2018.
- [16] S. Romanenko, D. Appadoo, N. Lawler, S. I. Hodgetts, A. R. Harvey and V. P. Wallace, "Terahertz Radiation Stimulates Neurite Growth in PC12 Derived Neurons During Development Phase: Preliminary Study," in *45th International Conference on Infrared, Millimeter, and Terahertz Waves (IRMMW-THz)*, Paris, France, 2020.
- [17] R. Philips, J. Kondev, J. Theriot and H. Garcia, *Physical Biology of the Cell*, New York, NY: Garland Science, 2013.
- [18] D. A. Fletcher and R. D. Mullins, "Cell mechanics and the cytoskeleton," *Nature*, vol. 463, no. 7280, pp. 485 - 492, 2010.
- [19] R. L. Margolis and L. Wilson, "Microtubule treadmilling: what goes around comes around," *BioEssays*, vol. 20, no. 10, pp. 830 - 836, 1998.
- [20] H. M. Berman, J. Westbrook, Z. Feng, G. Gilliland, T. N. Bhat, H. Weissig, I. N. Shindyalov and P. E. Bourne, "The Protein Data Bank," *Nucleic Acids Research*, vol. 28, pp. 235 - 242, 2000.
- [21] A. Ayoub, T. Craddock, M. Klobukowski and J. Tuszynski, "Analysis of the strength of interfacial hydrogen bonds between tubulin dimers using quantum theory of atoms in molecules," *Biophysics Journal*, vol. 107, no. 3, pp. 740 - 750, 2014.
- [22] J. M. Moix, J. E. Parker and I. Echchgadda, "Qualitative Behavior of the Low-Frequency Vibrational Dynamics of Microtubules and the Surrounding Water," *Journal of Physical Chemistry B*, vol. 121, pp. 3024 - 3031, 2017.
- [23] O. Smolyanskaya, N. Chernomyrdin, A. Konovko, K. Zaytsev, I. Ozheredov, O. Cherkasova, M. Nazarov, J.-P. Guillet, S. Kozlov, Y. V. Kistenev, J.-L. Coutaz, P. Mounaix, V. Vaks, J.-H. Son, H. Cheon and V. Wallace, "Terahertz biophotonics as a tool for studies of dielectric and spectral properties of biological tissues and liquids," *Progress in Quantum Electronics*, vol. 62, pp. 1-77, 2018.

- [24] J.-H. Son, *Terahertz Biomedical Science and Technology*, Boca Raton, FL: CRC Press, 2014.
- [25] J. J. Timmons, J. Preto, J. A. Tuszynski and E. T. Wong, "Tubulin's response to external electric fields by molecular dynamics simulations," *PLoS ONE*, vol. 13, no. 9, pp. 1 - 17, 2018.
- [26] P. Marracino, D. Havelka, J. Prusa, M. Liberti, J. Tuszynski, A. T. Ayoub, F. Apollonio and M. Cifra, "Tubulin response to intense nanosecond-scale electric field in molecular dynamics simulation," *Scientific Reports*, vol. 9, no. 1, pp. 1 - 14, 2019.
- [27] J. Prusa, A. T. Ayoub, D. E. Chafai, D. Havelka and M. Cifra, "Electro-opening of a microtubule lattice in silico," *Computational and Structural Biotechnology Journal*, vol. 19, pp. 1488 - 1496, 2021.
- [28] L. Rems and D. Miklavcic, "Tutorial: Electroporation of cells in complex materials and tissue," *Journal of Applied Physics*, vol. 119, no. 201101, pp. 1 - 21, 2016.
- [29] P. Vernier, Z. Levine, M.-C. Ho, S. Xiao, I. Semenov and A. Pakhomov, "Picosecond and Terahertz Perturbation of Interfacial Water and Electroporation of Biological Membranes," *Journal of Membrane Biology*, vol. 248, no. 5, pp. 837 - 848, 2015.
- [30] Cytoskeleton Inc. - The Protein Experts, "Fluorescent Microtubules Biochem Kit 4.2," 2012.
- [31] J. Hebling, G. Almasi, I. Z. Kozma and J. Kuhl, "Velocity matching by pulse front tilting for large-area THz-pulse generation," *Optics express*, vol. 10, no. 21, pp. 1161 - 1166, 2002.
- [32] H. Hirori, A. Doi, F. Blanchard and K. Tanaka, "Single-cycle terahertz pulses with amplitudes exceeding 1 MV/cm generated by optical rectification in LiNbO₃," *Applied Physics Letters*, vol. 98, no. 9, 2011.
- [33] M. N. Afsar and J. B. Hasted, "Measurements of the optical constants of liquid H₂O and D₂O between 6 and 450 cm⁻¹," *Journal of the Optical Society of America*, vol. 67, pp. 902 - 904, 1977.
- [34] T. Tachizaki, R. Salagicjo, S. Terada, K. -I. Kamei and H. Hirori, "Terahertz pulse-altered gene networks in human induced pluripotent stem cells," *Optics Letters*, vol. 45, no. 21, pp. 6078 - 6081, 2020.
- [35] D. R. Dalzell, J. McQuade, R. Vincelette, B. Ibey, J. Payne, R. Thomas, W. P. Roach, C. L. Roth and G. J. Wilmink, "Damage thresholds for terahertz radiation," in *Proceedings of SPIE: Optical Interactions with Tissues and Cells XI*, San Francisco, California, 2010.
- [36] I. Echchgadda, J. E. Grundt, C. Z. Cerna, C. C. Roth, J. A. Payne, B. L. Ibey and G. J. Wilmink, "Terahertz Radiation: A Non-contact Tool for Selective Stimulation of Biological Responses in Human Cells," *IEEE Transactions on Terahertz Science and Technology*, vol. 6, no. 1, pp. 54 - 68, 2016.

- [37] T. T. L. Kristensen, W. Withayachumnankul, P. U. Jepsen and D. Abbott, "Modeling terahertz heating effects on water," *Optics Express*, vol. 18, no. 5, pp. 4727 - 4739, 2010.
- [38] M. Tsubouchi, H. Hoshina, M. Nagai and G. Isoyama, "Plane photoacoustic wave generation in liquid water using irradiation of terahertz pulses," *Scientific Reports*, vol. 10, no. 18537, pp. 1 - 9, 2020.
- [39] C. M. Hough, D. N. Purschke, C. Huang, L. V. Titova, O. V. Kovalchuk, B. J. Warkentin and F. A. Hegmann, "Intense Terahertz Pulses Inhibit Ras Signaling and Other Cancer-associated Signaling Pathways in Human Skin Models," *Journal of Physics: Photonics*, vol. 3, no. 034004, pp. 1 - 14, 2021.
- [40] C. M. Hough, D. N. Purschke, C. Huang, L. V. Titova, O. V. Kovalchuk, B. J. Warkentin and F. A. Hegmann, "Topology-based prediction of pathway dysregulation induced by intense terahertz pulses in human skin tissue models," *Journal of Infrared, Millimeter, and Terahertz Waves*, vol. 39, pp. 887 - 898, 2018.
- [41] A. Ben-Ze'ev, S. R. Farmer and S. Penman, "Mechanisms of regulating tubulin synthesis in cultured mammalian cells," *Cell*, vol. 17, no. 2, pp. 319 - 325, 1979.
- [42] T. J. Yen, P. S. Machlin and D. W. Cleveland, "Autoregulated instability of beta-tubulin mRNAs by recognition of the nascent amino terminus of beta-tubulin," *Nature*, vol. 334, no. 6183, pp. 580 - 585, 1988.
- [43] D. W. Cleveland, "Autoregulated control of tubulin synthesis in animal cells," *Current Opinions in Cell Biology*, vol. 1, pp. 10 - 14, 1989.
- [44] I. Gasic, S. A. Boswell and T. J. Mitchison, "Tubulin mRNA stability is sensitive to change in microtubule dynamics caused by multiple physiological and toxic cues," *PLoS Biology*, vol. 17, no. 4, pp. 1 - 23, 2019.
- [45] G. Stelzer, N. Rosen, I. Plaschkes, S. Zimmerman, M. Twik, S. Fishilevich, T. I. Stein, R. Nudel, I. Lieder, Y. Mazor, S. Kaplan, D. Dahary, D. Warshawsky, Y. Guan-Golan, A. Kohn, N. Rappaport, M. Safran and D. Lancet, "The GeneCards Suite: From Gene Data Mining to Disease Genome Sequence Analysis," *Current Protocols in Bioinformatics*, vol. 54, pp. 1.30.1 - 1.30.33, 2016.
- [46] P. P. Gan, J. A. McCarroll, S. T. Po'uha, K. Kamath, M. A. Jordan and M. Kavallaris, "Microtubule Dynamics, Mitotic Arrest, and Apoptosis: Drug-Induced Differential Effects of BIII-Tubulin," *Molecular Cancer Therapeutics*, vol. 9, no. 5, pp. 1339 - 1348, 2010.
- [47] P. P. Gan and M. Kavallaris, "Tubulin-Targeted Drug Action: Functional Significance of Class II and Class IVb B-Tubulin in Vinca Alkaloid Sensitivity," *Cancer Research*, vol. 68, no. 23, pp. 9817 - 9824, 2008.
- [48] S. Carbon, A. Ireland, C. J. Mungall, S. Shu, B. Marshall and S. Lewis, "AmiGO: Online access to ontology and annotation data," *Bioinformatics*, vol. 25, no. 2, pp. 288 - 289, 2009.

- [49] G. Orr, P. Verdier-Pinard, H. McDaid and S. Horwitz, "Mechanisms of Taxol resistance related to microtubules," *Oncogene*, vol. 22, no. 47, pp. 7280 - 7295, 2003.
- [50] S. Punganuru, H. Madala and K. Srivenugopal, "Colchicine-Based Hybrid Anticancer Drugs to Combat Tumor Heterogeneity," *Medicinal Chemistry*, vol. 6, no. 3, 2016.
- [51] M. Jordan and L. Wilson, "Microtubules as a target for anticancer drugs," *Nature Review Cancer*, vol. 4, pp. 253 - 265, 2004.

10 Summary and Conclusions

10.1 Thesis summary and contribution

The investigations and results reported in this thesis advanced the study of the interaction of biological systems with THz radiation primarily along two avenues: (1) Design and implementation of an intense THz pulse source dedicated to real-time biological exposure analysis, including comprehensive beam characterization and a novel quantitative dosimetry framework, and (2) Contributions of experimental datasets of biological effects induced by intense THz pulses at three scales of biological structural organization, in the context of potential therapeutic mechanisms of intense THz pulses for cancer. The former comprised the topics discussed in Chapters 3 – 6, while the latter was the focus of Chapters 7 – 9. Chapters 1 and 2 provided introductory, background, and review material to contextualize the project's precedent and goals.

The primary goals of this thesis stated above were achieved. A radiation source that generates single-cycle, picosecond-duration EM pulses with high pulse energy and peak electric fields (1.5 μJ , 640 kV/cm), and a broad low-frequency energy spectrum ($\sim 0.1 - 2$ THz), was designed and constructed. This source was integrated into a biological exposure system with multiple modes of exposure operation, and several types of real-time analysis capabilities. Biological exposure studies were performed on skin tissue models, cells, and microtubules.

The THz bio-exposure system described in Chapter 5 was designed to integrate a laser-based radiation source with a system for real-time analysis of multiple types of biological samples (protein complexes in solution, cell culture, or 3D tissue models). Intense THz pulses were generated by optical rectification of tilted-pulse-front infrared laser pulses in lithium niobate, and coherently detected by electro-optic sampling in gallium phosphide, as described in Chapters 3 and 4. A novel component of the system design was the rotating off-axis parabolic mirror, which allowed the ability to direct the THz focus in a 360° annulus, providing multiple modes for source operation with a relatively small table footprint. Real-time biological effects were monitored via fluorescence microscopy from above the sample location (with THz exposure from below), and the system may also be operated for normal-incidence THz reflection spectroscopy of biological samples. The use of long-working-distance objectives with the microscope provided sufficient space to place a sharp conductive tip for local THz field enhancement, which induced dramatic structural change to microtubules and cell membranes.

In Chapter 6, a theoretical formalism of quantitative dose calculation for coherent THz pulse interactions was outlined. By modeling radiation propagation through stratified media as a binary decision tree, a set of all relevant transfer function terms may be recursively generated, and used to simulate coherent THz propagation and interaction in many optically thin materials, which is relevant to our exposure studies. Comparison to conventional spectroscopy models and measured THz transmission data showed good agreement, and simulations of real exposure scenarios predict that the exposure environment significantly impacts the THz field and energy seen by the sample.

For the exposure experiments, significant biological effects were observed at all investigated levels of biological structure. At the tissue level (Chapter 7), global differential gene expression measurements were performed for varying THz pulse energies. Of 9311 genes present in control probes, 1681 were significantly differentially expressed by intense THz pulses. These data were used as inputs for bioinformatics analyses. Signal Pathway Impact Analysis (SPIA) and Gene Ontology (GO) analysis predicted cellular signaling pathways and processes likely to be dysregulated, and THz effects were generally categorized as activation of pro-inflammatory and inhibition of pro-mitotic signaling. Clustering analysis of the pathway edge matrix identified particularly important genes that dominantly drive the predicted dysregulation to cancer-signaling, as discussed in the next section. These phenotypic effects were related to more fundamental interaction mechanisms with biomolecular and cellular structures.

At the cellular-level (Chapter 8), in THz-exposed human and rat cell lines, changes to cell membrane permeability were monitored with membrane-traversing fluorescent probes. Mathematical descriptions of field-induced membrane electropermeabilization were discussed, and provided a framework to understand the measured data. In A-431 epithelial carcinoma cells, THz exposure resulted in a significant but small (~2%), dose-dependent increase of membrane permeability that persisted for 24 hours post-exposure. In RBL-2H3 rat leukemia cells, utilizing a sharp conductive tip for local field-enhancement, evidence of dramatic, potentially reversible membrane permeabilization was observed in the target cell in real-time. These results were discussed in the context of the gene expression measurements from the previous chapter, and suggest that the predicted suppression of mitotic activity in skin may arise due to compromised cellular membranes.

At the molecular level (Chapter 9), in microtubules (MTs), intensity- and frequency-dependent disassembly at room temperature was observed within minutes of THz irradiation. Exposures with THz bandpass filters additionally indicated significant dependence on the pulse frequency content. These results were discussed in the context of measured downregulation of MT-related genes in

tissue (Chapter 7), and suggest that the biological effects observed in higher-level systems may arise in response to THz-induced disruption of essential cytoskeletal structures like MTs or actin.

In all cases, biological effects were not explained by the calculated or measured levels of heating associated with the beam exposure parameters. Thus, effects are attributed to non-thermal interaction mechanisms, such as the coupling and dysregulation of structural dynamics that occur in cellular systems at similar frequencies.

The dominant fundamental interaction mechanisms underlying phenotypic effects observed in cells and tissues remain to be elucidated. This is a difficult question to answer; due to the prevalence of a large range of oscillatory dynamics, THz excitations couple to a wide variety of potentially important biological structures that may influence the overall cellular response. Results from this thesis identified three key targets of THz interactions: microtubules, cellular membranes (including the outer plasma membrane and interior organelle membranes), and gene/protein targets for regulation of pro-mitotic gene expression that encode for proteins in the Ras and calmodulin superfamilies.

Observations of biological effects induced by intense THz pulses were often discussed in the context of potential therapeutic applications for skin diseases. The suppression of pro-mitotic signaling in target tissue, potentially via interaction with mitosis-regulating structures like microtubules or membranes, is the most promising avenue of novel therapeutic technologies utilizing THz radiation. If a predictable, repeatable effect can be established that is therapeutically effective, it may provide promising alternative treatment options for some cancers in the future, and should therefore be further explored.

10.2 Proposed future directions

There are many opportunities for academic, industrial, or clinical research and application that follow from the discussions presented in this thesis. Results motivate continuation along several particularly promising avenues, as discussed in the following sections.

10.2.1 Targeted protein expression assays for “terahertz targets”

In Chapter 7, it was shown that intense THz pulses induce a large genomic response in human skin, with 1681 genes significantly differentially expressed at the highest THz intensity. Of those, a subset of 23 genes were identified as the dominant drivers of THz-induced dysregulation of cancer signaling, termed “terahertz targets” (see Table 7.4). However, these experiments only characterize gene expression at the mRNA transcript level, and so future experiments investigating expression dynamics at the functional protein level is a natural progression to pursue these exciting results. Immunofluorescence assays that counter-stain for these target proteins in single cells is one potential method of directly assessing the functional role these gene targets potentially play in THz-induced skin dysregulation (and potentially other cell types). Fluorescence detection modalities may then be used to quantify spatiotemporal protein expression dynamics that are affected by THz exposure, and differential effects may be studied for varying THz dose, pulse repetition rate, pulse intensity, field strength, or spectral content.

Results from the analyses reported in Chapter 7 suggest that, for skin studies, THz-induced effects on mitotic and inflammatory processes are likely to be fruitful research avenues. For the former, central or terminal node proteins in the *Ras signaling* pathway (KRAS, MAPK3), calmodulin-/calmodulin-like calcium-binding proteins in the *Calcium signaling* pathway (CALML, CALML), or growth factors (HGF, FGF, PGF) are predicted to be dominant drivers of THz-induced suppression of mitotic activity. For inflammatory processes, chemokines, cytokines (CCL, CXCL), interleukins (IL6), and interferons (IL24) are the likely gene-level sources of THz-induced immune responses, as well as the associated receptors (CCR, CXCR, ILR).

10.2.2 Terahertz spectroscopy of cell media solutions: Influence of media conductivity on biological response to intense terahertz pulses

One experimental parameter that may significantly influence the biological response to intense THz pulses is the conductivity of the surrounding environment. Recall that microtubules (Chapter 9) were grown in an electrolytic tubulin buffer (80 mM PIPES, 2 mM MgCl₂, 0.5 mM EGTA), and 1 mM guanosine triphosphate (GTP) to facilitate polymerization. Epithelial tissues (Chapter 7) and cell cultures (Chapter 8) were grown in DMEM/EMEM supplemented with fetal bovine serum and penicillin/streptomycin. Further, recall from Chapter 2 that cellular and tissue systems themselves are broadly dispersive with conductivity increasing to ~100 S/m in the THz band. Therefore, samples studied in this thesis were in highly complex dielectric and conductive environments.

As described in Chapter 8, in cells, reduction in media conductivity increase the transmembrane voltage (TMV) decay constant in membranes. Further, in Chapter 6 it was demonstrated that the reflection properties of the materials surrounding the sample region significantly modulate the THz field and energy in the sample region. Therefore, variation of media conductivity may affect outcomes of THz exposure experiments in two ways: First, the alteration of back-reflected waves influences interaction duration and absorbed dose of the THz field in the sample region. Second, sufficiently low conductivity media increases cell membrane relaxation time from $\sim\mu\text{s}$ to potentially $\sim\text{ms}$ timescales. Therefore, a pulse train at 1 kHz repetition rate may induce a TMV build-up due to slower membrane relaxation that was not possible at higher conductivities.

For future experiments, it would therefore be useful to characterize the THz dielectric spectra of the sample media liquids, including verification of constancy of media conductivity over the course of an experiment duration. Moreover, media conductivity should be explicitly investigated as a variable in a controlled study due to the potential influence it may have on THz-induced outcomes, such as microtubule disassembly rate or cell membrane permeabilization. Measurements of media conductivity may be performed by operating the THz bio-exposure system in normal-incidence reflection spectroscopy mode, as described in Chapter 5.

10.2.3 Time-resolved, quantitative dielectric characterization of ionizing dose deposition in cells and tissue

THz spectroscopy may also provide useful characterizations of the structural or chemical changes that occur in cells or tissue in response to ionizing radiation. Due to the low penetration depth corresponding to large absorbed energy fractions within 10 – 100 μm of the tissue surface, and the sensitivity of THz spectral probes to chemical structures and concentrations, THz probes are well-suited to provide quantitative, high-SNR spectral measurements of dielectric parameter changes induced by ionizing radiation dose absorption in tissue. These studies may be performed with reflection spectroscopy on skin *in vivo*, or transmission spectroscopy with thin samples prepared *ex vivo*.

This concept can be extended to a pump-probe experimental scheme to characterize the time-evolution of the chemical and structural changes following absorption of ionizing photons. Photons interacting with atoms in tissue result in ejected electrons and scattered photons (typically via the photoelectric, Compton, or pair production effects, dependent on photon energy) [1, 2]. As the electrons travel, more ionizations occur as the charged particles' kinetic energies are absorbed by the medium, resulting in the creation of more scattered electrons and photons, and so on. The

electron-induced ionizations cause chemical change to tissue molecules either directly or via the production of free radicals [3]. These interact with essential biomolecular structures (e.g., DNA) causing cellular damage. Cellular systems activate response pathways and may attempt to repair radiation-induced damage. If the damage is sufficiently severe, the cell will activate a death protocol, resulting in the breakdown and recycling of cellular components in the final stage of the cell's life.

Therefore, during the dose deposition process, significant structural and chemical modifications occur in the tissue, predominantly during the phases in which biomolecules are chemically damaged and carrying out repair, which occur over ~ns – ms timescales following absorption [3]. Since THz spectroscopy is sensitive to chemical structure and concentrations [4, 5], and molecular signatures are often identifiable in the THz spectra [6], the dynamics of a THz spectrum of various tissues during dose deposition may be a novel approach to characterizing fundamental biochemical mechanisms of tissue/radiation interactions.

Several possibilities for medically interesting investigations exist. Quantitative dielectric information from THz spectroscopy could be used to:

- Characterize skin/surface dose,
- Correlate changes in the measured THz spectra to survival curve parameters (e.g., α/β ratio, BED, etc.) induced by varying dose, dose rate, fractionation, or LET (photons, electrons, protons, ions, or neutrons),
- Investigate differential THz spectra for varying cell and tissue types, cell cycle phase, or degrees of radiosensitization,
- Correlate differences in spectra modification to biological effectiveness and therapeutic efficacy.

10.2.4 Terahertz radiation as a sensitizing agent

Some observations reported in Chapters 7 – 9 suggest that THz irradiation may act as a sensitizing agent, or an agent combined with primary pharmacological or radiotherapy regimens that increases the therapeutic effectiveness by “sensitizing” the tissue to cytotoxic effects. For example, increased permeability of cell membranes is known to increase sensitivity to cytotoxic agents via ATP depletion, and so THz-induced permeabilization (Chapter 8) may influence the sensitivity of cellular response via similar mechanisms [7]. Similarly, disassembly of microtubules, or knockdown/inhibition of microtubule-related gene expressions, is a known anti-cancer

mechanism utilized in several forms of therapy, and increases sensitivity of cells to microtubule-targeting drugs [8, 9]. Therefore, THz-induced microtubule disassembly (Chapter 9) should be studied in the presence of these drugs to determine the existence of a combined effect.

10.2.5 Homogenizing the intensity and frequency distribution with raster-scan exposures

Maximizing the THz pulse intensity and field strength requires focusing the free-space THz beam to the smallest possible spot on the order of ~ 1 mm diameter, producing an approximately Gaussian intensity distribution. Moreover, it was shown in Chapter 4 that there is significant frequency variation within the focused spot. Therefore, the THz beam exposes a relatively low number of cells (~ 1000), and the cells that are exposed see differential energy and frequency distributions. Commonly utilized statistical assays that analyze the total population will therefore have compromised quality, as there is a small number of cells to begin with, and potentially large variations in exposure parameters that are pooled together in the global analysis.

This limitation may be addressed with single-cell assays, as suggested in Section 10.2.1. Another approach is to uniformly distribute the THz power to a larger area such that many more cells ($\sim 10^5$) see similar intensity and frequency profiles, and effects may be interpreted statistically with confidence. This can be achieved by raster-scanning the THz pulse train across the cell population, as commonly performed in THz imaging.

The following calculations may be used to design a programmable raster-scanning stage for implementation of the THz bio-exposure system.

First, the total exposure time can be expressed in terms of incremental step-scans as:

$$T = R \cdot N_{tot} \cdot \Delta t_{tot} \quad (10.1)$$

where R is the number of whole-scan repetitions and $N_{tot} = N_x \cdot N_y$ is the total number of step-and-shoot points determined by the desired step size of the sample stage ($\Delta x/\Delta y$) and exposure area. The total time between steps can be separated as $\Delta t_{tot} = \Delta t + t_{dwell}$, where Δt is the time for the stage to move between points, and t_{dwell} is the dwell time at a given point. The stage motion time can then be expressed as

$$\Delta t = \frac{T}{N_x N_y R} - t_{dwell} \quad (10.2)$$

which can then be related to the stage velocity and step size via $v = \Delta x / \Delta t$.

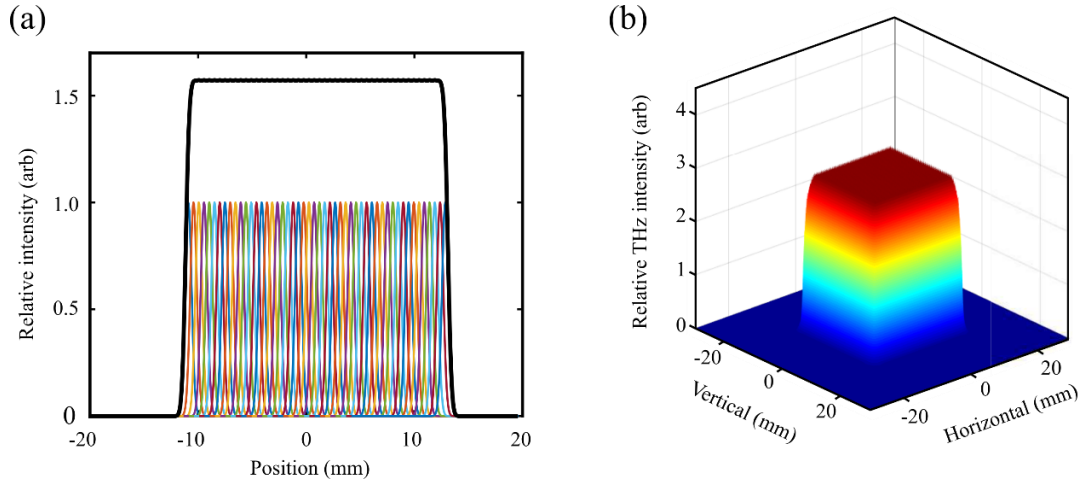


Figure 10.1. **Raster-scanning a gaussian THz spot uniform THz intensity/frequency distributions of arbitrary growth areas.** (a) 1D superposition of gaussian pulses with a step size of $\Delta x = 0.5$ mm, showing the creation of an approximately uniform energy distribution (black curve) from a raster-scanned THz pulse at dimensions suitable for large cell populations. (b) 2D superposition of Gaussian THz pulses showing uniform energy coverage of the desired geometry, and an enhanced intensity relative to single-spot exposures.

Therefore, by specifying the dish geometry and desired stage speed, step size, total scan time, and whole-scan repetition number, the optimal dwell time t_{dwell} is calculated by Equation (10.2) to determine the parameters leading to a uniform energy distribution for a given exposure area. Figure 10.1 shows a simulated energy distribution for a 10 minute single-scan ($R = 1$) exposure, using the geometry of the Ibidi optical plastic wells appropriate for THz exposures ($L_x = 24$ mm, $L_y = 22$ mm), a step size of $\Delta x = 0.5$ mm, and a typical commercial stage velocity of $v = 2.4$ mm/s [10]. The optimal dwell time is found to be $t_{dwell} = 52.5$ ms. These parameters correspond to a high degree of uniformity ($\sigma_I / \hat{I} = 1.8\%$), and an increase of overall THz energy deposition (Figure 10.1) without significantly increased heating to any single area of the dish.

10.3 Concluding statements

Recent innovations in THz generation have led to a renewed interest in THz interactions in biological systems. Intense THz pulses with high peak electric field strengths are capable of inducing biological effects via non-thermal mechanisms unique to the THz band, and these may be exploited for clinical application. However, even with the high intensity pulses utilized in this thesis, the biological effects induced in cellular and tissue systems were often relatively small, and required extended exposure times. Therefore, innovation in THz generation techniques and

efficiencies that allow higher intensities and peak field strengths, with high spectral density, particularly at lower THz band frequencies (0.1 – 0.5 THz), will predominantly drive the progression of biological effects research in the coming decades.

The investigations of this thesis led to observations of significant tissue-level effects of intense THz pulses, and identification of potential molecular or cellular mechanisms underlying these effects. However, the measurements, analyses, and interpretations are only directly relevant for the stated THz pulse parameters and biological systems under the stated exposure conditions. These may be generalizable to broader experimental parameters and cell-/tissue-types, but this must be verified case-by-case, rather than assumed. Therefore, much more work remains to be done, not only in establishing the existence of non-thermal biological effects at varying structural scales, but also the exploration of the THz parameter space that will assist in characterizing the precise nature of interaction.

The study of biological systems with terahertz radiation is a field still in its infancy, and is therefore a wide open research landscape. The significant growth of clinical interest in THz technologies observed in recent decades will only continue, and I am very excited to witness these progressions unfold. While the fruits of research science are their own reward, I cannot help but hope that these small additions may one day contribute in some way to improving the lives of cancer patients, or easing the burden that cancer continues to impose on the global population.

10.4 References

- [1] H. Johns and J. Cunningham, *Physics of Radiology*, Springfield, IL: Charles C Thomas Publisher, 1978.
- [2] F. Khan, *The physics of radiation therapy*, Philadelphia, PA: Lippincott Williams & Wilkins, 2003.
- [3] E. Alpen, *Radiation Biophysics*, San Francisco, CA: Academic Press, 1989.
- [4] E. Pickwell-MacPherson, B. E. Cole, A. J. Fitzgerald, V. P. Wallace and M. Pepper, "Simulation of terahertz pulse propagation in biological systems," *Applied Physics Letters*, vol. 84, no. 12, pp. 2190 - 2192, 2004.
- [5] B. Fischer, M. Walther and P. Jepsen, "Far-infrared vibrational modes of DNA components studied by terahertz time-domain spectroscopy," *Physics in Medicine and Biology*, vol. 47, no. 21, pp. 3807 - 3814, 2002.

- [6] P. Jepsen, D. Cooke and M. Koch, "Terahertz spectroscopy and imaging - Modern techniques and applications," *Laser and Photonics Reviews*, vol. 5, no. 1, pp. 124-166, 2011.
- [7] S. K. Frandsen, H. Gissel, P. Hojman, T. Tramm, J. Eriksen and J. Gehl, "Direct Therapeutic Applications of Calcium Electroporation to Effectively Induce Tumor Necrosis," *Cancer Research*, vol. 72, no. 6, pp. 1336 - 1341, 2012.
- [8] P. P. Gan and M. Kavallaris, "Tubulin-Targeted Drug Action: Functional Significance of Class II and Class IVb B-Tubulin in Vinca Alkaloid Sensitivity," *Cancer Research*, vol. 68, no. 23, pp. 9817 - 9824, 2008.
- [9] P. P. Gan, J. A. McCarroll, S. T. Po'uha, K. Kamath, M. A. Jordan and M. Kavallaris, "Microtubule Dynamics, Mitotic Arrest, and Apoptosis: Drug-Induced Differential Effects of BIII-Tubulin," *Molecular Cancer Therapeutics*, vol. 9, no. 5, pp. 1339 - 1348, 2010.
- [10] Thorlabs, Inc., "Motorized translation stages," Thorlabs, 2021. [Online]. Available: https://www.thorlabs.com/newgrouppage9.cfm?objectgroup_id=2163.

Bibliography

- T. Abbas and A. Dutta, "p21 in cancer: intricate networks and multiple activities," *Nature Reviews Cancer*, vol. 9, no. 6, pp. 400 - 414, 2009.
- G. Acbas, K. Niessen, E. Snell and A. Markelz, "Optical measurements of long-range protein vibrations," *Nature Communications*, vol. 5, no. 3076, pp. 1 - 7, 2014.
- A. Acheva, A. Aerts, C. Rombouts, S. Baatout, S. Salomaa, K. Manda, G. Hildebrandt and M. Kamarainen, "Human 3-D tissue models in radiation biology: current status and future perspectives," *International Journal of Radiation Research*, vol. 12, no. 2, 2014.
- M. N. Afsar and J. B. Hasted, "Measurements of the optical constants of liquid H₂O and D₂O between 6 and 450 cm⁻¹," *Journal of the Optical Society of America*, vol. 67, pp. 902 - 904, 1977.
- K. A. Ahmed, C. R. Correa, T. J. Dilling, N. G. Rao, R. Shridhar, A. M. Trotti, R. B. Wilder and J. J. Caudell, "Altered fractionation schedules in radiation treatment: a review," *Seminars in Oncology*, vol. 41, no. 6, pp. 730 - 750, 2014.
- R. J. Akhurst and A. Hata, "Targeting the TGFB signalling pathway in disease," *Nature Reviews Drug Discovery*, vol. 11, pp. 790 - 811, 2012.
- R. Albert, "Scale-free networks in cell biology," *Journal of cell science*, vol. 118, no. 21, pp. 4947 - 4957, 2005.
- B. Alberts, A. Johnson, J. Lewis, M. Raff, K. Roberts and P. Walter, *The Molecular Biology of the Cell*, 4th Edition, New York, NY: Garland Science, 2002.
- B. S. Alexandrov, V. Gelev, A. R. Bishop, A. Usheva and K. Ø. Rasmussen, "DNA breathing dynamics in the presence of a terahertz field," *Physics Letters A*, vol. 374, pp. 1214 - 1217, 2010.
- B. S. Alexandrov, V. Gelev, S. W. Yoo, A. R. Bishop, K. Ø. Rasmussen and A. Usheva, "Toward a Detailed Description of the Thermally Induced Dynamics of the Core Promoter," *Public Library of Science*, vol. 5, no. 3, pp. 1 - 10, 2009.
- B. S. Alexandrov, V. Gelev, S. W. Yoo, L. B. Alexandrov, Y. Fukuyo, A. R. Bishop, K. O. Rasmussen and A. Usheva, "DNA dynamics play a role as a basal transcription factor in the positioning and regulating of gene transcription initiation," *Nucleic Acids Research*, vol. 38, no. 6, pp. 1790 - 1795, 2009.

- B. S. Alexandrov, M. L. Phipps, L. B. Alexandrov, L. G. Booshehri, A. Erat, J. Zabolotny, C. H. Mielke, H. -T. Chen, G. Rodriguez, K. O. Rasmussen, J. M. Martinez, A. R. Bishop and A. Usheva, "Specificity and Heterogeneity of Terahertz Radiation Effect on Gene Expression in Mouse Mesenchymal Stem Cells," *Scientific Reports*, vol. 3, pp. 1 - 8, 2013.
- E. Almaas, "Biological impacts and context of network theory," *Journal of Experimental Biology*, vol. 210, no. 9, pp. 1548 - 1558, 2007.
- E. Alpen, Radiation Biophysics, San Francisco, CA: Academic Press, 1989.
- B. J. Altman, Z. E. Stine and C. V. Dang, "From Krebs to clinic: glutamine metabolism in cancer therapy," *Nature Reviews Cancer*, vol. 16, pp. 619 - 634, 2016.
- A. Amicis, S. D. Sanctis, S. D. Cristofaro, V. Franchini, F. Lista, E. Regalbuto, E. Giovenale, G. P. Gallerano, P. Nenzi, R. Bei, M. Fantini, M. Benvenuto, L. Masuelli, E. Coluzzi, C. Cicia and A. Sgura, "Biological effects of in vitro THz radiation exposure in human foetal fibroblasts," *Mutation Research/Genetic Toxicology and Environmental Mutagenesis*, vol. 793, pp. 150 - 160, 2015.
- A. A. Angeluts, A. B. Gapeyev, M. N. Esaulkov, O. G. Kosareva, S. N. Matyunin, M. M. Nazarov, T. N. Pashovkin, P. M. Solyankin, O. P. Cherkasova and A. P. Shkurinov, "Study of terahertz-radiation-induced DNA damage in human blood leukocytes," *Quantum Electronics*, vol. 44, no. 3, pp. 247 - 251, 2014.
- M. H. Arbab, T. C. Dickey, D. P. Winebrenner, A. Chen, M. B. Klein and P. D. Mourad, "Terahertz reflectometry of burn wounds in a rat model," *Biomedical optics express*, vol. 2, no. 8, pp. 2339 - 2347, 2011.
- M. H. Arbab, D. P. Winebrenner, T. C. Dickey, A. Chen, M. B. Klein and P. D. Mourad, "Terahertz spectroscopy for the assessment of burn injuries in vivo," *Journal of Biomedical Optics*, vol. 18, no. 7, 2013.
- P. Ashworth, E. Pickwell-MacPherson, E. Provenzano, E. Pinder, S. Purushotham and M. Pepper, "Terahertz pulsed spectroscopy of freshly excised human breast cancer," *Optics Express*, vol. 17, no. 5, pp. 12444 - 12454, 2009.
- F. H. Attix, Introduction to Radiological Physics and Radiation Dosimetry, New York, NY: John Wiley and Sons, Inc, 1986.
- D. H. Auston, K. P. Cheung, J. A. Valdmanis and D. A. Kleinman, "Cherenkov Radiation from Femtosecond Optical Pulses in Electro-Optic Media," *Physical Review Letters*, vol. 53, no. 16, 1984.

- A. Ayoub, T. Craddock, M. Klobukowski and J. Tuszynski, "Analysis of the strength of interfacial hydrogen bonds between tubulin dimers using quantum theory of atoms in molecules," *Biophysics Journal*, vol. 107, no. 3, pp. 740 - 750, 2014.
- BD Biosciences, "Spectrum Viewer," BD Biosciences, [Online]. Available: <https://www.bdbiosciences.com/en-us/applications/research-applications/multicolor-flow-cytometry/product-selection-tools/spectrum-viewer>.
- N. Bajwa, S. Sung, D. B. Ennis, M. C. Fishbein, B. Nowroozi, D. Ruan, A. Maccabi, J. Alger, M. A. St. John, W. S. Grundfest and Z. D. Taylor, "Terahertz Imaging of Cutaneous Edema: Correlation with Magnetic Resonance Imaging in Burn Wounds," *IEEE Transactions of Biomedical Engineering*, vol. 64, no. 11, pp. 2682 - 2694, 2017.
- J. Baselga and C. L. Arteaga, "Critical Update and Emerging Trends in Epidermal Growth Factor Receptor Targeting in Cancer," *Journal of Clinical Oncology*, vol. 23, no. 11, pp. 2445 - 2459, 2005.
- M. Baudelet, *Laser Spectroscopy for Sensing: Fundamentals, Techniques, and Applications*, Woodhead Publishing, 2014.
- M. Belehradec, C. Domenge, B. Luboinski, S. Orlowski, J. Belehradec and L. M. Mir, "Electrochemotherapy, a new antitumor treatment. First clinical phase I-II trial," *Cancer*, vol. 72, no. 12, pp. 694 - 700, 1993.
- A. Ben-Ze'ev, S. R. Farmer and S. Penman, "Mechanisms of regulating tubulin synthesis in cultured mammalian cells," *Cell*, vol. 17, no. 2, pp. 319 - 325, 1979.
- A. Beneduci, K. Cosentino, S. Romeo, R. Massa and G. Chidichimo, "Effect of millimetre waves on phosphatidylcholine membrane models: a non-thermal mechanism of interaction," *Soft Matter*, vol. 10, pp. 5559 - 5567, 2014.
- D. B. Bennett, Z. D. Taylor, P. Tewari, R. S. Singh, M. O. Culjat, W. S. Grundfest, D. J. Sassoon, R. D. Johnson, J. -P. Hubschman and E. R. Brown, "Terahertz sensing in corneal tissues," *Journal of Biomedical Optics*, vol. 16, no. 5, 2011.
- H. M. Berman, J. Westbrook, Z. Feng, G. Gilliland, T. N. Bhat, H. Weissig, I. N. Shindyalov and P. E. Bourne, "The Protein Data Bank," *Nucleic Acids Research*, vol. 28, pp. 235 - 242, 2000.
- D. D. Bikle, Z. Xie and C.-L. Tu, "Calcium regulation of keratinocyte differentiation," *Expert Review of Endocrinology and Metabolism*, vol. 7, no. 4, pp. 461 - 472, 2013.
- F. Blanchard, G. Sharma, L. Razzari, X. Ropagnol, H. -C. Bandulet, F. Vidal, R. Morandotti, J. -C. Kieffer, T. Ozaki, H. Tiedje, H. Haugen, M. Reid and F. Hegmann, "Generation of Intense

- Terahertz Radiation via Optical Methods," *IEEE Journal of Selected Topic in Quantum Electronics*, vol. 17, no. 1, pp. 5 - 16, 2011.
- J. Bock, Y. Fukuyo, S. Kang, M. L. Phipps, L. B. Alexandrov, K. O. Rasumussen, A. R. Bishop, E. D. Rosen, J. S. Martinez, H. -T. Chen, G. Rodriguez, B. S. Alexandrov and A. Usheva, "Mammalian Stem Cells Reprogramming in Response to Terahertz Radiation," *Public Library of Science (PLoS) ONE*, vol. 5, no. 12, pp. 1 - 6, 2010.
- R. A. Bockmann, B. L. de Groot, S. Kakorin, E. Neumann and H. Grubmuller, "Kinetics, Statistics, and Energetics of Lipid Membrane Electroporation Studied by Molecular Dynamics Simulations," *Biophysical Journal*, vol. 95, no. 4, pp. 1837 - 1850, 2008.
- A. N. Bogomazova, E. M. Vassina, T. N. Goryachkovskaya, V. M. Popik, A. S. Sokolov, N. A. Kolchanov, M. A. Lagarkova, S. L. Kiselev and S. E. Peltek, "No DNA damage response and negligible genome-wide transcriptional changes in human embryonic stem cells exposed to terahertz radiation," *Scientific Reports*, vol. 5, no. 7749, pp. 1 - 6, 2015.
- T. Bortfeld, "IMRT: a review and preview," *Physics in Medicine and Biology*, vol. 51, pp. R363 - R379, 2006.
- T. Bortfeld and R. Jeraj, "The physical basis and future of radiation therapy," *British Journal of Radiology*, vol. 84, no. 1002, pp. 485 - 498, 2011.
- O. Bottauscio, M. Chiampi and L. Zilberti, "Thermal Analysis of Human Tissues Exposed to Focused Beam THz Radiations," *IEEE Transactions on Magnetics*, vol. 51, no. 3, pp. 1 - 4, 2015.
- T. Bowman, T. Chavez, K. Khan, J. Wu, A. Chakraborty, N. Rajaram, K. Bailey and M. El-Shenawee, "Pulsed terahertz imaging of breast cancer in freshly excised murine tumors," *Journal of Biomedical Optics*, vol. 23, no. 2, pp. 1 - 13, 2018.
- W. E. Boyce and R. C. DiPrima, *Elementary Differential Equations and Boundary Value Problems*, 9th Ed., US: John Wiley and Sons, Inc., 2009.
- R. W. Boyd, *Nonlinear Optics*, 3rd Ed., Orlando, FL: Academic Press Inc., 2008.
- R. A. Bradshaw and E. A. Dennis, *Handbook of Cell Signaling*, Amsterdam, Netherlands: Academic Press, 2010.
- B. H. Bransden and C. J. Joachain, *Quantum Mechanics*, 2nd Ed., Pearson Education Limited, 2000.

- D. R. Brenner, H. K. Weir, A. A. Demers, L. F. Ellison, C. Louzado, A. Shaw, D. Turner, R. R. Woods and L. M. Smith, "Projected estimates of cancer in Canada in 2020," *Canadian Medical Association Journal*, vol. 192, no. 9, pp. E199 - E205, 2020.
- S. G. Brown, "Clinical review: Science, medicine, and the future. New techniques in laser therapy," *British Medical Journal*, vol. 316, pp. 754 - 757, 1998.
- M. -A. Brun, F. Formanek, A. Yasuda, M. Sekine, N. Ando and Y. Eishii, "Terahertz imaging applied to cancer diagnosis," *Physics in Medicine and Biology*, vol. 55, no. 16, pp. 4615 - 4623, 2010.
- V. Buschmann, H. Hempel, A. Knigge, C. Kraft, M. Roczen, M. Weyers, T. Siebert and F. Koberling, "Characterization of semiconductor devices and wafer materials via sub-nanosecond time-correlated single-photon counting," *Journal of Applied Spectroscopy*, vol. 80, pp. 449 - 457, 2013.
- COMSOL, Inc., Introduction to the Wave Optics Module, COMSOL 5.1 Documentation, 2015.
- C. Y. Calvet and L. M. Mir, "The promising alliance of anti-cancer electrochemotherapy with immunotherapy," *Cancer Metastasis Review*, vol. 35, pp. 165 - 177, 2016.
- Canadian Agency for Drugs and Technologies in Health, "Magnetic Resonance Guided Radiotherapy: MR-simulation and MR-linac," *CADTH Issues in Emerging Health Technologies*, no. 181, pp. 1 - 14, 2020.
- Canadian Cancer Society's Advisory Committee on Cancer Statistics, "Canadian Cancer Statistics 2019," Canadian Cancer Society, Statistics Canada, Toronto, ON, 2019.
- Canadian Cancer Society's Advisory Committee on Cancer Statistics, "Canadian Cancer Statistics 2014 Special Topic: Skin cancers," Canadian Cancer Society, Statistics Canada, Toronto, ON, 2014.
- Y. Cao, P. Huang, X. Li, W. Ge, D. Hou and G. Zhang, "Terahertz spectral unmixing based method for identifying gastric cancer," *Physics in Medicine and Biology*, vol. 63, no. 035016, pp. 1 - 10, 2018.
- S. Carbon, A. Ireland, C. J. Mungall, S. Shu, B. Marshall and S. Lewis, "AmiGO: Online access to ontology and annotation data," *Bioinformatics*, vol. 25, no. 2, pp. 288 - 289, 2009.
- A. Carpinteri, G. Lacidogna, G. Piana and A. Bassani, "Terahertz mechanical vibrations in lysozyme: Raman spectroscopy vs modal analysis," *Journal of Molecular Structure*, vol. 1139, pp. 222 - 230, 2017.

- C. Z. Cerna, D. P. Elam, I. Echchgadda, M. A. Sloan and G. J. Wilmink, "State-of-the-art Exposure Chamber for Highly Controlled and Reproducible THz Biological Effects Studies," *Proceedings of SPIE*, vol. 8941, pp. H1 - H9, 2014.
- J. Chamberlain, R. Miles, C. Collins and D. Steenson, "Introduction to Terahertz Solid-state Devices," in *New Directions in Terahertz Technology*, Netherlands, Kluwer Academic Publishers, 1997, pp. 3-27.
- J. Chamberlain, "Where optics meets electronics: recent progress in decreasing the terahertz gap," *Philosophical Transactions of the Royal Society*, vol. 362, pp. 199 - 213, 2004.
- W. -T. Chang, I. -S. Hwang, M. -T. Chang, C. -Y. Lin, W. -H. Hsu and J. -L. Hou, "Method of electrochemical etching of tungsten tips with controllable profiles," *Review of Scientific Instruments*, vol. 83, no. 083704, pp. 1 - 6, 2012.
- A. Charkhesht, C. K. Regmi, K. R. Mitchell-Koch, S. Cheng and N. Q. Vinh, "High-Precision Megahertz-to-Terahertz Dielectric Spectroscopy of Protein Collective Motions and Hydration Dynamics," *The Journal of Physical Chemistry B*, vol. 122, pp. 6341 - 6350, 2018.
- C. Chen, J. A. Evans, M. P. Robinson, S. W. Smye and P. O'Toole, "Electroporation of cells using EM induction of ac fields by a magnetic stimulator," *Physics in Medicine and Biology*, vol. 55, pp. 1219 - 1229, 2010.
- H. Cheon, H.-j. Yang, S.-H. Lee, Y. A. Kim and J.-H. Son, "Terahertz molecular resonance of cancer DNA," *Scientific Reports*, vol. 6, no. 37103, pp. 1 - 10, 2016.
- M. Chergui, "Ultrafast structural dynamics of biological systems," *Comprehensive Biophysics*, vol. 1, pp. 398 - 424, 2012.
- O. P. Cherkasova, D. S. Serdyukov, A. S. Ratushnyak, E. F. Nemova, E. N. Kozlov, Y. V. Shidlovskii, K. I. Zaytsev and V. V. Tuchin, "Effects of Terahertz Radiation on Living Cells: a Review," *Optics and Spectroscopy*, vol. 128, no. 6, pp. 855 - 866, 2020.
- O. P. Cherkasova, V. I. Fedorov, E. F. Nemova, S. S. Popova, A. S. Pogodin and A. G. Khamoyan, "Terahertz radiation influence on peptide conformation," *Proceedings of SPIE*, vol. 6727, pp. 1 - 5, 2007.
- A. Christofides, M. Kosmopoulos and C. Piperi, "Pathophysiological mechanisms regulated by cytokines in gliomas," *Cytokine*, vol. 71, pp. 377 - 384, 2015.
- N. Citri, "Conformational adaptability in enzymes," *Advances in Enzymology and Related Areas of Molecular Biology*, vol. 37, pp. 397 - 648, 1973.
- D. Clapham, "Calcium Signaling," *Cell*, vol. 131, no. 6, pp. 1047 - 1058, 2007.

- D. W. Cleveland, "Autoregulated control of tubulin synthesis in animal cells," *Current Opinions in Cell Biology*, vol. 1, pp. 10 - 14, 1989.
- M. Cohen and N. G. Trott, "Radiology, physical science, and the emergence of medical physics," *Medical Physics*, vol. 22, no. 11, pp. 1889 - 1897, 1995.
- S. J. Cook and P. J. Lockyer, "Recent advances in Ca²⁺-dependent Ras regulation and cell proliferation," *Cell Calcium*, vol. 39, pp. 101 - 112, 2006.
- S. Cui, H. -H. Tseng, J. Pakela, R. K. Ten Haken and I. E. Naqa, "Introduction to machine and deep learning for medical physicists," *Medical Physics*, vol. 47, no. 5, pp. e127 - e147, 2020.
- C. Cui, R. Merritt, L. Fu and Z. Pan, "Targeting calcium signaling in therapy," *Acta Pharmaceutica Sinica B*, vol. 7, no. 1, pp. 3 - 17, 2017.
- Cytoskeleton Inc. - The Protein Experts, "Fluorescent Microtubules Biochem Kit 4.2," 2012.
- D. R. Dalzell, J. McQuade, R. Vincelette, B. Ibey, J. Payne, R. Thomas, W. P. Roach, C. L. Roth and G. J. Wilkink, "Damage thresholds for terahertz radiation," in Proceedings of SPIE: Optical Interactions with Tissues and Cells XI, San Francisco, California, 2010.
- T. Dauxois, M. Peyrard and A. R. Bishop, "Entropy-driven DNA denaturation," *Physical Review E*, vol. 47, pp. R44 - R47, 1993.
- L. A. Dawson and D. A. Jaffray, "Advances in Image-Guided Radiation Therapy," *Journal of Clinical Oncology*, vol. 25, no. 8, pp. 938 - 946, 2007.
- E. V. Demidova, T. N. Goryachkovskaya, T. K. Malup, S. V. Bannikova, A. I. Semenov, N. A. Vinokurov, V. M. Popik and S. E. Peltek, "Studying the Non-Thermal Effects of Terahertz Radiation on E. coli/pKatG-gfp Biosensor Cells," *Bioelectromagnetics*, vol. 34, pp. 15 - 21, 2013.
- S. S. Dhillon, M. S. Vitiello, E. H. Linfield, A. G. Davies, M. C. Hoffmann, J. Booske, C. Paoloni, M. Gensch, P. Weightman, G. P. Williams, E. Castro-Camus, D. R. Cumming, F. Simoens, I. Escorcia-Carranza, J. Grant, S. Lucyszyn, M. Kuwata-Gonokami, K. Konishi, M. Koch, C. A. Schmuttenmaer, T. L. Cocker, R. Huber, A. G. Markelz, Z. D. Taylor, V. P. Wallace, J. A. Zeitler, J. Sibik, T. M. Korter, B. Ellison, S. Rea, P. Goldsmith, K. B. Cooper, R. Appleby, D. Pardo, P. G. Huggard, V. Krozer, H. Shams, M. Fice, C. Renaud, A. Seeds, A. Stöhr, M. Naftaly, N. Ridler, R. Clarke, J. E. Cunningham and M. B. Johnston, "The 2017 terahertz science and technology roadmap," *Journal of Physics D: Applied Physics*, vol. 50, no. 043001, pp. 1 - 49, 2017.

- T. Ding, T. Huber, A. P. J. Middelberg and R. J. Falconer, "Characterization of Low-Frequency Modes in Aqueous Peptides Using Far-Infrared Spectroscopy and Molecular Dynamics Simulation," *Journal of Physical Chemistry A*, vol. 115, pp. 11559 - 11565, 2011.
- A. Dobroiu, M. Yamashita, Y. N. Ohshima, Y. Morita, C. Otani and K. Kawase, "Terahertz imaging system based on a backward-wave oscillator," *Applied Optics*, vol. 43, no. 30, pp. 5637 - 5646, 2004.
- J. Downward, "Targeting ras signalling pathways in cancer therapy," *Nature Reviews Cancer*, vol. 3, pp. 11 - 22, 2003.
- G. Dranoff, "Cytokines in Cancer Pathogenesis and Cancer Therapy," *Nature Reviews Cancer*, vol. 4, no. 1, pp. 11 - 22, 2004.
- M. Drosten, C. G. Lechuga and M. Barbacid, "Ras in epidermal proliferation," *Oncotarget*, vol. 5, no. 14, pp. 5194 - 5195, 2014.
- F. A. Duck, "The origins of medical physics," *Physica Medica*, vol. 30, pp. 397 - 402, 2014.
- M. V. Duka, L. N. Dvoretzkaya, N. S. Balbekin, M. K. Khodzitskii, S. A. Chivilikhin and O. A. Smolyanskaya, "Numerical and experimental studies of mechanisms underlying the effect of pulsed broadband terahertz radiation on nerve cells," *Quantum Electronics*, vol. 44, no. 8, pp. 707 - 712, 2014.
- L. Duvillaret, F. Garet and J. -L. Coutaz, "Highly precise determination of optical constants and sample thickness in terahertz time-domain spectroscopy," *Applied Optics*, vol. 38, no. 2, pp. 409 - 415, 1999.
- B. Dörschel, D. Hermsdorf, S. Pieck, S. Starke and H. Thiele, "Thickness measurements on cell monolayers using CR-39 detectors," *Nuclear Instruments and Methods in Physics Research B*, vol. 187, no. 4, pp. 525 - 534, 2002.
- L. H. Eadie, C. Reid, A. Fitzgerald and V. Wallace, "Optimizing multi-dimensional terahertz imaging analysis for colon cancer diagnosis," *Expert Systems with Applications*, vol. 40, pp. 2043 - 2050, 2013.
- Eales, S. et al., "The Herschel ATLAS," *Publications of the Astronomical Society of the Pacific*, vol. 122, pp. 499 - 515, 2010.
- I. Echchgadda, J. E. Grundt, C. Z. Cerna, C. C. Roth, J. A. Payne, B. L. Ibey and G. J. Wilmink, "Terahertz Radiation: A Non-contact Tool for Selective Stimulation of Biological Responses in Human Cells," *IEEE Transactions on Terahertz Science and Technology*, vol. 6, no. 1, pp. 54 - 68, 2016.

- I. Echchgadda, C. Cerna, M. Sloan, D. Elam and B. Ibey, "Effects of different terahertz frequencies on gene expression in human keratinocytes," *Proceedings of the Society of Photo-Optical Instrumentation Engineers*, vol. 9321, pp. Q1 - Q9, 2015.
- I. Echchgadda, C. C. Roth, C. Z. Cerna and G. J. Wilmink, "Temporal Gene Expression Kinetics for Human Keratinocytes Exposed to Hyperthermic Stress," *Cells*, vol. 2, no. 2, pp. 224 - 243, 2013.
- Edmund Optics, "Understanding Microscopes and Objectives," Edmund Optics, 2021. [Online]. Available: <https://www.edmundoptics.com/knowledge-center/application-notes/microscopy/understanding-microscopes-and-objectives/>.
- A. Einstein, "Translated: On the quantum theory of radiation," *Physikalische Zeitschrift*, vol. 18, pp. 121 - 128, 1917.
- A. Einstein, "Translated: Radiation emission and absorption according to quantum theory," *Verhandlungen der Deutschen Physikalischen Gesellschaft*, vol. 18, pp. 318 - 323, 1916.
- Electrophysics, PV-320 Operating Manual, Fairfield, New Jersey, 2006.
- D. Eriksson and T. Stigbrand, "Radiation-induced cell death mechanisms," *Tumor Biology*, vol. 31, no. 4, pp. 363 - 372, 2010.
- E. Evans and A. Yeung, "Hidden dynamics in rapid changes of bilayer shape," *Chemistry and Physics of Lipids*, vol. 73, pp. 39 - 56, 1994.
- R. J. Falconer and A. G. Markelz, "Terahertz Spectroscopic Analysis of Peptides and Proteins," *Journal of Infrared and Millimeter Waves*, vol. 33, pp. 973 - 988, 2012.
- S. Fan, Y. He, B. S. Ung and E. Pickwell-MacPherson, "The growth of biomedical terahertz research," *Journal of Physics D: Applied Physics*, vol. 47, pp. 1 - 11, 2014.
- S. Fan, B. S. Y. Ung, E. P. J. Parrott, V. P. Wallace and E. Pickwell-MacPherson, "In vivo terahertz reflection imaging of human scars during and after the healing process," *Journal of Biophotonics*, vol. 10, no. 9, pp. 1143 - 1151, 2017.
- J. F. Federici, B. Schulkin, F. Huang, D. Gary, R. Barat, F. Oliveira and D. Zimdars, "THz imaging and sensing for security applications - explosives, weapons, and drugs," *Semiconductor Science and Technology*, vol. 20, pp. S266 - S280, 2005.
- S. Feng and H. G. Winful, "Physical origin of the Gouy phase shift," *Optics Letters*, vol. 26, no. 8, pp. 485 - 487, 2001.

- B. Fischer, M. Walther and P. Jepsen, "Far-infrared vibrational modes of DNA components studied by terahertz time-domain spectroscopy," *Physics in Medicine and Biology*, vol. 47, no. 21, pp. 3807 - 3814, 2002.
- A. Fitzgerald, V. Wallace, M. Jimenez-linan, L. Bobrow, R. Pye and A. Purushotham, "Terahertz Pulsed Imaging of human breast tumors," *Radiology*, vol. 239, no. 2, pp. 533 - 540, 2006.
- D. A. Fletcher and R. D. Mullins, "Cell mechanics and the cytoskeleton," *Nature*, vol. 463, no. 7280, pp. 485 - 492, 2010.
- R. L. Fork, B. I. Greene and C. V. Shank, "Generation of optical pulses shorter than 0.1 psec by soliding pulse mode locking," *Applied Physics Letters*, vol. 38, no. 9, pp. 671 - 672, 1981.
- S. K. Frandsen, H. Gissel, P. Hojman, T. Tramm, J. Eriksen and J. Gehl, "Direct Therapeutic Applications of Calcium Electroporation to Effectively Induce Tumor Necrosis," *Cancer Research*, vol. 72, no. 6, pp. 1336 - 1341, 2012.
- P. A. Franken, A. E. Hill, C. W. Peters and G. Weinreich, "Generation of Optical Harmonics," *Physical Review Letters*, vol. 7, pp. 118 - 119, 1961.
- H. Fröhlich, "Long-Range Coherence and Energy Storage in Biological Systems," *International Journal of Quantum Chemistry*, vol. 2, pp. 641 - 649, 1968.
- E. Fuchs and S. Raghavan, "Getting Under the Skin of Epidermal Morphogenesis," *Nature Reviews Genetics*, vol. 3, no. 3, pp. 199 - 209, 2002.
- C. Gabriel, S. Gabriel and E. Corthout, "The dielectric properties of biological tissues: I. Literature survey," *Physics in Medicine and Biology*, vol. 41, pp. 2231 - 2249, 1996.
- S. Gabriel, R. W. Lau and C. Gabriel, "The dielectric properties of biological tissues: III. Parametric models for the dielectric spectrum of tissues," *Physics in Medicine and Biology*, vol. 41, pp. 2251 - 2269, 1996.
- S. Gabriel, R. W. Lau and C. Gabriel, "The dielectric properties of biological tissues: II. Measurements in the frequency range 10 Hz to 20 GHz," *Physics in Medicine and Biology*, vol. 41, pp. 2251 - 2269, 1996.
- G. Gallerano, A. Doria, E. Giovenale and I. Spassovsky, "High power THz sources and applications at ENEA-Frascati," *Journal of Infrared Millimeter and Terahertz Waves*, vol. 35, pp. 17 - 24, 2014.
- L. Galluzzi et al., "Essential versus accessory aspects of cell death: recommendations of the NCCD 2015," *Cell Death and Differentiation*, vol. 22, pp. 58 - 73, 2015.

- P. P. Gan, J. A. McCarroll, S. T. Po'uha, K. Kamath, M. A. Jordan and M. Kavallaris, "Microtubule Dynamics, Mitotic Arrest, and Apoptosis: Drug-Induced Differential Effects of BIII-Tubulin," *Molecular Cancer Therapeutics*, vol. 9, no. 5, pp. 1339 - 1348, 2010.
- P. P. Gan and M. Kavallaris, "Tubulin-Targeted Drug Action: Functional Significance of Class II and Class IVb B-Tubulin in Vinca Alkaloid Sensitivity," *Cancer Research*, vol. 68, no. 23, pp. 9817 - 9824, 2008.
- I. Gasic, S. A. Boswell and T. J. Mitchison, "Tubulin mRNA stability is sensitive to change in microtubule dynamics caused by multiple physiological and toxic cues," *PLoS Biology*, vol. 17, no. 4, pp. 1 - 23, 2019.
- Gentec-EO, "Energy detectors: QE-I-USB v1.02," QC, Canada, 2011.
- I. A. Geyko, O. A. Smolyanskaya, M. I. Sulatskiy, S. E. Parakhuda, E. A. Sedykh, E. L. Odlyanitskiy, M. K. Khodzitskiy and A. G. Zabolotniy, "Impact of terahertz radiation on the epithelialization rate of scarified cornea," *Proceedings of SPIE*, vol. 9542, pp. 1 - 7, 2015.
- I. M. Ghobrial, T. E. Witzig and A. A. Adjei, "Targeting Apoptosis Pathways in Cancer Therapy," *CA Cancer Journal for Clinicians*, vol. 55, no. 3, pp. 178 - 194, 2005.
- M. Giladi, R. S. Schneiderman, T. Voloshin, Y. Porat, M. Munster, R. Blat, S. Sherbo, Z. Bomzon, N. Urman, A. Itzhaki, S. Cahal, A. Shteingauz, A. Chaudhry, E. D. Kirson, U. Weinberg and Y. Palti, "Mitotic Spindle Disruption by Alternating Electric Fields Leads to Improper Chromosome Segregation and Mitotic Catastrophe in Cancer Cells," *Scientific Reports*, vol. 5, no. 18046, 2015.
- A. Gothelf, L. M. Mir and J. Gehl, "Electrochemotherapy: results of cancer treatment using enhanced delivery of bleomycin by electroporation," *Cancer Treatment Reviews*, vol. 29, pp. 371 - 387, 2003.
- L. G. Gouy, Translated: On a new property of light waves, Paris, France: Gauthier-Villars, 1890.
- M. Grandolfo, S. M. Michaelson and A. Rindi, Biological Effects and Dosimetry of Nonionizing Radiation, New York, NY: NATO Scientific Affairs & Plenum Press, 1983.
- D. J. Griffiths, Introduction to Electrodynamics, Glenview, IL: Pearson Education, Inc., 2013.
- M. Grootendorst, A. J. Fitzgerald, S. G. Brouwer de Koning, A. Santaolalla, A. Portieri, M. Van Hemelrijck, M. R. Young, J. Owen, M. Cariati, M. Pepper, V. P. Wallace, S. E. Pinder and A. Purushotham, "Use of a handheld terahertz pulsed imaging device to differentiate benign and malignant breast tissue," *Biomedical Optics Express*, vol. 8, no. 6, 2017.

- D. Gross, L. M. Loew and W. W. Webb, "Optical Imaging of Cell Membrane Potential Changes Induced by Applied Electric Fields," *Biophysical Journal*, vol. 50, no. 2, pp. 339 - 348, 1986.
- C. Grosse and H. P. Schwan, "Cellular membrane potentials induced by alternating fields," *Biophysical Journal*, vol. 63, no. 6, pp. 1632 - 1642, 1992.
- F. Guo, C. Yao, C. Bajracharya, S. Polisetty, K. H. Schoenbach and S. Xiao, "Simulation Study of Delivery of Subnanosecond Pulses to Biological Tissues With an Impulse Radiating Antenna," *Bioelectromagnetics*, vol. 35, pp. 145 - 159, 2014.
- S. Hahn, "Hilbert transforms," in *The Transforms and Applications Handbook*, Boca Raton, FL, CRC Press, 1996.
- E. Hall, *Radiobiology for the Radiologist*, Philadelphia, PA: Lippincott, Williams & Wilkins, 2000.
- E. J. Hall and C. -S. Wu, "Radiation-induced second cancers: the impact of 3D-CRT and IMRT," *International Journal of Radiation Oncology Biology Physics*, vol. 56, no. 1, pp. 83 - 88, 2003.
- D. Hanahan and R. A. Weinberg, "The Hallmarks of Cancer," *Cell*, vol. 100, pp. 57 - 70, 2000.
- D. Hanahan and R. A. Weinberg, "Hallmarks of Cancer: The Next Generation," *Cell*, vol. 144, pp. 646 - 674, 2011.
- C. B. Harley, "Telomerase and cancer therapeutics," *Nature Reviews Cancer*, vol. 8, no. 3, pp. 167 - 179, 2008.
- N. Hay, "Reprogramming glucose metabolism in cancer: can it be exploited for cancer therapy?," *Nature Reviews Cancer*, vol. 16, pp. 635 - 649, 2016.
- L. He, Q. Zhang, P. Lan, W. Cao, X. Zhu, C. Zhai, F. Wang, W. Shi, M. Li, X. -B. Bian, P. Lu and A. D. Bandrauk, "Monitoring ultrafast vibrational dynamics of isotopic molecules with frequency modulation high-order harmonics," *Nature Communications*, vol. 9, no. 1108, 2018.
- J. Hebling, G. Almasi and I. Kozma, "Velocity matching by pulse front tilting for large-area THz-pulse generation," *Optics express*, vol. 10, no. 21, pp. 1161 - 1166, 2002.
- J. Hebling, A. G. Stepanov, G. Almasi, B. Bartal and J. Kuhl, "Tunable THz pulse generation by optical rectification of ultrashort laser pulses with tilted pulse fronts," *Applied Physics B: Lasers and Optics*, vol. 78, no. 5, pp. 593 - 599, 2004.
- J. Hebling, G. Almasi, I. Z. Kozma and J. Kuhl, "Velocity matching by pulse front tilting for large-area THz-pulse generation," *Optics express*, vol. 10, no. 21, pp. 1161 - 1166, 2002.

- E. Hecht, *Optics*, Reading, MA: Addison Wesley Longman, 1998.
- E. Hecht, *Optics*, Essex: Pearson Education, 2017.
- R. Heller and L. C. Heller, "Gene Electrotransfer Clinical Trials," *Advances in Genetics*, vol. 89, pp. 235 - 262, 2015.
- G. G. Hernandez-Cardoso, S. C. Rojas-Landeros, M. Alfaro-Gomez, A. I. Hernandez-Serrano, I. Salas-Gutierrez, E. Lemus-Bedolla, A. R. Castillo-Guzman, H. L. Lopez-Lemus and E. Castro-Camus, "Terahertz imaging for early screening of diabetic foot syndrome: A proof of concept," *Scientific Reports*, vol. 7, no. 42124, 2017.
- "Herschel," European Space Agency, [Online]. Available: <https://sci.esa.int/web/herschel>.
- M. Heyden and M. Havenith, "Combining THz spectroscopy and MD simulations to study protein-hydration coupling," *Methods*, vol. 52, pp. 74 - 83, 2010.
- H. Hintzsche, C. Jastrow, B. Heinen, K. Baaske, T. Kleine-Ostmann, M. Schwerdtfeger, M. K. Shakfa, U. Karst, M. Koch, T. Schrader and H. Stopper, "Terahertz Radiation at 0.380 THz and 2.520 THz Does Not Lead to DNA Damage in Skin Cells In Vitro," *Radiation Research*, vol. 179, no. 1, pp. 38 - 45, 2013.
- H. Hintzsche, C. Jastrow, T. Kleine-Ostmann, H. Stopper, E. Schmid and T. Schrader, "Terahertz Radiation Induces Spindle Disturbances in Human-Hamster Hybrid Cells," *Radiation Research*, vol. 175, no. 5, pp. 569 - 574, 2011.
- H. Hirori, A. Doi, F. Blanchard and K. Tanaka, "Single-cycle terahertz pulses with amplitudes exceeding 1 MV/cm generated by optical rectification in LiNbO₃," *Applied Physics Letters*, vol. 98, no. 9, 2011.
- M. Hoffmann and J. Fülöp, "Intense ultrashort terahertz pulses: generation and applications," *Journal of Physics D: Applied Physics*, vol. 44, no. 8, p. 083001, 2011.
- G. Hong, W. Zhang, H. Li, X. Shen and Z. Guo, "Separate enrichment analysis of pathways for up- and downregulated genes," *Journal of the Royal Society Interface*, vol. 11, no. 92, pp. 1 - 11, 2014.
- I. Hosako, N. Sekine, M. Patrashin, S. Saito, K. Fukunaga, Y. Kasai, P. Baron, T. Seta, J. Mendrok, S. Ochiai and H. Yasuda, "At the Dawn of a New Era in Terahertz Technology," *Proceedings of the IEEE*, vol. 95, no. 8, pp. 1611 - 1623, 2007.
- S. Hosseinpour and L. J. Walsh, "Laser-assisted nucleic acid delivery: A systematic review," *Journal of Biophotonics*, vol. 14, pp. 1 - 17, 2020.

- C. M. Hough, D. N. Purschke, C. Bell, A. P. Kalra, P. J. Oliva, C. Huang, J. A. Tuszynski, B. J. Warkentin and F. A. Hegmann, "Disassembly of microtubules by intense terahertz pulses," Accepted by *Biomedical Optics Express*, 2021.
- C. M. Hough, D. N. Purschke, C. Huang, L. V. Titova, O. V. Kovalchuk, B. J. Warkentin and F. A. Hegmann, "Topology-based prediction of pathway dysregulation induced by intense terahertz pulses in human skin tissue models," *Journal of Infrared, Millimeter, and Terahertz Waves*, vol. 39, pp. 887 - 898, 2018.
- C. M. Hough, D. N. Purschke, C. Huang, L. V. Titova, O. V. Kovalchuk, B. J. Warkentin and F. A. Hegmann, "Intense Terahertz Pulses Inhibit Ras Signaling and Other Cancer-associated Signaling Pathways in Human Skin Models," *Journal of Physics: Photonics*, vol. 3, no. 034004, pp. 1 - 14, 2021.
- C. M. Hough, D. N. Purschke, C. Huang, L. V. Titova, O. V. Kovalchuk, B. J. Warkentin and F. A. Hegmann, "Invited Paper: Global gene expression in human skin tissue induced by intense terahertz pulses," *Terahertz Science and Technology*, vol. 11, no. 1, pp. 28 - 33, 2018.
- Z. Hu, P. A. Ott and C. J. Wu, "Towards personalized, tumour-specific therapeutic vaccines for cancer," *Nature Reviews Immunology*, vol. 18, no. 3, pp. 168 - 182, 2018.
- Y. Hwang, J. Ahn, J. Mun, S. Bae, Y. U. Jeong, N. A. Vinokurov and P. Kim, "In vivo analysis of THz wave irradiation induced acute inflammatory response in skin by laser-scanning confocal microscopy," *Optics Express*, vol. 22, no. 10, pp. 11465 - 11475, 2014.
- G. J. Hyland, "Herbert Frohlich, FRS (1905 - 1991) - A Physicist Ahead of His Time," *Electromagnetic Biology and Medicine*, vol. 24, no. 3, pp. 161 - 182, 2005.
- International Agency for Research on Cancer, "List of Classifications, Agents classified by the IARC Monographs, Volumes 1 - 124," *IARC Monographs on the Evaluation of Risk to Humans*, 2021.
- International Commission on Non-Ionizing Radiation Protection, "Exposure to high frequency electromagnetic fields, biological effects and health consequences," International Commission on Non-Ionizing Radiation Protection, Germany, 2009.
- International Commission on Non-Ionizing Radiation Protection, "ICNIRP Guidelines for limiting exposure to time-varying electric, magnetic and electromagnetic fields (up to 300 GHz)," *Health Physics*, vol. 74, no. 4, pp. 494 - 522, 1998.
- V. Jelic, K. Iwaszczuk, P. Nguyen, C. Rathje, G. Hornig, H. Sharum, J. Hoffman, M. Freeman and F. Hegmann, "Ultrafast terahertz control of extreme tunnel currents through single atoms on a silicon surface," *Nature Physics*, vol. 13, no. 6, pp. 591 - 598, 2017.

- W. P. Jencks, "Binding energy, specificity, and enzymic catalysis: the circe effect," *Advances in Enzymology and Related Areas of Molecular Biology*, vol. 43, pp. 219 - 410, 1975.
- P. Jepsen, D. Cooke and M. Koch, "Terahertz spectroscopy and imaging - Modern techniques and applications," *Laser and Photonics Reviews*, vol. 5, no. 1, pp. 124-166, 2011.
- P. Jepsen and H. Merbold, "Terahertz Reflection Spectroscopy of Aqueous NaCl and LiCl Solutions," *Journal of Infrared, Millimeter, and Terahertz Waves*, vol. 31, no. 4, pp. 430-440, 2010.
- E. St. John, T. Athanasiou, D. Hadjiminias and D. Leff, "Diagnostic Accuracy of Intraoperative Techniques for Margin Assessment in Breast Cancer Surgery: A Meta-analysis," *Annals of Surgery*, vol. 265, no. 2, pp. 300 - 310, 2017.
- H. Johns and J. Cunningham, *Physics of Radiology*, Springfield, IL: Charles C Thomas Publisher, 1978.
- W. E. Johnson, C. Li and A. Rabinovic, "Adjusting batch effects in microarray expression data using empirical Bayes methods," *Biostatistics*, vol. 8, no. 1, pp. 118 - 127, 2007.
- M. Jordan and L. Wilson, "Microtubules as a target for anticancer drugs," *Nature Review Cancer*, vol. 4, pp. 253 - 265, 2004.
- M. Kanahisa and S. Goto, "KEGG: Kyoto Encyclopedia of Genes and Genomes," *Nucleic Acids Research*, vol. 28, no. 1, pp. 29 - 34, 2000.
- M. Kanehisa and S. Goto, "KEGG: Kyoto Encyclopedia of Genes and Genomes," *Nucleic Acids Research*, vol. 28, no. 1, pp. 27 - 30, 2000.
- N. Karpowicz, H. Zhong, J. Xu, K.-I. Lin, J.-S. Hwang and X.-C. Zhang, "Non-destructive sub-THz CW imaging," *Proceedings of SPIE*, vol. 5727, 2005.
- T. Kawasaki, K. Tsukiyama and A. Irizawa, "Dissolution of a fibrous peptide by terahertz free electron laser," *Scientific Reports*, vol. 9, no. 1, pp. 1 - 8, 2019.
- F. Khan, *The physics of radiation therapy*, Philadelphia, PA: Lippincott Williams & Wilkins, 2003.
- K. -T. Kim, J. Park, S. J. Jo, S. Jung, O. S. Kwon, G. P. Gallerano, W. -Y. Park and G. -S. Park, "High-power femtosecond-terahertz pulse induces a wound response in mouse skin," *Scientific Reports*, vol. 3, no. 2296, pp. 1 - 7, 2013.

- N. Kimizuka, T. Kawasaki and T. Kunitake, "Self-Organization of Bilayer Membranes from Amphiphilic Networks of Complementary Hydrogen Bonds," *Journal of the American Chemical Society*, vol. 115, no. 10, pp. 4387 - 4388, 1993.
- T. Kleine-Ostmann, C. Jastrow, K. Baaske, B. Heinen, M. Schwerdtfeger, U. Karst, H. Hintzsche, H. Stopper, M. Koch and T. Schrader, "Field Exposure and Dosimetry in the THz Frequency Range," *IEEE Transactions on Terahertz Science and Technology*, vol. 4, no. 1, pp. 12 - 25, 2014.
- T. Kleine-Ostmann and T. Nagatsuma, "A review on terahertz communication research," *Journal of Infrared, Millimeter, and Terahertz Waves*, vol. 32, no. 2, pp. 143 - 171, 2011.
- J. R. Knab, J. -Y. Chen, H. Yunfen and A. G. Markelz, "Terahertz Measurements of Protein Relaxational Dynamics," *Proceedings of the IEEE*, vol. 95, no. 8, pp. 1605 - 1610, 2007.
- H. P. Kok, P. Wust, P. R. Stauffer, F. Bardati, G. C. van Rhoon and J. Crezee, "Current state of the art of regional hyperthermia treatment planning: a review," *Radiation Oncology*, vol. 10, no. 196, pp. 1 - 14, 2015.
- K. Konig, "Multiphoton microscopy in life sciences," *Journal of Microscopy*, vol. 200, no. 2, pp. 83 - 104, 2000.
- A. Korenstein-Ilan, A. Barbul, P. Hasin, A. Eliran, A. Gover and R. Korenstein, "Terahertz Radiation Increases Genomic Instability in Human Lymphocytes," *Radiation Research*, vol. 170, pp. 224 - 234, 2008.
- A. L. Kormos and C. M. Hanson, "Semi-opaque chopper for thermal imaging system and method". United States Patent 6034371, 7 March 2000.
- T. M. Korter, R. Balu, M. B. Campbell, M. C. Beard, S. K. Gregurick and E. J. Heilweil, "Terahertz spectroscopy of solid serine and cysteine," *Chemical Physics Letters*, vol. 418, pp. 65 - 70, 2006.
- T. Kotnik, L. Rem, M. Tarek and D. Miklavcic, "Membrane Electroporation and Electropermeabilization," *Annual Review of Biophysics*, vol. 48, pp. 63 - 91, 2019.
- T. Kotnik, G. Pucihar and D. Miklavcic, "Induced Transmembrane Voltage and Its Correlation with Electroporation-Mediated Molecular Transport," *Journal of Membrane Biology*, vol. 236, no. 3, pp. 3 - 13, 2010.
- T. Kotnik, D. Maklavcic and T. Slivnik, "Time course of transmembrane voltage induced by time-varying electric fields - a method for theoretical analysis and its application," *Bioelectricity and Bioenergetics*, vol. 45, pp. 3 - 16, 1998.

- T. Kotnik, F. Bobanovic and D. Makilavcic, "Sensitivity of transmembrane voltage induced by applied electric fields - a theoretical analysis," *Bioelectrochemistry and Bioenergetics*, vol. 43, pp. 285 - 291, 1997.
- T. Kotnik, D. Milavcic and L. M. Mir, "Cell membrane electropermeabilization by symmetrical bipolar rectangular pulses. Part II. Reduced electrolytic contamination," *Bioelectrochemistry*, vol. 54, pp. 91 - 95, 2001.
- T. Kotnik and D. Maklavcic, "Theoretical Evaluation of Voltage Inducement on Internal Membranes of Biological Cells Exposed to Electric Fields," *Biophysical Journal*, vol. 90, no. 2, pp. 480 - 491, 2006.
- S. Koyama, E. Narita, Y. Shimizu, T. Shiina, M. Taki, N. Shinohara and J. Miyakoshi, "Twenty Four-Hour Exposure to a 0.12 THz Electromagnetic Field Does Not Affect the Genotoxicity, Morphological Changes, or Expression of Heat Shock Protein in HCE-T Cells," *International Journal of Environmental Research and Public Health*, vol. 13, no. 793, pp. 1 - 9, 2016.
- T. T. L. Kristensen, W. Withayachumnankul, P. U. Jepsen and D. Abbott, "Modeling terahertz heating effects on water," *Optics Express*, vol. 18, no. 5, pp. 4727 - 4739, 2010.
- G. Kroemer, L. Galluzzi, P. Vandenabeele, J. Abrams, E. S. Alnemri, E. H. Baehrecke, M. V. Blagosklonny, W. S. El-Deiry, P. Golstein, D. R. Green, M. Hengartner, R. A. Knight, S. Kumar, S. A. Lipton, W. Malorni, G. Nunez, M. E. Peter, J. Tschopp, J. Yuan, M. Piacentini, B. Zhivotovsky and G. Melino, "Classification of cell death: recommendations of the Nomenclature Committee on Cell Death 2009," *Cell Death and Differentiation*, vol. 16, pp. 3 - 11, 2009.
- K. Krushelnick and V. Malka, "Laser wakefield plasma accelerators," *Laser & Photonics Review*, vol. 4, no. 1, pp. 42 - 52, 2010.
- D. Laage, T. Elsaesser and J. Hynes, "Water Dynamics in the Hydration Shells of Biomolecules," *Chemical Reviews*, vol. 117, no. 16, pp. 10694 - 10725, 2017.
- A. Lajevardipour, A. W. Wood, R. L. McIntosh and S. Iskra, "Estimation of Dielectric Values for Tissue Water in the Terahertz Range," *Bioelectromagnetics*, vol. 37, pp. 563 - 567, 2016.
- Y. Lee, *Principles of Terahertz Science and Technology*, New York, NY: Springer, 2009.
- A. J. Lee, D. J. Spence and H. M. Pask, "Terahertz sources based on stimulated polariton scattering," *Progress in Quantum Electronics*, vol. 71, pp. 1 - 23, 2020.
- A. W. M. Lee, Q. Qin, S. Kumar, B. S. Williams and Q. Hu, "Real-time terahertz imaging over a standoff distance (>25 meters)," *Applied Physics Letters*, vol. 89, no. 141125, 2006.

- K. Lee and G. A. Piazza, "The interaction between the Wnt/B-catenin signaling cascade and PKG activation in cancer," *Journal of Biomedical Research*, vol. 31, pp. 189 - 196, 2016.
- Z. L. Levine and P. T. Vernier, "Life Cycle of an Electropore: Field-Dependent and field-Independent Steps in Pore Creation and Annihilation," *Journal of Membrane Biology*, vol. 236, pp. 27 - 36, 2010.
- R. A. Lewis, "A review of terahertz sources," *Journal of Physics D: Applied Physics*, vol. 47, 2014.
- X. Li, J. F. Lovell, J. Yoon and X. Chen, "Clinical development and potential of photothermal and photodynamic therapies for cancer," *Nature Reviews Clinical Oncology*, vol. 17, pp. 657 - 674, 2020.
- A. Likas, N. Vlassis and J. Verbeek, "The global k-means clustering algorithm," *Pattern Recognition*, vol. 36, no. 2, pp. 451 - 461, 2003.
- L. Lins and R. Brasseur, "The hydrophobic effect in protein folding," *FASEB Journal*, vol. 9, pp. 535 - 540, 1995.
- Z. Lojewska, D. L. Farkas, B. Ehrenberg and L. M. Loew, "Analysis of the effect of medium and membrane conductance on the amplitude and kinetics of membrane potentials induced by externally applied electric fields," *Biophysical Journal*, vol. 56, no. 1, pp. 121 - 128, 1989.
- I. V. Lundholm, H. Rodilla, W. Y. Wahlgren, A. Duelli, G. Bourenkov, J. Vukusic, R. Friedman, J. Stake, T. Schneider and G. Katona, "Terahertz radiation induces non-thermal structural changes associated with Fröhlich condensation in a protein crystal," *Structural Dynamics*, vol. 2, no. 054702, pp. 1 - 12, 2015.
- A. P. Lyubartsev and A. L. Rabinovich, "Recent development in computer simulations of lipid bilayers," *Soft Matter*, vol. 7, pp. 25 - 39, 2011.
- J. Ma, R. Shrestha, L. Moeller and D. M. Mittleman, "Invited Article: Channel performance for indoor and outdoor terahertz wireless links," *APL Photonics*, vol. 3, no. 051601, 2018.
- K. Ma, Artist, Animal Cell. [Art]. Wikimedia Commons, 2012.
- L. E. MacConaill and L. A. Garraway, "Clinical Implications of the Cancer Genome," *Journal of Clinical Oncology*, vol. 28, no. 35, pp. 5219 - 5228, 2010.
- T. H. Maiman, "Stimulated Optical Radiation in Ruby," *Nature*, vol. 187, no. 4736, pp. 493 - 494, 1960.

- H. H. Mantsch and R. N. McElhaney, "Phospholipid phase transitions in model and biological membranes as studied by infrared spectroscopy," *Chemistry and Physics of Lipids*, vol. 57, pp. 213 - 226, 1992.
- R. L. Margolis and L. Wilson, "Microtubule treadmilling: what goes around comes around," *BioEssays*, vol. 20, no. 10, pp. 830 - 836, 1998.
- A. Markelz, S. Whitmire, J. Hillebrecht and R. Birge, "THz time domain spectroscopy of biomolecular conformational modes," *Physics in Medicine and Biology*, vol. 47, pp. 3797 - 3805, 2002.
- A. Markelz and Z. Taylor, "The 2017 terahertz science and technology roadmap - Biological applications of THz technology," *Journal of Physics D: Applied Physics*, vol. 50, 2017.
- L. B. Marks and J. Ma, "Challenges in the clinical application of advanced technologies to reduce radiation-associated normal tissue injury," *International Journal of Radiation Oncology Biology Physics*, vol. 69, no. 1, pp. 4 - 12, 2007.
- P. Marracino, D. Havelka, J. Prusa, M. Liberti, J. Tuszynski, A. T. Ayoub, F. Apollonio and M. Cifra, "Tubulin response to intense nanosecond-scale electric field in molecular dynamics simulation," *Scientific Reports*, vol. 9, no. 1, pp. 1 - 14, 2019.
- F. H. Martini, J. L. Nath and E. F. Bartholomew, *Fundamentals of Anatomy and Physiology 9th Ed.*, Benjamin Cummings, 2012.
- J. C. Mather, E. S. Cheng, R. E. Eplee, R. B. Isaacman, S. S. Meyer, R. A. Shafer, R. Weiss, E. L. Wright, C. L. Bennett, N. W. Beggess, E. Dwek, S. Gulkis, M. G. Hauser, M. Janssen, T. Kelsall, P. M. Lubin, S. H. Moseley, T. L. Murdock, R. F. Silverberg, G. F. Smoot and D. T. Wilkinson, "A preliminary measurement of the cosmic microwave background spectrum by the Cosmic Background Explorer (COBE) satellite," *The Astrophysical Journal*, vol. 354, pp. L37 - L40, 1990.
- M. Mattsson, O. Zeni and M. Simko, "Is there a biological basis for therapeutic applications of millimeter waves and THz waves?," *Journal of Infrared, Millimeter, and Terahertz Waves*, vol. 39, pp. 863 - 878, 2018.
- M. -O. Mattsson and M. Simko, "Emerging medical applications based on non-ionizing electromagnetic fields from 0 Hz to 10 THz," *Medical Devices: Evidence and Research*, vol. 12, pp. 347 - 368, 2019.
- K. Mazur, I. A. Heisler and S. R. Meech, "Ultrafast Dynamics and Hydrogen-Bond Structure in Aqueous Solutions of Model Peptides," *Journal of Physical Chemistry B*, vol. 114, no. 32, pp. 10684 - 10691, 2010.

- J. A. McCammon, P. G. Wolynes and M. Karplus, "Picosecond Dynamics of Tyrosine Side Chains in Proteins," *Biochemistry*, vol. 18, no. 6, pp. 927 - 942, 1979.
- H. T. McMahon and J. L. Gallop, "Membrane curvature and mechanisms of dynamic cell membrane remodelling," *Nature*, vol. 438, pp. 590 - 596, 2005.
- A. M. Melo, A. L. Gobbi, M. H. Piazzetta and A. M. P. A. da Silva, "Cross-Shaped Terahertz Metal Mesh Filters: Historical Review and Results," *Advances in Optical Techniques*, vol. 2012, no. 530512, pp. 1 - 12, 2012.
- J. Michl, K. C. Park and P. Swietach, "Evidence-based guidelines for controlling pH in mammalian live-cell culture systems," *Communications Biology*, vol. 2, no. 144, pp. 1 - 12, 2019.
- R. Milo and R. Phillips, "Cell biology by the numbers," [Online]. Available: <http://book.bionumbers.org/>.
- D. M. Mittleman, M. Gupta, R. Neelamani, R. G. Baraniuk, J. V. Rudd and M. Koch, "Recent advances in terahertz imaging," *Applied Physics B: Lasers and Optics*, vol. 68, pp. 1085 - 1094, 1999.
- J. M. Moix, J. E. Parker and I. Echchgadda, "Qualitative Behavior of the Low-Frequency Vibrational Dynamics of Microtubules and the Surrounding Water," *Journal of Physical Chemistry B*, vol. 121, pp. 3024 - 3031, 2017.
- P. -A. Monnard and D. W. Deamer, "Membrane self-assembly processes: Steps toward the first cellular life," *Anatomical Record*, vol. 268, no. 3, pp. 196 - 207, 2002.
- P. Moulton, "Spectroscopic and laser characteristics of Ti:Al₂O₃," *Journal of Optical Society B*, vol. 3, no. 1, pp. 125 - 133, 1986.
- S. Mukherjee, *The Emperor of All Maladies: A Biography of Cancer*, New York, NY: Scribner, 2011.
- B. A. Munk, *Frequency Selective Surfaces: Theory and Design*, John Wiley & Sons, Inc., 2000.
- M. Naftaly, "An international intercomparison of THz time-domain spectrometers," in *International Conference on Infrared, Millimeter, and Terahertz Waves*, Copenhagen, Denmark, 2016.
- M. Naftaly, *Terahertz Metrology*, Boston, MA: Artech House, 2015.
- M. Naftaly and R. Miles, "Terahertz Time-Domain Spectroscopy for Material Characterization," *Proceedings of the IEEE*, vol. 95, no. 8, pp. 1658 - 1665, 2007.

- N. Nasir and M. A. Ahmad, "Cells Electrical Characterization: Dielectric Properties, Mixture, and Modeling Theories," *Journal of Engineering*, vol. 2020, no. 9475490, pp. 1 - 17, 2020.
- National Aeronautics and Space Administration, "NASA Missions - Herschel," [Online]. Available: https://www.nasa.gov/mission_pages/Herschel/index.html.
- National Institutes of Health: National Cancer Institute, "The Ras Initiative," 2020. [Online]. Available: <https://www.cancer.gov/research/key-initiatives/ras>.
- J. Neu and C. A. Schmuttenmaer, "Tutorial: An introduction to terahertz time domain spectroscopy (THz-TDS)," *Journal of Applied Physics*, vol. 124, no. 23, 2018.
- W. D. Newhauser and M. Durante, "Assessing the risk of second malignancies after modern radiotherapy," *Nature Reviews Cancer*, vol. 11, pp. 438 - 448, 2011.
- W. D. Newhauser and R. Zhang, "The physics of proton therapy," *Physics in Medicine and Biology*, vol. 60, pp. R155 - R209, 2015.
- G. L. Nicolson, "The Fluid-Mosaic Model of Membrane Structure: Still relevant to understanding the structure, function and dynamics of biological membranes after more than 40 years," *Biochimica et Biophysica Acta*, vol. 1838, pp. 1451 - 1466, 2014.
- A. I. Nikitkina, P. Y. Bikmulina, E. R. Gafarova, N. V. Kosheleva, Y. M. Efremov, E. A. Bezrukov, D. V. Butnaru, I. N. Dolganova, N. V. Chernomyrdin, O. P. Cherkasova, A. A. Gavdush and P. S. Timashev, "Terahertz radiation and the skin: a review," *Journal of Biomedical Optics*, vol. 26, no. 4, pp. 1 - 26, 2021.
- H. Nyquist, "Certain topics in telegraph transmission theory," *Transactions of AIEE*, vol. 47, no. 2, pp. 617-644, 1928.
- S. A. Ochsner, D. Abraham, K. Martin, W. Ding, A. McOwiti, W. Kankanamge, Z. Wang, K. Andreano, R. A. Hamilton, Y. Chen, A. Hamilton, M. L. Gantner, M. Dehart, S. Qu, S. G. Hilsenbeck, L. B. Becnel, D. Bridges, A. Ma'ayan, J. M. Huss, F. Stossi, C. E. Foulds, A. Kralli, D. P. McDonnell and N. J. McKenna, "The Signaling Pathways Project, an integrated 'omics knowledgebase for mammalian cellular signaling pathways," *Scientific data*, vol. 6, no. 252, pp. 1 - 21, 2019.
- "Operator's Manual: Legend Laser System - Kilohertz, Diode-Pumped, Ultrafast Ti:Sapphire Amplifier," Coherent, Inc., Santa Clara, CA.
- "Operator's Manual: Micra Modelocked Ti:Sapphire Laser," Coherent, Inc., Santa Clara, CA.
- G. Orr, P. Verdier-Pinard, H. McDaid and S. Horwitz, "Mechanisms of Taxol resistance related to microtubules," *Oncogene*, vol. 22, no. 47, pp. 7280 - 7295, 2003.

- O. B. Osman, T. J. Tan, S. Henry, A. Warsen, N. Farr, A. M. McClintic, Y. -N. Wang, S. Arbabi and M. H. Arbab, "Differentiation of burn wounds in an in vivo porcine model using terahertz spectroscopy," *Biomedical Optics Express*, vol. 11, no. 11, pp. 6528 - 6535, 2020.
- K. Otto, "Volumetric modulated arc therapy: IMRT in a single gantry arc," *Medical Physics*, vol. 35, no. 1, pp. 310 - 317, 2008.
- A. Panwar, A. Singh, A. Kumar and H. Kim, "Terahertz Imaging System for Biomedical Applications: Current Status," *International Journal of Engineering and Technology*, vol. 13, no. 2, pp. 33 - 39, 2013.
- R. A. Parikh, P. Wang, J. H. Beumer, E. Chu and L. J. Appleman, "The potential roles of hepatocyte growth factor (HGF)-MET pathway inhibitors in cancer treatment," *OncoTargets and Therapy*, vol. 7, pp. 969 - 983, 2014.
- M. Pavlin, V. Leven and D. Miklavcic, "Electroporation in dense cell suspension - Theoretical and experimental analysis of ion diffusion and cell permeabilization," *Biochimica et Biophysica Acta*, vol. 1770, pp. 12 - 23, 2007.
- X. G. Peralta, J. C. Cantu, C. Z. Cerna and I. Echchgadda, "Impact of Sub-Millimeter Waves on the Assembly Kinetic of Microtubules," in *43rd International Conference on Infrared, Millimeter, and Terahertz Waves (IRMMW-THz)*, Nagoya, Japan, 2018.
- R. Philips, J. Kondev, J. Theriot and H. Garcia, *Physical Biology of the Cell*, New York, NY: Garland Science, 2013.
- E. Pickwell, B. E. Cole, A. J. Fitzgerald, V. P. Wallace and M. Pepper, "Simulation of terahertz pulse propagation in biological systems," *Applied Physics Letters*, vol. 84, no. 12, pp. 2190 - 2192, 2004.
- E. Pickwell, B. Cole, A. Fitzgerald, M. Peppe and V. Wallace, "In vivo study of human skin using pulsed terahertz radiation," *Physics in Medicine and Biology*, vol. 49, no. 9, pp. 1595-1607, 2004.
- E. Pickwell and V. P. Wallace, "Biomedical applications of terahertz technology," *Journal of Physics D: Applied Physics*, vol. 39, no. 17, pp. R301 - R310, 2006.
- E. Pickwell-MacPherson, B. E. Cole, A. J. Fitzgerald, V. P. Wallace and M. Pepper, "Simulation of terahertz pulse propagation in biological systems," *Applied Physics Letters*, vol. 84, no. 12, pp. 2190 - 2192, 2004.
- E. Pickwell-MacPherson and V. Wallace, "Terahertz pulsed imaging - A potential medical imaging modality?," *Photodiagnosis and Photodynamic Therapy*, vol. 6, no. 2, pp. 128 - 134, 2009.

- G. L. Pilbratt, J. R. Riedinger, T. Passvogel, G. Crone, D. Doyle, U. Gageur, A. M. Heras, C. Jewell, L. Metcalfe, S. Ott and M. Schmidt, "Herschel Space Observatory: An ESA facility for far-infrared and submillimetre astronomy," *Astronomy and Astrophysics*, vol. 518, pp. 1 - 6, 2010.
- M. Pless, C. Droege, R. von Moos, M. Salzberg and D. Betticher, "A phase I/II trial of Tumor Treating Fields (TTFields) therapy in combination with pemetrexed for advanced non-small cell lung cancer," *Lung Cancer*, vol. 81, pp. 445 - 450, 2013.
- D. F. Plusquellic, K. Siegrist, E. J. Heilweil and O. Esenturk, "Applications of Terahertz Spectroscopy in Biosystems," *ChemPhysChem*, vol. 8, pp. 2412 - 2431, 2007.
- D. Popescu, C. Rucareanu and G. H. Victor, "A model for the appearances of statistical pores in membranes due to self-oscillations," *Bioelectrochemistry and Bioenergetics*, vol. 25, no. 1, pp. 91 - 103, 1991.
- J. Prusa, A. T. Ayoub, D. E. Chafai, D. Havelka and M. Cifra, "Electro-opening of a microtubule lattice in silico," *Computational and Structural Biotechnology Journal*, vol. 19, pp. 1488 - 1496, 2021.
- S. Punganuru, H. Madala and K. Srivenugopal, "Colchicine-Based Hybrid Anticancer Drugs to Combat Tumor Heterogeneity," *Medicinal Chemistry*, vol. 6, no. 3, 2016.
- E. R. Purba, E. -I. Saita and I. N. Maruyama, "Activation of the EGF Receptor by Ligand Binding and Oncogenic Mutations: The "Rotation Model"," *Cells*, vol. 6, no. 2, 2017.
- D. N. Purschke, M. Na, A. Longman, L. V. Titova and F. A. Hegmann, "Enhancement of hot-carrier photoluminescence with intense terahertz pulses," *Applied Physics Letters*, vol. 112, no. 072105, pp. 1 - 5, 2018.
- A. Ramundo-Orlando, G. P. Gallerano, P. Stano, A. Doria, E. Giovenale, G. Messina, M. Cappelli, M. D'Arienzo and I. Spassovsky, "Permeability Changes Induced by 130 GHz Pulsed Radiation on Cationic Liposomes Loaded With Carbonic Anhydrase," *Bioelectromagnetics*, vol. 28, no. 8, pp. 587 - 598, 2007.
- C. B. Reid, G. Reese, A. P. Gibson and V. P. Wallace, "Terahertz Time-Domain Spectroscopy of Human Blood," *IEEE Journal of Biomedical and Health Informatics*, vol. 17, no. 4, pp. 774 - 778, 2013.
- C. B. Reid, A. Fitzgerald, G. Reese, R. Goldin, P. Tekkis, P. S. O'Kelly, E. Pickwell-MacPherson, A. P. Gibson and V. P. Wallace, "Terahertz pulsed imaging of freshly excised human colonic tissues," *Physics in Medicine and Biology*, vol. 56, no. 14, 2011.
- J. Reimers, L. McKemmish, R. McKenzie, A. Mark and N. Hush, "Weak, strong, and coherent regimes of Fröhlich condensation and their applications to terahertz medicine and quantum

- consciousness," *Proceedings of the National Library of Science*, vol. 106, no. 11, pp. 4219 - 4224, 2009.
- L. Rems and D. Miklavcic, "Tutorial: Electroporation of cells in complex materials and tissue," *Journal of Applied Physics*, vol. 119, no. 201101, pp. 1 - 21, 2016.
- Y. Ren, J. Zheng, X. Yao, G. Weng and L. Wu, "Essential role of the cGMP/PKG signaling pathway in regulating the proliferation and survival of human renal carcinoma cells," *International Journal of Molecular Medicine*, vol. 34, pp. 1430 - 1438, 2014.
- P. L. Richards, "Bolometers for infrared and millimeter waves," *Journal of Applied Physics*, vol. 76, no. 1, 1994.
- M. E. Ritchie, M. J. Dunning, M. L. Smith, W. Shi and A. G. Lynch, "BeadArray Expression Analysis Using Bioconductor," *PLoS Computational Biology*, vol. 7, no. 12, pp. 1 - 6, 2011.
- M. Roark and S. E. Feller, "Molecular Dynamics Simulation Study of Correlated Motions in Phospholipid Bilayer Membranes," *Journal of Physical Chemistry B*, vol. 113, pp. 13229 - 13234, 2009.
- P. J. Roberts and C. J. Der, "Targeting the Raf-MEK-ERK mitogen-activated protein kinase cascade for the treatment of cancer," *Oncogene*, vol. 26, pp. 3291 - 3310, 2007.
- T. Rog, K. Murzyn and M. Pasenkiewicz-Gierula, "The dynamics of water at the phospholipid bilayer surface: a molecular dynamics simulation study," *Chemical Physics Letters*, vol. 3523, pp. 323 - 327, 2002.
- M. S. Rogers, T. Kobayashi, M. R. Pittelkow and E. E. Strehler, "Human Calmodulin-like Protein Is an Epithelial-Specific Protein Regulated during Keratinocyte Differentiation," *Experimental Cell Research*, vol. 267, no. 2, pp. 216 - 224, 2001.
- S. Romanenko, D. Appadoo, N. Lawler, S. I. Hodgetts, A. R. Harvey and V. P. Wallace, "Terahertz Radiation Stimulates Neurite Growth in PC12 Derived Neurons During Development Phase: Preliminary Study," in *45th International Conference on Infrared, Millimeter, and Terahertz Waves (IRMMW-THz)*, Paris, France, 2020.
- S. Romanenko, R. Begley, A. H. Harvey, L. Hool and V. P. Wallace, "The interaction between electromagnetic fields at megahertz, gigahertz and terahertz frequencies with cells, tissues and organisms: risks and potential," *Journal of the Royal Society Interface*, vol. 14, no. 137, pp. 1 - 22, 2017.
- S. Romanenko, P. Siegel, D. A. Wagenaar and V. P. Pikov, "Effects of millimeter wave irradiation and equivalent thermal heating on the activity of individual neurons in the leech ganglion," *Journal of Neurophysiology*, vol. 112, pp. 2423 - 2431, 2014.

- I. B. Roninson, E. V. Broude and B. -D. Chang, "If not apoptosis, then what? Treatment-induced senescence and mitotic catastrophe in tumor cells," *Drug Resistance Updates*, vol. 4, no. 5, pp. 303 - 313, 2001.
- A. -K. Roos, F. Eriksson, J. A. Timmons, J. Gerhardt, U. Nyman, L. Gudmundsdotter, A. Brave, B. Wahren and P. Pisa, "Skin Electroporation: Effects on Transgene Expression, DNA Persistence and Local Tissue Environment," *PLoS One*, vol. 4, no. 9, pp. 1 - 10, 2009.
- L. B. Rosen, D. D. Ginty, M. J. Weber and M. E. Greenberg, "Membrane Depolarization and Calcium Influx Stimulate MEK and MAP Kinase via Activation of Ras," *Neuron*, vol. 12, pp. 1207 - 1221, 1994.
- M. Ruas and G. Peters, "The p16INK4a/CDKN2A tumor suppressor and its relatives," *Biochimica et Biophysica Acta - Reviews on Cancer*, vol. 1378, pp. F115 - F177, 1998.
- H. Rubens and E. Nichols, "Heat rays of great wave-length," *Physical Review (Series I)*, vol. 4, no. 4, pp. 314 - 323, 1897.
- M. Ruden and N. Puri, "Novel anticancer therapeutics targeting telomerase," *Cancer Treatment Reviews*, vol. 39, no. 5, pp. 444 - 456, 2013.
- M. A. Salhi, T. Kleine-Ostmann and T. Schrader, "Propagation Channel Measurements in the mm- and Sub-mm Wave Range for Different Indoor Communication Scenarios," *Journal of Infrared, Millimeter, and Terahertz Waves*, vol. 42, pp. 357 - 370, 2021.
- L. S. Sawant, "Applications of Laplace Transform in Engineering Fields," *International Research Journal of Engineering and Technology*, vol. 5, no. 5, pp. 3100 - 3105, 2018.
- G. V. Scagliotti, S. Novello and J. von Pawel, "The emerging role of MET/HGF inhibitors in oncology," *Cancer Treatment Reviews*, vol. 39, no. 7, pp. 793 - 801, 2013.
- H. Schneckenburger, "Laser-assisted optoporation of cells and tissues - a mini-review," *Biomedical Optics Express*, vol. 10, no. 6, pp. 2883 - 2888, 2019.
- H. P. Schwan, "Electrical Properties of Tissue and Cell Suspensions," *Advances in Biological and Medical Physics*, vol. 5, pp. 147 - 209, 1957.
- Y. Schweitzer, A. D. Lieber, K. Keren and M. M. Kozlov, "Theoretical Analysis of Membrane Tension in Moving Cells," *Biophysical Journal*, vol. 106, pp. 84 - 92, 2014.
- P. Sebastian-Leon, E. Vidal, P. Minguez, A. Conesa, S. Tarazona, A. Amadoz, C. Armero, F. Salavert, A. Vidal-Puig, D. Montaner and J. Dopazo, "Understanding disease mechanisms with models of signaling pathway activities," *BMC Systems Biology*, vol. 8, no. 121, pp. 1 - 19, 2014.

- E. -Y. Seo, J. -H. Namkung, K. -M. Lee, W. -H. Lee, M. Im, S. -H. Hee, G. T. Park, J. -M. Yang, Y. -J. Seo, J. -K. Park, C. D. Kim and J. -H. Lee, "Analysis of calcium-inducible genes in keratinocytes using suppression subtractive hybridization and cDNA microarray," *Genomics*, vol. 86, no. 5, pp. 528 - 538, 2005.
- A. A. Serga, V. S. Tiberkevich, C. W. Sandweg, V. I. Vasyuchka, D. A. Bozhko, A. V. Chumak, T. Neumann, B. Obry, G. A. Melkov, A. N. Slavin and B. Hillebrands, "Bose-Einstein condensation in an ultra-hot gas of pumped magnons," *Nature communications*, vol. 5, no. 3452, 2014.
- Z. Shankayi and S. M. P. Firoozabadi, "The Effect of Pulsed Magnetic Field on the Molecular Uptake and Medium Conductivity of Leukemia Cell," *Cell Biochemistry and Biophysics*, vol. 65, pp. 211 - 216, 2013.
- C. E. Shannon, "Communication in the presence of noise," *Proceedings of the IRE*, vol. 37, no. 1, pp. 10 - 21, 1949.
- G. Sharma, I. Al-Naib, H. Hafez, R. Morandotti, D. G. Cooke and T. Ozaki, "Carrier density dependence of the nonlinear absorption of intense THz radiation in GaAs," *Optics Express*, vol. 20, no. 16, pp. 18016 - 18024, 2012.
- G. Sherbet, Calcium signaling in cancer, Boca Raton, FL: CRC Press, 2001.
- M. Shibuya, "VEGF-VEGFR Signals in Health and Disease," *Biomolecules and Therapeutics*, vol. 22, no. 1, pp. 1 - 9, 2014.
- P. H. Siegel, "Terahertz Technology in Biology and Medicine," *IEEE Transactions on Microwave Theory and Techniques*, vol. 4, pp. 1575 - 1578, 2004.
- P. H. Siegel and V. Pikov, "THz in Biology and Medicine: Towards Quantifying and Understanding the Interaction of Millimeter- and Submillimeter-Waves with Cells and Cell Processes," *Proc. of SPIE: Optical Interactions with Tissues and Cells XXI*, vol. 7562, no. 75620H, pp. 1 - 13, 2010.
- D. W. Siemann and M. R. Horsman, "Modulation of the tumor vasculature and oxygenation to improve therapy," *Pharmacology & Therapeutics*, vol. 153, pp. 107 - 124, 2015.
- K. Simons and E. Ilkonen, "Functional rafts in cell membranes," *Nature*, vol. 387, pp. 569 - 572, 1997.
- S. Singer and G. Nicolson, "The Fluid Mosaic Model of the Structure of Cell Membranes," *Science*, vol. 175, no. 4027, pp. 1208 - 1215, 1972.

- D. S. Sitnikov, I. V. Ilina and A. A. Pronkin, "Experimental system for studying bioeffects of intense terahertz pulses with electric field strength up to 3.5 MV/cm," *Optical Engineering*, vol. 59, no. 6, pp. 1 - 10, 2020.
- J. B. Sleiman, J. -B. Perraud, B. Bousquet, J. -P. Guillet, N. Palka and P. Mounaix, "Identifying explosives by chemometrics with terahertz spectral imaging," *Proceedings of SPIE*, no. 10.1117, 2015.
- O. Smolyanskaya, N. Chernomyrdin, A. Konovko, K. Zaytsev, I. Ozheredov, O. Cherkasova, M. Nazarov, J.-P. Guillet, S. Kozlov, Y. V. Kistenev, J.-L. Coutaz, P. Mounaix, V. Vaks, J.-H. Son, H. Cheon and V. Wallace, "Terahertz biophotonics as a tool for studies of dielectric and spectral properties of biological tissues and liquids," *Progress in Quantum Electronics*, vol. 62, pp. 1-77, 2018.
- J.-H. Son, *Terahertz Biomedical Science and Technology*, Boca Raton, FL: CRC Press, 2014.
- Spectrum/Gentec-DO, "Cross-reference product list," QC, Canada, 2014.
- G. Stelzer, N. Rosen, I. Plaschkes, S. Zimmerman, M. Twik, S. Fishilevich, T. I. Stein, R. Nudel, I. Lieder, Y. Mazor, S. Kaplan, D. Dahary, D. Warshawsky, Y. Guan-Golan, A. Kohn, N. Rappaport, M. Safran and D. Lancet, "The GeneCards Suite: From Gene Data Mining to Disease Genome Sequence Analysis," *Current Protocols in Bioinformatics*, vol. 54, pp. 1.30.1 - 1.30.33, 2016.
- J. C. Stone, "Regulation and Function of the RasGRP Family of Ras Activators in Blood Cells," *Genes and Cancer*, vol. 2, no. 3, pp. 320 - 334, 2011.
- M. R. Stratton, P. J. Campbell and P. A. Futreal, "The cancer genome," *Nature*, vol. 458, no. 7239, pp. 719 - 724, 2009.
- D. Strickland and G. Mourou, "Compression of amplified chirped optical pulses," *Optics Communications*, vol. 56, no. 3, pp. 219 - 221, 1985.
- I. P. Sugar and E. Neumann, "Stochastic model for electric field-induced membrane pores electroporation," *Biophysical Chemistry*, vol. 19, no. 3, pp. 211 - 225, 1984.
- N. Sultanova, S. Kasarova and I. Nikolov, "Characterization of optical properties of optical polymers," *Optical and Quantum Electronics*, vol. 45, pp. 221 - 232, 2013.
- J. Sun and S. Lucyszyn, "Extracting Complex Dielectric Properties From Reflection-Transmission Mode Spectroscopy," *IEEE Access.*, vol. 6, pp. 8302-8321, 2018.

- O. Sushko, R. Dubrovka and R. S. Donnan, "Terahertz Spectral Domain Computational Analysis of Hydration Shell of Proteins with Increasingly Complex Tertiary Structure," *Journal of Physical Chemistry B*, vol. 117, pp. 16486 - 16492, 2013.
- O. Svelto, *Principles of Lasers*, New York, NY: Springer, 2010.
- K. D. Swanson, E. Lok and E. T. Wong, "An Overview of Alternating Electric Fields Therapy (NovoTTF Therapy) for the Treatment of Malignant Glioma," *Current Neurology and Neuroscience Reports*, vol. 16, no. 8, pp. 1 - 10, 2016.
- T. Tachizaki, R. Salagicjo, S. Terada, K. -I. Kamei and H. Hirori, "Terahertz pulse-altered gene networks in human induced pluripotent stem cells," *Optics Letters*, vol. 45, no. 21, pp. 6078 - 6081, 2020.
- A. Takashima and D. Faller, "Targeting the RAS Oncogene," *Expert Opinion on Therapeutic Targets*, vol. 17, no. 5, pp. 507 - 531, 2013.
- H. Takeshima and T. Ushijima, "Accumulation of genetic and epigenetic alterations in normal cells and cancer risk," *Precision Oncology*, vol. 3, no. 7, pp. 1 - 8, 2019.
- J. Tang, H. Yin, J. Ma, W. Bo, Y. Yang, J. Xu, Y. Liu and Y. Gong, "Terahertz Electric Field-Induced Membrane Electroporation by Molecular Dynamics Simulation," *Journal of Membrane Biology*, vol. 251, pp. 681 - 693, 2018.
- J. Tang, J. Ma, L. Guo, K. Wang, Y. Yang, W. Bo, L. Yang, Z. Wang, H. Jiang, Z. Wu, B. Zeng and Y. Gong, "Interpretation of the molecular mechanism of the electroporation induced by symmetrical bipolar picosecond pulse trains," *BBA - Biomembranes*, vol. 1862, no. 183213, pp. 1 - 9, 2020.
- Y. H. Tao, S. I. Hodgetts, A. R. Harvey and V. P. Wallace, "Reproducibility of Terahertz Peaks in a Frozen Aqueous Solution of 5-Methylcytidine," *Journal of Infrared, Millimeter, and Terahertz Waves*, vol. 42, pp. 588 - 606, 2021.
- A. L. Tarca, S. Draghici, P. Kahtri, S. S. Hassan, P. Mittal, J. -S. Kim, C. J. Kim, J. P. Kusanovic and R. Romero, "A novel signaling pathway impact analysis," *Bioinformatics*, vol. 25, no. 1, pp. 75 - 82, 2009.
- "Tera-Hertz radiation in Biological Research, Investigations on Diagnostics and study on potential Genotoxic Effects (THz-BRIDGE), Final Report," [Online]. Available: <https://www.frascati.enea.it/THz-BRIDGE/>.
- The Ibidi Company, "Instructions u-Slide 2 Well (PDF) V3.1," Ibidi, 2020.

- The Nobel Foundation, "The Nobel Prize in Physics 2018," Nobel Prize Outreach, [Online]. Available: <https://www.nobelprize.org/prizes/physics/2018/summary/>.
- M. D. Thomson, M. Kress, T. Löffler and H. G. Roskos, "Broadband THz emission from gas plasmas induced by femtosecond optical pulses: From fundamentals to applications," *Laser & Photonics Review*, vol. 1, no. 4, pp. 349 - 368, 2007.
- M. D. Thomson, M. Kreß, T. Löffler and H. G. Roskos, "Broadband THz emission from gas plasmas induced by femtosecond optical pulses: From fundamentals to applications," *Laser and Photonics Reviews*, vol. 1, no. 4, pp. 349 - 368, 2007.
- Thorlabs, Inc., "Motorized translation stages," Thorlabs, 2021. [Online]. Available: https://www.thorlabs.com/newgrouppage9.cfm?objectgroup_id=2163.
- "THz Bandpass Filters: 10 um - 590 um Center Wavelength," Thorlabs, 2018. [Online]. Available: <https://www.thorlabs.com/catalogpages/obsolete/2018/FB19M10.pdf>.
- R. D. Timmerman, B. D. Kavanagh, C. Cho, L. Papiez and L. Xing, "Stereotactic Body Radiation Therapy in Multiple Organ Sites," *Journal of Clinical Oncology*, vol. 25, no. 8, pp. 947 - 952, 2007.
- J. J. Timmons, J. Preto, J. A. Tuszyński and E. T. Wong, "Tubulin's response to external electric fields by molecular dynamics simulations," *PLoS ONE*, vol. 13, no. 9, pp. 1 - 17, 2018.
- L. V. Titova, F. A. Hegmann and O. Kovalchuk, "Biological Effects of Broadband Terahertz Pulses," in *Terahertz Biomedical Science and Technology*, Boca Raton, FL, CRC Press, 2014, pp. 241 - 263.
- L. Titova, A. Ayesheshim, A. Golubov, R. Rodriguez-Juarez, R. Woycicki, F. Hegmann and O. Kovalchuk, "Intense THz pulses down-regulate genes associated with skin cancer and psoriasis: a new therapeutic avenue?," *Scientific Reports*, vol. 3, no. 2363, pp. Q1 - Q10, 2013.
- L. Titova, A. Ayesheshim, A. Golubov, D. Fogen, R. Rodriguez-Juarez, F. Hegmann and O. Kovalchuk, "Intense THz pulses cause H2AX phosphorylation and activate DNA damage response in human skin tissue," *Biomedical Optics Express*, vol. 4, no. 4, pp. 559 - 568, 2013.
- M. Tokman, J. H. Lee, Z. A. Levine, M. -C. Ho, M. E. Colvin and P. T. Vernier, "Electric Field-Driven Water Dipoles: Nanoscale Architecture of Electroporation," *PLoS One*, vol. 8, no. 4, pp. 1 - 9, 2013.
- B. C. Truong, H. D. Tuan, H. H. Kha and H. T. Nguyen, "Debye Parameter Extraction for Characterizing Interaction of Terahertz Radiation With Human Skin Tissue," *IEEE Transactions on Biomedical Engineering*, vol. 60, no. 6, pp. 1528 - 1537, 2013.

- B. C. Q. Truong, H. D. Tuan, A. J. Fitzgerald, V. P. Wallace and H. T. Nguyen, "A Dielectric Model of Human Breast Tissue in Terahertz Regime," *IEEE Transactions on Biomedical Engineering*, vol. 62, no. 2, pp. 699 - 707, 2015.
- M. Tsubouchi, H. Hoshina, M. Nagai and G. Isoyama, "Plane photoacoustic wave generation in liquid water using irradiation of terahertz pulses," *Scientific Reports*, vol. 10, no. 18537, pp. 1 - 9, 2020.
- F. O. Tzul, D. Vasilechuk and G. I. Makhatadze, "Evidence for the principle of minimal frustration in the evolution of protein folding landscapes," *Proceedings of the National Academy of Science*, vol. 114, no. 9, pp. E1627 - E1632, 2017.
- M. G. Vander-Heiden, L. C. Cantley and C. B. Thompson, "Understanding the Warburg Effect: The Metabolic Requirements of Cell Proliferation," *Science*, vol. 324, no. 5930, pp. 1029 - 1033, 2009.
- M. Vengris, I. H. van Stokkum, X. He, A. F. Bell, P. J. Tonge, R. van Grondelle and D. S. Larsen, "Ultrafast excited and ground-state isomerization dynamics of the green fluorescent protein chromophore in solution," *Journal of Physical Chemistry A*, vol. 108, no. 4587, 2004.
- I. Vermes, C. Haanen and C. Reutelingsperger, "Flow cytometry of apoptotic cell death," *Journal of Immunological Methods*, vol. 243, pp. 167 - 190, 2000.
- P. T. Vernier, Y. Sun and M. A. Gundersen, "Nanoelectropulse-driven membrane perturbation and small molecule permeabilization," *BMC Cell Biology*, vol. 7, no. 37, pp. 1 - 16, 2006.
- P. Vernier, Z. Levine, M.-C. Ho, S. Xiao, I. Semenov and A. Pakhomov, "Picosecond and Terahertz Perturbation of Interfacial Water and Electropermeabilization of Biological Membranes," *Journal of Membrane Biology*, vol. 248, no. 5, pp. 837 - 848, 2015.
- C. Voichita, S. Ansari and S. Draghici, "ROntoTools: R Onto-Tools suite," R Package version 2.6.0, 2017.
- C. Voichita, M. Donato and S. Draghici, "Incorporating gene significance in the impact analysis of signaling pathways," *11th International Conference on Machine Learning and Applications. ICMLA 2012*, pp. 126 - 131, 2012.
- A. Wade, A. Robinson, A. Engler, J. Petritsch, C. James and J. Phillips, "Proteoglycans and their roles in brain cancer," *FEBS Journal*, vol. 280, pp. 2399 - 2417, 2013.
- A. D. Waldman, J. M. Fritz and M. J. Lenardo, "A guide to cancer immunotherapy: from T cell basic science to clinical practice," *Nature Reviews Immunology*, vol. 20, pp. 651 - 668, 2020.

- K. F. Wall and A. Sanchez, "Titanium Sapphire Lasers," *The Lincoln Laboratory Journal*, vol. 3, no. 3, pp. 447 - 462, 1990.
- V. P. Wallace, A. J. Fitzgerald, E. Pickwell, R. J. Pye, P. F. Taday, N. Flanagan and T. Ha, "Terahertz Pulsed Spectroscopy of Human Basal Cell Carcinoma," *Applied Spectroscopy*, vol. 60, no. 10, pp. 1127 - 1133, 2006.
- V. Wallace, A. Fitzgerald, S. Shankar, N. Flanagan, R. Pye, J. Cluff and D. Arnone, "Terahertz pulsed imaging of basal cell carcinoma ex vivo and in vivo," *British Journal of Dermatology*, vol. 151, pp. 424-432, 2004.
- H. Wang, X. Mu, H. He and X. -D. Zhang, "Cancer Radiosensitizers," *Trends in Pharmacological Sciences*, vol. 39, no. 1, pp. 24 - 48, 2018.
- J. Wang, H. Lindley-Hatcher, X. Chen and E. Pickwell-MacPherson, "THz Sensing of Human Skin: A Review of Skin Modeling Approaches," *Sensors*, vol. 21, no. 3624, pp. 1 - 26, 2021.
- Z. Wang, "Ultrafast Imaging of Terahertz Pulses," PhD Thesis, University of Alberta, Edmonton, AB, 2013.
- Z. Wang, J. Lu, W. Huang, Z. Wu, J. Gong, Q. Wang, Q. Liu, C. Wang, Y. Zhu, X. Ding and Z. Wang, "A retrospective study of CT-guided percutaneous irreversible electroporation (IRE) ablation: clinical efficacy and safety," *BMC Cancer*, vol. 21, no. 1, pp. 1 - 8, 2021.
- S. Webb, M. Stoneham and H. Fröhlich, "Evidence for Non-thermal Excitation of Energy Levels in Active Biological Systems," *Physics Letters*, vol. 63A, no. 3, pp. 407 - 408, 1977.
- S. Webb and D. Dodds, "Inhibition of Bacterial Cell Growth by 136 gc Microwaves," *Nature*, vol. 218, pp. 374 - 375, 1968.
- P. Weightman, "Prospects for the study of biological systems with high power sources of terahertz radiation," *Physical Biology*, vol. 9, pp. 1 - 10, 2012.
- R. Wheeler, Artist, DNA Structure. [Art]. Wikimedia Commons, 2019.
- S. H. White and W. C. Wimley, "Membrane Protein Folding and Stability," *Annual Review of Biophysical and Biomolecular Structure*, vol. 28, pp. 319 - 365, 1999.
- D. Williams, "Radiation carcinogenesis: lessons from Chernobyl," *Oncogene*, vol. 27, pp. S9 - S18, 2009.
- R. Williams, A. Schofield, G. Holder, J. Downes, D. Edgar, P. Harrison, M. Siggel-King, M. Surman, D. Dunning, S. Hill, D. Holder, F. Jackson, J. Jones, J. McKenzie, Y. Saveliev, N.

- Thomsen, P. Williams and P. Weightman, "The influence of high intensity terahertz radiation on mammalian cell adhesion, proliferation and differentiation," *Physics in Medicine and Biology*, vol. 58, pp. 373 - 391, 2013.
- G. J. Wilmink, B. D. Rivest, C. C. Roth, B. L. Ibey, J. A. Payne, L. X. Cundin, J. E. Grundt, X. Peralta, D. G. Mixon and W. P. Roach, "In Vitro Investigation of the Biological Effects Associated With Human Dermal Fibroblasts Exposed to 2.52 THz Radiation," *Lasers in Surgery and Medicine*, vol. 43, no. 2, pp. 152 - 163, 2011.
- G. J. Wilmink, B. L. Ibey, C. L. Roth, R. L. Vincelette, B. D. Rivest, C. B. Horn, J. Bernhard, D. Roberson and W. P. Roach, "Determination of Death Thresholds and Identification of Terahertz (THz)-Specific Gene Expression Signatures," *Proceedings of the Society of Photo-Optical Instrumentation Engineers*, vol. 7562, pp. K1 - K8, 2010.
- G. J. Wilmink, B. D. Rivest, C. C. Roth, B. L. Ibey, J. A. Payne, L. X. Cundin, J. E. Grundt, X. Peralta, D. G. Mixon and W. P. Roach, "In Vitro Investigation of the Biological Effects Associated With Human Dermal Fibroblasts Exposed to 2.52 THz Radiation," *Lasers in Surgery and Medicine*, vol. 43, no. 2, pp. 152 - 163, 2011.
- G. Wilmink and J. Grundt, "Invited Review Article: Current State of Research on Biological Effects of Terahertz Radiation," *Journal of Infrared, Millimeter, and Terahertz Waves*, vol. 32, no. 10, pp. 1074 - 1122, 2011.
- B. Wong and Schawlow, "Far-infrared spectrum of $\text{Al}_2\text{O}_3:\text{V}^{4+}$," *The Journal of Chemical Physics*, vol. 49, no. 2, pp. 835 - 842, 1968.
- R. M. Woodward, B. E. Cole, V. P. Wallace, R. J. Pye, D. D. Arnone, E. H. Linfield and M. Pepper, "Terahertz pulse imaging in reflection geometry of human skin cancer and skin tissue," *Physics in Medicine and Biology*, vol. 47, no. 21, pp. 3853 - 3863, 2002.
- D. Woolard, E. Brown, M. Pepper and M. Kemp, "Invited Paper: Terahertz frequency sensing and imaging: A time of reckoning for future applications?," *Proceedings of IEEE*, vol. 93, no. 10, pp. 1722 - 1745, 2005.
- X. -J. Wu, J. -L. Ma, B. -L. Zhang, S. -S. Chai, Z. -J. Fang, C. -Y. Xia, D. -Y. Kong, J. -G. Wang, H. Liu, C. -Q. Zhu, X. Wang, C. -J. Ruan and Y. -T. Li, "Highly efficient generation of 0.2 mJ terahertz pulses in lithium niobate at room temperature with sub-50 fs chirped Ti:sapphire laser pulses," *Optics Express*, vol. 26, no. 6, pp. 7107 - 7116, 2018.
- T. Wu and S. Austin, "Bose-Einstein condensation in biological systems," *Journal of Theoretical Biology*, vol. 71, pp. 209 - 214, 1978.
- Q. Wu and X.-C. Zhang, "Free-space electro-optic sampling of terahertz beams," *Applied Physics Letters*, vol. 67, no. 3523, 1995.

- S. Xiao, S. Guo, V. Nesin, R. Heller and K. H. Schoenbach, "Subnanosecond Electric Pulses Cause Membrane Permeabilization and Cell Death," *IEEE Transactions on Biomedical Engineering*, vol. 58, no. 5, pp. 1239 - 1245, 2011.
- S. Yamazaki, M. Harata, Y. Ueno, M. Tsubouchi, K. Konagaya, Y. Ogawa, G. Isoyama, C. Otani and H. Hoshina, "Propagation of THz irradiation energy through aqueous layers: Demolition of actin filaments in living cells," *Scientific Reports*, vol. 10, no. 9008, pp. 1 - 10, 2020.
- S. Yamazaki, M. Harata, T. Idehara, K. Konagaya, G. Yokoyama, H. Hoshina and Y. Ogawa, "Actin polymerization is activated by terahertz irradiation," *Scientific Reports*, vol. 8, no. 9990, pp. 1 - 7, 2018.
- X. Yang, X. Zhao, K. Yang, Y. Liu, Y. Liu, W. Fu and Y. Luo, "Biomedical Applications of Terahertz Spectroscopy and Imaging," *Trends in Biotechnology*, vol. 34, no. 10, pp. 810 - 824, 2016.
- K. H. Yang, P. L. Richards and S. Y. R., "Generation of Far-Infrared Radiation by Picosecond Light Pulses in LiNbO₃," *Applied Physics Letters*, vol. 19, no. 9, 1971.
- Y. Yang, Y. Xiang and M. Xu, "From red to green: the propidium iodide-permeable membrane of *Shewanella decolorationis* S12 is repairable," *Scientific Reports*, vol. 5, no. 18583, pp. 1 - 5, 2015.
- M. L. Yarmush, A. Golberg, G. Sersa, T. Kotnik and D. Miklavcic, "Electroporation-Based Technologies for Medicine: Principles, Applications, and Challenges," *Annual Review of Biomedical Engineering*, vol. 16, pp. 295 - 320, 2014.
- K.-L. Yeh, M. Hoffmann and K. Nelson, "Generation of 10 uJ ultrashort terahertz pulses by optical rectification," *Applied Physics Letters*, vol. 90, no. 171121, pp. 1 - 3, 2007.
- T. J. Yen, P. S. Machlin and D. W. Cleveland, "Autoregulated instability of beta-tubulin mRNAs by recognition of the nascent amino terminus of beta-tubulin," *Nature*, vol. 334, no. 6183, pp. 580 - 585, 1988.
- K. I. Zaytsev, I. N. Dolganova, N. V. Chernomyrdin, G. M. Katyba, A. A. Gavidush, O. P. Cherkasova, G. A. Komandin, M. A. Shchedrina, A. N. Khodan, D. S. Ponomarev, I. V. Reshetov, V. E. Karasik, M. Skorobogatiy, V. N. Kurlov and V. V. Tuchin, "The progress and perspectives of terahertz technology for diagnosis of neoplasms: a review," *Journal of Optics*, vol. 22, no. 013001, pp. 1 - 44, 2020.
- O. Zeni, G. P. Gallerano, A. Perrotta, M. Romano, A. Sannino, M. Sarti, M. D'Arienzo, A. Doria, E. Giovenale, A. Lai, G. Messina and M. R. Scarfi, "Cytogenetic observations in human peripheral blood leukocytes following in vitro exposure to THz radiation: a pilot study," *Health Physics*, vol. 92, no. 4, pp. 349 - 357, 2007.

- M. Zhang, S. -M. Zhou and T. Qu, "What Do We Mean When We Talk About Linac Isocenter?," *International Journal of Medical Physics, Clinical Engineering and Radiation Oncology*, vol. 4, pp. 233 - 242, 2015.
- Y. -L. Zhang, R. -C. Wang, K. Cheng, B. Z. Ring and L. Su, "Roles of Rap1 signaling in tumor cell migration and invasion," *Cancer Biology and Medicine*, vol. 14, no. 1, pp. 90 - 99, 2017.
- V. F. Zhu, J. Yang, D. G. LeBrun and M. Li, "Understanding the role of cytokines in Glioblastoma Multiforme pathogenesis," *Cancer Letters*, vol. 316, no. 2, pp. 139 - 150, 2012.

A. Appendix

Here, additional details on calculations, derivations, analyses, or discussions that were not included in the main body of the thesis are provided.

A.1 Fourier series expansion

The Fourier transform, and the computational Fast Fourier Transform (FFT), are used extensively throughout this thesis to characterize the frequency-space THz exposure parameters, and to model THz pulse propagation in experimental geometries. Fourier series expansion is a set of mathematical operations that decomposes a given function into a superposition of sinusoids expressed in the original functions' conjugate space (e.g., $f(r) \rightarrow F(k)$, or $f(t) \rightarrow F(\omega)$). For time-domain signals, the FT determines the harmonic content of the waveform in terms of a set of amplitudes and phases for each frequency component.

Consider a time-series signal $f(t)$ that is defined (along with its derivative $f'(t)$) in the interval $-T \leq t \leq T$ and is periodic with period $2T$. The Fourier series expansion is [1]

$$f(t) = \frac{1}{2}A_0 + \sum_{n=1}^{\infty} \left[A_n \cos\left(\frac{n\pi t}{T}\right) + B_n \sin\left(\frac{n\pi t}{T}\right) \right] \quad (\text{A.1})$$

which converges assuming $f(t)$ and $f'(t)$ are continuous on $(-T, T)$. Multiplying by $\cos mt$ ($\sin mt$) and integrating solves for the series coefficients A_n (B_n)

$$\begin{aligned} A_m &= \frac{1}{\pi} \int_{-T}^{+T} f(t) \cos\left(\frac{m\pi t}{T}\right) dt, & m = 0, 1, \dots \\ B_m &= \frac{1}{\pi} \int_{-T}^{+T} f(t) \sin\left(\frac{m\pi t}{T}\right) dt, & m = 1, 2, \dots \end{aligned} \quad (\text{A.2})$$

or in terms of complex exponentials, since $e^{\pm int} = \cos(nt) \pm i \sin(nt)$,

$$f(t) = \frac{1}{\sqrt{2\pi}} \sum_{n=-\infty}^{\infty} C_n \exp\left(\frac{in\pi t}{T}\right) \quad (\text{A.3})$$

with complex coefficients given by

$$C_m = \frac{1}{T} \sqrt{\frac{\pi}{2}} \int_{-T}^T f(t) \exp\left(-\frac{im\pi t}{T}\right) dt \quad (\text{A.4})$$

where the pre-factor in front of the integral sign is chosen with foresight to simplify integration factors from the exponential term.

A.1.1 The Fourier transform

For practical purposes, any signal may be arbitrarily defined as pseudo-periodic by defining a finite single-period time window, T . While this sacrifices continuity of frequency-space representations, the time window may be chosen such that the transformed space has sufficient resolution, Δf , and the sampling width, Δt , may be chosen such that sufficiently high frequencies are achieved. To exactly reconstruct a time-domain signal from frequency-domain data, the Nyquist criterion requires that the sampling frequency be at least twice the maximum frequency, f_{max} [2, 3]. The corresponding expressions relating time and frequency space steps and windows are:

$$f_{max} = \frac{1}{2\Delta t} \quad (\text{A.5})$$

$$T = t_{max} - t(0) = \frac{1}{2\Delta f}$$

An example of typical time-domain parameters for THz pulse acquisition as described in this thesis may be $\Delta t = 100$ fs and $T = 20$ ps. By the above equations, the resulting frequency-space

parameters are $f_{max} = 5$ THz and $\Delta f = 0.025$ THz, which are sufficient for practical experimental scenarios presented in this thesis.

A.1.1.1 Fast fourier transform of terahertz pulse data in Matlab

The following Matlab code computes and displays the measured THz pulse and associated power spectrum from raw data collected from the electro-optic sampling LabView VI in the THz lab.

```
function [t y f Y P enr]=ComputePulseFFT(file)

%file - a string filename containing data from electro-optic sampling
%acquisition. Column 1 is the time vector, column 2 is the field
%amplitude data

%load data, and assign variables time, t, and field, y
data=dlmread(file);
t=data(:,1);
y=data(:,2);

%shift pulse maximum to t=0
[val ind]=max(y);
t=-t+t(ind);

% determine frequency vector
NFFT=2^nextpow2(length(t)); % fft length
Fs=1/mean(diff(t)); % sampling frequency
f=Fs/2*linspace(0,1,NFFT/2+1);% frequency array from DC to Nyquist

% compute amplitude/power spectra, and total energy
Y=fft(y-mean(y),NFFT); % subtract any DC offset
Y=Y(1:NFFT/2+1); % keep the positive part
P=abs(Y).^2; % compute power spectrum
enr=trapz(f,P); % compute total energy as integral of the power
%spectrum, via the trapezoidal method
P=P./enr; % normalize power spectrum to total energy

% display the pulse and power spectrum
figure
subplot(1,2,1)
plot(t,y,'b-','linewidth',2)
xlim([-5 15])
xlabel('Time (ps)')
ylabel('Field (arb.)')
set(gca,'fontsize',13,'fontname','Timesnewroman')

subplot(1,2,2)
```

```

semilogy(f,P,'r-','linewidth',2)
xlim([0 3])
xlabel('Frequency (THz)')
ylabel('Power (norm.)')
set(gca,'fontsize',13,'fontname','Timesnewroman')

```

A.1.1.2 The Laplace transform

In Chapter 8, a model of cell membrane electroporation was introduced that utilized convenient properties of the Laplace transform (a generalized frequency-space transformation of which the Fourier transform is a special case) [4]. The Laplace Transform (LT) of a function $g(t)$ is computed by

$$\mathcal{L}\{g(t)\} = G(s) = \int_0^{\infty} g(t) \exp(-st) dt \quad (\text{A.6})$$

where s is a complex frequency parameter $s = s_0 + i\omega$. The LT is therefore a generalization of the Fourier transform, for which only the imaginary component of the transformation parameter is utilized to extract harmonic information from $g(t)$. Preserving the real part additionally extracts first-order amplitude-decay information, and characterizes relaxation processes.

A.1.1.3 Laplace transforms for modeling cellular trans-membrane voltages (TMVs)

The property of LTs relevant for the analysis of cell membranes is the transformation of the derivative operator [4, 5]. The n^{th} -order derivative of a function $g(t)$ is expressed as an algebraic polynomial in powers of the complex frequency parameter s :

$$\mathcal{L}\{g^{(n)}(t)\} = s^n G(s) - s^{n-1}g(0) - \dots - g^{(n-1)}(0). \quad (\text{A.7})$$

In Chapter 8, the Ampere-Maxwell equation was used to determine solutions for the potential, V , in various cellular regions with permittivity ϵ and conductivity σ [6]:

$$\nabla \cdot \left(\left(\sigma + \epsilon \frac{\partial}{\partial t} \right) \nabla V(x, y, z, t) \right) = 0. \quad (\text{A.8})$$

Recall, in the steady state, Equation (A.8) reduces to Laplace's equation, $\nabla^2 V = 0$, and the induced TMV from a step-on field, E , for spherical cells with radius R is the Schwan equation:

$$\Delta V_m = fER \cos \theta \quad (\text{A.9})$$

where f is the purely conductive form-factor [6]

$$f = \frac{3\sigma_{ex}[3dR^2\sigma_{in} + (3d^2R - d^3)(\sigma_m - \sigma_{in})]}{2R^3(\sigma_m + 2\sigma_{ex})\left(\sigma_m + \frac{\sigma_{in}}{2}\right) - 2(R - d)^3(\sigma_{ex} - \sigma_m)(\sigma_{in} - \sigma_m)} \quad (\text{A.10})$$

and σ_{ex} , σ_{in} , and σ_m , are the conductivities of the extracellular space, intracellular space, and membrane, respectively, as defined in Chapter 8.

Equation (A.10) can be expressed as a functional differential operator by substituting σ with an admittivity operator associated with Equation (A.8), defined as $\Sigma = \sigma + \epsilon \frac{\partial}{\partial t}$ for each region, as

$$f = \frac{3\Sigma_{ex}[3dR^2\Sigma_{in} + (3d^2R - d^3)(\Sigma_m - \Sigma_{in})]}{2R^3(\Sigma_m + 2\Sigma_{ex})\left(\Sigma_m + \frac{1}{2}\Sigma_{in}\right) - 2(R - d)^3(\Sigma_{ex} - \Sigma_m)(\Sigma_{in} - \Sigma_m)} \quad (\text{A.11})$$

which accounts for the region's permittivity and preserves the model's time-dependence.

By the property of the LT in Equation (A.7), the frequency-space admittivity operator is $\Sigma(s) = \sigma + \epsilon s$. With this, applying the LT to Equation (A.11) returns an expression of the form

$$\mathcal{L}\{f\} = F(s) = \frac{a_1 s^2 + a_2 s + a_3}{b_1 s^2 + b_2 s + b_3} \quad (\text{A.12})$$

with coefficients [6]:

$$\begin{aligned} a_1 &= 3d\sigma_{ex}[\sigma_{in}(3R^2 - 3dR + d^2) + \sigma_m(3dR - d^2)], \\ a_2 &= 3d[(\sigma_{in}\epsilon_{ex} + \sigma_{ex}\epsilon_{in})(3R^2 - 3dR + d^2) + (\sigma_m\epsilon_{ex} + \sigma_{ex}\epsilon_m)(3dR - d^2)], \\ a_3 &= 3d\epsilon_{ex}[(\epsilon_{in}(3R^2 - 3dR + d^2) + \epsilon_m(3dR - d^2)], \\ b_1 &= 2R^3(\sigma_m + 2\sigma_{ex})\left(\sigma_m + \frac{1}{2}\sigma_{in}\right) + 2(R - d)^3(\sigma_m - \sigma_{ex})(\sigma_{in} - \sigma_m), \\ b_2 &= 2R^3\left[\sigma_{in}\left(\frac{1}{2}\epsilon_m + \epsilon_{ex}\right) + \sigma_m\left(\frac{1}{2}\epsilon_{in} + 2\epsilon_m + 2\epsilon_{ex}\right) + \sigma_{ex}(\epsilon_{in} + 2\epsilon_m)\right] \\ &\quad + 2(R - d)^3 \dots \\ &\quad \times [\sigma_{in}(\epsilon_m - \epsilon_{ex}) + \sigma_m(\epsilon_{in} - 2\epsilon_m + \epsilon_{ex}) - \sigma_{ex}(\epsilon_{in} - \epsilon_m)], \\ b_3 &= 2R^3(\epsilon_m + 2\epsilon_{ex})\left(\epsilon_m + \frac{1}{2}\epsilon_{in}\right) + 2(R - d)^3(\epsilon_m - \epsilon_{ex})(\epsilon_{in} - \epsilon_m). \end{aligned} \quad (\text{A.13})$$

The induced TMV is computed in complex frequency space as

$$\frac{\Delta V_m(s)}{R \cos \theta} = F(s)E(s). \quad (\text{A.14})$$

Therefore, as long as the Laplace transform of the incident field $\mathcal{L}\{E(t)\} = E(s)$ exists, the normalized TMV is determined by the inverse Laplace transform of the product $F(s)E(s)$. The result is then be scaled by the cell radius and $\cos \theta$ to determine the spatial distribution of $\Delta V_m(t)$.

The advantage of this approach relative to Equation (A.9) is that it allows the mathematical model of membrane electroporation to be generalized from strictly step-on/off square fields to one that can characterize the more complex electrical dynamics resulting from more complex fields

(see Figure 8.3(b)). These time-dependent solutions provide significant insight into fast, complex field interactions that may result from realistic THz pulses.

A.2 Bioinformatics analysis of gene expression microarrays: Signal Pathway Perturbation Analysis (SPIA)

A.2.1 Pathway perturbation analysis in R

The following script was created for implementation in R (RStudio platform) to perform the signal pathway perturbation analysis (or “signal pathway impact analysis”, SPIA) [7]. From measured gene expression data (gene name, expression magnitude, and p-value), this script accesses pathway information from the Kyoto Encyclopedia of Genes and Genomes (KEGG) [8], and calculates the total accumulated pathway perturbation, A_{tot} , using the software package, *ROntoTools*, as described in Chapter 7.

```
# Differential gene expression data is prepared as columns in a
#text or csv file, "ExpressionData.csv". Pathways perturbation
#utilizes the KEGG database functions in the ROntoTools package

#Access R/Bioconductor platform
source("http://www.bioconductor.org/biocLite.R")
biocLite()

#install ROntoTools
biocLite("ROntoTools")
library(ROntoTools)

#load pathway data
kpg<-keggPathwayGraphs("hsa",updateCache = T,verbose=T)
kpg<-setEdgeWeights(kpg,edgeTypeAttr = "subtype",edgeWeightByType
= list(activation=1,inhibition=-1,expression=1,repression=-
1),defaultWeight = 0)
kpn<-keggPathwayNames("hsa")

#load data
allgeneData<-read.csv("~/ExpressionData.csv",sep="," ,header=TRUE)

#Define fold-change and p-value data
fc<-allgeneData$logFC
pv<-allgeneData$P.Value

#Define reference set of Entrez gene IDs
```

```

ref<-as.character(allgeneData$ENTREZ_GENE_ID)

### Implementation of ROntolTools
#Set node weights based on p-value
kpg<-
setNodeWeights(kpg,weights=alphaMLG(pv,threshold=max(pv)),default
Weight=1)

#Calculate perturbation scores (using pathway express - pe)
peRes<-pe(x=fc,graphs=kpg,ref=ref,nboot=5000,verbose=TRUE)

#Print the results, sort by magnitude of total accumulated
#perturbation
Summary(peRes, pathNames = kpn,order.by="pAcc")

#Save data as a comma-separated file for later analysis
write.csv(peRes, "peRes.csv")

```

A.2.2 Details on transcript-level dysregulation of cancer-related signaling pathways

In Chapter 7, eight signaling pathways related to the initiation, progression, or development of human cancer were identified that are predicted to be dysregulated from the differential gene expression profiles induced by exposure to intense THz pulses. Here, each of these pathways is described, and plots of the transcript-level sources of dysregulation that result from THz exposure are provided. Figure A.1 below provides an illustrative example to assist the interpretation of the similar figures associated with each of the pathway discussions in following subsections. The magnitude of gene expression of significantly upregulated and downregulated genes at the highest THz intensity will be shown in the left plot, along with the ratio of THz-affected to total genes in the considered pathway. The two-way plot at right will show the perturbation of the genes in the context of the larger pathway interaction. The vertical axis indicates magnitude of THz-expression, and the horizontal axis represents the corresponding perturbation magnitude of that gene in the pathway under consideration.

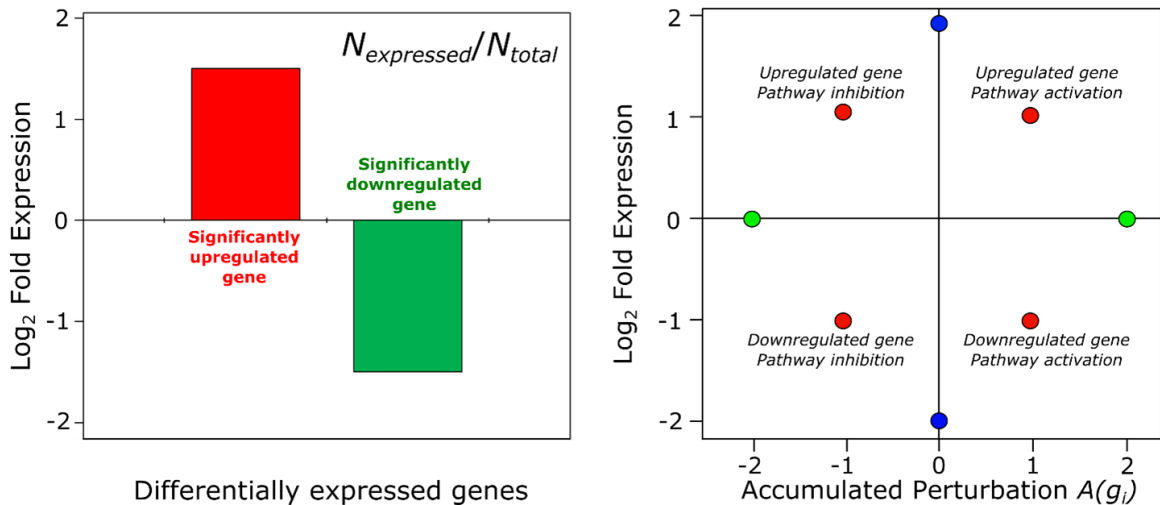


Figure A.1. **Plot legend to assist the following pathway discussions.** *Left:* A bar plot displaying the expression magnitude of genes within the considered pathway determined to be significantly differentially expressed by the highest THz intensity. In the top-right corner of each plot is the ratio of THz-affected genes to the total number of genes in the pathway. *Right:* A two-way plot, displaying expression levels of all genes in the pathway, and the resulting accumulated perturbation assigned to each gene. Blue datapoints indicate genes that were affected by intense THz pulses and did not receive additional perturbation from upstream genes, but may contribute to downstream perturbation. Green points are genes that were not affected by THz, but were affected by upstream perturbations in the relevant network (but cannot cause further downstream perturbation). Red points are genes that were both expressed by THz exposure (and so may contribute to downstream perturbation) and were further affected by upstream perturbations in the associated gene interaction network.

A.2.2.1 Cytokine-cytokine receptor interaction

The cytokine-cytokine receptor interaction pathway regulates the immune response to acute inflammatory stimulus, and is predicted to be activated by intense THz pulses. Several studies have reported observation of THz-induced inflammatory responses at the cellular [9], tissue [10], and organism [11] level in epidermal cell and tissue systems.

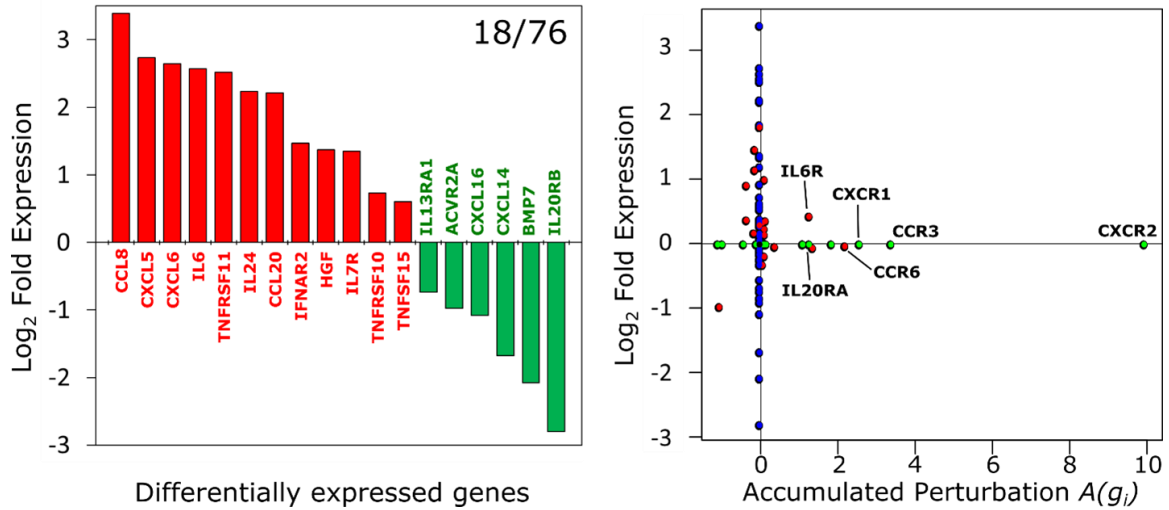


Figure A.2. **Transcript-level sources of THz-induced dysregulation to *Cytokine-cytokine receptor interaction signaling*.**

18 of 76 genes considered in this pathway are differentially expressed by the highest THz intensity, and these are largely localized to differential expression of the chemokine and inflammatory cytokine families (CCL, CXCL), interleukins (IL6), and interferons (IL24). From this initial perturbation, the predicted activation of the cytokine-cytokine receptor interaction pathway is due to the accumulated perturbation at downstream nodes, which predominantly include the corresponding receptors of the aforementioned ligand families (CCR, CXCR, ILR). Therefore, the dominant source of the predicted activation of an inflammatory response were not due to genes that were directly affected by THz exposures, but rather due to downstream targets of directly affected genes. This indicates that extended exposure to intense THz pulses is recognized and responded to as an acute immune response. Previous studies comparing responses to varying inflammatory stimuli in mouse skin have shown that the inflammatory response to THz exposures is most genomically similar to a wound response, and dissimilar to responses stimulated by burns or exposure to other types of radiation (UV, neutrons) [11].

A.2.2.2 *Proteoglycans in cancer*

Proteoglycans (i.e., glycosylated proteins) are found in connective tissues such as the dermis, and regulate molecular motility, protein activity/stability, and signaling [12]. Although they are key molecules in regulating cancer progression, relatively little information in skin is available in the literature. Proteoglycans have been observed to amplify tumor growth via interaction with growth factors, cytokines, and enzymes, as well as inhibit tumor growth via activation of tumor suppressor proteins [8].

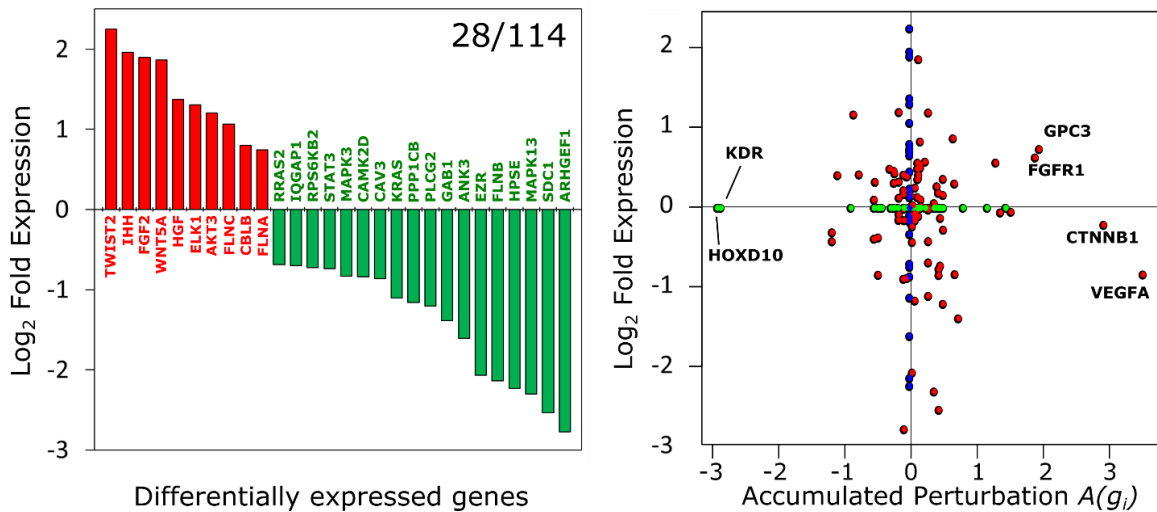


Figure A.3. Transcript-level sources of THz-induced dysregulation to *Proteoglycan signaling in cancer*.

28 of 114 genes in this pathway were differentially expressed at the highest THz intensity, and the pathway is predicted to be activated.

A.2.2.3 *cGMP-PKG signaling*

Protein kinase G (PKG) is a signaling protein activated by intracellular cyclic guanosine monophosphate (cGMP). Limited information in skin is available, however some individual studies have found that in skin cancer, cGMP influences anti-proliferative and pro-apoptotic mechanisms,

and downregulation of PKG-activated genes induces pro-apoptotic effects [13, 14]. The activity of this pathway is predicted to be suppressed by intense THz pulses.

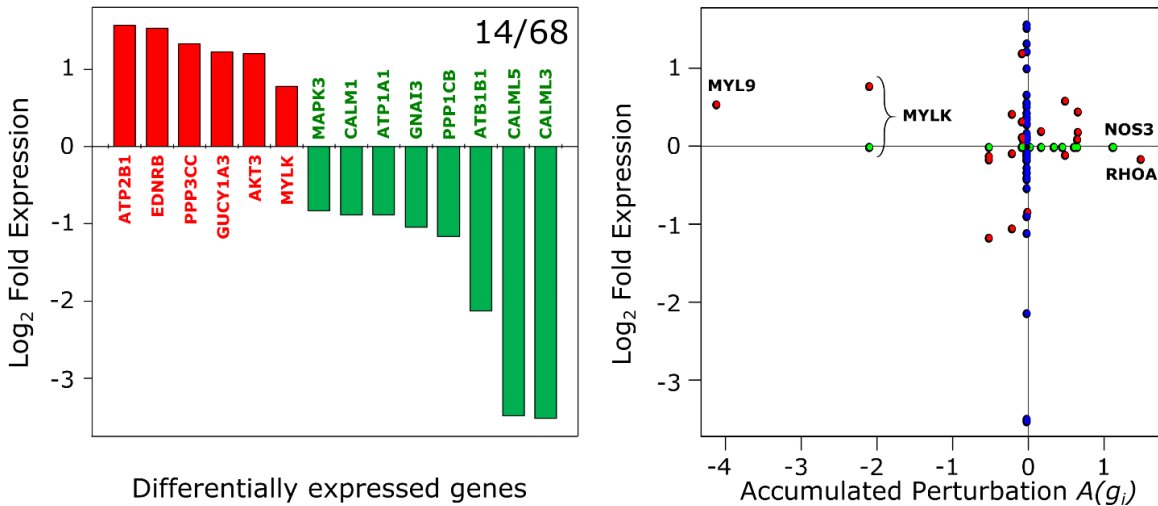


Figure A.4. Transcript-level sources of THz-induced dysregulation to *cGMP-PKG* signaling.

14 of the 68 genes considered in this network are differentially expressed by intense THz pulses, predominantly in the Ras and Calcium-binding family (MAPK3, CALM1, CALML3, CALML5).

A.2.2.4 Calcium signaling

The *Calcium signaling* pathway refers to the regulatory function of calcium-binding proteins (CBPs), or proteins that are activated upon binding a calcium ion. CBPs regulate a wide range of cellular functions such as protein phosphorylation, cytoskeleton dynamics/motility, viability, and proliferation/apoptosis [15]. In skin, epidermal differentiation is regulated by a strong calcium gradient across the epidermis that triggers sequential expression of essential structural and binding proteins necessary for stability and formation of the skin barrier.

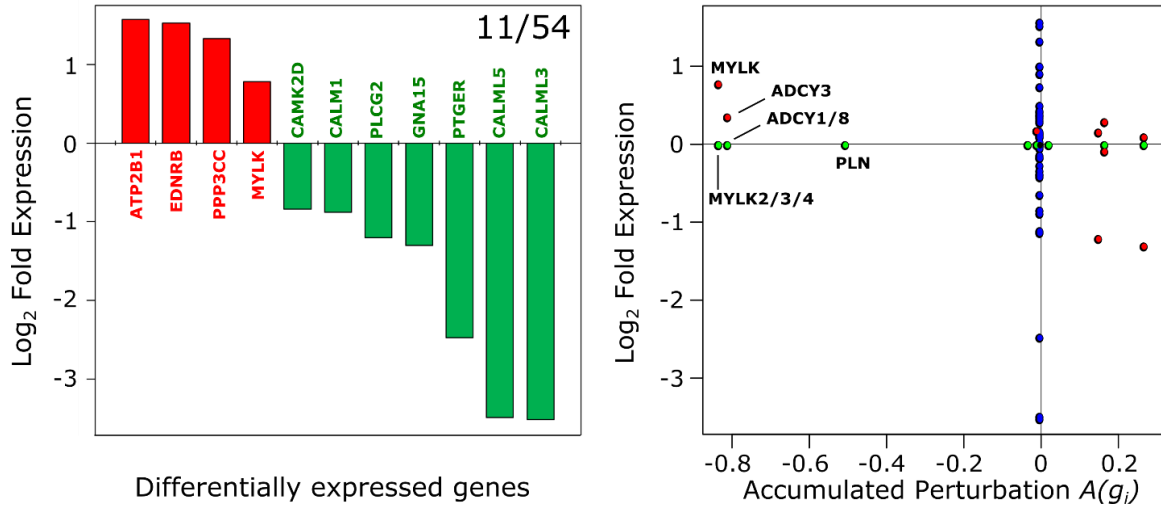


Figure A.5. Transcript-level sources of THz-induced dysregulation to *Calcium signaling*.

11 of 54 genes in this pathway were significantly expressed at the highest THz intensity, and these are largely represented by downregulation of calmodulin and calmodulin-like proteins (CAMK2D, CALM1, CALML3, CALML5). This gene expression profile, and resulting inhibition of associated signaling, may be a genomic response to field-induced membrane permeation and increased influx of calcium ions into the intracellular space, as suggested in Chapter 8.

A.2.2.5 Regulation of actin cytoskeleton

Actin is one of three main protein complexes that comprise the cellular cytoskeleton (along with microtubules and intermediate filaments) and is abundant in all cell types. These complexes provide structural support, shape, and resistance to mechanical stress, and additionally regulates division, motility, and intracellular chemical transport. The actin structure is regulated by the Rho family (a subfamily of the Ras superfamily), while actin dynamics are calcium-regulated [8].

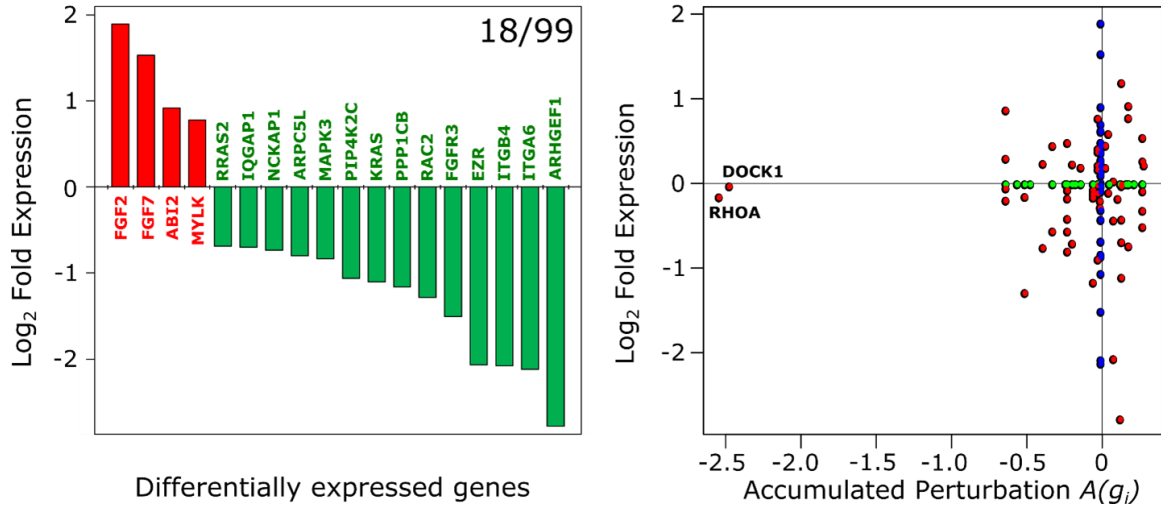


Figure A.6. **Transcript-level sources of THz-induced dysregulation to the *Regulation of actin cytoskeleton* pathway.**

18 of 99 genes in this network were significantly affected by intense THz pulses. The majority of THz-induced suppression is due to perturbation accumulation at genes associated with Ras activation: DOCK1 (“dedicator of cytokinesis 1”, encodes for a GEF-activator for the Rho family), and RHOA (“ras homology family member A”, a small GTPase that acts as a molecular switch in signal transduction). Overexpression of these are associated with tumor proliferation and metastasis [16].

A.2.2.6 *Rap1* signaling

The Ras-associated protein-1 (Rap1), like Ras, is a small GTPase that functions as a molecular switch to regulate signal transduction activation. The *Rap1* signaling pathway has diverse cellular functions, regulating cell adhesion, cytoskeletal dynamics, motility, migration, and polarization [17].

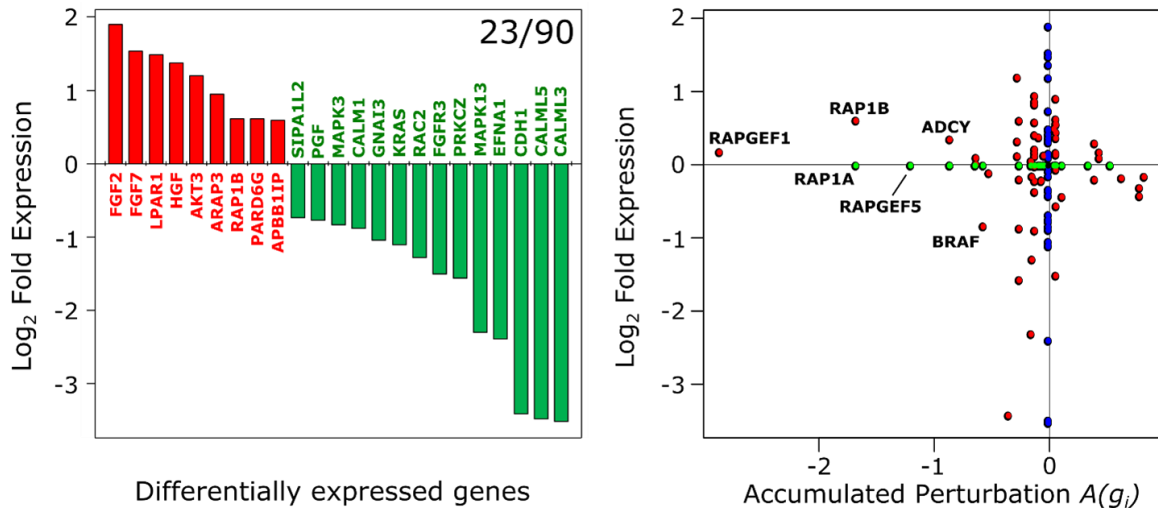


Figure A.7. Transcript-level sources of THz-induced dysregulation to *Rap1* signaling.

23 of the 90 genes in this pathway were differentially expressed by intense THz pulses. Genes directly affected by intense THz pulses in this pathway include growth factors (upregulation of FGF and HGF, and downregulation of PGF), Ras family (KRAS, MAPK3), and CBPs (CALM1, CALML3, CALML5). The majority of the negative perturbation in this pathway occurs at nodes/genes that are not directly expressed by intense THz pulses (RAP1A, RAP1B, RAPGEF1, RAPGEF2).

A.2.2.7 *Ras* signaling

The *Ras* signaling network regulates cell division, proliferation, and survival, and is found in nearly all eukaryotic cell types [18, 19]. The Ras protein is a small GTPase and central hub protein that acts as a molecular “on/off” switch to regulate signal transduction in the network. Due to the ubiquitous general function in regulating cell division, it is also one of the most commonly implicated pathways in the development of human cancer [20].

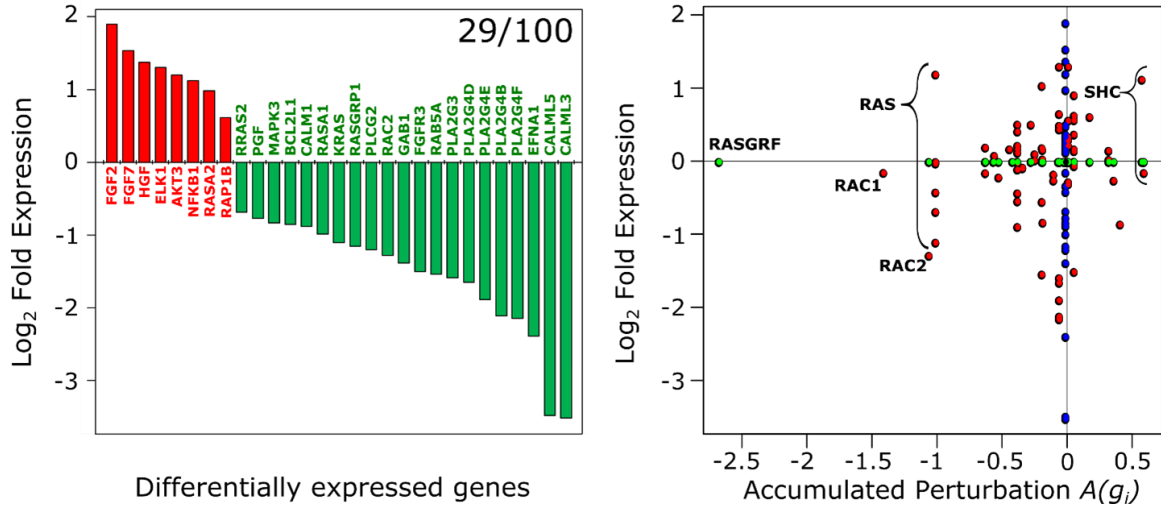


Figure A.8. Transcript-level sources of THz-induced dysregulation to *Ras* signaling.

Of the 100 genes present in the network, 29 were significantly affected by the highest THz intensity. THz-affected genes in the Ras superfamily include members of the Ras (KRAS, RAP1B, RRAS2), Rap (RAP1B), and Rho (RAC2) families. Associated Ras-dependent families (RASA1, RASA2, RASGRP1) additionally regulate the binding and activity of Ras-related proteins.

A.2.2.8 Glioma

The *Glioma* pathway describes the gene-level signaling responsible for the initiation and development of gliomas, a common primary brain tumor, and is the pathway that is predicted to be most inhibited by intense THz pulses, as quantified by the total accumulated perturbation score, A_{tot} , as discussed in Chapter 7. This is a cancer-specific network that contains the more general *Calcium* and *MAPK/Ras Signaling* pathways ubiquitous in nearly all cell/tissue types to promote cell cycle progression [8].

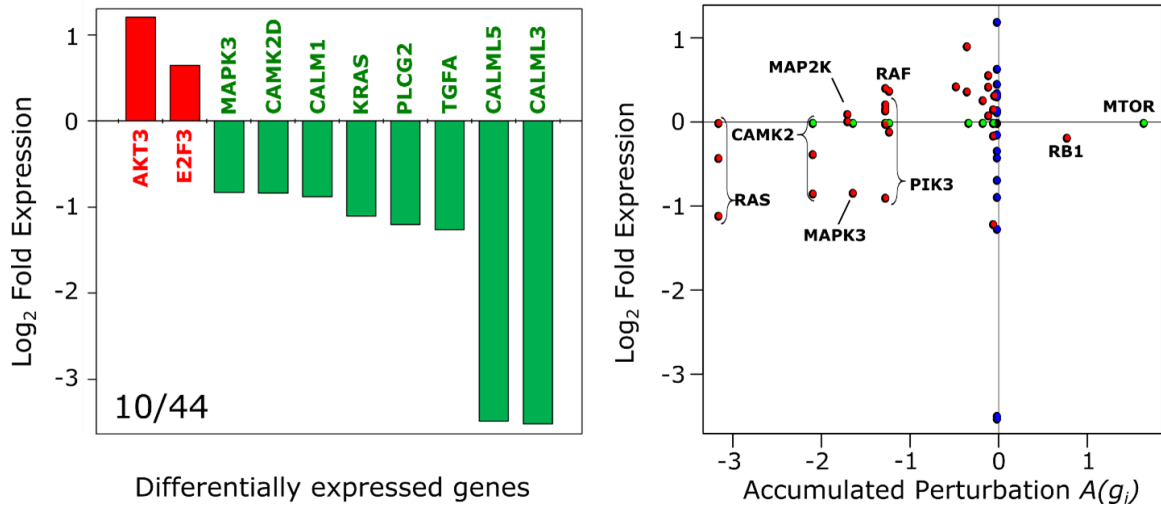


Figure A.9. Transcript-level sources of THz-induced dysregulation to *Glioma* signaling.

Of the 44 genes in the network, 10 are significantly differentially expressed by the highest THz intensity. Although the *Glioma* pathway describes gene/protein signaling in cell types belonging to neural tissue, the THz-induced suppression of this pathway is due to individual suppression of distinct signaling pathways that are ubiquitous in nearly all cell/tissue types. Suppression of this network is predominantly due to downregulation of the Ras family (KRAS, MAPK3), calcium-binding proteins in the *Calcium signaling* pathway (CAMK2D, CALM1, CALML3, CALML5), and tumor growth factor α (TGF α).

A.2.3 Conventional thresholds vs. cut-off free analysis (COFA)

Pathway analysis techniques often utilize a subset of “significant” genes that rely on arbitrary thresholds, typically $|\log(FC)| > 0.58$ and $p < 0.05$, where FC is the expression fold-change, and p is the associated p-value (adjusted for multiple hypothesis testing, if necessary). Measurements for genes that do not meet these criteria are excluded from significance-based analyses. However, since small variations of these chosen thresholds may influence the results, accuracy is often dependent on the choice of threshold. An advantage of Signal Pathway Impact Analysis (SPIA) is

the opportunity to use cut-off free analysis (COFA) [7, 21]. This is achieved by modifying the original SPIA equation:

$$PF(g_i) = \Delta E(g_i) + A(g_i) \quad (\text{A.15})$$

where $PF(g_i)$ is the total perturbation factor for i^{th} gene in the network, $\Delta E(g_i)$ is the measured gene expression (log-fold change), and

$$A(g_i) = \sum_{j < i} \beta_{ij} \frac{PF(g_j)}{N_{ds}} \quad (\text{A.16})$$

is the accumulated perturbation from upstream nodes.

In COFA, gene significance is incorporated by weighting gene expression measurements [21]

$$PF(g_i) = \alpha \cdot \Delta E(g_i) + A(g_i) \quad (\text{A.17})$$

where α is a p-value-based weighting factor

$$\alpha = -\log\left(\frac{p}{p_{max}}\right). \quad (\text{A.18})$$

In Equation (A.18), p is the adjusted p-value associated with the pathway dysregulation result, and p_{max} is the maximum (i.e., least significant) value in the dataset. In this formalism, there are no “significant” or “insignificant” genes, but rather the pathway perturbation contribution from all genes is weighted by the measured significance.

To test the validity of this method, both conventional thresholds and COFA were performed on gene expression profiles measured from the highest intensity THz exposure, as described in

Sections 7.3.1.1 – 7.3.1.4 of Chapter 7. A comparison between the results of the two methods is shown in Figure A.10. 99 significantly dysregulated pathways were identified using conventional significance thresholds, and 42 pathways were identified using node-weighting in COFA. There is near-total inclusion (40 of the 42) of the pathways identified by COFA (see Venn diagram in inset of Figure A.10). Further, the calculated total accumulation ($A_{tot} = \sum_i A(g_i)$) are approximately consistent for most identified overlapping pathways, as seen by the bar chart in Figure A.10. The overlapping pathways, total accumulated perturbation (A_{tot}), and associated p-values are given in Table A.1. Pathways identified by only one of the individual analyses are listed in Table A.2 and Table A.3.

The correspondence shown in Figure A.10 verifies consistency of COFA when compared with pathways identified using conventional thresholds. Moreover, COFA identifies a relatively smaller number of significantly dysregulated pathways ($p < 0.05$), and is therefore a conservative estimate of signaling pathways that may be dysregulated by THz exposure. As COFA is shown to be consistent with conventional methods for the THz exposure with the highest dose, it is assumed to be valid for calculation using all measured gene expressions for lower doses (see Figure 7.5).

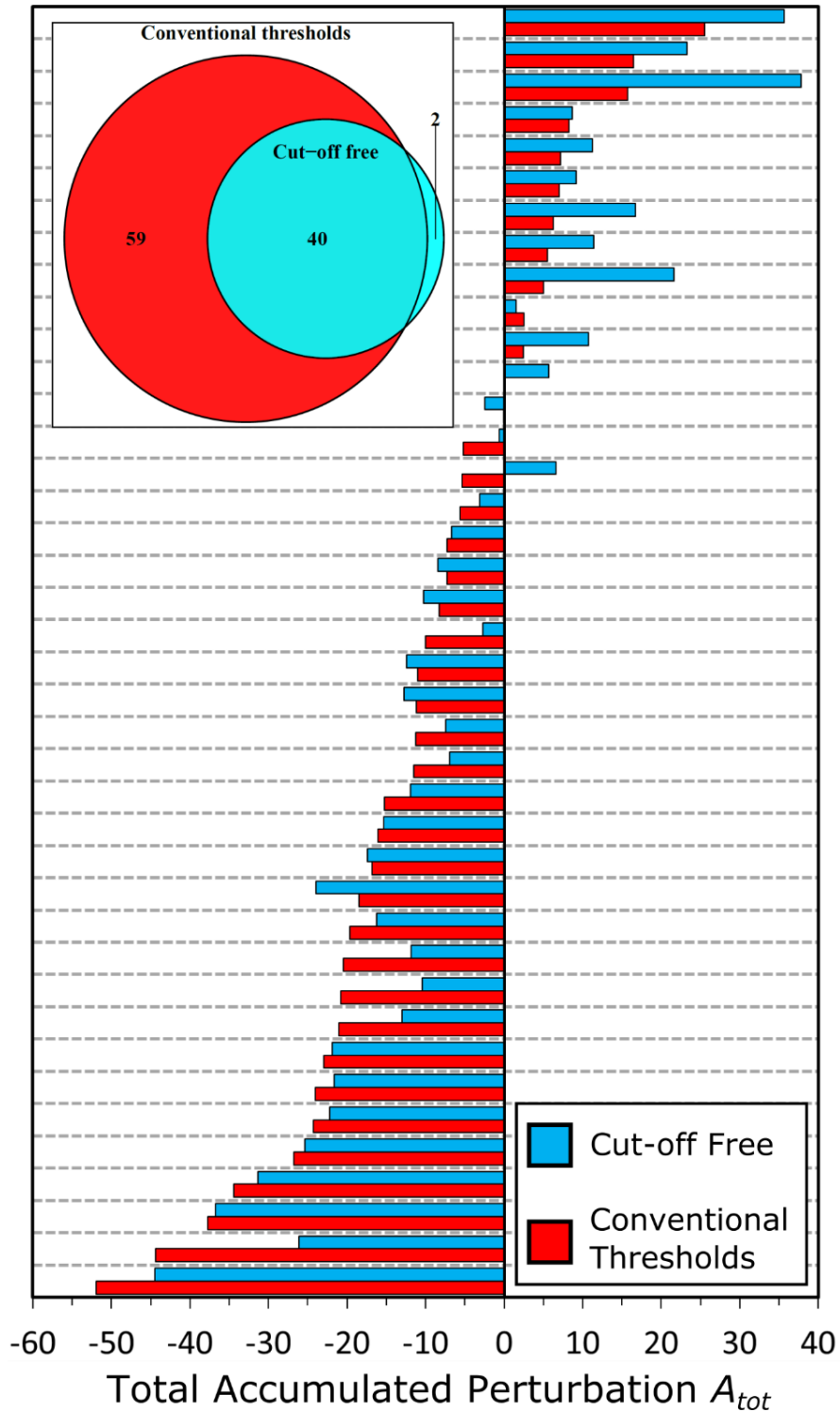


Figure A.10. **Correspondence between SPIA analysis using conventional thresholds compared to cut-off free analysis (COFA).** The main plot shows comparisons of the total accumulated perturbation between 40 pathways identified using both of the two methods ($p < 0.05$). The activation/inhibition status are consistent, with the exception of one pathway (*Axon guidance*; see Table A.1). *Inset:* The Venn diagram shows near total overlap of pathways identified using COFA with those identified with conventional thresholds.

Table A.1. Pathways identified using both Conventional Thresholds and Cut-off Free Analysis (COFA)

Path ID	Pathway Name	Accumulated Perturbation		p-value	
		<i>Thresholds</i>	<i>Cut-off Free</i>	<i>Thresholds</i>	<i>Cut-off Free</i>
05034	Alcoholism	-51.98	-44.48	0.0031	0.0043
04014	Ras signaling pathway	-44.38	-26.08	0.0011	0.015
05214	Glioma	-37.78	-36.76	0.0045	0.0041
04713	Circadian entrainment	-34.39	-31.34	0.0023	0.0043
04722	Neurotrophin signaling pathway	-26.78	-25.40	0.0022	0.0041
05152	Tuberculosis	-24.31	-22.20	0.0094	0.012
04921	Oxytocin signaling pathway	-24.06	-21.64	0.0013	0.012
04925	Aldosterone synthesis and secretion	-22.95	-21.87	0.0045	0.0077
04270	Vascular smooth muscle contraction	-21.04	-13.03	0.0011	0.0043
04810	Regulation of actin cytoskeleton	-20.77	-10.45	0.0050	0.048
05161	Hepatitis B	-20.48	-11.86	0.025	0.016
04015	Rap1 signaling pathway	-19.62	-16.22	0.0029	0.023
05130	Pathogenic Escherichia coli infection	-18.50	-23.97	0.0081	0.016
04261	Adrenergic signaling in cardiomyocytes	-16.83	-17.37	0.0011	0.012
05031	Amphetamine addiction	-16.09	-15.34	0.0074	0.0043
05010	Alzheimer's disease	-15.27	-11.92	0.0074	0.0043
04020	Calcium signaling pathway	-11.49	-6.91	0.0046	0.047
05133	Pertussis	-11.24	-7.46	0.0017	0.030
04370	VEGF signaling pathway	-11.20	-12.77	0.0048	0.048
04933	AGE-RAGE signaling pathway in diabetic complications	-10.97	-12.44	0.012	0.046
04022	cGMP-PKG signaling pathway	-10.04	-2.69	0.0046	0.012
04970	Salivary secretion	-8.30	-10.24	0.0023	0.0041
04924	Renin secretion	-7.25	-8.40	0.0026	0.0043
04971	Gastric acid secretion	-7.25	-6.68	0.0011	0.0077
04728	Dopaminergic synapse	-5.62	-3.13	0.0023	0.0043
04360	Axon guidance	-5.35	6.61	0.0011	0.012
04922	Glucagon signaling pathway	-5.23	-0.61	0.0046	0.0041
04114	Oocyte meiosis	-0.07	-2.48	0.010	0.016
04010	MAPK signaling pathway	0.10	5.65	0.0021	0.044
04071	Sphingolipid signaling pathway	2.44	10.76	0.0023	0.036
04916	Melanogenesis	2.51	1.50	0.014	0.036

05205	Proteoglycans in cancer	5.05	21.63	0.0032	0.016
04932	Non-alcoholic fatty liver disease (NAFLD)	5.54	11.39	0.011	0.036
04210	Apoptosis	6.24	16.70	0.040	0.047
04740	Olfactory transduction	7.01	9.21	0.0048	0.0041
05146	Amoebiasis	7.15	11.23	0.0029	0.0043
04744	Phototransduction	8.30	8.65	0.0048	0.0041
04062	Chemokine signaling pathway	15.76	37.80	0.0042	0.0041
04060	Cytokine-cytokine receptor interaction	16.51	23.27	0.0031	0.0041
04621	NOD-like receptor signaling pathway	25.52	35.64	0.0021	0.0041

Table A.2. Pathways identified by Cut-off Free Analysis not identified using Conventional Thresholds

Path ID	Pathway Name	Accumulated Perturbation	p-value
04610	Complement and coagulation cascades	-5.81	0.026
04950	Maturity onset diabetes of the young	-6.81	0.035

Table A.3. Pathways identified using Conventional Thresholds not identified using Cut-off Free Analysis

Path ID	Pathway Name	Accumulated Perturbation	p-value
04657	IL-17 signaling pathway	2.85	0.00095
03320	PPAR signaling pathway	-2.17	0.0011
04530	Tight junction	0	0.0017
04972	Pancreatic secretion	0	0.0017
04976	Bile secretion	0	0.0017
05202	Transcriptional misregulation in cancer	-1.37	0.0021
05418	Fluid shear stress and atherosclerosis	-2.45	0.0021
05323	Rheumatoid arthritis	0	0.0023
05412	Arrhythmogenic right ventricular cardiomyopathy (ARVC)	-1.95	0.0026
04080	Neuroactive ligand-receptor interaction	-1.94	0.0032
05206	MicroRNAs in cancer	0	0.0032
04668	TNF signaling pathway	-3.17	0.0045
04024	cAMP signaling pathway	-8.14	0.0045
05165	Human papillomavirus infection	25.73	0.0057
05203	Viral carcinogenesis	-0.46	0.0074
04371	Apelin signaling pathway	-18.81	0.0074

05144	Malaria	1.37	0.0074
04912	GnRH signaling pathway	-16.51	0.0074
05160	Hepatitis C	0.85	0.0078
04913	Ovarian steroidogenesis	0	0.0078
04218	Cellular senescence	-16.67	0.0083
05164	Influenza A	2.01	0.0089
04630	Jak-STAT signaling pathway	5.97	0.0094
04611	Platelet activation	-25.66	0.011
05200	Pathways in cancer	11.32	0.012
04390	Hippo signaling pathway	-6.28	0.012
04512	ECM-receptor interaction	2.78	0.013
04216	Ferroptosis	0	0.013
04724	Glutamatergic synapse	3.87	0.013
04910	Insulin signaling pathway	-6.39	0.013
05132	Salmonella infection	-6.78	0.014
04152	AMPK signaling pathway	2.57	0.014
04960	Aldosterone-regulated sodium reabsorption	-1.10	0.015
05150	Staphylococcus aureus infection	0	0.018
04720	Long-term potentiation	-18.81	0.030
05142	Chagas disease (American trypanosomiasis)	9.86	0.030
04923	Regulation of lipolysis in adipocytes	2.25	0.030
04623	Cytosolic DNA-sensing pathway	0	0.031
04072	Phospholipase D signaling pathway	-1.92	0.032
04115	p53 signaling pathway	3.65	0.034
04380	Osteoclast differentiation	-13.26	0.034
05140	Leishmaniasis	-0.83	0.034
04742	Taste transduction	-1.11	0.035
05221	Acute myeloid leukemia	-3.73	0.036
01523	Antifolate resistance	1.12	0.036
05414	Dilated cardiomyopathy (DCM)	0	0.037
05134	Legionellosis	-4.94	0.037
05168	Herpes simplex infection	-1.37	0.037
05231	Choline metabolism in cancer	-4.66	0.039
04730	Long-term depression	-2.91	0.039
04918	Thyroid hormone synthesis	0	0.041
04664	Fc epsilon RI signaling pathway	-7.82	0.047
04723	Retrograde endocannabinoid signaling	-0.087	0.049
04620	Toll-like receptor signaling pathway	0.18	0.049
05162	Measles	-8.04	0.049
04217	Necroptosis	-1.50	0.049
04151	PI3K-Akt signaling pathway	12.36	0.049
04622	RIG-I-like receptor signaling pathway	-0.64	0.050
04650	Natural killer cell mediated cytotoxicity	-13.54	0.050

A.3 References

- [1] B. H. Bransden and C. J. Joachain, Quantum Mechanics, 2nd Ed., Pearson Education Limited, 2000.
- [2] H. Nyquist, "Certain topics in telegraph transmission theory," *Transactions of AIEE*, vol. 47, no. 2, pp. 617-644, 1928.
- [3] C. E. Shannon, "Communication in the presence of noise," *Proceedings of the IRE*, vol. 37, no. 1, pp. 10 - 21, 1949.
- [4] W. E. Boyce and R. C. DiPrima, Elementary Differential Equations and Boundary Value Problems, 9th Ed., US: John Wiley and Sons, Inc., 2009.
- [5] L. S. Sawant, "Applications of Laplace Transform in Engineering Fields," *International Research Journal of Engineering and Technology*, vol. 5, no. 5, pp. 3100 - 3105, 2018.
- [6] T. Kotnik, D. Maklavcic and T. Slivnik, "Time course of transmembrane voltage induced by time-varying electric fields - a method for theoretical analysis and its application," *Bioelectricity and Bioenergetics*, vol. 45, pp. 3 - 16, 1998.
- [7] C. Voichita, S. Ansari and S. Draghici, "ROntoTools: R Onto-Tools suite," *R Package version 2.6.0*, 2017.
- [8] M. Kanahisa and S. Goto, "KEGG: Kyoto Encyclopedia of Genes and Genomes," *Nucleic Acids Research*, vol. 28, no. 1, pp. 29 - 34, 2000.
- [9] I. Echchgadda, C. Cerna, M. Sloan, D. Elam and B. Ibey, "Effects of different terahertz frequencies on gene expression in human keratinocytes," *Proceedings of the Society of Photo-Optical Instrumentation Engineers*, vol. 9321, pp. Q1 - Q9, 2015.
- [10] L. Titova, A. Ayesheshim, A. Golubov, R. Rodriguez-Juarez, R. Woycicki, F. Hegmann and O. Kovalchuk, "Intense THz pulses down-regulate genes associated with skin cancer and psoriasis: a new therapeutic avenue?," *Scientific Reports*, vol. 3, no. 2363, pp. Q1 - Q10, 2013.
- [11] K. -T. Kim, J. Park, S. J. Jo, S. Jung, O. S. Kwon, G. P. Gallerano, W. -Y. Park and G. -S. Park, "High-power femtosecond-terahertz pulse induces a wound response in mouse skin," *Scientific Reports*, vol. 3, no. 2296, pp. 1 - 7, 2013.
- [12] A. Wade, A. Robinson, A. Engler, J. Petritsch, C. James and J. Phillips, "Proteoglycans and their roles in brain cancer," *FEBS Journal*, vol. 280, pp. 2399 - 2417, 2013.
- [13] Y. Ren, J. Zheng, X. Yao, G. Weng and L. Wu, "Essential role of the cGMP/PKG signaling pathway in regulating the proliferation and survival of human renal carcinoma cells," *International Journal of Molecular Medicine*, vol. 34, pp. 1430 - 1438, 2014.

- [14] K. Lee and G. A. Piazza, "The interaction between the Wnt/B-catenin signaling cascade and PKG activation in cancer," *Journal of Biomedical Research*, vol. 31, pp. 189 - 196, 2016.
- [15] G. Sherbet, *Calcium signaling in cancer*, Boca Raton, FL: CRC Press, 2001.
- [16] G. Stelzer, N. Rosen, I. Plaschkes, S. Zimmerman, M. Twik, S. Fishilevich, T. I. Stein, R. Nudel, I. Lieder, Y. Mazor, S. Kaplan, D. Dahary, D. Warshawsky, Y. Guan-Golan, A. Kohn, N. Rappaport, M. Safran and D. Lancet, "The GeneCards Suite: From Gene Data Mining to Disease Genome Sequence Analysis," *Current Protocols in Bioinformatics*, vol. 54, pp. 1.30.1 - 1.30.33, 2016.
- [17] Y. -L. Zhang, R. -C. Wang, K. Cheng, B. Z. Ring and L. Su, "Roles of Rap1 signaling in tumor cell migration and invasion," *Cancer Biology and Medicine*, vol. 14, no. 1, pp. 90 - 99, 2017.
- [18] A. Takashima and D. Faller, "Targeting the RAS Oncogene," *Expert Opinion on Therapeutic Targets*, vol. 17, no. 5, pp. 507 - 531, 2013.
- [19] P. J. Roberts and C. J. Der, "Targeting the Raf-MEK-ERK mitogen-activated protein kinase cascade for the treatment of cancer," *Oncogene*, vol. 26, pp. 3291 - 3310, 2007.
- [20] National Institutes of Health: National Cancer Institute, "The Ras Initiative," 2020. [Online]. Available: <https://www.cancer.gov/research/key-initiatives/ras>.
- [21] C. Voichita, M. Donato and S. Draghici, "Incorporating gene significance in the impact analysis of signaling pathways," *11th International Conference on Machine Learning and Applications. ICMLA 2012*, pp. 126 - 131, 2012.